UC Berkeley

Title

Stereochemical Effects on Eu(III) 1,2-HOPO Luminescence

Permalink

https://escholarship.org/uc/item/3bh6q5cn

Author

Tatum, David Sherrod

Publication Date

2014

Peer reviewed|Thesis/dissertation

Stereochemical Effects on Eu^{III} 1,2-HOPO Luminescence

by

David Sherrod Tatum

A dissertation submitted in partial satisfaction of the

requirements for the degree of

Doctor of Philosophy

in

Chemistry

in the

Graduate Division

of the

University of California, Berkeley

Committee in charge:

Professor Kenneth N. Raymond, Chair
Professor Richard A. Andersen
Professor Gerard Marriott

Fall 2014

Stereochemical Effects on Eu^{III} 1,2-HOPO Luminescence

Copyright © 2014

by

David Sherrod Tatum

Abstract

Stereochemical Effects on Eu[III] 1,2-HOPO Luminescence

by

David Sherrod Tatum

Doctor of Philosophy in Chemistry

University of California, Berkeley

Professor Kenneth N. Raymond, Chair

The bonding in lanthanide coordination complexes is often approximated as involving only non-directional ionic bonds between the ligands and the metal. In the following report, we take a critical view of this Ln[III] point charge approximation. We develop the idea that d_π/p_π covalent interactions between the Ln[III] metals and the ligands are essential to understanding the geometry found in solution. Since the luminescence of Eu[III] is found to depend strongly on the ligand geometry, we propose that any model neglecting the treatment of ligand-metal covalent interaction is necessarily incomplete.

Chapter 1. First, an overview of lanthanide coordination complexes and their application in homogenous time-resolved fluorescence (HTRF) assays is presented. Several examples of commercially relevant luminescent Eu[III] complexes are compared to the bright 1-hydroxypyridin-2-one (1,2-HOPO) complexes described in this report.

Chapter 2. Our group has previously reported an automated shape analysis for eight-coordinate systems using the angles between the normals of adjacent polytopal faces (δ dihedral angles). Herein we extend that automated analysis to coordination numbers four through nine, and we demonstrate its functional equivalence to the parent Muetterties and Guggenberger analysis. The shape parameters defined here are linearly correlated along intramolecular rearrangement paths between related pairs of idealized shapes. Derivations of the ideal shapes, particularly for the troublesome eight-coordinate C_{2v} geometry, are also discussed.

Chapter 3. We report the novel 5LImXy-1,2-HOPO ligand, which forms one of the brightest Eu[III] 1,2-HOPO complexes (aqueous quantum yield of 22%). The DFT minimized coordinates provide a better structural model than the XRD coordinates for fitting the ^{1}H-NMR isotropic shifts, confirming that the dodecahedral (Dod) ground state geometry predominates in solution. All of the lanthanide 5LImXy-1,2-HOPO complexes are found to be fluxional within the NMR timescale and solvent temperature limits, varying widely as a function of lanthanide size. Slow exchange ^{1}H-NMR spectra were collected for all but **La** and **Ce**, representing the first opportunity to study M(bidentate)$_4$-type twist-inversion rearrangements with trivalent metal ions. The slowness of the rearrangement barrier for **Eu** confirms that the Dod structure may be important for efficient energy transfer from ligand to metal.

Chapter 4. The racemization process characterized in chapter 3 is found to occur by either an intramolecular low temperature process (LTP) or a high temperature process (HTP) involving ligand dissociation. Two new groups of ligands are characterized, toward finding a system where the HTP can be conveniently measured by ^{1}H-NMR selective inversion recovery (SIR) experiments. PEG linked versions of 5LImXy-1,2-HOPO are found to rearrange by an intramolecular mechanism, despite expectations that the PEG linker would shut down the LTP for these systems. The 2LImTHF-1,2-HOPO ligand allowed measurement of the HTP for most of the lanthanide series, and the associated barriers are 2.5-3 kcal/mol larger than those found for the LTP in chapter 3. DFT calculated structures of the 2LImTHF-1,2-HOPO complexes are used to model the ^{1}H-NMR isotropic shifts, confirming that the Dod ground state geometry predominates in solution. For both groups of ligands, differences in geometry are found to affect the sensitization efficiency rather than the metal centered efficiency of Eu^{III} photoluminescence.

Chapter 5. We demonstrate measureable stereochemical differences for 5LImXy-1,2-HOPO complexes of d^0 and d^{10} metals, both by XRD and by DFT. In general, the d^{10} complexes tend toward the square antiprism (SA), while the d^0 complexes tend toward Dod, once differences in normalized bites have been considered. The measured and calculated barriers for intramolecular racemization (LTP) are smaller for the d^{10} metal complexes, compared to d^0 complexes. All of these effects can be rationalized by DFT, suggesting that the Dod stereochemistry uniquely maximizes d$_\pi$/p$_\pi$ bonding between the ligands and the metal. Preference for Dod coordination and the associated strengthening of d$_\pi$/p$_\pi$ bonding is proposed to maximize efficiency of energy transfer from ligand to metal in the photoluminescence of **Eu**.

Chapter 6. We report time-resolved X-ray absorption near edge structure (TR-XANES) measurements at the Eu L_3 edge upon photoexcitation of several Eu^{III}-based luminescent lanthanide complexes. We find an unambiguous signature of the 4f intrashell excitation that occurs upon energy transfer from the photoactive organic antennas to the lanthanide species. Phenomenologically, this observation provides the basis for direct investigation of a crucial step in the energy transfer pathways that lead to sensitized luminescence in lanthanide-based dyes. Interestingly, the details of the TR-XANES feature suggest that the degree of 4f−5d hybridization may itself vary depending on the excited state of the Eu^{III} ion.

Chapter 7. We report two novel 1,2-HOPO ligands for the sensitization of Eu^{III} photoluminescence. We find that the [Eu(2LIS-1,2-HOPO)$_2$]$^-$ complex exhibits a remarkably high quantum yield of 38% in aqueous solution, much larger than the previous record of 23% for these systems. The ^{1}H-NMR contact shifts and DFT structural parameters are used to rationalize the large differences in quantum yields among these structurally similar systems. These complexes challenge the luminescence model developed in previous chapters, which states that structures closer to Dod should exhibit brighter luminescence. Very small differences in ligand architecture for these extremely rigid ligands can have dramatic effects on the efficiency of Eu^{III} photosensitization.

Stereochemical Effects on Eu^{III} 1,2-HOPO Luminescence

Table of Contents

Chapter 1

Introduction to Lanthanide Luminescence and Applications in Homogenous Time-resolved Fluorescence (HTRF) Assays

The lanthanides (less commonly called the lanthanoids) are a chemically similar series of fifteen metals occupying the *4f* block of the periodic table. The lanthanides belong to a broader group of elements called the rare earths (REs), which also includes the group III elements yttrium and scandium. The name of the lanthanide series comes from the Greek word λανθανειν (*lanthanein*) meaning "to lie hidden," referring to the way lanthanum was first discovered in 1839 "lying hidden" within samples of cerium oxide. An appropriate name for the entire series, the remaining naturally occurring lanthanides were not fully isolated and identified until the early 1900s. It is evident even from their individual names that the REs are commonly found mixed together in naturally occurring ores. Consider that four of the seventeen REs (yttrium, terbium, erbium, and ytterbium) are all named after the same village of Ytterby, Sweden, where they were first mined. Similarly, the names praseodymium and neodymium come from Greek meaning "leek-green twin" and "new twin" respectively. Lanthanides are commonly found in the 3+ oxidation state, leading to $[Xe]4f^n$ electron configurations where n ranges from 0 to 14 for La[III] to Lu[III] respectively. The size of lanthanide ions decreases in a smooth curve from La to Lu, resulting from a steady increase in effective nuclear charge (Fig. 1.1).[1,2] Although lanthanides have relatively high natural abundance, the similarities in charge, size, and relative inertness toward redox chemistry make separation of the lanthanides a difficult and expensive process. Older methods relied on fractional crystallization, while newer methods use ion exchange chromatography or countercurrent exchange liquid-liquid extraction.

$$y = 19.872(22) - 0.146(7)*x + 0.0034(5)*x^2$$

$$R^2 = 0.9978, \text{weigthed red. } \chi^2 = 0.5406$$
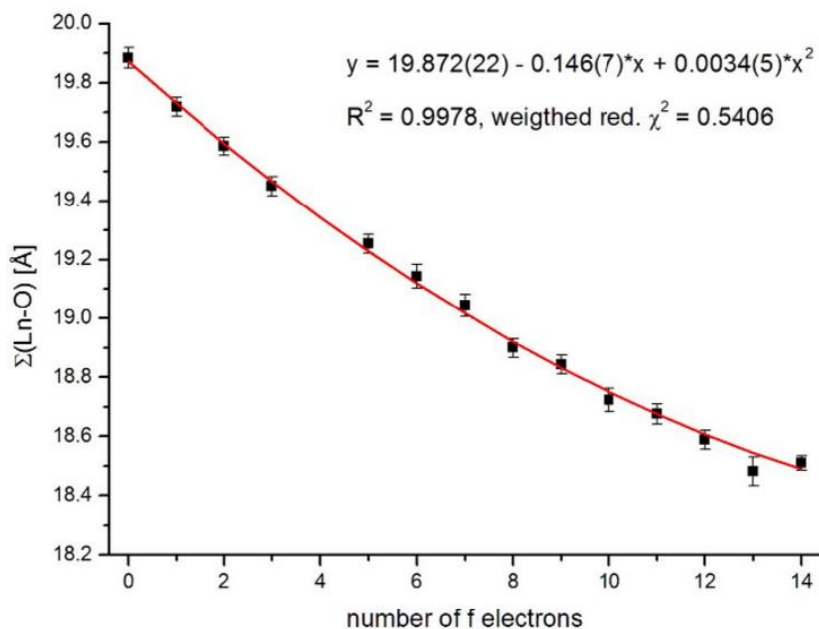
Figure 1.1. The lanthanide contraction, measured for TREN-1,2-HOIQO complexes.[1]

Steadily falling prices (excepting some recent volatility due to monopolized production) of REs has engendered uses in a wide variety of important technologies. The red phosphor of cathode ray televisions has depended upon Eu[III] since the 1960s. [3–6] Other lighting applications include the development of lanthanide doped organic light emitting diodes (OLEDs). First demonstrated in 1964 at Bell Laboratories, Nd:YAG and related lasers are now ubiquitous.[7–11] Extremely strong RE permanent magnets like SmCo or NdFeB are critical for the electric motors of hybrid vehicles and wind turbines, among other high technology uses.[12] Erbium-doped fiber

amplifiers have enabled critical improvements in telecommunications since 1987.[13,14] Lanthanide phosphors with tailored up-conversion or down-conversion have also been used for enhancement of photovoltaic cells.[15–19]

Recent interest in the coordination chemistry of discrete lanthanide complexes has stemmed largely from their use as luminescent reporters applicable to biological systems.[20–29] The valence *4f* electrons of Ln[III] complexes have little interaction with the ligand field due to effective screening by the 5s and 5p subshells, and so *4f-4f* transitions are characterized by sharp, line-like emission and absorption lines. The ligand field can affect the bandshape and relative intensities of the *4f-4f* absorption/emission spectra, but the energies of these spectral bands are fixed across all complexes of the same metal. We can therefore refer to the absorption spectra of simple Ln[III] doped LaF_3 salts as representative of all Ln[III] complexes (Fig. 1.2).
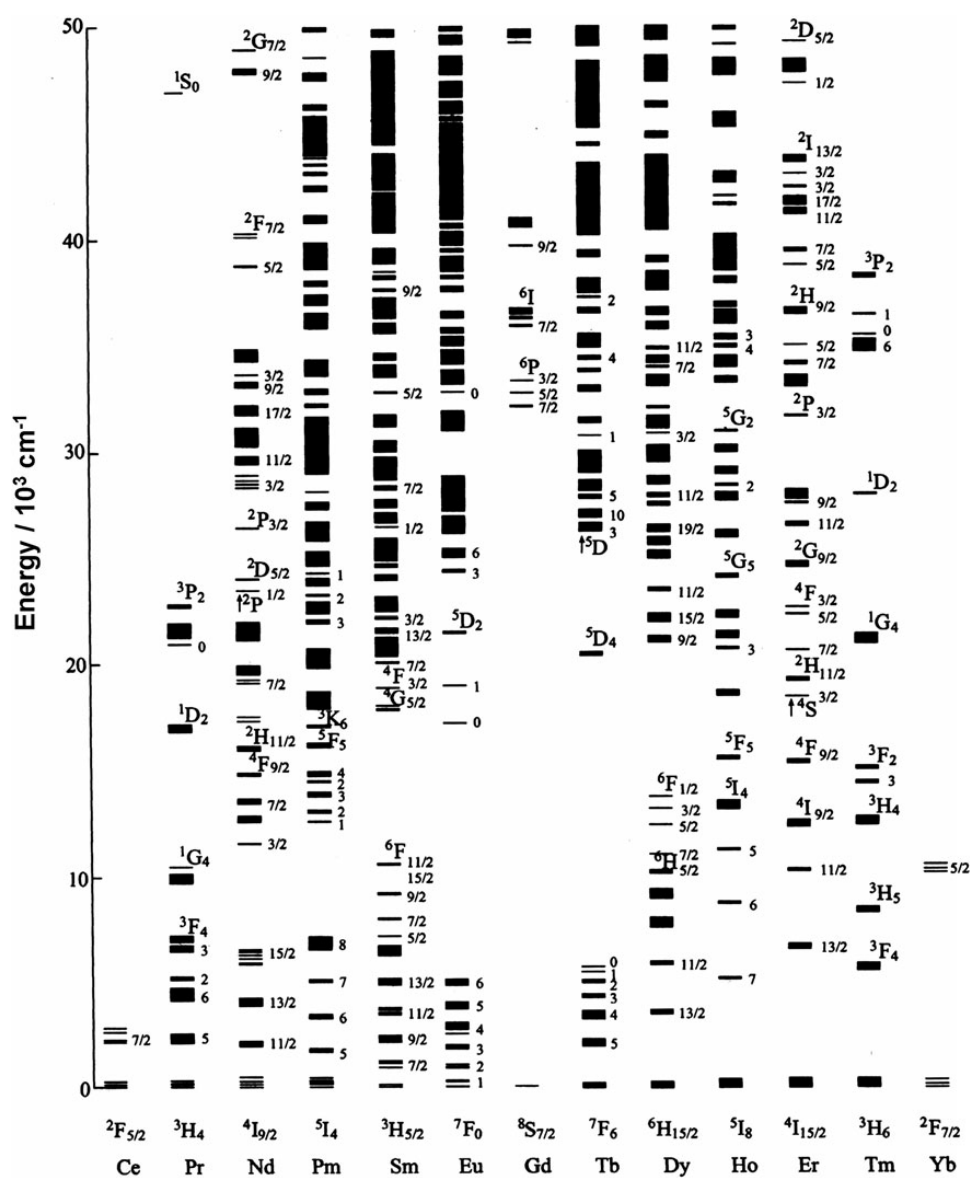
Figure 1.2. Partial energy level diagram for Ln[III] ions doped into a low symmetry crystal (LaF_3).[25,30]

3

Atomic term symbols are used to describe *4f-4f* transitions, since the energy states are dominated by Russell-Saunders spin orbit coupling rather than ligand field effects. Transitions between states of the same angular momentum, like the *4f-4f* transitions, are forbidden by parity and sometimes by spin. While the selection rules for analogous *d-d* transitions of d-block metal complexes are relaxed by coupling to vibrations of the ligand field, the selection rules for the *4f-4f* transitions remain relatively rigid, resulting in small molar extinction coefficients (typically less than 10 $M^{-1}cm^{-1}$). In order to make practical use of luminescent lanthanide reporters, the excited state(s) must be populated indirectly. It has been recognized since 1942 that indirect excitation of Eu^{III} can be accomplished by energy transfer from nearby organic ligands, called the antenna effect.[31] A general Jablonski diagram, shown below, depicts the many various energetic pathways that are relevant to Ln^{III} photosensitization and emission.
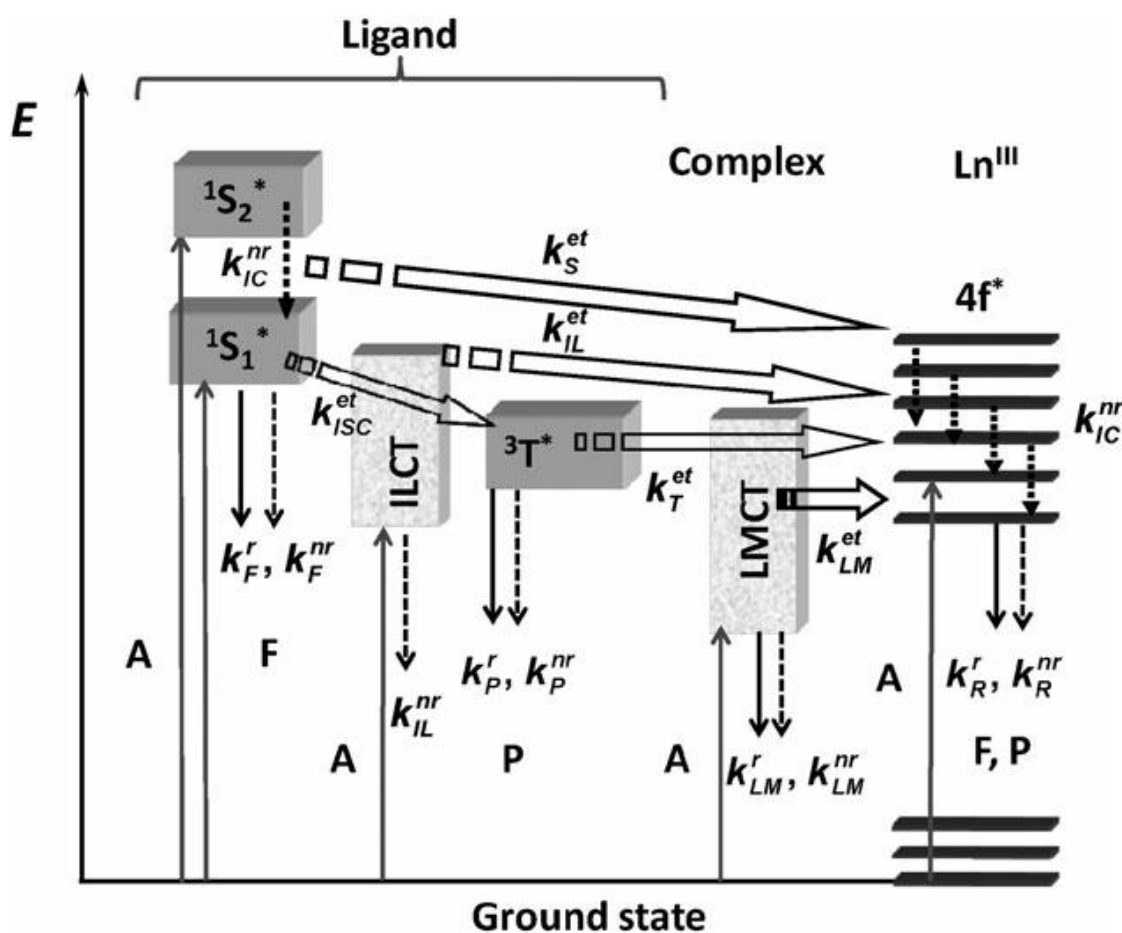
Figure 1.3. Schematic representation of energy absorption, migration, emission (plain arrows) and dissipation (dotted arrows) processes in a lanthanide complex. $^1S^*$ or S = singlet state, 3T* or T = triplet state, A = absorption, F = fluorescence, P = phosphorescence, k = rate constant, r = radiative, nr = non-radiative, IC = internal conversion, ISC = intersystem crossing, ILCT (indices IL) = intraligand charge transfer, LMCT (indices LM) = ligand-to-metal charge transfer. Back transfer processes are not drawn for the sake of clarity.[25]

Related to the forbidden nature of the *4f-4f* transitions, the excited states of Ln^{III} ions are generally long lived. The visible emitters Eu^{III} and Tb^{III} exhibit the longest lifetimes, typically on the order of 1 millisecond or longer. Eu^{III} and Tb^{III} have some of the largest energy gaps between

the emissive excited state and the ground state, which reduces the efficiency of nonradiative quenching processes. The utility of these long lifetimes for time-resolved luminescent immunoassays was first proposed in 1970s.[32–34] Long lifetimes allow for temporal discrimination of the luminescent lanthanide signal from the short lived autofluorescence (on the order of ns) of the background biological media. Early examples of these assays involved a two-step procedure, where the lanthanide is first carried through the immunological reaction by EDTA or DTPA derivatives. The formation of a luminescent complex is then achieved after the immunological reaction has occurred, by introducing media containing surfactants and organic ligands.[32] More recently, homogenous time-resolved fluorescence (HTRF) assays have emerged, where the lanthanide is bound to sensitizing polydentate ligand-antibody conjugate from the start.[35–41] HTRF assays have the advantage of allowing lanthanide luminescence to be observed during the course of an immunological reaction. Additionally, the long lived lanthanide excited state can be used as a donor in Förster resonance energy transfer (FRET) to a nearby organic dye. Using long-lived lanthanide complexes as FRET donors causes the acceptor dye to also be long-lived, allowing temporal discrimination of both donor and acceptor from the background (Fig. 1.4).[42,43]
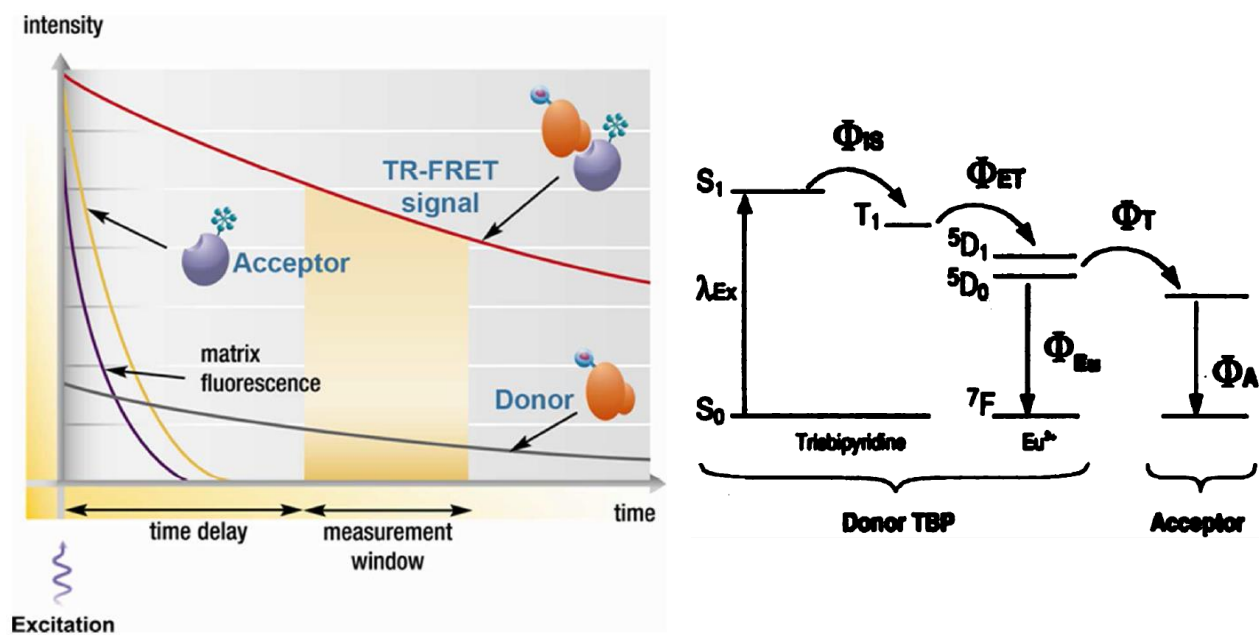
Figure 1.4. Schematic view of timing in HTRF assays, using lanthanide chelates as long-lived energy donors.[35]

As a representative example of HTRF immunoassays, consider the following schematic.[35] Upon stimulating a cell receptor of interest, cAMP is generated in a sample. After cell-lyses, the organic dye labeled cAMP and lanthanide chelate labeled anti-cAMP antibody are added to solution. Unlabeled cAMP competes with dye labeled cAMP causing attenuation of the TR-FRET signal, which can be used to determine the amount of unlabeled cAMP generated by the cells.
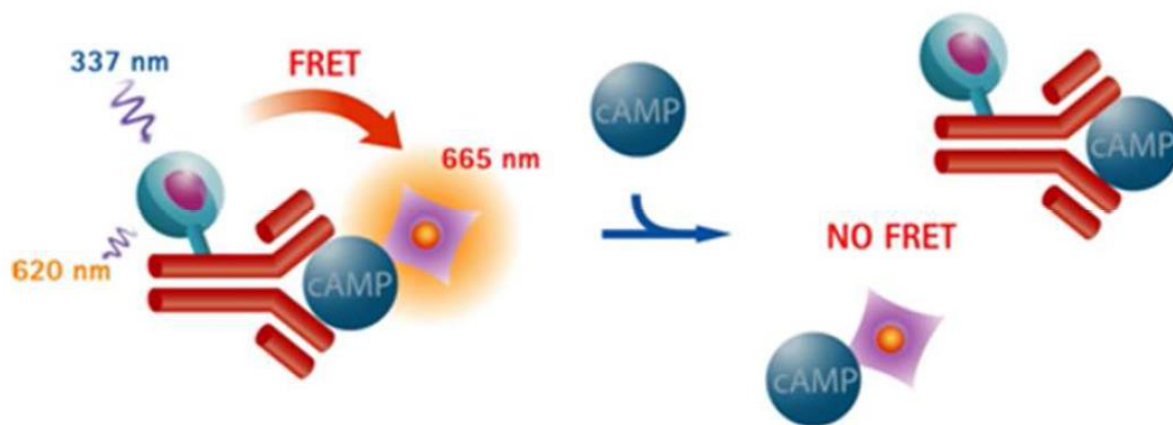
Figure 1.5. The cAMP HTRF assay principle.[35]

A similar assay principle can be used to probe binding events at membrane bound proteins, shown in the following figure. Like the antibodies in the cAMP assays, the membrane bound proteins are first covalently labeled with the lanthanide chelate. Binding strength of the fluorescent CCK(26-23) ligand to the protein receptor can be directly followed by HTRF. Competition experiments using non-labeled competitor ligands allow determination of binding constants with a large dynamic range. The HTRF principles can also be applied to microscopy, where localization of lanthanide tagged proteins can be followed in live cells.
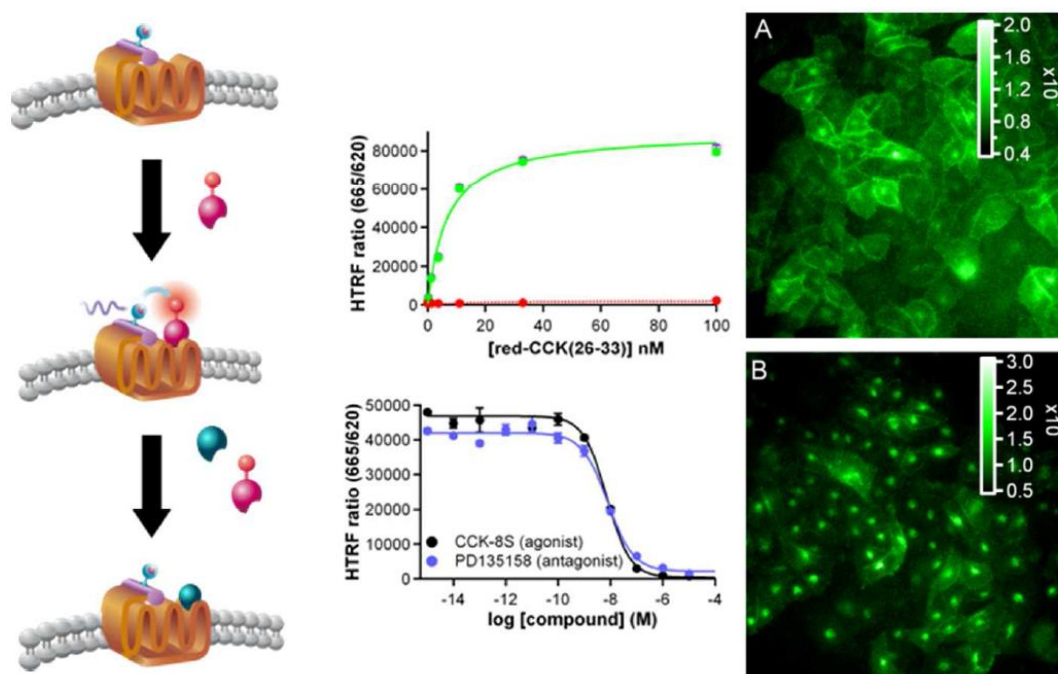
Figure 1.6. Tag-lite binding assay for the Cholecystokinin2 (CCK-2) receptor (left) and internalization of vasoactive intestinal peptides imaged by time resolved microscopy of the Lumi4-Tb tags.[35]

One of the key design principles behind HTRF assays is the dual wavelength detection from the sample. Changes in turbidity or other scattering effects can be corrected for internally

by simultaneous detection of both the lanthanide donor and organic acceptor channels. Lanthanides are ideal donors for these dual wavelength measurements due to their sharp emission bands compared to organic dyes. These turbidity corrections are especially critical for applications in drug discovery, where variances in aqueous solubility of drug candidates can present a significant challenge.[44,45]
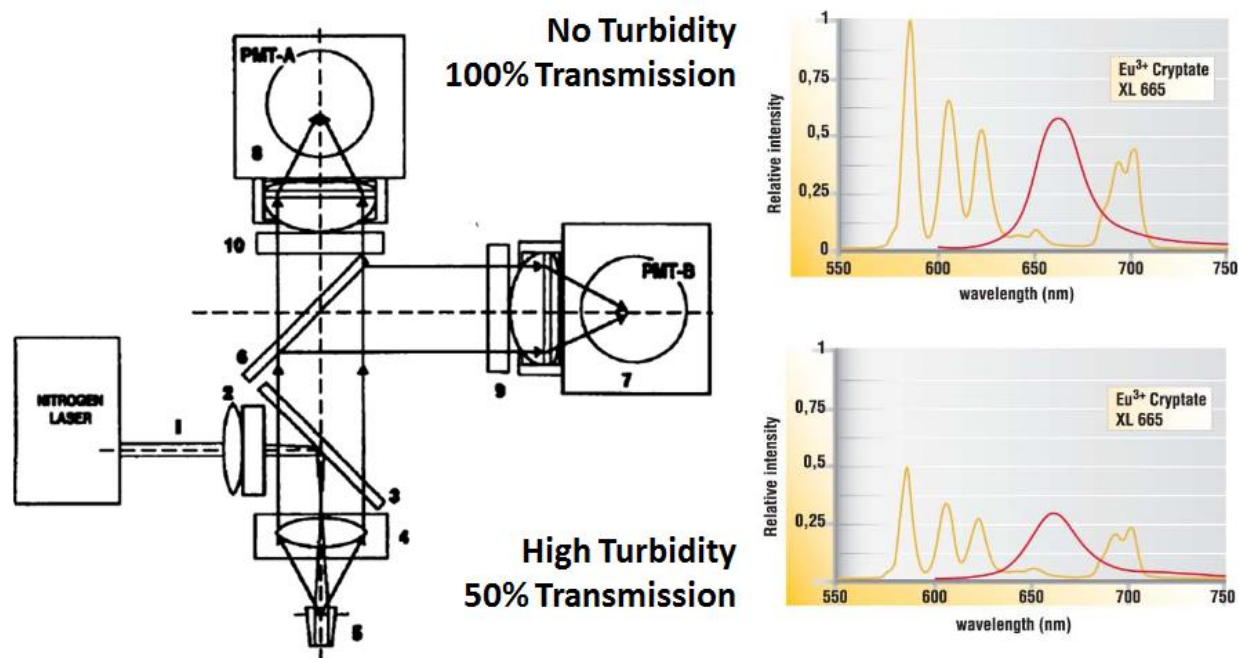
Figure 1.7. Dual wavelength detection of lanthanide donor and organic acceptor allow for turbidity corrections.[35]

A selection of the Eu[III] and Tb[III] coordination complexes developed for use in HTRF technologies is shown in the following figure, which can be divided into a few basic design categories. Compounds **1**, **2**, and **3** are derivatives of the well-known Lehn cryptates, which make use of bipyridyl units to absorb light and transfer energy to bound Eu[III] ions.[46–49] While these cryptate complexes have good kinetic stability in aqueous solution, they leave the Eu[III] coordinatively unsaturated due to their low denticities. Lanthanide ions are found to be 8- or 9-coordinate in aqueous solution, which means a few units of water can bind directly to the Eu[III] center when these 5- and 6-coordinate cryptates are used. Water is an efficient quencher of lanthanide luminescence, due to the relatively high energy of O-H bond vibrations and the hydrophilic nature of lanthanide cations. Thus, the Lehn cryptates exhibit low brightness levels unless fluoride is added to the solution as a competitor for water coordination. Compounds **4**, **5**, and **6** are 1,4,7,10-tetraazacyclododecane-1,4,7,10-tetraacetic acid (DOTA) derivatives incorporating various azaxanthone dyes as Eu[III] sensitizers.[50,51] These compounds are reasonably bright with quantum yields up to 10% in aqueous buffer, but they exhibit poor luminescence in the presence of divalent cations like Mn[II] making them unsuitable for HTRF applications. Compounds **7** and **8** are derivatives of diethylenetriaminepentaacetic acid (DTPA), which have similar quantum yields with Eu[III] (around 15%) and similar stability issues as the DOTA derivatives.[52,53] Compounds **10** through **13**, members of the so called EuroTracker dyes, exhibit bright Eu[III] luminescence (quantum yields around 25%), but exhibit some stability and nonspecific binding issues .[36,54,55]
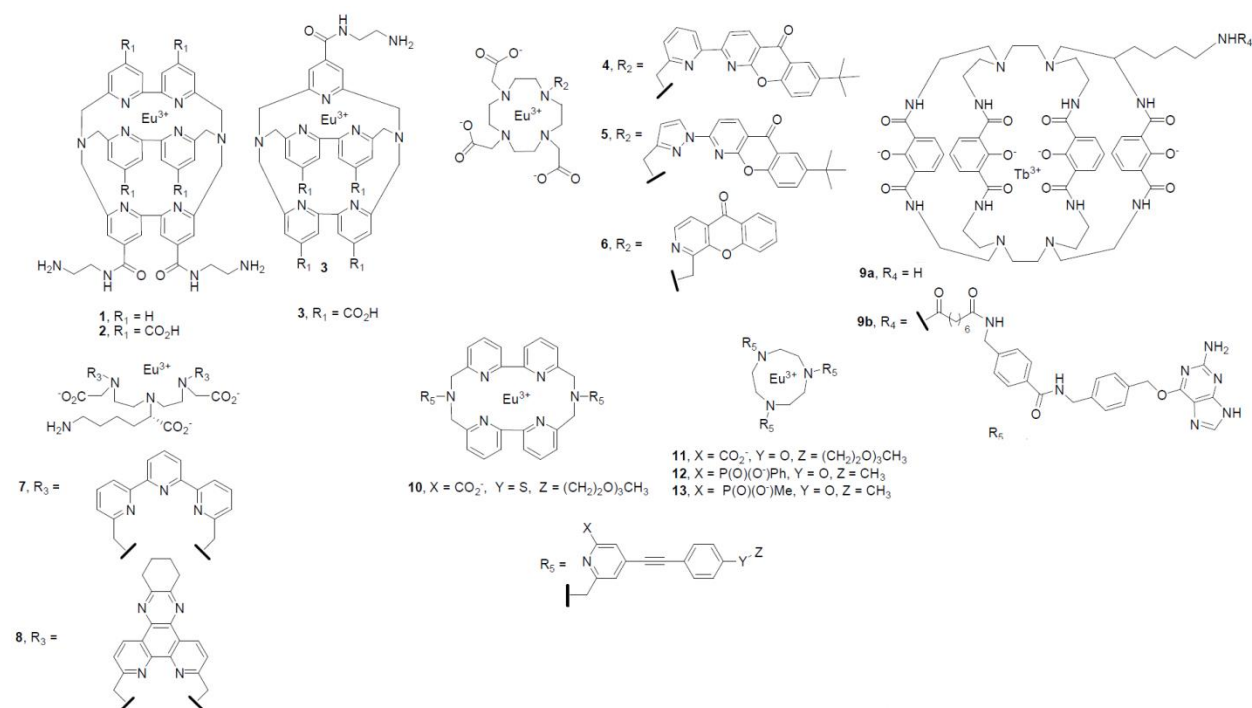
Figure 1.8. A selection of Eu[III] and Tb[III] coordination compounds developed for HTRF assays and imaging.[35]

Over the past 12 years, the Raymond group has investigated the use various binding units commonly found in Fe[III] binding siderophores as sensitizers for Ln[III] photoluminescence.[56–71] The hard lewis acid character of Ln[III] ions is well-matched by these hard all oxygen donor ligands (Fig. 1.9), leading to thermodynamically stable complexes. Derivatives of the 2-hydroxyisophthalamide (IAM) chelate have been found to sensitize extremely bright Tb[III] photoluminescence, with quantum yields as high as 60% found for compound **9** in the above figure. The favorable macrocyclic ligand architecture ensures high kinetic stability, which is crucial for HTRF assays and microscopy applications. It has also been found that derivatives of the 1-hydroxypyridin-2-one (1,2-HOPO) chelate are efficient sensitizers of Eu[III] photoluminescence. Quantum yields for reported 1,2-HOPO Eu[III] complexes have been found as high as 23% in aqueous buffer, making them competitive with the bright EuroTracker dyes as candidates for HTRF applications.
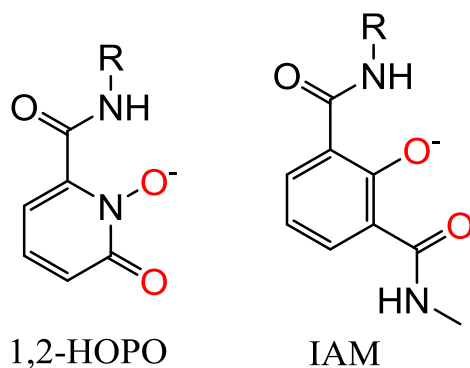
Figure 1.9. Structures of the 1,2-HOPO (left) chelate used for Eu[III] luminescence and the IAM (right) chelate used for Tb[III] luminescence; binding oxygen atoms are shown in red.

Understanding the factors that govern high quantum yields of Eu^{III} 1,2-HOPO chelates toward the design of brighter luminescence agents is the primary focus of this report. Analysis of Eu^{III} luminescence is greatly simplified by the presence of a purely magnetic dipole transition ($^5D_0 \rightarrow {}^7F_1$). With an intensity that is unaffected by the ligand field, the $^5D_0$ to $^7F_1$ transition acts as an internal reference for estimating the radiative lifetime (τ_{rad}). The radiative lifetime, inversely related to the radiative rate (k_{rad}), is the expected Eu^{III} lifetime in the absence of all nonradiative quenching, and it is calculated according to the following equation.[66,72–74]

$$k_{rad} = 1/\tau_{rad} = A[I_{tot}/I_{MD}] \qquad \textbf{(Equation 1.1)}$$

Here, I_{tot} and I_{MD} are the integrated intensities of the total Eu^{III} emission and of the magnetic dipole transition (580 to 600 nm) respectively. The constant, A, is the spontaneous emission probability of the $^5D_0$ to $^7F_1$ transition, which is 32.4 s^{-1} in water.[73] By comparing the observed luminescent lifetime to the radiative lifetime, we can define the probability that the excited Eu^{III} ion will decay radiatively (η_{Eu}) as

$$\eta_{Eu} = \tau_{obs}/\tau_{rad} = k_{rad}/k_{obs}. \qquad \textbf{(Equation 1.2)}$$

The overall quantum yields (Φ_{tot}) can be experimentally determined by the optically dilute method using quinine sulfate as the fluorescence standard. The quantum yield is simply the probability that an absorbed UV photon generates an emitted red photon from Eu^{III}, and it can be broken down into two component probabilities, the metal efficiency η_{Eu} defined above and the sensitization efficiency η_{sens}.

$$\Phi_{tot} = (\eta_{sens})(\eta_{Eu}) \qquad \textbf{(Equation 1.3)}$$

The sensitization efficiency (η_{sens}) is the probability that the energy of an absorbed photon is successfully transferred onto the Eu^{III} center. The extent of nonradiative quenching of the Eu^{III} excited state can be quantified in two ways. First, the rate of nonradiative decay can be calculated using the observed lifetime and calculated radiative lifetime according to the following equation.

$$k_{nonrad} = k_{obs} - k_{rad} = 1/\tau_{obs} - 1/\tau_{rad} \qquad \textbf{(Equation 1.4)}$$

More specific to aqueous solution, the lifetimes of each complex in H_2O and D_2O can be used to determine the degree of Eu^{III} hydration. Since O–H oscillators resonate at high energy, water is a particularly efficient quencher of Eu^{III} luminescence.[75–77] Consequently, luminescent complexes show a shorter luminescent lifetimes in water than deuterated water. The number of inner-sphere water molecules, q, is calculated using the empirically derived Horrocks equation,[78]

$$q = 1.11(1/\tau_{H2O} - 1/\tau_{D2O} - 0.31) \qquad \textbf{(Equation 1.5)}$$

where τ_{H2O} and τ_{D2O}, the observed luminescent lifetimes in the two solvents, are in milliseconds. Quantum yields reported for 1,2-HOPO Eu^{III} complexes range from 4% up to 23% in aqueous buffer. In some cases the lower quantum yields can be attributed to a bound water molecule present within the first coordination sphere of the Eu^{III} ion.[62,66] In other cases, lower quantum yield can be attributed to diminished sensitization efficiency (η_{sens}). Since all of these 1,2-HOPO complexes have similar singlet and triplet state energies, structural changes between the various ligands must be important factors affecting luminescence.

That the sensitization efficiency of Eu[III] chelates can be strongly affected by ligand geometry is supported by the Dexter-type mutual exchange model of ligand to metal energy transfer. The selection rules for Dexter-type mutual exchange implicate the triplet state of the ligand as the preferred energy donor. Malta has recently demonstrated temperature dependent luminescence studies that support a Dexter-type mechanism for related $[Eu(acac)_3(H_2O)_2]$ systems.[79,80] However, other authors have concluded that the ligand excited singlet state is the privileged donor state.[81–83] For chelate chromophore systems, like the 1,2-HOPO complexes, it is difficult to sort out which states are most important, since the ligand-metal donor-acceptor distances are fixed by the metal-ligand bonds. However, the large quantum yield changes brought about by 1,2-HOPO ligand structural modifications are more consistent with a Dexter-type transfer, since the donor-acceptor distances do not change significantly from complex to complex.

The current state of the art for modeling the rates of energy transfer from ligand to metal have been recently compiled into the LUMPAC software package.[84–86] The first step involved in these calculations involves geometry optimization, where the Ln[III] ion is modeled as a simple point 3+ charge called a SPARKLE. The authors find better correspondence between XRD coordinates and those calculated by the SPARKLE model, compared to coordinates calculated by semi-empirical DFT methods.[87,88] From these studies the authors conclude that, "in contrast to what would be expected, the results showed that by enlarging the size of the basis set, or by including electron correlation, or both, deviations of the predicted coordination polyhedrons with respect to the crystallographic ones consistently increased, reducing the quality of the results." However, these conclusions are rooted in the assumption that the XRD coordinates are the best models for these coordination complexes in solution.

In the following report, we take a critical view of the Ln[III] point charge approximation. We find that coordinates minimized by DFT offer a better structural model for rationalizing the ^{1}H-NMR isotropic shifts, than the XRD coordinates. Throughout the document, we develop the idea that covalent interactions between the Ln[III] metals and the ligands are essential to understanding the geometry found in solution. Since the luminescence of Eu[III] is found to depend strongly on the ligand geometry we conclude that any model neglecting the treatment of ligand-metal covalent interaction is necessarily incomplete.

References

(1) Seitz, M.; Oliver, A. G.; Raymond, K. N. *J. Am. Chem. Soc.* **2007**, *129*, 11153.
(2) Raymond, K. N.; Wellman, D. L.; Sgarlata, C.; Hill, A. P. *Comptes Rendus Chim.* **2010**, *13*, 849.
(3) Ronda, C. R.; Jüstel, T.; Nikol, H. *J. Alloys Compd.* **1998**, *275–277*, 669.
(4) Shur, M. S.; Zukauskas, R. *Proc. IEEE* **2005**, *93*, 1691.
(5) Kim, J. S.; Jeon, P. E.; Park, Y. H.; Choi, J. C.; Park, H. L.; Kim, G. C.; Kim, T. W. *Appl. Phys. Lett.* **2004**, *85*, 3696.
(6) Miniscalco, W. J. *J. Light. Technol.* **1991**, *9*, 234.
(7) Geusic, J. E.; Marcos, H. M.; Uitert, L. G. V. *Appl. Phys. Lett.* **1964**, *4*, 182.
(8) Reisfeld, R.; Jørgensen, C. K. In *Lasers and Excited States of Rare Earths*; Inorganic Chemistry Concepts; Springer Berlin Heidelberg, 1977; pp. 64–122.
(9) Kuriki, K.; Koike, Y.; Okamoto, Y. *Chem. Rev.* **2002**, *102*, 2347.

(10) Weber, J. K. R.; Felten, J. J.; Cho, B.; Nordine, P. C. *Nature* **1998**, *393*, 769.

(11) Slooff, L. H.; Blaaderen, A. van; Polman, A.; Hebbink, G. A.; Klink, S. I.; Veggel, F. C. J. M. V.; Reinhoudt, D. N.; Hofstraat, J. W. *J. Appl. Phys.* **2002**, *91*, 3955.

(12) Fraden, J. *Handbook of Modern Sensors: Physics, Designs, and Applications*; Springer Science & Business Media, 2010.

(13) Mears, R. J.; Reekie, L.; Jauncey, I. M.; Payne, D. N. *Electron. Lett.* **1987**, *23*, 1026.

(14) Becker, P. M.; Olsson, A. A.; Simpson, J. R. *Erbium-Doped Fiber Amplifiers: Fundamentals and Technology*; Academic Press, 1999.

(15) Wegh, R. T.; Donker, H.; Oskam, K. D.; Meijerink, A. *Science* **1999**, *283*, 663.

(16) Trupke, T.; Shalav, A.; Richards, B. S.; Würfel, P.; Green, M. A. *Sol. Energy Mater. Sol. Cells* **2006**, *90*, 3327.

(17) Richards, B. S. *Sol. Energy Mater. Sol. Cells* **2006**, *90*, 2329.

(18) Richards, B. S. *Sol. Energy Mater. Sol. Cells* **2006**, *90*, 1189.

(19) Ende, B. M. van der; Aarts, L.; Meijerink, A. *Phys. Chem. Chem. Phys.* **2009**, *11*, 11081.

(20) Eliseeva, S. V.; Bünzli, J.-C. G. *New J. Chem.* **2011**, *35*, 1165.

(21) Bünzli, J.-C. G.; Eliseeva, S. V. *J. Rare Earths* **2010**, *28*, 824.

(22) Bünzli, J.-C. G.; Piguet, C. *Chem. Soc. Rev.* **2005**, *34*, 1048.

(23) Binnemans, K. *Chem. Rev.* **2009**, *109*, 4283.

(24) De Sá, G. .; Malta, O. .; de Mello Donegá, C.; Simas, A. .; Longo, R. .; Santa-Cruz, P. .; da Silva, E. . *Coord. Chem. Rev.* **2000**, *196*, 165.

(25) Eliseeva, S. V.; Bünzli, J.-C. G. *Chem. Soc. Rev.* **2009**, *39*, 189.

(26) Montgomery, C. P.; Murray, B. S.; New, E. J.; Pal, R.; Parker, D. *Acc. Chem. Res.* **2009**, *42*, 925.

(27) Handl, H. L.; Gillies, R. J. *Life Sci.* **2005**, *77*, 361.

(28) Parker, D.; Williams, J. A. G. *J. Chem. Soc. Dalton Trans.* **1996**, 3613.

(29) Selvin, P. R. *Annu. Rev. Biophys. Biomol. Struct.* **2002**, *31*, 275.

(30) Liu, G. In *Spectroscopic Properties of Rare Earths in Optical Materials*; Hull, P. R.; Parisi, P. J.; Jr, P. R. M. O.; Warlimont, P. H.; Liu, D. G.; Jacquier, P. B., Eds.; Springer Series in Materials Science; Springer Berlin Heidelberg, 2005; pp. 1–94.

(31) Weissman, S. I. *J. Chem. Phys.* **1942**, *10*, 214.

(32) Soini, E.; Hemmilä, I. *Clin. Chem.* **1979**, *25*, 353.

(33) Soini, E.; Kojola, H. *Clin. Chem.* **1983**, *29*, 65.

(34) Soini, E.; Lövgren, T.; Reimer, C. B. *C R C Crit. Rev. Anal. Chem.* **1987**, *18*, 105.

(35) Zwier, J. M.; Bazin, H.; Lamarque, L.; Mathis, G. *Inorg. Chem.* **2014**, *53*, 1854.

(36) Delbianco, M.; Sadovnikova, V.; Bourrier, E.; Mathis, G.; Lamarque, L.; Zwier, J. M.; Parker, D. *Angew. Chem. Int. Ed.* **2014**, *53*, 10718.

(37) Alpha, B.; Lehn, J.-M.; Mathis, G. *Angew. Chem. Int. Ed. Engl.* **1987**, *26*, 266.

(38) Prat, O.; Lopez, E.; Mathis, G. *Anal. Biochem.* **1991**, *195*, 283.

(39) Mathis, G. *Clin. Chem.* **1993**, *39*, 1953.

(40) Vila-Nova, S. P.; Pereira, G. A. .; Albuquerque, R. Q.; Mathis, G.; Bazin, H.; Autiero, H.; Sá, G. F. d.; Alves, S. *J. Lumin.* **2004**, *109*, 173.

(41) Guillaumont, D.; Bazin, H.; Benech, J.-M.; Boyer, M.; Mathis, G. *ChemPhysChem* **2007**, *8*, 480.

(42) *Biochemical fluorescence: concepts*; Chen, R. F.; Edelhoch, H., Eds.; M. Dekker: New York, 1975.

(43) Morrison, L. E. *Anal. Biochem.* **1988**, *174*, 101.

(44) Mathis, G. *Clin. Chem.* **1995**, *41*, 1391.

(45) Degorce, F. *Curr. Chem. Genomics* **2009**, *3*, 22.

(46) Bazin, H.; Préaudat, M.; Trinquet, E.; Mathis, G. *Spectrochim. Acta. A. Mol. Biomol. Spectrosc.* **2001**, *57*, 2197.

(47) Lehn, J.-M.; Regnouf de Vains, J.-B. *Tetrahedron Lett.* **1989**, *30*, 2209.

(48) Prodi, L.; Maestri, M.; Balzani, V.; Lehn, J.-M.; Roth, C. *Chem. Phys. Lett.* **1991**, *180*, 45.

(49) Lehn, J.-M.; De Vains, J.-B. R. *Helv. Chim. Acta* **1992**, *75*, 1221.

(50) Montgomery, C. P.; New, E. J.; Palsson, L. O.; Parker, D.; Batsanov, A. S.; Lamarque, L. *Helv. Chim. Acta* **2009**, *92*, 2186.

(51) Parker, D.; Walton, J. W.; Lamarque, L.; Zwier, J. M. *Eur. J. Inorg. Chem.* **2010**, *2010*, 3961.

(52) Galaup, C.; Couchet, J.-M.; Bedel, S.; Tisnès, P.; Picard, C. *J. Org. Chem.* **2005**, *70*, 2274.

(53) Deslandes, S.; Galaup, C.; Poole, R.; Mestre-Voegtlé, B.; Soldevila, S.; Leygue, N.; Bazin, H.; Lamarque, L.; Picard, C. *Org. Biomol. Chem.* **2012**, *10*, 8509.

(54) Walton, J. W.; Bourdolle, A.; Butler, S. J.; Soulie, M.; Delbianco, M.; McMahon, B. K.; Pal, R.; Puschmann, H.; Zwier, J. M.; Lamarque, L.; Maury, O.; Andraud, C.; Parker, D. *Chem. Commun.* **2013**, *49*, 1600.

(55) Butler, S. J.; Delbianco, M.; Lamarque, L.; McMahon, B. K.; Neil, E. R.; Pal, R.; Parker, D.; Walton, J. W.; Zwier, J. M. *Dalton Trans.* **2014**.

(56) Petoud, S.; Cohen, S. M.; Bünzli, J.-C. G.; Raymond, K. N. *J. Am. Chem. Soc.* **2003**, *125*, 13324.

(57) Johansson, M. K.; Cook, R. M.; Xu, J.; Raymond, K. N. *J. Am. Chem. Soc.* **2004**, *126*, 16451.

(58) Petoud, S.; Muller, G.; Moore, E. G.; Xu, J.; Sokolnicki, J.; Riehl, J. P.; Le, U. N.; Cohen, S. M.; Raymond, K. N. *J. Am. Chem. Soc.* **2006**, *129*, 77.

(59) Moore, E. G.; Xu, J.; Jocher, C. J.; Werner, E. J.; Raymond, K. N. *J. Am. Chem. Soc.* **2006**, *128*, 10648.

(60) Seitz, M.; Moore, E. G.; Ingram, A. J.; Muller, G.; Raymond, K. N. *J. Am. Chem. Soc.* **2007**, *129*, 15468.

(61) Samuel, A. P. S.; Moore, E. G.; Melchior, M.; Xu, J.; Raymond, K. N. *Inorg. Chem.* **2008**, *47*, 7535.

(62) Moore, E. G.; Jocher, C. J.; Xu, J.; Werner, E. J.; Raymond, K. N. *Inorg. Chem.* **2007**, *46*, 5468.

(63) Moore, E. G.; Xu, J.; Jocher, C. J.; Castro-Rodriguez, I.; Raymond, K. N. *Inorg. Chem.* **2008**, *47*, 3105.

(64) D'Aléo, A.; Xu, J.; Moore, E. G.; Jocher, C. J.; Raymond, K. N. *Inorg. Chem.* **2008**, *47*, 6109.

(65) Samuel, A. P. S.; Xu, J.; Raymond, K. N. *Inorg. Chem.* **2008**, *48*, 687.

(66) D'Aléo, A.; Moore, E. G.; Szigethy, G.; Xu, J.; Raymond, K. N. *Inorg. Chem.* **2009**, *48*, 9316.

(67) Moore, E. G.; Samuel, A. P. S.; Raymond, K. N. *Acc. Chem. Res.* **2009**, *42*, 542.

(68) Samuel, A. P. S.; Lunkley, J. L.; Muller, G.; Raymond, K. N. *Eur. J. Inorg. Chem.* **2010**, *2010*, 3343.

(69) Moore, E. G.; Xu, J.; Jocher, C. J.; Corneillie, T. M.; Raymond, K. N. *Inorg. Chem.* **2010**, *49*, 9928.

(70) Xu, J.; Corneillie, T. M.; Moore, E. G.; Law, G.-L.; Butlin, N. G.; Raymond, K. N. *J. Am. Chem. Soc.* **2011**, *133*, 19900.

(71) Law, G.-L.; Andolina, C. M.; Xu, J.; Luu, V.; Rutkowski, P. X.; Muller, G.; Shuh, D. K.; Gibson, J. K.; Raymond, K. N. *J. Am. Chem. Soc.* **2012**, *134*, 15545.

(72) Werts, M. H. V. In *Lanthanide Luminescence*; Hänninen, P.; Härmä, H., Eds.; Springer Series on Fluorescence; Springer Berlin Heidelberg, 2011; pp. 133–159.

(73) Beeby, A.; Bushby, L. M.; Maffeo, D.; Williams, J. A. G. *J. Chem. Soc. Dalton Trans.* **2002**, 48.

(74) Pacold, J. I.; Tatum, D. S.; Seidler, G. T.; Raymond, K. N.; Zhang, X.; Stickrath, A. B.; Mortensen, D. R. *J. Am. Chem. Soc.* **2014**, *136*, 4186.

(75) Heller, A. *J. Am. Chem. Soc.* **1966**, *88*, 2058.

(76) Haas, Y.; Stein, G. *J. Phys. Chem.* **1971**, *75*, 3677.

(77) Kropp, J. L.; Windsor, M. W. *J. Chem. Phys.* **1965**, *42*, 1599.

(78) Supkowski, R. M.; Horrocks Jr., W. D. *Inorganica Chim. Acta* **2002**, *340*, 44.

(79) Malta, O. L. *J. Non-Cryst. Solids* **2008**, *354*, 4770.

(80) Faustino, W. M.; Nunes, L. A.; Terra, I. A. A.; Felinto, M. C. F. C.; Brito, H. F.; Malta, O. L. *J. Lumin.* **2013**, *137*, 269.

(81) Kleinerman, M. *J. Chem. Phys.* **1969**, *51*, 2370.

(82) Yang, C.; Fu, L.-M.; Wang, Y.; Zhang, J.-P.; Wong, W.-T.; Ai, X.-C.; Qiao, Y.-F.; Zou, B.-S.; Gui, L.-L. *Angew. Chem. Int. Ed.* **2004**, *43*, 5010.

(83) Rodríguez-Cortiñas, R.; Avecilla, F.; Platas-Iglesias, C.; Imbert, D.; Bünzli, J.-C. G.; de Blas, A.; Rodríguez-Blas, T. *Inorg. Chem.* **2002**, *41*, 5336.

(84) Dutra, J. D. L.; Bispo, T. D.; Freire, R. O. *J. Comput. Chem.* **2014**, *35*, 772.

(85) Dutra, J. D. L.; Ferreira, J. W.; Rodrigues, M. O.; Freire, R. O. *J. Phys. Chem. A* **2013**, *117*, 14095.

(86) Dutra, J. D. L.; Freire, R. O. *J. Photochem. Photobiol. Chem.* **2013**, *256*, 29.

(87) Freire, R. O.; Rocha, G. B.; Simas, A. M. *J. Mol. Model.* **2006**, *12*, 373.

(88) Rodrigues, D. A.; da Costa, N. B.; Freire, R. O. *J. Chem. Inf. Model.* **2011**, *51*, 45.

Chapter 2

The Shape49 Program: Automated δ Dihedral Angle Shape Analysis for Coordination Numbers Four through Nine

Introduction

Chemical reasoning relies on quantifiable comparisons and with regard to shape these comparisons can be difficult to make. The structure of a typical coordination complex can resemble multiple idealized forms with varying degrees of distortion. A popular method for quantifying this distortion was reported in 1974 by Muetterties and Guggenberger, based on a specific application by Porai-Koshits and Aslanov in 1972.[1–3] Therein, the authors classify shapes by considering the angles between normals of adjacent triangles comprising the convex coordination polyhedron, i.e. the dihedral angles (δ) along each external edge (Fig. 2.1). There are 6, 9, 12, 15, 18, and 21 such angles (and edges) for 4-, 5-, 6-, 7-, 8-, and 9-coordinate geometries respectively. A subset of these angles (between two and six) was chosen as "shape determining" for each coordination number, and these subsets were tabulated for comparing measured and ideal geometries. The authors emphasized the utility of these δ angles for mapping the paths of intramolecular rearrangements.
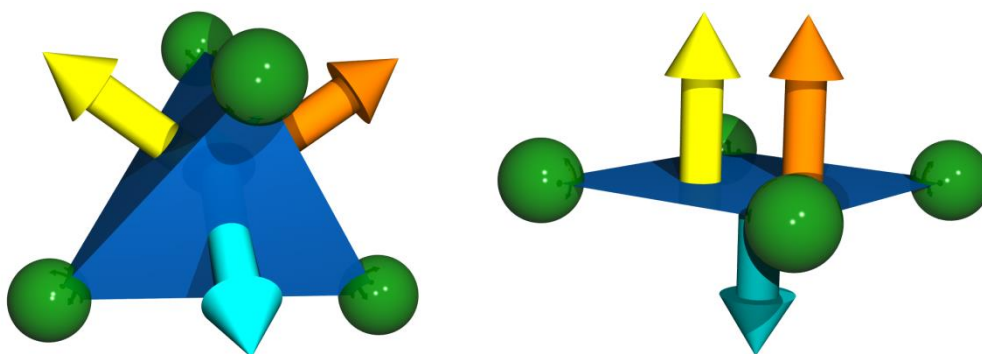
Figure 2.1. The angles (δ) between the yellow, orange, and cyan normal vectors are all equal to ~109.5^{o} in the tetrahedron (left). In the square planar geometry (right), the δ angle between parallel yellow and orange vectors is zero, while pairings of either the orange or yellow with the antiparallel cyan vector are 180°.

More recently, three distinct albeit related types of automated shape analysis have been reported. Eisenstein and coworkers reported a Fortran program for assigning seven-coordinate geometries using L-M-L (θ) angles.[4] A popular program developed by Avnir and coworkers called continuous shape measures (CShM) considers the distances between superimposed coordinates of measured and scaled ideal shapes.[5–16] Our group has previously reported a Matlab script that assigns common eight-coordinate geometries using the full set of dihedral (δ) angles described above.[17,18] The Raymond and Eisenstein routines rely on the same, well-known root-mean-square deviation (RMSD) function shown below:

$$S(\delta, \hat{\delta}) = min\left(\sqrt{\frac{1}{N}\sum_{i=1}^{N}(\delta_i - \hat{\delta}_i)^2} \right) \qquad \textbf{(Equation 2.1)}$$

where δ_i and $\hat{\delta}_i$ are the ith angles (θ or δ) of measured and reference structures respectively, and N is the total number of unique angles. Angles are constant with respect to isotropic scaling, which means size normalization of investigated coordinates is not required. Distances, however, vary with isotropic scaling, so the CShM program uses the normalized RMSD function shown below:

$$S(Q, P) = min\left(\frac{\sum_{i=1}^{N}|Q_i - P_i|^2}{\sum_{i=1}^{N}|Q_i - Q_0|^2}\right) \times 100 \qquad \text{(\textbf{Equation 2.2})}$$

where Q_i and P_i are the ith coordinate vectors of measured and reference respectively, and Q_0 is the centroid position. The function $S(Q,P)$ in Avnir's program takes on unitless values from 0 to a maximum of 100. The function $S(\delta,\hat{\delta})$ in Eisenstein's and Raymond's programs has units of degrees without an obvious maximum. All three routines employ the same basic principle. The difference (in angles or distances) between a measured set of coordinates (X) and an ideal shape (Y) is calculated for every unique relative orientation to find the smallest possible least-squares difference, $S(X,Y)$. A small minimum value of $S(X,Y)$ indicates that the shape of a measured set of coordinates X is close to the shape of ideal Y and vice versa. By calculating S with respect to several ideal shapes, a measured set of coordinates can be quantitatively assigned as closest to a particular ideal. The low energy pathways between two related ideal geometries (e.g. 5-coordinate D_{3h} and C_{4v} geometries via the Berry pseudorotation) can be examined by plotting the corresponding S functions against one another, called a "shape map".[5,11–16] On a shape map, the shortest distance between the position of a measured coordinate set and the low energy rearrangement path between the two plotted ideal shapes can be found. This shortest distance, called the deviation function in CShM, is another useful metric for categorizing the shapes of coordination polyhedra, especially those with no clear closest ideal.

Herein, we extend our automated δ angle analysis to coordination numbers four through nine, and we expand the scope of our original eight-coordinate analysis. In addition to the shape measures, S, the program can print the total sets of δ angles. Inclusion of these angles improves the transparency of our program, since the values of S can be independently verified from them (Eq. 1). These lists of angles demonstrate the program's equivalence to the Muetterties analysis, and they facilitate quick comparison to δ angles that have been reported previously. Twist angles (φ) for six- and certain eight-coordinate systems are also calculated by the program. Like CShM, the δ angle analysis requires the specification of explicit ideal shapes. Here, we have replaced the hard sphere model (HSM) ideals used in the Muetterties and CShM analyses with more chemically reasonable ones according to Kepert's methods.[19–23] We compare several possible ideal geometries for the eight-coordinate C_{2v} bicapped trigonal prism (BCTP) and determine that Drew's most favorable polyhedron (MFP) works best in our program.[24] Some authors have noted that the δ angle analysis gives misleading results when significant differences in M-L bond distances are present.[24,25] We include an optional automatic normalization procedure to overcome this limitation. Finally, we find an excellent linear correlation between values of S along 14 intramolecular rearrangement pathways, demonstrating the utility of the δ angles and S values derived from them.

Results and Discussion

Derivation of the ideal shapes. If only the angular parameters are considered, shapes belonging to the cubic point groups T_d and O_h, are completely defined by symmetry, i.e. there is only one ideal tetrahedron, one ideal octahedron, and one ideal cube. Similarly, the shape of the 4-coordinate D_{4h} square plane is uniquely defined. By restricting the coordinates of ideal geometries to lie on the surface of a unit sphere, the bipyramids (5-coordinate D_{3h}, 7-coordinate

D_{5h}, and 8-coordinate D_{6h}) join the ranks of symmetry defined shapes. All other shapes considered here require at least one additional shape parameter not defined by the symmetry.

The important role of ligand-ligand repulsion in determining coordination geometry has been appreciated for some time.[26–31] By treating ligand atoms (or bonds) as mutually repulsive points on a unit sphere, shapes can be defined by minimizing the following expression:

$$U = \sum_{ij}^{m} d_{ij}^{-n}, \; (i > j) \qquad \textbf{(Equation 2.3)}$$

where d_{ij} is the distance between points i and j, m is the total number of points, and n is a chosen parameter. The most generally appropriate value of n cannot be known exactly, and calculating ideal shapes requires that its value be chosen somewhat arbitrarily. At one end of the spectrum lies $n=1$, which represents Coulombic repulsion between the ligand points. At the other end lies $n=\infty$, describing incompressible ligand spheres and commonly called the (infinitely) hard sphere model (HSM). Chemically reasonable values of n fall somewhere between these two extremes. The repulsion energy expression (Eq. 2) was originally adapted from the Born-Landé equation by Hoard and Silverton in 1963.[30] There, the value $n=7$ was chosen, since crystal compressibility measurements indicate $n=7$ as the appropriate Born exponent for Ne shell ions (cyanide ligands of $K_4Mo(CN)_8$ being closest to the [Ne] electronic configuration).[32] This idea was greatly expanded upon in the following years by Kepert and others.[19–23] In one account, Kepert suggests that experiment typically falls between $n=6$ and $n=10$, leading to the previous use of $n=8$ in our eight-coordinate program.[17,22] Here, we take Kepert's later suggestion of $n=6$ as the most generally appropriate value.[33]

Here we provide the calculated shape parameters for several possible values of n (see Appendix 2). Our repulsion energy minimizations are consistent with those reported previously for all available comparisons. We include the corresponding δ angles for each value of n, and we note an important error in the Muetterties analysis. The shape determining δ angles of the 7-coordinate C_{3v} geometry ($n=6$) were erroneously calculated as 24.2°; we show here that they are actually 16.1°.[1] We report the shape parameters to an excessive number of digits so that compounded rounding errors by the program are minimized when analyzing ideal shapes and the paths between them. The A-M-L Φ values shown on the left side of each table are relative to the high symmetry axis (A) shown in red.
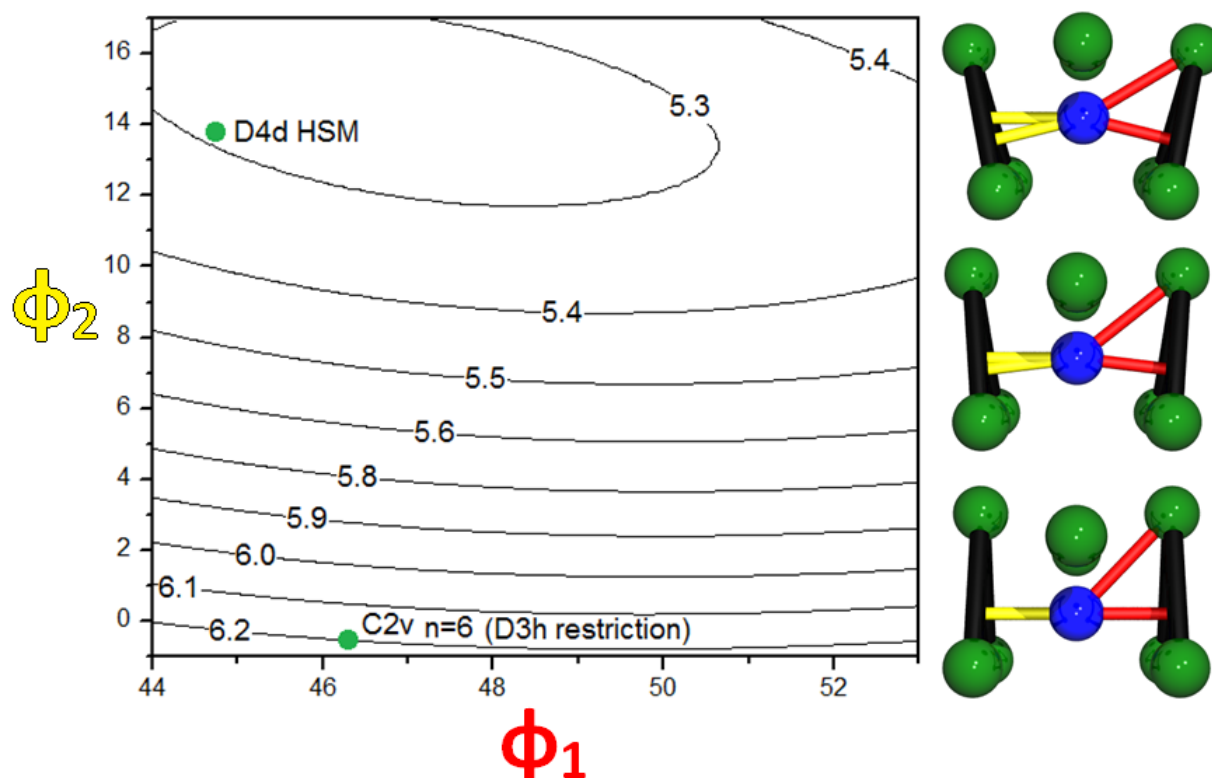
Figure 2.2. Repulsion energy surface showing the D_{3h} restricted C_{2v} bicapped trigonal prism and its subsequent collapse to the D_{4d} HSM upon lifting the D_{3h} restriction

Calculating the 8-coordinate C_{2v} bicapped trigonal prism (BCTP) geometry presents a problem if the trigonal prism subset is not constrained to have local D_{3h} symmetry (as in Table S5). Every coordination number has only one global repulsion energy minimum. In the absence of the D_{3h} restriction, all repulsion energy C_{2v} models minimize to the D_{4d} antiprism global minimum (Fig. 2.2). For this reason, Kepert makes little mention of the BCTP, except for the special case of M(monodentate)$_4$(bidentate)$_2$ compounds.[22,33] Others have acknowledged the issue and argue for the shape's existence on the basis of particularly favorable σ-bonding.[34] Drew gives an excellent discussion of the topic.[24] He notes that the D_{3h} restriction is unrealistic, but also that the repulsion energy derivation is impossible in its absence. Drew proposes a "most favorable" polyhedron (MFP) based on representative BCTP crystal structures. He reports the average L-L distances from normalized atomic coordinates, which we use to derive the shape and δ angle parameters of Drew's MFP (Table 11). We compare those MFP values to the n=6 D_{3h} restricted, the HSM D_{3h} restricted, and our previously reported BCTP.[17]

Table 2.1. Finding the nearest points-on-a-sphere model BCTP for Drew's MFP and comparison of the associated δ angles with other possible BCTP ideals

Edge, (Table 6 code)	Drew MFP edge lengths (Å)	Drew MFP nearest unit sphere fit (Å)	δ Angles Drew MFP (°)	δ Angles HSM (°)	δ Angles n=6 (°)	δ Angles Raymond Reported[17] (°)
t	1.78	1.78	-	-	-	-
v_2 (D)	1.25	1.25	71.8	70.9	74.4	62.2
v_1 (A)	1.50	1.50	26.6	21.8	28.9	18.0
h_1, h_3 (B)	1.36	1.34	46.5	48.2	47.3	46.3
h_2 (E)	1.13	1.13	84.1	90	90	88.7
c_1 (C)	1.18	1.18	67.7	60.8	59.1	64.2
c_2 (C)	1.21	1.22	56.6	60.8	59.1	69.2

In the following table, we report the shape analysis of 15 well-documented BCTP examples from the literature using the four possible C_{2v} ideals shown above. The much lower values for $S(C_{2v})$ using Drew's MFP support its use as the ideal bicapped trigonal prism in our program. We find this troublesome shape of particular importance for the δ angle analysis reported here, since the primary aim of Porai-Koshits and Aslanov's original dihedral angle (δ) and twist angle (φ) criteria was to distinguish the bicapped trigonal prism (C_{2v}) from the other common 8-coordinate geometries (D_{2d} and D_{4d}).

Table 2.2. Shape Analysis comparison of possible C_{2v} idealized geometries

CCSD or ICSD Ref. Code	Compound	$S(D_{4d})$ (°)	$S(D_{2d})$ (°)	$S(C_{2v})$ Drew MFP (°)	$S(C_{2v})$ D_{3h} Rest. HSM (°)	$S(C_{2v})$ D_{3h} Rest. (n=6) (°)	$S(C_{2v})$ Raymond Reported (°)
30338[35]	Li_4UF_8	12.48	12.46	3.73	4.15	3.20	7.30
80398[36]	Li_4ZrF_8	12.18	12.48	3.45	4.27	3.12	7.69
85718[37]	Ba_2ZrF_8	11.25	12.25	2.58	3.70	3.08	7.18
NICHOC10[38]	$Ho(isonic)_3(OH_2)_2$	8.99	11.81	1.76	4.30	4.43	7.72
DTPACV10[39]	$V(S_2CCH_2Ph)_4$	10.62	10.90	2.98	5.08	5.28	7.16
TMNHYW10[40]	$WMe_4[ON(Me)NO]_2$	9.15	10.81	2.19	5.33	5.76	7.51
HYZCSC[41]	$Sc(thacox)_4$	7.72	9.27	4.14	6.98	7.68	8.76
HTROPS01[42]	$[Sc(trop)_4]^-$	11.18	8.78	4.60	6.18	6.32	8.05
TRONBC[43]	$[Nb(trop)_4]^+$	9.39	7.64	6.49	8.67	9.37	9.79
YACACT[44]	$Y(acac)_3(OH_2)_2$	9.26	8.82	3.94	6.07	6.47	8.33
AQACAL[45]	$La(acac)_3(OH_2)_2$	10.04	9.62	4.64	6.48	6.84	8.40
NDACAT10[46]	$Nd(acac)_3(OH_2)_2$	9.86	9.76	4.31	6.23	6..52	8.40
EUACAC10[47]	$Eu(acac)_3(OH_2)_2$	9.50	9.27	3.83	5.88	6.30	8.05
ACACCE02[48]	$α-Ce(acac)_4$	7.28	8.75	4.95	7.84	8.41	9.81
ACACTH01[49]	$α-Th(acac)_4$	7.09	9.85	4.06	7.23	7.62	9.67

The Shape49 Program. Like our original eight-coordinate routine, the program reported here is coded in Matlab script (see Appendix 2). The program is also compatible with GNU Octave, a Linux based freeware alternative to Matlab, which can run on a Windows machine

using freeware Cygwin. The first two lines of code specify normalization and analysis options. If the string *longanalysis* is set to 1, the program will print the shape measures S, the full set of δ angles, and (if applicable) the φ twist angles. If *longanalysis* is set to 0 only S values will be printed. Coordinates may be submitted with or without one central atom. If a central atom is included and the string *autonormalize* is set to 0, then the central atom is simply ignored. If *autonormalize* is set to 1 and a central atom is present, the coordinates will be normalized with respect to the central atom. If *autonormalize* is set to 1 and a central atom is not present, the coordinates will be normalized with respect to the calculated centroid of the ligand coordinates. Note that while normalization is optional, it should always be used for certain types of structures, e.g. the actinyls, since the trans oxo ligand bond distances are considerably shorter than for the equatorial ligands. Regardless of the normalization option selected, subsequent shape analysis does not involve the central atom.

Once a set of coordinates have been submitted (and optionally normalized), the program computes the shape analysis in three steps. First, the L-L edges belonging to the convex coordination polyhedron are found, which generates the critically important "edge number" of each vertex. For all edges AB, all possible triangles ABC are tested to see if any of them are external faces. An external face is found by considering the projection of all possible vectors CD onto the normal of ABC and verifying that the all projections are either positive or negative. An important limitation of this procedure is that the submitted coordinates must describe a convex polyhedron with only three or four sided faces. Second, the dihedral (δ) angles are computed for all found external edges. These first two stages are essentially unchanged from our original eight-coordinate analysis. In the third stage, which comprises the bulk of the program, the shape analysis is calculated for all unique pairings of the measured δ angles with those of the ideal shapes to find the minimum value. We refer to this process as alignment, but note that it is a discrete pairing problem distinct from the alignment and scaling required in CShM. Each coordination number requires a different alignment (third stage) procedure, which we explore in more detail in Appendix 2.

Intramolecular Rearrangement Pathways. An important property of any shape analysis is that the shape measure X of an ideal shape Y must be equivalent to the shape measure Y of an ideal X, i.e. $S(X,Y) = S(Y,X)$. Here we demonstrate that our program meets this requirement. Using default $n=6$ ideals, four-coordinate D_{4h} and T_d are 85.50^o apart, five-coordinate D_{3h} and C_{4v} are 26.99^o apart, six-coordinate O_h and D_{3h} are 45.22^o apart, and nine-coordinate D_{3h} and C_{4v} are 9.26^o apart. Shape distances for seven- and eight-coordination are shown in the following tables.

Table 2.3. Shape analyses of seven-coordinate ideals

$n = 6$	C_{2v}	D_{5h}
C_{3v}	12.42	26.28
C_{2v}		27.48
D_{5h}		0

Table 2.4. Shape analyses of eight-coordinate ideals

$n = 6$	C_{2v} (MFP)	D_{2d}	O_h	D_{6h}	D_{3h}
D_{4d}	8.92	15.20	31.48	33.01	45.37
C_{2v} (MFP)	0	11.88	33.48	30.67	43.44
D_{2d}		0	30.58	29.61	43.37
O_h			0	37.05	45.58
D_{6h}				0	43.24
D_{3h}					0

Since the ideal shapes are constructed as points on a unit sphere, we can similarly generate intermediates between two shapes as points on a unit sphere. For each intramolecular rearrangement considered, some element of symmetry is maintained throughout the transformation (Table 15). Here, we generate intermediates along these rearrangement paths by first minimally aligning the two ideals (with regard to the path symmetry) and then changing the angular coordinates from one shape to another in linear steps. For low coordination numbers (four and five), this method exactly generates the lowest repulsion energy path between the two shapes. For higher coordination numbers we note that the true lowest energy path does not necessarily involve linear changes in the associated angles.[33] The approximate pathways generated here are close enough to the energy minimum to afford good linear correlations between idealized shapes. We examine each intramolecular rearrangement path in thirteen steps, and in the following table we show linear regression statistics from the shape analyses of the 15 paths investigated.

Table 2.5. Linear correlation of the δ shape analysis along intramolecular rearrangement pathways

Coord#	Ideal1	Ideal2	Path Sym	Slope	Intercept (°)	R^2	Max Dev. (°)	Max Dev. (%)
4	T_d	D_{4h}	D_{2d}	-1.0004(3)	85.56(1)	0.999999	0.08	0.09
5	D_{3h}	C_{4v}	C_{2v}	-1.0003(6)	27.02(1)	0.999997	0.05	0.19
6	O_h	D_{3h}	D_3	-1.002(1)	45.36(3)	0.999986	0.17	0.38
7	C_{2v}	D_{5h}	C_2	-1.000(1)	27.55(2)	0.999980	0.12	0.44
7	C_{3v}	D_{5h}	C_s	-1.07(3)	28.2(5)	0.990941	3.15	12.0
7	C_{3v}	C_{2v}	C_s	-1.0000(6)	12.429(4)	0.999996	0.02	0.16
8	D_{4d}	D_{2d}	D_2	-1.000(1)	15.23(1)	0.999987	0.05	0.33
8	D_{2d}	C_{2v}	C_2	-1.0002(6)	11.893(4)	0.999996	0.02	0.17
8	D_{4d}	C_{2v}	C_{2v}	-1	8.92	1	0	0
8	D_{2d}	O_h	D_{2d}	-1.0003(4)	30.603(7)	0.999998	0.04	0.13
8	D_{4d}	O_h	D_4	-1.002(1)	31.59(3)	0.999978	0.14	0.44
8	C_{2v}	O_h	C_2	-1.001(1)	33.58(2)	0.999982	0.13	0.39
8	O_h	D_{3h}	D_3	-0.999(1)	45.65(3)	0.999984	0.16	0.35
8	O_h	D_{6h}	D_{3d}	-0.9998(6)	37.09(1)	0.999995	0.07	0.19
9	D_{3h}	C_{4v}	C_{2v}	-1.0002(5)	9.266(3)	0.999997	0.01	0.11

We observe excellent correlation (R > 0.99997) for 14 of the 15 investigated paths. Relative deviations are less than 0.5% and absolute deviations are small. For these 14 paths with good linear correlation we note that the two ideal endpoints share the same external edges. We find a relatively poor correlation for the 7-coordinate C_s path between C_{3v} and D_{5h}, which we ascribe to the difference in external edges between these two shapes. We note here that the maximum deviation occurs near the transition point from one external edge to the other. The perfect correlation found for the 8-coordinate C_{2v} path between D_{4d} and C_{2v} is likely due to the small absolute magnitude of $S(D_{4d},C_{2v})$, since the values of S are reported to the nearest hundredth. From these linear correlations we can define the deviation (Δ) of a real structure, R, from the path between ideal shapes X and Y as follows:

$$\Delta(R,XY) = \frac{\sqrt{2}}{2} * [S(R,X) + S(R,Y) - S(X,Y)] \qquad \textbf{(Equation 2.4)}$$

Similarly, we can define the relative positioning (P) of structure R along a reaction path toward ideal X as a percentage:

$$P(R,X) = \left[\frac{S(R,Y) - \sqrt{2}/2 * \Delta(R,XY)}{S(X,Y)}\right] * 100\% \qquad \textbf{(Equation 2.5)}$$

In the following figure we show a representative visualization of one these 15 intramolecular rearrangement paths. Visualizations of the remaining paths are reported in the supplementary material.

Linear correlation between values of S(X) along intramolecular rearrangement paths
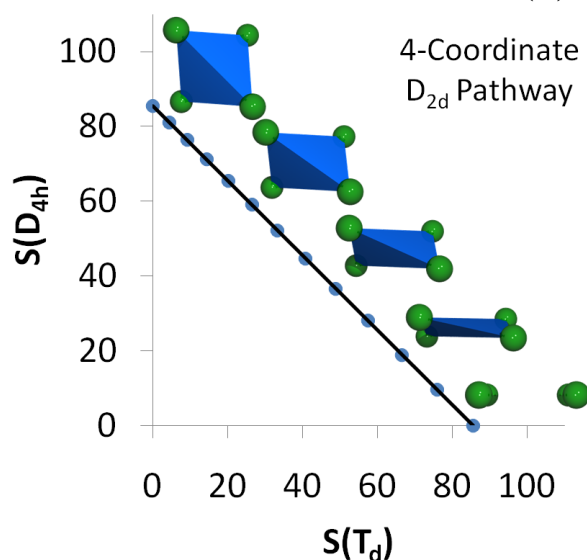
Figure 2.3. 4-Coordinate D_{2d} pathway
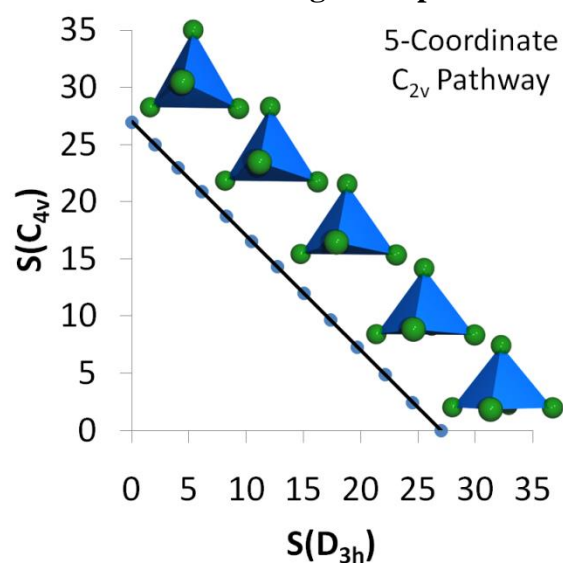
Figure 2.4. 5-Coordinate C_{2v} pathway
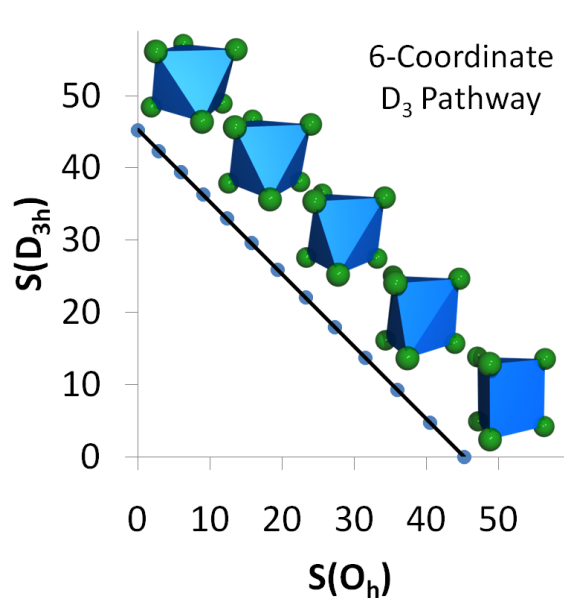
Figure 2.5. 6-Coordinate D_3 pathway
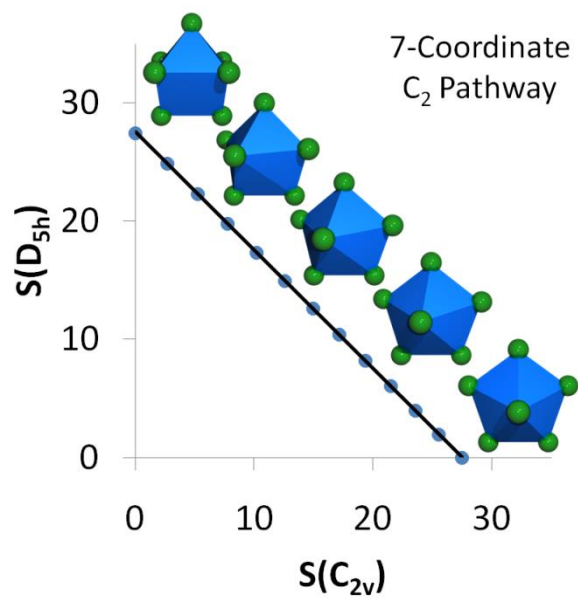
Figure 2.6. 7-Coordinate C_2 pathway
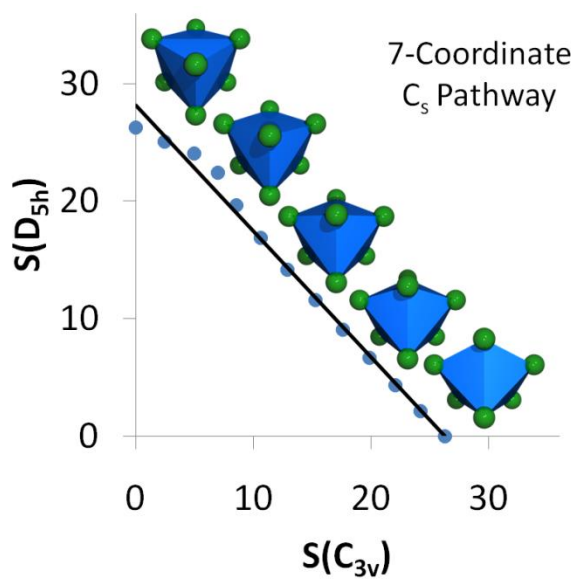
Figure 2.7. 7-Coordinate C_s pathway
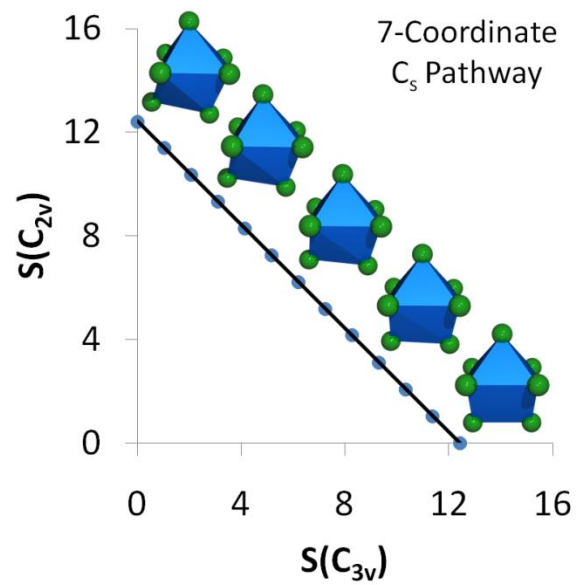
Figure 2.8. 7-Coordinate C_s pathway
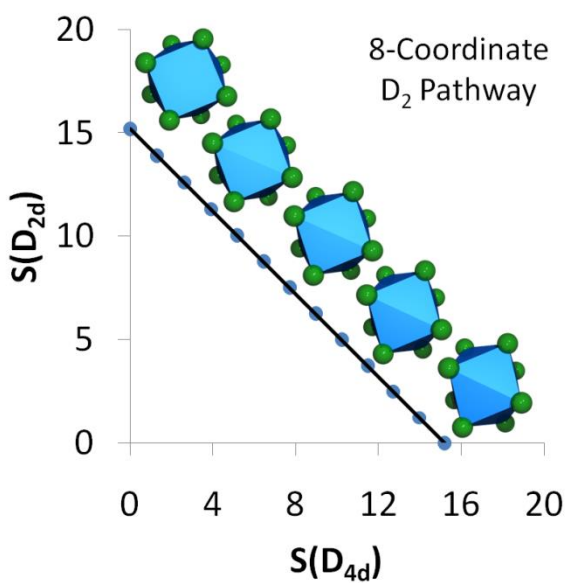
Figure 2.9. 8-Coordinate D_2 pathway
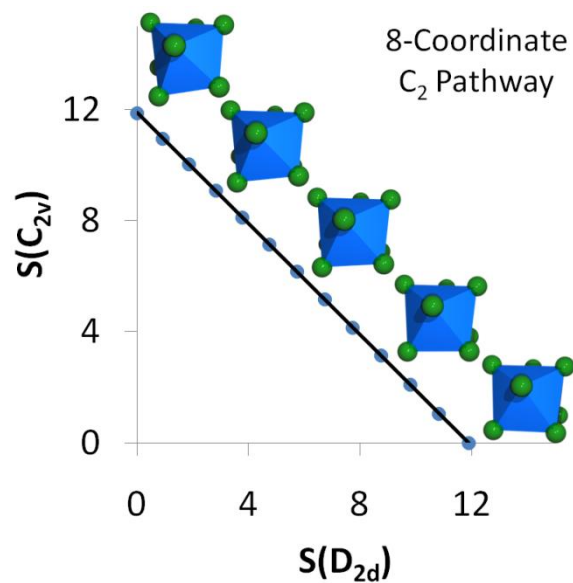
Figure 2.10. 8-Coordinate C_2 pathway
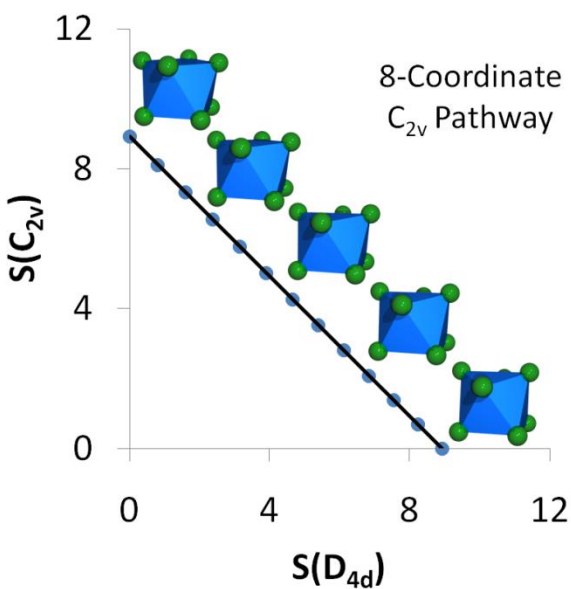
Figure 2.11. 8-Coordinate C_{2v} pathway
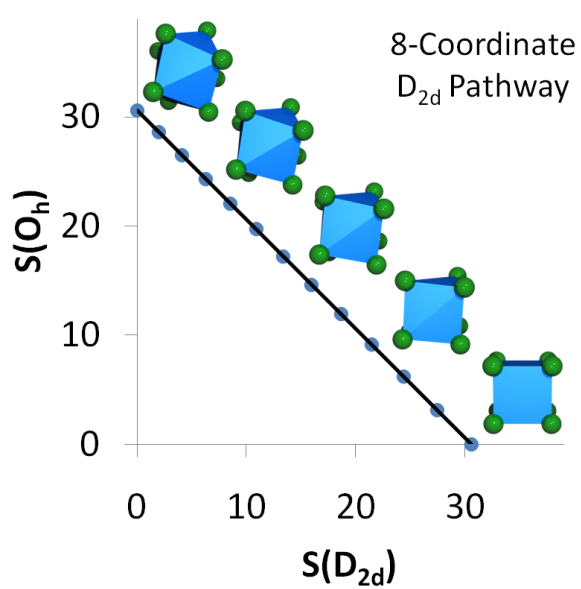
Figure 2.12. 8-Coordinate D_{2d} pathway
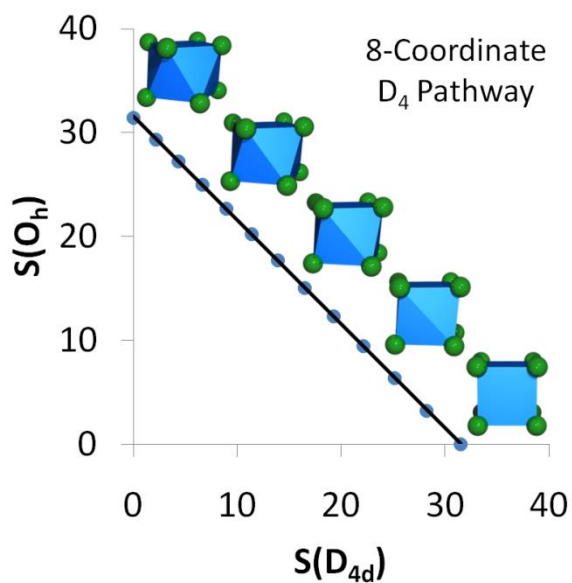
Figure 2.13. 8-Coordinate D_4 pathway
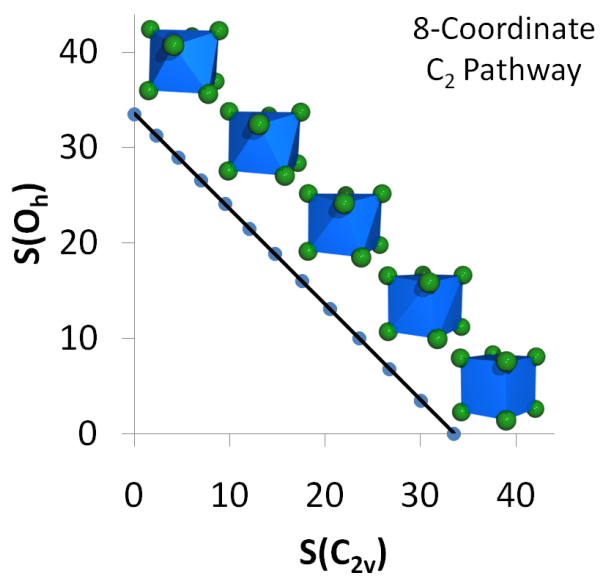
Figure 2.14. 8-Coordinate C_2 pathway
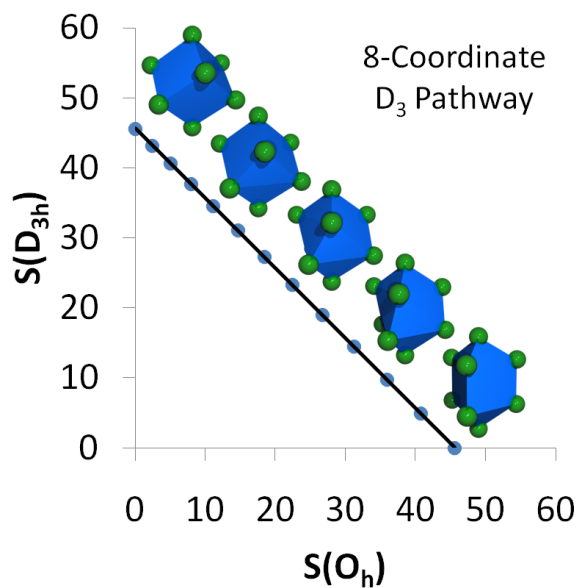
Figure 2.15. 8-Coordinate D_3 pathway
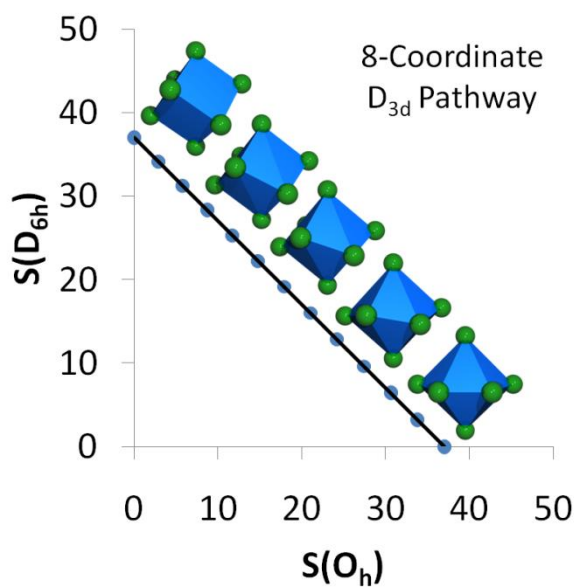
Figure 2.16. 8-Coordinate D_{3d} pathway
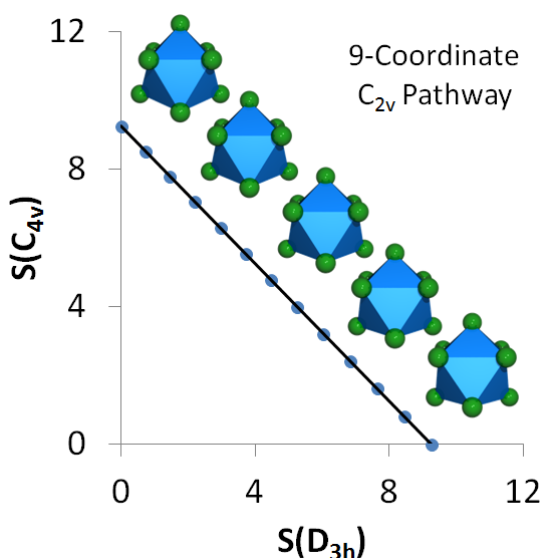
Figure 2.17. 9-Coordinate C_{2v} pathway

Conclusion

We have extended our automated δ angle analysis to coordination numbers four through nine, expanding the scope and transparency of the original eight-coordinate analysis. The choice of ideal shapes was critically analyzed, and we revise our previously reported C_{2v} bicapped trigonal prism to that of Drew's MFP. The issue of bond length differences was addressed by introducing an optional automatic normalization procedure. Equivalence to the parent Muetterties δ analysis has been demonstrated by printing the full set of δ angles for measured and ideal structures. Finally, we find excellent linear correlation between values of S along 14 intramolecular rearrangement pathways, which were used to define deviation (Δ) and path position (P) functions. We have demonstrated that the δ angle criterion, and the shape measures S derived from them are useful metrics for following the paths of intramolecular rearrangements.

References

(1)   Muetterties, E. L.; Guggenberger, L. J. *J. Am. Chem. Soc.* **1974**, *96*, 1748–1756.
(2)   Guggenberger, L. J.; Muetterties, E. L. *J. Am. Chem. Soc.* **1976**, *98*, 7221–7225.
(3)   Porai-Koshits, M. A.; Aslanov, L. A. *J. Struct. Chem.* **1972**, *13*, 244–253.
(4)   Maseras, F.; Eisenstein, O. *New J. Chem.* **1997**, *21*, 961–967.
(5)   Casanova, D.; Cirera, J.; Llunell, M.; Alemany, P.; Avnir, D.; Alvarez, S. *J. Am. Chem. Soc.* **2004**, *126*, 1755–1763.
(6)   Zabrodsky, H.; Peleg, S.; Avnir, D. *J. Am. Chem. Soc.* **1992**, *114*, 7843–7851.
(7)   Zabrodsky, H.; Peleg, S.; Avnir, D. *J. Am. Chem. Soc.* **1993**, *115*, 8278–8289.
(8)   Pinsky, M.; Avnir, D. *Inorg. Chem.* **1998**, *37*, 5575–5582.
(9)   Pinsky, M.; Lipkowitz, K. B.; Avnir, D. *J. Math. Chem.* **2001**, *30*, 109–120.
(10)   Pinsky, M.; Dryzun, C.; Casanova, D.; Alemany, P.; Avnir, D. *J. Comput. Chem.* **2008**, *29*, 2712–2721.
(11)   Cirera, J.; Alemany, P.; Alvarez, S. *Chem. – Eur. J.* **2004**, *10*, 190–207.
(12)   Alvarez, S.; Llunell, M. *J. Chem. Soc. Dalton Trans.* **2000**, 3288–3303.

(13) Alvarez, S.; Avnir, D.; Llunell, M.; Pinsky, M. *New J. Chem.* **2002**, *26*, 996–1009.

(14) Casanova, D.; Alemany, P.; Bofill, J. M.; Alvarez, S. *Chem. – Eur. J.* **2003**, *9*, 1281–1295.

(15) Casanova, D.; Llunell, M.; Alemany, P.; Alvarez, S. *Chem. – Eur. J.* **2005**, *11*, 1479–1494.

(16) Ruiz-Martínez, A.; Casanova, D.; Alvarez, S. *Chem. – Eur. J.* **2008**, *14*, 1291–1303.

(17) Xu, J.; Radkov, E.; Ziegler, M.; Raymond, K. N. *Inorg. Chem.* **2000**, *39*, 4156–4164.

(18) Xu, J.; Whisenhunt, D. W.; Veeck, A. C.; Uhlir, L. C.; Raymond, K. N. *Inorg. Chem.* **2003**, *42*, 2665–2674.

(19) Favas, M. C.; Kepert, D. L. *Prog. Inorg. Chem.* **1980**, *27*, 325–463.

(20) Kepert, D. L. *Prog. Inorg. Chem.* **1977**, *23*, 1–65.

(21) Kepert, D. L. *Prog. Inorg. Chem.* **1979**, *25*, 41–144.

(22) Kepert, D. L. *Prog. Inorg. Chem.* **1978**, *24*, 179–249.

(23) Favas, M. C.; Kepert, D. L. *Prog. Inorg. Chem.* **1981**, *28*, 309–367.

(24) Drew, M. G. B. *Coord. Chem. Rev.* **1977**, *24*, 179–275.

(25) Kouba, J. K.; Wreford, S. S. *Inorg. Chem.* **1976**, *15*, 1463–1465.

(26) Föppl, L. *J. Für Reine Angew. Math. Crelles J.* **1912**, *1912*, 251–302.

(27) Schütte, K.; Waerden, B. L. van der *Math. Ann.* **1951**, *123*, 96–124.

(28) Gillespie, R. J.; Nyholm, R. S. *Q. Rev. Chem. Soc.* **1957**, *11*, 339–380.

(29) Gillespie, R. J. *Can. J. Chem.* **1960**, *38*, 818–826.

(30) Hoard, J. L.; Silverton, J. V. *Inorg. Chem.* **1963**, *2*, 235–242.

(31) Thompson, H. B.; Bartell, L. S. *Inorg. Chem.* **1968**, *7*, 488–491.

(32) Pauling, L. *The Nature of the Chemical Bond and the Structure of Molecules and Crystals: An Introduction to Modern Structural Chemistry*; Cornell University Press, 1960.

(33) Kepert, D. L. *Inorganic stereochemistry*; Springer-Verlag, 1982.

(34) Burdett, J. K.; Hoffmann, R.; Fay, R. C. *Inorg. Chem.* **1978**, *17*, 2553–2568.

(35) Brunton, G. *J. Inorg. Nucl. Chem.* **1967**, *29*, 1631–1636.

(36) Dugat, P.; El-Ghozzi, M.; Metin, J.; Avignant, D. *J. Solid State Chem.* **1995**, *120*, 187–196.

(37) Le Bail, A.; Laval, J.-P. *Eur. J. Solid State Inorg. Chem.* **1998**, *35*, 357–372.

(38) Kay, J.; Moore, J. W.; Glick, M. D. *Inorg. Chem.* **1972**, *11*, 2818–2827.

(39) Bonamico, M.; Dessy, G.; Fares, V.; Scaramuzza, L. *J. Chem. Soc. Dalton Trans.* **1974**, 1258–1263.

(40) Fletcher, S. R.; Skapski, A. C. *J. Organomet. Chem.* **1973**, *59*, 299–307.

(41) Barlic, B.; Golic, L.; Lazarini, F. *Cryst. Struct. Commun.* **1974**, *3*, 407.

(42) Davis, A. R.; Einstein, F. W. B. *Inorg. Chem.* **1974**, *13*, 1880–1884.

(43) Davis, A. R.; Einstein, F. W. B. *Inorg. Chem.* **1975**, *14*, 3030–3035.

(44) Cunningham, J. A.; Sands, D. E.; Wagner, W. F. *Inorg. Chem.* **1967**, *6*, 499–503.

(45) Phillips, T.; Sands, D. E.; Wagner, W. F. *Inorg. Chem.* **1968**, *7*, 2295–2299.

(46) Aslanov, L. A.; Porai-Koshits, M. A.; Dekaprilevich, M. O. *J. Struct. Chem.* **1971**, *12*, 470.

(47) Il'inskii, A. L.; Aslanov, L. A.; Ivanov, V. I.; Khalilov, A. D.; Petrukhin, O. M. *J. Struct. Chem.* **1969**, *10*, 263–266.

(48) Titze, H. *Acta Chem. Scand.* **1974**, *28*, 1079.

(49) Allard, B. *Acta Chem. Scand.* **1976**, *30*, 461.

Chapter 3

**Structure, Kinetics, and Luminescence of Eight-Coordinate
1,2-HOPO Complexes in Solution**

Introduction

As discussed in chapter 1, luminescent lanthanide complexes are important materials for a variety of applications ranging from telecommunications and lighting to biological imaging and assays.[1–9] Lanthanide dyes have several advantageous properties, such as sharp atomic-like emission bands, long-lived luminescence, and relative insensitivity to quenching by molecular oxygen. The 4f-4f transitions responsible for lanthanide luminescence are dipole forbidden by parity, and sometimes by spin, and these selection rules are more rigid than for analogous d-d transitions due to electronic screening of the buried 4f orbitals by the filled 5s and 5p orbitals. The molar absorptivities of the 4f-4f transitions are small, so photoluminescence of lanthanides typically relies on energy transfer from a nearby strongly absorbing chromophore, a process known as the antenna effect. Ideal chromophore containing ligands must also protect the excited lanthanide ion from nonradiative solvent quenching, since high energy O-H bond vibrations present in water and other solvents are particularly efficient quenchers of lanthanide luminescence. Despite all that is known about the important factors governing efficient luminescence, the development of bright complexes that reliably perform in aqueous solution at low concentrations remains an open challenge.

We have previously reported tetradentate ligands based on diamides of 1-hydroxypyridin-2-one (1,2-HOPO, Fig. 3.1), which form very stable (pEu = 18-19) eight coordinate EuL_2 complexes exhibiting bright photoluminescence upon excitation at 330 nm.[10–15] The total quantum yields of previously reported Eu(III) complexes in this family range from 4% to 23% in aqueous TRIS buffer.[14] Here we report the novel 5LImXy-1,2-HOPO ligand (L), which forms an Eu(III) complex with an aqueous quantum yield of 22%. All of our previously reported 1,2-HOPO ligands have similar optical properties (e.g. extinction coefficients, singlet and triplet state energies) indicating that stereochemical effects are likely responsible for the observed differences in quantum efficiency. Structural investigations of luminescent lanthanide complexes are typically limited to solid state XRD crystal structures. However, crystal packing forces can play a dominant role in determining the coordination polyhedron observed in the solid state, since the low energy conformations of eight-coordination (D_{4d}, D_{2d}, C_{2v}) are relatively close in energy. Thirteen new metal complexes of the 5LImXy-1,2-HOPO ligand (**La**, **Ce**, **Pr, Nd, Sm, Eu, Tb, Dy, Ho, Er, Tm, Yb,** and **Lu**) are characterized here by single crystal X-ray diffraction (XRD), DFT, and ^{1}H-NMR. The ^{1}H-NMR isotropic shifts of the paramagnetic complexes were measured in the slow exchange regime to characterize the ground state geometries of these complexes in solution. We demonstrate that the calculated DFT structures, free from the confounding effects of crystal packing, offer a better structural model for rationalizing the ^{1}H-NMR data than do the XRD structures.

Discrete, homoleptic eight-coordinate complexes (like those reported here) are notorious for being stereochemically nonrigid in solution, meaning the energy barriers for reversible intramolecular rearrangement are small enough (less than 20 kcal/mol) to preclude the isolation of stereoisomers at room temperature.[16–19] Eight-coordinate complexes of the form M(bidentate)$_4$ rearrange quickly, but the rearrangement barriers are substantially larger than for examples containing monodentate ligands.[18–24] In some cases, slow exchange of M(bidentate)$_4$ complexes has been observed in solution by ^{1}H-NMR.[25–30] Very low temperatures, nonpolar solvents, and high oxidation state (IV, V. or VI) metals are typically required. Intramolecular rearrangement of eight-coordinate M(bidentate)$_4$ complexes is directly analogous to the Bailar twist rearrangement

of six-coordinate M(bidentate)$_3$ complexes and the tetrahedral inversion of four-coordinate M(bidentate)$_2$ complexes.[31–35] Here we present the first examples of low oxidation state (III) metal complexes with large enough M(bidentate)$_4$-type intramolecular rearrangement barriers to be characterized by ^{1}H-NMR. The barriers associated with intramolecular rearrangement are measured by ^{1}H-NMR selective inversion recovery (SIR) experiments, and the impact of these rearrangement rates on the structure and luminescence of **Eu** is discussed.

Results and Dicussion

Luminescence. Over the past 12 years, our group has reported a family of tetradentate 1,2-HOPO based ligands that form monoanionic eight-coordinate complexes with trivalent lanthanide ions. In general, the ligands are made from previously reported 1,2-HOPOBn thiaz according to Scheme 1.[36] The Eu^{III} complexes of these tetradentate 1,2-HOPO ligands have been found to exhibit bright red luminescence, both as a solid and in buffered aqueous solution. The aqueous quantum yields of previously reported Eu^{III} complexes in this family range from 4% to 23%.[14] The rather large variation in quantum yields is surprising, given that both the singlet and triplet state energies of the previously investigated ligands remain relatively constant. The high energy O-H bond vibrations of water and other solvents are good quenchers of Eu^{III} luminescence, thus bright complexes must use ligands that coordinatively saturate the Eu^{III} metal center. The lower quantum yields of certain 1,2-HOPO complexes we have previously reported can be explained by the presence of a bound water molecule (q=1), Eu^{III} being typically 8- or 9-coordinate with oxygen-sized ligands. We have also reported Eu^{III} complexes that have low quantum yields but no bound water molecules (q=0). For these systems we are forced to conclude that the differences in quantum yields are related to stereochemical differences of the Eu^{III} complexes.
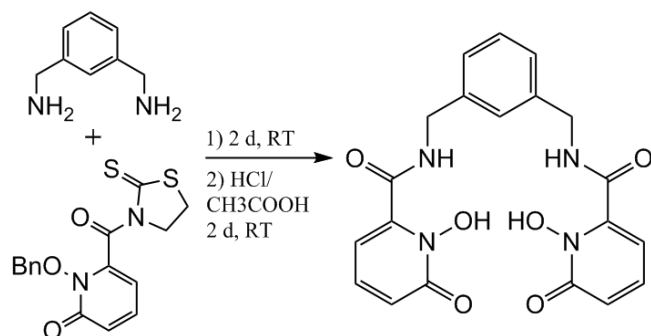
Scheme 3.1. Synthesis of tetradentate 1,2-HOPO ligands

We have previously reported the [Eu(5LIO-1,2-HOPO)$_2$]$^-$ complex with an impressive quantum yield of 0.215 in aqueous solution.[10] Structurally related complexes [Eu(5LI-1,2-HOPO)$_2$]$^-$ and [Eu(5LINMe-1,2-HOPO)$_2$]$^-$ are similarly bright (0.20 and 0.19 respectively).[12] The Eu^{III} complex (**Eu**) of the novel 5LImXy-1,2-HOPO ligand reported here has an aqueous quantum yield of 0.22, making all four of these compounds among the brightest Eu^{III} 1,2-HOPO complexes that we have found. Here we compare the aqueous photophysical parameters found for [Eu(5LIO-1,2-HOPO)$_2$]$^-$ and **Eu**, revealing that they are all nearly equivalent (Table 3.1). We note that the band shapes of the luminescence spectra are also nearly identical (Fig. 3.1). Both complexes exhibit a two band pattern for the $^5D_0$ to $^7F_1$ transition, which is consistent with a D$_{2d}$

dodecahedral ground state structure in solution. We take the correspondence of these values and spectra as evidence that the forthcoming solution state structural conclusions of the [Ln(5LLmXy-1,2-HOPO)$_2$]$^-$ complexes can be extended to [Eu(5LIO-1,2-HOPO)$_2$]$^-$, [Eu(5LI-1,2-HOPO)$_2$]$^-$ and [Eu(5LINMe-1,2-HOPO)$_2$]$^-$. That is, we find it likely that the similarity of the luminescence properties among these structurally related Eu^{III} complexes is consistent with a common ground state structure in solution.

Table 3.1. Comparison of Luminescence Data for [Eu(5LIO-1,2-HOPO)$_2$][NMe4][10] and [Eu(5LImXy-1,2-HOPO)$_2$][NMe$_4$] (**Eu**)

	Eu	[Eu(5LIO-1,2-HP)$_2$]$^-$
λ_{max} (nm)	333	333
ε_{max} (M^{-1}cm^{-1})	22000	19000
Φ_{total} in H$_2$O	21.8 ± 0.2 %	21.5 ± 3 %
τ_{obs} in H$_2$O (μs)	733 ± 3	727 ± 1.2
τ_{obs} in D$_2$O (μs)	1022 ± 3	1012 ± 2.5
Calcd τ_{rad} (μs)	1730	1640
Calcd k_{rad} (s^{-1})	577	609
Calcd k_{nonrad} (s^{-1})	789	807
η_{Eu}	0.422	0.443
η_{sens}	0.504	0.485
q	0.1	0.1
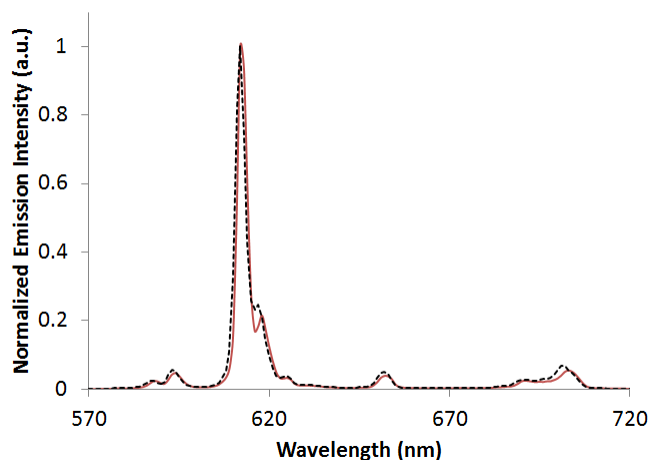
Figure 3.1. Comparison of Luminescence Spectra for [Eu(5LIO-1,2-HOPO)$_2$]$^-$ (dashed) and **Eu** (solid) in aqueous solution.

Structure. The stereochemistry of eight-coordination has been extensively reviewed over the years.[37–43] For spherical eight-coordinate ions, i.e. excluding ions containing linear moieties like the actinyls, there are three commonly encountered coordination geometries: the D$_{4d}$ square antiprism (SAP), the D$_{2d}$ trigonal face dodecahedron (DD), and the C$_{2v}$ bicapped trigonal prism (BCTP). For the DD, SAP, and BCTP, defining each idealized shape requires the determination of one or more shape parameters, since the eight ligand positions are not uniquely defined by their respective symmetries. In order to derive these shape parameters, the repulsion energy model was adapted from the Born-Lande equation by Hoard and Silverton, and later expanded by Kepert and others, shown below.[37,38]

31

$$U = \sum r_{ij}^{-n} \text{ for } i > j \qquad \textbf{(Equation 3.1)}$$

Minimizing the value of U maximizes the ligand-ligand distances (r_{ij}). The maximum values of these L-L distances are limited by constraining all ligands to ride the surface of a unit sphere. The repulsion energy model is directly related to the hard sphere model (HSM) that many authors rely on for ideal shapes. The Born exponent (n) applicable to most ligands falls between n=4 and 12, while the HSM represents an unrealistic repulsion potential of n=∞. Following Kepert's suggestion, we choose n=6 for our modeling here.[44] In addition to defining the ideal shapes of a given symmetry, the repulsion energy model is useful for testing the effects of additional positional constraints. Rigid bidentate ligands, for example, have a fixed bite distance between the two coordinating atoms, as is the case with the 1,2-HOPO ligand family. The normalized bite is defined as the distance between bidentate donors atoms (L-L) divided by the average M-L distance. The repulsion energy minimum can be calculated as a function of normalized bite for each crystal structure reported here (**La** through **Lu**). The shape analyses of these repulsion energy minimized structures are plotted as a function of normalized bite in the following figure.
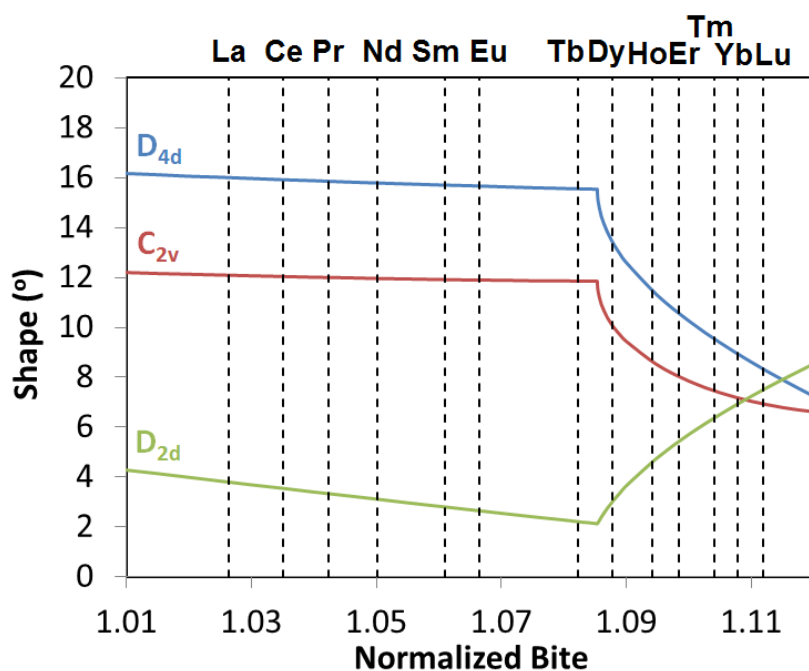
Figure 3.2. Shape analysis of repulsion energy minimized structures as a function of normalized bite. Dashed lines represent the normalized bite determined from each XRD structure reported here.

As the normalized bite is decreased, the repulsion energy minimum approaches the tetrahedral limit at b=0. Bites ranging from 0 to 1.08 show a clear DD shape with a corresponding *mmmm* ligand wrapping pattern. As the normalized bite is further increased, the minimum structure begins to shift towards the *ssss*-SA, coincident with the $c_1c_1h_2h_2$- and $c_1h_2c_1h_2$-BCTPs. All of these structures are related by very small atomic displacements known as Hoard-Silverton rearrangements, and they are the most likely candidates for the ground state structure of an M(bidentate)$_4$ complex within the normalized bite range considered. As M(tetradentate)$_2$ systems, the compounds reported here are slightly more complicated than the

M(bidentate)$_4$ case, in that the direction of the distortion changes the possible ligand wrapping patterns. The complexes reported here are best thought of as an M(bidentate)$_4$ system with a flexible linker connecting two pairs of bidentate ligands together. For instance, the *mmmm*-DD wrapping pattern for M(bidentate)$_4$ complexes becomes the *mgm,mgm*-DD wrapping pattern for the M(tetradentate)$_2$ system reported here. Depending on the direction of distortion from DD, the *ssss*-SA becomes either the *sss,sss*-SA or the *sls,sls*-SA. The $c_1c_1h_2h_2$- and $c_1h_2c_1h_2$-BCTP become $c_1c_1c_1,h_2v_2h_2$- and $c_1h_1h_2,c_1h_1h_2$-BCTP respectively.
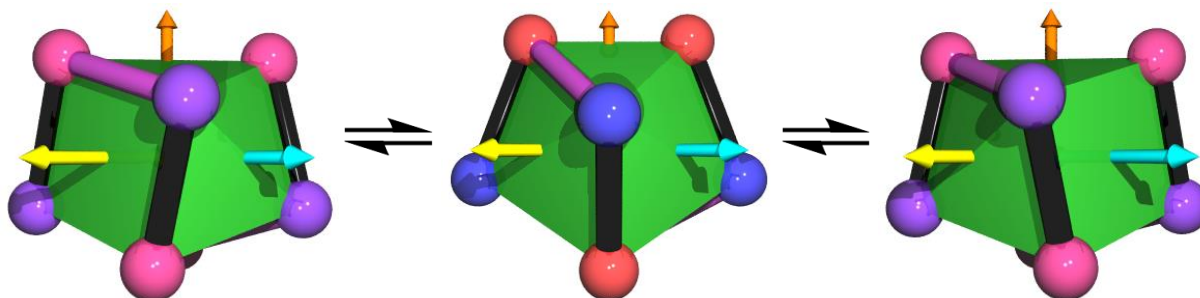
Figure 3.3. The *mgm,mgm*-DD (center) is converted to the *sss,sss*-SA (left) or the *sls,sls*-SA (right). The DD high symmetry axis is shown in orange, while the SA axes are shown in yellow (left) and cyan (right). 1,2-HOPO chelates are represented by black bars, *m*-xylyl backbones by magenta bars.

All twelve complexes reported here crystallize in monoclinic P2$_1$/c or the P2$_1$/n setting, with similar cell constants, cell volumes, calculated densities, and solvent content. As a representative example, the ORTEP of **Lu** is provided.
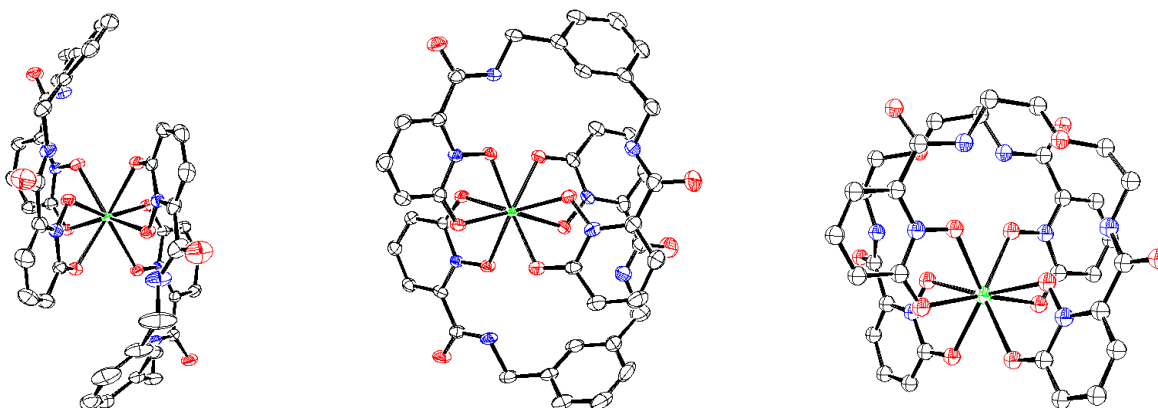
Figure 3.4. ORTEP of **Lu** (left and middle) and [Sm(5LIO-1,2-HOPO)$_2$]$^-$ drawn at 50% probability, counterion and hydrogen atoms have been removed for clarity. **Lu** has a trans orientation of the connecting *m*-xylyl backbones while [Sm(5LIO-1,2-HOPO)$_2$]$^-$ has a cis configuration.[12]

The complexes sit on general positions (Z=4), with no imposed crystallographic symmetry. Superimposing the crystal structures (Fig. 3.5) reveals that the two ligands are more distinguishable in the earlier lanthanide (**Sm, Nd**, **Pr**, **Ce**, and **La)** structures than in the later lanthanide (**Eu**, **Tb**, **Dy**, **Ho**, **Er**, **Tm**, **Yb**, and **Lu**) structures.
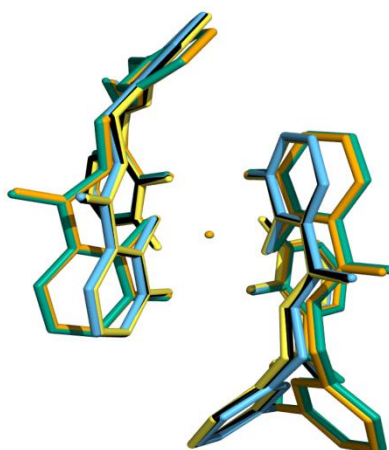
Figure 3.5. Superimposed XRD crystal structures of **La** (blue-green), **Sm** (orange), **Eu** (sky blue), **Ho** (black), and **Lu** (yellow)

In the crystal structures of the later lanthanide complexes, the *m*-xylyl backbones of both ligands bend towards the opposing ligands, while in the earlier lanthanide complexes the *m*-xylyl backbone of one ligand bends away from the opposing ligand. The ^{1}H-NMR spectra of all twelve complexes are consistent with a single preferred geometry in solution having two indistinguishable ligands related by C_2 symmetry. DFT geometry optimizations of the earlier lanthanide complexes reveal a small preference (1.4 kcal/mol on average) for the more symmetric C_2 geometry of the later lanthanide complexes. The calculated transition state between the two *m*-xylyl backbone orientations (1.9 kcal/mol on average) was also found to be small for the entire lanthanide series. Consequently, the less symmetric orientation found in the crystal structures of the earlier lanthanides may be attributed to crystal packing effects.

The crystal structures confirm that the *m*-xylyl backones are in opposing (trans), rather than adjacent (cis) positions (Fig. 3.4). We have previously reported examples of both cis and trans orientations for related luminescent 5LI-type 1,2-HOPO complexes.[12] The presence of only the trans orientation here is likely due to the cis form having unfavorable steric interactions between the two *m*-xylyl backbone rings. The trans isomer was calculated as 2.8 kcal/mol lower in energy than the cis isomer for **Eu**. Although only the trans isomer is found, the complexes are chiral and crystallize as a racemate. Only the Λ enantiomers are shown in Figure 3.4. Like the nearest dodecahedral structure, the oxygen donors are split into four apical A and four equatorial B sites. No significant difference in average M-O bond length was observed between these A and B sites ($0.99 <$ M-O$_B$/M-O$_A < 1.01$). Additionally, no difference was observed between average M-ON and M-OC bond lengths ($1.00 <$ M-ON/M-OC < 1.01), supporting the notion that both types of pyridyl oxygen donors are equally anionic (Table 3.2).

Table 3.2. Structure and Shape Analysis for the 5LImXy-1,2-HOPO Ln complexes found for by XRD and DFT derived coordinates.

Complex	M-O (Å)	M-ON/ M-OC	M-O$_B$/ M-O$_A$	φ Twist (deg.)	Muetterties δ Angles (deg.)				δ Shape Measure (deg.)		
									D$_{4d}$	C$_{2v}$	D$_{2d}$
D$_{4d}$ (n=6 ideal)	-	1	1	24.4	0,	0,	51.4,	51.4	0	8.92	15.20
C$_{2v}$ (Drew MFP)	-	1	1	15.9	0,	26.6,	46.5,	46.5	8.92	0	11.88
D$_{2d}$ (n=6 ideal)	-	1	1	0	29.9,	29.9,	29.9,	29.9	15.20	11.88	0
La XRD	2.49	1.00	0.99	8.6, 10.8	22.0,	25.6,	44.1,	49.5	12.74	9.07	10.01
Ce XRD	2.47	1.00	1.01	8.0, 10.4	21.8,	26.1,	43.8,	48.7	12.87	9.03	9.64
Pr XRD	2.45	1.00	1.01	8.2, 10.9	21.9,	26.2,	43.9,	48.8	12.70	8.87	9.62
Nd XRD	2.43	1.00	0.99	8.4, 11.1	21.3,	26.2,	44.3,	49.1	12.65	8.73	9.77
Sm XRD	2.41	1.01	1.00	8.3, 11.1	21.6,	26.4,	44.5,	48.6	12.48	8.54	9.36
Eu XRD	2.40	1.00	1.00	11.3, 14.5	17.6,	20.5,	46.5,	49.0	10.29	7.47	10.28
Tb XRD	2.36	1.00	1.01	11.6, 14.2	17.3,	21.5,	47.1,	48.7	10.29	7.14	10.12
Dy XRD	2.35	1.00	1.01	11.9, 14.5	17.3,	21.8,	47.5,	48.5	10.29	7.13	10.23
Ho XRD	2.34	1.00	1.01	12.2, 14.5	17.5,	21.8,	47.9,	48.7	10.27	7.12	10.26
Er XRD	2.33	1.01	1.01	12.4, 14.7	17.6,	21.6,	48.1,	48.7	10.17	7.10	10.25
Tm XRD	2.32	1.00	1.01	12.4, 14.4	17.9,	21.5,	48.1,	48.5	10.19	7.18	10.12
Yb XRD	2.31	1.01	1.01	13.0, 14.9	17.3,	21.0,	48.3,	48.6	9.88	7.01	10.24
Lu XRD	2.30	1.01	1.01	12.9, 15.0	17.3,	21.0,	48.5,	48.6	9.77	6.91	10.14
La DFT	2.54	1.00	1.01	5.9, 6.1	30.7,	30.8,	40.6,	46.4	15.60	11.64	9.67
Ce DFT	2.52	1.00	1.01	5.8, 6.0	30.7,	30.8,	40.5,	45.9	15.52	11.56	9.41
Pr DFT	2.50	1.00	1.01	5.7, 5.9	30.7,	30.7,	40.5,	45.5	15.37	11.40	9.13
Nd DFT	2.49	1.00	1.01	5.7, 5.9	30.6,	30.6,	40.6,	45.2	15.24	11.27	8.88
Sm DFT	2.46	1.00	1.01	5.7, 5.9	30.2,	30.4,	40.7,	44.6	14.97	11.01	8.45
Eu DFT	2.44	1.00	1.01	5.7, 5.9	30.1,	30.3,	40.6,	44.3	14.85	10.88	8.22
Tb DFT	2.41	1.00	1.01	5.7, 5.9	29.7,	30.0,	40.7,	43.7	14.59	10.64	7.85
Dy DFT	2.40	1.00	1.01	5.8, 5.9	29.6,	29.8,	40.7,	43.5	14.47	10.54	7.68
Ho DFT	2.39	1.00	1.01	5.8, 6.0	29.5,	29.7,	40.8,	43.3	14.36	10.44	7.52
Er DFT	2.38	1.00	1.01	5.9, 6.0	29.3,	29.5,	40.8,	43.1	14.25	10.35	7.37
Tm DFT	2.37	1.00	1.01	5.9, 6.1	29.1,	29.3,	40.8,	42.9	14.14	10.25	7.24
Yb DFT	2.35	1.00	1.01	6.0, 6.1	29.0,	29.1,	40.8,	42.8	14.03	10.17	7.11
Lu DFT	2.34	1.00	1.01	6.1, 6.2	28.8,	28.9,	40.9,	42.7	13.90	10.07	7.00

The DFT calculated structures have average M-O bond lengths that are 4 to 5 pm longer than those found by XRD. Shape analysis indicates that the XRD structures are all closest to the C$_{2v}$ $c_1c_1c_1,h_2v_2h_2$-BCTP, while the DFT structures are closest to the D$_{2d}$ *mgm,mgm*-DD. The *sss,sss*-SA is the closest D$_{4d}$ square antiprism found for both the XRD and DFT coordinates.

Since we are most interested in the structures of the lanthanide complexes in solution, we now turn to ^{1}H-NMR to sort out which structural model (XRD or DFT) is most representative of the solution state data. The amide-methylene coupling system is electronically isolated from the aromatic ring protons of the connecting backbone and from the protons on the HOPO rings, which yields easily interpreted coupling patterns in the ^{1}H-NMR spectra, shown for **Lu** in Fig. 3.6 as a representative plot. The ^{1}H-NMR spectra of the remaining complexes are available in the SI. The bilateral symmetry of the 5LI*m*Xy-1,2-HOPO ligand is broken when bound to the metal, and the two ligands are related by a C$_2$ symmetry axis. Consequently there are two amide

resonances (11.77 and 13.47 ppm), four *m*-xylyl resonances (8.13 to 8.56 ppm), six HOPO resonances (6.28 to 8.26 ppm), and four diasteriotopic methylene resonances (4.84 to 6.14 ppm) for **Lu** at room temperature. In total, there are five isolated coupling systems. Two sets of HOPOs in an ABX pattern, two sets of methylenes/amides in an AMX pattern, and 1 set of aromatic protons in an ABMX pattern. There is a significant upfield shift (1.22 ppm) of HOPO resonance L compared to its exchange partner K, which is attributed to the ring current of the aromatic *m*-xylyl backbones. In the DFT minimized structure of **Lu**, HOPO resonance L is only 3.64 Å from the *m*-xylyl ring centroid. Assignment of HOPO resonance L is critical for assigning the rest of the HOPO resonances.
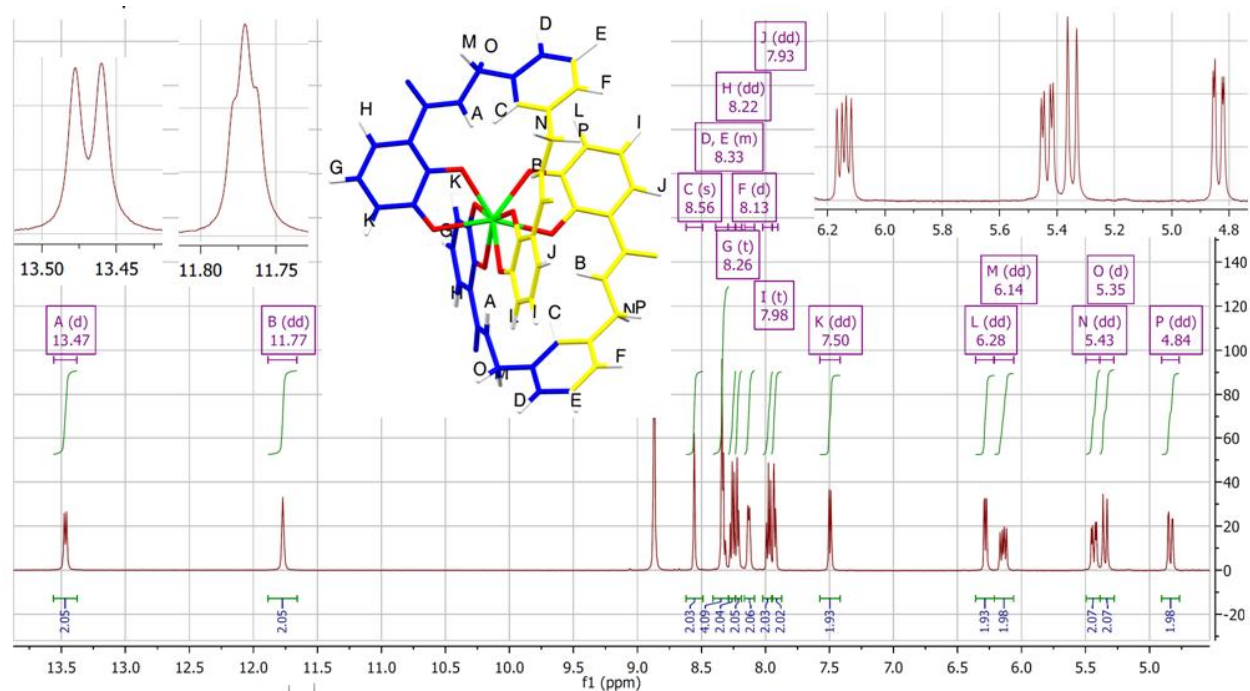
Figure 3.6. . ^{1}H-NMR spectra and assignments for **Lu** at -15 °C, 500 MHz, 1:2 DMF:acetone

Assignment of the amide and methylene resonances is made possible by considering the coupling between them. Each methylene resonance appears as an AMX doublet of doublets, with one large $^2J_{HH}$ coupling constant for the geminal partner and a smaller $^3J_{HH}$ coupling constant for the adjacent amide. The $^3J_{HH}$ methylene-amide coupling constants contain important structural information, since the methylene carbons participate in the only rotatable bonds of the complex. The amide function maintains planarity with the HOPO ring due to strong hydrogen bonding between the amide hydrogen and pyridine oxide. Amide protons A and B are inequivalent in regard to their coupling with the vicinal methylene protons. Amide proton A couples strongly to proton M, but hardly at all to proton O. Amide B on the other hand, couples about equally strong to protons N and P. The strength of amide-methylene [1]H-^{1}H coupling depends upon the H-C-N-H dihedral angle according to the well-known Karplas equation. These four coupling constants were calculated by DFT for **Lu**, and they are compared to experimental values below (Table 3.3).

Table 3.3. Summary of observed and calculated coupling constants for **Lu** at -15 ^{o}C

	Observed $^3J_{HH}$ (Hz)	DFT Calcd. $^3J_{HH}$ (Hz)	Dihedral Angles DFT (^{o})	Dihedral Angles XRD (^{o})
H_A-H_M	9.0	8.6	165.8	136.9
H_A-H_O	<0.5	0.3	78.4	105.0
H_B-H_N	4.5	2.1	122.6	119.3
H_B-H_P	2.9	2.4	122.5	122.8

Having the largest ^3J coupling constant, resonance M was assigned by considering which methylene had an H-C-N-H dihedral angle closest to 180° in the XRD and DFT structures. The remaining three methylenes are assigned with the aid of COSY and EXSY spectra (see Appendix 3). The reasonable agreement between calculated and observed coupling constants indicates that the DFT minimized geometry is a good structural model for **Lu** in solution.

As mentioned above, the XRD and DFT structures are closest to the $c_1c_1c_1,h_2v_2h_2$-BCTP, the *mgm,mgm*-DD and the *sss,sss*-SA coordination geometries. The DD is distinguishable from the BCTP and SA in regard to the direction of the high symmetry axis. That is, the high symmetry axes for the BCTP and SA are coincident, and they are both perpendicular to the high symmetry axis for the DD geometry (Fig. 3.3). By modeling the ^{1}H-NMR isotropic shifts, the orientation of the magnetic easy axis can be evaluated, and the best-fit assignment of that orientation can help discriminate between the possible geometrical forms of these complexes in solution. An isotropic shift is defined as the total displacement (in ppm) of a resonance in a paramagnetic substance relative to the same resonance in an analogous diamagnetic compound.[45] Isotropic shifts are composed of two components, the through-space dipolar pseudocontact shifts and the through-bond Fermi contact shifts. Fermi contact shifts are large and important for paramagnetic transition metal complexes, since the *d*-orbitals orbitals containing the unpaired spin can participate directly in bonding with ligands. Unpaired spin in paramagnetic lanthanides is localized in the *4f* orbitals, so contact shifts are regarded as negligible beyond the primary coordination sphere for most lanthanide systems. As many authors have done previously, we neglect to treat the contact shifts in our fitting procedure, making the assumption that the isotropic shifts are dominated by the dipolar contributions.[46–49] The ^{1}H-NMR dipolar shifts depend on the angle (θ) between the magnetic axis and the M-H vector, and the shifts are inversely proportional to the cube of the M-H distance (*r*). The equation that governs this angular dependence is shown below.

$$\delta_{dip} = D_1 \frac{(3\cos^2\theta - 1)}{r^3}$$ **(Equation 3.1)**

Unambiguous assignment of the **Eu** and **Sm** ^{1}H-NMR spectra was made possible by EXSY and COSY characterization. Moving towards more paramagnetic metals broadens away the apparent coupling constants of each peak, and the COSY signals drop off accordingly. However, the EXSY signals between exchange partners remains strong, and these proved vital for assigning the remaining lanthanide complexes. Once assignments were made, the isotropic shifts were all calculated using the shifts of **Lu** as the diamagnetic reference. The following table summarizes the observed isotropic shifts for each resonance.

Table 3.4. Summary of observed ^{1}H-NMR isotropic shifts

^{1}H	Pr	Nd	Sm	Eu	Tb	Dy	Ho	Er	Tm	Yb
A	-54.93	-17.35	-1.58	18.45	-252.16	-237.82	-74.25	41.12	80.66	27.39
B	17.58	16.52	1.92	-10.11	136.05	93.35	72.48	-8.09	-73.49	-22.63
C	-13.98	-3.26	-0.27	4.41	-59.76	-72.23	-19.34	14.73	17.26	7.75
D	-8.71	-2.63	-0.05	3.40	-37.20	-36.62	-12.25	6.88	13.03	4.74
E	-4.33	-0.87	-0.04	1.78	-16.78	-18.00	-5.05	4.17	5.81	2.29
F	-1.55	0.89	-0.01	0.51	-1.01	-5.92	2.02	3.07	-1.73	-0.04
G	9.48	4.97	0.50	-5.13	40.33	31.87	17.25	-5.86	-20.06	-6.40
H	4.02	2.76	0.34	-2.36	5.39	14.07	1.93	-1.91	-6.97	-1.56
I	0.89	2.73	0.17	-2.03	8.69	-0.17	6.40	-0.72	-3.80	-1.77
J	6.57	4.91	0.53	-3.49	29.22	31.71	11.63	-3.23	-10.89	-3.64
K	15.46	5.97	0.84	-3.30	80.68	75.57	32.15	-6.71	-24.26	-8.78
L	-18.34	-6.35	-0.53	8.42	-73.02	-67.06	-21.29	12.18	25.64	8.59
M	-9.27	-2.54	-0.23	3.03	-45.10	-41.44	-13.36	7.39	15.05	5.15
N	2.76	2.92	0.31	-1.50	17.14	13.25	10.64	0.77	-8.70	-2.85
O	-17.21	-5.51	-0.52	6.23	-73.78	-73.01	-24.26	12.28	23.91	8.65
P	1.74	3.62	0.44	-1.47	24.77	12.59	14.27	1.6	-15.34	-4.12

Note that the lanthanide complexes can be split into two different groups based on the direction of the isotropic shift for each resonance. The shifts for **Pr**, **Nd**, **Sm**, **Tb**, **Dy**, and **Ho** are all similar in sign, while the shifts for **Eu**, **Er**, **Tm**, and **Yb** are in the opposite direction, as expected. Nonlinear least squares fitting of these shifts to the equation shown above was performed by minimizing the agreement factor, R, shown below

$$R = \sqrt{\frac{\sum(\delta_{iso}^{obs} - \delta_{dip}^{calc})^2}{\sum(\delta_{iso}^{obs})^2}}$$ **(Equation 3.2)**

Amide resonances A and B, show the largest isotropic shifts, ranging from -252 to 136 ppm for **Tb**. These especially large ^{1}H-NMR shifts are a result of short M-H distances (3.85 Å). At such short distances, the contact shifts contribute significantly to the observed isotropic shift. Since these large contact shifts cannot be easily quantified, we have omitted the amide peaks from our fitting procedure. By minimizing the agreement factor R, we have fit the isotropic shift data along the three possible axis choices.

Table 3.5. Fitting the isotropic shifts to the three possible high symmetry axes

		Pr	Nd	Sm	Eu	Tb	Dy	Ho	Er	Tm	Yb
S_4	D_1	-2124	-729	-71	768	-9464	-9339	-3228	1513	3135	1140
	R	0.203	0.517	0.595	0.430	0.230	0.146	0.364	0.275	0.380	0.287
C_2	D_1	3168	1168	115	-1139	14787	14396	5205	-2236	-4954	-1799
	R	0.441	0.538	0.600	0.568	0.359	0.349	0.385	0.487	0.439	0.371
S_8	D_1	4059	1259	121	-1478	16983	17084	5525	-2925	-5535	-2018
	R	0.447	0.707	0.757	0.557	0.557	0.502	0.648	0.458	0.625	0.586

It is clear from the one parameter fits that the best choice for the magnetic easy axis is the S_4 axis of the *mgm,mgm*-DD. Interestingly, the closest alternative structures identified for the XRD and DFT coordinates ($c_1c_1c_1,h_2v_2h_2$-BCTP and *sss,sss*-SA) have high symmetry axes coincident with the S_8 axis in Table 3.5, representing the worst possible fit to the isotropic shift data. The difference between these two possible high symmetry axes can also be shown in the following two parameter fit. Now, the orientation of the magnetic easy axis is allowed to rotate about the C_2 symmetry axis relating the two ligands. An α angle of 0 (or 180) corresponds to the S_4 axis shown above, while an α angle of 90 (or 270) corresponds to the S_8 axis.

Table 3.6. Fitting the isotropic shifts to the two parameter model

		Pr	Nd	Sm	Eu	Tb	Dy	Ho	Er	Tm	Yb
	D1	-2234	-819	-80	861	-9847	-9496	-3356	1507	3415	1190
S_4	α	5.4	10.2	10.2	9.9	4.5	2.2	4.5	-0.6	8.1	4.8
	R	0.123	0.439	0.536	0.322	0.187	0.132	0.343	0.274	0.301	0.252

The R value predictably improves with the addition of the extra fitting parameter. The values found for α range from 10.2 to -0.6, which are all clearly much closer to 0 than 90. Both of these fitting procedures are consistent with a common *mgm,mgm*-DD structure in solution for these lanthanide complexes.

SIR experiments. The analogy between previously reported M(bidentate)$_4$ systems and our M(tetradentate)$_2$ system reported here is supported by the presence of a common DD ground state geometry. We now turn our focus to the kinetic behavior of these lanthanide complexes in solution. As a representative plot, the variable temperature of **Lu** is provided.
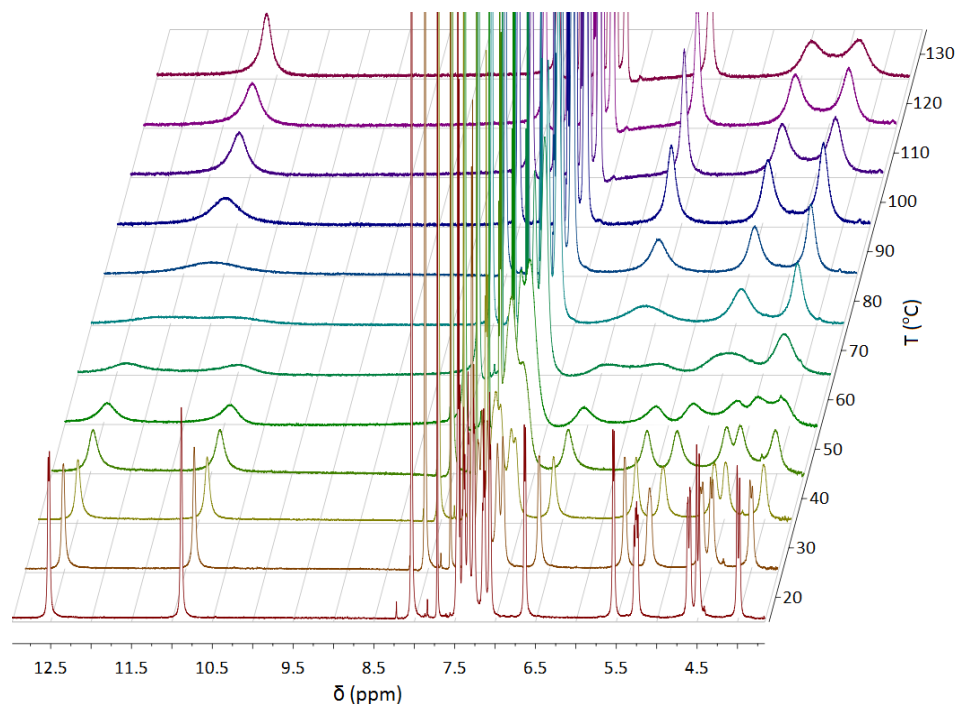
Figure 3.7. VT ^{1}H-NMR Spectrum of **Lu** in d$_7$-DMF

From the VT plot, we note that there are two exchange processes present. The two processes can be most easily distinguished by their respective effects on the methylene resonance peaks. For the low temperature process (LTP), methylene protons M and O are exchanged (likewise N and P are exchanged), but neither M nor O exchanges with N and P. For the high temperature process (HTP), all four methylenes are exchanged. Similar to the tetrahedral inversion of $M(bidentate)_2$ complexes reported previously, we take the lack of full exchange between methylenes for the LTP as evidence of an intramolecular mechanism.

The kinetics of the LTP were followed by selective inversion recovery for all complexes excepting **La**, **Pr**, and **Nd**, which were too stereochemically nonrigid to measure within the solvent temperature window. The Eyring plot and corresponding linear fits reveal that the slope of **Sm** is significantly different from the rest of the metals (Fig. 3.8).
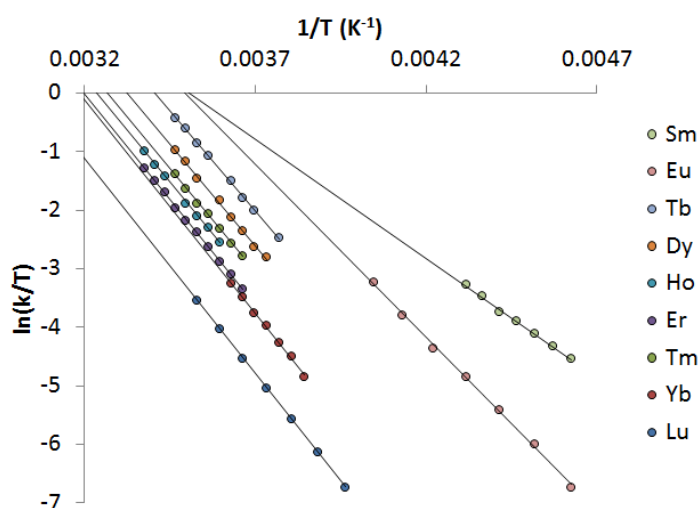
Figure 3.8. Eyring plot for **Sm**, **Eu**, **Tb**, **Dy**, **Ho**, **Er**, **Tm**, **Yb**, and **Lu**.

Table 3.7. Linear fits of the kinetic data and the activation constants derived from them

	Sm	**Eu**	**Tb**	**Dy**	**Ho**	**Er**	**Tm**	**Yb**	**Lu**
Slope	-4070	-5910	-6840	-6950	-7080	-7200	-7040	-7290	-7340
Intercept	14.3	20.6	23.3	23.1	22.9	23.0	23.0	23.2	22.4
R	0.998	0.9990	0.9990	0.998	0.9995	0.9997	0.998	0.998	0.99995
$\Delta H^{\ddagger}$	8.1(2)	11.7(2)	13.6(2)	13.8(3)	14.1(1)	14.30(8)	14.0(3)	14.5(3)	14.57(4)
$\Delta S^{\ddagger}$	-18.8(7)	-6.2(7)	-0.9(7)	-1.3(10)	-1.7(5)	-1.5(3)	-1.6(10)	-1.0(12)	-2.8(2)
$\Delta G^{\ddagger}$ (298 K)	13.7	13.6	13.9	14.2	14.6	14.7	14.4	14.8	15.4

From the kinetic data, we observe that the $\Delta G^{\ddagger}$ for the intramolecular rearrangement is relatively constant across the lanthanide series. From **Tb** to **Lu** the $\Delta S^{\ddagger}$ values are slightly negative and very close to zero, consistent with the intramolecular exchange process involving no change in coordination number for these metals (eight-coordinate transition state). As a result, the $\Delta G^{\ddagger}$ is primarily enthalpic from **Tb** to **Lu**, which begins to change at **Eu** (Fig. 3.9). The $\Delta S^{\ddagger}$ value for **Sm** is relatively large and negative, which implies that **Sm** has a more crowded

transition state. Increasing the metal size from **Lu** to **Sm** yields more available surface area for solvent to coordinate. The significantly different kinetics of **Sm** are indicative of a 9-coordinate, solvent-assisted transition state during intramolecular rearrangement. Therefore **Eu** marks the inflection point between these two extreme cases.
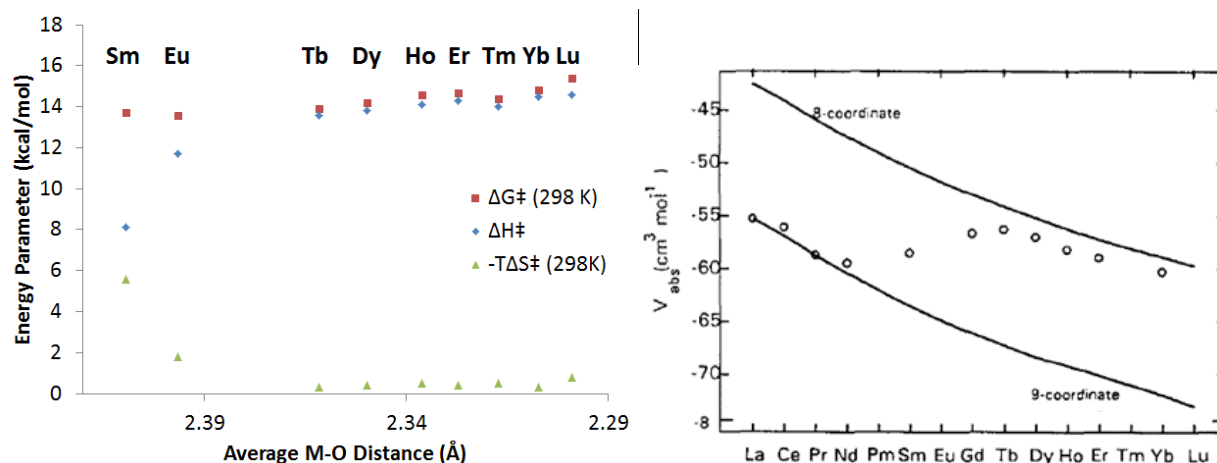
Figure 3.9. Plot of activation energy parameters versus the average M-O distance for each complex, compared to absolute partial molar volumes of the Ln^{III} aqua ions in $LnCl_3$ solutions.[50]

The sudden change in $\Delta S^{\ddagger}$ is reminiscent of the change in V_{abs} for the lanthanide aquo ions found by Merbach and coworkers.[50] These authors found that Sm and Eu span the gap between eight and nine coordination in aqueous solution. The size of Eu is in a special position within the lanthanide series, particularly when paired with all oxygen donors as in these two examples. This critical size helps explain why relatively small changes to the ligand backbone result in a 9-coordinate ground state for previously reported $[Eu(4LIoXy-1,2-HOPO)_2]^-$.
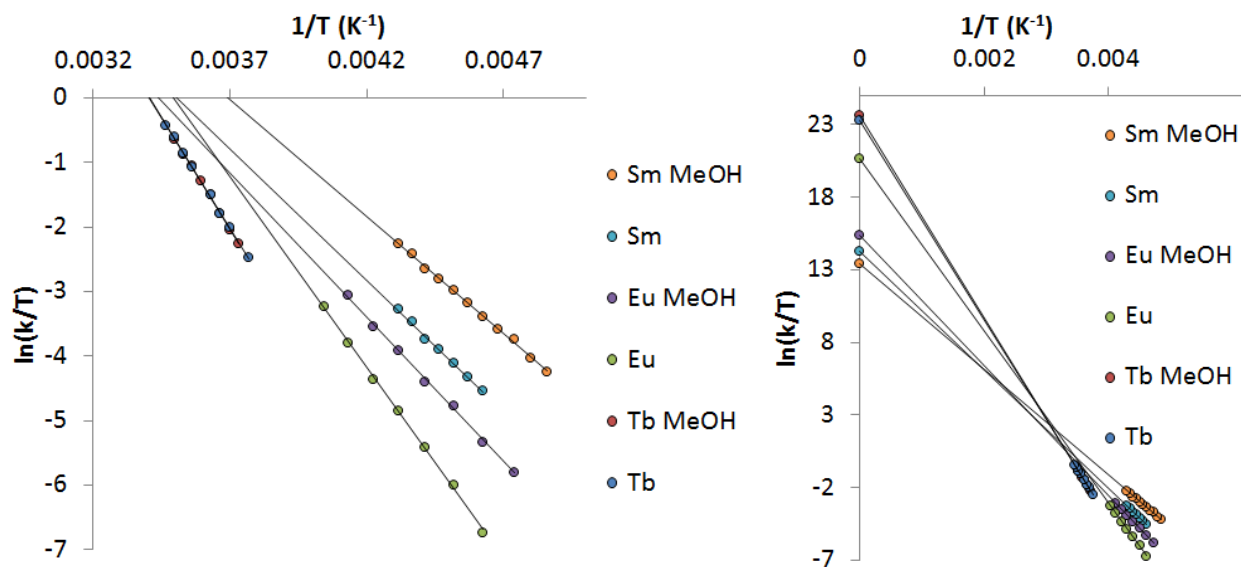
Figure 3.10. Eyring plot for solvent study of **Sm**, **Eu**, and **Tb** in 1:2 DMF:acetone and 1:2 DMF:MeOH

41

In order to take a closer look at the change in LTP mechanism, we measured the rates for **Sm**, **Eu**, and **Tb** in a 1:2 DMF:MeOH mixture. Activation parameters are essentially unchanged for **Tb** in the more polar MeOH solvent, where $\Delta H^{\ddagger}$, $\Delta S^{\ddagger}$, and $\Delta G^{\ddagger}$ at 298 K were found to be 13.8 kcal/mol, -0.2 cal/molK, and 13.8 kcal/mol respectively. The rates of exchange for **Sm** in the MeOH solvent were significantly increased ($\Delta H^{\ddagger}$, $\Delta S^{\ddagger}$, and $\Delta G^{\ddagger}$ at 298 K were found to be 7.2 kcal/mol, -20.6 cal/molK, and 13.3 kcal/mol respectively). Interestingly, the **Eu** complex shows a change in mechanism in the new solvent system, where activation parameters $\Delta H^{\ddagger}$, $\Delta S^{\ddagger}$, and $\Delta G^{\ddagger}$ at 298 K were found to be 8.9 kcal/mol, -16.7 cal/molK, and 13.8 kcal/mol respectively. Methanol is a better ligand for lanthanides than acetone, so it is better able to assist with the LTP of **Eu**. The fact that the rates for **Tb** remain unchanged between the two solvent systems lends strong support for 8-coordinate, nondissociative transition state. It expected that all metals smaller than **Tb** would show similar invariance with changes in solvent.

Modeling the Intramolecular Exchange Process. The intramolecular exchange process for M(bidentate)$_4$ compounds is directly analogous to the Bailar twist of M(bidentate)$_3$ and the tetrahedral inversion of M(bidentate)$_2$ compounds. The eight-coordinate rearrangement has previously been characterized in terms of discrete steps involving individual Hoard-Silverton rearrangements. Here we will take a more continuous approach. The Bailar twist is defined as the D_3 symmetric reaction path relating octahedral and trigonal prismatic coordination geometries.[31] The twist angle (θ) can be visualized by imagining that ligand donors of each bidentate unit are placed on either end of a helicopter blade. The shafts of the helicopters blades are all planted into the central atom at 120$^{\mathrm{o}}$ to each other, and their mutual rotation gives rise to the twist (the trigonal prismatic geometry being found at $\theta = 0$). Likewise, tetrahedral inversion is defined as the D_{2d} symmetric reaction path relating tetrahedral and square planar coordination geometries.[35] Here the inversion angle φ can be thought of as the deviation of all four ligands from the plane of the nearest square planar geometry (the square plane being found at $\varphi=0$). By combining these two ideas, we arrive at our model for the eight-coordinate twist-inversion rearrangement. Imagine four helicopter shafts (with a donor on the end of each blade) planted into the central atom along a square plane. We can calculate the repulsion energy for this new combined model as a function of the angles θ and φ, which is shown in the following figure.
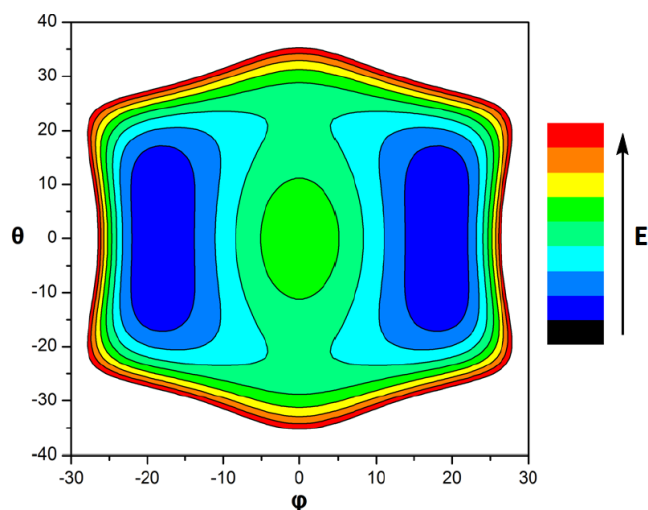
Figure 3.11. Plot of the repulsion energy (n=6) as a function of twist (θ) and inversion (φ) angles for fixed bite distance of **Tb**.

With the repulsion energy surface in hand, we can derive a continuous series of structures along the lowest energy path relating the two *mmmm*-DD ground states (shown in blue). These structures were submitted to the shape analysis (as with Fig. 3.2), and the results are plotted as a function of the φ inversion angle.
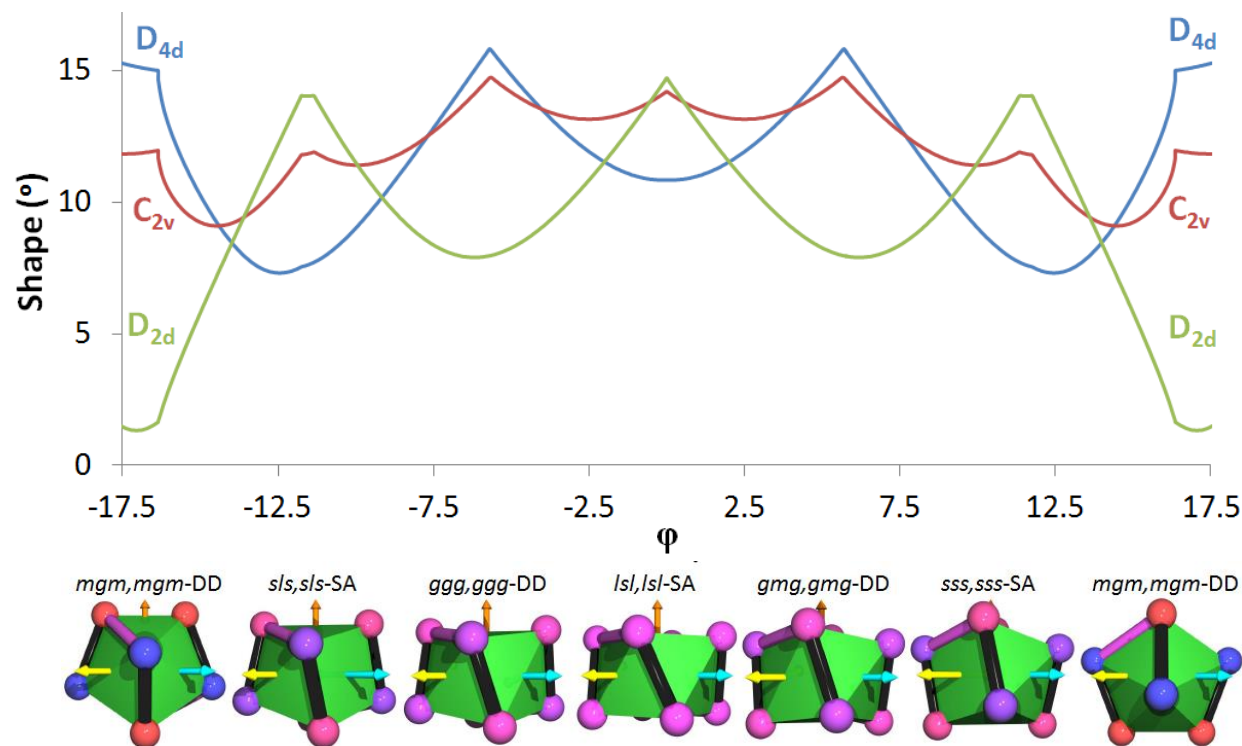
Figure 3.12. Shape analysis of the intermediate structures along the reaction lowest energy path of Fig. 3.10.

The bottom of each well in the shape plot corresponds to a discrete Hoard-Silverton rearrangement products previously outlined by Fay and others. Polyhedral models of these discrete points along the D_2 twist-inversion reaction path are also shown. An important difference to realize between the M(tetradentate)$_2$ complexes reported here and M(bidetntate)$_4$ complexes reported by others is that the M(tetradentate)$_2$ complexes are chiral even in the *mgm,mgm*-DD ground state. The symmetry of the M(tetradentate)$_2$ complexes is C_2 throughout the intramolecular rearrangement, meaning that the symmetry of the plot reported in Fig. 3.10 would be C_2 rather than C_{2v} as shown. This leads us to an odd observation, that two ground state enantiomers can be exchanged by way of an enantiomeric pair of transition states. We have struggled to think of another good example of such a system.

We have established that the structure of the very bright **Eu** complex is clearly *mgm,mgm*-DD, and that the complex is fluxional on the NMR timescale at accessible temperatures. The lifetime of the rearrangement process is calculated to be 1.5 ms at room temperature, which is more than twice as long as the photoluminescent lifetime of **Eu** in aqueous solution (0.7 ms). This observation is consistent with the DD structural assignment based on the two band shape of the $^5D_0$ to $^7F_1$ transition. That is, the structure is rearranging slowly enough that the ground state symmetry affects the long-lived luminescence. It is also important to note that the rearrangement occurs many orders of magnitude slower than the energy transfer step

from the ligand to the metal. Although eight-coordinate lanthanide complexes are often highly fluxional with ill-defined coordination geometries, the **Eu** complex reported here is remarkably rigid in solution. We find this unexpected rigidity of **Eu** to support our hypothesis that the variability in quantum yield for our family of 1,2-HOPO complexes is related to subtle differences in the ground state geometries. That **Eu** prefers DD coordination and is also one of our brightest complexes suggests that perhaps the DD geometry favors efficient sensitization of the metal. We develop this idea further in chapter 5, where we show that the DD coordination geometry offers the greatest d_π/p_π bonding, which may be important for ligand to metal energy transfer in these luminescent systems.

Conclusions

We have previously reported a family of 1,2-HOPO ligands than form luminescent Eu^{III} complexes ranging in quantum yield from 4% to 23% in aqueous TRIS buffer. Here we report the novel 5LI*m*Xy-1,2-HOPO ligand (**L**), which forms one of our brightest Eu^{III} complex with an aqueous quantum yield of 22%. The luminescence spectrum and repulsion energy calculations suggested a DD ground state structure, but the XRD coordinates indicated a BCTP structure in the solid state. The DFT coordinates minimized to a *mgm,mgm*-DD ground state structure, and these coordinates were useful for fitting the isotropic shifts of the entire lanthanide series. The isotropic shift data confirmed the *mgm,mgm*-DD ground state structure for the entire lanthanide series in solution. All of the lanthanide complexes were found to be fluxional within NMR timescale and solvent temperature limits, which varied widely as a function of lanthanide size. Slow exchange spectra were collected for all but **La**, representing the first opportunity to study M(bidentate)$_4$ inversion-twist rearrangements with trivalent metal ions. The slowness of the rearrangement barrier for **Eu** confirmed that the DD structure may be important for efficient energy transfer from ligand to metal.

Experimental

General Methods. The 1,2-HOPOBn-thiazolide precursor was synthesized according to previously reported methods.[36] All other solvents and reagents were purchased from commercial sources and used as received unless otherwise noted. ^{1}H-NMR and ^{13}C-NMR spectra were obtained at 500 MHz and 125 MHz respectively, using either Bruker AV-500 or DRX-500 spectrometers. ^{1}H (or ^{13}C) chemical shifts of the ligand and precursor are measured relative to residual solvent signals, taken as 7.24 (77.23) and 2.50 (39.51) ppm for CDCl$_3$ and DMSO-d$_6$ respectively. ^{1}H chemical shifts of the lanthanide complexes are reported in ppm relative to a coaxial sealed capillary of CDCl$_3$ (containing 1% TMS). High resolution electrospray ionization mass spectra (HRMS-ESI) and elemental analyses were performed by the Microanalytical Laboratory at the University of California, Berkeley.

5LI*m*Xy-1,2-HOPOBn (LBn). Neat *m*-xylylenediamine (1.96 g, 1.44 mmol) was added to 1,2-HOPOBn-thiazolide (10.0 g, 28.9 mmol) in methylene chloride (200 mL). After two days at room temperature, the pale yellow solution was loaded directly onto a silica column. A solvent gradient of 0 to 2% methanol in methylene chloride afforded the desired product as hardened beige foam of **LBn**. Yield: 8.16 g, 96% ^{1}H NMR (300 MHz, CDCl$_3$, 25 °C): δ 4.21 (d, $^3J = 6.2$ Hz, 4H, CH_2), 5.20 (s, 4H, CH_2), 5.98 (t, $^3J = 6.2$ Hz, 2H, NH), 6.24 (dd, $^3J = 6.8$ Hz, ^4J= 1.6 Hz, 2H, =CH), 6.73 (dd, $^3J = 9.2$ Hz, ^4J= 1.6 Hz, 2H, =CH), 6.96 (t, $^4J = 1.1$ Hz, 1H, ArH), 7.08 (dd,

^3J = 7.7 Hz, ^4J= 1.1 Hz, 2H, Ar*H*), 7.19 (dd, ^3J = 9.2 Hz, ^3J= 6.8 Hz, 2H, =C*H*), 7.21-7.40 (m, 11H, Ar*H*). ^{13}C NMR (100 MHz, CDCl3, 25 °C): δ 43.3, 78.9, 105.6, 123.8, 125.7, 126.6, 128.4, 128.7, 129.2, 130.3, 133.2, 137.6, 137.9, 142.5, 158.3, 160.4. HRMS-ESI (*m/z*, [M+H]$^+$) Calcd for $C_{34}H_{31}N_4O_6$: 591.2238, Found: 591.2240. Anal. Calcd (Found) for $C_{34}H_{30}N_4O_6 \cdot 0.3H_2O$: C 68.51 (68.70), H 5.17 (5.39), N 9.40 (9.35) %.

5LI*m*Xy-1,2-HOPO (L). The benzyl protected ligand (8.00 g, 13.5 mmol) was dissolved into glacial acetic acid (150 mL) and concentrated hydrochloric acid (150 mL). After two days, the acid was removed under vacuum, and water (150 mL) was added to precipitate the product. The precipitate was vigorously stirred, collected by filtration, washed with water, and dried to afford a free flowing white powder of **L**. Yield: 5.26 g, 95%. ^{1}H NMR (300 MHz, CDCl$_3$, 25 °C): δ 4.43 (d, ^3J = 6.0 Hz, 4H, C*H$_2$*), 6.34 (dd, ^3J = 6.9 Hz, ^4J= 1.7 Hz, 2H, =C*H*), 6.58 (dd, ^3J = 9.1 Hz, ^4J= 1.7 Hz, 2H, =C*H*), 7.19-7.34 (m, 4H, Ar*H*). 7.39 (dd, ^3J = 9.1 Hz, ^3J= 6.9 Hz, 2H, =C*H*), 9.32 (t, ^3J = 6.0 Hz, 2H, N*H*). ^{13}C NMR (100 MHz, CDCl3, 25 °C): δ 42.3, 103.8, 119.4, 125.7, 125.8, 128.4, 137.2, 138.6, 142.1, 157.4, 160.4. HRMS-ESI (*m/z*, [M-H]$^-$) Calcd for $C_{20}H_{17}N_4O_6$: 409.1154, Found: 409.1140. Anal. Calcd (Found) $C_{20}H_{18}N_4O_6 \cdot 1.3H_2O$: C, 55.37 (55.45); H, 4.79 (4.63); N, 12.92 (12.74) %.

General Method for the Preparation of Metal Complexes. The 5LI*m*Xy-1,2-HOPO ligand (172 mg, 0.42 mmol), the appropriate metal chloride hydrate (0.20 mmol), and pyridine (100 mg, 1.3 mmol) were mixed into methanol (10 mL), and the reaction was heated to reflux for 4 hours. Upon cooling the product was collected by filtration, washed with methanol (3x2 mL), and dissolved into 7 mL of *N,N*-dimethylformamide. A solution of NMe$_4$OH·5H$_2$O (36 mg, 0.20 mmol) in methanol (0.25 mL) was added to the DMF solution, and crystals were grown by gaseous diffusion of diethyl ether. Crystallization was repeated to ensure purity of the final products.

[La(5LI*m*Xy-1,2-HOPO)$_2$][NMe$_4$] (La). Colorless crystals. Yield: 138 mg, 59 %. ^{1}H NMR (500 MHz, 2:1 acetone-d$_6$:DMF-d$_7$, 25 °C): δ 12.49 (t, *J* = 4.0 Hz, 4H), 8.46 (s, 2H), 8.23 (t, *J* = 7.5 Hz, 2H), 8.14 (d, *J* = 7.5 Hz, 4H), 8.03-8.09 (m, 8H), 7.01 (dd, *J* = 7.1 Hz, *J* = 3.2 Hz, 4H), 5.40 (s, 8H, C*H$_2$*), 4.25 (s, 12H, N*Me$_4$*). ^{13}C NMR (125 MHz, 2:1 acetone-d$_6$:DMF-d$_7$, 25 °C): 164.25, 161.06, 140.07, 139.00, 132.76, 129.52, 128.28, 125.68, 117.18, 111.37, 55.99, 44.57. HRMS-ESI (*m/z*, [M]$^-$) Calcd for $C_{40}H_{32}N_8O_{12}{}^{139}$La: 955.1209, Found: 955.1187. Anal. Calcd (Found) for $[La(C_{20}H_{16}N_4O_6)_2][C_4H_{12}N] \cdot 1.75C_3H_7NO \cdot 0.05C_4H_{10}O \cdot 1.75H_2O$: C 49.75 (49.66), H 5.07 (4.86), N 12.65 (12.44) %.

[Ce(5LI*m*Xy-1,2-HOPO)$_2$][NMe$_4$] (Ce). Orange crystals. Yield: 138 mg, 66 %. Calcd for $C_{40}H_{32}N_8O_{12}{}^{140}$Ce: 956.1200, Found: 956.1228. Anal. Calcd (Found) for $[Ce(C_{20}H_{16}N_4O_6)_2][C_4H_{12}N] \cdot 0.5C_3H_7NO \cdot 0.05C_4H_{10}O \cdot 3H_2O$: C 48.78 (48.70), H 4.84 (4.66), N 11.82 (11.65) %.

[Pr(5LI*m*Xy-1,2-HOPO)$_2$][NMe$_4$] (Pr). Pale green crystals. Yield: 164 mg, 73 %. ^{1}H NMR (500 MHz, 2:1 acetone-d$_6$:DMF-d$_7$, -70 °C): δ 29.30 (s, 2H), 22.91 (s, 2H), 17.71 (s, 2H), 14.49 (s, 2H), 12.24 (s, 2H), 8.86 (s, 2H), 8.16 (s, 2H), 6.56 (s, 4H), 4.02 (s, 2H), 3.70 (s, 12H), -0.37 (s, 2H), -3.10 (s, 2H), -5.36 (s, 2H), -11.84 (s, 2H), -11.93 (s, 2H), -41.18 (s, 2H). HRMS-ESI (*m/z*, [M]$^-$) Calcd for $C_{40}H_{32}N_8O_{12}{}^{141}$Pr: 957.1222, Found: 957.1204. Anal. Calcd (Found) for

$[Pr(C_{20}H_{16}N_4O_6)_2][C_4H_{12}N]\cdot2C_3H_7NO\cdot0.05C_4H_{10}O\cdot1.25H_2O$: C 50.07 (50.07), H 5.09 (5.07), N 12.83 (12.87) %.

[Nd(5LI*m*Xy-1,2-HOPO)$_2$][NMe$_4$] (Nd). Pale blue crystals. Yield: 144 mg, 64 %. ^{1}H NMR (500 MHz, 2:1 acetone-d$_6$:DMF-d$_7$, -60 °C): 28.26 (s, 2H), 13.46 (s, 2H), 13.22 (s, 2H), 12.84 (s, 2H), 10.97 (s, 2H), 10.71 (s, 2H), 9.02 (s, 2H), 8.45 (s, 2H), 8.34 (s, 2H), 7.46 (t, J = 6.5 Hz, 2H), 5.69 (s, 2H), 5.30 (s, 2H), 4.20 (s, 12H), 3.60 (s, 2H), -0.05 (s, 2H), -0.18 (s, 2H), -3.87 (s, 2H). HRMS-ESI (*m/z*, [M]$^-$) Calcd for C$_{40}$H$_{32}$N$_8$O$_{12}^{142}$Nd: 958.1222, Found: 958.1210. Anal. Calcd (Found) for $[Nd(C_{20}H_{16}N_4O_6)_2][C_4H_{12}N]\cdot2C_3H_7NO\cdot0.1C_4H_{10}O\cdot H_2O$: C 50.16 (50.23), H 5.09 (5.12), N 12.77 (12.67) %.

[Sm(5LI*m*Xy-1,2-HOPO)$_2$][NMe$_4$] (Sm). Pale yellow crystals. Yield: 178 mg, 74 %. ^{1}H NMR (500 MHz, 2:1 acetone-d$_6$:DMF-d$_7$, -35 °C): δ 13.69 (s, 2H), 11.88 (d, J = 8.6 Hz, 2H), 8.75 (t, J = 8.1 Hz, 2H), 8.56 (d, J = 7.2 Hz, 2H), 8.46 (d, J = 7.2 Hz, 2H), 8.34 (d, J = 8.4 Hz, 2H), 8.30 – 8.25 (m, 6H), 8.15 (t, 2H), 8.13 (d, J = 5.6 Hz, 2H), 5.91 (dd, J = 15.7, 8.9 Hz, 2H), 5.75 (d, J = 6.4 Hz, 2H), 5.72 (d, 2H), 5.28 (d, J = 13.2 Hz, 2H), 4.82 (d, J = 15.7 Hz, 2H), 4.29 (s, 12H). ^{13}C NMR (125 MHz, 2:1 acetone-d$_6$:DMF-d$_7$, -35 °C): δ 168.85, 164.62, 161.31, 160.57, 140.04, 139.82, 139.75, 138.84, 133.97, 132.89, 129.27, 128.83, 127.64, 125.17, 118.03, 117.56, 111.92, 111.91, 55.02, 45.58, 42.92. HRMS-ESI (*m/z*, [M]$^-$) Calcd for C$_{40}$H$_{32}$N$_8$O$_{12}^{144}$Sm: 960.1265, Found: 960.1260. Anal. Calcd (Found) for $[Sm(C_{20}H_{16}N_4O_6)_2][C_4H_{12}N]\cdot1.75C_3H_7NO\cdot0.25C_4H_{10}O\cdot H_2O$: C 50.06 (50.10), H 5.08 (4.87), N 12.49 (12.38) %.

[Eu(5LI*m*Xy-1,2-HOPO)$_2$][NMe$_4$] (Eu). Colorless crystals. Yield: 168 mg, 70 %. ^{1}H NMR (500 MHz, 2:1 acetone-d$_6$:DMF-d$_7$, -35 °C): δ 31.92 (s, 2H), 14.72 (s, 2H), 12.97 (s, 2H), 11.73 (d, J = 7.6 Hz, 2H), 11.59 (d, J = 13.1 Hz, 2H), 10.11 (t, J = 7.7 Hz, 2H), 9.18 (d, J = 14.3 Hz, 2H), 8.63 (d, J = 6.7 Hz, 2H), 5.95 (s, 2H), 5.85 (d, J = 6.0 Hz, 2H), 4.76 (s, 12H), 4.43 (s, 2H), 4.18 (s, 2H), 3.93 (s, 2H), 3.35 (d, J = 13.4 Hz, 2H), 3.12 (s, 2H), 1.62 (s, 2H). ^{13}C NMR (125 MHz, 2:1 acetone-d$_6$:DMF-d$_7$, -35 °C): δ 234.96, 200.20, 166.73, 156.58, 145.87, 140.17, 131.82, 131.74, 130.22, 129.81, 126.58, 125.10, 101.97, 99.15, 90.47, 88.95, 60.96, 56.01, 52.13, 49.26, 43.80. HRMS-ESI (*m/z*, [M]$^-$) Calcd for C$_{40}$H$_{32}$N$_8$O$_{12}^{151}$Eu: 967.1344, Found: 967.1327. Anal. Calcd (Found) for $[Eu(C_{20}H_{16}N_4O_6)_2][C_4H_{12}N]\cdot1.75C_3H_7NO\cdot0.25C_4H_{10}O\cdot H_2O$: C 49.99 (49.94), H 5.07 (5.04), N 12.47 (12.38) %.

[Tb(5LI*m*Xy-1,2-HOPO)$_2$][NMe$_4$] (Tb). Colorless crystals. Yield: 160 mg, 75 %. ^{1}H NMR (500 MHz, 2:1 acetone-d$_6$:DMF-d$_7$, 5 °C): δ 88.21 (s, 0H), 48.59 (s, 3H), 37.15 (s, 57H), 29.63 (s, 0H), 22.59 (s, 3H), 16.68 (s, 55H), 13.61 (s, 6H), 7.12 (s, 54H), 1.89 (s, 388H), -8.45 (s, 66H), -28.86 (s, 60H), -38.96 (s, 3H), -51.08 (s, 1H), -66.76 (s, 0H), -68.42 (s, 1H). HRMS-ESI (*m/z*, [M]$^-$) Calcd for C$_{40}$H$_{32}$N$_8$O$_{12}^{159}$Tb: 975.1399, Found: 975.1374. Anal. Calcd (Found) for $[Tb(C_{20}H_{16}N_4O_6)_2][C_4H_{12}N]\cdot C_3H_7NO\cdot0.25C_4H_{10}O\cdot0.5H_2O$: C 50.11 (49.98), H 4.77 (4.52), N 12.18 (12.28) %.

[Dy(5LI*m*Xy-1,2-HOPO)$_2$][NMe$_4$] (Dy). Colorless crystals. Yield: 139 mg, 65 %. ^{1}H NMR (500 MHz, 2:1 acetone-d$_6$:DMF-d$_7$, 20 °C): δ 105.12 (s, 2H), 83.09 (s, 2H), 40.13 (s, 2H), 39.63 (s, 2H), 22.29 (s, 2H), 18.68 (s, 2H), 17.43 (s, 2H), 7.81 (s, 2H), 2.22 (s, 2H), 1.87 (s, 12H), -9.67 (s, 2H), -28.29 (s, 2H), -35.29 (s, 2H), -60.83 (s, 2H), -63.67 (s, 2H), -67.68 (s, 2H), -224.35 (s, 2H). HRMS-ESI (*m/z*, [M]$^-$) Calcd for C$_{40}$H$_{32}$N$_8$O$_{12}^{164}$Dy: 980.1437, Found: 980.1427. Anal.

Calcd (Found) for [Dy(C$_{20}$H$_{16}$N$_4$O$_6$)$_2$][C$_4$H$_{12}$N]·C$_3$H$_7$NO·0.25C$_4$H$_{10}$O·0.5H$_2$O: C 49.96 (49.98), H 4.76 (4.62), N 12.14 (12.35) %.

[Ho(5LImXy-1,2-HOPO)$_2$][NMe$_4$] (Ho). Pink crystals. Yield: 137 mg, 64 %. ^{1}H NMR (500 MHz, 2:1 acetone-d$_6$:DMF-d$_7$, 20 °C): δ 84.25 (s, 2H), 39.63 (s, 2H), 25.50 (s, 2H), 19.55 (s, 2H), 19.09 (s, 2H), 16.07 (s, 2H), 14.38 (s, 2H), 10.15 (s, 4H), 3.79 (s, 12H), 3.28 (s, 2H), -3.93 (s, 2H), -7.23 (s, 2H), -10.80 (s, 2H), -15.05 (s, 2H), -18.91 (s, 2H), -60.78 (s, 2H). HRMS-ESI (*m/z*, [M]$^-$) Calcd for C$_{40}$H$_{32}$N$_8$O$_{12}$^{165}Ho: 981.1448, Found: 981.1428. Anal. Calcd (Found) for [Ho(C$_{20}$H$_{16}$N$_4$O$_6$)$_2$][C$_4$H$_{12}$N]·C$_3$H$_7$NO·0.25C$_4$H$_{10}$O·0.5H$_2$O: C 49.85 (49.76), H 4.75 (4.63), N 12.11 (12.27) %.

[Er(5LImXy-1,2-HOPO)$_2$][NMe$_4$] (Er). Pink crystals. Yield: 151 mg, 68 %. ^{1}H NMR (500 MHz, 2:1 acetone-d$_6$:DMF-d$_7$, 7.5 °C): δ 54.72 (s, 2H), 23.59 (s, 2H), 18.77 (s, 2H), 17.94 (s, 2H), 15.52 (s, 2H), 13.83 (s, 2H), 12.80 (s, 2H), 11.50 (s, 4H), 9.71 (s, 2H), 7.57 (s, 2H), 6.74 (s, 2H), 6.61 (s, 2H), 6.50 (s, 2H), 5.80 (s, 12H), 4.99 (s, 2H), 2.70 (s, 2H), 1.11 (s, 2H). HRMS-ESI (*m/z*, [M]$^-$) Calcd for C$_{40}$H$_{32}$N$_8$O$_{12}$^{166}Er: 982.1448, Found: 982.1448. Anal. Calcd (Found) for [Er(C$_{20}$H$_{16}$N$_4$O$_6$)$_2$][C$_4$H$_{12}$N]·1.5C$_3$H$_7$NO·0.25C$_4$H$_{10}$O·H$_2$O: C 49.37 (49.26), H 4.94 (4.91), N 12.21 (12.25) %.

[Tm(5LImXy-1,2-HOPO)$_2$][NMe$_4$] (Tm). Colorless crystals. Yield: 149 mg, 69 %. ^{1}H NMR (500 MHz, 2:1 acetone-d$_6$:DMF-d$_7$, 5 °C): δ 94.15 (s, 2H), 31.90 (s, 2H), 29.25 (s, 2H), 25.83 (s, 2H), 21.36 (s, 2H), 21.20 (s, 2H), 14.13 (s, 2H), 7.22 (s, 12H), 6.39 (s, 2H), 4.18 (s, 2H), 1.26 (s, 2H), -2.96 (s, 2H), -3.30 (s, 2H), -10.50 (s, 2H), -11.80 (s, 2H), -16.72 (s, 2H), -61.60 (s, 2H). HRMS-ESI (*m/z*, [M]$^-$) Calcd for C$_{40}$H$_{32}$N$_8$O$_{12}$^{169}Tm: 985.1487, Found: 985.1472. Anal. Calcd (Found) for [Tm(C$_{20}$H$_{16}$N$_4$O$_6$)$_2$][C$_4$H$_{12}$N]·C$_3$H$_7$NO·0.25C$_4$H$_{10}$O·0.75H$_2$O: C 49.49 (49.48), H 4.76 (4.60), N 12.02 (12.16) %.

[Yb(5LImXy-1,2-HOPO)$_2$][NMe$_4$] (Yb). Colorless crystals. Yield: 134 mg, 61 %. ^{1}H NMR (500 MHz, 2:1 acetone-d$_6$:DMF-d$_7$, -2.5 °C): δ 40.86 (s, 2H), 16.31 (s, 2H), 14.85 (s, 2H), 14.00 (s, 2H), 13.07 (d, *J* = 8.0 Hz, 2H), 11.30 (s, 2H), 10.62 (t, *J* = 7.6 Hz, 2H), 8.09 (s, 2H), 6.66 (s, 2H), 6.21 (s, 2H), 5.27 (s, 12H), 4.29 (s, 2H), 2.57 (s, 2H), 1.86 (s, 2H), 0.72 (s, 2H), -1.28 (s, 2H), -10.85 (s, 2H). HRMS-ESI (*m/z*, [M]$^-$) Calcd for C$_{40}$H$_{32}$N$_8$O$_{12}$^{174}Yb: 990.1534, Found: 990.1524. Anal. Calcd (Found) for [Yb(C$_{20}$H$_{16}$N$_4$O$_6$)$_2$][C$_4$H$_{12}$N]·1.25C$_3$H$_7$NO·0.25C$_4$H$_{10}$O·H$_2$O: C 49.13 (49.08), H 4.84 (4.82), N 12.05 (12.13) %.

[Lu(5LImXy-1,2-HOPO)$_2$][NMe$_4$] (Lu). Colorless crystals. Yield: 178 mg, 72 %. ^{1}H NMR (500 MHz, 2:1 acetone-d$_6$:DMF-d$_7$, -15 °C): δ 13.47 (d, *J* = 8.7 Hz, 2H), 11.77 (s, 2H), 8.56 (s, 2H), 8.37 − 8.30 (m, 4H), 8.26 (t, 2H), 8.22 (dd, *J* = 7.5, 1.9 Hz, 2H), 8.13 (d, *J* = 5.9 Hz, 2H), 7.98 (t, *J* = 7.9 Hz, 2H), 7.93 (dd, *J* = 7.4, 1.9 Hz, 2H), 7.50 (dd, *J* = 8.3, 1.9 Hz, 2H), 6.28 (dd, *J* = 8.3, 1.7 Hz, 2H), 6.14 (dd, *J* = 16.0, 9.1 Hz, 2H), 5.43 (dd, *J* = 15.6, 4.8 Hz, 2H), 5.35 (d, *J* = 15.8 Hz, 2H), 4.84 (dd, *J* = 15.7, 3.2 Hz, 2H), 4.29 (s, 12H). ^{13}C NMR (125 MHz, 2:1 acetone-d$_6$:DMF-d$_7$, -15 °C): δ 163.17, 163.12, 161.00, 160.46, 140.62, 138.98, 138.47, 137.96, 133.11, 132.53, 129.40, 128.52, 127.78, 125.14, 117.18, 116.86, 111.24, 111.10, 55.46, 45.26, 43.65. HRMS-ESI (*m/z*, [M]$^-$) Calcd for C$_{40}$H$_{32}$N$_8$O$_{12}$^{175}Lu: 991.1553, Found: 991.1519. Anal. Calcd (Found) for [Lu(C$_{20}$H$_{16}$N$_4$O$_6$)$_2$][C$_4$H$_{12}$N]·1.5C$_3$H$_7$NO·0.25C$_4$H$_{10}$O·H$_2$O: C 49.05 (48.92), H 4.91 (4.84), N 12.13 (12.21) %.

Luminescence Measurements. Instrumentation details have been reported elsewhere.[14] Samples were first dissolved into DMSO, and then diluted into aqueous TRIS buffer (final concentration DMSO < 0.05%). The TRIS buffer was prepared by dissolving TRIS hydrochloride (20 mM) and sodium chloride (100 mM) into Millipore water and adjusting the pH to 7.4 with sodium hydroxide. Quinine sulfate in 0.05 M H_2SO_4 ($\Phi = 0.508$) was used as an aqueous fluorescence quantum yield reference.[51] Quantum yields were determined by the optically dilute method (with optical density at λ_{ex} <0.05) according to the following equation:

$$\Phi_x = \frac{A_r(\lambda)}{A_x(\lambda)}\frac{I_x}{I_r}\Phi_r$$

where $A(\lambda)$ is the absorbance of sample x and reference r at the excitation wavelength λ, and I is the total integrated emission of the sample and quantum yield reference. The same excitation wavelength λ and slit widths were used for sample and reference, removing the need to correct for the incident power of the excitation source. Similarly, the refractive indices for sample and reference are assumed identical, both being aqueous. A 5 cm quartz cuvette was used to measure the absorption spectra in order to increase the signal-to-noise for these dilute solutions. Luminescence measurements were made using a 1 cm quartz fluorescence cuvette. Quantum yields of **Eu** and **Sm** were determined in triplicate at an excitation wavelength of 333 nm (see Appendix 3).

2D-NMR. The temperature probe was calibrated from 0 to -70 ^{o}C using methanol (Appendix 3). Selective inversion recovery (SIR) experiments were collected at forty two different mixing times (Appendix 3). Integrated peak data for inverted and exchanging resonances were fit to a two site exchange model within the program CIFIT2.[52,53] Reported ^{1}H-COSY and [1]H-EXSY/NOESY spectra are averaged over 128 scans or more. For [1]H-EXSY/NOESY spectra, mixing times were set to the middle of the observed T_1 relaxation times.

DFT Calculations. Ground state geometry optimization and frequency calculations were performed using Gaussian 09 at the Molecular Graphics and Computation Facility at University of California, Berkeley, CA.[54] Coordinates were optimized from the XRD structures as starting points. The B3LYP functional was used, treating the light atoms with the 6-31G(d,p) basis set and the metal atoms with quasi relativistic effective core pseudopotentials, specifically: **La** (ECP46MWB), **Ce** (ECP47MWB), **Pr** (ECP48MWB), **Nd** (ECP49MWB), **Sm** (ECP51MWB), **Eu** (ECP52MWB), **Tb** (ECP54MWB), **Dy** (ECP55MWB), **Ho** (ECP56MWB), **Er** (ECP57MWB), **Tm** (ECP58MWB), **Yb** (ECP59MWB), and **Lu** (ECP60MWB).[55,56] Lanthanide basis sets were taken directly from the Stuttgart/Köln group website. The larger 6311++G(d,p) basis set was also tested, but the far greater computational expense was not matched by a significant change in the ground state geometry. The functional B3PW91 was also tested, again without significant structural differences. All calculations were run with no symmetry constraints.

XRD Methods. Single crystal X-ray diffraction data were collected on a Bruker APEX or QUAZAR diffractometer equipped with a Bruker APEX-I or APEX-II CCD detector respectively. Structures were solved with SIR-97,[57] refined with SHELX-97,[58] and the refined atomic positions are displayed as 50% thermal ellipsoids using ORTEP-32.[59] Publication

materials were generated with WinGX.[60] For all structures the refinement tool SQUEEZE was used to remove disordered solvent electron density from the .hkl file used for final refinement.[61]

References

(1)   Eliseeva, S. V.; Bünzli, J.-C. G. *Chem. Soc. Rev.* **2009**, *39*, 189.
(2)   Bünzli, J.-C. G.; Piguet, C. *Chem. Soc. Rev.* **2005**, *34*, 1048.
(3)   Binnemans, K. *Chem. Rev.* **2009**, *109*, 4283.
(4)   De Sá, G. .; Malta, O. .; de Mello Donegá, C.; Simas, A. .; Longo, R. .; Santa-Cruz, P. .; da Silva, E. . *Coord. Chem. Rev.* **2000**, *196*, 165.
(5)   Hemmilä, I.; Laitala, V. In *Lanthanide Luminescence*; Hänninen, P.; Härmä, H., Eds.; Springer Series on Fluorescence; Springer Berlin Heidelberg, 2011; pp. 361–380.
(6)   Stenman, U.-H. In *Lanthanide Luminescence*; Hänninen, P.; Härmä, H., Eds.; Springer Series on Fluorescence; Springer Berlin Heidelberg, 2011; pp. 329–341.
(7)   Tanke, H. J. In *Lanthanide Luminescence*; Hänninen, P.; Härmä, H., Eds.; Springer Series on Fluorescence; Springer Berlin Heidelberg, 2011; pp. 313–328.
(8)   Werts, M. H. V. In *Lanthanide Luminescence*; Hänninen, P.; Härmä, H., Eds.; Springer Series on Fluorescence; Springer Berlin Heidelberg, 2011; pp. 133–159.
(9)   Zwier, J. M.; Bazin, H.; Lamarque, L.; Mathis, G. *Inorg. Chem.* **2014**, 140106154502005.
(10) Moore, E. G.; Xu, J.; Jocher, C. J.; Werner, E. J.; Raymond, K. N. *J. Am. Chem. Soc.* **2006**, *128*, 10648.
(11) Moore, E. G.; Jocher, C. J.; Xu, J.; Werner, E. J.; Raymond, K. N. *Inorg. Chem.* **2007**, *46*, 5468.
(12) Moore, E. G.; Xu, J.; Jocher, C. J.; Castro-Rodriguez, I.; Raymond, K. N. *Inorg. Chem.* **2008**, *47*, 3105.
(13) D'Aléo, A.; Xu, J.; Moore, E. G.; Jocher, C. J.; Raymond, K. N. *Inorg. Chem.* **2008**, *47*, 6109.
(14) D'Aléo, A.; Moore, E. G.; Szigethy, G.; Xu, J.; Raymond, K. N. *Inorg. Chem.* **2009**, *48*, 9316.
(15) Abergel, R. J.; D'Aléo, A.; Ng Pak Leung, C.; Shuh, D. K.; Raymond, K. N. *Inorg. Chem.* **2009**, *48*, 10868.
(16) Muetterties, E. L. *Inorg. Chem.* **1974**, *13*, 1011.
(17) *IUPAC Compendium of Chemical Terminology: Gold Book*; Nič, M.; Jirát, J.; Košata, B.; Jenkins, A.; McNaught, A., Eds.; 2.1.0 ed.; IUPAC: Research Triagle Park, NC, 2009.
(18) Fay, R. C. *Coord. Chem. Rev.* **1996**, *154*, 99.
(19) Muetterties, E. L. *Inorg. Chem.* **1973**, *12*, 1963.
(20) Fay, R. C.; Howie, J. K. *J. Am. Chem. Soc.* **1977**, *99*, 8110.
(21) Fay, R. C.; Howie, J. K. *J. Am. Chem. Soc.* **1979**, *101*, 1115.
(22) Adams, A. C.; Larsen, E. M. *Inorg. Chem.* **1966**, *5*, 228.
(23) Pinnavaia, T. J.; Fay, R. C. *Inorg. Chem.* **1966**, *5*, 233.
(24) Adams, A. C.; Larsen, E. M. *Inorg. Chem.* **1966**, *5*, 814.
(25) Bhat, A. N.; Fay, R. C.; Lewis, D. F.; Lindmark, A. F.; Strauss, S. H. *Inorg. Chem.* **1974**, *13*, 886.
(26) Fay, R. C.; Lewis, D. F.; Weir, J. R. *J. Am. Chem. Soc.* **1975**, *97*, 7179.
(27) Lewis, D. F.; Fay, R. C. *Inorg. Chem.* **1976**, *15*, 2219.
(28) Hawthorne, S. L.; Bruder. Alan H.; Fay, R. C. *Inorg. Chem.* **1978**, *17*, 2114.

(29) Weir, J. R.; Fay, R. C. *Inorg. Chem.* **1986**, *25*, 2969.

(30) Hawthorne, S. L.; Bruder, A. H.; Fay, R. C. *Inorg. Chem.* **1983**, *22*, 3368.

(31) Davis, A. V.; Firman, T. K.; Hay, B. P.; Raymond, K. N. *J. Am. Chem. Soc.* **2006**, *128*, 9484.

(32) Eaton, S. S.; Hutchison, J. R.; Holm, R. H.; Muetterties, E. L. *J. Am. Chem. Soc.* **1972**, *94*, 6411.

(33) Eaton, S. S.; Eaton, G. R.; Holm, R. H.; Muetterties, E. L. *J. Am. Chem. Soc.* **1973**, *95*, 1116.

(34) Basolo, F.; Pearson, R. G. *Mechanisms of Inorganic Reactions: Study of Metal Complexes in Solution*; 2nd edition.; John Wiley & Sons Inc: New York etc., 1967.

(35) Holm, R. H.; O'Connor, M. J. In *Progress in Inorganic Chemistry*; Lippard, S. J., Ed.; John Wiley & Sons, Inc.: Hoboken, NJ, USA, 1971; Vol. 14, pp. 241–401.

(36) Xu, J.; Durbin, P. W.; Kullgren, B.; Ebbe, S. N.; Uhlir, L. C.; Raymond, K. N. *J. Med. Chem.* **2002**, *45*, 3963.

(37) Hoard, J. L.; Silverton, J. V. *Inorg. Chem.* **1963**, *2*, 235.

(38) Kepert, D. L. *Prog. Inorg. Chem.* **1978**, *24*, 179.

(39) Drew, M. G. B. *Coord. Chem. Rev.* **1977**, *24*, 179.

(40) Burdett, J. K.; Hoffmann, R.; Fay, R. C. *Inorg. Chem.* **1978**, *17*, 2553.

(41) Muetterties, E. L.; Wright, C. M. *Q. Rev. Chem. Soc.* **1967**, *21*, 109.

(42) Lippard, S. J. In *Progress in Inorganic Chemistry*; Cotton, F. A., Ed.; John Wiley & Sons, Inc.: Hoboken, NJ, USA, 1967; Vol. 8, pp. 109–193.

(43) Blight, D. G.; Kepert, D. L. *Inorg. Chem.* **1972**, *11*, 1556.

(44) Kepert, D. L. *Inorganic Stereochemistry*; Softcover reprint of the original 1st ed. 1982 edition.; Springer: Berlin, Heidelberg, 1982.

(45) Bertini, I.; Luchinat, C. *Nmr of Paramagnetic Molecules in Biological Systems*; Benjamin/Cummings Publishing Company, 1986.

(46) Kemple, M. D.; Ray, B. D.; Lipkowitz, K. B.; Prendergast, F. G.; Rao, B. D. N. *J. Am. Chem. Soc.* **1988**, *110*, 8275.

(47) Lisowski, J.; Sessler, J. L.; Lynch, V.; Mody, T. D. *J. Am. Chem. Soc.* **1995**, *117*, 2273.

(48) Lisowski, J.; Sessler, J. L.; Mody, T. D. *Inorg. Chem.* **1995**, *34*, 4336.

(49) Forsberg, J. H.; Delaney, R. M.; Zhao, Q.; Harakas, G.; Chandran, R. *Inorg. Chem.* **1995**, *34*, 3705.

(50) Hugh Powell, D.; Favre, M.; Graeppi, N.; Ni Dhubhghaill, O. M.; Pubanz, D.; Merbach, A. *J. Alloys Compd.* **1995**, *225*, 246.

(51) Velapoldi, R. A.; Tønnesen, H. H. *J. Fluoresc.* **2004**, *14*, 465.

(52) Mugridge, J. S.; Szigethy, G.; Bergman, R. G.; Raymond, K. N. *J. Am. Chem. Soc.* **2010**, *132*, 16256.

(53) Bain, A. D.; Cramer, J. A. *J. Magn. Reson. A* **1996**, *118*, 21.

(54) *Gaussian 09, Revision D.01,*.

(55) Dolg, M.; Stoll, H.; Savin, A.; Preuss, H. *Theor. Chim. Acta* **1989**, *75*, 173.

(56) Dolg, M.; Stoll, H.; Preuss, H. *Theor. Chim. Acta* **1993**, *85*, 441.

(57) Altomare, A.; Burla, M. C.; Camalli, M.; Cascarano, G. L.; Giacovazzo, C.; Guagliardi, A.; Moliterni, A. G. G.; Polidori, G.; Spagna, R. *J. Appl. Crystallogr.* **1999**, *32*, 115.

(58) Sheldrick, G. M. *Acta Crystallogr. A* **2008**, *64*, 112.

(59) Farrugia, L. J. *J. Appl. Crystallogr.* **1997**, *30*, 565.

(60) Farrugia, L. J. *J. Appl. Crystallogr.* **1999**, *32*, 837.

(61)   Van der Sluis, P.; Spek, A. L. *Acta Crystallogr. A* **1990**, *46*, 194.

Chapter 4

Searching for the Rearrangement High-Temperature Process (HTP)

Introduction

In chapter 3, we demonstrated that the 5LImXy-1,2-HOPO ligand forms 8-coordinate lanthanide complexes which racemize by way of a low temperature process (LTP) and a high temperature process (HTP). The LTP was characterized by ^{1}H-^{1}H EXSY and ^{1}H selective inversion recovery (SIR) experiments. In that chapter we provided evidence that the LTP occurs without dissociation of the coordinating 1,2-HOPO units. The HTP, on the other hand, requires at least partial ligand dissociation, since there is no other way to account for the observed mutual exchange of all four diastereotopic methylene protons at elevated temperatures (Fig. 1). Regardless of the exact mechanism, ligand dissociation occurring in the HTP is expected to leave coordination sites open for solvent molecules. Since the efficiency of photoluminescence by lanthanide complexes depends partly upon the hydration state of the lanthanide ion, we were interested to characterize the HTP of the 5LImXy-1,2-HOPO complexes as representative samples. Unfortunately, we could find no suitable way to model the HTP for the 5LImXy-1,2-HOPO complexes directly. Modeling the exchange of coupled systems by lineshape analysis is problematic when the number of exchange processes is greater than one, in addition to the complications of line broadening associated with the paramagnetism of most of the lanthanides. Selective inversion is similarly problematic, due to the incompatible broadness of the methylene resonances in the slow HTP/fast LTP regime (Fig. 4.1).
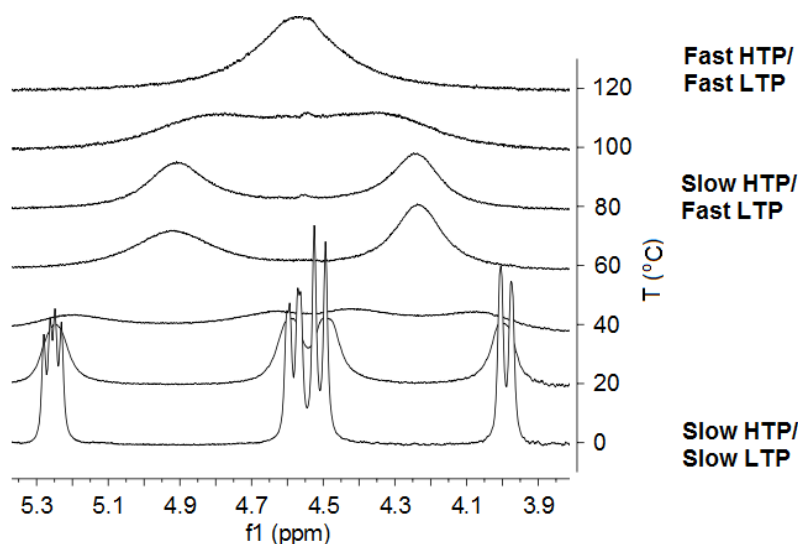
Figure 4.1. Variable Temperature ^{1}H-NMR of [Y(5LImXy-1,2-HOPO)$_2$][NMe4] in DMF-d_7 showing the effects of the LTP and HTP on the diastereotopic methylene peaks, 500 MHz

We were therefore interested in finding new 1,2-HOPO complexes where the HTP could be investigated directly, by designing a system that cannot participate in the LTP. Two new ligand systems were developed, and their lanthanide complexes are characterized here by luminescence and ^{1}H-NMR. For the first ligand system, the tetradentate 5LImXy-1,2-HOPO ligand was modified by covalently linking two units together with a polyethylene glycol (PEG) linker, generating octadentate ligands like the one shown in Fig. 4.2.
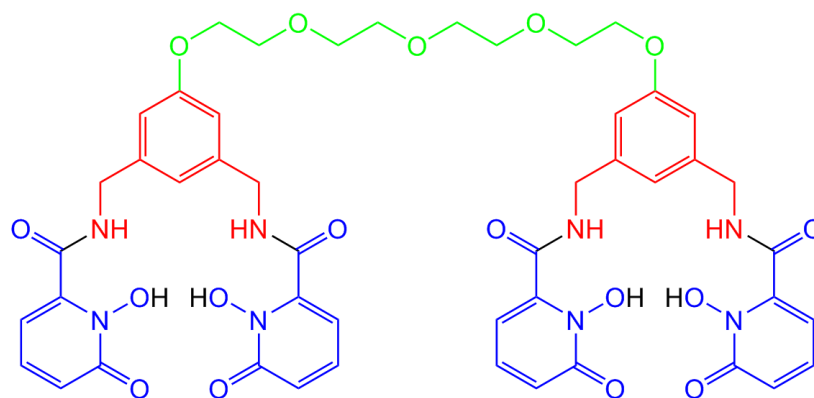
Figure 4.2. Octadentate tetraethylene glycol (green) linked PEG4-1,2-HOPO ligand

Introduction of the PEG linker was expected to shut down the LTP, since the PEG linker would have to somehow pass through the metal center during the rearrangement. That expectation is emphasized in Fig. 4.3, showing the two enantiomers of [Eu(PEG4-5LImXy-1,2-HOPO)]- rotated to demonstrate the impossibility of the LTP pathway.
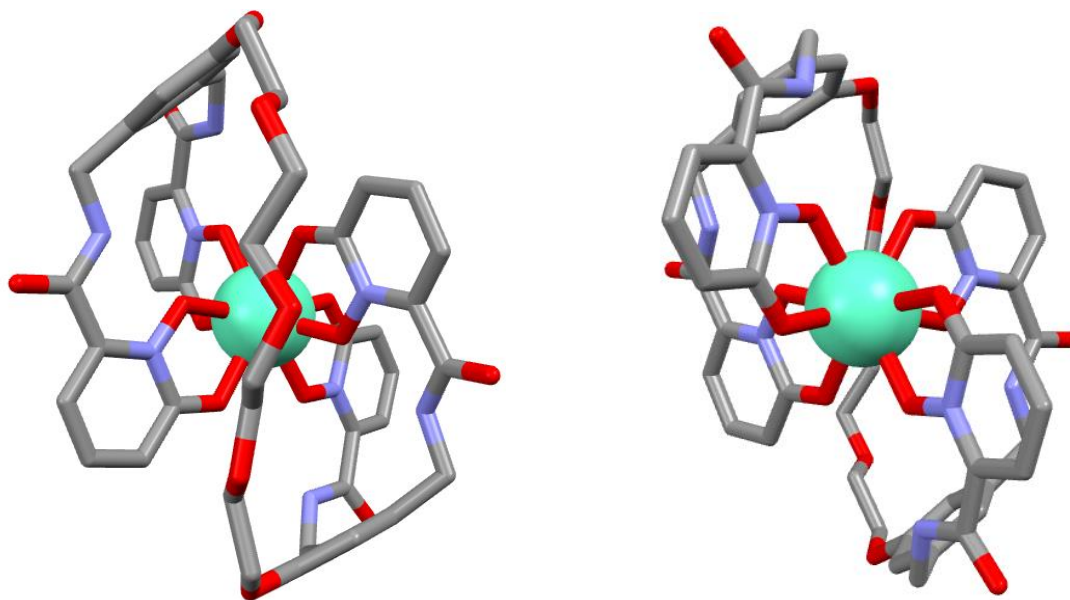
Figure 4.3. The two enantiomers of [Eu(PEG4-5LImXy-1,2-HOPO)]- rotated to demonstrate the proposed LTP shut down

A second ligand type was also investigated for measurement of the HTP. Making use of *meso*-tetrahydrofuran (mTHF) diamine, the 2LImTHF-1,2-HOPO ligand shown in the following figure was synthesized. Like the 5LImXy-1,2-HOPO ligand, the 2LImTHF-1,2-HOPO ligand is achiral, since the two halves of the ligand are related by mirror symmetry. That mirror symmetry is broken upon binding to a lanthanide, resulting in a C_2 symmetric complex (Fig. 4.4).
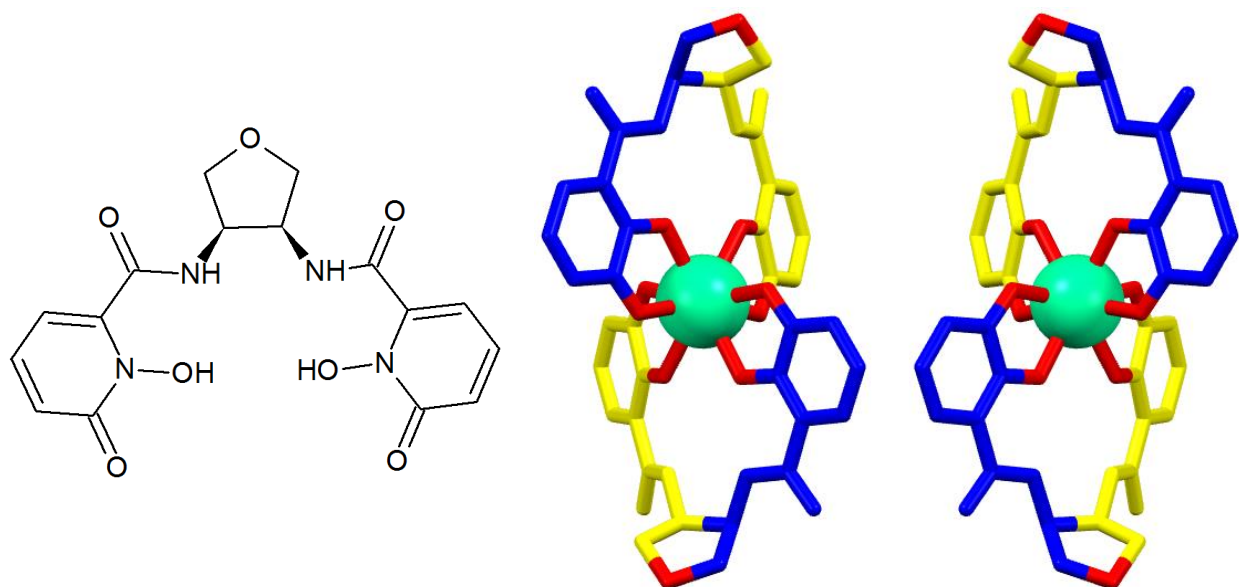
Figure 4.4. The 2LImTHF-1,2-HOPO ligand (left) and the two enantiomers of [Eu(2LImTHF-1,2-HOPO)$_2$]$^-$ (right)

The 2LImTHF-1,2-HOPO complexes cannot undergo the LTP observed for 5LImXy-1,2-HOPO complexes, due to differences in the preferred edges spanned by the diamine backbones. The LTP requires breaking the *a* edges of the dodecahedron, since these edges become the face diagonals of the *llll*-edge antiprismatic transition state.[1–3] These *a* edges, however, cannot be broken for complexes of the 2LImTHF-1,2-HOPO ligand, since the *a* edges are spanned by covalent linkage to the mTHF backbones. Chemical exchange between the two inequivalent ligand arms of 2LImTHF-1,2-HOPO complexes requires at least partial ligand dissociation. The process is therefore most similar to the HTP found for the 5LImXy-1,2-HOPO complexes in chapter 3, and it will be called the HTP even though only one kind of exchange process is observed for the 2LImTHF-1,2-HOPO systems.

Results and Discussion

PEG-1,2-HOPO Complexes. Before synthesis was attempted, geometry optimized structures of the Eu^{III} complexes with varying PEG linker lengths were calculated. In the following table, the structures and shape analyses of the proposed PEG-linked ligand Eu^{III} complexes are compared to the Eu^{III} complexes of the unsubstituted 5LImXy-1,2-HOPO ligand. As expected, the shape analysis numbers approach those of the unsubstituted compound as the PEG linker is increased in length.
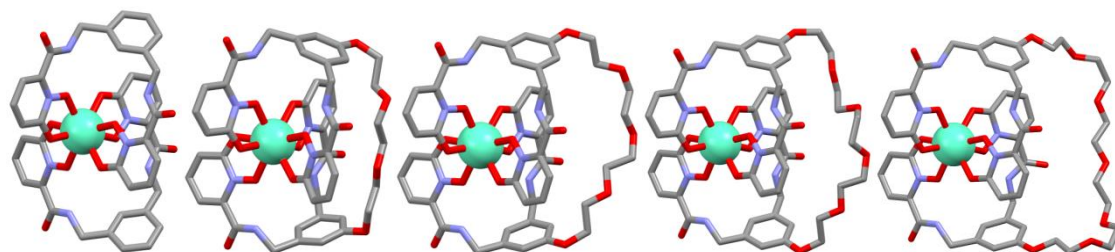
	5LImXy	**PEG3**	**PEG4**	**PEG5**	**PEG6**
D_{4d}	14.9	19.2	19.4	16.7	17.0
C_{2v}	10.9	12.4	13.2	12.1	12.7
D_{2d}	8.2	11.4	10.1	9.1	8.9

Figure 4.5. Structural comparison of PEG linked and unsubstituted [Eu(5LImPhen-1,2-HOPO)$_2$]$^-$ complexes

The synthesis and characterization of the PEG4 and PEG5 ligands are described in this report. The syntheses of the requisite tetramines were adapted from procedures reported for similar 3,2-HOPO ligands.[4] The Eu^{III} complexes of the PEG4 and PEG5 ligands were also synthesized and characterized by luminescence. The optical properties and observed quantum yield are summarized in the following table.[5–7]

Table 4.1. Summary of the optical properties for Eu(III) complexes of the PEG-type ligands

	[Eu(5LImXy-1,2-HOPO)$_2$]$^-$	[Eu(PEG4-1,2-HOPO)]$^-$	[Eu(PEG5-1,2-HOPO)]$^-$
λ_{max} (nm)	333	333	333
Φ_{tot} H$_2$O	0.220	0.160	0.178
τ_{obs} H$_2$O (µs)	733	740	742
τ_{obs} D$_2$O (µs)	1020	1000	1010
τ_{rad} (µs)	1730	1840	1770
k_{rad} (s^{-1})	577	544	564
k_{nonrad} (s^{-1})	787	807	784
η_{Eu}	0.422	0.402	0.420
η_{sens}	0.504	0.398	0.423
q (# of H$_2$O)	0.1	0.1	0.1

The luminescence parameters for the Eu^{III} PEG4- and PEG5-1,2-HOPO complexes are nearly identical to those of the unsubstituted 5LImXy-1,2-HOPO complex, except for two parameters. There are significant differences in the η_{sens} values and quantum yields. The η_{sens} values are affected by the rate of intersystem crossing and the rate of energy transfer, but it is unlikely that the rates of intersystem crossing are different among these samples given the similarities of the ligand structures. The identical λ_{max} values (333 nm) support the notion that the PEG chain has little or no influence on the photophysics of the 1,2-HOPO chromophores (Fig. 5). Instead, we infer that the differences in η_{sens} values are due entirely to the different rates

of energy transfer to the metal. A shorter PEG chain causes greater distortion of the complex from that of the unsubstituted version, resulting in lower rates of energy transfer.
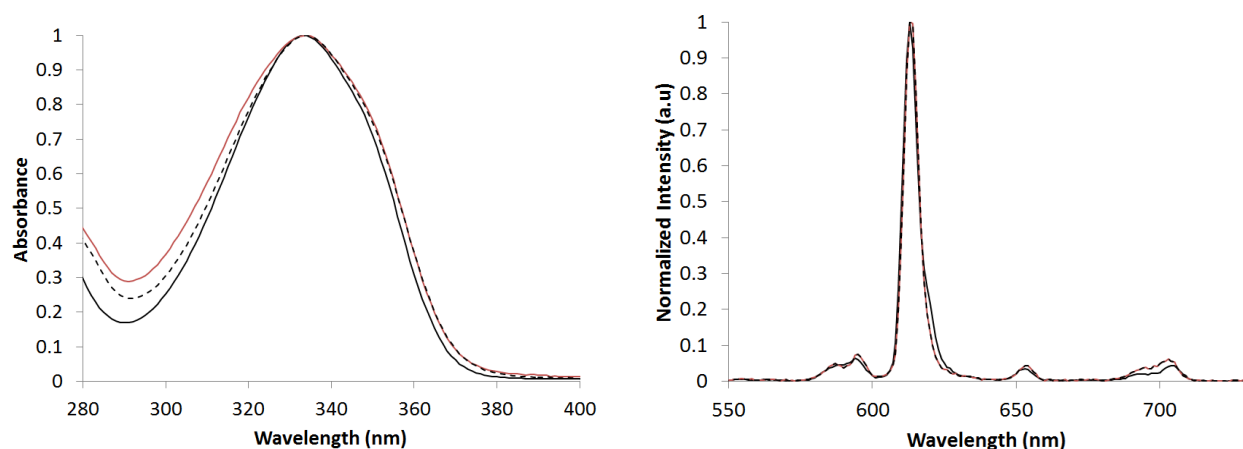
Figure 4.6. UV-visible absorption (left) and luminescent emission (right) spectra of [Eu(5LImXy-1,2-HOPO)$_2$]$^-$ (solid black line), [Eu(PEG4-1,2-HOPO)]$^-$ (black dashed line), and [Eu(PEG5-1,2-HOPO)]$^-$ (red solid line).

The ^{1}H-^{1}H COSY spectra at -15 ^{o}C are shown for [Lu(PEG4-1,2-HOPO)][pyH] and [Lu(5LImXy-1,2-HOPO)$_2$][NMe$_4$] below. The apparent similarity between these two spectra (disregarding peaks for the different counterions) supports the notion that the structures of [Lu(PEG4-1,2-HOPO)]$^-$ and [Lu(5LImXy-1,2-HOPO)$_2$]$^-$ are similar in solution.
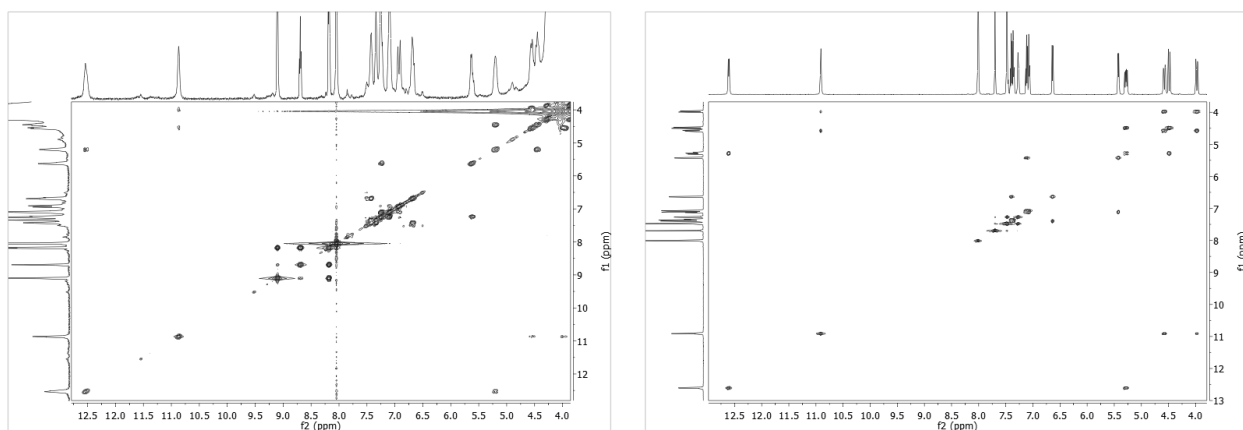
Figure 4.7. ^{1}H-^{1}H COSY of [Lu(PEG4-1,2-HOPO)][pyH] (left) and [Lu(5LImXy-1,2-HOPO)$_2$][NMe$_4$] (right)

In order to test whether the LTP is shut down by presence of the PEG linker in [Lu(PEG4-1,2-HOPO)]$^-$, selective inversion recovery experiments were performed. The results of these experiments are summarized in the following Eyring plot.
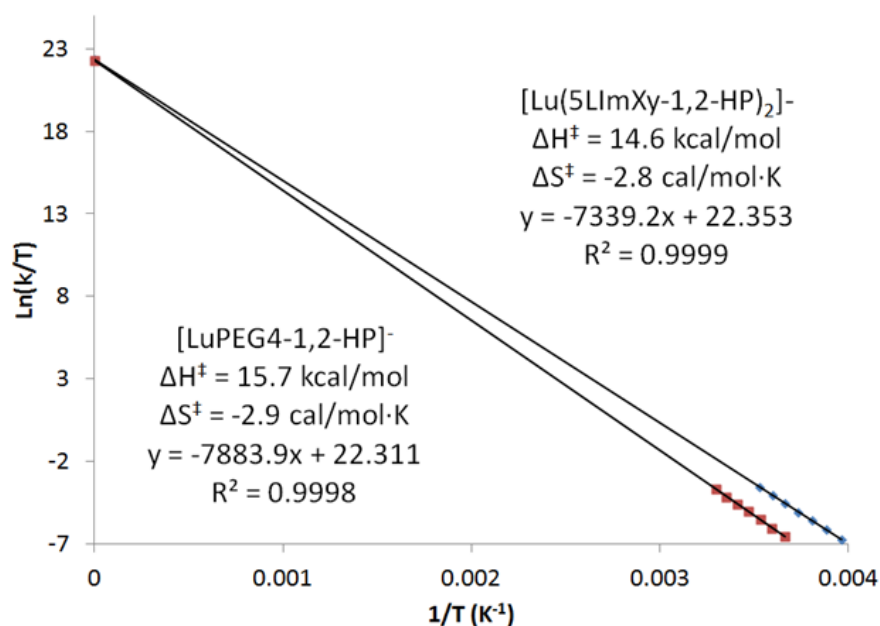
Figure 4.8. Eyring plot of [Lu(PEG4-1,2-HOPO)]⁻ (red) and [Lu(5LImPhen-1,2-HOPO)₂]⁻ (blue)

The Eyring plot demonstrates that the rearrangement processes for [Lu(PEG4-1,2-HOPO)]⁻ and [Lu(5LImXy-1,2-HOPO)₂]⁻ are actually quite similar. The small, negative $\Delta S^{\ddagger}$ values are consistent with intramolecular rearrangements involving no change in coordination number for both complexes. The 1.1 kcal/mol difference in $\Delta H^{\ddagger}$ values indicates a small amount of additional strain for the transition state of the [Lu(PEG4-1,2-HOPO)]⁻ complex compared to unsubstituted [Lu(5LIXy-1,2-HOPO)₂]⁻. This small energy difference can be rationalized by the following proposed mechanism, investigated by DFT optimized structures of likely intermediates involved in the process.
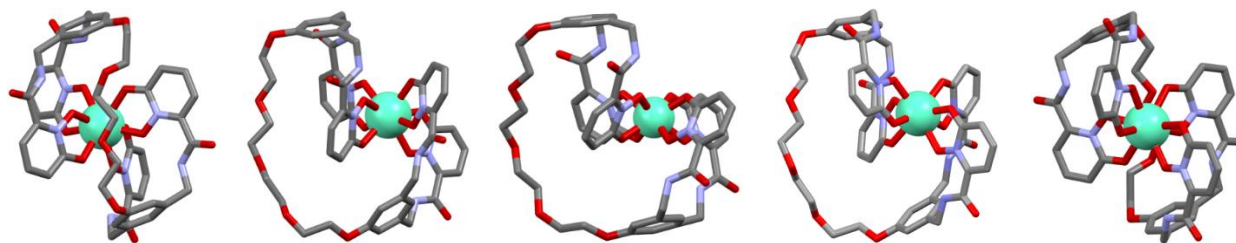
Figure 4.9. Proposed intermediates (middle) between the two enantiomers of [Eu(PEG4-1,2-HOPO)]⁻ (ends)

In the proposed mechanism one of the phenyl rings flips outward, allowing the PEG linker to move around the back side of the 1,2-HOPO units. Essentially, the PEG chain acts like a jump rope that is being held by the two phenyl ring "hands." The fixed length of the PEG chain engenders a more strained transition state than the analogous unsubstituted complex, which explains the 1.1 kcal/mol difference in $\Delta H^{\ddagger}$ values.

2LImTHF-1,2-HOPO Complexes. Although we were not able to grow single crystals of the 2LImTHF-1,2-HOPO complexes, structures of the lanthanide complexes were calculated by DFT. The average M-O distances were found to be slightly longer (0.003 Å on average) than for the corresponding calculated 5LImXy-1,2-HOPO complexes. All of the 2LImTHF-1,2-HOPO complexes are closest to an D_{2d} dodecahedral structure although the D_{2d} shape angles are larger than found in chapter 3, which can be attributed to the reduced flexibility of the mTHF backbone.

Table 4.2. Shape analyses of the DFT calculated 2LImTHF-1,2-HOPO structures

Complex	M-O (Å)	δ Shape Measure (deg.)		
		D_{4d}	C_{2v}	D_{2d}
La	2.54	19.38	15.21	13.43
Ce	2.52	18.97	14.82	13.06
Pr	2.51	18.60	14.47	12.72
Nd	2.49	18.24	14.13	12.41
Sm	2.46	17.59	13.53	11.87
Eu	2.44	17.23	13.20	11.60
Tb	2.42	16.67	12.68	11.16
Dy	2.40	16.37	12.42	10.95
Ho	2.39	16.07	12.16	10.76
Er	2.38	15.78	11.90	10.57
Tm	2.37	15.51	11.66	10.41
Yb	2.36	15.21	11.41	10.25
Lu	2.35	14.93	11.17	10.11

As expected, we find 14 inequivalent resonances in the ^{1}H-NMR spectrum of [Lu(2LImTHF-1,2-HOPO)$_2$]$^-$ at room temperature (Fig. 10). Unlike the 5LImXy-1,2-HOPO complexes, we are not able to make definite assignments due to lack of distinguishable features between the exchange partners. The very similar chemical environments for the two inequivalent arms cause the exchange partners to be very close together, most within 0.05 ppm. The largest gap between partners, found for resonances G and H, is 0.16 ppm.
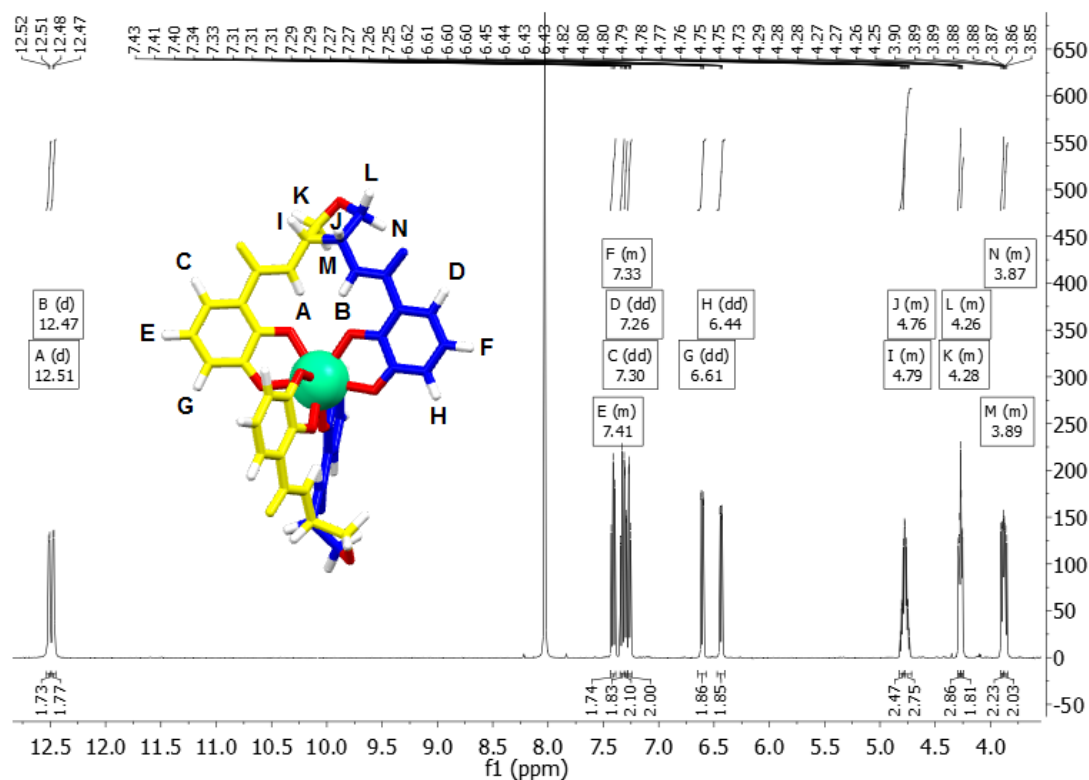
Figure 4.10. ^{1}H-NMR of [Lu(2LImTHF-1,2-HOPO)$_2$]$^-$ at RT, note that assignments distinguishing exchange partners (e.g. A and B, C and D, etc.) are arbitrarily made, 500 MHz

As with the 5LImXy-1,2-HOPO complexes in chapter 3, modeling the ^{1}H-NMR isotropic shifts allows orientation of the magnetic easy axis to be found, and the best-fit assignment of that orientation can help discriminate between the possible geometrical forms of these complexes in solution. Isotropic shifts are composed of two components, the through-space dipolar pseudocontact shifts and the through-bond Fermi contact shifts. As many authors have done previously, we neglect to treat the contact shifts in our fitting procedure, making the assumption that the isotropic shifts are dominated by the dipolar contributions. The ^{1}H-NMR dipolar shifts depend on the angle (θ) between the magnetic axis and the M-H vector, and the shifts are inversely proportional to the cube of the M-H distance (r). The equation that governs this angular dependence is shown below.

$$\delta_{dip} = D_1 \frac{(3\cos^2\theta - 1)}{r^3}$$

(**Equation 4.1**)

Assignments of the ^{1}H-NMR spectra were made possible by EXSY and COSY characterization. Moving towards more paramagnetic metals broadens away the apparent coupling constants of each peak, and the COSY signals drop off accordingly. However, the EXSY signals remain strong throughout the series, and these proved vital for identifying exchange partners the remaining lanthanide complexes. Due to the lack of definite assignments between exchange partners, the experimental values were averaged for both the diamagnetic [Lu(2LImTHF-1,2-HOPO)$_2$]$^-$ reference and the paramagnetic samples. The isotropic shifts were calculated from these average values and are summarized in the following table.

Table 4.3. Summary of observed ^{1}H-NMR isotropic shifts for [M(2LImTHF-1,2-HOPO)$_2$]$^-$ complexes.

^{1}H	Ce	Pr	Nd	Sm	Eu	Tb	Dy	Ho	Er	Tm	Yb
A/B	-15.80	-29.60	-4.21	-0.50	4.13	-90.99	-89.52	-	-17.19	13.56	-2.59
C/D	0.31	0.62	1.17	0.14	-0.91	8.56	1.31	1.51	-5.62	-1.86	-2.94
E/F	2.70	4.46	2.29	0.18	-2.43	18.48	9.60	2.39	-4.69	-3.99	-3.24
G/H	5.13	8.15	1.89	0.57	0.34	49.65	36.63	15.24	-5.30	-9.09	-2.81
I/J	-2.94	-5.58	-0.36	0.0	0.55	-15.6	-17.22	-1.76	8.86	2.92	2.22
K/L	-1.88	-3.52	-0.31	0.01	0.53	-7.82	-10.37	-0.44	3.16	2.60	0.83
M/N	-3.05	-5.60	-0.70	-0.04	0.83	-16.01	-17.33	-2.37	4.64	2.36	2.83

As in chapter 3, the lanthanide complexes can be split into two different groups based on the direction of the isotropic shift for each resonance. The shifts observed for the compounds reported here are smaller in magnitude by about a factor of 2 compared to shifts found in chapter 3. Shifts for the Ce, Pr, Nd, Sm, Tb, Dy, and Ho complexes are all similar in sign, while shifts for the Eu, Er, Tm, and Yb complexes are in the opposite direction, as expected. Nonlinear least squares fitting of these shifts to the equation shown above was performed by minimizing the agreement factor, R, shown below

$$R = \sqrt{\frac{\sum(\delta_{iso}^{obs}-\delta_{dip}^{calc})^2}{\sum(\delta_{iso}^{obs})^2}}$$ **(Equation 4.2)**

Amide resonances A and B show the largest isotropic shifts, reaching -91 ppm for the Tb complex. These especially large ^{1}H-NMR shifts are a result of short M-H distances (3.81 Å). At such short distances, the contact shifts contribute significantly to the observed isotropic shift. Since these large contact shifts cannot be easily quantified, we have omitted the amide peaks from our fitting procedure. By minimizing the agreement factor R, we have fit the isotropic shift data along the three possible axis choices.

Table 4.4. Fitting the isotropic shifts to the three possible high symmetry axes

		Ce	Pr	Nd	Sm	Eu	Tb	Dy	Ho	Er	Tm	Yb
S_4	D_1	-555	-919	-136	-30	122	-3301	-2849	-907	912	463	394
	R	0.260	0.090	0.466	0.770	0.526	0.180	0.161	0.670	0.526	0.384	0.602
C_2	D_1	734	1631	250	49	-215	5920	5107	1360	-1169	-856	-532
	R	0.439	0.214	0.432	0.692	0.564	0.229	0.211	0.622	0.641	0.333	0.653
S_8	D_1	772	1836	258	-	-247	6511	5624	940	-1340	-880	-528
	R	0.743	0.304	0.590	-	0.568	0.393	0.360	0.924	0.782	0.543	0.846

It is clear from most of the one parameter fits that the best choice for the magnetic easy axis is the S_4 axis of the *mam,mam*-DD. Some of the metals with large contact shift components (Nd, Sm, Er, and Ho) were found to favor the true C_2 symmetry axis rather than the pseudo S_8 axis. Interestingly, the closest alternative structures identified for the DFT coordinates (*c$_1$h$_3$v$_2$*, *c$_1$h$_3$v$_2$*-BCTP and *sls,sls*-SA) have high symmetry axes coincident with the S_8 axis in Table 3, representing the worst possible fit to the isotropic shift data. The difference between the S_4 and S_8 high symmetry axes can also be shown in the following two parameter fit. Now, the

orientation of the magnetic easy axis is allowed to rotate about the C_2 symmetry axis relating the two ligands. An α angle of 0 (or 180) corresponds to the S_4 axis shown above, while an α angle of 90 (or 270) corresponds to the S_8 axis.

Table 4.5. Fitting the isotropic shifts to the two parameter model

		Ce	Pr	Nd	Sm	Eu	Tb	Dy	Ho	Er	Tm	Yb
	D1	-566	-920	-136	-33	122	-3305	-2853	-989	928	464	395
S_4	α	6.0	2.7	1.3	14.2	0.0	3.2	3.1	13.9	5.7	2.9	-2.5
	R	0.247	0.083	0.466	0.762	0.526	0.175	0.156	0.656	0.521	0.383	0.601

The R value predictably improves with the addition of the extra fitting parameter. The values found for α range from 14.2 to -2.5, which are all clearly much closer to 0 than 90. Both of these fitting procedures are consistent with a common *mam,mam*-DD structure in solution for these lanthanide complexes. However, these fits are of much poorer quality than the analogous fits of the 5LImXy-1,2-HOPO complexes in chapter 3. We attribute part of the difference to the greater deviation from DD found for the DFT structures in Table 1. It is also likely that the averaged values used to generate the experimental isotropic shifts contribute to the poorer fits seen here.

SIR experiments. The kinetics of the HTP were followed by selective inversion recovery for all except the La and Ce complexes, which were too stereochemically nonrigid to measure within the solvent temperature window. Some of the metals (Ho, Er, and Yb) did not have the well-spaced peaks necessary for clean inversions, and so reliable data could not be collected for these samples. The Eyring plot and corresponding linear fits reveal that the slopes and intercepts change gradually moving across the lanthanide series. Changes in the absolute positions of the lines are more pronounced for the largest members (Nd and Pr) evaluated here (Fig. 11).
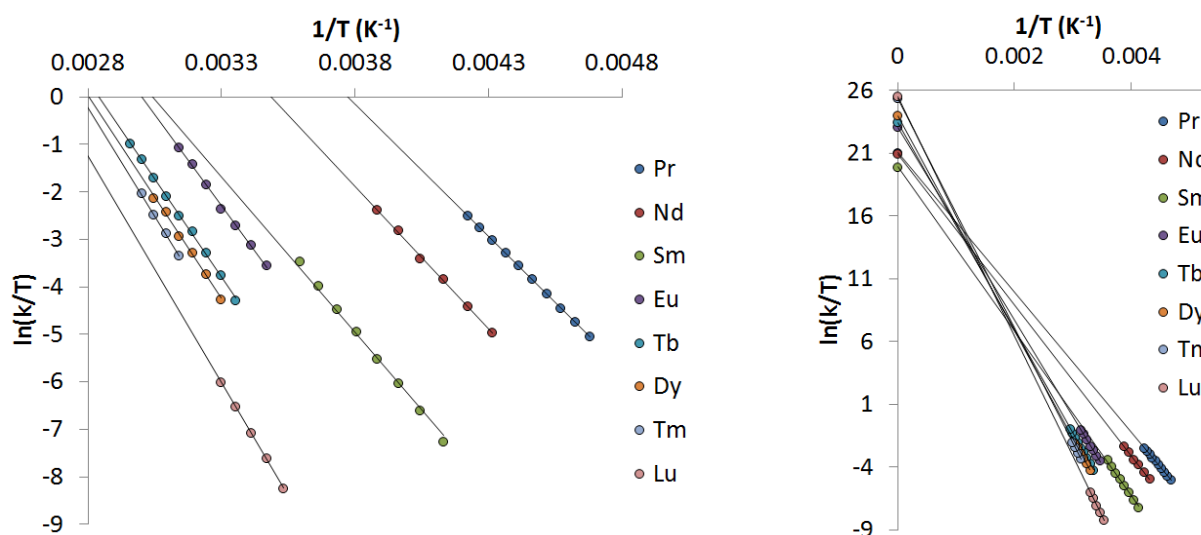
Figure 4.11. Eyring plot for Pr, Nd, Sm, Eu, Tb, Dy, Tm, and Lu complexes of 2LImTHF-1,2-HOPO

Table 4.6. Linear fits of the SIR kinetic data and the activation constants derived from them

	Pr	Nd	Sm	Eu	Tb	Dy	Tm	Lu
Slope	-5570	-6000	-7010	-7680	-8260	-8560	-9130	-9540
Intercept	21.0	20.9	21.7	23.0	23.5	24.0	25.4	25.5
R	0.99990	0.9990	0.9997	0.997	0.9990	0.996	0.9995	0.9994
$\Delta H^{\ddagger}$	11.06(5)	11.9(2)	13.9(1)	15.2(3)	16.4(2)	17.0(5)	18.1(3)	19.0(3)
$\Delta S^{\ddagger}$	-5.4(2)	-5.6(8)	-4.1(4)	-1.4(11)	-0.6(7)	0.4(17)	3.2(9)	3.4(9)
$\Delta G^{\ddagger}$ (298 K)	12.7	13.6	15.1	15.7	16.6	16.9	17.2	17.9
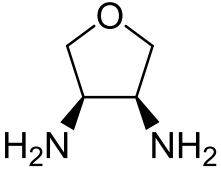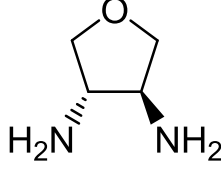
The $\Delta G^{\ddagger}$ barrier at 298 K gradually increases across the lanthanide series. Larger changes in the $\Delta G^{\ddagger}$ barrier are noted for early lanthanides, consistent with the steepness of the lanthanide contraction in that region. In general, these HTP barriers are 2.5-3 kcal/mol larger than found for the LTP in chapter 3. The $\Delta S^{\ddagger}$ values are slightly negative toward the larger metals Pr and Nd, while values are slightly positive for the smaller metals Tm and Lu. We have determined $\Delta G^{\ddagger}$ at 298 K for a wet sample of the Lu complex to be 15.8 kcal/mol, much lower than the 17.9 kcal/mol found for sample reported in Table 5. This large change in $\Delta G^{\ddagger}$ as a function of solvent is consistent with the expectation that the HTP observed for the 2LImTHF-1,2-HOPO complexes involves ligand dissociation and solvent participation.

Luminescence. The aqueous photoluminescent properties of [Eu(2LImTHF-1,2-HOPO)$_2$]$^-$ and [Eu(2LIssTHF-1,2-HOPO)$_2$]$^-$ were evaluated, and we compare the normalized absorption and emission profiles of the two complexes below. The luminescence parameters derived from these spectra are also tabulated below. The DFT calculated structure of [Eu(2LIssTHF-1,2-HOPO)$_2$]$^-$ yielded shape parameters similar to the structure of [Eu(2LImTHF-1,2-HOPO)$_2$]$^-$ ($D_{4d}/C_{2v}/D_{2d}$ = 18.19/13.79/10.31 compared to 17.23/13.20/11.60 respectively), and the overall symmetry of Eu(2LIssTHF-1,2-HOPO)$_2$]$^-$ complex was found to be D_2.
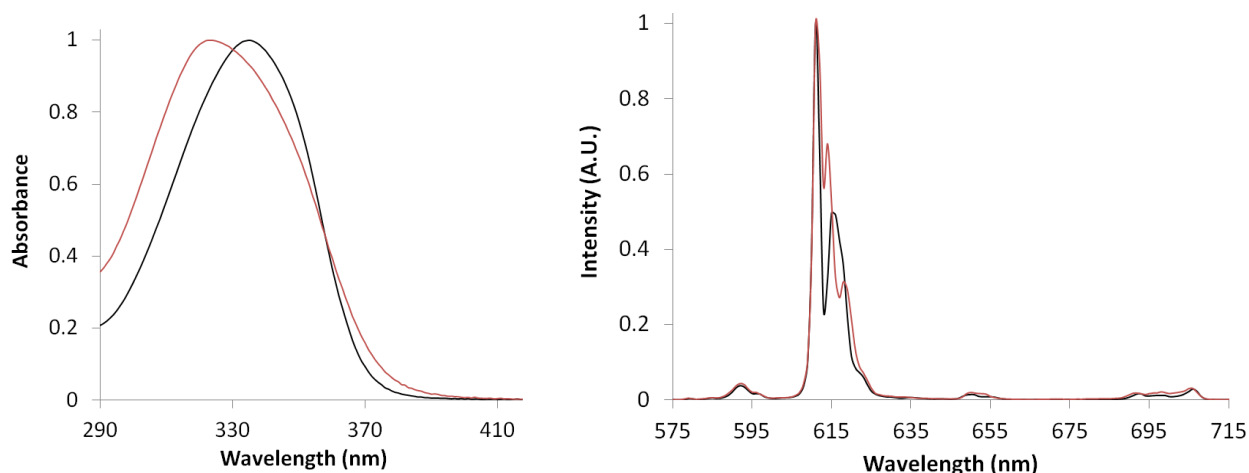
Figure 4.12. UV-visible absorption (left) and luminescent emission (right) spectra of [Eu(2LImTHF-1,2-HOPO)$_2$]$^-$ (black) and [Eu(2LIssTHF-1,2-HOPO)$_2$]$^-$ (red).

Table 4.7. Summary of the optical properties for Eu^{III} complexes of the THF-type ligands

	[Eu(2LImTHF-1,2-HOPO)$_2$]$^-$	[Eu(2LIssTHF-1,2-HOPO)$_2$]$^-$
λ_{max} (nm)	335	323
Φ_{tot} H$_2$O	0.202	0.096
τ_{obs} H$_2$O (µs)	600	582
τ_{obs} D$_2$O (µs)	795	781
τ_{rad} (µs)	1380	1390
k_{rad} (s^{-1})	726	717
k_{nonrad} (s^{-1})	941	1001
η_{Eu}	0.435	0.417
η_{sens}	0.466	0.229
q (# of H$_2$O)	0.1	0.1

As with the PEG ligands in the previous section, we note that most of the luminescent parameters for the Eu^{III} THF complexes are nearly identical, except for two. There are significant differences in the η_{sens} values and quantum yields. The η_{sens} values are affected by the rate of intersystem crossing and the rate of energy transfer, but it is unlikely that the rates of intersystem crossing are different among these samples given the similarities of the ligands. These complexes provide further evidence that small changes in ligand geometry can have large effects on the Eu^{III} photoluminescence.

Conclusions

We have synthesized and characterized two new groups of ligands, toward finding a system where the HTP could be measured by ^{1}H-NMR SIR experiments. The PEG ligands were found to rearrange by an intramolecular mechanism, despite expectations that the PEG linker would shut down the LTP for these systems. The 2LImTHF-1,2-HOPO ligand allowed measurement of the HTP for most of the lanthanide series, and the associated barriers were found to be 2.5-3 kcal/mol larger than those found for the LTP in chapter 3. Modeling the ^{1}H-NMR isotropic shifts confirmed the DFT calculations, which predicted a D_{2d} dodecahedral structures for Ln^{III} complexes of the 2LImTHF-1,2-HOPO ligand. The Eu^{III} photoluminescence measurements for both the PEG and THF show differences in quantum yield that are associated with differences in sensitization efficiency rather than differences in metal centered efficiency. These results indicate that ligand geometry can play a large role in determining the overall quantum yield of these luminescent systems.

Experimental

General Methods. The hydrated Ln^{III} chloride salts were purchased from Sigma-Aldrich. Tetraethylene glycol, pentaethylene glycol, and dimethyl 5-hydroxyisophthalate were purchased

from Alfa Aesar. All other solvents and reagents were purchased from VWR and were used as received. Thin-layer chromatography (TLC) was performed using precoated Kieselgel 60 F$_{254}$ plates. Flash chromatography was performed using Silicycle SiliaFlash P60 silica (230-400 mesh). ^{1}H- and ^{13}C-NMR spectra were collected on Bruker AV-500, DRX-500 spectrometers, operating at 500 (125) MHz for ^{1}H (or ^{13}C) respectively. ^{1}H (or ^{13}C) chemical shifts are reported in parts per million relative to the solvent resonances, taken as δ 7.24 (δ 77.23), δ 2.50 (δ 39.51), and δ 2.75 (δ 29.76), for CDCl$_3$, DMSO-d$_6$, and DMF-d$_7$ respectively. A sealed capillary of 1% TMS in CDCl$_3$ was used to standardize the chemical shifts of the paramagnetic compounds. Coupling constants (*J*) are reported in hertz. The following standard abbreviations are used for characterization of ^{1}H NMR signals: s=singlet, d=doublet, t=triplet, m=multiplet, dd = doublet of doublets. High resolution electrospray ionization mass spectra (HRMS-ESI) and elemental analyses were performed by the Microanalytical Laboratory, University of California, Berkeley, CA.

PEG5-ester. The PEG5-ditosylate was synthesized from p-toluenesulfonyl chloride and pentaethylene glycol according to an adapted literature procedure and was used without purification.[8] In a 250 mL round bottom flask, PEG5-ditosylate (14.8 g, 27.0 mmol), dimethyl 5-hydroxyisophthalate (11.35 g, 54.0 mmol), and potassium carbonate (14.9 g, 108 mmol) were combined in DMF (125 mL) and heated to 120 °C overnight with stirring. Once cooled, the reaction was poured into water (500 mL), and the product was extracted with ethyl acetate (3x200 mL). The volume was reduced and then loaded onto a column. Unreacted dimethyl 5-hydroxyisophthalate was eluted with 1:2 ethyl acetate:hexanes, then the desired product was eluted with neat ethyl acetate. Solvent removal afforded a colorless oil. Yield: 7.37 g, 44 %. ^{1}H NMR (400 MHz, DMSO-d$_6$): δ 3.51 (s, 4H, OC*H$_2$*), 3.51-3.55 (m, 4H, OC*H$_2$*), 3.56-3.61 (m, 4H, OC*H$_2$*), 3.73-3.78 (m, 4H, OC*H$_2$*), 3.86 (s, 12H, C*H$_3$*), 4.16-4.21 (m, 4H, OC*H$_2$*), 7.62 (d, ^4J = 1.4 Hz, 4H, Ar*H*), 8.00 (t, ^4J = 1.4 Hz, 2H, Ar*H*). ^{13}C NMR (100 MHz, DMSO-d$_6$): δ 52.49, 67.94, 68.72, 69.80, 69.81, 69.95, 119.26, 121.74, 128.30, 131.38, 158.72, 165.11. HRMS-ESI (*m/z*, [M+Na]$^+$) Calcd for ^{12}C$_{30}$H$_{38}$O$_{14}$^{23}Na: 645.2154, Found: 645.2152.

PEG5-bromide. In a round bottom flask, PEG5-ester (7.22 g, 11.6 mmol) was dissolved in toluene (60 mL) and cooled on ice under N$_2$. RedAl (57.9 mmol, 17.25 mL) was then added dropwise to the stirring solution, causing precipitation of an insoluble glop, which was left to warm to RT overnight. The reaction was quenched by adding water (50 mL) all at once, causing dissolution of the glop, and was then stirred at RT for several hours. The aluminum salts were filtered off on a pad of celite, and the pad was washed several times with water. The combined filtrate was acidified with a minimal amount of HCl and was then evaporated to dryness. PBr$_3$ (7.81 g, 28.9 mmol) dissolved in dichloromethane (250 mL) was added to the resulting oil, and the reaction was stirred at RT overnight. The reaction was quenched by addition of aqueous bicarbonate, and the organic layer was separated and concentrated. Column chromatography using dichloromethane, then 5% ether, then 10% ether afforded excellent separation of the desired product. Concentration of the eluent resulted in a colorless oil. Yield: 4.58 g, 52 %. ^{1}H NMR (400 MHz, DMSO-d$_6$): δ 3.52 (s, 4H, OC*H$_2$*), 3.52-3.55 (m, 4H, OC*H$_2$*), 3.56-3.60 (m, 4H, OC*H$_2$*), 3.71-3.75 (m, 4H, OC*H$_2$*), 4.06-4.11 (m, 4H, OC*H$_2$*), 4.64 (s, 8H, C*H$_2$*), 6.98 (d, ^4J = 1.4 Hz, 4H, Ar*H*), 7.10 (t, ^4J = 1.4 Hz, 2H, Ar*H*). ^{13}C NMR (100 MHz, DMSO-d$_6$): δ 33.86, 67.32, 68.80, 69.78, 69.79, 69.92, 115.26, 122.34, 139.77, 158.50. HRMS-ESI (*m/z*, [M+Na]$^+$) Calcd for ^{12}C$_{26}$H$_{34}$O$_6$^{79}Br$_2$^{81}Br$_2$^{23}Na: 784.8940, Found: 784.8947.

65

PEG5-azide. In a round bottom flask, PEG5-bromide (4.17 g, 5.47 mmol) and sodium azide (3.56 g, 54.7 mmol) were combined with acetone (150 mL). The reaction was heated to reflux overnight with stirring. Upon cooling, the salts were filtered off and the filtate was concentrated. The resulting oil was dissolved into diethyl ether, filtered, and concentrated again to yield a colorless oil. Yield: 3.27 g, 98 %. ^{1}H NMR (400 MHz, DMSO-d$_6$): δ 3.51 (s, 4H, OCH_2), 3.51-3.55 (m, 4H, OCH_2), 3.56-3.60 (m, 4H, OCH_2), 3.72-3.76 (m, 4H, OCH_2), 4.08-4.13 (m, 4H, OCH_2), 4.43 (s, 8H, CH_2), 6.94 (s, 6H, ArH). ^{13}C NMR (100 MHz, DMSO-d$_6$): δ 53.30, 67.29, 68.82, 69.78, 69.79, 69.93, 114.11, 120.35, 137.60, 158.82. HRMS-ESI (*m/z*, [M+Na]$^+$) Calcd for [12]C$_{26}$H$_{34}$N$_{12}$O$_6$[23]Na: 633.2616, Found: 633.2613.

PEG5-amine. In round bottom flask, PEG5-azide (3.27 g, 5.36 mmol) and 5% Pd/C (1.15 g) were combined in methanol (100 mL). The reaction vessel was placed into a bomb and pressurized with H$_2$ to 200 psi. After stirring at RT for two days, the bomb was depressurized and the Pd/C was filtered off. Evaporation of the solvent left a colorless oil. Yield: 2.66 g, 98 %. ^{1}H NMR (400 MHz, DMSO-d$_6$): δ 3.52 (s, 4H, OCH_2), 3.52-3.55 (m, 4H, OCH_2), 3.56-3.60 (m, 4H, OCH_2), 3.63 (s, 8H, CH_2), 3.69-3.74 (m, 4H, OCH_2), 4.01-4.08 (m, 4H, OCH_2), 6.75 (s, 4H, ArH), 6.82 (s, 2H, ArH). ^{13}C NMR (100 MHz, DMSO-d$_6$): δ 45.75, 66.88, 69.03, 69.81, 69.82, 69.94, 110.87, 118.01, 145.57, 158.52.

PEG5-1,2-HOPOBn. Note that even though the amine starting material is aliphatic, it does not seem to react with 1,2-HOPOBn thiaz as would be expected, possibly due to poor insolubility in dichloromethane. In a 250 mL round bottom flask, PEG5-amine (572 mg, 1.13 mmol) was dissolved into water (20 mL) containing potassium carbonate (1.62 g, 11.74 mmol), and the flask was cooled in an ice bath with stirring. In a separate flask, 1,2-HOPOBn acid chloride (1.55 g, 5.87 mmol) was dissolved into dichloromethane (20 mL). The acid chloride was added to the amine solution dropwise, and the reaction was stirred with warming to RT overnight. The organic layer was separated and loaded onto column using dichloromethane. Slowly increasing the methanol concentration to 5% afforded the desired product as a colorless foam upon solvent removal. Yield: 898 mg, 56 %. ^{1}H NMR (400 MHz, DMSO-d$_6$): δ 3.46-3.54 (m, 12H, OCH_2), 3.57-3.61 (m, 4H, OCH_2), 3.81-3.86 (m, 4H, OCH_2), 4.34 (d, ^3J = 5.9 Hz, 8H, CH_2), 5.24 (s, 8H, CH_2), 6.34 (dd, ^3J = 6.7 Hz, ^4J = 1.6 Hz, 4H, =CH), 6.66 (dd, ^3J = 9.3 Hz, ^4J = 1.6 Hz, 4H, =CH), 6.77 (s, 4H, ArH), 6.84 (s, 2H, ArH), 7.33-7.41 (m, 20H, BnH), 7.48 (dd, ^3J = 9.2 Hz, ^3J = 6.7 Hz, 4H, =CH), 9.36 (t, ^3J = 6.0 Hz, 4H, NH). ^{13}C NMR (100 MHz, DMSO-d$_6$): δ 42.38, 66.86, 68.78, 69.73, 69.77, 69.87, 78.36, 104.07, 112.04, 118.57, 122.56, 128.41, 128.98, 129.59, 133.79, 138.93, 139.91, 143.86, 157.50, 158.68, 160.46. HRMS-ESI (*m/z*, [M+Na]$^+$) Calcd for [12]C$_{78}$H$_{78}$N$_8$O$_{18}$[23]Na: 1437.5326, Found: 1437.5360.

THF ligands. The THF ligands were prepared in a manner similar to the PEG5-1,2-HOPOBn ligand shown above, using 10 mmol of the requisite diamines. The *m*THF diamine starting material was synthesized from 1,4-anhydroerythritol according to published procedures.[9] Similarly, the ssTHF diamine starting material was synthesized from 1,4-anhydrothreiotol, following reduction and condensation of (+)-dimethyl L-tartrate according to published procedures.[9,10]

2LImTHF-1,2-HOPOBn. Yield:4.9 g, 88 %. ^{1}H NMR (500 MHz, CDCl$_3$) δ 7.96 (d, J = 6.7 Hz, 2H, NH), 7.39 – 7.22 (m, 10H, BnH), 7.01 (dd, J = 9.2, 6.9 Hz, 2H, =CH), 6.34 (dd, J = 9.2, 1.6 Hz, 2H, =CH), 6.09 (dd, J = 6.8, 1.6 Hz, 2H, =CH), 5.21 (d, J = 8.6 Hz, 2H, CH_2), 5.01 (d, J =

8.5 Hz, 2H, CH_2), 4.81 (h, J = 7.4 Hz, 2H, CH), 3.93 (dd, J = 9.3, 5.7 Hz, 2H, CH_2), 3.60 (dd, J = 9.5, 3.7 Hz, 2H, CH_2). ^{13}C NMR (125 MHz, CDCl$_3$): δ 160.30, 158.43, 142.21, 138.45, 132.92, 130.01, 129.50, 128.63, 123.37, 106.74, 79.44, 71.52, 51.42. HRMS-ESI (*m/z*, [M+Na]$^+$) Calcd for ^{12}C$_{30}$H$_{28}$N$_4$O$_7$^{23}Na: 579.1850, Found: 579.1846.

2LIssTHF-1,2-HOPOBn. Yield: 4.8 g, 86 %. ^{1}H NMR (500 MHz, CDCl$_3$) δ 7.81 (d, J = 5.7 Hz, 2H, NH), 7.44 – 7.26 (m, 10H, BnH), 7.24 (dd, J = 9.2, 6.9 Hz, 2H, =CH), 6.67 (dd, J = 9.2, 1.6 Hz, 2H, =CH), 6.50 (dd, J = 6.8, 1.6 Hz, 2H, =CH), 5.31 (d, J = 9.0 Hz, 2H, CH_2), 5.20 (d, J = 9.0 Hz, 2H, CH_2), 4.34 (h, J = 4.0 Hz, 2H, CH), 4.04 (dd, J = 9.7, 5.9 Hz, 2H, CH_2), 3.57 (dd, J = 9.7, 4.6 Hz, 2H, CH_2). ^{13}C NMR (125 MHz, CDCl$_3$): δ 160.13, 158.52, 141.41, 138.12, 132.86, 130.10, 129.62, 128.75, 124.48, 107.39, 79.34, 71.47, 57.05. HRMS-ESI (*m/z*, [M-H]$^-$) Calcd for ^{12}C$_{30}$H$_{27}$N$_4$O$_7$: 555.1885, Found: 555.1894.

Method for Deprotection of Ligands. The appropriate benzyl protected ligand was dissolved into glacial acetic acid (20 mL) at room temperature. Fuming hydrochloric acid (20 mL) was added to the homogenous solution, and the reaction was stirred at room temperature for three days. The solvent was removed, and the resulting glass was dissolved into methanol (5 mL). The product was precipitated by adding the methanolic solution dropwise to a flask of anhydrous diethyl ether (250 mL) with vigorous stirring. The suspension was stirred overnight, filtered, washed with ether (3x10 mL), and dried to afford free flowing white powder.

PEG4-1,2-HOPO. Yield: 570 mg, 89 %. ^{1}H NMR (400 MHz, DMSO-d$_6$): δ 3.51-3.62 (m, 8H, OCH_2), 3.74 (m, 4H, OCH_2), 4.06 (m, 4H, OCH_2), 4.40 (d, ^3J = 5.9 Hz, 8H, CH_2), 6.34 (dd, ^3J = 6.9 Hz, ^4J = 1.5 Hz, 4H, =CH), 6.59 (dd, ^3J = 9.1 Hz, ^4J = 1.5 Hz, 4H, =CH), 6.81 (s, 4H, ArH), 6.87 (s, 2H, ArH), 7.40 (dd, ^3J = 9.1 Hz, ^3J = 6.9 Hz, 4H, =CH), 9.30 (t, ^3J = 5.9 Hz, 4H, NH). ^{13}C NMR (100 MHz, DMSO-d$_6$): δ 42.25, 67.07, 68.93, 69.80, 69.92, 103.72, 111.62, 117.98, 119.40, 137.29, 140.11, 142.13, 157.43, 158.70, 160.41. HRMS-ESI (*m/z*, [M+Na]$^+$) Calcd for ^{12}C$_{48}$H$_{50}$N$_8$O$_{17}$^{23}Na: 1033.3186, Found: 1033.3199. Anal. Calcd (Found) for C$_{48}$H$_{50}$N$_8$O$_{17}$·1.75H$_2$O: C 55.30 (55.14), H 5.17 (4.97), N 10.75 (10.58) %.

PEG5-1,2-HOPO. Yield: 576 mg, 86 %. ^{1}H NMR (400 MHz, DMSO-d$_6$): δ 3.47-3.61 (m, 12H, OCH_2), 3.74 (m, 4H, OCH_2), 4.06 (m, 4H, OCH_2), 4.40 (d, ^3J = 6.0 Hz, 8H, CH_2), 6.34 (dd, ^3J = 6.9 Hz, ^4J = 1.6 Hz, 4H, =CH), 6.59 (dd, ^3J = 9.1 Hz, ^4J = 1.6 Hz, 4H, =CH), 6.81 (s, 4H, ArH), 6.87 (s, 2H, ArH), 7.40 (dd, ^3J = 9.1 Hz, ^3J = 6.9 Hz, 4H, =CH), 9.30 (t, ^3J = 6.0 Hz, 4H, NH). ^{13}C NMR (100 MHz, DMSO-d$_6$): δ 42.25, 67.06, 68.93, 69.77, 69.78, 69.92, 103.74, 111.63, 117.98, 119.41, 137.30, 140.11, 142.14, 157.43, 158.71, 160.41. HRMS-ESI (*m/z*, [M+Na]$^+$) Calcd for ^{12}C$_{50}$H$_{54}$N$_8$O$_{18}$^{23}Na: 1077.3448, Found: 1077.3467. Anal. Calcd (Found) for C$_{50}$H$_{54}$N$_8$O$_{18}$·2.9H$_2$O: C 54.24 (54.68), H 5.44 (5.42), N 10.12 (9.66) %.

2LImTHF-1,2-HOPO. Yield: 3.1 g, 91%. ^{1}H NMR (500 MHz, DMSO-d$_6$) δ 8.85 (d, J = 7.5 Hz, 2H, NH), 7.40 (dd, J = 9.0, 7.0 Hz, 2H, =CH), 6.61 (dd, J = 9.1, 1.6 Hz, 2H, =CH), 6.39 (dd, J = 6.9, 1.6 Hz, 2H, =CH), 4.65 (h, J = 6.3 Hz, 2H, CH), 4.01 (dd, J = 8.8, 6.4 Hz, 2H, CH_2), 3.64 (dd, J = 8.9, 5.1 Hz, 2H, CH_2). ^{13}C NMR (125 MHz, DMSO-d$_6$): δ 160.33, 157.43, 141.66, 137.07, 119.47, 104.63, 69.85, 50.97. HRMS-ESI (*m/z*, [M-H]$^-$) Calcd for ^{12}C$_{16}$H$_{15}$N$_4$O$_7$: 375.0946, Found: 375.0952. Anal. Calcd (Found) for C$_{16}$H$_{16}$N$_4$O$_7$·1.5H$_2$O: C 47.65 (47.73), H 4.75 (4.74), N 13.89 (13.78) %.

2LIssTHF-1,2-HOPO. Yield: 3.3 g, 94%. ^{1}H NMR (500 MHz, DMSO-d$_6$) δ 9.24 (d, J = 6.7 Hz, 2H, NH), 7.41 (dd, J = 9.1, 6.9 Hz, 2H, =CH), 6.58 (dd, J = 9.1, 1.6 Hz, 2H, =CH), 6.31 (dd, J = 6.9, 1.6 Hz, 2H, =CH), 4.37 (dq, J = 7.5, 3.3 Hz, 2H, CH), 4.03 (dd, J = 9.1, 5.7 Hz, 2H, CH_2), 3.61 (dd, J = 9.2, 3.9 Hz, 2H, CH_2). ^{13}C NMR (125 MHz, DMSO-d$_6$): δ 160.28, 157.48, 142.04, 137.38, 119.64, 103.72, 71.28, 55.18. HRMS-ESI (*m/z*, [M-H]$^-$) Calcd for ^{12}C$_{16}$H$_{15}$N$_4$O$_7$: 375.0946, Found: 375.0952. Anal. Calcd (Found) for C$_{16}$H$_{16}$N$_4$O$_7$·2.7H$_2$O: C 45.22 (44.84), H 5.08 (4.7), N 13.18 (12.92) %.

Preparation of the PEG Complexes. The appropriate PEG ligand (0.10 mmol) was dissolved into DMF (2 mL) and metal chloride salt (0.10 mmol) was dissolved into MeOH (2 mL). Excess pyridine was added, and the two solutions were combined and heated to 80 ^{o}C overnight under N$_2$. After cooling, the volatiles were removed under vacuum, leaving behind a residue containing pyridinium chloride and the desired metal complexes.

[Lu(PEG4-1,2-HOPO)][pyH]. HRMS-ESI (*m/z*, [M]$^-$) Calcd for ^{12}C$_{48}$H$_{46}$N$_8$O$_{17}$^{175}Lu: 1181.2389, Found: 1181.2366.

[Eu(PEG4-1,2-HOPO)][pyH]. HRMS-ESI (*m/z*, [M]$^-$) Calcd for ^{12}C$_{48}$H$_{46}$N$_8$O$_{17}$^{151}Eu: 1159.2193, Found: 1159.2178.

[Eu(PEG5-1,2-HOPO)][pyH]. HRMS-ESI (*m/z*, [M]$^-$) Calcd for ^{12}C$_{50}$H$_{50}$N$_8$O$_{18}$^{151}Eu: 1203.2456, Found: 1203.2482.

Preparation of the THF Complexes. The THF ligand (0.21 mmol) and the appropriate metal chloride salt (0.1 mmol) were dissolved into MeOH (3 mL). Excess pyridine was added, and the reaction was heated to reflux for four hours. Upon cooling, the solvent was decanted off, and fresh MeOH (3 mL) was added, along with NMe$_4$OH·5H$_2$O (0.5 mmol). The reaction was again heated briefly and then cooled. The precipitate was collected by filtration and washed with ice cold MeOH (3x1 mL).

[La(2LImTHF-1,2-HOPO)$_2$][NMe$_4$]. Yield: 76 mg, 75 %. ^{1}H NMR (500 MHz, DMF-d$_7$, 20 °C): δ 12.23 (d, J = 4.5 Hz, 4H), 7.39 (dd, J = 8.4, 7.6 Hz, 4H), 7.29 (dd, J = 7.5, 1.8 Hz, 4H), 6.57 (dd, J = 8.5, 1.7 Hz, 4H), 4.80 (q, J = 5.5 Hz, 4H), 4.25 (dd, J = 8.9, 6.0 Hz, 4H), 3.89 (dd, J = 8.9, 5.1 Hz, 4H). HRMS-ESI (*m/z*, [M]$^-$) Calcd for C$_{32}$H$_{28}$N$_8$O$_{14}$^{139}La: 887.0794, Found: 887.0809. Anal. Calcd (Found) for [La(C$_{16}$H$_{14}$N$_4$O$_7$)$_2$][C$_4$H$_{12}$N]·3H$_2$O: C 42.57 (42.30), H 4.56 (4.31), N 12.41 (12.47) %.

[Ce(2LImTHF-1,2-HOPO)$_2$][NMe$_4$]. Yield: 63 mg, 62 %. ^{1}H NMR (500 MHz, DMF-d$_7$, -50 °C): δ 11.82 (s, 2H), 11.47 (s, 2H), 10.35 (s, 2H), 9.78 (s, 2H), 7.99 (s, 2H), 7.18 (s, 2H), 2.47 (s, 2H), 2.30 (s, 2H), 1.96 (s, 2H), 1.72 (s, 2H), 0.94 (s, 2H), 0.70 (s, 2H), -2.36 (s, 2H), -4.27 (s, 2H). HRMS-ESI (*m/z*, [M]$^-$) Calcd for C$_{32}$H$_{28}$N$_8$O$_{14}$^{140}Ce: 888.0785, Found: 888.0806. Anal. Calcd (Found) for [Ce(C$_{16}$H$_{14}$N$_4$O$_7$)$_2$][C$_4$H$_{12}$N]·2.4H$_2$O: C 42.98 (42.95), H 4.49 (4.49), N 12.53 (12.59) %.

[Pr(2LImTHF-1,2-HOPO)$_2$][NMe$_4$]. Yield: 78 mg, 77 %. ^{1}H NMR (500 MHz, DMF-d$_7$, -45 °C): δ 14.67 (s, 4H), 12.16 (s, 2H), 11.51 (s, 2H), 8.41 (d, J = 7.5 Hz, 2H), 7.40 (d, J = 6.8 Hz, 2H), 0.88 (s, 2H), 0.61 (s, 2H), -0.63 (s, 2H), -0.97 (s, 2H), -1.51 (s, 2H), -1.93 (s, 2H), -15.80 (s, 2H), -18.41 (s, 2H). HRMS-ESI (*m/z*, [M]$^-$) Calcd for C$_{32}$H$_{28}$N$_8$O$_{14}$^{141}Pr: 889.0807, Found:

889.0818. Anal. Calcd (Found) for [Pr(C$_{16}$H$_{14}$N$_4$O$_7$)$_2$][C$_4$H$_{12}$N]·3.2H$_2$O: C 42.37 (42.14), H 4.58 (4.34), N 12.35 (12.17) %.

[Nd(2LImTHF-1,2-HOPO)$_2$][NMe$_4$]. Yield: 79 mg, 77 %. ^{1}H NMR (500 MHz, DMF-d_7, -35 °C) δ 9.82 (s, 2H), 9.50 (s, 2H), 8.94 (s, 2H), 8.68 (d, J = 7.2 Hz, 2H), 8.44 (s, 2H), 8.38 (s, 2H), 8.22 (d, J = 7.2 Hz, 2H), 7.63 (s, 2H), 4.50 (s, 2H), 4.34 (s, 2H), 4.04 (t, J = 7.2 Hz, 2H), 3.89 (t, J = 7.1 Hz, 2H), 3.28 (s, 2H), 3.07 (s, 2H). HRMS-ESI (*m/z*, [M]$^-$) Calcd for C$_{32}$H$_{28}$N$_8$O$_{14}$^{142}Nd: 890.0808, Found: 890.0820. Anal. Calcd (Found) for [Nd(C$_{16}$H$_{14}$N$_4$O$_7$)$_2$][C$_4$H$_{12}$N]·0.5CH$_3$OH·5H$_2$O: C 42.64 (42.40), H 4.54 (4.33), N 12.35 (12.11) %.

[Sm(2LImTHF-1,2-HOPO)$_2$][NMe$_4$]. Yield: 71 mg, 69 %. ^{1}H NMR (500 MHz, DMF-d_7, -25 °C) δ 12.05 (d, J = 3.4 Hz, 2H), 11.93 (d, J = 3.4 Hz, 2H), 7.60 (t, J = 8.0 Hz, 2H), 7.51 (t, J = 8.0 Hz, 2H), 7.46 (dd, J = 7.5, 1.4 Hz, 2H), 7.38 (dd, J = 7.5, 1.4 Hz, 2H), 7.14 (dd, J = 8.4, 1.4 Hz, 2H), 7.05 (dd, J = 8.4, 1.4 Hz, 2H), 4.81-4.78 (m, 2H), 4.77-4.74 (m, 2H), 4.32 – 4.28 (m, 2H), 4.28 – 4.24 (m, 2H), 3.86 (dd, J = 9.0, 4.9 Hz, 2H), 3.82 (dd, J = 9.0, 5.0 Hz, 2H). HRMS-ESI (*m/z*, [M]$^-$) Calcd for C$_{32}$H$_{28}$N$_8$O$_{14}$^{152}Sm: 900.0928, Found: 900.0946. Anal. Calcd (Found) for [Sm(C$_{16}$H$_{14}$N$_4$O$_7$)$_2$][C$_4$H$_{12}$N]·0.5CH$_3$OH·3.5H$_2$O: C 41.66 (41.62), H 4.69 (4.66), N 11.98 (11.93) %.

[Eu(2LImTHF-1,2-HOPO)$_2$][NMe$_4$]. Yield: 77 mg, 75 %. ^{1}H NMR (500 MHz, DMF-d_7, 15 °C) δ 16.99 (s, 2H), 16.26 (s, 2H), 7.00 (d, J = 7.7 Hz, 2H), 6.71 (d, J = 7.7 Hz, 2H), 6.42 (d, J = 7.2 Hz, 2H), 6.32 (d, J = 7.2 Hz, 2H), 5.41-5.33 (s, 2H), 5.32 – 5.24 (m, 2H), 4.97 (t, J = 7.5 Hz, 2H), 4.90 (t, J = 7.5 Hz, 2H), 4.86-4.81 (m, 2H), 4.79-4.74 (m, 4H), 4.69 – 4.63 (m, 2H). HRMS-ESI (*m/z*, [M]$^-$) Calcd for C$_{32}$H$_{28}$N$_8$O$_{14}$^{151}Eu: 899.0929, Found: 899.0928. Anal. Calcd (Found) for [Eu(C$_{16}$H$_{14}$N$_4$O$_7$)$_2$][C$_4$H$_{12}$N]·0.25CH$_3$OH·3.3H$_2$O: C 41.78 (41.75), H 4.60 (4.56), N 12.10 (12.05) %.

[Tb(2LImTHF-1,2-HOPO)$_2$][NMe$_4$]. Yield: 68 mg, 66 %. ^{1}H NMR (500 MHz, DMF-d_7, 35 °C) δ 49.82 (s, 2H), 49.55 (s, 2H), 19.15 (s, 2H), 17.81 (s, 2H), 10.18 (s, 2H), 6.95 (s, 2H), -7.26 (s, 2H), -8.39 (s, 2H), -14.98 (s, 2H), -15.11 (s, 2H), -16.23 (s, 2H), -16.91 (s, 2H), -85.77 (s, 2H), -96.21 (s, 2H). HRMS-ESI (*m/z*, [M]$^-$) Calcd for C$_{32}$H$_{28}$N$_8$O$_{14}$^{159}Tb: 907.0984, Found: 907.1001. Anal. Calcd (Found) for [Tb(C$_{16}$H$_{14}$N$_4$O$_7$)$_2$][C$_4$H$_{12}$N]·0.25CH$_3$OH·3.5H$_2$O: C 41.36 (41.31), H 4.60 (4.55), N 11.97 (11.95) %.

[Dy(2LImTHF-1,2-HOPO)$_2$][NMe$_4$]. Yield: 80 mg, 77 %. ^{1}H NMR (500 MHz, DMF-d_7, 40 °C) δ 43.40 (s, 2H), 42.92 (s, 2H), 17.68 (s, 2H), 16.26 (s, 2H), 10.26 (s, 2H), 6.91 (s, 2H), -5.53 (s, 2H), -6.66 (s, 2H), -11.79 (s, 2H), -12.53 (s, 2H), -13.09 (s, 2H), -14.37 (s, 2H), -71.44 (s, 2H), -82.61 (s, 2H). HRMS-ESI (*m/z*, [M]$^-$) Calcd for C$_{32}$H$_{28}$N$_8$O$_{14}$^{161}Dy: 909.1000, Found: 909.1007. Anal. Calcd (Found) for [Dy(C$_{16}$H$_{14}$N$_4$O$_7$)$_2$][C$_4$H$_{12}$N]·0.35CH$_3$OH·3.75H$_2$O: C 41.03 (41.04), H 4.63 (4.65), N 11.85 (11.85) %.

[Ho(2LImTHF-1,2-HOPO)$_2$][NMe$_4$]. Yield: 73 mg, 70 %. ^{1}H NMR (500 MHz, DMF-d_7, 25 °C) δ 22.75 (s, 2H), 20.77 (s, 2H), 9.76 (s, 4H), 9.56 (s, 2H), 8.01 (s, 2H), 3.83 (s, 4H), 3.02 (s, 4H), 2.15 (s, 2H), 0.87 (s, 2H). HRMS-ESI (*m/z*, [M]$^-$) Calcd for C$_{32}$H$_{28}$N$_8$O$_{14}$^{165}Ho: 913.1034, Found: 913.1053. Anal. Calcd (Found) for [Ho(C$_{16}$H$_{14}$N$_4$O$_7$)$_2$][C$_4$H$_{12}$N]·2H$_2$O: C 42.24 (42.12), H 4.33 (4.20), N 12.31 (12.16) %.

[Er(2LImTHF-1,2-HOPO)$_2$][NMe$_4$]. Yield: 74 mg, 71 %. ^{1}H NMR (500 MHz, DMF-d_7, 50 °C) δ 14.33 (s, 2H), 12.95 (s, 2H), 8.59 (s, 2H), 8.44 (s, 2H), 7.71 (s, 2H), 7.14 (s, 2H), 2.79 (s, 2H), 2.57 (s, 2H), 1.74 (s, 2H), 1.58 (s, 2H), 1.38 (s, 2H), 1.07 (s, 2H), -3.60 (s, 2H), -5.45 (s, 2H). HRMS-ESI (*m/z*, [M]$^-$) Calcd for C$_{32}$H$_{28}$N$_8$O$_{14}$^{166}Er: 914.1034, Found: 914.1059. Anal. Calcd (Found) for [Er(C$_{16}$H$_{14}$N$_4$O$_7$)$_2$][C$_4$H$_{12}$N]·4H$_2$O: C 40.71 (40.52), H 4.56 (4.40), N 11.87 (11.70) %.

[Tm(2LImTHF-1,2-HOPO)$_2$][NMe$_4$]. Yield: 70 mg, 67 %. ^{1}H NMR (500 MHz, DMF-d_7, 45 °C) δ 26.05 (s, 4H), 7.70 (s, 4H), 7.01 (s, 2H), 6.73 (s, 2H), 6.31 (s, 2H), 6.16 (s, 2H), 5.88 (s, 2H), 4.95 (s, 2H), 3.76 (s, 2H), 3.00 (s, 2H), -2.18 (s, 2H), -2.97 (s, 2H). HRMS-ESI (*m/z*, [M]$^-$) Calcd for C$_{32}$H$_{28}$N$_8$O$_{14}$^{169}Tm: 917.1073, Found: 917.1087. Anal. Calcd (Found) for [Tm(C$_{16}$H$_{14}$N$_4$O$_7$)$_2$][C$_4$H$_{12}$N]·0.3CH$_3$OH·3.6H$_2$O: C 40.89 (40.89), H 4.58 (4.58), N 11.82 (11.83) %.

[Yb(2LImTHF-1,2-HOPO)$_2$][NMe$_4$]. Yield: 77 mg, 73 %. ^{1}H NMR (500 MHz, DMF-d_7, 30 °C) δ 10.28 (s, 2H), 9.52 (s, 2H), 7.11 (s, 2H), 6.89 (s, 2H), 6.80 (d, *J* = 6.8 Hz, 2H), 6.63 (d, *J* = 6.6 Hz, 2H), 5.33 (s, 2H), 4.86 (s, 2H), 4.37 (s, 2H), 4.30 (s, 2H), 4.17 (t, *J* = 6.8 Hz, 2H), 4.08 (t, *J* = 6.8 Hz, 2H), 3.79 (s, 2H), 3.64 (s, 2H). HRMS-ESI (*m/z*, [M]$^-$) Calcd for C$_{32}$H$_{28}$N$_8$O$_{14}$^{174}Yb: 922.1119, Found: 922.1149. Anal. Calcd (Found) for [Yb(C$_{16}$H$_{14}$N$_4$O$_7$)$_2$][C$_4$H$_{12}$N]·3H$_2$O: C 41.19 (40.93), H 4.42 (4.04), N 12.01 (11.80) %.

[Lu(2LImTHF-1,2-HOPO)$_2$][NMe$_4$]. Yield: 72 mg, 68 %. ^{1}H NMR (500 MHz, DMF-d_7, 25 °C) δ 12.51 (d, *J* = 5.3 Hz, 2H), 12.47 (d, *J* = 5.0 Hz, 2H), 7.41 (dd, *J* = 8.5, 7.5 Hz, 2H), 7.33 (dd, *J* = 8.5, 7.5 Hz, 2H), 7.30 (dd, *J* = 7.5, 1.7 Hz, 2H), 7.26 (dd, *J* = 7.5, 1.8 Hz, 2H), 6.61 (dd, *J* = 8.5, 1.7 Hz, 2H), 6.44 (dd, *J* = 8.5, 1.8 Hz, 2H), 4.83 – 4.72 (m, 4H), 4.30 – 4.24 (m, 4H), 3.91 – 3.84 (m, 4H). HRMS-ESI (*m/z*, [M]$^-$) Calcd for C$_{32}$H$_{28}$N$_8$O$_{14}$^{175}Lu: 923.1138, Found: 923.1157. Anal. Calcd (Found) for [Lu(C$_{16}$H$_{14}$N$_4$O$_7$)$_2$][C$_4$H$_{12}$N]·4.25H$_2$O: C 40.25 (40.08), H 4.55 (4.36), N 11.73 (11.60) %.

[Eu(2LIssTHF-1,2-HOPO)$_2$][NMe$_4$]. Yield: 87 mg, 89 %. HRMS-ESI (*m/z*, [M]$^-$) Calcd for C$_{32}$H$_{28}$N$_8$O$_{14}$^{151}Eu: 899.0929, Found: 899.0911.

DFT Calculations. Ground state geometry optimization and frequency calculations were performed using Gaussian 09 at the Molecular Graphics and Computation Facility at University of California, Berkeley, CA.[11] The B3LYP functional was used, treating the light atoms with the 6-31G(d,p) basis set and the metal atoms with quasi relativistic effective core pseudopotentials, specifically: **La** (ECP46MWB), **Ce** (ECP47MWB), **Pr** (ECP48MWB), **Nd** (ECP49MWB), **Sm** (ECP51MWB), **Eu** (ECP52MWB), **Tb** (ECP54MWB), **Dy** (ECP55MWB), **Ho** (ECP56MWB), **Er** (ECP57MWB), **Tm** (ECP58MWB), **Yb** (ECP59MWB), and **Lu** (ECP60MWB).[12,13]

2D-NMR. The temperature probe was calibrated from 0 to -70 °C using methanol. Selective inversion recovery (SIR) experiments were collected at forty two different mixing times, which were adjusted based on the T_1 relaxation time of the inverted peak. Integrated peak data for inverted and exchanging resonances were fit to a two site exchange model within the program CIFIT2.[14,15] Reported ^{1}H-COSY and [1]H-EXSY/NOESY spectra are averaged over 128 scans or more. For [1]H-EXSY/NOESY spectra, mixing times were set to the middle of the observed T_1

relaxation times. The DFT calculated structure for [Ho(2LImTHF-1,2-HOPO)$_2$]$^-$ was used to model the geometric parameters used to fit the isotropic shifts for all complexes reported here.

Luminescence Measurements. Instrumentation details have been reported elsewhere.[6] Samples were first dissolved into DMSO, and then diluted into aqueous TRIS buffer (final concentration DMSO < 0.05%). The TRIS buffer was prepared by dissolving TRIS hydrochloride (20 mM) and sodium chloride (100 mM) into Millipore water and adjusting the pH to 7.4 with sodium hydroxide. Quinine sulfate in 0.05 M H$_2$SO$_4$ ($\Phi = 0.508$) was used as an aqueous fluorescence quantum yield reference.[16] Quantum yields were determined by the optically dilute method (with optical density at λ_{ex} <0.05) according to the following equation:

$$\Phi_x = \frac{A_r(\lambda)}{A_x(\lambda)} \frac{I_x}{I_r} \Phi_r$$

where $A(\lambda)$ is the absorbance of sample x and reference r at the excitation wavelength λ, and I is the total integrated emission of the sample and quantum yield reference. The same excitation wavelength λ and slit widths were used for sample and reference, removing the need to correct for the incident power of the excitation source. Similarly, the refractive indices for sample and reference are assumed identical, both being aqueous. A 5 cm quartz cuvette was used to measure the absorption spectra in order to increase the signal-to-noise for these dilute solutions. Luminescence measurements were made using a 1 cm quartz fluorescence cuvette.

References

(1)   Kepert, D. L. *Inorganic stereochemistry*; Springer-Verlag, 1982.
(2)   Fay, R. C.; Howie, J. K. *J. Am. Chem. Soc.* **1979**, *101*, 1115.
(3)   Weir, J. R.; Fay, R. C. *Inorg. Chem.* **1986**, *25*, 2969.
(4)   Szigethy, G.; Raymond, K. N. *Chem. – Eur. J.* **2011**, *17*, 1818.
(5)   Beeby, A.; Bushby, L. M.; Maffeo, D.; Williams, J. A. G. *J. Chem. Soc. Dalton Trans.* **2002**, 48.
(6)   D'Aléo, A.; Moore, E. G.; Szigethy, G.; Xu, J.; Raymond, K. N. *Inorg. Chem.* **2009**, *48*, 9316.
(7)   Werts, M. H. V.; Jukes, R. T. F.; Verhoeven, J. W. *Phys. Chem. Chem. Phys.* **2002**, *4*, 1542.
(8)   Snow, A. W.; Foos, E. E. *Synthesis* **2003**, *2003*, 0509.
(9)   Zhang, Z.; Du, X.; Chopiuk, G. Heteropolycyclic Inhibitors. WO0202562 (A2), January 10, 2002.
(10) Terfort, A. *Synthesis* **1992**, *1992*, 951.
(11) *Gaussian 09, Revision D.01,*.
(12) Dolg, M.; Stoll, H.; Savin, A.; Preuss, H. *Theor. Chim. Acta* **1989**, *75*, 173.
(13) Dolg, M.; Stoll, H.; Preuss, H. *Theor. Chim. Acta* **1993**, *85*, 441.
(14) Mugridge, J. S.; Szigethy, G.; Bergman, R. G.; Raymond, K. N. *J. Am. Chem. Soc.* **2010**, *132*, 16256.
(15) Bain, A. D.; Cramer, J. A. *J. Magn. Reson. A* **1996**, *118*, 21.
(16) Velapoldi, R. A.; Tønnesen, H. H. *J. Fluoresc.* **2004**, *14*, 465.

Chapter 5

**d-Orbital Effects on the Stereochemistry of
Eight Coordinate 1,2-HOPO Chelates**

Introduction

Although six-coordinate metal complexes have been known for more than a century, it was not until recently that nonoctahedral structures of unidentate homoleptic ML_6 metal complexes were seriously considered.[1–6] An extended Hückel calculation predicted a trigonal prismatic structure for $[TiH_6]^{2-}$, which directly opposes VSEPR expectations given the lack of lone electron pairs on the metal center.[7,8] Experimental evidence for nonoctahedral structures soon followed, found first for the lithium salt of the $[ZrMe_6]^{2-}$ ion and later more convincingly for the neutral WMe_6 species.[9–12] In the absence of significant π-bonding or sterically demanding ligands, second-order Jahn-Teller distortion causes a mixing of the t_{1u} HOMO and t_{2g} LUMO, stabilizing the D_{3h} or C_{3v} coordination geometries.[13–15] For ligands that are able to participate in π-donation, the O_h geometry allows the most favorable d_π/p_π interaction between the metal and ligand t_{2g} orbitals (Fig. 1).
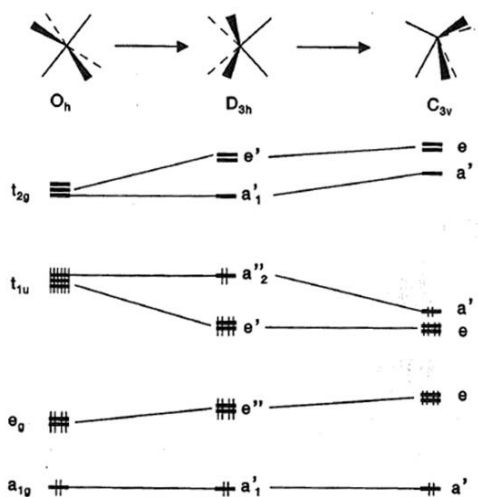
Figure 5.1. Walsh diagram of d^0 metals showing energetic preference for C_{3v} in the absence of ligand π-donation.[15]

In contrast to six-coordination, the variable stereochemistry of eight-coordinate unidentate homoleptic ML_8 complexes has been known for more than half a century. The structure of Na_3TaF_8 has fluoride ligands positioned at the vertices of a D_{4d} square antiprism (SA), resulting in eight symmetry equivalent ligands.[16–18] The structure of $K_4[Mo(CN)_8]$ and isostructural $K_4[W(CN)_8]$ exhibit a lower symmetry D_{2d} trigonal dodecahedral (Dod) coordination, resulting in two distinct sets of four equivalent cyanide ligands. Shown below are sketches of these two coordination modes, along with accompanying labels for the distinguishable vertices and edges. Kepert's repulsion energy calculations very nearly match the values found in Hoard's original treatment, finding that the SA geometry is slightly favored over the Dod form for homoleptic ML_8 complexes.[19]
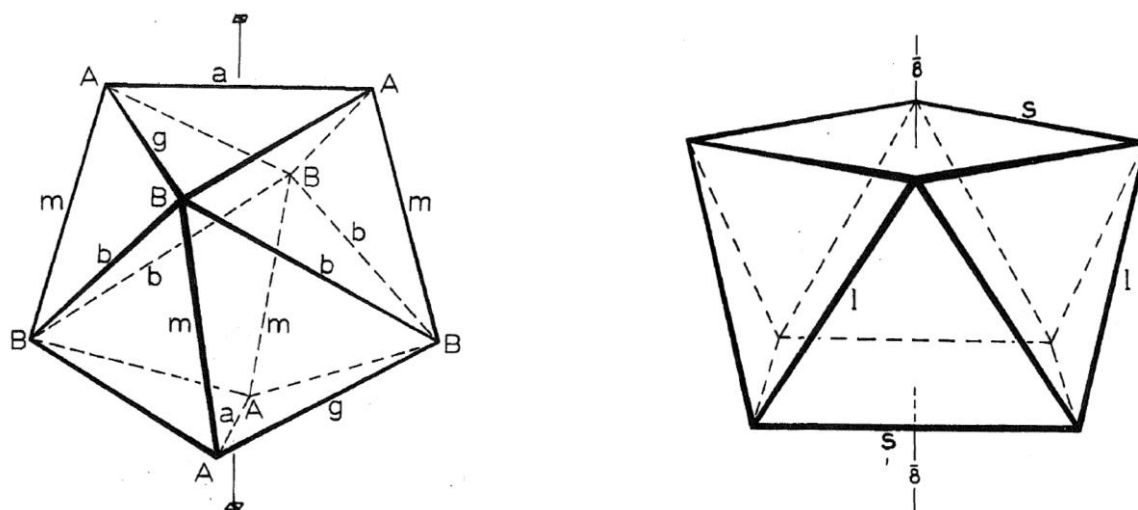
Figure 5.2. Schematics of D_{2d} dodecahedral (Dod, left) and D_{4d} antiprismatic (SA, right) coordination polyhedra.[18]

Many studies have been performed on the $[Mo(CN)_8]^{4-}$ ion in particular, attempting to determine the stereochemistry in solution by UV-vis,[20] Raman,[21,22] infrared,[22,23] NMR,[24–26] and by theoretical treatments.[27,28] To date, it is still unknown whether the Dod or SA is the ground state structure in the absence of crystal packing effects. For example, the structure of $K_4Mo(CN)_8$ is found to be dodecahedral in the solid state while the structure of $Tl_4Mo(CN)_8$ shows antiprismatic coordination of the cyanide ligands.[29,30] These two solid state examples have also been recently characterized by solid state ^{95}Mo NMR.[31] All stereochemical studies of $Mo(CN)_8^{4-}$ and related species are inherently complicated by the monodentate nature of the cyanide ligands, which results in fast rearrangement kinetics and moderate lability in solution.[27,31] The ligand field splitting of the metal valence d-orbitals is shown in the following figure for the two possible stereoisomers of $Mo(CN)_8^{4-}$.
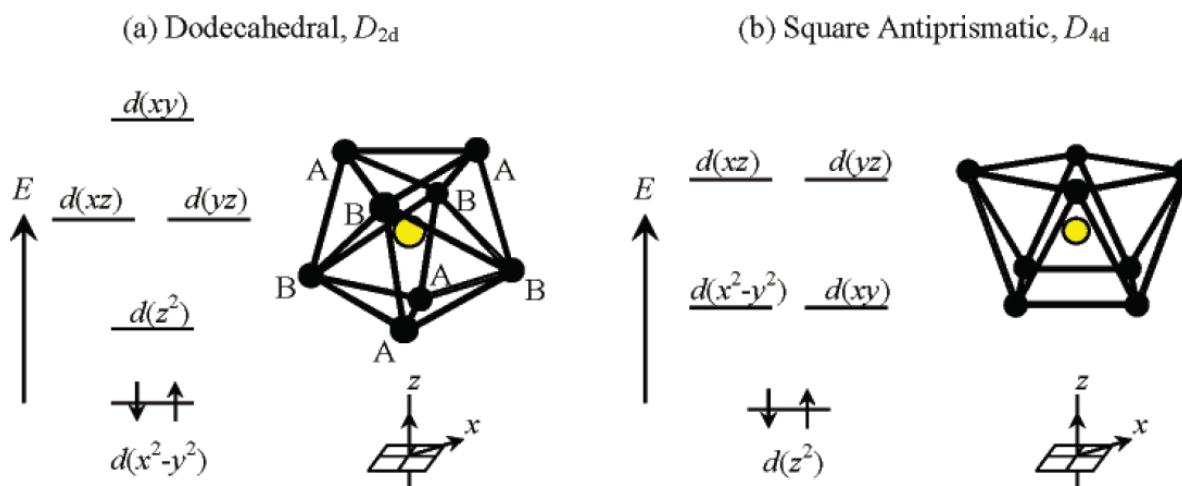
Figure 5.3. Ligand field splitting of valence metal d-orbitals in stereoisomers of $Mo(CN)_8^{4-}$.[31]

For both the Dod and SA forms, the HOMO of $Mo(CN)_8^{4-}$ is nonbonding with respect to the σ-bonding interactions of the ligands. However, C-bonded cyanide can act as a π-acceptor using the unoccupied π^* orbitals of the C-N triple bond. The electron pair occupying the HOMO of $Mo(CN)_8^{4-}$ can delocalize out onto the cyanide ligands in both Dod and SA forms through π-backbonding, but to differing degrees. The inequivalence of the A and B sites in the Dod form creates four strong π-backbonding interactions between the B site cyanides and the filled $d(x^2-y^2)$ orbital of Mo^{IV}. The increase in B site interaction comes at the cost of weakened π-type interaction with the A sites, leading to an observation known as Orgel's rule.[32] Orgel's rule states that complexes of the form $[MX_4Y_4]$ will prefer Dod coordination, and that the ligands X and Y will sort into the A and B sites of the Dod depending upon the π-bonding preferences of the ligands and metal. That is, the better π donors will occupy B sites for d^0 metal complexes, while the better π acceptors will occupy B sites for d^2 metal complexes. Exceptions to the rule have been found when sterically demanding ligands are used, but in general Orgel's rule is supported by experimental results.

An implied extension of Orgel's rule states that the Dod stereochemistry is universally preferred when favorable π-bonding exists, even for homoleptic ML_8 complexes. The extended rule bears analogy to six-coordination in that Dod and octahedral may dominate when favorable metal-ligand π-type interactions exist, whereas C_{3v}/D_{3h} and D_{4d} may dominate when favorable π-type interactions are absent. If true, the extended rule suggests that the Dod stereochemistry of $K_4Mo(CN)_8$ may be the ground state structure in solution, despite the SA preferences of repulsion energy. Hoard openly disagrees with the extended rule, but experimental evidence one way or another is lacking.[29] The question remains: do the four strong B-site π bonds and four weak A-site π bonds in Dod stereochemistry confer greater stabilization than eight intermediate π bonds in the SA form? We attempt to address this question here.

In the following report, we provide the crystal structures, ^{1}H-NMR, and DFT calculations of d^0 and d^{10} metal complexes using the 5LImXy-1,2-HOPO ligand previously described in chapter 3. Specifically, we report the Sc^{III}, Y^{III}, Ti^{IV}, Zr^{IV}, Hf^{IV}, Ce^{IV} d^0 metal complexes, as well as the In^{III}, Tl^{III} and Sn^{IV} d^{10} complexes. Relevant to the present study of 8-coordinate complexes are the constraints of having a fixed donor-donor distance bidentate chelator, rather than unidentate ligands. Given the relative edge lengths of the idealized polyhedra ($m < s < g < l$), small bites favor m-edge spanned Dod structures while larger bites favor s- or even l-edge spanned SA forms (see Fig. 4). By comparing similarly sized metals, we remove the effects of these edge preferences and isolate the stereochemical effects of different electronic structures between the d^0 and d^{10} metals. For the π donating ligand used here we find that the d^0 metals favor Dod geometries whereas the d^{10} metals favor SA forms, lending support to the extension of Orgel's rule. The effects of π-bonding on the rates of the LTP racemization characterized in chapter 3 are also evaluated here for these complexes, likewise measured by ^{1}H-NMR selective inversion recovery (SIR) experiments. We propose that the maximized d_π/p_π interaction between the d^0 metal and ligand in the Dod form is related to the high quantum yields found for Dod Eu^{III} complexes described in chapters 3 and 4.

Results and Discussion

Structure Analysis. With the ionic radius of the HOPO oxygen atoms taken as 1.20 Å, the average M-O distances found by XRD match well with the expected values based on the

Shannon ionic radii (within 0.01 Å).[33] M-O distances for Ce^{IV} were found to be 0.02 Å longer than expected, while radii of **Y** and **Lu** were found to be 0.02 Å shorter than expected. These values along with unit cell parameters for the nine new reported crystal structures are summarized in the following table.

Table 5.1. Ionic radii and unit cell parameters for [M(5LImXy-1,2-HOPO)$_2$] complexes

L^1 Metal Complex	Ionic Radius (pm)	Found Radius (pm)	Space Group	Unit Cell Parameters			
				a	b	c	β (°)
	Ti^{IV}	88	88	P2$_1$/c	12.0736(8)	19.3293(12)	16.0885(10)	105.0010(10)
	Hf^{IV}	97	97	P2$_1$/c	12.097(3)	19.590(4)	16.135(4)	104.525(9)
d^0 metals	Zr^{IV}	98	98	P2$_1$/c	12.9852(5)	16.8744(7)	18.5054(8)	106.438(2)
	Ce^{IV}	111	113	P2$_1$/c	12.1717(4)	19.9261(6)	16.1952(5)	103.590(2)
	Sc^{III}	101	101	P2$_1$/c	14.6094(6)	14.7981(6)	24.6083(10)	101.2280(10)
	Y^{III}	116	114	P2$_1$/c	14.6265(11)	14.7375(11)	24.9826(19)	101.1190(10)
d^{10} metals	Sn^{IV}	95	96	C2/c	23.6140(8)	14.3621(5)	24.3046(8)	90.980(2)
	In^{III}	106	105	P2$_1$/c	14.796(3)	15.042(3)	24.057(5)	101.734(3)
	Tl^{III}	112	113	P2$_1$/n	17.1508(8)	10.7064(5)	28.8293(14)	96.2040(10)

It is important to note that all M^{III} complexes were crystallized from the same DMF/Et$_2$O solvent system, and tetramethylammonium was used as the couterion in all cases. Similarly, all M^{IV} complexes were crystallized in the same way from DMSO/MeOH. The similarity of unit cell parameters for **Ti**, **Hf**, and **Ce** point to a common structure, and we found that all three of these crystallized without the incorporation of solvent. Crystals of **Zr** were found to contain a unit of methanol in the crystal structure, which may be due to a lower starting concentration of **Zr** in the DMSO soluble phase. Even though the size of **Sn** falls between **Ti** and **Hf**, the unit cell of **Sn** differs dramatically from those of the d^0 M^{IV} metal complexes, giving the first indication that the d^0 and d^{10} complexes have different structural preferences. The unit cells of **Y** and **Sc** are both isomorphous with the unit cells found for the late lanthanides (**Eu** to **Lu**) in Chapter 3. Both **In** and **Tl** fall between the sizes of **Y** and **Sc**, and like **Sn** these d^{10} metal complexes exhibit cells that differ significantly from those of the d^0 metals. As a representative example, the ORTEPs of **Y** and **Tl** are shown in the following figure.
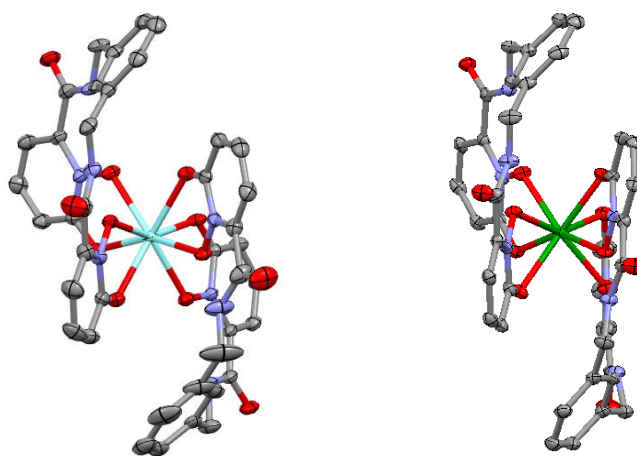

Figure 5.4. Comparison of ORTEPs for **Y** (left) and **Tl** (right)

Comparing the ORTEP plots of **Y** and **Tl** reveals that the **Tl** structure appears significantly flattened compared to the structure of **Y**. Given the similarity in sizes and crystallization conditions for these two metals, the differences in structure are not attributed to crystal packing effects. The following table summarizes shape analyses of the XRD determined crystal structures, as well as the corresponding DFT minimized structures. The average M-O bond distances, average bite distance, and corresponding normalized bites are also tabulated. The average bite distance for Ln^{III} complexes reported in chapter 3 was 2.56 Å. Here we that find bite distances for the d^0 metals are all smaller than Ln^{III} average, with the largest difference (2.46 Å) occurring for the smallest complex (**Ti)**. Bite distances for the majority of the d^{10} metals are larger than the Ln^{III} average, the only exception being the smallest d^{10} complex **Sn**.

Table 5.2. Normalized bite, bite angle, and shape measure parameters for solid state and calculated gas-phase structures of $[M(5LImXy-1,2-HOPO)_2]$ complexes. *calculated values

	M	Normalized Bite	M-O Avg. Bond Distance (Å)	Bite Distance (Å)	Shape Analysis of XRD Structures			Shape Analysis of DFT Structures			
					D_{4d}	C_{2v}	D_{2d}	D_{4d}	C_{2v}	D_{2d}	Twist Angle φ
	Ti^{IV}	1.18	2.08	2.46	10.2	4.75	9.83	10.8	7.96	6.78	10.2
	Hf^{IV}	1.15	2.17	2.50	11.7	5.96	9.17	13.4	9.65	6.17	6.43
d^0	Zr^{IV}	1.14	2.18	2.49	12.8	5.58	10.1	13.6	9.82	6.17	6.13
metals	Ce^{IV}	1.08	2.33	2.53	13.5	7.28	10.4	15.2	11.2	8.08	5.24
	Sc^{III}	1.14	2.21	2.52	8.52	6.54	10.3	12.1	8.78	6.47	8.12
	Y^{III}	1.09	2.34	2.55	10.3	7.12	10.2	14.2	10.3	7.17	5.89
	Sn^{IV}	1.16	2.16	2.52	8.31	6.18	8.73	9.93	5.59	7.80	11.7
d^{10}	In^{III}	1.14	2.25	2.57	6.23	5.99	11.6	10.3	5.68	8.34	11.4
metals	Pb^{IV}	1.12*	2.30*	2.58*	-	-	-	9.53	5.10	9.31	13.1
	Tl^{III}	1.12	2.33	2.60	4.92	6.81	12.2	11.2	6.68	10.2	12.3

The shape analyses of the d^0 XRD crystal structures are all closest to a C_{2v} bicapped trigonal prism (BCTP). Focusing on the D_{4d} and D_{2d} values, the larger normalized bites favor the *ssss*-SA (as for **Sc**) while smaller normalized bites favor the *mmmm*-Dod (as for **Ce^{IV}**), which is in agreement with the predictions of repulsion energy (Fig. 4). The DFT calculated structures for the d^0 complexes are all definitively *mmmm*-Dod. The shape analyses of the d^{10} XRD crystal structures are close to the BCTP, but also show a clear preference for *ssss*-SA over the *mmmm*-Dod, an effect that is most pronounced in the **Tl** structure. The DFT calculated d^{10} structures are closest to the BCTP with a slight preference for Dod over the SA, but show significant skewing along each mirror plane (larger φ twist angles) compared to the calculated d^0 complexes. In order to remove the complicating effects that the *m*-xylyl backbone imposes upon the structure, these metal complexes were also calculated without the connecting backbone as the $[M(1,2-HOPO)_4]$ complexes. The shape analyses of these structures are summarized in the following table.

Table 5.3. Shape analysis and ligand wrapping pattern of calculated [M(1,2-HOPO)$_4$] complexes. *calculated values

	L^1 Metal Complex	Normalized Bite from XRD	Shape Analysis of Free HOPO DFT Structures			Ligand Wrapping Pattern
			D$_{4d}$	C$_{2v}$	D$_{2d}$	
d^0 metals	Ti^{IV}	1.18	11.01	6.81	6.68	*mmmm*-Dod
	Hf^{IV}	1.15	13.86	9.6	5.34	*mmmm*-Dod
	Zr^{IV}	1.14	15.2	10.81	4.95	*mmmm*-Dod
	Ce^{IV}	1.08	17.24	12.64	6.69	*mmmm*-Dod
	Sc^{III}	1.14	7.43	3.03	10.58	BCTP
	Lu^{III}	1.11	16.24	11.68	5.2	*mmmm*-Dod
	Y^{III}	1.09	16.04	11.51	5.43	*mmmm*-Dod
d^{10} metals	Sn^{IV}	1.16	4.72	6.74	11.78	*ssss*-SA
	In^{III}	1.14	4.57	6.85	12.13	*ssss*-SA
	Pb^{IV}	1.12*	4.05	7.12	12.79	*ssss*-SA
	Tl^{III}	1.12	3.89	7.67	13.68	*ssss*-SA
d^2 metals	V^{III}	1.20*	2.42	9.12	14.25	*llll*-SA
	Nb^{III}	1.17*	2.82	9.15	14.04	*llll*-SA
	Ta^{III}	1.18*	2.59	8.99	14.02	*llll*-SA
	Mo^{IV}	1.20*	2.82	9.26	14.11	*llll*-SA
	W^{IV}	1.19*	2.65	9.19	14.15	*llll*-SA

For the d^0 metal complexes, the shape analyses are all closest to *mmmm*-Dod structures except for [Sc(HOPO)$_4$]$^-$, which is consistent with the larger normalized bite of **Sc** (Fig. 4). Note, however, that the M^{IV} d^0 complexes maintain an *mmmm*-Dod structure well beyond the bite found for **Sc**. The d^{10} metal complexes are all closest to the *ssss*-SA, regardless of bite size. Likewise, the d^2 metal complexes are all closest to an *llll*-SA, regardless of bite. In making comparisons between the groups, it is important to choose metals of similar size so that the effects of differing normalized bite can be removed. The following figure shows the repulsion energy minimized (n=6) shape as a function of normalized bite for the range of sizes considered here. For normalized bites less than 1.084, the *mmmm*-Dod structure is the repulsion energy calculated minimum. The *ssss*-SA is the calculated minimum at a bite of 1.188. Bites between 1.084 and 1.188 are expected to be intermediate between the *mmmm*-Dod and *ssss*-SA forms. Although not shown in the following figure, the *llll*-SA is predicted to be a minimum when normalized bite reaches 1.262 or larger. The repulsion energy calculations used to generate the shape analysis curves are all in agreement with Kepert's earlier treatment.[19]
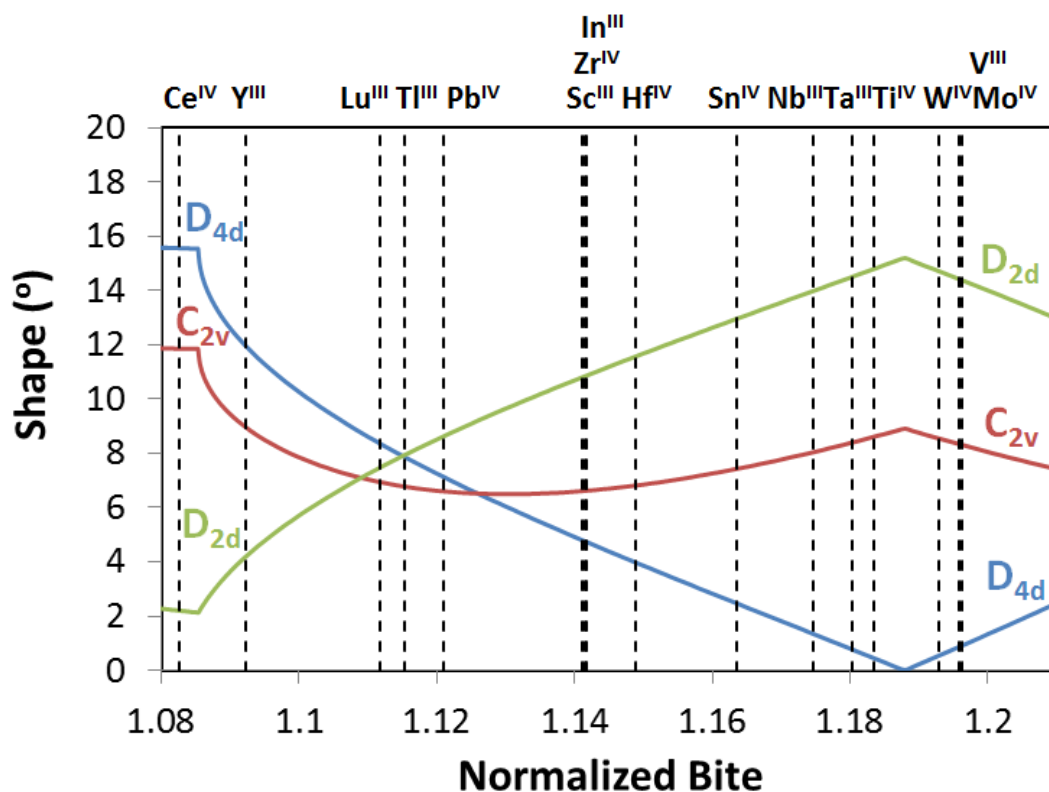
Figure 5.5. Repulsion energy minima (n=6) as a function of normalized bite, taken from crystal structures where available

Tl and **Lu** are a good comparison due to similar size and charge. The only difference in electronic configuration between the two is an empty (**Lu**) or filled (**Tl**) 5d subshell. By repulsion energy both should be close to the same intermediate form between Dod and SA, but XRD and DFT structures show large differences between them. Note that **Ti** is expected to be very close to the *ssss*-SA ideal based on normalized bite (Fig. 5.5), yet the DFT calculation of both **Ti** and [Ti(1,2-HOPO)$_4$] indicates a clear *mmmm*-Dod preference. Likewise all of the d^2 metal complexes are expected to be closest to a *ssss*-SA by repulsion energy, yet DFT calculations predict the *llll*-SA form. Representative [M(1,2-HOPO)$_4$] DFT structures from the three groups of metals are shown in the following figure.
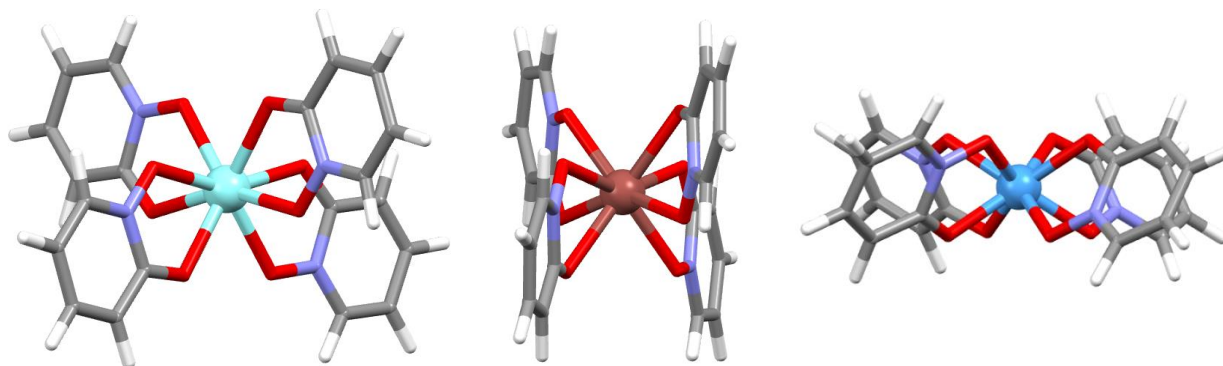
Figure 5.6. Calculated structures of d^0 Y[HOPO]$_4^-$ (left) and d^{10} Tl[HOPO]$_4^-$ (middle) and d^2 Ta[HOPO]$_4^-$ (right)

^{1}**H-NMR.** Slow exchange ^{1}H-NMR spectra were accessible for all but **Ce^{IV}** which starts to decoalesce around -50 $^{\circ}$C, similar to what was found for **La** in chapter 3. In general the differences in slow exchange ^{1}H-NMR spectra between the remaining samples were unremarkable. The largest methylene-amide coupling constant was found to decrease by 1 Hz going from d^{0} to d^{10} metals, consistent with a shift towards the *ssss*-SA geometry in solution. As in chapter 3, SIR experiments allowed the characterization of the LTP in the slow exchange regime. Mutual exchange rates were extracted to generate the following Eyring analysis (Fig. 5).
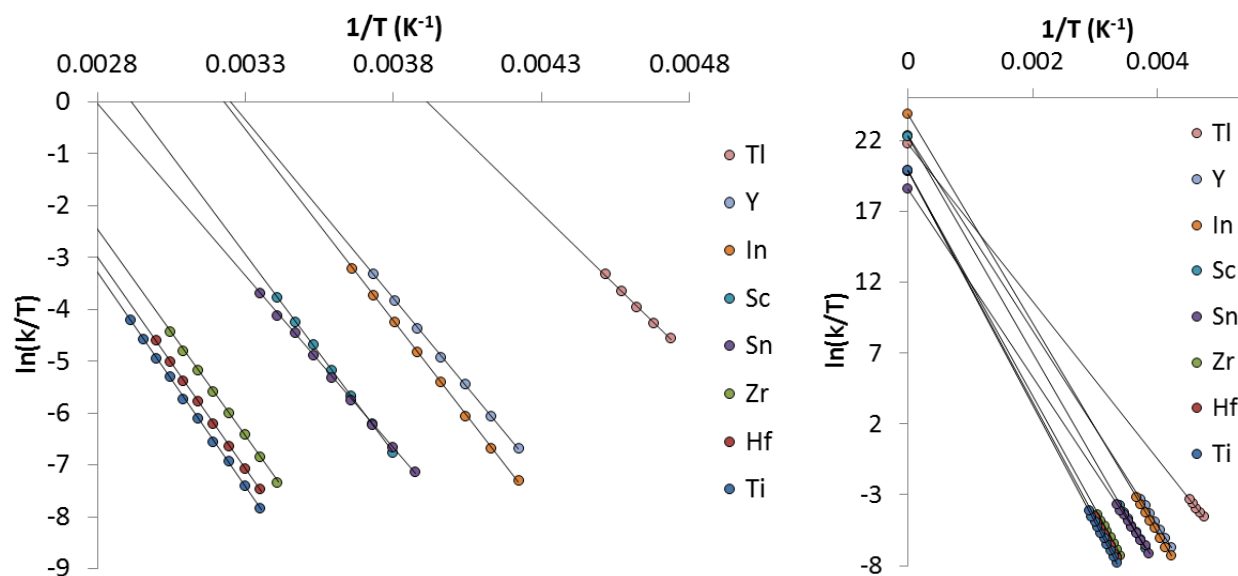
Figure 5.7. Eyring plot for M^{III} complexes in 1:2 DMF:acetone and M^{IV} complexes in DMF

Table 5.4. Linear fits of the SIR kinetic data and the activation constants derived from them

|	Ti	Hf	Zr	Sn	Sc	In	Y	Tl
Slope	-8270	-8160	-7970	-6640	-7640	-7380	-6880	-5560
Intercept	19.9	19.8	19.9	18.6	22.3	23.8	22.4	21.8
R	0.9998	0.9993	0.99992	0.9996	0.99990	0.9998	0.99990	0.9990
$\Delta H^{\ddagger}$ (kcal/mol)	16.4	16.2	15.8	13.2	15.2	14.7	13.7	11.0
$\Delta S^{\ddagger}$ (cal/mol·K)	-7.7	-7.8	-7.7	-10	-3.0	0.1	-2.8	-4.0
$\Delta G^{\ddagger}$ at 298 K	18.7	18.5	18.1	16.3	16.0	14.6	14.5	12.2

Activation energy parameters for the M^{III} complexes are consistent with the intramolecular rearrangement LTP found for the analogous lanthanide complexes in chapter 3. That is, the small negative $\Delta S^{\ddagger}$ values are consistent with an intramolecular transition state that is neither associative nor dissociative. Barriers were also determined for [Sc(2LImTHF-1,2-HOPO)$_2$]$^{-}$ and [Y(2LImTHF-1,2-HOPO)$_2$]$^{-}$ HTP surrogates as 19.4 and 17.2 kcal/mol respectively, consistent with the values found for the lanthanides in chapter 4. Activation parameters for the M^{IV} complexes are all similar, with $\Delta S^{\ddagger}$ values ranging from -10 to to -8 cal/mol·K. Although these entropy values are greater in absolute magnitude those found for the M^{III} complexes, the exchange processes are likely to be analogous. The higher charge on the metal should disfavor ligand dissociation in solution, an assumption supported by the

observation that [Zr(2LImTHF-1,2-HOPO)$_2$] and [Hf(2LImTHF-1,2-HOPO)$_2$] exhibit slow exchange spectra even up to 140 $^\circ$C in DMF. The LTP $\Delta G^\ddagger$ barriers at room temperature are compared as a function of normalized bite in the following plot.
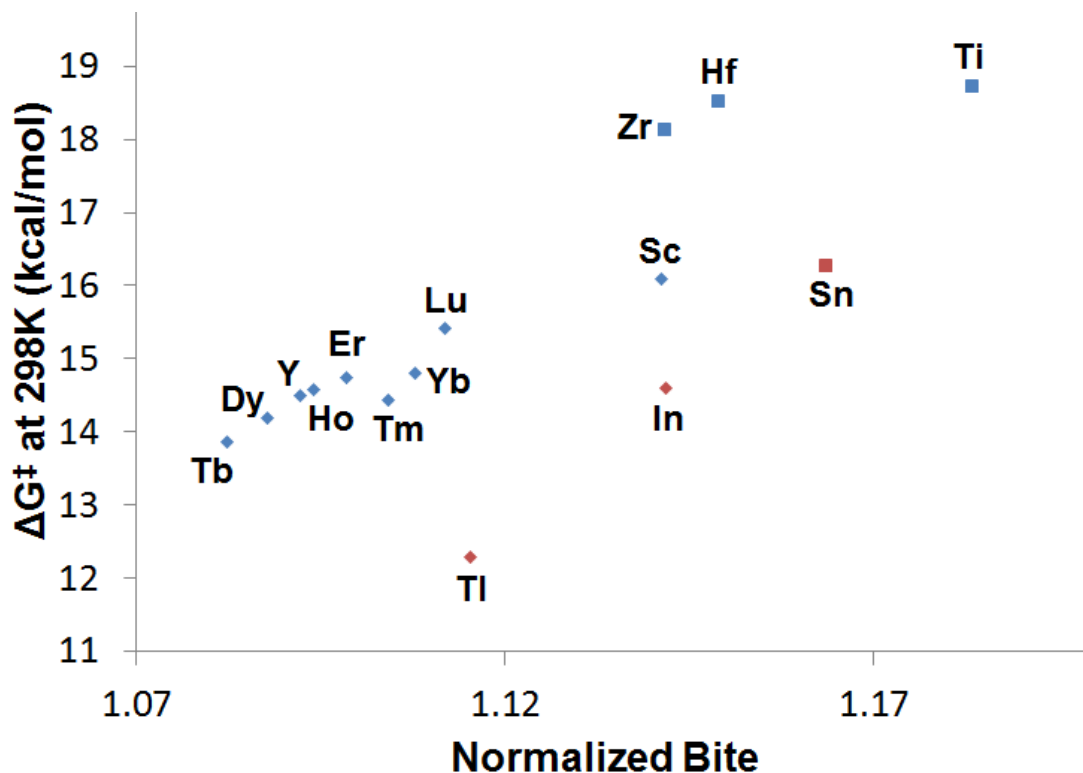
Figure 5.8. LTP intramolecular racemization barriers as a function of normalized bite for the complexes reported here and in chapter 3. M^{III} complex are represented by diamonds, M^{IV} by squares, d^0 complexes are blue, and d^{10} are red.

The barriers found for the d^{10} metal complexes are all significantly lower than those of the d^0 metals. Specifically, the barrier for **Tl** is 3.2 kcal/mol lower than similarly sized **Lu**, while **In** showed a smaller difference of 1.4 kcal/mol compared to similarly sized **Sc**. The barrier for **Sn** is 2.3 kcal/mol lower than similarly sized **Hf** and **Ti**. Comparing **In** and **Sn**, the larger drop in barrier height for **Sn** supports a bonding explanation, since M-O covalent interactions are expected to increase with higher charge on the metal. Increased nuclear charge lowers the metal valence orbital energies, better matching them to mix with the donor orbitals on the ligands. Similarly, the larger drop in barrier height for **Tl** compared to **In** is consistent with a covalent bonding model, since radial extension of the valence *d*-orbitals is expected to increase as one moves to later members of the same group. In order to investigate the LTP in more detail, DFT calculations of ground and transition states for the full [M(5LImXy-1,2-HOPO)$_2$] complexes and [M(1,2-HOPO)$_4$] models were performed, and the calculated rearrangement barriers are tabulated below.

Table 5.5. Comparison of calculated and experimentally determined racemization barriers.

		Normalized Bite	[M(5LImXy-1,2-HOPO)$_2$] Complexes			[M(1,2-HOPO)$_4$] Complexes	
			Measured Barrier (kcal/mol)	Calculated Barrier (kcal/mol)	Twist Angle (°)	Calculated Barrier (kcal/mol)	Twist Angle (°)
M^{III} Complexes	**Tb**	1.08	13.9	10.1	18.6	5.70	25.6
	Dy	1.09	14.2	10.2	19.0	5.63	25.7
	Ho	1.09	14.6	10.3	19.4	5.56	25.9
	Y	1.09	14.5	10.1	19.8	5.37	25.9
	Er	1.10	14.7	10.4	19.7	5.47	26.0
	Tm	1.10	14.4	10.5	20.0	5.41	26.1
	Yb	1.11	14.8	10.7	20.2	5.37	26.2
	Lu	1.11	15.4	10.7	20.6	5.29	26.4
	Sc	1.14	16.0	11.2	23.7	4.79	27.8
	In	1.14	14.6	9.94	21.8	3.82	26.7
	Tl	1.12	12.2	9.24	19.2	3.63	23.0
M^{IV} Complexes	**Ce^{IV}**	1.08	-	13.4	20.8	8.43	24.0
	Zr	1.14	18.1	14.7	24.7	7.41	27.8
	Hf	1.15	18.5	14.7	24.4	7.73	27.5
	Ti	1.18	18.7	14.3	27.3	7.28	29.0
	Sn	1.16	16.3	12.0	24.4	4.52	27.7

DFT Calculations. The calculated barriers for the full complexes underestimate the measured barriers by about 4 kcal/mol, but the trends are in good agreement with the experimental values. The increasing barrier height for the full complexes contrasts with the decreasing height for [M(1,2-HOPO)$_4$] models, moving from smaller to larger normalized bites. We attribute the differences between the two models to the calculated twist angles. These angles are smaller for the full complexes compared to [M(1,2-HOPO)$_4$] models, and show wider variance from sample to sample. We propose that the fixed distance *m*-xylene backbone is too short to adequately bridge the *s* edge of the calculated SA transition state, except for very small metals like Ti^{IV}. Note that the difference in twist angles between the two models is much smaller for **Ti** than for the larger metals. As the size of the metal is increased, the twist angle is decreased toward the cubic limit at 0°, because the edges of a cube are 3% shorter than the *s* edges of the same sized SA. The calculated barriers for the [M(1,2-HOPO)$_4$] models are roughly half the magnitude of the barriers calculated for the full complexes, further evidence that the connecting -*m*-xylene backbone contributes a large amount of strain to the rearrangement process. The tetradenticity of the ligand used here is an important contributing factor for why the barriers are large enough to measure by ^{1}H-NMR SIR experiments compared to true M(bidentate)$_4$ systems.
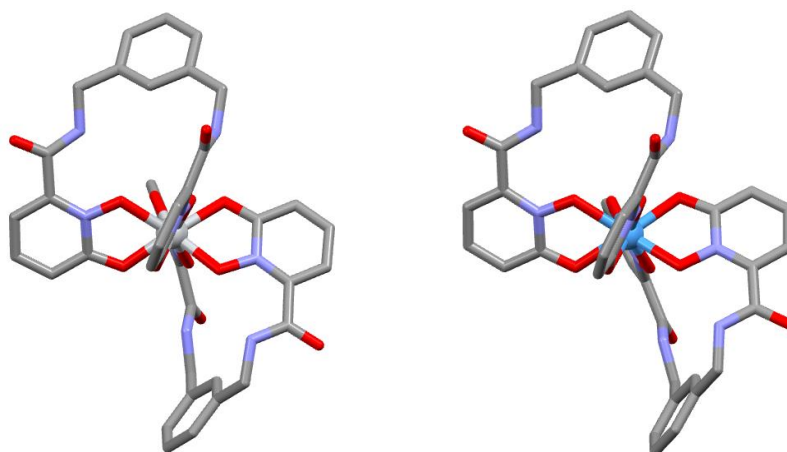
Figure 5.9. Comparison of the TS for **Ti** (left) and the GS for **Ta** (right).

In order to rationalize the different barriers for the d^0 and d^{10} metals, we first compare the transition state of d^0 **Ti** to the similarly sized ground state of d^2 **Ta** (Fig. 7). The TS of **Ti** and the GS of **Ta** are both closest to an *llll*-SA. For d^2 metals like Ta the lone pair of electrons occupy the lowest lying d-orbital on the metal, either a B_1 symmetric dx^2-y^2 orbital or an A_1 symmetric dz^2 orbital depending on the ligand field (Fig. 2). In both cases, the orbitals are incapable of σ bonding by symmetry. However, in order to avoid π interaction with the oxygen π-donating ligands, the lone pair on Ta occupies an A_1 symmetric dz^2 orbital, overcoming a significant repulsion energy penalty given the relatively large bite of **Ta** (Fig. 4). Apparently the *llll*-edge SA allows the greatest reprieve from π-interactions between metal and ligand (Fig. 8).
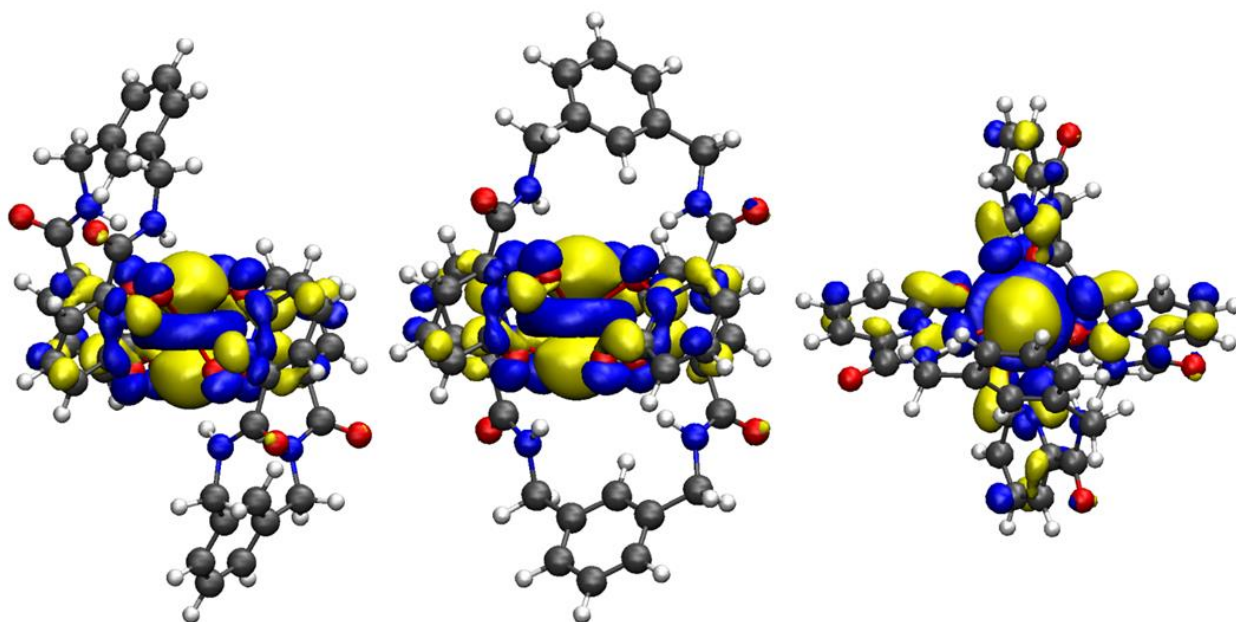
Figure 5.10. Calculated HOMO of **Ta** viewed along C_2 axes (left and middle) and along C_4 (right)
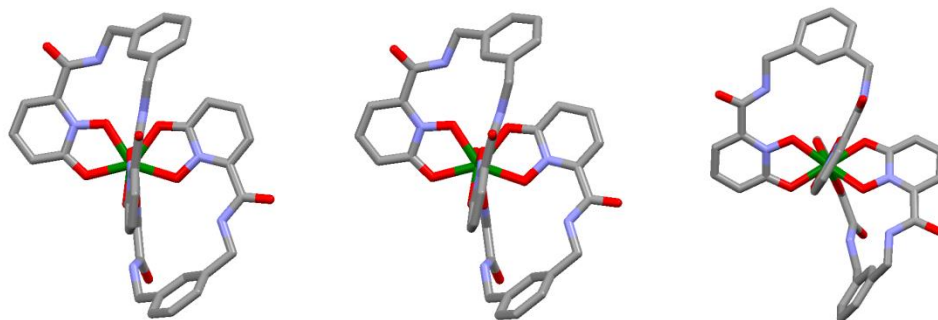
Figure 5.11. Calculated structures of **Ta**^{V} (left), **Ta**^{IV} (middle), and **Ta**^{III} (right)

As a demonstration of the influence that the *d*-orbital lone pair has on stereochemistry, consider the change in geometry calculated going from **Ta**^{V}, to **Ta**^{IV} to **Ta**^{III} shown above. For d^0 **Ta**^{V} the *mmmm*-Dod geometry dominates, while a skewed Dod is found for d^1 Ta^{IV}. Recognizing that the *llll*-edge SA provides the least amount of π interaction for **Ta**^{III} informs our expectations for the d^0 metal complexes. That is, we expect maximum favorable π-bonding for the *mmmm*-Dod ground state and minimum favorable interaction in the *llll*-SA transition state. For the ground state structures of the d^0 complexes, there are four p orbitals on the B-site oxygens that are important for d_π/p_π bonding. Those orbitals transform as A_2, B_1, and E irreducible representations, shown in the following figure. Only the B_1 representation has appropriate symmetry and positioning to form significant d_π/p_π overlap with the metal.
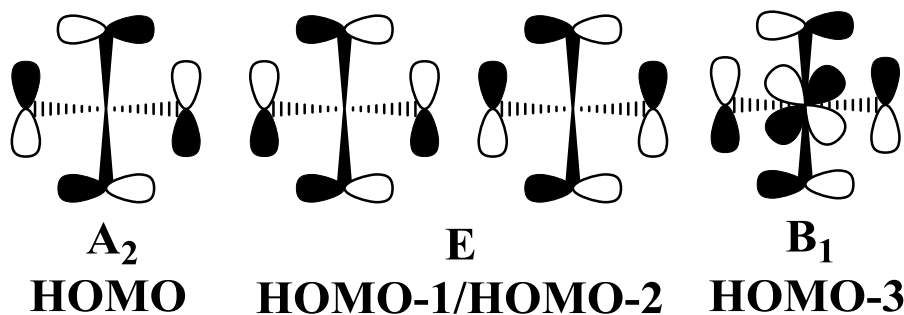
Figure 5.12. Irreducible representations of the four orbitals on the B-site oxygens capable of strong d_π/p_π bonding
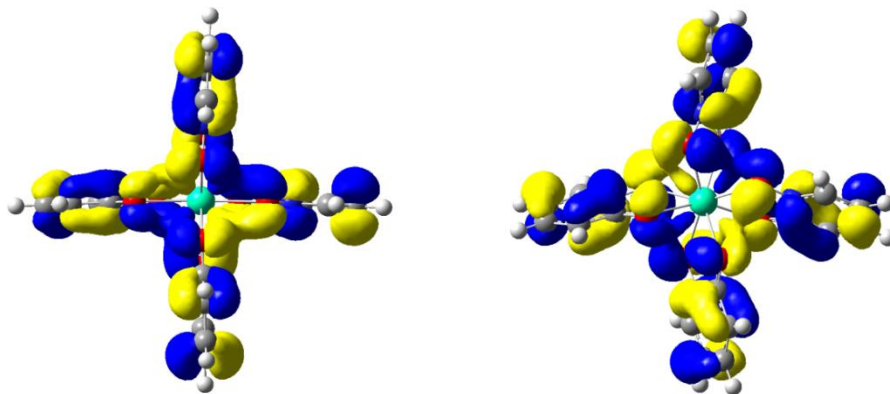
Figure 5.13. B_1 symmetric HOMO-3 molecular orbitals calculated for [Hf(1,2-HOPO)$_4$] in the ground state (left) and transition state (right).

Using [Hf(1,2-HOPO)$_4$] as a representative model, the calculated HOMO-3 molecular orbital is found to have B$_1$ symmetry, and shows significant covalent interaction between ligand π orbitals and the d(x^2-y^2) orbital of the metal as expected. The π overlap with the metal is visibly weakened upon moving to the transition state. The ground state HOMO-3 was calculated to have 6% Hf d-orbital contribution, while the transition state has only 4% Hf d-orbital contribution. The effect of this weakened covalent interaction can also be quantified by calculating the total nuclear charges on the metal for GS and TS structures. The results of total nuclear charge calculated by natural bond order (NBO) calculations are summarized in the following table.

Table 5.6. Comparison of total nuclear charges on the metal for the full complexes and [M(1,2-HOPO)$_4$] models

|		[M(5LImXy-1,2-HOPO)$_2$] Complexes			[M(1,2-HOPO)$_4$] Complexes		
		GS	TS	Diff	GS	TS	Diff
d^0 metals	Ti^{IV}	0.950	1.031	0.081	0.928	1.001	0.073
	Hf^{IV}	1.823	1.892	0.069	1.808	1.889	0.081
	Zr^{IV}	1.686	1.758	0.072	1.671	1.757	0.086
	Ce^{IV}	1.921	1.998	0.077	1.894	1.978	0.084
	Sc^{III}	1.037	1.098	0.061	1.014	1.064	0.050
	Lu^{III}	1.460	1.527	0.067	1.431	1.489	0.058
	Y^{III}	1.603	1.651	0.049	1.587	1.636	0.049
d^{10} metals	Sn^{IV}	2.114	2.136	0.023	2.080	2.111	0.031
	In^{III}	1.623	1.640	0.017	1.588	1.608	0.020
	Pb^{IV}	1.923	1.921	-0.002	1.907	1.927	0.020
	Tl^{III}	1.450	1.458	0.008	1.430	1.438	0.008
d^2 metals	V^{III}	0.681	-	-	0.643	-	-
	Nb^{III}	1.108	-	-	1.057	-	-
	Ta^{III}	1.911	-	-	1.485	-	-
	Mo^{IV}	0.904	-	-	0.895	-	-
	W^{IV}	1.070	-	-	1.063	-	-

From NBO analysis, we find that in all cases the charge on the central metal atom increases upon going from GS to TS, consistent with diminished covalent interaction between the metal and ligands. We note a much larger difference between GS and TS for the d^0 metals than found for the d^{10} metals. The M^{IV} d^0 compounds show the largest increases in charge, with an average of 0.08 charge units. The M^{III} d^0 metals show an average increase of 0.06 charge units going from GS to TS, while d^{10} metals show an average change of 0.02 charge units.

Conclusions

We have demonstrated measureable stereochemical differences for 5LImXy-1,2-HOPO complexes of d^0 and d^{10} metals, both by XRD and by DFT. In general, the d^{10} complexes tend toward *ssss*-SA, while the d^0 complexes tend toward *mmmm*-Dod, once differences in normalized bites have been considered. The measured and calculated barriers for intramolecular racemization are lower for the d^{10} metal complexes, compared to d^0. All of these effects can be rationalized by DFT, suggesting that the *mmmm*-Dod stereochemistry uniquely maximizes d$_\pi$/p$_\pi$ bonding interaction for these systems, lending support to the extension of Orgel's rule. Preference for Dod coordination and related strengthening of d$_\pi$/p$_\pi$ bonding may be related to maximizing efficiency of energy transfer from ligand to metal in the photoluminescence of **Eu**.

Experimental

General Methods. The 5LImXy-1,2-HOPO ligand was synthesized according to methods reported in chapter 3. Scandium(III) chloride hexahydrate was purchased from REacton. Yttrium(III) chloride hexahydrate, indium(III) chloride tetrahydrate, titanium(IV) diisopropoxide bis(acetylacetonate), hafnium(IV) trifluoromethanesulfonate, thallium(III) chloride hydrate, and tin(IV) bis(acetylacetonate) dichloride were purchased from Sigma-Aldrich. Zirconium(IV) acetylacetonate was purchased from Strem Chemicals. Cerium(IV) acetylacetonate was stolen from Xu. All other solvents and reagents were purchased from VWR and were used as received. ^{1}H-NMR spectra were obtained using Bruker AV-500 spectrometers operating at 500 MHz. ^{1}H chemical shifts are reported in parts per million relative to the solvent resonances, taken as δ = 2.75, 2.92, 8.03 for DMF-d_7 and δ = 2.50 for DMSO-d_6. Coupling constants (J) are reported in hertz. The following standard abbreviations are used for characterization of ^{1}H NMR signals: s=singlet, d=doublet, t=triplet, m=multiplet, dd = doublet of doublets. High resolution electrospray ionization mass spectra (HRMS-ESI) and elemental analyses were performed by the Microanalytical Laboratory, University of California, Berkeley, CA.

General Method for the Preparation of Metal(III/IV) Complexes. The 5LImPhen-1,2-HOPO ligand (172 mg, 0.42 mmol) was suspended in methanol (8 mL) at room temperature. The appropriate metal salt (0.20 mmol) was separately dissolved into methanol (2 mL) and added to the ligand suspension. Pyridine (100 mg, 1.3 mmol) was added dropwise, and the reaction was heated to reflux for 4 hours. Upon cooling in an ice bath the product was collected by filtration and washed with methanol (3x2 mL). M(III) products were dissolved into 2 mL of dimethylformamide (DMF). A solution of NMe$_4$OH·5H$_2$O (1 mol. equiv.) in methanol (0.25 mL) was added to the DMF solution, and crystals were grown by gaseous diffusion of diethyl ether. M(IV) products were dissolved into 2 mL of dimethylsulfoxide (DMSO) and crystals were grown by gaseous diffusion of methanol.

Sc[5LImXy-1,2-HOPO]$_2$[NMe$_4$] (Sc): Scandium(III) trichloride hydrate yielded colorless crystals of **Sc**. Yield: 139 mg, 63%. ^{1}H NMR (500 MHz, 1:2 DMF-d_7:acetone-d_6, -10 ^{o}C): δ 12.55 (d, J = 8.1 Hz, 2H, NH), 10.88 (s, 2H, NH), 7.75 (s, 2H, ArH), 7.49 − 7.43 (m, 4H, ArH), 7.33 (t, J = 7.9 Hz, 2H, =CH), 7.30 (dd, J = 7.4, 1.9 Hz, 2H, =CH), 7.28 − 7.24 (m, 2H, ArH), 7.07 (t, J = 7.9 Hz, 2H, =CH), 7.03 (dd, J = 7.3, 1.7 Hz, 2H, =CH), 6.53 (dd, J = 8.2, 1.9 Hz, 2H, =CH), 5.33 (d, J = 7.9 Hz, 2H, =CH), 5.27 (dd, J = 16.1, 8.9 Hz, 2H, CH_2), 4.58 (dd, J = 15.8, 4.9 Hz, 2H, CH_2), 4.46 (d, J = 16.1 Hz, 2H, CH_2), 3.97 (dd, J = 15.8, 3.0 Hz, 2H, CH_2), 3.41 (s, 12H). HRMS-ESI (m/z, [M]$^-$) Calcd for C$_{40}$H$_{32}$N$_8$O$_{12}$^{45}Sc: 861.1704, Found: 861.1727. Anal. Calcd (Found) for [Sc(C$_{20}$H$_{16}$N$_4$O$_6$)$_2$][C$_4$H$_{12}$N]·2.6H$_2$O: C 53.78 (53.61), H 5.05 (4.91), N 12.83 (12.78) %.

Y[5LImXy-1,2-HOPO]$_2$[NMe$_4$] (Y): Yttrium(III) trichloride hydrate yielded colorless crystals of **Y**. Yield: 165 mg, 72%. ^{1}H NMR (500 MHz, 1:2 DMF-d_7:acetone-d_6, -35 ^{o}C): δ 12.59 (d, J = 9.0 Hz, 2H, NH), 10.89 (t, J = 3.8 Hz, 2H, NH), 7.66 (s, 2H, ArH), 7.51 − 7.45 (m, 4H, ArH), 7.43 (t, J = 8.0 Hz, 2H, =CH), 7.37 (dd, J = 7.4, 1.6 Hz, 2H, =CH), 7.27 (d, J = 6.7 Hz, 2H, ArH), 7.12 (t, J = 7.9 Hz, 2H, =CH), 7.07 (dd, J = 7.4, 1.7 Hz, 2H, =CH), 6.66 (dd, J = 8.4, 1.7 Hz, 2H, =CH), 5.40 (dd, J = 8.3, 1.5 Hz, 2H, =CH), 5.26 (dd, J = 15.9, 9.1 Hz, 2H, CH_2), 4.54 (dd, J = 15.5, 4.6 Hz, 2H, CH_2), 4.49 (d, J = 15.7 Hz, 2H, CH_2), 3.96 (dd, J = 15.5, 3.3 Hz, 2H, CH_2). HRMS-ESI (m/z, [M]$^-$) Calcd for C$_{40}$H$_{32}$N$_8$O$_{12}$^{89}Y: 905.1204, Found: 905.1189. Anal.

Calcd (Found) for $Y[C_{20}H_{16}N_8O_{12}]_2[C_4H_{12}N]\cdot1.75C_3H_7NO\cdot0.25C_4H_8O\cdot H_2O$: C 52.75 (52.73), H 5.35 (5.40), N 13.16 (13.14) %.

In[5LImXy-1,2-HOPO]$_2$[NMe$_4$] (In): Indium(III) trichloride hydrate yielded pale yellow crystals of **In**. Yield: 152 mg, 65%. ^{1}H NMR (500 MHz, 1:2 DMF-d_7:acetone-d_6, -15 ^{o}C): δ 12.28 (s, 2H, N*H*), 10.87 (s, 2H, N*H*), 7.74 (s, 2H, Ar*H*), 7.49 − 7.44 (m, 4H, Ar*H*), 7.36 − 7.27 (m, 6H), 7.14 − 7.05 (m, 4H, =C*H*), 6.54 (dd, *J* = 7.0, 3.0 Hz, 2H, =C*H*), 5.50 (s, 2H, =C*H*), 5.22 (dd, *J* = 15.8, 8.5 Hz, 2H, C*H*$_2$), 4.52 (dd, *J* = 15.8, 4.4 Hz, 2H, C*H*$_2$), 4.47 (d, *J* = 16.3 Hz, 2H, C*H*$_2$), 4.09 (dd, *J* = 15.8, 3.4 Hz, 2H, C*H*$_2$). HRMS-ESI (*m/z*, [M]$^-$) Calcd for $C_{40}H_{32}N_8O_{12}{}^{115}In$: 931.1184, Found: 931.1210. Anal. Calcd (Found) for $[In(C_{20}H_{16}N_4O_6)_2][C_4H_{12}N]\cdot0.5C_3H_7NO\cdot3H_2O$: C 49.85 (49.98), H 4.92 (4.79), N 12.14 (11.99) %.

Tl[5LImXy-1,2-HOPO]$_2$[NMe$_4$] (Tl): Thallium(III) trichloride hydrate yielded yellow crystals of **Tl**. Yield: 136 mg, 54%. ^{1}H NMR (500 MHz, 1:2 DMF-d_7:acetone-d_6, -65 °C): δ 12.00 (s, 2H, N*H*), 10.82 (s, 2H, N*H*), 7.77 (s, 2H, Ar*H*), 7.57 − 7.33 (m, 10H), 7.28 − 7.05 (m, 4H), 6.47 (dd, *J* = 39.0, 6.6 Hz, 2H, =C*H*), 5.58 (dd, *J* = 38.7, 7.3 Hz, 2H, =C*H*), 5.20 (dd, *J* = 14.9, 8.0 Hz, 2H, C*H*$_2$), 4.56 (d, *J* = 15.4 Hz, 2H, C*H*$_2$), 4.45 (d, *J* = 14.2 Hz, 2H, C*H*$_2$), 4.25 (d, *J* = 13.2 Hz, 2H, C*H*$_2$). HRMS-ESI (*m/z*, [M]$^-$) Calcd for $C_{40}H_{32}N_8O_{12}{}^{205}Tl$: 1021.1889, Found: 1021.1907. Anal. Calcd (Found) for $[Tl(C_{20}H_{16}N_4O_6)_2][C_4H_{12}N]\cdot0.5C_3H_7NO\cdot3.5H_2O$: C 45.74 (45.71), H 4.60 (4.56), N 11.14 (11.20) %.

Ti[5LImXy-1,2-HOPO]$_2$ (Ti): Titanium(IV) bisacetylacetonate diisopropoxide yielded orange crystals of **Ti**. Yield: 128 mg, 72%. ^{1}H NMR (500 MHz, DMF-d_7, 25 °C): δ 10.66 (d, *J* = 8.1 Hz, 2H, N*H*), 9.28 (t, *J* = 3.5 Hz, 2H, N*H*), 7.85 (s, 2H, Ar*H*), 7.77 (t, *J* = 8.1 Hz, 2H), 7.66 − 7.60 (m, 2H), 7.59 (d, *J* = 7.6 Hz, 2H), 7.55 (d, *J* = 7.6 Hz, 2H), 7.52 (d, *J* = 8.5 Hz, 2H), 7.39 − 7.34 (m, 4H), 6.84 (d, *J* = 8.6 Hz, 2H, =C*H*), 5.41 (d, *J* = 8.4 Hz, 2H, =C*H*), 5.32 (dd, *J* = 15.9, 8.4 Hz, 2H, C*H*$_2$), 4.56 (dd, *J* = 15.2, 3.6 Hz, 2H, C*H*$_2$), 4.54 (d, *J* = 15.7 Hz, 2H, C*H*$_2$), 4.18 (dd, *J* = 15.4, 4.5 Hz, 2H, C*H*$_2$). HRMS-ESI (*m/z*, [M+Na]$^+$) Calcd for $C_{40}H_{32}N_8O_{12}{}^{23}Na^{48}Ti$: 887.1511, Found: 887.1489. Anal. Calcd (Found) for $[Ti(C_{20}H_{16}N_4O_6)_2]\cdot0.35H_2O$: C 55.16 (55.08), H 3.78 (3.59), N 12.87 (12.68) %.

Zr[5LImXy-1,2-HOPO]$_2$ (Zr): Zirconium(IV) tetraacetylacetonate yielded colorless crystals of **Zr**. Yield 162 mg, 87%. ^{1}H NMR (500 MHz, DMF-d_7, 40 °C): δ 10.92 (d, *J* = 8.4 Hz, 2H, N*H*), 9.34 (s, 2H, N*H*), 7.82 − 7.76 (m, 4H), 7.68 (dd, *J* = 7.5, 1.5 Hz, 2H, =C*H*), 7.61 − 7.50 (m, 6H), 7.38 (dd, *J* = 7.5, 1.5 Hz, 2H, =C*H*), 7.33 (d, *J* = 7.4 Hz, 2H, Ar*H*), 7.00 (dd, *J* = 8.6, 1.5 Hz, 2H, =C*H*), 5.65 (d, *J* = 8.3 Hz, 2H, =C*H*), 5.30 (dd, *J* = 15.8, 8.6 Hz, 2H, C*H*$_2$), 4.59 (dd, *J* = 15.5, 4.4 Hz, 2H, C*H*$_2$), 4.54 (d, *J* = 15.8 Hz, 2H, C*H*$_2$), 4.13 (dd, *J* = 15.2, 4.1 Hz, 2H, C*H*$_2$). HRMS-ESI (*m/z*, [M+Na]$^+$) Calcd for $C_{40}H_{32}N_8O_{12}{}^{23}Na^{90}Zr$: 929.1079, Found: 929.1059. Anal. Calcd (Found) for $[Zr(C_{20}H_{16}N_4O_6)_2]\cdot3.3H_2O$: C 49.66 (49.89), H 4.02 (3.77), N 11.58 (11.32) %.

Hf[5LImXy-1,2-HOPO]$_2$ (Hf): Hafnium(IV) trifluoromethanesulfonate yielded colorless crystals of **Hf**. Yield 161 mg, 81%. ^{1}H NMR (500 MHz, DMF-d_7, 30 °C): δ 10.94 (d, *J* = 7.6 Hz, 2H, N*H*), 9.36 (s, 2H, N*H*), 7.83 − 7.77 (m, 4H), 7.68 (dd, *J* = 7.6, 1.7 Hz, 2H, =C*H*), 7.61 − 7.52 (m, 6H), 7.37 (dd, *J* = 7.6, 1.7 Hz, 2H, =C*H*), 7.34 (d, *J* = 7.4 Hz, 2H, Ar*H*), 7.01 (dd, *J* = 8.6, 1.7 Hz, 2H, =C*H*), 5.62 (d, *J* = 8.2 Hz, 2H, =C*H*), 5.30 (dd, *J* = 15.8, 8.6 Hz, 2H, C*H*$_2$), 4.59 (dd, *J* = 15.3, 4.2 Hz, 2H, C*H*$_2$), 4.54 (d, *J* = 15.7 Hz, 2H, C*H*$_2$), 4.12 (dd, *J* = 15.2, 4.1 Hz, 2H, C*H*$_2$).

HRMS-ESI (*m/z*, [M+Na]$^+$) Calcd for $C_{40}H_{32}N_8O_{12}{}^{23}Na^{180}Hf$: 1019.1497, Found: 1019.1482. Anal. Calcd (Found) for $[Hf(C_{20}H_{16}N_4O_6)_2]\cdot0.25H_2O$: C 48.06 (47.79), H 3.28 (2.99), N 11.21 (11.08) %.

Ce[5LImXy-1,2-HOPO]$_2$ (Ce^{IV}): Cerium(IV) tetraacetylacetonate yielded violet crystals of **Ce**. Yield: 112 mg, 59%. ^{1}H NMR (500 MHz, DMF-d_7, 20 °C): δ 10.27 (s, 4H, N*H*), 7.72 (s, 2H, Ar*H*), 7.68 – 7.61 (m, 4H, =C*H*), 7.51 – 7.47 (m, 2H, Ar*H*), 7.44 – 7.38 (m, 8H), 6.30 (d, *J* = 6.1 Hz, 4H, =C*H*), 4.63 (s, 8H, C*H*$_2$). HRMS-ESI (*m/z*, [M+Na]$^+$) Calcd for $C_{40}H_{32}N_8O_{12}{}^{23}Na^{140}Ce$: 979.1086, Found: 979.1072. Anal. Calcd (Found) for $[Ce(C_{20}H_{16}N_4O_6)_2]\cdot1.5H_2O$: C 48.83 (49.04), H 3.59 (3.55), N 11.39 (11.21) %.

Sn[5LImXy-1,2-HOPO]$_2$ (Sn): Tin(IV) bisacetylacetonate dichloride yielded colorless crystals of **Sn**. Yield 167 mg, 89%. ^{1}H NMR (500 MHz, DMF-d_7, -10 °C): δ 10.66 (d, *J* = 6.5 Hz, 2H, N*H*), 9.33 (s, 2H, N*H*), 7.85 – 7.78 (m, 4H), 7.70 (d, *J* = 7.5 Hz, 2H), 7.66 – 7.54 (m, 6H), 7.46 (d, *J* = 7.3 Hz, 2H), 7.39 (d, *J* = 6.5 Hz, 2H), 7.01 (d, *J* = 8.1 Hz, 2H, =C*H*), 5.62 (d, *J* = 7.8 Hz, 2H, =C*H*), 5.23 (dd, *J* = 15.4, 7.6 Hz, 2H, C*H*$_2$), 4.60 (d, *J* = 15.3 Hz, 2H, C*H*$_2$), 4.50 (d, *J* = 12.6 Hz, 2H, C*H*$_2$), 4.29 (dd, *J* = 14.8, 4.8 Hz, 2H, C*H*$_2$). HRMS-ESI (*m/z*, [M+Na]$^+$) Calcd for $C_{40}H_{32}N_8O_{12}{}^{23}Na^{120}Sn$: 959.1054, Found: 959.1050. Anal. Calcd (Found) for $[Sn(C_{20}H_{16}N_4O_6)_2]\cdot0.4CH_3OH\cdot4.6H_2O$: C 47.06 (46.63), H 4.18 (3.74), N 10.87 (10.44) %.

Zr[2LImTHF-1,2-HOPO]$_2$ (Zr): Zirconium(IV) tetraacetylacetonate yielded colorless crystals of **Zr**. Yield 139 mg, 80%. ^{1}H NMR (500 MHz, DMF-d_7, 30 °C): δ 10.49 (d, *J* = 5.5 Hz, 2H, N*H*), 10.45 (d, *J* = 5.7 Hz, 2H, N*H*), 7.76 (dd, *J* = 8.6, 7.6 Hz, 2H, =C*H*), 7.71 (dd, *J* = 8.6, 7.6 Hz, 2H, =C*H*), 7.50 (dd, *J* = 7.6, 1.5 Hz, 2H, =C*H*), 7.47 (dd, *J* = 7.6, 1.5 Hz, 2H, =C*H*), 6.89 (dd, *J* = 8.6, 1.5 Hz, 2H, =C*H*), 6.84 (dd, *J* = 8.6, 1.5 Hz, 2H, =C*H*), 4.99 – 4.89 (m, 4H, C*H*), 4.34 – 4.26 (m, 4H, C*H*$_2$), 3.92 – 3.84 (m, 4H, C*H*$_2$). HRMS-ESI (*m/z*, [M+Na]$^+$) Calcd for $C_{32}H_{28}N_8O_{14}{}^{23}Na^{90}Zr$: 861.0664, Found: 861.0659. Anal. Calcd (Found) for $[Zr(C_{16}H_{14}N_4O_7)_2]\cdot3.3H_2O$: C 42.74 (42.68), H 3.88 (3.77), N 12.46 (12.53) %.

Hf[2LImTHF-1,2-HOPO]$_2$ (Hf): Hafnium(IV) trifluoromethanesulfonate yielded colorless crystals of **Hf**. Yield 132 mg, 71%. ^{1}H NMR (500 MHz, DMF-d_7, 30 °C): δ 10.52 (d, *J* = 5.7 Hz, 2H, N*H*), 10.48 (d, *J* = 5.8 Hz, 2H, N*H*), 7.76 (dd, *J* = 8.6, 7.6 Hz, 2H, =C*H*), 7.71 (dd, *J* = 8.6, 7.6 Hz, 2H, =C*H*), 7.50 (dd, *J* = 7.6, 1.5 Hz, 2H, =C*H*), 7.47 (dd, *J* = 7.6, 1.5 Hz, 2H, =C*H*), 6.89 (dd, *J* = 8.6, 1.5 Hz, 2H, =C*H*), 6.84 (dd, *J* = 8.6, 1.5 Hz, 2H, =C*H*), 5.00 – 4.89 (m, 4H, C*H*), 4.34 – 4.27 (m, 4H, C*H*$_2$), 3.91 – 3.85 (m, 4H, C*H*$_2$). HRMS-ESI (*m/z*, [M+Na]$^+$) Calcd for $C_{32}H_{28}N_8O_{14}{}^{23}Na^{180}Hf$: 951.1083, Found: 951.1074. Anal. Calcd (Found) for $[Hf(C_{16}H_{14}N_4O_7)_2]\cdot2.9H_2O$: C 39.25 (39.12), H 3.48 (3.29), N 11.44 (11.37) %.

Ce[2LImTHF-1,2-HOPO]$_2$ (Ce): Cerium(IV) tetraacetylacetonate yielded violet crystals of **Ce**. Yield 96 mg, 54%. ^{1}H NMR (500 MHz, DMF-d_7, -50 °C): δ 10.53 (d, *J* = 6.0 Hz, 2H, N*H*), 10.35 (d, *J* = 6.4 Hz, 2H, N*H*), 7.72 (t, *J* = 8.0 Hz, 2H, =C*H*), 7.62 (t, *J* = 8.0 Hz, 2H, =C*H*), 7.29 (d, *J* = 6.6 Hz, 2H, =C*H*), 7.14 (d, *J* = 6.7 Hz, 2H, =C*H*), 6.84 (d, *J* = 8.4 Hz, 2H, =C*H*), 6.57 (d, *J* = 8.2 Hz, 2H, =C*H*), 4.99-4.88 (m, 4H, C*H*), 4.34-4.26 (m, 2H, C*H*$_2$), 4.27-4.19 (m, 2H, C*H*$_2$), 3.86 – 3.74 (m, 4H, C*H*$_2$). HRMS-ESI (*m/z*, [M+Na]$^+$) Calcd for $C_{32}H_{28}N_8O_{14}{}^{23}Na^{140}Ce$: 911.0672, Found: 911.0659. Anal. Calcd (Found) for $[Ce(C_{16}H_{14}N_4O_7)_2]\cdot3.4H_2O$: C 40.46 (40.01), H 3.69 (3.22), N 11.80 (11.98) %.

^{1}H-NMR SIR Experiments. The temperature probe was calibrated from 0 to -70 ^{o}C using methanol. Selective inversion recovery (SIR) experiments were collected at forty two different mixing times. Integrated peak data for inverted and exchanging resonances were fit to a two site exchange model within the program CIFIT2.[34,35]

Crystal Data. Single crystal X-ray diffraction data were collected on a Bruker APEX or QUAZAR diffractometer equipped with a Bruker APEX-I or APEX-II CCD detector respectively. Structures were solved (using the WinGX[36] software package) with SIR-97,[37] refined with SHELX-97,[38] and the refined atomic positions are displayed as 50% thermal ellipsoids using ORTEP-32.[39] For the crystal structures of **Sc**, **In**, **Tl**, **Y**, **Eu**, **Sn**, and **Zr**, the refinement tool SQUEEZE was used to remove electron density due to disordered solvent from the .hkl file used for final refinement.[40] The following table shows the results of the SQUEEZE routine, as well as estimation of the removed disordered solvent from NMR and/or elemental analysis.

Table 5.7. Calculated void volumes and electron counts from SQUEEZE routine

Complex	Void Volume ($\mathring{A}^3$)	SQUEEZE Electron Count	Estimated Disordered Solvent per unit cell	Solvent Electron Count
Sc	718	170	3DMF+Et$_2$O+H$_2$O	172
In	1229	304	7DMF+Et$_2$O+H$_2$O	332
Lu	1255	360	7DMF+Et$_2$O+H$_2$O	332
Tl	1290	227	7DMF+Et$_2$O+H$_2$O	332
Y	1254	316	7DMF+Et$_2$O+H$_2$O	332
Zr	230	66	4MeOH	72

DFT Calculations. Ground and transition state geometry optimization and frequency calculations were performed using Gaussian 09 at the Molecular Graphics and Computation Facility at University of California, Berkeley, CA.[41] Coordinates were optimized from the XRD structures as starting points. The B3LYP functional was used, treating the light atoms with the 6-31G(d,p) basis set and the metal atoms with quasi relativistic effective core pseudopotentials, specifically: **Sc**, **Ti**, **V** (ECP10MDF[42]); **Y, Zr, Nb, Mo** (ECP28MWB[43,44]); **In** and **Sn** (ECP28MDF[45]); **Ce^{IV}** (ECP46MWB-AVQZ[46]); **Tb** (ECP54MWB[47,48]); **Dy** (ECP55MWB[47,48]); **Ho** (ECP56MWB[47,48]); **Er** (ECP57MWB[47,48]); **Tm** (ECP58MWB[47,48]); **Yb** (ECP59MWB[47,48]); **Hf**, **Lu**, **Ta**, **W** (ECP60MWB[47,48]); **Tl** (ECP60MWB[49]) and **Pb** (ECP60MDF[45]). Lanthanide basis sets were taken directly from the Stuttgart/Köln group website. All calculations were run with no symmetry constraints. Transition state calculations were verified by the presence of only one imaginary frequency.

References

(1)   Hoffmann, R.; Howell, J. M.; Rossi, A. R. *J. Am. Chem. Soc.* **1976**, *98*, 2484.
(2)   Demolliens, A.; Jean, Y.; Eisenstein, O. *Organometallics* **1986**, *5*, 1457.
(3)   Kang, S. K.; Albright, T. A.; Eisenstein, O. *Inorg. Chem.* **1989**, *28*, 1611.
(4)   Shen, M.; Iii, H. F. S.; Partridge, H. *J. Chem. Phys.* **1993**, *98*, 508.
(5)   Kang, S. K.; Tang, H.; Albright, T. A. *J. Am. Chem. Soc.* **1993**, *115*, 1971.
(6)   Maseras, F.; Lledós, A.; Clot, E.; Eisenstein, O. *Chem. Rev.* **2000**, *100*, 601.

(7)   Gillespie, R. J.; Nyholm, R. S. *Q. Rev. Chem. Soc.* **1957**, *11*, 339.

(8)   Gillespie, R. J.; Robinson, E. A. *Angew. Chem. Int. Ed. Engl.* **1996**, *35*, 495.

(9)   Morse, P. M.; Girolami, G. S. *J. Am. Chem. Soc.* **1989**, *111*, 4114.

(10) Haaland, A.; Hammel, A.; Rypdal, K.; Volden, H. V. *J. Am. Chem. Soc.* **1990**, *112*, 4547.

(11) Pfennig, V.; Seppelt, K. *Science* **1996**, *271*, 626.

(12) Kleinhenz, S.; Pfennig, V.; Seppelt, K. *Chem. - Eur. J.* **1998**, *4*, 1687.

(13) Kaupp, M. *Angew. Chem. Int. Ed.* **1999**, *38*, 3034.

(14) Kaupp, M. *Angew. Chem. Int. Ed.* **2001**, *40*, 3534.

(15) Seppelt, K. *Acc. Chem. Res.* **2003**, *36*, 147.

(16) Hoard, J. L.; Nordsieck, H. H. *J. Am. Chem. Soc.* **1939**, *61*, 2853.

(17) Hoard, J. L.; Martin, W. J.; Smith, M. E.; Whitney, J. F. *J. Am. Chem. Soc.* **1954**, *76*, 3820.

(18) Hoard, J. L.; Silverton, J. V. *Inorg. Chem.* **1963**, *2*, 235.

(19) Kepert, D. L. *Inorganic stereochemistry*; Springer-Verlag, 1982.

(20) Perumareddi, J. R.; Liehr, A. D.; Adamson, A. W. *J. Am. Chem. Soc.* **1963**, *85*, 249.

(21) Parish, R. V.; Simms, P. G.; Wells, M. A.; Woodward, L. A. *J. Chem. Soc. Inorg. Phys. Theor.* **1968**, 2882.

(22) König, E. *Theor. Chim. Acta* **1962**, *1*, 23.

(23) Kettle, S. F. A.; Parish, R. V. *Spectrochim. Acta* **1965**, *21*, 1087.

(24) Muetterties, E. L. *Inorg. Chem.* **1965**, *4*, 769.

(25) Muetterties, E. L. *Inorg. Chem.* **1973**, *12*, 1963.

(26) Brownlee, R. T. C.; Shehan, B. P.; Wedd, A. G. *Inorg. Chem.* **1987**, *26*, 2022.

(27) Hendrickx, M. F. A.; Mironov, V. S.; Chibotaru, L. F.; Ceulemans, A. *Inorg. Chem.* **2004**, *43*, 3142.

(28) Gołcebiewski, A.; Kowalski, H. *Theor. Chim. Acta* **1968**, *12*, 293.

(29) Hoard, J. L.; Hamor, T. A.; Glick, M. D. *J. Am. Chem. Soc.* **1968**, *90*, 3177.

(30) Meske, W.; Babel, D. *J. Alloys Compd.* **1992**, *183*, 158.

(31) Forgeron, M. A. M.; Wasylishen, R. E. *J. Am. Chem. Soc.* **2006**, *128*, 7817.

(32) Orgel, L. E. *J. Inorg. Nucl. Chem.* **1960**, *14*, 136.

(33) Shannon, R. D. *Acta Crystallogr. Sect. A* **1976**, *32*, 751.

(34) Mugridge, J. S.; Szigethy, G.; Bergman, R. G.; Raymond, K. N. *J. Am. Chem. Soc.* **2010**, *132*, 16256.

(35) Bain, A. D.; Cramer, J. A. *J. Magn. Reson. A* **1996**, *118*, 21.

(36) Farrugia, L. J. *J. Appl. Crystallogr.* **1999**, *32*, 837.

(37) Altomare, A.; Burla, M. C.; Camalli, M.; Cascarano, G. L.; Giacovazzo, C.; Guagliardi, A.; Moliterni, A. G. G.; Polidori, G.; Spagna, R. *J. Appl. Crystallogr.* **1999**, *32*, 115.

(38) Sheldrick, G. M. *Acta Crystallogr. A* **2008**, *64*, 112.

(39) Farrugia, L. J. *J. Appl. Crystallogr.* **1997**, *30*, 565.

(40) Van der Sluis, P.; Spek, A. L. *Acta Crystallogr. A* **1990**, *46*, 194.

(41) *Gaussian 09, Revision D.01,*.

(42) Dolg, M.; Wedig, U.; Stoll, H.; Preuss, H. *J. Chem. Phys.* **1987**, *86*, 866.

(43) Andrae, D.; Haeussermann, U.; Dolg, M.; Stoll, H.; Preuss, H., H. *Theor. Chim. Acta* **1990**, *77*, 123.

(44) Martin, J. M. L.; Sundermann, A. *J. Chem. Phys.* **2001**, *114*, 3408.

(45) Metz, B.; Stoll, H.; Dolg, M. *J. Chem. Phys.* **2000**, *113*, 2563.

(46) Hülsen, M.; Weigand, A.; Dolg, M. *Theor. Chem. Acc.* **2009**, *122*, 23.

(47) Dolg, M.; Stoll, H.; Savin, A.; Preuss, H. *Theor. Chim. Acta* **1989**, *75*, 173.

(48) Dolg, M.; Stoll, H.; Preuss, H. *Theor. Chim. Acta* **1993**, *85*, 441.
(49) Leininger, T.; Berning, A.; Nicklass, A.; Stoll, H.; Werner, H.-J.; Flad, H.-J. *Chem. Phys.* **1997**, *217*, 19.

Chapter 6

Direct Observation of 4f Intrashell Excitation in Luminescent Eu Complexes by Time‑Resolved X‑ray Absorption Near Edge Spectroscopy

Preface

The following chapter has been previously published. I decided on which compounds to measure, and I synthesized the necessary gram quantities of the materials. I also completed the DFT modeling shown in Appenedix 6. Joe Pacold measured these compounds by TR-XANES, and he and Jerry Seidler came up with the 4f/5d mixing analysis of the results. Joe and I both contributed significantly to writing and revising the document in its current form, although Joe contributed more. The introduction repeats some of the ideas covered in previous chapters, but we mostly preserve the document here in its published form for the sake of clarity.

Introduction

As discussed in chapter 1, many of the lanthanide elements have useful spectroscopic properties that have spurred broad development of novel luminescent molecules and materials.[1–6] Examples include "standard" phosphors with applications in lighting and communication,[7–10] phosphors with tailored up-conversion or down-conversion properties for the enhancement of photovoltaic cell efficiency,[11–15] and luminescent lanthanide dyes for biological assays,[16–21] in addition to decades of work on laser materials.[22–25] Despite the development of numerous applications, elucidating the energy transfer pathways in luminescent lanthanide materials remains challenging. Most of these systems exploit transitions within the partially filled 4f shells of the trivalent lanthanide ions. The optical cross sections for direct excitation (or de-excitation) of 4f–4f transitions are very weak, since they are electric dipole forbidden by parity and, in some cases, by spin. It is more efficient to indirectly excite the lanthanide by coupling to a sensitizer, i.e., another species that strongly absorbs photons and then transfers energy nonradiatively to the lanthanide.[26–28]

To rationally design efficient luminescent lanthanide materials, it is crucial to understand the underlying mechanisms of energy transfer (which vary from system to system). After initial photoexcitation, the sensitizer may undergo intersystem crossing to lower energy excited states before transferring energy to the lanthanide, creating uncertainty about which particular states contribute most. There are several possible mechanisms for the sensitizer to lanthanide energy transfer, such as resonant Coulomb interactions including Förster dipole–dipole transfer and resonance between higher multipole transitions,[29,30] or charge exchange (Dexter transfer). [31] Resonance conditions and selection rules may constrain these possibilities, but it is often not clear a priori which mechanism is dominant.[32–35] Following energy transfer, the excited state of the lanthanide may relax to a lower excited state before emitting a photon, or be nonradiatively quenched without any photoemission.[36–38]

Here, we report a time-resolved X-ray absorption near edge spectroscopy (TR-XANES) signature of the ligand-to-lanthanide energy transfer (ET) step in a set of luminescent Eu^{III} complexes. Specifically, we find that photoexcitation of the sensitizing ligand leads to a long-lived (> 100 μs) transient change in the XANES at the Eu L_3 (2p$_{3/2}$) edge, and that the magnitude of the change is correlated with the efficiency of the ligand-to-lanthanide ET. TR-XANES directly interrogates the metal ion and is complementary to time-resolved optical measurements that indirectly provide information about the ET step. While the result we report here is a purely phenomenological observation, we aim to use this ultrafast technique as a time-resolved probe

for the excited state electronic structure of Eu^{III} and other lanthanides, toward establishing a more detailed understanding of energy transfer in these systems.

Over the past two decades, TR-XANES has emerged as a powerful technique for studies of transient photoinduced effects, including chemical reactions[39,40] and spin crossover in photoactive transition metal complexes.[41–44] All of these phenomena involve significant distortions in local structure (e.g., dissociation, or bond length changes larger than 0.1 Å) that are driven by interatomic charge transfer or by electronic occupancy changes in bonding orbitals. Here, we find that TR-XANES can be used to observe a qualitatively different process, the nonradiative transfer of energy to a lanthanide ion, involving no intermediate charge transfer state. Because the long-lived Eu^{III} excitation is confined to *non*bonding 4f orbitals, we expect no significant structural change relative to the ground state at the 100-µs time scale of the observed signal (Appendix 6). The nonbonding nature of the 4f orbitals is well documented and self-evident from the atomic-like spectroscopic properties, which is why atomic term symbols are used to label the observed transitions. We note that lanthanide phosphors in general, including those that are sensitized via intermediate charge transfer states, show no difference in configuration coordinate between 4f intrashell excited states.[45–47] It is therefore significant that we observe a clear TR-XANES feature at all.

The functional form of the transient signal raises questions about the nature of 4f coupling to other atomic orbitals and to the local environment (e.g., the ligand). In particular, we consider whether the degree of 4f mixing with the bonding s- and d-orbitals, and consequently the energies of the nominal 4f and 5d manifolds, may itself be a function of 4f excitation.

Luminescent lanthanide dyes[16–21,48–52] such as the ones used in this study provide an illustration of the difficulties involved in understanding the photophysics of a general luminescent lanthanide system. An organic ligand attached to a trivalent lanthanide ion (Eu^{III} here) serves as a light-harvesting antenna[18,26,53] by absorbing broadband UV light (Figure 6.1). Ideally, this excitation is eventually transferred to the Eu^{III}, which can later emit a visible photon (Figure 6.1 (a)). The quantum efficiency of this process is limited by the existence of other pathways for radiative and nonradiative dissipation of energy, which we will now summarize. The initial excited singlet state (S) of the ligand may quickly undergo intersystem crossing to the triplet state (T). However, it may also transfer energy directly to the lanthanide, or decay back to the ground state (Figure 6.1 (c)). When sufficient coupling exists between the ligand and the Eu^{III} ion, a portion of the energy in the ligand S or T state is converted to a 4f intrashell excitation on the Eu^{III}.
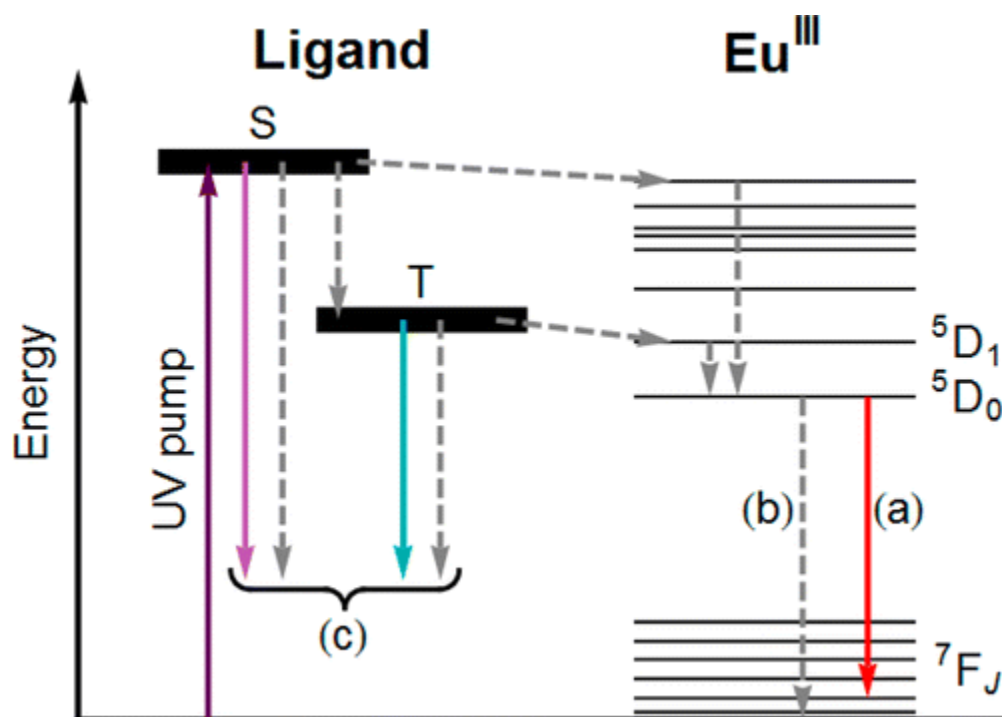
Figure 6.1. A schematic representation of the different possible energy transfer pathways in photoactive luminescent lanthanide complexes. Solid arrows represent radiative transitions, while dashed arrows represent nonradiative transitions. Three possible outcomes of photoexcitation (a, b, c) are described in the text.
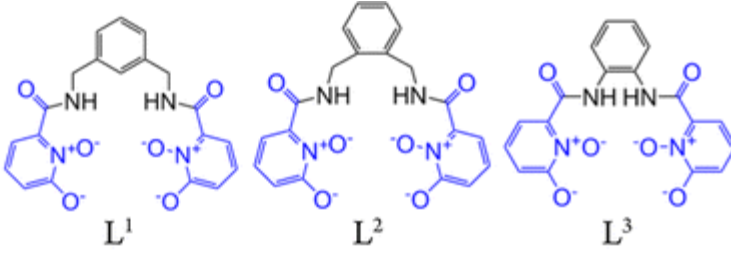
The long-lived Eu^{III} excited state requires substantial isolation from solvent species that have vibrational modes capable of quenching the excitation through nonradiative channels[36–38] (Figure 6.1 (b)). Ligands used for lanthanide luminescence must therefore be carefully designed to minimize nonradiative solvent coupling. In cases where the excited lanthanide is not quenched, the lanthanide may emit a photon upon 4f intrashell de-excitation along narrow, atomic-like emission lines (Figure 6.1 (a)). In this final emission step, the intensities of certain 4f–4f transitions, the "hypersensitive" lines (e.g., $^5D_0$ to $^7F_2$ of Eu^{III}), are strongly dependent on the local environment of the lanthanide atom.[28,54–56]

Each step in this process has been investigated experimentally by UV/visible spectroscopy[28,36,57–59] and by extensive theoretical calculations.[60–64] The overall efficiency of the antenna-to-lanthanide energy transfer has been estimated through calculations based on optical photoemission measurements (as outlined under Materials and Methods) and on the efficiency of energy transfer to a second fluorescent species.[65] Additionally, transient absorption measurements have been used to determine the lifetimes of the various ligand excited states responsible for energy transfer.[58,66] There have been no complementary metal-specific absorption spectroscopy observations of the lanthanide excited state electronic structure, likely due to the very weak, dipole-forbidden nature of the 4f intrashell transitions.

Materials and Methods

The samples are listed in Table 6.1. The three ligands are similar in that they each bear two 1-hydroxypyridin-2-one amide antennas (Table 6.1, shown in blue) which bind the Eu^{III} ion through both types of pyridyl oxygen donors. Each ligand has four donors, leading to 8-coordinate 1:2 metal:ligand complexes in the solid state.[48,67] Note that upon solvation, the coordination number of $[Eu(L^2)_2]^-$ increases to nine (Appendix 6). The UV–visible absorption and photoluminescent emission properties of the three complexes are similar. In particular, all three show broadband absorption in the near UV, with the absorption maxima (λ_{max}) occurring at wavelengths near 340 nm and similar peak molar absorptivities (ε_{max}). Combined spectra of $[Eu(L^1)_2]^-$ in aqueous buffer are provided in Figure 6.1 as a representative plot. A notable feature of the luminescence spectrum is the large $^5D_0 \rightarrow {}^7F_2$ transition, which accounts for 79% of the total emission.

Table 6.1. Ligand Structures and Photophysical Parameters of the Luminescent Eu^{III} Complexes

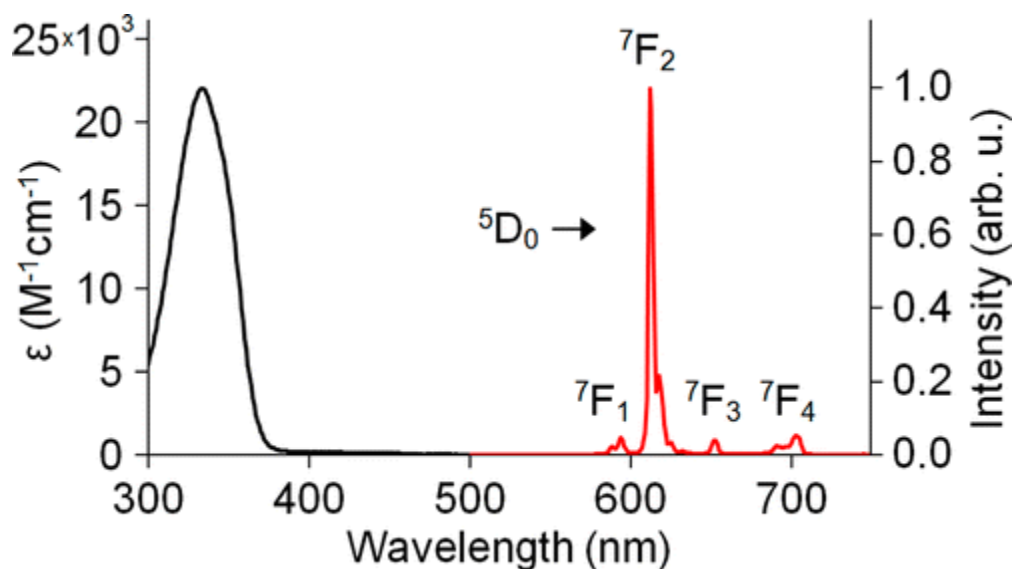| Complex	$[Eu(L^1)_2]^-$	$[Eu(L^2)_2]^-$	$[Eu(L^3)_2]^-$
λ_{max} (nm)	333	337	342
ε_{max} ($M^{-1}cm^{-1}$)	22,000	19,000	21,000
τ_{obs} H_2O (μs)	733	234	536
τ_{obs} D_2O (μs)	1022	317	734
Φ_{tot} H_2O	0.22	0.051	0.062
τ_{rad} (μs)	1680	1740	1470
k_{rad} (s^{-1})	596	573	680
k_{nonrad} (s^{-1})	768	3700	1190
η_{Eu}	0.436	0.134	0.365
η_{sens}	0.500	0.380	0.170
q (# of H_2O)	0.1	0.9	0.2

Figure 6.2. Photoabsorption spectrum (black) and photoluminescence spectrum (red) at 333 nm excitation, collected from a 2 µM solution of $[Eu(L^1)_2]^-$ in 0.1 M Tris buffer (pH = 7.4). Note that the hypersensitive line at 612 nm ($^5D_0 \rightarrow {}^7F_2$ transition) dominates the photoemission.

As discussed in chapter 1, analysis of Eu^{III} luminescence is greatly simplified by the presence of a purely magnetic dipole transition ($^5D_0 \rightarrow {}^7F_1$). With an intensity that is unaffected by the ligand field, the $^5D_0$ to $^7F_1$ transition acts as an internal reference for estimating the radiative lifetime (τ_{rad}). The radiative lifetime, inversely related to the radiative rate (k_{rad}), is the expected Eu^{III} lifetime in the absence of all nonradiative quenching, and it is calculated according to the following equation.[48,56,68]

$$k_{rad} = 1/\tau_{rad} = A[I_{tot}/I_{MD}] \qquad \textbf{(Equation 6.1)}$$

Here, I_{tot} and I_{MD} are the integrated intensities of the total Eu^{III} emission and of the magnetic dipole transition (580 to 600 nm) respectively. The constant, A, is the spontaneous emission probability of the $^5D_0$ to $^7F_1$ transition, which is 32.4 s^{-1} in water.[68] By comparing the observed luminescent lifetime to the radiative lifetime, we can define the probability that the excited Eu^{III} ion will decay radiatively (η_{Eu}) as

$$\eta_{Eu} = \tau_{obs}/\tau_{rad} = k_{rad}/k_{obs} \qquad \textbf{(Equation 6.2)}$$

The overall quantum yields (Φ_{tot}) were experimentally determined by the optically dilute method using quinine sulfate as the fluorescence standard. The quantum yield is simply the probability that an absorbed UV photon generates an emitted red photon from Eu^{III}, and it can be broken down into two component probabilities, the metal efficiency η_{Eu} defined above and the sensitization efficiency η_{sens}.

$$\Phi_{tot} = (\eta_{sens})(\eta_{Eu}) \qquad \textbf{(Equation 6.3)}$$

The sensitization efficiency (η_{sens}) is the probability that the energy of an absorbed photon is successfully transferred onto the Eu^{III} center. The extent of nonradiative quenching of the Eu^{III} excited state can be quantified in two ways. First, the rate of nonradiative decay can be

calculated using the observed lifetime and calculated radiative lifetime according to the following equation.

$$k_{nonrad} = k_{obs} - k_{rad} = 1/\tau_{obs} - 1/\tau_{rad}$$ (**Equation 6.4**)

More specific to aqueous solution, the lifetimes of each complex in H_2O and D_2O can be used to determine the degree of Eu^{III} hydration. Since O–H oscillators resonate at high energy, water is a particularly efficient quencher of Eu^{III} luminescence.[36–38] Consequently, each complex shows a shorter luminescent lifetime in water than deuterated water. The number of inner-sphere water molecules, q, is calculated using the empirically derived Horrocks equation,[59]

$$q=1.11(1/\tau_{H2O} - 1/\tau_{D2O} - 0.31)$$ (**Equation 6.5**)

where τ_{H2O} and τ_{D2O}, the observed luminescent lifetimes in the two solvents, are in milliseconds. Comparing k_{nonrad} and q in Table 6.1 shows that water coordination leads to increased rates of nonradiative quenching.

Comparing the values η_{sens} and η_{Eu} in Table 6.1 reveals the rationale for choosing these three complexes to study. Complex $[Eu(L^1)_2]^-$ is approximately four times brighter than $[Eu(L^2)_2]^-$ and $[Eu(L^3)_2]^-$ due to efficient sensitization (large η_{sens}) and minimal quenching (large η_{Eu}; q close to zero; small k_{nonrad}). Complex $[Eu(L^2)_2]^-$ has efficient sensitization (large η_{sens}), but a low quantum yield due to quenching by a bound water molecule (small η_{Eu}; q close to one; large k_{nonrad}). Finally, $[Eu(L^3)_2]^-$ has minimal quenching (large η_{Eu}; q close to zero; small k_{nonrad}) but also a low quantum yield due to inefficient sensitization of the metal (low η_{sens}). Thus, complex $[Eu(L^1)_2]^-$ is representative of pathway (a) in Figure 6.1, $[Eu(L^2)_2]^-$ is representative of (b), and $[Eu(L^3)_2]^-$ is representative of (c). Synthesis and characterization of $[Eu(L^2)_2]^-$ and $[Eu(L^3)_2]^-$ have been reported previously (including further details on the photophysical measurements summarized in Table 6.1), while $[Eu(L^1)_2]^-$ has been reported in chapter 3.[48,67]

Time-resolved Eu L_3-edge XANES measurements were performed in total fluorescence mode at beamline 11-ID-D of the Advanced Photon Source (APS) using a flowing jet of each sample in solution, at concentrations varying from 0.3 to 1 mM. The energy of the incident X-ray beam was scanned through the Eu L_3 edge (i.e., the $2p_{3/2}$ binding energy) in 0.25 eV steps, and the total X-ray fluorescence (proportional to the absorption for a dilute sample) was measured at each step. Avalanche photodiodes were used to record the time-resolved incident X-ray flux and the fluorescence from the sample. A pulsed 351 nm laser was used to excite the chromophore. Data were collected for 300 μs before and after each laser pulse. This collection time was limited by the height of the laser-illuminated volume of sample (approximately 750 μm) and the minimum jet flow rate needed to sustain laminar flow (approximately 3 m/s), rather than the luminescence lifetimes of the samples (τ_{obs} H_2O, Table 6.1). Additional experimental details are given in Appendix 6.

Results and Discussion

Typical L_3 XANES spectra for $[Eu(L^1)_2]^-$ are shown in Figure 6.3a. The "white line" peak at 6987 eV corresponds to the $2p_{3/2} \rightarrow 5d$ excitations dominating the spectrum, since the 5d shell is unoccupied. The width of the peak is determined largely by the splitting of the 5d levels.

There is an additional intrinsic broadening of the entire spectrum due to the lifetime of the $2p_{3/2}$ core hole; the implications of this effect are discussed below.
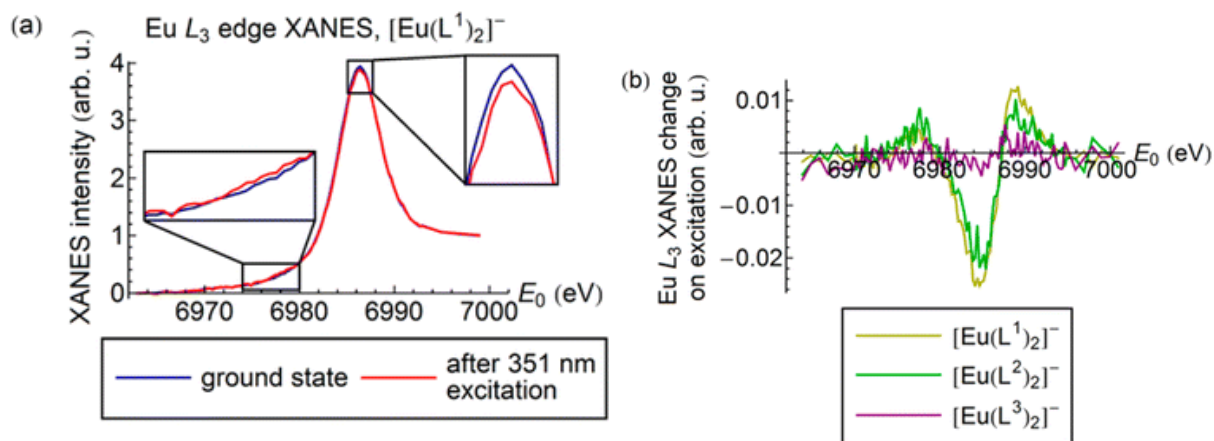

Figure 6.3. (a) Eu L_3 edge XANES collected from a 1 mM solution of $[Eu(L^1)_2]^-$. The sample was excited by a 351 nm laser with a fluence per pulse of approximately 20 mJ/cm^2. Two sections of the spectrum are magnified (insets) to show part of the change induced by the UV pump. (b) Fractional differences in the excited-state and ground-state XANES from the three complexes used in this study. To mitigate sample damage, the laser fluence was decreased to approximately 12 mJ/cm^2 while collecting these spectra, giving a smaller change than the one seen in (a). Data were averaged over 75 μs after the pump pulse to generate the excited-state spectra.

The UV photoexcitation caused a suppression of the white line and additional smaller changes, which are visible in the difference spectra shown in Figure 6.3b. The difference scales with the pump laser power, saturating (but not changing functional form) near a fluence per shot of 20 mJ/cm^2; the spectra in Figure 6.3a were collected at this fluence. The data shown in in Figure 6.3b were collected at a fluence per shot of 12 mJ/cm^2.

The UV pump laser gradually caused sample damage, observed as precipitation of unidentified Eu-containing material out of each solution. Monitoring the intensity of the total fluorescence over time showed that during a typical ten-minute long XANES scan the concentration of Eu in solution decreased by approximately 0.05% (an amount we regard as negligible). The total white line intensity changed by approximately 1% following each laser pulse (Figure 6.3b). In addition, we observed visible luminescence extending approximately 2 mm along the sample jet below the laser spot. On the basis of the jet flow rate (approximately 3 m/s), we estimate the luminescence lifetime to be on the order of 0.5 ms, consistent with optical measurements.

We first note that the signals from $[Eu(L^1)_2]^-$ and $[Eu(L^2)_2]^-$ have similar magnitudes and shapes, while the signal from $[Eu(L^3)_2]^-$ is strongly suppressed. We find this to be consistent with the calculated η_{sens} values discussed above; specifically, there is a clear correlation between the magnitude of the transient XANES signal and the efficiency of energy transfer from the ligand to the Eu^{III} ion. The long lifetime (>100 μs) of the TR-XANES signal is also inconsistent with the short lifetimes of the ligand excited states of related systems at room temperature (<2 ns).[58,66] We conclude that the transient signal is a feature of the Eu^{III} 4f-4f intrashell excitation that follows photoexcitation of the antenna, and that X-ray absorption spectroscopy is a useful probe of the transient 4f electronic state of the lanthanide atom in these systems.

Furthermore, we again emphasize that this method specifically targets the lanthanide, and it is therefore complementary to transient absorption and time-resolved photoemission measurements. As a possible application, we suggest that measurements at higher time resolution (available at XFEL facilities) should be able to determine the time delay between UV activation of the ligand and population of the lanthanide 4f excited state(s). This would directly probe the ligand-to-lanthanide energy transfer mechanism in complexes of this type.[32–35,57,69]

Before concluding, it is interesting to consider possible mechanisms for the sensitivity of the L_3 XANES to the 4f intrashell configuration. Recall that this effect is unexpected in light of the insignificant structural differences between the ground state and the excited states of each complex (Appendix 6). We therefore consider mechanisms driven purely by changes in electronic structure.

Figure 6.4a shows a simplified schematic of the density of states of Eu^{III} in the presence of a ligand. The ion has several narrow, atomic-like unoccupied 4f states near the Fermi level E_F, and a large unfilled 5d band. For clarity, we have plotted a small number of arbitrarily positioned 4f states rather attempting to show the entire 4f manifold. A simple broadening of the 5d band (Figure 6.4b) would lead to suppression of the associated XANES peak. This might be caused, for example, by an increase in the crystal field splitting due to a change in the symmetry of the chelating cage around the Eu^{III} ion. However, no such distortion is expected here (Appendix 6). As an alternative explanation of our result, we first note that there is a TR-XANES peak at 6977 eV. We expect unoccupied 4f states (or mixed 4f–5d states) to contribute to the XANES near this energy, since FEFF calculations[70] (Appendix 6) show a concentration of Eu f states there. In addition, this energy is 10 eV below the white-line peak, and the gap between the 4f and 5d levels of Eu^{III} is on the order of 10 eV in solid-state systems.[71–73]
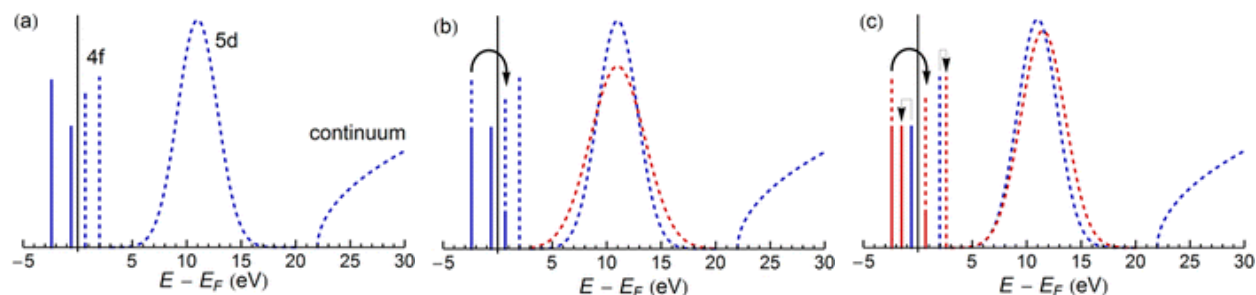
Figure 6.4. (a) Schematic representation of the density of states for ground-state Eu^{III}, including atomic-like occupied 4f states (solid lines), unoccupied 4f states (dashed), and unoccupied 5d and continuum bands. (b) Effect of a 4f–4f transition accompanied by a change in 5d crystal field splitting. (c) Effect of a 4f–4f excitation accompanied by a change in the degree of 4f–5d hybridization. The curved arrows indicate the change in electron occupancy upon excitation, while the orthogonal arrows indicate reorganization of the 4f manifold due to a changed 4f–5d hybridization.

Taken together, the TR-XANES features of the long-lived Eu^{III} excited state indicate a change in both the 4f and 5d states, as would be associated with an increase of 4f–5d mixing (Figure 6.4c). As support for this hypothesis, we note that *static* orbital hybridization effects in lanthanide materials have been extensively studied.[74–76] In particular, quantitative interpretations of visible lanthanide emission spectra[77–80] use 4f wave functions that are mixed with opposite-parity 5d states due to perturbation by the ligand field. The observation of a *time-dependent*

change in the degree of orbital mixing would have important consequences for theoretical calculations of the energy transfer rate, as well as for treatments of the emission spectrum in these complexes.

The total fluorescence detection method used in this experiment gives spectra with an energy resolution intrinsically limited by the 3.91 eV lifetime of the $2p_{3/2}$ vacancy. The low resolution destroys some information about the density of states, especially changes of the hypothetical type shown in Figure 6.4. The present data therefore do not distinguish unambiguously between the possible scenarios. Existing data on lanthanide compounds,[81–84] including europium(III) oxide,[73] show that it is possible to resolve 2p to 4f excitations with high detection energy resolution; further studies are ongoing.

Conclusions

We have identified a transient XANES signal associated with the 4f–4f intrashell transition that precedes hypersensitive emission in a family of luminescent Eu complexes. The functional form of the transient signal suggests that excitation-induced orbital hybridization effects may play an unexpected role in systems of the type studied here. More fundamentally, the existence of the signal demonstrates that time-resolved X-ray absorption spectroscopy is a promising tool for directly studying the excited states of lanthanides in luminescent materials. DFT-minimized structures of the ground states; structure comparison of the S and T state for $[Eu(L^1)_2]^-$; additional details on collection of TR-XANES; analysis of laser-induced and X-ray-induced sample damage; results of FEFF calculations of the l-projected density of states. This material is available

References

(1) Eliseeva, S. V.; Bünzli, J.-C. G. *New J. Chem.* **2011**, *35*, 1165.
(2) Bünzli, J.-C. G.; Eliseeva, S. V. *J. Rare Earths* **2010**, *28*, 824.
(3) Bünzli, J.-C. G.; Piguet, C. *Chem. Soc. Rev.* **2005**, *34*, 1048.
(4) Binnemans, K. *Chem. Rev.* **2009**, *109*, 4283.
(5) De Sá, G. .; Malta, O. .; de Mello Donegá, C.; Simas, A. .; Longo, R. .; Santa-Cruz, P. .; da Silva, E. . *Coord. Chem. Rev.* **2000**, *196*, 165.
(6) Eliseeva, S. V.; Bünzli, J.-C. G. *Chem. Soc. Rev.* **2009**, *39*, 189.
(7) Ronda, C. R.; Jüstel, T.; Nikol, H. *J. Alloys Compd.* **1998**, *275–277*, 669.
(8) Shur, M. S.; Zukauskas, R. *Proc. IEEE* **2005**, *93*, 1691.
(9) Kim, J. S.; Jeon, P. E.; Park, Y. H.; Choi, J. C.; Park, H. L.; Kim, G. C.; Kim, T. W. *Appl. Phys. Lett.* **2004**, *85*, 3696.
(10) Miniscalco, W. J. *J. Light. Technol.* **1991**, *9*, 234.
(11) Wegh, R. T.; Donker, H.; Oskam, K. D.; Meijerink, A. *Science* **1999**, *283*, 663.
(12) Trupke, T.; Shalav, A.; Richards, B. S.; Würfel, P.; Green, M. A. *Sol. Energy Mater. Sol. Cells* **2006**, *90*, 3327.
(13) Richards, B. S. *Sol. Energy Mater. Sol. Cells* **2006**, *90*, 2329.
(14) Richards, B. S. *Sol. Energy Mater. Sol. Cells* **2006**, *90*, 1189.
(15) Ende, B. M. van der; Aarts, L.; Meijerink, A. *Phys. Chem. Chem. Phys.* **2009**, *11*, 11081.
(16) Soini, E.; Lövgren, T.; Reimer, C. B. *C R C Crit. Rev. Anal. Chem.* **1987**, *18*, 105.
(17) Handl, H. L.; Gillies, R. J. *Life Sci.* **2005**, *77*, 361.

(18) Petoud, S.; Cohen, S. M.; Bünzli, J.-C. G.; Raymond, K. N. *J. Am. Chem. Soc.* **2003**, *125*, 13324.

(19) Parker, D.; Williams, J. A. G. *J. Chem. Soc. Dalton Trans.* **1996**, 3613.

(20) Moore, E. G.; Samuel, A. P. S.; Raymond, K. N. *Acc. Chem. Res.* **2009**, *42*, 542.

(21) Selvin, P. R. *Annu. Rev. Biophys. Biomol. Struct.* **2002**, *31*, 275.

(22) Reisfeld, R.; Jørgensen, C. K. In *Lasers and Excited States of Rare Earths*; Inorganic Chemistry Concepts; Springer Berlin Heidelberg, 1977; pp. 64–122.

(23) Kuriki, K.; Koike, Y.; Okamoto, Y. *Chem. Rev.* **2002**, *102*, 2347.

(24) Weber, J. K. R.; Felten, J. J.; Cho, B.; Nordine, P. C. *Nature* **1998**, *393*, 769.

(25) Slooff, L. H.; Blaaderen, A. van; Polman, A.; Hebbink, G. A.; Klink, S. I.; Veggel, F. C. J. M. V.; Reinhoudt, D. N.; Hofstraat, J. W. *J. Appl. Phys.* **2002**, *91*, 3955.

(26) Weissman, S. I. *J. Chem. Phys.* **1942**, *10*, 214.

(27) *Fundamentals of phosphors*; Yen, W. M.; Shionoya, S.; Yamamoto, H., Eds.; CRC Press: Boca Raton, FL, 2007.

(28) Bünzli, J.-C. G.; Eliseeva, S. V. In *Lanthanide Luminescence*; Hänninen, P.; Härmä, H., Eds.; Springer Series on Fluorescence; Springer Berlin Heidelberg, 2011; pp. 1–45.

(29) Főrster, T. *Discuss. Faraday Soc.* **1959**, *27*, 7.

(30) Förster, T. *Chem. Phys. Lett.* **1971**, *12*, 422.

(31) Dexter, D. L. *J. Chem. Phys.* **1953**, *21*, 836.

(32) Lima, P. P.; Nobre, S. S.; Freire, R. O.; Júnior, S. A.; Sá Ferreira, R. A.; Pischel, U.; Malta, O. L.; Carlos, L. D. *J. Phys. Chem. C* **2007**, *111*, 17627.

(33) Ward, M. D. *Coord. Chem. Rev.* **2010**, *254*, 2634.

(34) Hebbink, G. A.; Klink, S. I.; Grave, L.; Oude Alink, P. G. B.; van Veggel, F. C. J. M. *ChemPhysChem* **2002**, *3*, 1014.

(35) Hebbink, G. A.; Grave, L.; Woldering, L. A.; Reinhoudt, D. N.; van Veggel, F. C. J. M. *J. Phys. Chem. A* **2003**, *107*, 2483.

(36) Heller, A. *J. Am. Chem. Soc.* **1966**, *88*, 2058.

(37) Haas, Y.; Stein, G. *J. Phys. Chem.* **1971**, *75*, 3677.

(38) Kropp, J. L.; Windsor, M. W. *J. Chem. Phys.* **1965**, *42*, 1599.

(39) Stickrath, A. B.; Mara, M. W.; Lockard, J. V.; Harpham, M. R.; Huang, J.; Zhang, X.; Attenkofer, K.; Chen, L. X. *J. Phys. Chem. B* **2013**, *117*, 4705.

(40) Chen, L. X.; Zhang, X.; Lockard, J. V.; Stickrath, A. B.; Attenkofer, K.; Jennings, G.; Liu, D.-J. *Acta Crystallogr. A* **2010**, *66*, 240.

(41) Bressler, C.; Milne, C.; Pham, V.-T.; ElNahhas, A.; Veen, R. M. van der; Gawelda, W.; Johnson, S.; Beaud, P.; Grolimund, D.; Kaiser, M.; Borca, C. N.; Ingold, G.; Abela, R.; Chergui, M. *Science* **2009**, *323*, 489.

(42) Huse, N.; Kim, T. K.; Jamula, L.; McCusker, J. K.; de Groot, F. M. F.; Schoenlein, R. W. *J. Am. Chem. Soc.* **2010**, *132*, 6809.

(43) Monat, J. E.; McCusker, J. K. *J. Am. Chem. Soc.* **2000**, *122*, 4092.

(44) Gawelda, W.; Pham, V.-T.; Benfatto, M.; Zaushitsyn, Y.; Kaiser, M.; Grolimund, D.; Johnson, S. L.; Abela, R.; Hauser, A.; Bressler, C.; Chergui, M. *Phys. Rev. Lett.* **2007**, *98*, 057401.

(45) Blasse, G. *Luminescent materials*; Springer-Verlag: Berlin ; New York, 1994.

(46) Fonger, W. H.; Struck, C. W. *J. Chem. Phys.* **1970**, *52*, 6364.

(47) Struck, C. W.; Fonger, W. H. *J. Chem. Phys.* **1976**, *64*, 1784.

(48) D'Aléo, A.; Moore, E. G.; Szigethy, G.; Xu, J.; Raymond, K. N. *Inorg. Chem.* **2009**, *48*, 9316.

(49) Moore, E. G.; Xu, J.; Jocher, C. J.; Werner, E. J.; Raymond, K. N. *J. Am. Chem. Soc.* **2006**, *128*, 10648.

(50) Moore, E. G.; Xu, J.; Jocher, C. J.; Castro-Rodriguez, I.; Raymond, K. N. *Inorg. Chem.* **2008**, *47*, 3105.

(51) Fernández-Moreira, V.; Song, B.; Sivagnanam, V.; Chauvin, A.-S.; Vandevyver, C. D. B.; Gijs, M.; Hemmilä, I.; Lehr, H.-A.; Bünzli, J.-C. G. *Analyst* **2009**, *135*, 42.

(52) Moore, E. G.; Xu, J.; Jocher, C. J.; Corneillie, T. M.; Raymond, K. N. *Inorg. Chem.* **2010**, *49*, 9928.

(53) Crosby, G. A.; Kasha, M. *Spectrochim. Acta* **1958**, *10*, 377.

(54) Moeller, T.; Ulrich, W. F. *J. Inorg. Nucl. Chem.* **1956**, *2*, 164.

(55) Sonesson, A.; Hamoir, G.; Nilsson, I. M.; Pispa, J. *Acta Chem. Scand.* **1958**, *12*, 1937.

(56) Werts, M. H. V. In *Lanthanide Luminescence*; Hänninen, P.; Härmä, H., Eds.; Springer Series on Fluorescence; Springer Berlin Heidelberg, 2011; pp. 133–159.

(57) Yang, C.; Fu, L.-M.; Wang, Y.; Zhang, J.-P.; Wong, W.-T.; Ai, X.-C.; Qiao, Y.-F.; Zou, B.-S.; Gui, L.-L. *Angew. Chem. Int. Ed.* **2004**, *43*, 5010.

(58) Moore, E. G.; Grilj, J.; Vauthey, E.; Ceroni, P. *Dalton Trans.* **2013**, *42*, 2075.

(59) Supkowski, R. M.; Horrocks Jr., W. D. *Inorganica Chim. Acta* **2002**, *340*, 44.

(60) Malta, O. L. *J. Lumin.* **1997**, *71*, 229.

(61) Malta, O. L. *J. Non-Cryst. Solids* **2008**, *354*, 4770.

(62) Rodrigues, M. O.; da Costa Júnior, N. B.; de Simone, C. A.; Araújo, A. A. S.; Brito-Silva, A. M.; Paz, F. A. A.; de Mesquita, M. E.; Júnior, S. A.; Freire, R. O. *J. Phys. Chem. B* **2008**, *112*, 4204.

(63) Malta, O. L.; Legendziewicz, J.; Huskowska, E.; Turowska-Tyrk, I.; Albuquerque, R. Q.; de Mello Donegá, C.; e Silva, F. R. G. *J. Alloys Compd.* **2001**, *323–324*, 654.

(64) Malta, O. L.; Batista, H. J.; Carlos, L. D. *Chem. Phys.* **2002**, *282*, 21.

(65) Xiao, M.; Selvin, P. R. *J. Am. Chem. Soc.* **2001**, *123*, 7067.

(66) Foley, T. J.; Harrison, B. S.; Knefely, A. S.; Abboud, K. A.; Reynolds, J. R.; Schanze, K. S.; Boncella, J. M. *Inorg. Chem.* **2003**, *42*, 5023.

(67) D'Aléo, A.; Xu, J.; Moore, E. G.; Jocher, C. J.; Raymond, K. N. *Inorg. Chem.* **2008**, *47*, 6109.

(68) Beeby, A.; Bushby, L. M.; Maffeo, D.; Williams, J. A. G. *J. Chem. Soc. Dalton Trans.* **2002**, 48.

(69) Rodríguez-Cortiñas, R.; Avecilla, F.; Platas-Iglesias, C.; Imbert, D.; Bünzli, J.-C. G.; de Blas, A.; Rodríguez-Blas, T. *Inorg. Chem.* **2002**, *41*, 5336.

(70) Rehr, J. J.; Kas, J. J.; Vila, F. D.; Prange, M. P.; Jorissen, K. *Phys. Chem. Chem. Phys.* **2010**, *12*, 5503.

(71) Thiel, C. W.; Cone, R. L. *J. Lumin.* **2011**, *131*, 386.

(72) Dorenbos, P. *J. Lumin.* **2000**, *91*, 91.

(73) Yamaoka, H.; Taguchi, M.; M. Vlaicu, A.; Oohashi, H.; Yokoi, K.; Horiguchi, D.; Tochio, T.; Ito, Y.; Kawatsura, K.; Yamamoto, K.; Chainani, A.; Shin, S.; Shiga, M.; Wada, H. *J. Phys. Soc. Jpn.* **2006**, *75*, 034702.

(74) Strange, P.; Svane, A.; Temmerman, W. M.; Szotek, Z.; Winter, H. *Nature* **1999**, *399*, 756.

(75) Brown, S. D.; Strange, P.; Bouchenoire, L.; Zarychta, B.; Thompson, P. B. J.; Mannix, D.; Stockton, S. J.; Horne, M.; Arola, E.; Ebert, H.; Szotek, Z.; Temmerman, W. M.; Fort, D. *Phys. Rev. Lett.* **2007**, *99*, 247401.

(76) Brown, S. D.; Strange, P.; Bouchenoire, L.; Thompson, P. B. J. *Phys. Rev. B* **2013**, *87*, 165111.

(77) Judd, B. R. *J. Chem. Phys.* **1966**, *44*, 839.

(78) Judd, B. R. *J. Chem. Phys.* **1979**, *70*, 4830.

(79) Ofelt, G. S. *J. Chem. Phys.* **1962**, *37*, 511.

(80) Mason, S. F.; Peacock, R. D.; Stewart, B. *Mol. Phys.* **1975**, *30*, 1829.

(81) Krisch, M. H.; Kao, C. C.; Sette, F.; Caliebe, W. A.; Hämäläinen, K.; Hastings, J. B. *Phys. Rev. Lett.* **1995**, *74*, 4931.

(82) Bartolomé, F.; Krisch, M. H.; Raoux, D.; Tonnerre, J.-M. *Phys. Rev. B* **1999**, *60*, 13497.

(83) Dallera, C.; Krisch, M. H.; Rogalev, A.; Gauthier, C.; Goulon, J.; Sette, F.; Sole, A. *Phys. Rev. B* **2000**, *62*, 7093.

(84) Hämäläinen, K.; Siddons, D. P.; Hastings, J. B.; Berman, L. E. *Phys. Rev. Lett.* **1991**, *67*, 2850.

Chapter 7

Rationalizing the Brightest Eu^{III} 1,2-HOPO Complex

Introduction

Over the past 5 chapters, we have built a working model for the stereochemical and associated electronic factors important for realizing high quantum yield Eu^{III} 1,2-HOPO complexes. Specifically, high quantum yields are associated with dodecahedral structures in solution (chapters 3 and 4) and that preference may be related to favorable π bonding in these d^0 Eu^{III} complexes (chapter 5). In chapter 6, we found that the emissive metal centered excited state exhibits features of increased 4f/5d hybridization in the TR-XANES spectra. Assuming all of these factors are related, it stands to reason that decreasing the deviation from dodecahedral coordination will favor d$_\pi$/p$_\pi$ bonding between ligand and metal. We expect the increased π interaction will lead to an increased rate of energy transfer from ligand to metal. We introduce two new ligands here, 2LIfurazan-1,2-HOPO and 2LIS-1,2-HOPO, in order to test this model. The diamine linkers for these, and previously studied 2LIoPhen-1,2-HOPO are shown in the following figure. Like the THF backbones discussed in chapter 4, these short 2LI-type 1,2-HOPO ligands form Ln^{III} complexes where the backbones bridge the *a* edges of the dodecahedron. Unlike the THF ligands, the backbone rings for these ligands are flat, leading to structures that have apparent D$_{2d}$ symmetry in solution by ^{1}H-NMR.
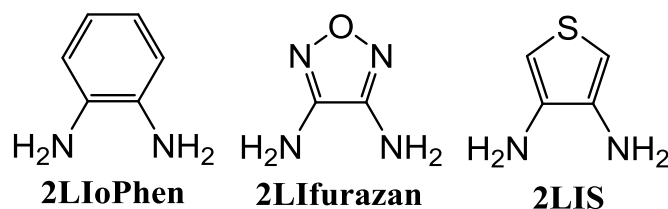

Figure 7.1. Diamine linkers used in the synthesis of the indicated 2LI-type 1,2-HOPO ligands

Results and Discussion

The crystal structure for [Eu(2LIoPhen-1,2-HOPO)$_2$][NMe$_4$] has been reported previously.[1] We have crystallized the [Eu(2LIS-1,2-HOPO)$_2$][pyH] complex and report the structure here. Shown below is a table of the shape analyses for the XRD coordinates of these two complexes, and the DFT calculated coordinates of all three Eu^{III} complexes reported here.

Table 7.1. Summary shape analysis parameters for Eu^{III} complexes of the 2LI-type ligands

	Ave. XRD M-O Dist. (Å)	Ave. DFT M-O Dist. (Å)	XRD Shape Analysis			DFT Shape Analysis		
			D$_{4d}$	C$_{2v}$	D$_{2d}$	D$_{4d}$	C$_{2v}$	D$_{2d}$
[Eu(2LIoPhen-1,2-HOPO$_2$)]$^-$	2.392	2.438	20.29	13.59	14.01	19.46	15.00	11.37
[Eu(2LIfurazan-1,2-HOPO$_2$)]$^-$	-	2.442	-	-	-	19.71	15.10	10.41
[Eu(2LIS-1,2-HOPO$_2$)]$^-$	2.396	2.441	21.88	14.44	15.29	19.98	15.36	10.82

The shape analysis numbers offer little discrimination between the three Eu^{III} complexes. Shape analyses of the DFT calculated structures are all closest to D$_{2d}$ dodecahedral, while shape analyses of the XRD coordinates show slight preferences for the C$_{2v}$ bicapped trigonal prism. We therefore might expect that the luminescence efficiencies to be similar based on the current model.

Luminescence. The absorption and emission properties of the 2LI-type Eu(III) complexes are summarized in the following plots and table.
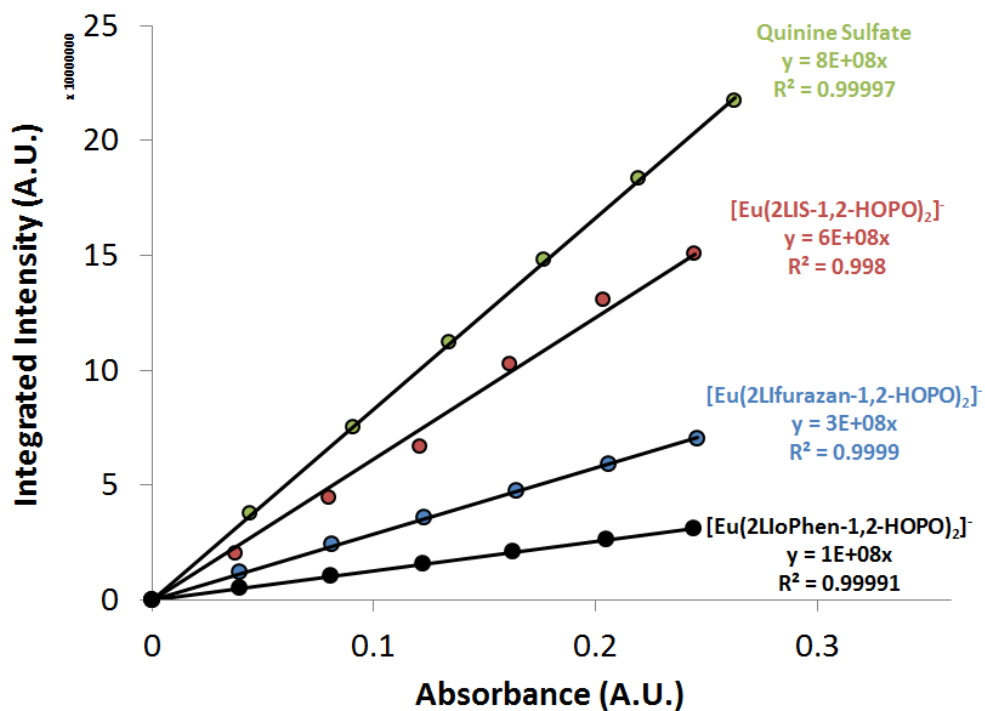

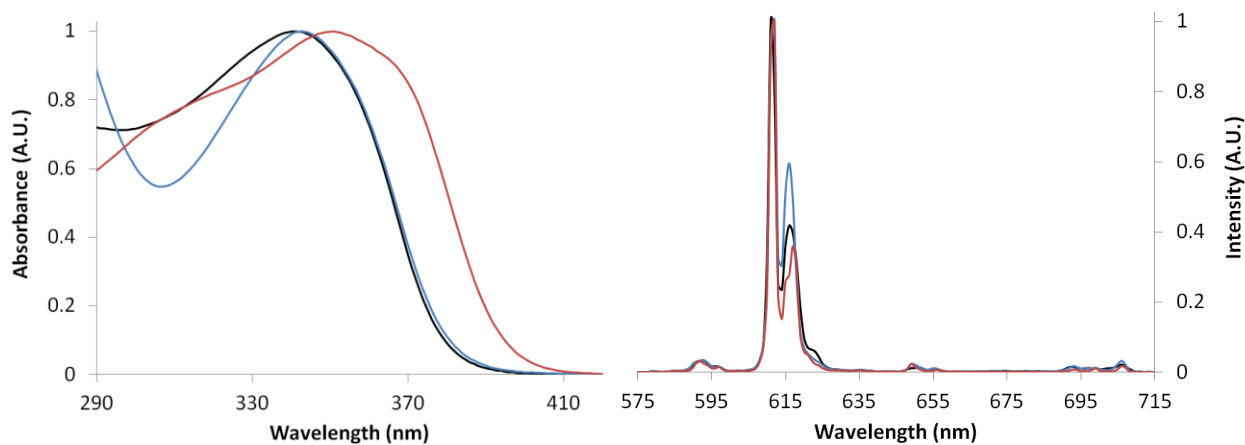**Figure 7.2.** Quantum yield determination for Eu^{III} complexes of the 2LI-type ligands reported here
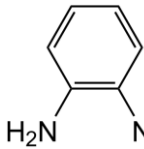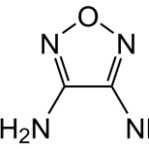

Figure 7.3. Combination UV-vis absorption (left) and luminescent emission (right) of [Eu(2LIoPhen-1,2-HOPO$_2$)]$^-$ (black), [Eu(2LIfurazan-1,2-HOPO$_2$)]$^-$ (blue), and [Eu(2LIS-1,2-HOPO$_2$)]$^-$ (red)

Table 7.2. Summary of the optical properties for the Eu^{III} complexes

Eu Complex	2LIoPhen	2LIfurazan	2LIS
λ_{max} (nm)	342	342	350
τ_{obs} H$_2$O (μs)	548	523	606
τ_{obs} D$_2$O (μs)	706	707	745
Φ_{tot} H$_2$O	0.077	0.173	0.370
τ_{rad} (μs)	1380	1370	1350
k_{rad} (s^{-1})	722	730	742
k_{nonrad} (s^{-1})	1100	1180	623
η_{Eu}	0.396	0.382	0.449
η_{sens}	0.195	0.453	0.824
q (# of H$_2$O)	0.11	0.21	0.00

The luminescent parameters of the complexes reported here share many similarities. Specifically, the observed lifetimes, radiative lifetimes, q values, and η_{Eu} values are all similar. We note small changes in the λ_{max} value, which may be indicative of electronic differences between these ligands. The most striking differences among these samples are the quantum yields and η_{sens} values, similar to what was found in chapter 4. To emphasize the connection between these two values, the quantum yields and η_{sens} values for these three complexes are plotted against each other in the following figure.

Figure 7.4. Plot of quantum yield vs. η_{sens} for the Eu^{III} complexes of 2LI-type ligands reported here

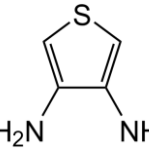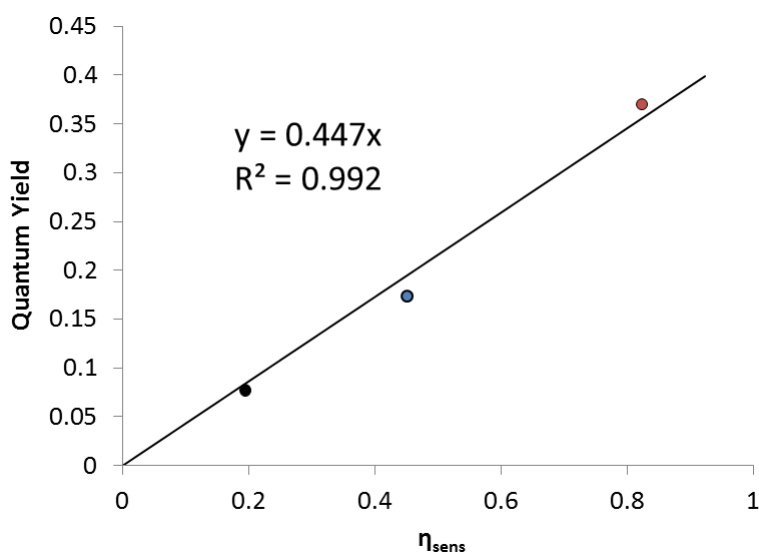The above plot shows that the dramatic difference in quantum yields across this series is almost entirely due to the differences in η_{sens} values. Previous explanations for the low quantum yield of [Eu(2LIoPhen-1,2-HOPO)$_2$]$^-$ were somewhat inconclusive.[1,2] There are small differences in the excited singlet and triplet state energies compared to complexes with aliphatic linkers, which might be caused by conjugation of the phenyl ring π system with that of the 1,2-HOPO chromophore. However, it was noted that these electronic differences are small, and they do not fully account for the observed differences in quantum yield.[2] The low η_{sens} values of [Eu(2LIoPhen-1,2-HOPO)$_2$]$^-$ indicate that the photoexcited ligand is strongly quenched before the energy is transferred onto the Eu^{III} center. Since η_{sens} is a product of the ligand intersystem crossing rate and the rate of energy transfer to the metal, one or both of these processes must be causing the low η_{sens} values. Likewise, one or both of these processes must be much faster for the [Eu(2LIS-1,2-HOPO)$_2$]$^-$ complex. We attempt to rationalize these differences by taking a closer look at the DFT and XRD structures for these rigid systems.

Structure. In the following figure we compare the crystal structures of [Eu(2LIS-1,2-HOPO)$_2$]$^-$ (largest quantum yield) and [Eu(2LIoPhen-1,2-HOPO)$_2$]$^-$ (smallest quantum yield), as well as the corresponding DFT minimized structures.
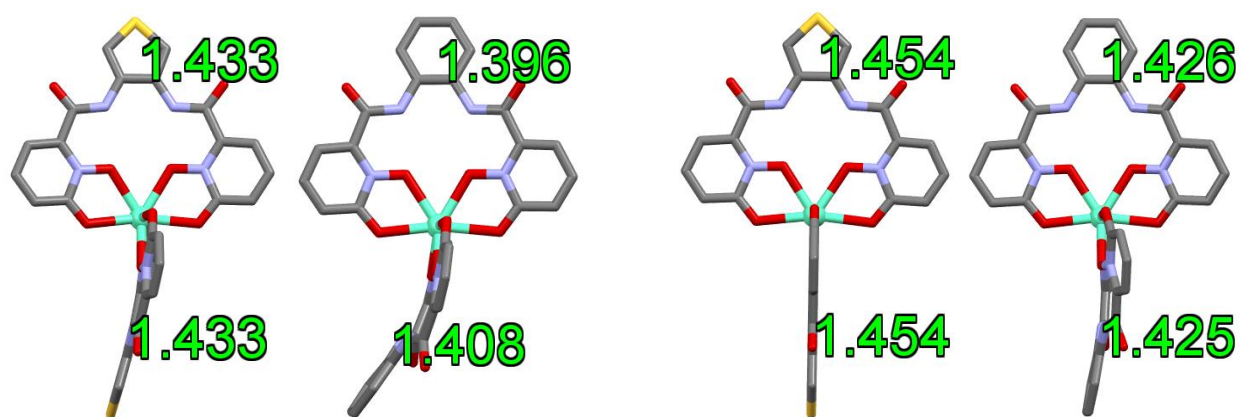
Figure 7.5. Comparison of the 2LI bridge lengths (Å) for XRD (left) and DFT (right) structures of [Eu(2LIS-1,2-HOPO)$_2$]$^-$ and [Eu(2LIoPhen-1,2-HOPO)$_2$]$^-$

From both sets of structures we note a difference in the planarity of the two complexes. The DFT structure of [Eu(2LIS-1,2-HOPO)$_2$]$^-$ is perfectly flat, with only minor buckling observed in the solid state. The structure of [Eu(2LIoPhen-1,2-HOPO)$_2$]$^-$ is significantly buckled in both XRD and DFT structures. The origin of this buckling likely arises from the 0.3 Å difference in bond length across the 2LI bridge. From the DFT structures, the lengths of the bridge are 1.425, 1.448, and 1.454 Å for the calculated structures of [Eu(2LIoPhen-1,2-HOPO)$_2$]$^-$, [Eu(2LIfurazan-1,2-HOPO)$_2$]$^-$, and [Eu(2LIS-1,2-HOPO)$_2$]$^-$ respectively. These differences are due to the different bond orders of the 2LI bridge in each system, which are closer to single bonds for the [Eu(2LIfurazan-1,2-HOPO)$_2$]$^-$ and [Eu(2LIS-1,2-HOPO)$_2$]$^-$ complexes. The longer bonds in [Eu(2LIS-1,2-HOPO)$_2$]$^-$ allow the amide hydrogens to better avoid one another, which reduces the amount of mutual repulsion between them. In line with previous rationalizations of Eu^{III} quantum yields, the more planar (closer to D$_{2d}$) structure of [Eu(2LIS-1,2-HOPO)$_2$]$^-$

109

correlates with higher quantum yield, possibly due to the associated increase in π-bonding with the Eu(III) metal.

The ^{1}H-NMR isotropic shifts for the three HOPO resonances are tabulated below. We note that the largest differences between the complexes occur for resonance C. Since resonance C is closest to the B-site oxygens participating in π-bonding, we expect resonance C to exhibit the largest contact shifts via delocalization of the unpaired spin out onto the ring.[3] By modeling the isotropic shifts for [Eu(2LIfurazan-1,2-HOPO)$_2$]$^-$ (D_1 = 346), we are able to extract contact shifts for resonance C as 2.8, 0.8 and 1.8 ppm for [Eu(2LIoPhen-1,2-HOPO)$_2$]$^-$, [Eu(2LIfurazan-1,2-HOPO)$_2$]$^-$, and [Eu(2LIS-1,2-HOPO)$_2$]$^-$ respectively. These contact shifts can be treated as surrogates for the strength of π-bonding observed by ^{1}H-NMR.

Table 7.3. Summary of the ^{1}H-NMR isotropic shifts observed for the Eu^{III} complexes of the 2LI-type ligands

[1]H	[Eu(2LIoPhen-1,2-HOPO$_2$)]$^-$	[Eu(2LIfurazan-1,2-HOPO$_2$)]$^-$	[Eu(2LIS-1,2-HOPO$_2$)]$^-$	
A	-0.61	-0.49	-0.6	
B	-2.19	-2.62	-3.1	
C	0.25	-0.81	-1.84	
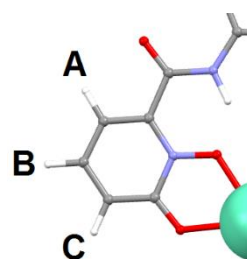
The contact shifts can be rationalized by considering the 2LI bridge N-C-C bond angles for these three complexes (Fig. 5). That is, the contact shifts are inversely proportional to the N-C-C angles. As the angle is widened, one expects the π-bonding between the Eu^{III} and B-site oxygens to diminish, which should reduce the delocalization of unpaired spin out onto the HOPO ring.
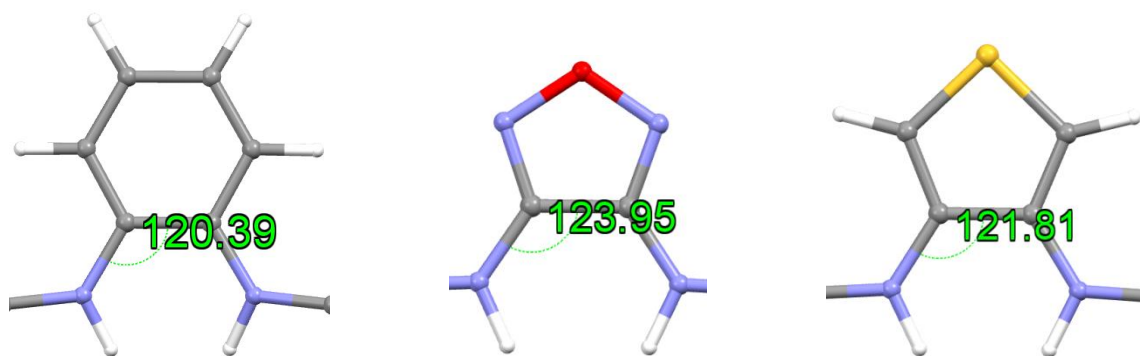
Figure 7.6. Comparison of the 2LI bridge angles (^{o}) for DFT structures of [Eu(2LIoPhen-1,2-HOPO)$_2$]$^-$ (left), [Eu(2LIfurazan-1,2-HOPO)$_2$]$^-$ (middle), and [Eu(2LIS-1,2-HOPO)$_2$]$^-$ (right).

Taking the information from the 2LI bridge lengths and N-C-C angles together, we can arrive at a "Goldilocks" explanation for the observed trends in quantum yield. The [Eu(2LIoPhen-1,2-HOPO)$_2$]$^-$ complex exhibits the greatest π-bonding on the NMR timescale (largest resonance C contact shift) due to having the smallest N-C-C angle. However, the significant buckling (Fig. 5) observed due to short 2LI bridge length may greatly reduce this interaction on the much shorter timescales associated with energy transfer to the metal. The

[Eu(2LIfurazan-1,2-HOPO)$_2$]$^-$ complex exhibits the weakest π-bonding (smallest resonance C contact shift) due to having the widest N-C-C angle, but DFT calculations predict a perfectly planar structure similar to [Eu(2LIS-1,2-HOPO)$_2$]$^-$, due to the longer 2LI bridge length. The [Eu(2LIS-1,2-HOPO)$_2$]$^-$ complex falls somewhere in between the two other structures, and so the moderate level of π-bonding and flat structure make this complex "just right" for very efficient Eu^{III} sensitization. The ^{13}C-NMR peaks should be more sensitive to these differences in contact shifts, and efforts are ongoing to assign the ^{13}C-NMR spectra for that purpose.

Conclusions

We have reported two new 1,2-HOPO ligands for the sensitization of Eu^{III} photoluminescence. We find that the [Eu(2LIS-1,2-HOPO)$_2$]$^-$ complex exhibits a remarkably high quantum yield of 38% in aqueous solution, much larger than the previous record of 23% for these systems. ^{1}H-NMR contact shifts and DFT structural parameters are used to rationalize the large differences in quantum yields observed here. These complexes challenge the current luminescence model, which states that structures closer to D$_{2d}$ should exhibit brighter luminescence. Very small differences in ligand architecture for extremely rigid ligands (like those reported here) can have dramatic effects on Eu^{III} photosensitization efficiency.

Experimental

General Methods. Europium(III) chloride hexahydrate was purchased from REacton. Yttrium(III) chloride hexahydrate and 3,4-diaminofurazan were purchased from Sigma-Aldrich. The 3,4-diaminothiophene dihydrochloride was purchased from Acros. Synthesis and characterization of the 2LIoPhen-1,2-HOPO ligand has been reported previously.[2] All other solvents and reagents were purchased from VWR and were used as received. Thin-layer chromatography (TLC) was performed using precoated Kieselgel 60 F$_{254}$ plates. Flash chromatography was performed using Silicycle SiliaFlash P60 silica (230-400 mesh). NMR spectra were obtained using Bruker AVB-400 or DRX-500 spectrometers operating at 400 (100) or 500 (125) MHz for ^{1}H (or ^{13}C) respectively. ^{1}H (or ^{13}C) chemical shifts are reported in parts per million relative to the solvent resonances, taken as δ 7.24 (δ 77.23) and δ 2.50 (δ 39.51) for CDCl$_3$ and DMSO-d$_6$ respectively. A sealed capillary of 1% TMS in CDCl$_3$ was used as a coaxial ppm reference for the paramagnetic lanthanide samples. Coupling constants (J) are reported in hertz. The following standard abbreviations are used for characterization of ^{1}H NMR signals: s=singlet, d=doublet, t=triplet, m=multiplet, dd = doublet of doublets. High resolution electrospray ionization mass spectra (HRMS-ESI) and elemental analyses were performed by the Microanalytical Laboratory, University of California, Berkeley, CA.

2LIfurazan-1,2-HOPO. An adapted literature procedure was used, since diaminofurazan is especially non-nucleophilic.[4] In a round bottom flask, 1,2-HOPOBn acyl chloride (8.6 g, 33 mmol) was dissolved into dioxane (35 mL). The diaminofurazan (1.6 g, 16 mmol) was separately dissolved into 35 mL dioxane, and then added all at once to the acid chloride. A catalytic amount of BF$_3$·Et$_2$O (800 mg) was then added, and the reaction was heated to 100 °C overnight under N$_2$. Upon cooling the solvent was removed and DCM was added causing precipitation of the crude product. Acid and base wash followed by vigorous stirring yielded the crude product as a brown powder with significant (~15 %) 1,2-HOPO free acid contaminant. Yield: 1.68 g, 14 % over two steps. ^{1}H NMR (500 MHz, DMSO-d$_6$): δ 11.88 (s, 2H, N*H*), 7.49

(dd, ^3J = 7.4 Hz, ^3J = 5.2 Hz, 2H, =C*H*), 6.71 (dd, ^3J = 7.4 Hz, ^4J = 1.8 Hz, 2H, =C*H*), 6.58 (dd, ^3J = 5.2 Hz, 2H, =C*H*). ^{13}C NMR (125 MHz, DMSO-d$_6$): δ 158.73, 157.43, 145.78, 140.00, 137.20, 121.11, 105.56. HRMS-ESI (*m/z*, [M-H]$^-$) Calcd for ^{12}C$_{14}$H$_9$N$_6$O$_7$: 373.0538, Found: 373.0541.

2LIS-1,2-HOPOBn. In a 250 mL round bottom flask, 3,4-diaminothiophene dihydrochloride (836 mg, 4.47 mmol) was dissolved into water (40 mL). Potassium carbonate (3.21 g, 23.24 mmol) and dichloromethane (20 mL) were added, and the flask was cooled on ice with stirring for 1 hour. In a separate flask, 1,2-HOPOBn acid chloride (3.06 g, 11.6 mmol) was dissolved into dichloromethane (20 mL). The acid chloride was added to the amine solution dropwise, and the two-phase system was stirred with warming to RT overnight. The organic layer was separated and loaded onto column using dichloromethane. Slowly increasing the methanol concentration to 5% afforded the desired product as a colorless foam of **1** upon solvent removal. Yield: 1.59 g, 63 %. ^{1}H NMR (400 MHz, CDCl$_3$): δ 10.05 (s, 2H, N*H*), 7.84 (s, 2H, =C*H*), 7.10-7.27 (m, 10H, Bn*H*), 7.05 (dd, ^3J = 9.2 Hz, ^3J = 6.8 Hz, 2H, =C*H*), 6.39 (dd, ^3J = 9.2 Hz, ^4J = 1.6 Hz, 2H, =C*H*), 6.17 (dd, ^3J = 6.8 Hz, ^4J = 1.6 Hz, 2H, =C*H*), 5.09 (s, 4H, C*H$_2$*),. ^{13}C NMR (100 MHz, CDCl$_3$): δ 158.78, 157.98, 142.84, 138.70, 132.91, 130.22, 129.54, 128.63, 127.20, 123.52, 113.12, 106.89, 79.79. HRMS-ESI (*m/z*, [M-H]$^-$) Calcd for ^{12}C$_{30}$H$_{23}$N$_4$O$_6$^{32}S: 567.1344, Found: 567.1327.

2LIS-1,2-HOPO. The benzyl protected ligand **2LIS-1,2-HOPOBn** was dissolved into glacial acetic acid (20 mL) at room temperature. Concentrated hydrochloric acid (20 mL) was added to the homogenous solution, and the reaction was stirred at room temperature for three days. The solvent was removed, and the resulting glass was dissolved into methanol (5 mL). The product was precipitated by adding the methanolic solution dropwise to a flask of anhydrous diethyl ether (250 mL) with vigorous stirring. The suspension was stirred overnight, filtered, washed with ether (3x10 mL), and dried to afford free flowing white powder of **2**. Yield: 1.02 g, 92 %. ^{1}H NMR (400 MHz, DMSO-d$_6$): δ 10.53 (s, 2H, N*H*), 7.86 (s, 2H, =C*H*), 7.47 (dd, ^3J = 9.1 Hz, ^3J = 6.9 Hz, 2H, =C*H*), 6.67 (dd, ^3J = 9.1 Hz, ^4J = 1.6 Hz, 2H, =C*H*), 6.57 (dd, ^3J = 6.9 Hz, ^4J = 1.5 Hz, 2H, =C*H*). ^{13}C NMR (100 MHz, DMSO-d$_6$): δ 158.20, 157.43, 141.28, 137.27, 127.47, 120.19, 112.86, 104.76. HRMS-ESI (*m/z*, [M-H]$^-$) Calcd for ^{12}C$_{16}$H$_{11}$N$_4$O$_6$^{32}S: 387.0405, Found: 387.0400. Anal. Calcd (Found) for C$_{16}$H$_{12}$N$_4$O$_6$S: C 49.48 (49.32), H 3.11 (3.18), N 14.43 (14.19), S 8.26 (7.98) %.

Method for the Preparation of Metal Complexes. The ligand (0.21 mmol) was suspended in methanol (3 mL) at room temperature. The appropriate hydrated metal chloride (0.10 mmol) was separately dissolved into methanol (1 mL) and added to the ligand suspension. Pyridine (79 mg, 1 mmol) was added dropwise, and the reaction was heated to reflux for 4 hours. Upon cooling, the product was collected by filtration and washed with methanol (3x1 mL). Complexes of the 2LIfurazan-1,2-HOPO ligand were obtained in analytically pure form as the pyridinium salt, since the excess free ligand and 1,2-HOPO starting material are reasonably soluble in methanol. Complexes of the other two ligands were further treated with a 5-fold molar excess of tetramethylammonium hydroxide in methanol (3 mL), in order to solubilize the residual amount of free ligand present. Filtration followed by washing with methanol (3x1mL) afforded analytically pure samples of the tetramethylammonium salts.

[Y(2LIoPhen-1,2-HOPO)₂][NMe₄]. Yield: 75 mg, 74 %. ^{1}H NMR (500 MHz, DMSO-d₆): δ 13.77 (s, 4H, N*H*), 8.66 (dd, ^3J = 6.3 Hz, ^3J = 3.6 Hz, 4H, Ar*H*), 7.48 – 7.43 (m, 8H), 7.26 (dd, ^3J = 6.3 Hz, ^4J = 3.7 Hz, 4H, =C*H*), 6.73 (dd, ^3J = 6.5 Hz, ^4J = 3.9 Hz, 4H, =C*H*), 3.35 (s, 12H). ^{13}C NMR (125 MHz, DMSO-d₆): δ 161.48, 158.27, 136.62, 133.13, 127.76, 124.64, 122.23, 116.76, 111.81, 54.39. HRMS-ESI (*m/z*, [M]⁻) Calcd for $^{12}C_{36}H_{24}N_8O_{12}{}^{89}Y$: 849.0578, Found: 849.0597. Anal. Calcd (Found) for [Y(C₁₈H₁₂N₄O₆)₂][C₄H₁₂N]·0.5C₃H₇NO·2.7H₂O: C 49.41 (49.56), H 4.49 (4.41), N 13.19 (13.04) %.

[Eu(2LIoPhen-1,2-HOPO)₂][NMe₄]. Yield: 84 mg, 79 %. ^{1}H NMR (500 MHz, DMSO-d₆): δ 19.03 (s, 4H), 9.51 (s, 4H), 7.94 (s, 4H), 6.98 (s, 4H), 6.84 (d, *J* = 6.0 Hz, 4H), 5.26 (s, 4H), 3.75 (s, 12H). ^{13}C NMR (125 MHz, DMSO-d₆): δ 212.35, 162.98, 130.23, 129.67, 125.41, 122.88, 105.07, 100.17, 70.22, 54.80. HRMS-ESI (*m/z*, [M]⁻) Calcd for $^{12}C_{36}H_{24}N_8O_{12}{}^{151}Eu$: 911.0718, Found: 911.0721. Anal. Calcd (Found) for [Eu(C₁₈H₁₂N₄O₆)₂][C₄H₁₂N]·0.5C₃H₇NO·2.1H₂O: C 46.97 (46.90), H 4.15 (4.12), N 12.54 (12.51) %.

[Y(2LIfurazan-1,2-HOPO)₂][py-H]. Yield: 60 mg, 63 %. ^{1}H NMR (500 MHz, DMSO-d₆): δ 15.37 (s, 4H, N*H*), 8.89 (d, *J* = 5.0 Hz, 2H, py*H*), 8.50 (tt, *J* = 7.8, 1.5 Hz, 1H, py*H*), 8.03 – 7.95 (m, 2H, py*H*), 7.53 (dd, ^3J = 8.5 Hz, ^3J = 7.5 Hz, 4H, =C*H*), 7.47 (dd, ^3J = 7.5 Hz, ^4J = 1.8 Hz, 4H, =C*H*), 6.89 (dd, ^3J = 8.5 Hz, ^4J = 1.8 Hz, 4H, =C*H*). ^{13}C NMR (125 MHz, DMSO-d₆): δ 161.19, 156.26, 144.91, 143.40, 143.25, 135.07, 133.95, 126.75, 118.61, 112.50. HRMS-ESI (*m/z*, [M]⁻) Calcd for $^{12}C_{28}H_{16}N_{12}O_{14}{}^{89}Y$: 832.9973, Found: 832.9973. Anal. Calcd (Found) for [Y(C₁₄H₈N₆O₇)₂][C₅H₆N]·1.4H₂O: C 42.22 (42.02), H 2.66 (2.44), N 19.40 (19.45) %.

[Eu(2LIfurazan-1,2-HOPO)₂][py-H]. Yield: 65 mg, 64 %. ^{1}H NMR (500 MHz, DMSO-d₆): δ 30.08 (s, 4H), 9.29 (d, *J* = 5.0 Hz, 2H, py*H*), 8.84 (t, *J* = 7.8 Hz, 1H, py*H*), 8.41 – 8.29 (m, 2H, py*H*), 6.87 (d, *J* = 7.1 Hz, 4H), 5.05 (d, *J* = 7.3 Hz, 4H), 4.43 (t, *J* = 7.6 Hz, 4H). ^{13}C NMR (125 MHz, DMSO-d₆): δ 203.37, 163.48, 147.82, 144.49, 144.24, 129.51, 126.83, 105.82, 100.25, 68.04. HRMS-ESI (*m/z*, [M]⁻) Calcd for $^{12}C_{28}H_{16}N_{12}O_{14}{}^{151}Eu$: 895.0113, Found: 895.0126. Anal. Calcd (Found) for [Eu(C₁₄H₈N₆O₇)₂][C₅H₆N]·1.9H₂O: C 39.21 (39.27), H 2.57 (2.46), N 18.01 (17.94) %.

[Y(2LIS-1,2-HOPO)₂][NMe₄]. Yield: 70 mg, 72 %. ^{1}H NMR (500 MHz, DMSO-d₆): δ 14.57 (s, 4H, N*H*), 8.22 (s, 4H, =C*H*) 7.51-7.44 (m, 8H, =C*H*), 6.79 (dd, ^3J = 7.2 Hz, ^4J = 3.2 Hz, 4H, =C*H*), 3.34 (s, 12H). ^{13}C NMR (125 MHz, DMSO-d₆): δ 161.44, 156.98, 136.05, 133.30, 127.14, 117.06, 111.59, 110.83, 54.39. HRMS-ESI (*m/z*, [M]⁻) Calcd for $^{12}C_{32}H_{20}N_8O_{12}{}^{32}S_2{}^{89}Y$: 860.9706, Found: 860.9722. Anal. Calcd (Found) for [Y(C₁₆H₁₀N₄O₆S)₂][C₄H₁₂N]·1.7H₂O: C 44.75 (44.58), H 3.69 (3.48), N 13.04 (12.96), S 6.64 (6.46) %.

[Eu(2LIS-1,2-HOPO)₂][NMe₄]. Yield: 84 mg, 81 %. ^{1}H NMR (500 MHz, DMSO-d₆): δ 25.32 (s, 4H), 9.84 (s, 4H), 6.98 (d, *J* = 7.1 Hz, 4H), 5.98 (d, *J* = 7.3 Hz, 4H), 4.85 (t, *J* = 7.6 Hz, 4H), 3.85 (s, 12H). ^{13}C NMR (125 MHz, DMSO-d₆): δ 207.76, 163.21, 130.61, 129.82, 111.99, 104.80, 100.21, 67.96, 54.91. HRMS-ESI (*m/z*, [M]⁻) Calcd for $^{12}C_{32}H_{20}N_8O_{12}{}^{32}S_2{}^{151}Eu$: 922.9846, Found: 922.9857. Anal. Calcd (Found) for [Eu(C₁₆H₁₀N₄O₆S)₂][C₄H₁₂N]·2.3H₂O: C 41.57 (41.83), H 3.55 (3.37), N 12.12 (12.20), S 6.16 (5.89) %.

DFT Calculations. Ground state geometry optimization and frequency calculations were performed using Gaussian 09 at the Molecular Graphics and Computation Facility at University

of California, Berkeley, CA.[5] The B3LYP functional was used, treating the light atoms with the 6-31G(d,p) basis set and the metal atoms with quasi relativistic effective core pseudopotentials, specifically: **Eu** (ECP52MWB)[6,7] and **Y** (ECP28MWB[8,9]). All calculations were run with no symmetry constraints.

Luminescence Measurements. Instrumentation details have been reported elsewhere.[2] Samples were first dissolved into DMSO, and then diluted into aqueous TRIS buffer (final concentration DMSO < 0.05%). The TRIS buffer was prepared by dissolving TRIS base (1 mM) into Millipore water and adjusting the pH to 7.4 with hydrochloric acid. Quinine sulfate in 0.05 M H_2SO_4 (Φ = 0.508) was used as an aqueous fluorescence quantum yield reference.[10] Quantum yields were determined by the optically dilute method (with optical density at λ_{ex} <0.05) according to the following equation:

$$\Phi_x = \frac{A_r(\lambda)}{A_x(\lambda)}\frac{I_x}{I_r}\Phi_r$$

where $A(\lambda)$ is the absorbance of sample x and reference r at the excitation wavelength λ, and I is the total integrated emission of the sample and quantum yield reference. The same excitation wavelength λ and slit widths were used for sample and reference, removing the need to correct for the incident power of the excitation source. Similarly, the refractive indices for sample and reference are assumed identical, both being aqueous. A 5 cm quartz cuvette was used to measure the absorption spectra in order to increase the signal-to-noise for these dilute solutions. Luminescence measurements were made using a 1 cm quartz fluorescence cuvette.

Crystal Data. Single crystal X-ray diffraction data were collected on a Bruker APEX or QUAZAR diffractometer equipped with a Bruker APEX-I or APEX-II CCD detector respectively. Structures were solved (using the WinGX[11] software package) with SIR-97,[12] refined with SHELX-97,[13] and the refined atomic positions are displayed as 50% thermal ellipsoids using ORTEP-32.[14] The refinement tool SQUEEZE was used to remove electron density due to disordered solvent from the .hkl file used for final refinement.[15]
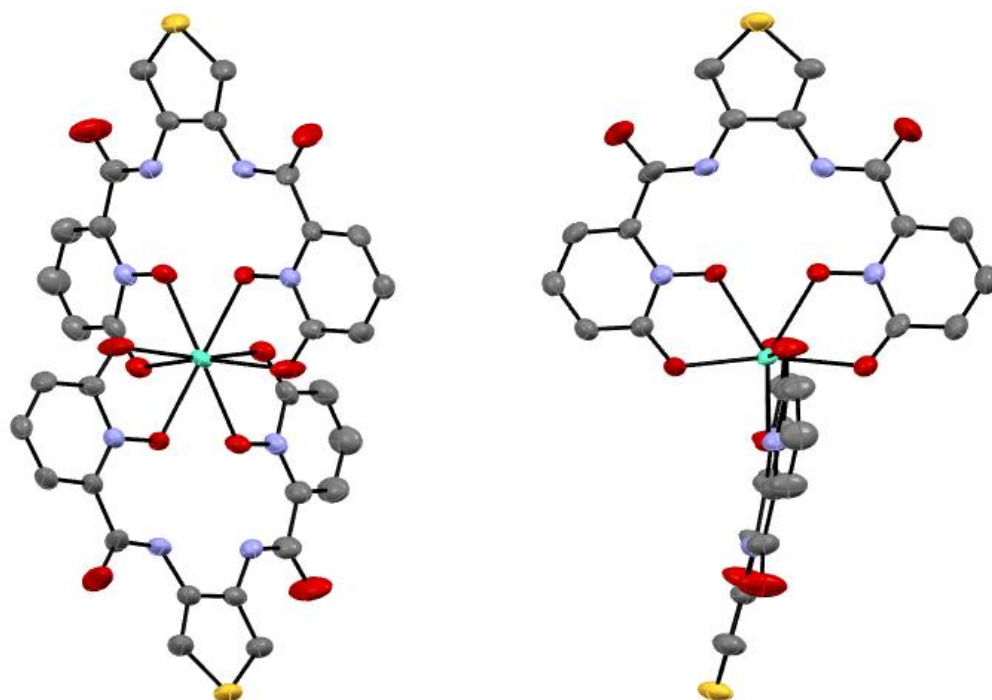
Figure 7.7. ORTEP for [Eu(2LIS-1,2-HOPO)₂][py-H]

Table 7.4. Crystal data and structure refinement for [Eu(2LIS-1,2-HOPO)₂][py-H].

Identification code	Eu2LIS
Empirical formula	C37 H26 Eu N9 O12 S2
Formula weight	1004.749
Temperature	100(2) K
Wavelength	0.71073 Å
Crystal system	Orthorhombic
Space group	Pbcn
Unit cell dimensions	a = 18.4501(10) Å $\alpha = 90°$.
	b = 9.1782(5) Å $\beta = 90°$.
	c = 23.1559(12) Å $\gamma = 90°$.
Volume	3921.2(4) Å^3
Z	4
Density (calculated)	1.492 Mg/m^3
Absorption coefficient	1.793 mm^{-1}
F(000)	2220
Crystal size	0.09 x 0.06 x 0.01 mm^3
Theta range for data collection	1.76 to 25.37°.
Index ranges	-22<=h<=22, -11<=k<=10, -25<=l<=27

115

Reflections collected	82067
Independent reflections	3591 [R(int) = 0.0434]
Completeness to theta = 25.00°	99.9 %
Absorption correction	Semi-empirical from equivalents
Max. and min. transmission	0.9823 and 0.8553
Refinement method	Full-matrix least-squares on F^2
Data / restraints / parameters	3591 / 0 / 281
Goodness-of-fit on F^2	1.069
Final R indices [I>2sigma(I)]	R1 = 0.0475, wR2 = 0.1112
R indices (all data)	R1 = 0.0691, wR2 = 0.1270
Largest diff. peak and hole	1.302 and -1.126 e.Å^{-3}

References

(1) D'Aléo, A.; Xu, J.; Moore, E. G.; Jocher, C. J.; Raymond, K. N. *Inorg. Chem.* **2008**, *47*, 6109.

(2) D'Aléo, A.; Moore, E. G.; Szigethy, G.; Xu, J.; Raymond, K. N. *Inorg. Chem.* **2009**, *48*, 9316.

(3) Bertini, I.; Luchinat, C. *Nmr of Paramagnetic Molecules in Biological Systems*; Benjamin/Cummings Publishing Company, 1986.

(4) Li, W.-S.; More, S. V.; Wang, C.-H.; Jen, Y. C.; Yao, C.-F.; Wang, T.-F.; Hung, C.-C.; Jao, S.-C. *Bioorg. Med. Chem. Lett.* **2010**, *20*, 1148.

(5) *Gaussian 09, Revision D.01,*.

(6) Dolg, M.; Stoll, H.; Savin, A.; Preuss, H. *Theor. Chim. Acta* **1989**, *75*, 173.

(7) Dolg, M.; Stoll, H.; Preuss, H. *Theor. Chim. Acta* **1993**, *85*, 441.

(8) Andrae, D.; Haeussermann, U.; Dolg, M.; Stoll, H.; Preuss, H., H. *Theor. Chim. Acta* **1990**, *77*, 123.

(9) Martin, J. M. L.; Sundermann, A. *J. Chem. Phys.* **2001**, *114*, 3408.

(10) Velapoldi, R. A.; Tønnesen, H. H. *J. Fluoresc.* **2004**, *14*, 465.

(11) Farrugia, L. J. *J. Appl. Crystallogr.* **1999**, *32*, 837.

(12) Altomare, A.; Burla, M. C.; Camalli, M.; Cascarano, G. L.; Giacovazzo, C.; Guagliardi, A.; Moliterni, A. G. G.; Polidori, G.; Spagna, R. *J. Appl. Crystallogr.* **1999**, *32*, 115.

(13) Sheldrick, G. M. *Acta Crystallogr. A* **2008**, *64*, 112.

(14) Farrugia, L. J. *J. Appl. Crystallogr.* **1997**, *30*, 565.

(15) Van der Sluis, P.; Spek, A. L. *Acta Crystallogr. A* **1990**, *46*, 194.

Chapter 2 Appendix

**Repulsion Energy Ideal Structures, Description of Alignment Procedure,
and Commented Code of Shape49 Program**

Repulsion Energy Minimized Ideal Structures

The Axis-M-L Φ angles shown on the left side of each table are relative to the high symmetry axis shown in red.

Table A2.1. 5-Coordinate C_{4v}
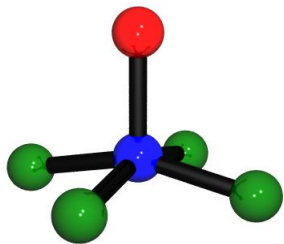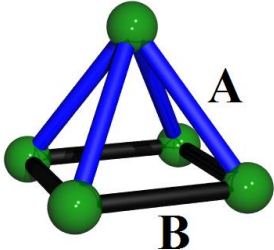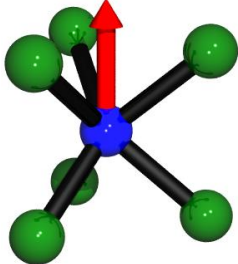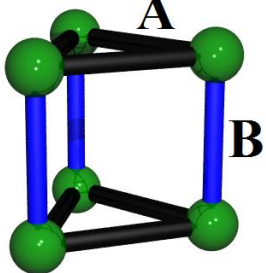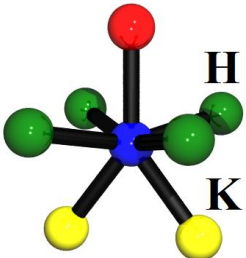
M-L Angles	n	Φ (°)	δ (°)		δ Edges
			A	**B**	
	1	104.0755	76.506	118.886	
	4	102.4153	75.867	119.613	
	5	101.8545	75.648	119.860	
	6	101.3220	75.437	120.095	
	7	100.8241	75.239	120.316	
	8	100.3629	75.054	120.521	
	12	98.8557	74.440	121.194	
	HSM	90	70.529	125.264	

Table A2.2. 6-Coordinate D_{3h}

M-L Angles	n	Φ (°)	δ (°)		δ Edges
			A	**B**	
	1	51.5651	90	120	
	4	50.7748	90	120	
	5	50.5972	90	120	
	6	50.4486	90	120	
	7	50.3233	90	120	
	8	50.2168	90	120	
	12	49.9196	90	120	
	HSM	49.1066	90	120	

Table A2.3. 7- Coordinate C$_{2v}$

M-L Angles	n	Φ_H (^{o})	θ_H (^{o})	Φ_K (^{o})
	1	80.8414	49.0407	144.1892
	4	79.9506	48.8141	143.6613
	5	79.6536	48.7645	143.4735
	6	79.3826	48.7268	143.2996
	7	79.1417	48.7008	143.1423
	8	78.9317	48.6864	143.0017
	12	78.3487	48.7249	142.5802
	HSM	77.3365	50.1792	141.3317
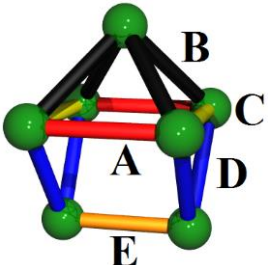
n	δ (^{o})					δ Edges
	A	**B**	**C**	**D**	**E**	
1	41.245	66.131	79.105	87.771	104.915	
4	41.410	65.630	79.008	88.034	105.812	
5	41.422	65.465	79.001	88.137	106.082	
6	41.423	65.314	79.002	88.235	106.321	
7	41.411	65.180	79.011	88.326	106.525	
8	41.389	65.064	79.027	88.410	106.694	
12	41.202	64.748	79.147	88.687	107.078	
HSM	38.668	64.364	80.671	90	106.307	

Table A2.4. 7- Coordinate C$_{3v}$
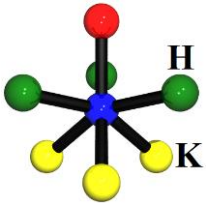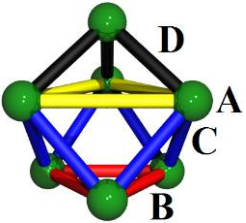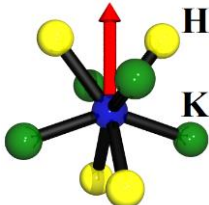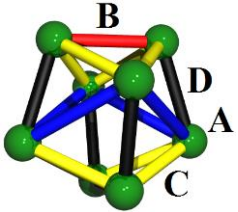
A-M-L Angles	n	Φ_H (^{o})	Φ_K (^{o})	δ (^{o})				δ Edges
				A	**B**	**C**	**D**	
	1	73.2823	128.7700	15.691	58.142	76.210	91.898	
	4	74.0721	129.6841	15.979	57.715	75.999	92.425	
	5	74.3580	129.9806	16.055	57.557	75.942	92.614	
	6	74.6256	130.2543	16.124	57.408	75.889	92.789	
	7	74.8703	130.5022	16.188	57.272	75.842	92.949	
	8	75.0910	130.7244	16.244	57.149	75.800	93.093	
	12	75.7635	131.3944	16.414	56.775	75.671	93.527	
	HSM	77.8695	133.4767	16.982	55.607	75.230	94.852	

Table A2.5. 8- Coordinate D$_{2d}$

M-L Angles	n	Φ_H (^{o})	Φ_K (^{o})	δ (^{o})				δ Edges
				A	**B**	**C**	**D**	
	1	38.3834	108.1458	29.145	52.870	61.591	75.113	
	4	37.5904	108.3875	29.803	53.369	61.310	74.597	
	5	37.4440	108.4970	29.893	53.374	61.308	74.485	
	6	37.3332	108.6079	29.948	53.340	61.327	74.393	
	7	37.2489	108.7165	29.978	53.282	61.359	74.318	
	8	37.1843	108.8207	29.990	53.210	61.399	74.254	
	12	37.0417	109.1774	29.955	52.882	61.582	74.088	
	HSM	36.8467	110.5402	29.462	51.271	62.482	73.693	

119

Table A2.6. 8- Coordinate C$_{2v}$
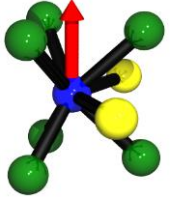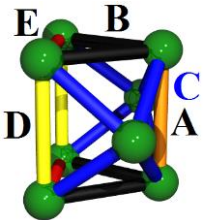
M-L Angles	n	Φ (^{o})	Twist φ (^{o})	δ (^{o})					δ Edges
				A	B	C	D	E	
	1	47.3036	13.42	30.359	46.992	58.755	75.179	90	
	4	46.7078	13.51	29.483	47.151	58.931	74.741	90	
	5	46.4988	13.55	29.172	47.205	58.995	74.586	90	
	6	46.2865	13.58	28.855	47.259	59.062	74.428	90	
	7	46.0731	13.61	28.535	47.312	59.131	74.268	90	
	8	45.8610	13.64	28.215	47.364	59.200	74.108	90	
	12	45.0711	13.75	27.009	47.550	59.472	73.504	90	
	HSM	41.8103	14.14	21.787	48.190	60.794	70.893	90	

Table A2.7. 8- Coordinate D$_{4d}$
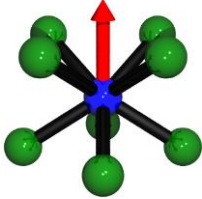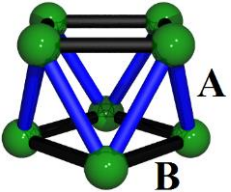
M-L Angles	n	Φ (^{o})	Twist φ (^{o})	δ (^{o})		δ Edges
				A	B	
	1	55.9140	24.29	50.896	77.789	
	4	56.7121	24.36	51.229	77.426	
	5	56.9352	24.38	51.326	77.322	
	6	57.1345	24.40	51.414	77.229	
	7	57.3111	24.41	51.494	77.145	
	8	57.4669	24.42	51.564	77.070	
	12	57.9267	24.44	51.779	76.846	
	HSM	59.2641	24.47	52.448	76.164	

Table A2.8. 8- Coordinate D$_{3h}$
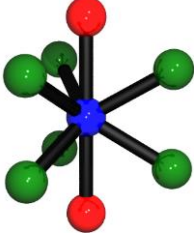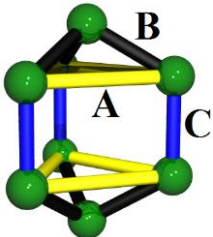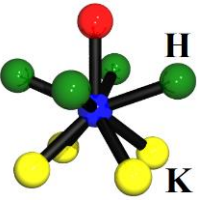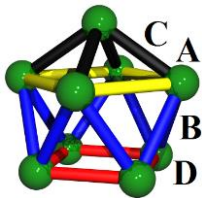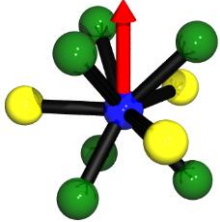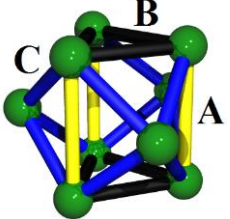
M-L Angles	n	Φ (^{o})	δ (^{o})			δ Edges
			A	B	C	
	1	61.2358	40.193	82.834	120	
	4	60.3110	40.716	82.053	120	
	5	60.1949	40.782	81.954	120	
	6	60.1220	40.824	81.891	120	
	7	60.0764	40.850	81.852	120	
	8	60.0479	40.866	81.828	120	
	12	60.0075	40.889	81.793	120	
	HSM	60.0000	40.893	81.787	120	

Table A2.9. 9- Coordinate C$_{4v}$

M-L Angles	n	Φ_H (^{o})	Φ_K (^{o})	δ (^{o})				δ Edges
				A	B	C	D	
	1	68.7663	127.6807	38.199	52.681	58.909	69.061	
	4	68.8181	127.2495	37.864	52.845	58.941	69.076	
	5	68.8380	127.1006	37.747	52.903	58.954	69.080	
	6	68.8615	126.9623	37.637	52.958	58.968	69.080	
	7	68.8886	126.8372	37.534	53.009	58.985	69.075	
	8	68.9187	126.7260	37.440	53.057	59.004	69.068	
	12	69.0552	126.4038	37.147	53.208	59.089	69.012	
	HSM	70.0747	125.7166	36.199	53.741	59.721	68.402	

Table A2.10. 9- Coordinate D_{3h}

M-L Angles	n	Φ (°)	δ (°)			δ Edges
			A	**B**	**C**	
	1	45.2795	27.329	47.502	59.399	
	4	44.9745	26.860	47.572	59.507	
	5	44.8373	26.647	47.602	59.557	
	6	44.6922	26.422	47.635	59.610	
	7	44.5440	26.191	47.667	59.665	
	8	44.3964	25.960	47.699	59.720	
	12	43.8619	25.117	47.810	59.926	
	HSM	41.8103	21.787	48.190	60.794	

More details about the third stage alignment procedure

Four-coordinate analysis does not require edge finding, since four vertices are always mutually connected along external edges. The tetrahedron is isotropic with respect to alignment, while the square plane has a unique symmetry axis. There are three possible orientations of the unique axis, requiring three alignments. In five-coordinate systems, the program expects three 4-edge vertices and two 3-edge vertices. The two 3-edge vertices are not connected to each other; they are related by mirror symmetry in the ideal D_{3h} and C_{4v} shapes, meaning specific assignment is not required. The remaining three 4-edge vertices are equivalent in D_{3h} but not C_{4v}. The C_{4v} principle rotation axis lies along one of these three 4-edge vertices, and so three alignments are required for 5-coordination.

Six-coordinate alignment is complicated by the presence of multiple 4-sided faces in the D_{3h} ideal. For the program to function, all 4-sided faces must be at least slightly creased along one of the two face diagonals. The presence of a perfectly flat 4-sided face causes incorrect edge number assignments, as one, both, or neither of the face diagonals may be counted as external edges. To accommodate shapes containing perfectly flat 4-sided faces, all input coordinates are anisotropically modified by about 10^{-9} units, i.e. an insignificant random crease is introduced to all ideally flat 4-sided faces. Considering all possible creases of the three 4-edge faces in D_{3h} symmetry, we find two unique structure types (Fig. A2.1).
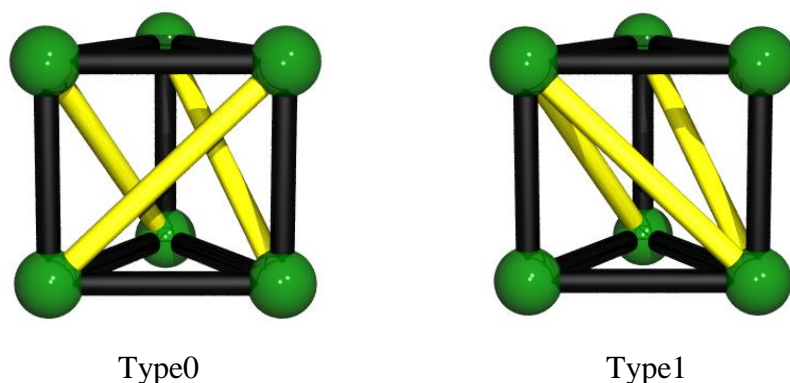
Type0   Type1

Figure A2.1. The two edge types considered for δ shape analysis of six coordination

The most common structure type for six-coordination is type0 shown to the left, which includes all structures close to O_h geometry (all six ligands sit on 4-edge vertices). For alignment, one vertex is chosen arbitrarily, and then the four vertices connected to it are found and labeled in sequence by connectivity. There are eight total ways to sequentially label the set of four vertices connected to the first, four ways rotating the labels clockwise and four ways rotating counterclockwise. The remaining sixth vertex is unique by not being connected to the first chosen vertex, thus eight total alignments are required. The less common structure type shown to the right has two 5-edge vertices, two 3-edge vertices, and two 4-edge vertices, and all eight possible alignments are tested. Seven-coordination also has two structure types due to the two flat faces of the C_{2v} monocapped trigonal prism, shown below.

Type0   Type1
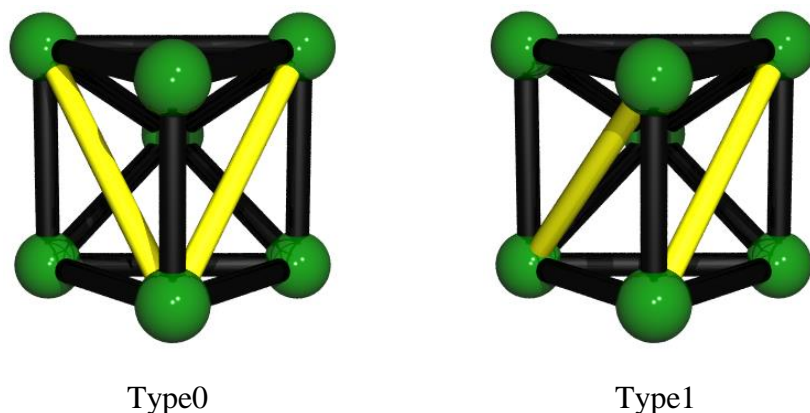
Figure A2.2. The two edge types considered for δ shape analysis of seven coordination

Type0 seven-coordinate structures (like the C_{3v} capped octahedron) have one 3-edge, three 5-edge, and three 4-edge vertices. The unique 3-edge vertex is labeled, then the three 5-edge vertices are labeled in the six possible ways. The 4-edge vertices are unambiguously found by connectivity to the 5-edge vertices, thus six total alignments are required. Type1 seven-coordinate structures (like the D_{5h} pentagonal bipyramid) have two 5-edge vertices and five 4-edge vertices. The 4-edge vertices are labeled sequentially by connectivity. Rotating the 4-edge labels to all five 4-edge vertices combined with the two possible 5-edge labels requires ten total alignments.

Eight-coordination is particularly complicated by the six 4-sided faces of the cube, the two 4-sided faces of the D_{4d} square antiprism, and the three 4-sided faces of the D_{3h} bicapped trigonal prism. There are 64 ways to crease the six 4-sided faces of a cube, resulting in seven unique structure types. There are four ways to crease the two 4-sided faces of the square antiprism, resulting in two distinct structure types (similar to seven-coordination), both of which are equivalent to two of the cubic types. There are two distinct D_{3h} structure types (similar to D_{3h} in six-coordiation), one of which is equivalent to a cubic type. The eight unique structure types for eight-coordination are shown below.
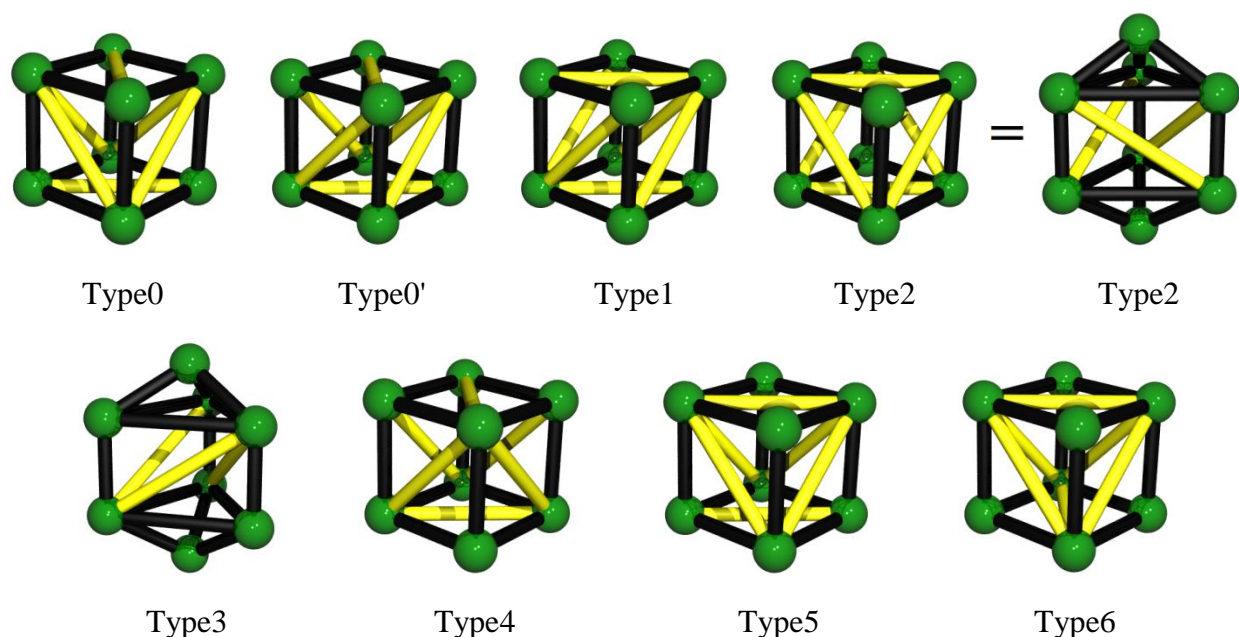
Figure A2.3. The eight edge types considered for δ shape analysis of eight coordination

Most common in eight coordination are type0 and type0' structures, which both have four 4-edge vertices and four 5-edge vertices. All structures near D_{2d}, C_{2v}, or D_{4d} geometries are one of these two structure types. The D_{6h} hexagonal bipyramid is representative of type1, having two 6-edge vertices and six 4-edge vertices. The D_{3h} bicapped trigonal prism is type2 or type3. Both type2 and type3 have two 3-edge vertices; type2 has and six 5-edge vertices, while type3 has two 4-edge, two 5-edge, and two 6-edge vertices. Structure types 4, 5, and 6 do not have associated ideal geometries other than the cube, but they are included nonetheless for completeness.

There are eight ways to label the four 4-edge vertices in type0 structures, and the corresponding 5-edge vertices are found unambiguously by connectivity, requiring eight total alignments. Type0' structures are aligned by transformation of the eight type0 permutations. Structure types 1, 2 and 3 are labeled similarly to seven-coordinate type1 structures, but six label rotations are required instead of five (meaning 12 alignments are required). Structure types 4, 5, and 6 are aligned by finding an initial set of arbitrary (but properly connected) labels and then applying all 48 possible symmetry operations of O_h to generate the possible permutations.

There is only one structure type considered for nine-coordination analysis, with six 5-edge and three 4-edge vertices. The alignment problem is directly analogous to that of five-coordination. Three alignments are required, since one of the three 4-edge vertices must be labeled as the unique capping atom of the C_{4v} monocapped square antiprism.

The Shape49 δ Dihedral Angle Shape Analysis Progra

```
clear
%----------------------------
%Choose analysis options below
%----------------------------
```

```
longanalysis=1; %enter 0 for short, 1 for long
autonormalize=0; %enter 0 for off, 1 for on


%--------------------------------------------
%Input xyz coordinates below (as P1, P2, etc.)
%--------------------------------------------


title1 = '4Coord Td Ideal';
P1 = [0   0.816496        0.577350
0          -0.816496       0.577350
0.816496         0         -0.577350
-0.816496        0         -0.577350];


title2 = '4Coord D4h Ideal';
P2 = [1   0 0
-1         0          0
0          1          0
0          -1         0];


title3 = '5Coord D3h Ideal';
P3 = [0   0          1
1          0          0
-1         0          0
0          0.866025         -0.5
0          -0.866025        -0.5];


title4 = '5Coord C4v Ideal (n=6)';
P4 = [0   0          1
0.980539         0          -0.196323
-0.980539        0          -0.196323
0          0.980539         -0.196323
0          -0.980539        -0.196323];


title5 = '6Coord Oh Ideal';
P5 = [1   0          0
-1         0          0
0          1          0
0          -1         0
0          0          1
0          0          -1];


title6 = '6Coord D3h Ideal (n=6)';
P6 = [0   0.771054        0.636770
0.667752         -0.385527        0.636770
-0.667752        -0.385527        0.636770
0          0.771054         -0.636770
0.667752         -0.385527        -0.636770
-0.667752        -0.385527        -0.636770];


title7 = '7Coord C3v Ideal (n=6)';
P7 = [0.000000   0.000000        1.000000
0.000000         0.964214         0.265125
-0.835034        -0.482107        0.265125
0.835034         -0.482107        0.265125
0.660937         0.381592         -0.646181
```

```
-0.660937        0.381592        -0.646181
0.000000        -0.763184        -0.646181];

title8 = '7Coord C2v Ideal (n=6)';
P8 = [0.000000   0.000000        1.000000
0.738705        0.648357        0.184250
-0.738705       0.648357        0.184250
-0.738705       -0.648357       0.184250
0.738705        -0.648357       0.184250
0.000000        0.597631        -0.801771
0.000000        -0.597631       -0.801771];

title9 = '7Coord D5h Ideal';
P9 = [0.000000   0.000000        1.000000
0.000000        0.951057        0.309017
-1.000000       0.000000        0.000000
0.000000        -0.951057       0.309017
1.000000        0.000000        0.000000
0.000000        0.587785        -0.809017
0.000000        -0.587785       -0.809017];

title10 = '8Coord D4d Ideal (n=6)';
P10 = [0.839947  0.000000        0.542669
-0.839947       0.000000        0.542669
0.000000        0.839947        0.542669
0.000000        -0.839947       0.542669
0.593932        0.593932        -0.542669
0.593932        -0.593932       -0.542669
-0.593932       0.593932        -0.542669
-0.593932       -0.593932       -0.542669];

title11 = '8Coord C2v Ideal (Drew MFP)';
P11 = [0.747682  0.000000        0.664057
-0.747682       0.000000        0.664057
0.623219        0.565650        -0.540035
-0.623219       0.565650        -0.540035
0.623219        -0.565650       -0.540035
-0.623219       -0.565650       -0.540035
0.000000        0.891561        0.452902
0.000000        -0.891561       0.452902];

title12 = '8Coord D2d Ideal (n=6)';
P12 = [0.606449  0.000000        0.795122
-0.606449       0.000000        0.795122
0.947724        0.000000        -0.319090
-0.947724       0.000000        -0.319090
0.000000        0.606449        -0.795122
0.000000        -0.606449       -0.795122
0.000000        0.947724        0.319090
0.000000        -0.947724       0.319090];

title13 = '8Coord Oh Ideal';
P13 = [0.577350  0.577350   0.577350
-0.577350   0.577350   0.577350
0.577350   -0.577350   0.577350
```

```
0.577350   0.577350  -0.577350
-0.577350  -0.577350   0.577350
-0.577350   0.577350  -0.577350
0.577350  -0.577350  -0.577350
-0.577350  -0.577350  -0.577350];

title14 = '8Coord D6h Ideal';
P14 = [0.000000 0.000000      1.000000
0.000000       0.000000      -1.000000
-0.500000      0.866025      0.000000
-0.500000      -0.866025     0.000000
1.000000       0.000000      0.000000
0.500000       0.866025      0.000000
0.500000       -0.866025     0.000000
-1.000000      0.000000      0.000000];

title15 = '8Coord D3h Ideal (n=6)';
P15 = [0.000000 0.000000      1.000000
0.000000       0.000000      -1.000000
0.000000       0.867088      0.498155
-0.750920      -0.433544     0.498155
0.750920       -0.433544     0.498155
0.000000       0.867088      -0.498155
0.750920       -0.433544     -0.498155
-0.750920      -0.433544     -0.498155];

title16 = '9Coord D3h Ideal (n=6)';
P16 = [-1.000000 0.000000      0.000000
0.500000       0.866025      0.000000
0.500000       -0.866025     0.000000
-0.351649      0.609074      0.710895
-0.351649      0.609074      -0.710895
-0.351649      -0.609074     0.710895
-0.351649      -0.609074     -0.710895
0.703298       0.000000      0.710895
0.703298       0.000000      -0.710895];

title17 = '9Coord C4v Ideal (n=6)';
P17 = [0.000000 0.000000      1.000000
-0.565000      0.565000      -0.601289
0.565000       -0.565000     -0.601289
-0.932711      0.000000      0.360624
0.000000       0.932711      0.360624
0.000000       -0.932711     0.360624
0.932711       0.000000      0.360624
0.565000       0.565000      -0.601289
-0.565000      -0.565000     -0.601289];

%----------------------------------------------------
%Specify which set of coordinates you want to run below
%----------------------------------------------------

P = [P1];
title=title1;
```

```
%--------------------------------------------------------------------
%!!!!!!!!!!!!!!!!!!!!!!!!!!!!!!!!!!!!!!!!!!!!!!!!!!!!!!!!!!!!!!!!!!!!!!
%Advanced: Do not edit below this line unless you know what you are doing
%!!!!!!!!!!!!!!!!!!!!!!!!!!!!!!!!!!!!!!!!!!!!!!!!!!!!!!!!!!!!!!!!!!!!!!
%--------------------------------------------------------------------


%-----------------------------------------
%Section A: Delta Angles of Ideal Structures
%-----------------------------------------

%Ideal delta angles for 5Coord C4v
a=75.437; b=120.0951; %Kepert repulsion model, n=6

ideal5c4v=zeros(5,5);
ideal5c4v(1,2)=a; ideal5c4v(1,3)=a;
ideal5c4v(1,4)=a; ideal5c4v(1,5)=a;
ideal5c4v(2,3)=0; ideal5c4v(2,4)=b;
ideal5c4v(2,5)=b; ideal5c4v(3,4)=b;
ideal5c4v(3,5)=b;

%Ideal delta angles for 7Coord C3v
a=16.124; b=57.408; c=75.889; d=92.789; %Kepert repulsion model, n=6

ideal7c3v=zeros(7,7);
ideal7c3v(1,2)=a; ideal7c3v(1,3)=a;
ideal7c3v(1,4)=d; ideal7c3v(1,5)=c;
ideal7c3v(1,6)=c; ideal7c3v(2,3)=a;
ideal7c3v(2,4)=d; ideal7c3v(2,5)=c;
ideal7c3v(2,7)=c; ideal7c3v(3,4)=d;
ideal7c3v(3,6)=c; ideal7c3v(3,7)=c;
ideal7c3v(5,6)=b; ideal7c3v(5,7)=b;
ideal7c3v(6,7)=b;

%Ideal delta angles for 7Coord C2v
a=41.423; b=65.314; c=79.002; d=88.235; e=106.321; %Kepert repulsion model, n=6

ideal7c2v=zeros(7,7);
ideal7c2v(1,2)=0; ideal7c2v(1,3)=0;
ideal7c2v(1,4)=e; ideal7c2v(1,5)=d;
ideal7c2v(1,6)=d; ideal7c2v(2,3)=a;
ideal7c2v(2,4)=d; ideal7c2v(2,5)=c;
ideal7c2v(2,7)=b; ideal7c2v(3,4)=d;
ideal7c2v(3,6)=c; ideal7c2v(3,7)=b;
ideal7c2v(5,6)=a; ideal7c2v(5,7)=b;
ideal7c2v(6,7)=b;

%Ideal delta angles for 8Coord D4d
a=51.414; b=77.229; %Kepert repulsion model, n=6

ideal8d4d=zeros(8,8);
ideal8d4d(1,2)=a; ideal8d4d(1,5)=a;
ideal8d4d(1,7)=b; ideal8d4d(1,8)=b;
ideal8d4d(2,8)=a; ideal8d4d(2,5)=b;
ideal8d4d(2,6)=b; ideal8d4d(3,4)=a;
ideal8d4d(3,7)=a; ideal8d4d(3,6)=b;
```

```
ideal8d4d(3,5)=b; ideal8d4d(4,6)=a;
ideal8d4d(4,7)=b; ideal8d4d(4,8)=b;
ideal8d4d(5,6)=0; ideal8d4d(5,7)=a;
ideal8d4d(6,8)=a; ideal8d4d(7,8)=0;

%Ideal delta angles for 8Coord C2v
%a=28.855; b=47.259; c=59.062; d=59.062; e=74.428; f=90;  %D3h Restriction, n=6
a=26.649; b=46.454; c=56.577; d=67.703; e=71.829; f=84.098;  %Drew MFP

ideal8c2v=zeros(8,8);
ideal8c2v(1,2)=c; ideal8c2v(1,5)=c;
ideal8c2v(1,7)=d; ideal8c2v(1,8)=d;
ideal8c2v(2,8)=b; ideal8c2v(2,5)=e;
ideal8c2v(2,6)=f; ideal8c2v(3,4)=c;
ideal8c2v(3,7)=b; ideal8c2v(3,6)=e;
ideal8c2v(3,5)=f; ideal8c2v(4,6)=c;
ideal8c2v(4,7)=d; ideal8c2v(4,8)=d;
ideal8c2v(5,6)=0; ideal8c2v(5,7)=b;
ideal8c2v(6,8)=b; ideal8c2v(7,8)=a;

%Ideal delta angles for 8Coord D2d
a=29.948; b=53.340; c=61.327; d=74.393; %Kepert repulsion model, n=6

ideal8d2d=zeros(8,8);
ideal8d2d(1,2)=b; ideal8d2d(1,5)=c;
ideal8d2d(1,7)=d; ideal8d2d(1,8)=c;
ideal8d2d(2,8)=c; ideal8d2d(2,5)=c;
ideal8d2d(2,6)=d; ideal8d2d(3,4)=b;
ideal8d2d(3,7)=c; ideal8d2d(3,6)=c;
ideal8d2d(3,5)=d; ideal8d2d(4,6)=c;
ideal8d2d(4,7)=c; ideal8d2d(4,8)=d;
ideal8d2d(5,6)=a; ideal8d2d(5,7)=a;
ideal8d2d(6,8)=a; ideal8d2d(7,8)=a;

%Ideal delta angles for 8Coord D3h
a=40.824; b=81.891; c=120; %Kepert repulsion model, n=6

ideal8d3h=zeros(8,8);
ideal8d3h(1,5)=b; ideal8d3h(1,7)=b;
ideal8d3h(1,8)=b; ideal8d3h(2,3)=a;
ideal8d3h(2,4)=a; ideal8d3h(2,5)=0;
ideal8d3h(2,6)=b; ideal8d3h(2,8)=c;
ideal8d3h(3,4)=a; ideal8d3h(3,5)=c;
ideal8d3h(3,6)=b; ideal8d3h(3,7)=0;
ideal8d3h(4,6)=b; ideal8d3h(4,7)=c;
ideal8d3h(4,8)=0; ideal8d3h(5,7)=a;
ideal8d3h(5,8)=a; ideal8d3h(7,8)=a;

%Ideal delta angles for 9Coord C4v
a=37.637; b=52.958; c=58.968; d=69.080; %Kepert repulsion model, n=6

ideal9c4v=zeros(9,9);
ideal9c4v(1,4)=c; ideal9c4v(1,5)=c;
ideal9c4v(1,8)=c; ideal9c4v(1,9)=c;
ideal9c4v(2,4)=b; ideal9c4v(2,5)=b;
```

```
ideal9c4v(2,6)=d; ideal9c4v(2,7)=d;
ideal9c4v(3,6)=d; ideal9c4v(3,7)=d;
ideal9c4v(3,8)=b; ideal9c4v(3,9)=b;
ideal9c4v(4,5)=a; ideal9c4v(4,8)=a;
ideal9c4v(4,6)=b; ideal9c4v(5,7)=b;
ideal9c4v(5,9)=a; ideal9c4v(6,7)=0;
ideal9c4v(6,8)=b; ideal9c4v(7,9)=b;
ideal9c4v(8,9)=a;

%Ideal delta angles for 9Coord D3h
a=26.422; b=47.635; c=59.610; %Kepert repulsion model, n=6

ideal9d3h=zeros(9,9);
ideal9d3h(1,4)=c; ideal9d3h(1,5)=c;
ideal9d3h(1,8)=c; ideal9d3h(1,9)=c;
ideal9d3h(2,4)=c; ideal9d3h(2,5)=c;
ideal9d3h(2,6)=c; ideal9d3h(2,7)=c;
ideal9d3h(3,6)=c; ideal9d3h(3,7)=c;
ideal9d3h(3,8)=c; ideal9d3h(3,9)=c;
ideal9d3h(4,5)=a; ideal9d3h(4,6)=b;
ideal9d3h(4,8)=b; ideal9d3h(5,7)=b;
ideal9d3h(5,9)=b; ideal9d3h(6,7)=a;
ideal9d3h(6,8)=b; ideal9d3h(7,9)=b;
ideal9d3h(8,9)=a;

%-------------------------------------------
%!!!!!!!!!!!!!!!!!!!!!!!!!!!!!!!!!!!!!!!!!!!!
%Editing should not be needed below this line
%!!!!!!!!!!!!!!!!!!!!!!!!!!!!!!!!!!!!!!!!!!!!
%-------------------------------------------

%Ideal delta angles for 4Coord Td
a=109.471;

ideal4td=zeros(4,4);
ideal4td(1,2)=a; ideal4td(1,3)=a;
ideal4td(1,4)=a; ideal4td(2,3)=a;
ideal4td(2,4)=a; ideal4td(3,4)=a;

%Ideal delta angles for 4Coord D4h
a=180;

ideal4d4h=zeros(4,4);
ideal4d4h(1,2)=a; ideal4d4h(1,3)=0;
ideal4d4h(1,4)=a; ideal4d4h(2,3)=a;
ideal4d4h(2,4)=0; ideal4d4h(3,4)=a;

%Ideal delta angles for 5Coord D3h
a=53.130; b=101.537;

ideal5d3h=zeros(5,5);
ideal5d3h(1,2)=a; ideal5d3h(1,3)=a;
ideal5d3h(1,4)=b; ideal5d3h(1,5)=b;
ideal5d3h(2,3)=a; ideal5d3h(2,4)=b;
ideal5d3h(2,5)=b; ideal5d3h(3,4)=b;
```

129

```
ideal5d3h(3,5)=b;

%Ideal delta angles for 6Coord Oh
a=70.529;

ideal6oh=zeros(6,6);
ideal6oh(1,2)=a; ideal6oh(1,3)=a;
ideal6oh(1,4)=a; ideal6oh(1,5)=a;
ideal6oh(2,3)=a; ideal6oh(2,5)=a;
ideal6oh(2,6)=a; ideal6oh(3,4)=a;
ideal6oh(3,6)=a; ideal6oh(4,5)=a;
ideal6oh(4,6)=a; ideal6oh(5,6)=a;

%Ideal delta angles for 6Coord D3h
a=90; b=120;

ideal6d3h=zeros(6,6);
ideal6d3h(1,2)=a; ideal6d3h(1,3)=a;
ideal6d3h(1,4)=b; ideal6d3h(1,5)=0;
ideal6d3h(2,3)=a; ideal6d3h(2,5)=b;
ideal6d3h(2,6)=0; ideal6d3h(3,4)=0;
ideal6d3h(3,6)=b; ideal6d3h(4,5)=a;
ideal6d3h(4,6)=a; ideal6d3h(5,6)=a;

%Ideal delta angles for 7Coord D5h
a=54.383; b=77.947;

ideal7d5h=zeros(7,7);
ideal7d5h(1,2)=a; ideal7d5h(1,6)=a;
ideal7d5h(1,4)=b; ideal7d5h(1,5)=b;
ideal7d5h(2,3)=a; ideal7d5h(2,4)=a;
ideal7d5h(2,5)=a; ideal7d5h(2,7)=a;
ideal7d5h(3,4)=b; ideal7d5h(3,6)=a;
ideal7d5h(3,7)=b; ideal7d5h(4,6)=a;
ideal7d5h(5,6)=a; ideal7d5h(5,7)=b;
ideal7d5h(6,7)=a;

%Ideal delta angles for 8Coord Oh
a=90;

ideal8oh=zeros(8,8);
ideal8oh(1,2)=0; ideal8oh(1,5)=a;
ideal8oh(1,7)=a; ideal8oh(1,8)=a;
ideal8oh(2,8)=a; ideal8oh(2,5)=a;
ideal8oh(2,6)=a; ideal8oh(3,4)=0;
ideal8oh(3,7)=a; ideal8oh(3,6)=a;
ideal8oh(3,5)=a; ideal8oh(4,6)=a;
ideal8oh(4,7)=a; ideal8oh(4,8)=a;
ideal8oh(5,6)=0; ideal8oh(5,7)=0;
ideal8oh(6,8)=0; ideal8oh(7,8)=0;

%Ideal delta angles for 8Coord D6h
a=44.4153; b=81.787;

ideal8d6h=zeros(8,8);
```

```
ideal8d6h(1,2)=a; ideal8d6h(1,3)=a;
ideal8d6h(1,4)=a; ideal8d6h(1,5)=a;
ideal8d6h(1,7)=a; ideal8d6h(1,8)=a;
ideal8d6h(2,5)=b; ideal8d6h(2,6)=a;
ideal8d6h(2,8)=b; ideal8d6h(3,5)=b;
ideal8d6h(3,6)=a; ideal8d6h(3,7)=b;
ideal8d6h(4,6)=a; ideal8d6h(4,7)=b;
ideal8d6h(4,8)=b; ideal8d6h(5,6)=a;
ideal8d6h(6,7)=a; ideal8d6h(6,8)=a;

nr=size(P,1); %determines which analysis to run

%---------------------------------------------
%Section B: Manipulation of loaded coordinates
%---------------------------------------------

%Normalize Section
fm=0;
centroid(1,1)=sum(P(:,1))/nr;
centroid(1,2)=sum(P(:,2))/nr;
centroid(1,3)=sum(P(:,3))/nr;
for i=1:nr,
NP(i,:)=P(i,:)-centroid;
normalize(i,1)=norm(NP(i,:));
end %for i
bd=sum(normalize(:,1))/nr;
for i=1:nr,
 if norm(NP(i,:))/bd<=0.5 %finds metal if within .5r of centroid
 fm=i;
 end %if norm
end %for i
if fm~=0
P=zeros(nr-1,3);
 for i=1:fm,
  if i~=fm
  P(i,:)=NP(i,:)+centroid;
  end %if
 end %for i
 for i=(fm+1):nr,
 P(i-1,:)=NP(i,:)+centroid; %found metal removed from coordinates
 end %for i
fm=NP(fm,:)+centroid;
nr=nr-1;
end %if fm

format short
if autonormalize==1 & fm~=0
 if longanalysis==1
 disp('Found Central Atom:')
 disp(fm);
 disp(' ');
 end %if longanalysis
NP=zeros(nr,3);
 for i=1:nr,
 NP(i,:)=P(i,:)-fm;
```

131

```
 normalize(i,1)=norm(NP(i,:));
 P(i,:)=NP(i,:)/normalize(i,1)+fm; %coordinates normalized to metal
 end %for i
end %if autonormalize

if autonormalize==1 & fm==0
 if longanalysis==1
 disp('Calculated Centroid:')
 disp(centroid);
 disp(' ');
 end %if longanalysis
 for i=1:nr,
 P(i,:)=NP(i,:)/normalize(i,1)+centroid; %normalized to centroid
 end %for i
end %if autonormalize

if autonormalize==1 & longanalysis==1
format short
disp('Normalized Coordinates:');
disp(P);
disp(' ');
end %if autonormalize

%Coordinates related by symmetry (e.g. crystallographically imposed) can cause
%a divide by zero error when generating the convex polyhedron. The following
%routine insignificantly modifies the coordinates to prevent such an error.
DS=[2 29 67
3 31 71
5 37 73
7 41 79
11 43 83
13 47 89
17 53 97
19 59 101
23 61 103];

for i=1:nr,
 for j=1:3,
 DT(i,j)=DS(i,j)*0.0000000001+1;
 AS(i,j)=DS(i,j)*0.0000000001;
 end %for j
end %for i
P=P+AS;
P=P.*DT;

%-------------------------------------------------------------
%Section C: Find the convex polyhedron from given set of vertices
%-------------------------------------------------------------

nr=size(P,1); %nr is coordination number
alledges=zeros(nr,nr);
for a=1:nr,
 for b=1:nr, %for all possible vertex combinations A,B
  if b~=a & alledges(a,b)~=1 %choose an edge AB that has not yet been found
  vertex1=P(a,:);
```

132

```matlab
  vertex2=P(b,:);
 edge=P(a,:)-P(b,:);
  for j=1:nr, %for all vertices not part of the chosen edge AB
   if j~=a & j~=b
   iskonvex=ones(nr,1);
   vertex3=P(j,:); %choose a vertex C
   oldprojection=zeros(1,3);
    for k=1:nr, %for all other possible vertices
     if k~=a & k~=b & k~=j %that are not A, B, or C
     vertex4=P(k,:); %choose a vertex D
     normal=cross(vertex3-vertex1,edge); %calculate normal of plane ABC
     AP=vertex4-vertex3;
            projection=normal*AP'; %calculate projection of CD onto normal of ABC
     faktor=oldprojection/projection; %faktor will be all + or all - if ABC is part of convex polyhedron
      if faktor < 0 %if any projections have a difference in sign
      iskonvex(k)=0; %then it will be marked 0 here
      break; %breaks out of k-loop
      end %if faktor
      oldprojection=projection;
     end %if k~=
    end %for k
    if sum(iskonvex)==nr %any 0 marks above means sum(iskonvex)<nr and AB is not an outer edge
    alledges(a,b)=1; alledges(b,a)=1; %otherwise the edge is found
    break; %breaks out of j-loop
    end % if sum(iskonvex)
   end %if j
  end % for j
 end %if b
 end % for b
end % for a


%--------------------------------------------------------------------
%Section D: Determine angles between adjacent faces for all found edges
%--------------------------------------------------------------------

allangles=zeros(nr); degallangles=zeros(nr); distance=zeros(nr);
triualledges=triu(alledges);
for i=1:nr,
 for j=1:nr,
  if triualledges(i,j)==1 %for all found edges
  kk=1;
   for k=1:nr,
    if alledges(k,i)==1 & alledges(k,j)==1 & kk<=2 %find two vertices connected to that edge
     if kk==1
     point1=P(k,:); %and label them
     else point2=P(k,:);
     end %if kk
     kk=kk+1;
    end %if
   end %loop k
%calculate dihedral angle
  edge=P(i,:)-P(j,:);
  distance(i,j)=norm(edge);
  normal1=cross(point1-P(i,:),edge);
  normal2=cross(edge,point2-P(i,:));
```

133

```
newangle=(normal1*normal2')/(norm(normal1)*norm(normal2));
degangle=acos(newangle)*180/pi;
allangles(i,j)=newangle;
degallangles(i,j)=degangle;
 end %if alledges(i,j)==1
end %for j
end %for i


%3-edge vertices can cause erroneous dihedral angles for certain edges.
%The following routine finds those vertices and fixes the associated errors.
if nr~=4 %these errors don't occur in four coordination
vertices3=0;
for i=1:nr,
 if sum(alledges(i,:))==3
 vertices3(1,1)=i;
  for j=1:nr,
   if sum(alledges(j,:))==3 & i~=j
   vertices3(1,2)=j;
          for k=1:nr,
           if sum(alledges(k,:))==3 & i~=j & j~=k & k~=i
           vertices3(1,3)=k;
            for m=1:nr,
             if sum(alledges(m,:))==3 & i~=j & i~=k & i~=m & j~=k & j~=m & k~=m
             vertices3(1,4)=m;
     end %if
            end %for m
           end %if
           end %for k
   end %if
  end %for j
 end %if
end %for i
v3=0;
if vertices3~=0
v3=size(vertices3,2); %v3 is number of 3-edge vertices
end %if
%fix dihedral angle errors due to presence of 3-edge vertices
if v3>=1
for i=1:nr,
 for j=1:nr,
  if triualledges(i,j)==1
  point1=0;
   for k=1:nr,
    if alledges(k,i)==1 & alledges(k,j)==1 & vertices3(1,1)==k
    point1=P(k,:);
    end %if
   end %loop k
   for k=1:nr,
    if alledges(k,i)==1 & alledges(k,j)==1 & vertices3(1,1)~=k & alledges(k,vertices3(1,1))~=1 & point1~=0
    point2=P(k,:);
    end %if
   end %loop k
%calculate angle
   if point1~=0
   edge=P(i,:)-P(j,:);
```

```
    normal1=cross(point1-P(i,:),edge);
    normal2=cross(edge,point2-P(i,:));
    newangle=(normal1*normal2')/(norm(normal1)*norm(normal2));
    degangle=acos(newangle)*180/pi;
    allangles(i,j)=newangle;
    degallangles(i,j)=degangle;
   end
  end %if alledges
 end %for j
end %for i
end %if v3
if v3>=2
for i=1:nr,
 for j=1:nr,
  if triualledges(i,j)==1
  point1=0;
   for k=1:nr,
    if alledges(k,i)==1 & alledges(k,j)==1 & vertices3(1,2)==k
    point1=P(k,:);
    end %if
   end %loop k
   for k=1:nr,
    if alledges(k,i)==1 & alledges(k,j)==1 & vertices3(1,2)~=k & alledges(k,vertices3(1,2))~=1 & point1~=0
    point2=P(k,:);
    end %if
   end %loop k
%calculate angle
   if point1~=0
   edge=P(i,:)-P(j,:);
   normal1=cross(point1-P(i,:),edge);
   normal2=cross(edge,point2-P(i,:));
   newangle=(normal1*normal2')/(norm(normal1)*norm(normal2));
   degangle=acos(newangle)*180/pi;
   allangles(i,j)=newangle;
   degallangles(i,j)=degangle;
   end
  end %if alledges
 end %for j
end %for i
end %if v3
if v3==4
for i=1:nr,
 for j=1:nr,
  if triualledges(i,j)==1
  point1=0;
   for k=1:nr,
    if alledges(k,i)==1 & alledges(k,j)==1 & vertices3(1,3)==k
    point1=P(k,:);
    end %if
   end %loop k
   for k=1:nr,
    if alledges(k,i)==1 & alledges(k,j)==1 & vertices3(1,3)~=k & alledges(k,vertices3(1,3))~=1 & point1~=0
    point2=P(k,:);
    end %if
   end %loop k
```

```matlab
%calculate angle
  if point1~=0
  edge=P(i,:)-P(j,:);
  normal1=cross(point1-P(i,:),edge);
  normal2=cross(edge,point2-P(i,:));
  newangle=(normal1*normal2')/(norm(normal1)*norm(normal2));
  degangle=acos(newangle)*180/pi;
  allangles(i,j)=newangle;
  degallangles(i,j)=degangle;
  end
 end %if alledges
 end %for j
end %for i
for i=1:nr,
 for j=1:nr,
 if triualledges(i,j)==1
 point1=0;
  for k=1:nr,
  if alledges(k,i)==1 & alledges(k,j)==1 & vertices3(1,4)==k
  point1=P(k,:);
  end %if
 end %loop k
 for k=1:nr,
  if alledges(k,i)==1 & alledges(k,j)==1 & vertices3(1,4)~=k & alledges(k,vertices3(1,4))~=1 & point1~=0
  point2=P(k,:);
  end %if
 end %loop k
%calculate angle
  if point1~=0
  edge=P(i,:)-P(j,:);
  normal1=cross(point1-P(i,:),edge);
  normal2=cross(edge,point2-P(i,:));
  newangle=(normal1*normal2')/(norm(normal1)*norm(normal2));
  degangle=acos(newangle)*180/pi;
  allangles(i,j)=newangle;
  degallangles(i,j)=degangle;
  end
 end %if alledges
 end %for j
end %for i
end %if v3
end %if nr~=4

%------------------------------------
%Section E: 4-Coordinate Shape Analysis
%------------------------------------

if nr==4
%generate all possible permutations
vertex=[1 2 3 4
2, 1, 3, 4
1 3 2 4];

%calculate shape measure
for vv=1:3,
```

```matlab
newalledges=zeros(nr);
 for i=1:nr,
  for j=1:nr,
  newalledges(i,j)=alledges(vertex(vv,i),vertex(vv,j));
   end %j
 end %i
 newalledges=triu(newalledges);
  for i=1:nr,
  for j=1:nr,
   if newalledges(i,j)==1
   angle=degallangles(vertex(vv,i),vertex(vv,j));
    if angle==0
    angle=degallangles(vertex(vv,j),vertex(vv,i));
    end %if angle
   diff4td(i,j)=ideal4td(i,j)-angle;
   diff4d4h(i,j)=ideal4d4h(i,j)-angle;
   end %if newalledges
  end %j
 end %i
 sum4td(vv)=sum(sum(diff4td.^2));
 sum4d4h(vv)=sum(sum(diff4d4h.^2));
end %for vv

%load the shape minimized alignment
kk=0;
i=min(sum4td);
j=min(sum4d4h);
for vv=1:3
 if (sum4td(1,vv)-i+sum4d4h(1,vv)-j)<=.000001 & (sum4td(1,vv)-i+sum4d4h(1,vv)-j)>=-.000001
 kk=vv;
 end %if
end %for vv
for i=1:nr,
 for j=1:nr,
 newalledges(i,j)=alledges(vertex(kk,i),vertex(kk,j));
 end %j
end %i
newalledges=triu(newalledges);
for i=1:nr,
 for j=1:nr,
  if newalledges(i,j)==1
  angle=degallangles(vertex(kk,i),vertex(kk,j));
   if angle==0
   angle=degallangles(vertex(kk,j),vertex(kk,i));
   end %if angle
   finalangles(i,j)=angle;
  end %if newalledges
 end %for j
end %for i

%print results
sindex(1,1)=sqrt(min(sum4td)/6);
sindex(1,2)=sqrt(min(sum4d4h)/6);

sindex1(1,1)=finalangles(1,3); sindex1(2,1)=finalangles(2,4); sindex2(1,1)=finalangles(1,2);
```

```
sindex2(2,1)=finalangles(1,4); sindex2(3,1)=finalangles(2,3); sindex2(4,1)=finalangles(3,4);

sindex3(1,1)=ideal4td(1,3); sindex3(2,1)=ideal4td(2,4); sindex4(1,1)=ideal4td(1,2);
sindex4(2,1)=ideal4td(1,4); sindex4(3,1)=ideal4td(2,3); sindex4(4,1)=ideal4td(3,4);

sindex5(1,1)=ideal4d4h(1,3); sindex5(2,1)=ideal4d4h(2,4); sindex6(1,1)=ideal4d4h(1,2);
sindex6(2,1)=ideal4d4h(1,4); sindex6(3,1)=ideal4d4h(2,3); sindex6(4,1)=ideal4d4h(3,4);

shapeangles=[sindex1,sindex3,sindex5];
otherangles=[sindex2,sindex4,sindex6];
format bank
disp(['Shape Analysis of ', title,' is:']);
disp('     Td    D4h'); disp(sindex);
disp(' ');
if longanalysis == 1
disp('Shape Determining Angles:');
disp(['Measured',' Td',' D4h']);
disp(shapeangles);
disp(' ');
disp('Other Angles:');
disp(['Measured',' Td',' D4h']);
disp(otherangles);
end %if
end %if nr=4


%--------------------------------------
%Section F: 5-Coordinate Shape Analysis
%--------------------------------------

if nr==5
%find the three 4-edge vertices
vertex=1;
for i=1:nr,
 if sum(alledges(i,:))==4
  for j=1:nr,
   if i~=j & sum(alledges(j,:))==4
    for k=1:nr,
     if i~=k & j~=k & sum(alledges(k,:))==4
     vertex(1,3)=i;
     vertex(1,2)=j;
     vertex(1,1)=k;
     end %if
    end %for k
   end %if
  end %for j
 end %if sum
end %for i
vertex(1,4)=vertices3(1,1);
vertex(1,5)=vertices3(1,2);

%generate all possible permutations
vertex(2,1)=vertex(1,2); vertex(2,2)=vertex(1,3);
vertex(2,3)=vertex(1,1); vertex(3,1)=vertex(1,3);
vertex(3,2)=vertex(1,1); vertex(3,3)=vertex(1,2);
vertex(2,4)=vertex(1,4); vertex(3,4)=vertex(1,4);
```

```
vertex(2,5)=vertex(1,5); vertex(3,5)=vertex(1,5);

%calculate shape measure
for vv=1:3,
 newalledges=zeros(nr);
 for i=1:nr,
  for j=1:nr,
  newalledges(i,j)=alledges(vertex(vv,i),vertex(vv,j));
  end %j
 end %i
newalledges=triu(newalledges);
 for i=1:nr,
  for j=1:nr,
  if newalledges(i,j)==1
  angle=degallangles(vertex(vv,i),vertex(vv,j));
   if angle==0
   angle=degallangles(vertex(vv,j),vertex(vv,i));
   end %if angle
  diff5c4v(i,j)=ideal5c4v(i,j)-angle;
  diff5d3h(i,j)=ideal5d3h(i,j)-angle;
  end %if
 end %j
 end %i
sum5c4v(vv)=sum(sum(diff5c4v.^2));
sum5d3h(vv)=sum(sum(diff5d3h.^2));
end %for vv

%load the shape minimized alignment
kk=0;
i=min(sum5c4v);
j=min(sum5d3h);
for vv=1:3
 if (sum5c4v(1,vv)-i+sum5d3h(1,vv)-j)<=0.001 & (sum5c4v(1,vv)-i+sum5d3h(1,vv)-j)>=-0.001
 kk=vv;
 end %if
end %for vv
for i=1:nr,
 for j=1:nr,
 newalledges(i,j)=alledges(vertex(kk,i),vertex(kk,j));
 end %for j
end %for i
newalledges=triu(newalledges);
for i=1:nr,
 for j=1:nr,
 if newalledges(i,j)==1
 angle=degallangles(vertex(kk,i),vertex(kk,j));
  if angle==0
  angle=degallangles(vertex(kk,j),vertex(kk,i));
  end %if angle
  finalangles(i,j)=angle;
 end %if newalledges
 end %for j
end %for i

%print results
```

```
sindex(1,1)=sqrt(min(sum5d3h)/9);
sindex(1,2)=sqrt(min(sum5c4v)/9);

sindex1(1,1)=finalangles(2,3); sindex1(2,1)=finalangles(1,2); sindex1(3,1)=finalangles(1,3);
sindex2(1,1)=finalangles(1,4); sindex2(2,1)=finalangles(1,5); sindex2(3,1)=finalangles(2,4);
sindex2(4,1)=finalangles(2,5); sindex2(5,1)=finalangles(3,4); sindex2(6,1)=finalangles(3,5);

sindex3(1,1)=ideal5d3h(2,3); sindex3(2,1)=ideal5d3h(1,2); sindex3(3,1)=ideal5d3h(1,3);
sindex4(1,1)=ideal5d3h(1,4); sindex4(2,1)=ideal5d3h(1,5); sindex4(3,1)=ideal5d3h(2,4);
sindex4(4,1)=ideal5d3h(2,5); sindex4(5,1)=ideal5d3h(3,4); sindex4(6,1)=ideal5d3h(3,5);

sindex5(1,1)=ideal5c4v(2,3); sindex5(2,1)=ideal5c4v(1,2); sindex5(3,1)=ideal5c4v(1,3);
sindex6(1,1)=ideal5c4v(1,4); sindex6(2,1)=ideal5c4v(1,5); sindex6(3,1)=ideal5c4v(2,4);
sindex6(4,1)=ideal5c4v(2,5); sindex6(5,1)=ideal5c4v(3,4); sindex6(6,1)=ideal5c4v(3,5);

shapeangles=[sindex1,sindex3,sindex5];
otherangles=[sindex2,sindex4,sindex6];
format bank
disp(['Shape Analysis of ', title,' is:']);
disp('    D3h    C4v'); disp(sindex);
disp(' ');
if longanalysis == 1
disp('Shape Determining Angles:');
disp(['Measured',' D3h',' C4v']);
disp(shapeangles);
disp(' ');
disp('Other Angles:');
disp(['Measured',' D3h',' C4v']);
disp(otherangles);
end %if
end %if nr==5


%-------------------------------------
%Section G: 6-Coordinate Shape Analysis
%-------------------------------------

if nr==6
%determine structure type
type=0;
for i=1:nr,
 if sum(alledges(i,:))==5
 type=1;
 end %if
end %for i

if type==0
%pick an arbitrary starting vertex
vertex(1,1)=1; vertex(2,1)=1; vertex(3,1)=1; vertex(4,1)=1;
vertex(5,6)=1; vertex(6,6)=1; vertex(7,6)=1; vertex(8,6)=1;
%find the four vertices connected to it in a sequential path
for i=1:nr,
 if alledges(i,1)==1
  for j=1:nr,
   if i~=j & alledges(j,1)==1 & alledges(j,i)==1
    for k=1:nr,
```

```matlab
    if i~=k & j~=k & alledges(k,1)==1 & alledges(k,j)==1 & alledges(k,i)~=1
     for m=1:nr,
      if i~=k & j~=k & j~=m & alledges(m,1)==1 & alledges(m,k)==1 & alledges(m,i)==1 & alledges(m,j)~=1
      vertex(1,5)=i;
              vertex(1,4)=j;
      vertex(1,3)=k;
      vertex(1,2)=m;
       end %if
      end %for m
     end %if
    end %for k
   end %if
  end %for j
 end %if
end %for i
for i=1:nr,
 if alledges(i,1)==0
 vertex(1,6)=i; vertex(2,6)=i; vertex(3,6)=i; vertex(4,6)=i;
 vertex(5,1)=i; vertex(6,1)=i; vertex(7,1)=i; vertex(8,1)=i;
 end %if
end %for i

%generate all possible permutations
vertex(2,3)=vertex(1,2); vertex(2,4)=vertex(1,3); vertex(2,5)=vertex(1,4); vertex(2,2)=vertex(1,5);
vertex(3,4)=vertex(1,2); vertex(3,5)=vertex(1,3); vertex(3,2)=vertex(1,4); vertex(3,3)=vertex(1,5);
vertex(4,5)=vertex(1,2); vertex(4,2)=vertex(1,3); vertex(4,3)=vertex(1,4); vertex(4,4)=vertex(1,5);
vertex(5,2)=vertex(1,2); vertex(5,3)=vertex(1,3); vertex(5,4)=vertex(1,4); vertex(5,5)=vertex(1,5);
vertex(6,3)=vertex(1,2); vertex(6,4)=vertex(1,3); vertex(6,5)=vertex(1,4); vertex(6,2)=vertex(1,5);
vertex(7,4)=vertex(1,2); vertex(7,5)=vertex(1,3); vertex(7,2)=vertex(1,4); vertex(7,3)=vertex(1,5);
vertex(8,5)=vertex(1,2); vertex(8,2)=vertex(1,3); vertex(8,3)=vertex(1,4); vertex(8,4)=vertex(1,5);
end %if type==0

if type==1
%find the 5-edge vertices
for i=1:nr,
 if sum(alledges(i,:))==5
  for j=1:nr,
   if i~=j & sum(alledges(j,:))==5
   vertex(1,1)=i; vertex(2,1)=j; vertex(3,1)=i; vertex(4,1)=j;
   vertex(5,1)=i; vertex(6,1)=j; vertex(7,1)=i; vertex(8,1)=j;
   vertex(1,6)=j; vertex(2,6)=i; vertex(3,6)=j; vertex(4,6)=i;
   vertex(5,6)=j; vertex(6,6)=i; vertex(7,6)=j; vertex(8,6)=i;
   end %if
  end %for j
 end %if
end %for i

%find the 3-edge vertices
for i=1:nr,
 if sum(alledges(i,:))==3
  for j=1:nr,
   if i~=j & sum(alledges(j,:))==3
   vertex(1,3)=i; vertex(2,3)=i; vertex(3,3)=j; vertex(4,3)=j;
   vertex(5,3)=i; vertex(6,3)=i; vertex(7,3)=j; vertex(8,3)=j;
   vertex(1,4)=j; vertex(2,4)=j; vertex(3,4)=i; vertex(4,4)=i;
```

```matlab
   vertex(5,4)=j; vertex(6,4)=j; vertex(7,4)=i; vertex(8,4)=i;
  end %if
 end %for j
 end %if
end %for i


%find the remaining 4-edge vertices by connectivity
for i=1:nr,
 if sum(alledges(i,:))==4 & alledges(i,vertex(1,3))==1
 vertex(1,2)=i; vertex(2,2)=i; vertex(3,2)=i; vertex(4,2)=i;
 vertex(5,5)=i; vertex(6,5)=i; vertex(7,5)=i; vertex(8,5)=i;
 end %if
 if sum(alledges(i,:))==4 & alledges(i,vertex(1,4))==1
 vertex(1,5)=i; vertex(2,5)=i; vertex(3,5)=i; vertex(4,5)=i;
 vertex(5,2)=i; vertex(6,2)=i; vertex(7,2)=i; vertex(8,2)=i;
 end %if
end %for i


%fix dihedral angle errors due to connected 5-edge vertices
edge=P(vertex(1,1),:)-P(vertex(1,6),:);
normal1=cross(P(vertex(1,3),:)-P(vertex(1,1),:),edge);
normal2=cross(edge,P(vertex(1,4),:)-P(vertex(1,1),:));
newangle=(normal1*normal2')/(norm(normal1)*norm(normal2));
degangle=acos(newangle)*180/pi;
allangles(vertex(1,1),vertex(1,6))=newangle; allangles(vertex(1,6),vertex(1,1))=newangle;
degallangles(vertex(1,1),vertex(1,6))=degangle; degallangles(vertex(1,6),vertex(1,1))=degangle;


edge=P(vertex(1,5),:)-P(vertex(1,1),:);
normal1=cross(P(vertex(1,2),:)-P(vertex(1,5),:),edge);
normal2=cross(edge,P(vertex(1,4),:)-P(vertex(1,5),:));
newangle=(normal1*normal2')/(norm(normal1)*norm(normal2));
degangle=acos(newangle)*180/pi;
allangles(vertex(1,5),vertex(1,1))=newangle; allangles(vertex(1,1),vertex(1,5))=newangle;
degallangles(vertex(1,5),vertex(1,1))=degangle; degallangles(vertex(1,1),vertex(1,5))=degangle;


edge=P(vertex(1,2),:)-P(vertex(1,6),:);
normal1=cross(P(vertex(1,3),:)-P(vertex(1,2),:),edge);
normal2=cross(edge,P(vertex(1,5),:)-P(vertex(1,2),:));
newangle=(normal1*normal2')/(norm(normal1)*norm(normal2));
degangle=acos(newangle)*180/pi;
allangles(vertex(1,2),vertex(1,6))=newangle; allangles(vertex(1,6),vertex(1,2))=newangle;
degallangles(vertex(1,2),vertex(1,6))=degangle; degallangles(vertex(1,6),vertex(1,2))=degangle;
allangles=triu(allangles);
degallangles=triu(degallangles);
end %if type==1


%calculate shape measure
ss=size(vertex,1);
newalledges=zeros(nr); diff6oh=zeros(nr); diff6d3h=zeros(nr);
for vv=1:ss,
 for i=1:nr,
  for j=1:nr,
  newalledges(i,j)=alledges(vertex(vv,i),vertex(vv,j));
  end %j
 end %i
```

```matlab
newalledges=triu(newalledges);
 for i=1:nr,
  for j=1:nr,
   if newalledges(i,j)==1
   angle=degallangles(vertex(vv,i),vertex(vv,j));
    if angle==0
    angle=degallangles(vertex(vv,j),vertex(vv,i));
    end %if angle
   diff6oh(i,j)=ideal6oh(i,j)-angle;
   diff6d3h(i,j)=ideal6d3h(i,j)-angle;
   end %if
  end %j
 end %i
 for i=1:nr,
  for j=1:nr,
   if diff6oh(i,j)==0 & ideal6oh(i,j)~=0
   diff6oh(i,j)=ideal6oh(i,j);
   end %if
   if diff6d3h(i,j)==0 & ideal6d3h(i,j)~=0
   diff6d3h(i,j)=ideal6d3h(i,j);
   end %if
  end %j
 end %i
sum6oh(vv)=sum(sum(diff6oh.^2));
sum6d3h(vv)=sum(sum(diff6d3h.^2));
end %for vv

%load the shape minimized alignment
kk=0;
i=min(sum6oh);
j=min(sum6d3h);
for vv=1:ss
 if abs(sum6oh(1,vv)-i+sum6d3h(1,vv)-j)<=0.001
 kk=vv;
 end %if
end %for vv
for i=1:nr,
 for j=1:nr,
 newalledges(i,j)=alledges(vertex(kk,i),vertex(kk,j));
 end %j
end %i
newalledges=triu(newalledges);
for i=1:nr,
 for j=1:nr,
  if newalledges(i,j)==1
  angle=degallangles(vertex(kk,i),vertex(kk,j));
   if angle==0
   angle=degallangles(vertex(kk,j),vertex(kk,i));
   end %if angle
   finalangles(i,j)=angle;
  end %if newalledges
 end %for j
end %for i

%calculate theta twist angle
```

```matlab
centroid1=(P(vertex(kk,1),:)+P(vertex(kk,2),:)+P(vertex(kk,3),:))/3;
centroid2=(P(vertex(kk,4),:)+P(vertex(kk,5),:)+P(vertex(kk,6),:))/3;
vector1=cross(centroid1-P(vertex(kk,1),:),centroid2-centroid1);
vector2=cross(centroid1-P(vertex(kk,2),:),centroid2-centroid1);
vector3=cross(centroid1-P(vertex(kk,3),:),centroid2-centroid1);
vector4=cross(centroid2-P(vertex(kk,4),:),centroid2-centroid1);
vector5=cross(centroid2-P(vertex(kk,5),:),centroid2-centroid1);
vector6=cross(centroid2-P(vertex(kk,6),:),centroid2-centroid1);
twist(1,1)=acos((vector1*vector4')/(norm(vector1)*norm(vector4)))*180/pi;
twist(1,2)=acos((vector2*vector5')/(norm(vector2)*norm(vector5)))*180/pi;
twist(1,3)=acos((vector3*vector6')/(norm(vector3)*norm(vector6)))*180/pi;

%print results
sindex(1,1)=sqrt(min(sum6oh)/12);
sindex(1,2)=sqrt(min(sum6d3h)/12);

sindex1(1,1)=finalangles(1,5); sindex1(2,1)=finalangles(2,6); sindex1(3,1)=finalangles(3,4);
sindex1(4,1)=finalangles(1,4); sindex1(5,1)=finalangles(2,5); sindex1(6,1)=finalangles(3,6);
sindex2(1,1)=finalangles(1,2); sindex2(2,1)=finalangles(1,3); sindex2(3,1)=finalangles(2,3);
sindex2(4,1)=finalangles(4,5); sindex2(5,1)=finalangles(4,6); sindex2(6,1)=finalangles(5,6);

sindex3(1,1)=ideal6oh(1,5); sindex3(2,1)=ideal6oh(2,6); sindex3(3,1)=ideal6oh(3,4);
sindex3(4,1)=ideal6oh(1,4); sindex3(5,1)=ideal6oh(2,5); sindex3(6,1)=ideal6oh(3,6);
sindex4(1,1)=ideal6oh(1,2); sindex4(2,1)=ideal6oh(1,3); sindex4(3,1)=ideal6oh(2,3);
sindex4(4,1)=ideal6oh(4,5); sindex4(5,1)=ideal6oh(4,6); sindex4(6,1)=ideal6oh(5,6);

sindex5(1,1)=ideal6d3h(1,5); sindex5(2,1)=ideal6d3h(2,6); sindex5(3,1)=ideal6d3h(3,4);
sindex5(4,1)=ideal6d3h(1,4); sindex5(5,1)=ideal6d3h(2,5); sindex5(6,1)=ideal6d3h(3,6);
sindex6(1,1)=ideal6d3h(1,2); sindex6(2,1)=ideal6d3h(1,3); sindex6(3,1)=ideal6d3h(2,3);
sindex6(4,1)=ideal6d3h(4,5); sindex6(5,1)=ideal6d3h(4,6); sindex6(6,1)=ideal6d3h(5,6);

if type==1
sindex2(7,1)=finalangles(1,6); sindex4(7,1)=ideal6oh(1,6); sindex6(7,1)=ideal6d3h(1,6);
end %if type==1

shapeangles=[sindex1,sindex3,sindex5];
otherangles=[sindex2,sindex4,sindex6];
format bank
disp(['Shape Analysis of ', title,' is:']);
disp('    Oh    D3h'); disp(sindex);
disp(' ');
if longanalysis == 1
disp('Shape Determining Angles:');
disp(['Measured','    Oh','    D3h']);
disp(shapeangles);
disp(' ');
disp('Other Angles:');
disp(['Measured','   Oh','   D3h']);
disp(otherangles);
disp(' ');
disp('Phi Twist Angles:');
disp(twist);
end %if
end %if nr==6
```

```
%--------------------------------------
%Section H: 7-Coordinate Shape Analysis
%--------------------------------------

if nr==7
if v3~=0 %type0 (here) and type1 (below) have already been determined above by v3
%find the three 5-edge vertices
for i=1:nr,
 if sum(alledges(i,:))==5
  for j=1:nr,
   if i~=j & sum(alledges(j,:))==5
    for k=1:nr,
     if i~=k & j~=k & sum(alledges(k,:))==5
     vertex(1,3)=i;
     vertex(1,2)=j;
     vertex(1,1)=k;
     end %if
    end %for k
   end %if
  end %for j
 end %if sum
end %for i
%number the unique 3-edge vertex
vertex(1,4)=vertices3(1,1); vertex(4,4)=vertices3(1,1);
vertex(2,4)=vertices3(1,1); vertex(5,4)=vertices3(1,1);
vertex(3,4)=vertices3(1,1); vertex(6,4)=vertices3(1,1);

%generate all possible permutations
vertex(2,1)=vertex(1,2); vertex(2,2)=vertex(1,3); vertex(2,3)=vertex(1,1);
vertex(3,1)=vertex(1,3); vertex(3,2)=vertex(1,1); vertex(3,3)=vertex(1,2);
vertex(4,1)=vertex(1,1); vertex(4,2)=vertex(1,3); vertex(4,3)=vertex(1,2);
vertex(5,1)=vertex(1,3); vertex(5,2)=vertex(1,2); vertex(5,3)=vertex(1,1);
vertex(6,1)=vertex(1,2); vertex(6,2)=vertex(1,1); vertex(6,3)=vertex(1,3);

for vv=1:6,
 for i=1:nr,
  if alledges(i,vertex(vv,4))==0 & i~=vertex(vv,4) & alledges(i,vertex(vv,1))==1 & alledges(i,vertex(vv,2))==1
  vertex(vv,5)=i;
  end % if
  if alledges(i,vertex(vv,4))==0 & i~=vertex(vv,4) & alledges(i,vertex(vv,1))==1 & alledges(i,vertex(vv,3))==1
  vertex(vv,6)=i;
  end % if
  if alledges(i,vertex(vv,4))==0 & i~=vertex(vv,4) & alledges(i,vertex(vv,2))==1 & alledges(i,vertex(vv,3))==1
  vertex(vv,7)=i;
  end % if
 end %for i
end %for vv
end %if v3

if v3==0 %if type1
%find the two 5-edge vertices
vertex=1;
for i=1:nr,
 if sum(alledges(i,:))==5
  for j=1:nr,
```

```matlab
  if i~=j & sum(alledges(j,:))==5
  vertex(1,2)=i; vertex(2,2)=i; vertex(3,2)=i; vertex(4,2)=i; vertex(5,2)=i;
  vertex(6,6)=i; vertex(7,6)=i; vertex(8,6)=i; vertex(9,6)=i; vertex(10,6)=i;
  vertex(1,6)=j; vertex(2,6)=j; vertex(3,6)=j; vertex(4,6)=j; vertex(5,6)=j;
  vertex(6,2)=j; vertex(7,2)=j; vertex(8,2)=j; vertex(9,2)=j; vertex(10,2)=j;
  end %if i
 end %for j
 end %if sum
end %for i
%find the remaining five vertices in a sequential path
for i=1:nr,
 if alledges(i,vertex(1,2))==1 & alledges(i,vertex(1,6))==1
 vertex(1,1)=i;
 end %if
end %for i
for i=1:nr,
 if alledges(i,vertex(1,2))==1 & alledges(i,vertex(1,6))==1 & alledges(i,vertex(1,1))==1
 vertex(1,5)=i;
 end %if
end %for i
for i=1:nr,
 if alledges(i,vertex(1,2))==1 & alledges(i,vertex(1,6))==1 & alledges(i,vertex(1,5))==1 & i~=vertex(1,1)
 vertex(1,7)=i;
 end %if
end %for i
for i=1:nr,
 if alledges(i,vertex(1,2))==1 & alledges(i,vertex(1,6))==1 & alledges(i,vertex(1,7))==1 & i~=vertex(1,5)
 vertex(1,3)=i;
 end %if
end %for i
for i=1:nr,
 if alledges(i,vertex(1,2))==1 & alledges(i,vertex(1,6))==1 & alledges(i,vertex(1,3))==1 & i~=vertex(1,7)
 vertex(1,4)=i;
 end %if
end %for i

%generate all possible permutations
vertex(2,5)=vertex(1,1); vertex(2,7)=vertex(1,5); vertex(2,3)=vertex(1,7); vertex(2,4)=vertex(1,3);
vertex(2,1)=vertex(1,4);
vertex(3,7)=vertex(1,1); vertex(3,3)=vertex(1,5); vertex(3,4)=vertex(1,7); vertex(3,1)=vertex(1,3);
vertex(3,5)=vertex(1,4);
vertex(4,3)=vertex(1,1); vertex(4,4)=vertex(1,5); vertex(4,1)=vertex(1,7); vertex(4,5)=vertex(1,3);
vertex(4,7)=vertex(1,4);
vertex(5,4)=vertex(1,1); vertex(5,1)=vertex(1,5); vertex(5,5)=vertex(1,7); vertex(5,7)=vertex(1,3);
vertex(5,3)=vertex(1,4);
vertex(6,1)=vertex(1,1); vertex(6,5)=vertex(1,5); vertex(6,7)=vertex(1,7); vertex(6,3)=vertex(1,3);
vertex(6,4)=vertex(1,4);
vertex(7,5)=vertex(1,1); vertex(7,7)=vertex(1,5); vertex(7,3)=vertex(1,7); vertex(7,4)=vertex(1,3);
vertex(7,1)=vertex(1,4);
vertex(8,7)=vertex(1,1); vertex(8,3)=vertex(1,5); vertex(8,4)=vertex(1,7); vertex(8,1)=vertex(1,3);
vertex(8,5)=vertex(1,4);
vertex(9,3)=vertex(1,1); vertex(9,4)=vertex(1,5); vertex(9,1)=vertex(1,7); vertex(9,5)=vertex(1,3);
vertex(9,7)=vertex(1,4);
vertex(10,4)=vertex(1,1); vertex(10,1)=vertex(1,5); vertex(10,5)=vertex(1,7); vertex(10,7)=vertex(1,3);
vertex(10,3)=vertex(1,4);
```

```
end %if v3

%calculate shape measure
ss=size(vertex,1);
newalledges=zeros(nr,nr);
diff7c2v=zeros(nr,nr); diff7c3v=zeros(nr,nr); diff7d5h=zeros(nr,nr);
for vv=1:ss
newalledges=zeros(9);
 for i=1:nr,
  for j=1:nr,
  newalledges(i,j)=alledges(vertex(vv,i),vertex(vv,j));
  end %for j
 end %for i
 newalledges=triu(newalledges);
 for i=1:nr,
  for j=1:nr,
   if newalledges(i,j)==1
   angle=degallangles(vertex(vv,i),vertex(vv,j));
    if angle==0
    angle=degallangles(vertex(vv,j),vertex(vv,i));
    end %if angle
   diff7c3v(i,j)=ideal7c3v(i,j)-angle;
   diff7c2v(i,j)=ideal7c2v(i,j)-angle;
   diff7d5h(i,j)=ideal7d5h(i,j)-angle;
   end %if newalledges
  end %for j
 end %for i
 for i=1:nr,
  for j=1:nr,
   if diff7c3v(i,j)==0 & ideal7c3v(i,j)~=0
   diff7c3v(i,j)=ideal7c3v(i,j);
   end %if
   if diff7c2v(i,j)==0 & ideal7c2v(i,j)~=0
   diff7c2v(i,j)=ideal7c2v(i,j);
   end %if
   if diff7d5h(i,j)==0 & ideal7d5h(i,j)~=0
   diff7d5h(i,j)=ideal7d5h(i,j);
   end %if
  end %for j
 end %for i
sum7c3v(vv)=sum(sum(diff7c3v.^2));
sum7c2v(vv)=sum(sum(diff7c2v.^2));
sum7d5h(vv)=sum(sum(diff7d5h.^2));
end %for vv

%load the shape minimized alignment
ii=0; jj=0; kk=0;
for vv=1:ss
 if sum7c2v(1,vv)==min(sum7c2v)
 ii=vv;
 end %if
 if sum7d5h(1,vv)==min(sum7d5h)
 jj=vv;
 end %if
 if sum7c3v(1,vv)==min(sum7c3v)
```

```
kk=vv;
 end %if
end %for vv
for vv=1:ss
 if abs(sum7c3v(1,vv)-min(sum7c3v)+sum7c2v(1,vv)-min(sum7c2v)+sum7d5h(1,vv)-min(sum7d5h))<=0.001
ii=vv;
jj=vv;
kk=vv;
 end %if
end %for vv
if abs(sum7c2v(1,kk)-min(sum7c2v))<=0.001
ii=kk;
 end %if
if abs(sum7d5h(1,kk)-min(sum7d5h))<=0.001
jj=kk;
 end %if

%sort the measured shape angles
finalangles=zeros(nr,nr);
for i=1:nr,
 for j=1:nr,
 newalledges(i,j)=alledges(vertex(kk,i),vertex(kk,j));
 end %for j
end %for i
newalledges=triu(newalledges);
for i=1:nr,
 for j=1:nr,
  if newalledges(i,j)==1
  angle=degallangles(vertex(kk,i),vertex(kk,j));
   if angle==0
   angle=degallangles(vertex(kk,j),vertex(kk,i));
   end %if angle
   finalangles(i,j)=angle;
  end %if newalledges
 end %for j
end %for i

%sort the c2v ideal angles
newideal7c2v=zeros(nr,nr);
for i=1:nr,
 for j=1:nr,
  if ideal7c2v(i,j)~=0
   for m=1:nr
    for n=1:nr
    if vertex(ii,i)==vertex(kk,m) & vertex(ii,j)==vertex(kk,n)
          newideal7c2v(m,n)=ideal7c2v(i,j);
          newideal7c2v(n,m)=ideal7c2v(i,j);
    end %if
    end %for n
   end %for m
  end %if ideal7c2v
 end %for j
end %for i
newideal7c2v=triu(newideal7c2v);
```

148

```matlab
%sort the d5h ideal angles
newideal7d5h=zeros(nr,nr);
for i=1:nr,
 for j=1:nr,
  if ideal7d5h(i,j)~=0
   for m=1:nr
    for n=1:nr
     if vertex(jj,i)==vertex(kk,m) & vertex(jj,j)==vertex(kk,n)
            newideal7d5h(m,n)=ideal7d5h(i,j);
            newideal7d5h(n,m)=ideal7d5h(i,j);
     end %if
    end %for n
   end %for m
  end %if ideal7d5h
 end %for j
end %for i
newideal7d5h=triu(newideal7d5h);


%print results
sindex(1,1)=sqrt(min(sum7c3v)/15);
sindex(1,2)=sqrt(min(sum7c2v)/15);
sindex(1,3)=sqrt(min(sum7d5h)/15);
str1=' C3v   C2v   D5h';
sindex1(1,1)=finalangles(2,3); sindex1(2,1)=finalangles(1,2); sindex1(3,1)=finalangles(1,3);
sindex1(4,1)=finalangles(4,6); sindex2(1,1)=finalangles(5,6); sindex2(2,1)=finalangles(6,7);
sindex2(3,1)=finalangles(5,7); sindex2(4,1)=finalangles(2,7); sindex2(5,1)=finalangles(3,7);
sindex2(6,1)=finalangles(2,5); sindex2(7,1)=finalangles(3,6); sindex2(8,1)=finalangles(1,5);
sindex2(9,1)=finalangles(1,6); sindex2(10,1)=finalangles(2,4); sindex2(11,1)=finalangles(3,4);
sindex2(12,1)=finalangles(1,4);

sindex3(1,1)=ideal7c3v(2,3); sindex3(2,1)=ideal7c3v(1,2); sindex3(3,1)=ideal7c3v(1,3);
sindex3(4,1)=ideal7c3v(4,6); sindex4(1,1)=ideal7c3v(5,6); sindex4(2,1)=ideal7c3v(6,7);
sindex4(3,1)=ideal7c3v(5,7); sindex4(4,1)=ideal7c3v(2,7); sindex4(5,1)=ideal7c3v(3,7);
sindex4(6,1)=ideal7c3v(2,5); sindex4(7,1)=ideal7c3v(3,6); sindex4(8,1)=ideal7c3v(1,5);
sindex4(9,1)=ideal7c3v(1,6); sindex4(10,1)=ideal7c3v(2,4); sindex4(11,1)=ideal7c3v(3,4);
sindex4(12,1)=ideal7c3v(1,4);

sindex5(1,1)=newideal7c2v(2,3); sindex5(2,1)=newideal7c2v(1,2); sindex5(3,1)=newideal7c2v(1,3);
sindex5(4,1)=newideal7c2v(4,6); sindex6(1,1)=newideal7c2v(5,6); sindex6(2,1)=newideal7c2v(6,7);
sindex6(3,1)=newideal7c2v(5,7); sindex6(4,1)=newideal7c2v(2,7); sindex6(5,1)=newideal7c2v(3,7);
sindex6(6,1)=newideal7c2v(2,5); sindex6(7,1)=newideal7c2v(3,6); sindex6(8,1)=newideal7c2v(1,5);
sindex6(9,1)=newideal7c2v(1,6); sindex6(10,1)=newideal7c2v(2,4); sindex6(11,1)=newideal7c2v(3,4);
sindex6(12,1)=newideal7c2v(1,4);

sindex7(1,1)=newideal7d5h(2,3); sindex7(2,1)=newideal7d5h(1,2); sindex7(3,1)=newideal7d5h(1,3);
sindex7(4,1)=newideal7d5h(4,6); sindex8(1,1)=newideal7d5h(5,6); sindex8(2,1)=newideal7d5h(6,7);
sindex8(3,1)=newideal7d5h(5,7); sindex8(4,1)=newideal7d5h(2,7); sindex8(5,1)=newideal7d5h(3,7);
sindex8(6,1)=newideal7d5h(2,5); sindex8(7,1)=newideal7d5h(3,6); sindex8(8,1)=newideal7d5h(1,5);
sindex8(9,1)=newideal7d5h(1,6); sindex8(10,1)=newideal7d5h(2,4); sindex8(11,1)=newideal7d5h(3,4);
sindex8(12,1)=newideal7d5h(1,4);

shapeangles=[sindex1,sindex3,sindex5,sindex7];
otherangles=[sindex2,sindex4,sindex6,sindex8];
format bank
disp(['Shape Analysis of ', title,' is:']);
```

```matlab
disp('    C3v    C2v    D5h'); disp(sindex);
disp(' ');
if longanalysis == 1
disp('Shape Determining Angles:');
disp(['Measured','   C3v ','   C2v ','   D5h']);
disp(shapeangles);
disp(' ');
disp('Other Angles:');
disp(['Measured','    C3v ','   C2v ','    D5h']);
disp(otherangles);
end %if
end %if nr==7


%-------------------------------------
%Section I: 8-Coordinate Shape Analysis
%-------------------------------------

if nr==8
%determine structure type
type=0;
for i=1:nr,
 if sum(alledges(i,:))==3
  for j=1:nr,
   if sum(alledges(j,:))==3 & i~=j
    for k=1:nr,
           if sum(alledges(k,:))==3 & i~=j & j~=k & k~=i
           type=6;
           end %if
           end %for k
   end %if
  end %for j
 end %if
end %for i
if type==0
 for i=1:nr,
  if sum(alledges(i,:))==3
   for j=1:nr,
    if sum(alledges(j,:))==3 & i~=j
    type=2; pt1=i; pt2=j;
           end %if
   end %for j
  end %if
 end %for i
end %if type
if type==2
 for i=1:nr,
  if sum(alledges(i,:))==6
   for j=1:nr,
    if sum(alledges(j,:))==6 & i~=j
    type=3; pt3=i; pt4=j;
           end %if
   end %for j
  end %if
 end %for i
end %if type
```

```matlab
if type==3
 if alledges(pt1,pt3)==1 & alledges(pt2,pt3)==1 & alledges(pt1,pt4)==1 & alledges(pt2,pt4)==1
 type=5;
 end %if
end %if type
if type==0
 for i=1:nr,
 if sum(alledges(i,:))==3
 type=4;
 end %if
 end %for i
end %if type
if type==0
 for i=1:nr,
 if sum(alledges(i,:))==6
 type=1;
 end %if
 end %for i
end %if type

if type==0
%find the two pairs of 4-edge vertices
found=zeros(1,nr);
kk=1;
for i=1:nr,
 if sum(alledges(i,:))==4 & found(i)==0
  for j=1:nr,
   if alledges(i,j)==1 & sum(alledges(j,:))==4 & found(j)==0
   vertex(1,2*kk-1)=i;
   vertex(1,2*kk)=j;
   found(i)=1;
   found(j)=1;
   kk=kk+1;
   break;
   end %if
  end %for j
 end %if sum
end %for i

%generate all possible permutations
vertex(2,1)=vertex(1,1); vertex(2,2)=vertex(1,2);
vertex(2,3)=vertex(1,4); vertex(2,4)=vertex(1,3);
vertex(3,1)=vertex(1,2); vertex(3,2)=vertex(1,1);
vertex(3,3)=vertex(1,3); vertex(3,4)=vertex(1,4);
vertex(4,1)=vertex(1,2); vertex(4,2)=vertex(1,1);
vertex(4,3)=vertex(1,4); vertex(4,4)=vertex(1,3);
vertex(5,1)=vertex(1,3); vertex(5,2)=vertex(1,4);
vertex(5,3)=vertex(1,1); vertex(5,4)=vertex(1,2);
vertex(6,1)=vertex(1,3); vertex(6,2)=vertex(1,4);
vertex(6,3)=vertex(1,2); vertex(6,4)=vertex(1,1);
vertex(7,1)=vertex(1,4); vertex(7,2)=vertex(1,3);
vertex(7,3)=vertex(1,1); vertex(7,4)=vertex(1,2);
vertex(8,1)=vertex(1,4); vertex(8,2)=vertex(1,3);
vertex(8,3)=vertex(1,2); vertex(8,4)=vertex(1,1);
```

151

```matlab
%find the 5-edge vertices by connectivity
for vv=1:8,
 for i=1:nr,
  if alledges(i,vertex(vv,1))==1 & alledges(i,vertex(vv,2))==1 & alledges(i,vertex(vv,3))==1
  vertex(vv,5)=i;
  end
  if alledges(i,vertex(vv,2))==1 & alledges(i,vertex(vv,3))==1 & alledges(i,vertex(vv,4))==1
  vertex(vv,6)=i;
  end
  if alledges(i,vertex(vv,1))==1 & alledges(i,vertex(vv,3))==1 & alledges(i,vertex(vv,4))==1
  vertex(vv,7)=i;
  end
  if alledges(i,vertex(vv,1))==1 & alledges(i,vertex(vv,2))==1 & alledges(i,vertex(vv,4))==1
  vertex(vv,8)=i;
  end
 end %for i
end %for vv


%check for type0' structure by transformation of above permutations
for vv=9:16
vertex(vv,1)=vertex(vv-8,1); vertex(vv,2)=vertex(vv-8,8); vertex(vv,3)=vertex(vv-8,3); vertex(vv,4)=vertex(vv-8,6);
vertex(vv,5)=vertex(vv-8,7); vertex(vv,6)=vertex(vv-8,4); vertex(vv,7)=vertex(vv-8,5); vertex(vv,8)=vertex(vv-8,2);
end %for vv
end %if type==0


if type==1
%find the two 6-edge vertices
for i=1:nr,
 if sum(alledges(i,:))==6
  for j=1:nr,
   if sum(alledges(j,:))==6 & i~=j
   vertex(1,1)=i; vertex(1,6)=j;
   end %if
  end %for j
 end %if sum
end %for i
for i=1:nr,
 if i~=vertex(1,1) & i~=vertex(1,6)
 vertex(1,2)=i;
 end %if
end %for i


%find the 4-edge vertices sequentially
 for i=1:nr,
  if alledges(i,vertex(1,1))==1 & alledges(i,vertex(1,2))==1 & alledges(i,vertex(1,6))==1
  vertex(1,5)=i;
  end %if
 end %for i
 for i=1:nr,
  if alledges(i,vertex(1,1))==1 & alledges(i,vertex(1,5))==1 & alledges(i,vertex(1,6))==1 & i~=vertex(1,2)
  vertex(1,3)=i;
  end %if
 end %for i
```

```matlab
for i=1:nr,
 if alledges(i,vertex(1,1))==1 & alledges(i,vertex(1,3))==1 & alledges(i,vertex(1,6))==1 & i~=vertex(1,5)
 vertex(1,7)=i;
 end %if
 end %for i
 for i=1:nr,
 if alledges(i,vertex(1,1))==1 & alledges(i,vertex(1,7))==1 & alledges(i,vertex(1,6))==1 & i~=vertex(1,3)
 vertex(1,4)=i;
 end %if
 end %for i
 for i=1:nr,
 if alledges(i,vertex(1,1))==1 & alledges(i,vertex(1,4))==1 & alledges(i,vertex(1,6))==1 & i~=vertex(1,7)
 vertex(1,8)=i;
 end %if
 end %for i
end %if type==1

if type==2
%find the two 3-edge vertices
for i=1:nr,
 if sum(alledges(i,:))==3
  for j=1:nr,
   if sum(alledges(j,:))==3 & i~=j
   vertex(1,1)=i; vertex(1,6)=j;
   end %if
  end %for j
 end %if sum
end %for i
%pick one 3-edge vertex arbitrarily and then find the three 4-edge vertices connected to it
for i=1:nr,
 if alledges(i,vertex(1,1))==1
  for j=1:nr,
   if alledges(j,vertex(1,1))==1 & i~=j
    for k=1:nr,
          if alledges(k,vertex(1,1))==1 & i~=j & i~=k & j~=k
 vertex(1,5)=i; vertex(1,7)=j; vertex(1,8)=k;
    end %if
   end %for k
  end %if
 end %for j
 end %if
end %for i

%find the remaining vertices by connectivity
for i=1:nr,
 if alledges(i,vertex(1,6))==1 & alledges(i,vertex(1,5))==1 & alledges(i,vertex(1,8))==1
 vertex(1,2)=i;
 end %if
 end %for i
 for i=1:nr,
 if alledges(i,vertex(1,6))==1 & alledges(i,vertex(1,7))==1 & alledges(i,vertex(1,8))==1
 vertex(1,4)=i;
 end %if
 end %for i
 for i=1:nr,
```

```
 if alledges(i,vertex(1,6))==1 & alledges(i,vertex(1,5))==1 & alledges(i,vertex(1,7))==1
 vertex(1,3)=i;
  end %if
 end %for i
end %if type==2

if type==3
%find the unique 3- and 6-edge vertices
for i=1:nr,
 if sum(alledges(i,:))==3
  for j=1:nr,
   if sum(alledges(j,:))==3 & i~=j
   vertex(1,1)=i; vertex(1,6)=j;
    end %if
  end %for j
 end %if sum
end %for i
for i=1:nr,
 if sum(alledges(i,:))==6 & alledges(i,vertex(1,1))==1
 vertex(1,5)=i;
 end %if
end %for i
for i=1:nr,
 if sum(alledges(i,:))==6 & alledges(i,vertex(1,6))==1
 vertex(1,4)=i;
 end %if
end %for i
for i=1:nr,
 if sum(alledges(i,:))==4 & alledges(i,vertex(1,1))==1
 vertex(1,7)=i;
 end %if
end %for i
for i=1:nr,
 if sum(alledges(i,:))==4 & alledges(i,vertex(1,6))==1
 vertex(1,3)=i;
 end %if
end %for i
for i=1:nr,
 if sum(alledges(i,:))==5 & alledges(i,vertex(1,1))==1
 vertex(1,8)=i;
 end %if
end %for i
for i=1:nr,
 if sum(alledges(i,:))==5 & alledges(i,vertex(1,6))==1
 vertex(1,2)=i;
 end %if
end %for i

%fix dihedral angle errors due to connected 6-edge vertices
edge=P(vertex(1,4),:)-P(vertex(1,5),:);
normal1=cross(P(vertex(1,3),:)-P(vertex(1,4),:),edge);
normal2=cross(edge,P(vertex(1,7),:)-P(vertex(1,4),:));
newangle=(normal1*normal2')/(norm(normal1)*norm(normal2));
degangle=acos(newangle)*180/pi;
allangles(vertex(1,4),vertex(1,5))=newangle; allangles(vertex(1,5),vertex(1,4))=newangle;
```

```
degallangles(vertex(1,4),vertex(1,5))=degangle; degallangles(vertex(1,5),vertex(1,4))=degangle;

edge=P(vertex(1,5),:)-P(vertex(1,2),:);
normal1=cross(P(vertex(1,8),:)-P(vertex(1,5),:),edge);
normal2=cross(edge,P(vertex(1,3),:)-P(vertex(1,5),:));
newangle=(normal1*normal2')/(norm(normal1)*norm(normal2));
degangle=acos(newangle)*180/pi;
allangles(vertex(1,5),vertex(1,2))=newangle; allangles(vertex(1,2),vertex(1,5))=newangle;
degallangles(vertex(1,5),vertex(1,2))=degangle; degallangles(vertex(1,2),vertex(1,5))=degangle;

edge=P(vertex(1,4),:)-P(vertex(1,8),:);
normal1=cross(P(vertex(1,2),:)-P(vertex(1,4),:),edge);
normal2=cross(edge,P(vertex(1,7),:)-P(vertex(1,4),:));
newangle=(normal1*normal2')/(norm(normal1)*norm(normal2));
degangle=acos(newangle)*180/pi;
allangles(vertex(1,4),vertex(1,8))=newangle; allangles(vertex(1,8),vertex(1,4))=newangle;
degallangles(vertex(1,4),vertex(1,8))=degangle; degallangles(vertex(1,8),vertex(1,4))=degangle;
allangles=triu(allangles);
degallangles=triu(degallangles);
end %if type==3

if type==4
%find the unique 3- and 6-edge vertices
for i=1:nr,
 if sum(alledges(i,:))==6
  for j=1:nr,
   if sum(alledges(j,:))==3
   vertex(1,1)=i; vertex(1,5)=j;
   end %if
  end %for j
 end %if sum
end %for i

%find the remaining vertices by connectivity
 for i=1:nr,
 if alledges(i,vertex(1,1))==0
 vertex(1,6)=i;
 end %if
 end %for i
 for i=1:nr,
  for j=1:nr,
  if alledges(i,vertex(1,5))==1 & alledges(j,vertex(1,5))==1 & i~=j & i~=vertex(1,5) & j~=vertex(1,5)
  vertex(1,2)=i; vertex(1,3)=j;
  end %if
 end %for j
 end %for i
 for i=1:nr,
  if alledges(i,vertex(1,2))==0 & alledges(i,vertex(1,3))==0 & i~=vertex(1,2) & i~=vertex(1,3)
  vertex(1,4)=i;
  end %if
 end %for i
 for i=1:nr,
 if sum(alledges(i,:))==4 & alledges(i,vertex(1,2))==1
 vertex(1,8)=i;
 end %if
```

```
 end %for i
 for i=1:nr,
  if sum(alledges(i,:))==4 & alledges(i,vertex(1,3))==1
  vertex(1,7)=i;
  end %if
 end %for i
end %if type==4

if type==5
%find the unique 3- and 6-edge vertices
for i=1:nr,
 if sum(alledges(i,:))==6
  for j=1:nr,
   if sum(alledges(j,:))==6 & i~=j
   vertex(1,1)=i; vertex(1,2)=j;
   end %if
  end %for j
 end %if sum
end %for i
for i=1:nr,
 if sum(alledges(i,:))==3
  for j=1:nr,
   if sum(alledges(j,:))==3 & i~=j
   vertex(1,5)=i; vertex(1,8)=j;
   end %if
  end %for j
 end %if sum
end %for i

%find the remaining vertices by connectivity
 for i=1:nr,
  if alledges(i,vertex(1,1))==0 & i~=vertex(1,1)
  vertex(1,6)=i;
  end %if
 end %for i
 for i=1:nr,
  if alledges(i,vertex(1,2))==0 & i~=vertex(1,2)
  vertex(1,7)=i;
  end %if
 end %for i
 for i=1:nr,
  if alledges(i,vertex(1,1))==1 & alledges(i,vertex(1,2))==1 & alledges(i,vertex(1,6))==1 &
alledges(i,vertex(1,7))==1 & alledges(i,vertex(1,8))==1
  vertex(1,4)=i;
  end %if
 end %for i
 for i=1:nr,
  if alledges(i,vertex(1,1))==1 & alledges(i,vertex(1,2))==1 & alledges(i,vertex(1,6))==1 &
alledges(i,vertex(1,7))==1 & alledges(i,vertex(1,5))==1
  vertex(1,3)=i;
  end %if
 end %for i

%fix dihedral angle errors due to connected 6-edge vertices
edge=P(vertex(1,1),:)-P(vertex(1,2),:);
```

```matlab
normal1=cross(P(vertex(1,5),:)-P(vertex(1,1),:),edge);
normal2=cross(edge,P(vertex(1,8),:)-P(vertex(1,1),:));
newangle=(normal1*normal2')/(norm(normal1)*norm(normal2));
degangle=acos(newangle)*180/pi;
allangles(vertex(1,1),vertex(1,2))=newangle; allangles(vertex(1,2),vertex(1,1))=newangle;
degallangles(vertex(1,1),vertex(1,2))=degangle; degallangles(vertex(1,2),vertex(1,1))=degangle;
allangles=triu(allangles);
degallangles=triu(degallangles);
end %if type==5

if type==6
%find the four 3-edge vertices
for i=1:nr,
 if sum(alledges(i,:))==3
  for j=1:nr,
   if sum(alledges(j,:))==3 & i~=j
    for k=1:nr,
     if sum(alledges(k,:))==3 & i~=k & k~=j
      for m=1:nr,
       if sum(alledges(m,:))==3 & i~=m & j~=m & k~=m
       vertex(1,1)=i; vertex(1,2)=j; vertex(1,3)=k; vertex(1,4)=m;
               end %if
              end %for m
             end %if
            end %for k
   end %if
  end %for j
 end %if
end %for i

%find the 6-edge vertices by connectivity
for i=1:nr,
 if sum(alledges(i,:))==6 & alledges(i,vertex(1,1))==1 & alledges(i,vertex(1,2))==1 & alledges(i,vertex(1,3))==1
 vertex(1,5)=i;
 end %if
 if sum(alledges(i,:))==6 & alledges(i,vertex(1,2))==1 & alledges(i,vertex(1,3))==1 & alledges(i,vertex(1,4))==1
 vertex(1,6)=i;
 end %if
 if sum(alledges(i,:))==6 & alledges(i,vertex(1,1))==1 & alledges(i,vertex(1,3))==1 & alledges(i,vertex(1,4))==1
 vertex(1,7)=i;
 end %if
 if sum(alledges(i,:))==6 & alledges(i,vertex(1,1))==1 & alledges(i,vertex(1,2))==1 & alledges(i,vertex(1,4))==1
 vertex(1,8)=i;
 end %if
end %for i

%fix dihedral angle errors due to connected 6-edge vertices
edge=P(vertex(1,6),:)-P(vertex(1,5),:);
normal1=cross(P(vertex(1,2),:)-P(vertex(1,6),:),edge);
normal2=cross(edge,P(vertex(1,3),:)-P(vertex(1,6),:));
newangle=(normal1*normal2')/(norm(normal1)*norm(normal2));
degangle=acos(newangle)*180/pi;
allangles(vertex(1,6),vertex(1,5))=newangle; allangles(vertex(1,5),vertex(1,6))=newangle;
degallangles(vertex(1,6),vertex(1,5))=degangle; degallangles(vertex(1,5),vertex(1,6))=degangle;
```

```
edge=P(vertex(1,7),:)-P(vertex(1,5),:);
normal1=cross(P(vertex(1,1),:)-P(vertex(1,7),:),edge);
normal2=cross(edge,P(vertex(1,3),:)-P(vertex(1,7),:));
newangle=(normal1*normal2')/(norm(normal1)*norm(normal2));
degangle=acos(newangle)*180/pi;
allangles(vertex(1,7),vertex(1,5))=newangle; allangles(vertex(1,5),vertex(1,7))=newangle;
degallangles(vertex(1,7),vertex(1,5))=degangle; degallangles(vertex(1,5),vertex(1,7))=degangle;

edge=P(vertex(1,8),:)-P(vertex(1,5),:);
normal1=cross(P(vertex(1,1),:)-P(vertex(1,8),:),edge);
normal2=cross(edge,P(vertex(1,2),:)-P(vertex(1,8),:));
newangle=(normal1*normal2')/(norm(normal1)*norm(normal2));
degangle=acos(newangle)*180/pi;
allangles(vertex(1,8),vertex(1,5))=newangle; allangles(vertex(1,5),vertex(1,8))=newangle;
degallangles(vertex(1,8),vertex(1,5))=degangle; degallangles(vertex(1,5),vertex(1,8))=degangle;

edge=P(vertex(1,6),:)-P(vertex(1,8),:);
normal1=cross(P(vertex(1,2),:)-P(vertex(1,6),:),edge);
normal2=cross(edge,P(vertex(1,4),:)-P(vertex(1,6),:));
newangle=(normal1*normal2')/(norm(normal1)*norm(normal2));
degangle=acos(newangle)*180/pi;
allangles(vertex(1,6),vertex(1,8))=newangle; allangles(vertex(1,8),vertex(1,6))=newangle;
degallangles(vertex(1,6),vertex(1,8))=degangle; degallangles(vertex(1,8),vertex(1,6))=degangle;

edge=P(vertex(1,7),:)-P(vertex(1,6),:);
normal1=cross(P(vertex(1,3),:)-P(vertex(1,7),:),edge);
normal2=cross(edge,P(vertex(1,4),:)-P(vertex(1,7),:));
newangle=(normal1*normal2')/(norm(normal1)*norm(normal2));
degangle=acos(newangle)*180/pi;
allangles(vertex(1,7),vertex(1,6))=newangle; allangles(vertex(1,6),vertex(1,7))=newangle;
degallangles(vertex(1,7),vertex(1,6))=degangle; degallangles(vertex(1,6),vertex(1,7))=degangle;

edge=P(vertex(1,7),:)-P(vertex(1,8),:);
normal1=cross(P(vertex(1,1),:)-P(vertex(1,7),:),edge);
normal2=cross(edge,P(vertex(1,4),:)-P(vertex(1,7),:));
newangle=(normal1*normal2')/(norm(normal1)*norm(normal2));
degangle=acos(newangle)*180/pi;
allangles(vertex(1,7),vertex(1,8))=newangle; allangles(vertex(1,8),vertex(1,7))=newangle;
degallangles(vertex(1,7),vertex(1,8))=degangle; degallangles(vertex(1,8),vertex(1,7))=degangle;
allangles=triu(allangles);
degallangles=triu(degallangles);
end %if type==6

if type~=0 & type~=4 & type~=5 & type~=6
%generate all possible permutations
vertex(2,1)=vertex(1,1); vertex(2,6)=vertex(1,6);
vertex(3,1)=vertex(1,1); vertex(3,6)=vertex(1,6);
vertex(4,1)=vertex(1,1); vertex(4,6)=vertex(1,6);
vertex(5,1)=vertex(1,1); vertex(5,6)=vertex(1,6);
vertex(6,1)=vertex(1,1); vertex(6,6)=vertex(1,6);
vertex(7,1)=vertex(1,6); vertex(7,6)=vertex(1,1);
vertex(8,1)=vertex(1,6); vertex(8,6)=vertex(1,1);
vertex(9,1)=vertex(1,6); vertex(9,6)=vertex(1,1);
vertex(10,1)=vertex(1,6); vertex(10,6)=vertex(1,1);
vertex(11,1)=vertex(1,6); vertex(11,6)=vertex(1,1);
```

```
vertex(12,1)=vertex(1,6); vertex(12,6)=vertex(1,1);

vertex(2,2)=vertex(1,5); vertex(2,3)=vertex(1,7); vertex(2,4)=vertex(1,8);
vertex(3,2)=vertex(1,3); vertex(3,3)=vertex(1,4); vertex(3,4)=vertex(1,2);
vertex(4,2)=vertex(1,7); vertex(4,3)=vertex(1,8); vertex(4,4)=vertex(1,5);
vertex(5,2)=vertex(1,4); vertex(5,3)=vertex(1,2); vertex(5,4)=vertex(1,3);
vertex(6,2)=vertex(1,8); vertex(6,3)=vertex(1,5); vertex(6,4)=vertex(1,7);
vertex(7,2)=vertex(1,2); vertex(7,3)=vertex(1,3); vertex(7,4)=vertex(1,4);
vertex(8,2)=vertex(1,5); vertex(8,3)=vertex(1,7); vertex(8,4)=vertex(1,8);
vertex(9,2)=vertex(1,3); vertex(9,3)=vertex(1,4); vertex(9,4)=vertex(1,2);
vertex(10,2)=vertex(1,7); vertex(10,3)=vertex(1,8); vertex(10,4)=vertex(1,5);
vertex(11,2)=vertex(1,4); vertex(11,3)=vertex(1,2); vertex(11,4)=vertex(1,3);
vertex(12,2)=vertex(1,8); vertex(12,3)=vertex(1,5); vertex(12,4)=vertex(1,7);

vertex(2,5)=vertex(1,3); vertex(2,7)=vertex(1,4); vertex(2,8)=vertex(1,2);
vertex(3,5)=vertex(1,7); vertex(3,7)=vertex(1,8); vertex(3,8)=vertex(1,5);
vertex(4,5)=vertex(1,4); vertex(4,7)=vertex(1,2); vertex(4,8)=vertex(1,3);
vertex(5,5)=vertex(1,8); vertex(5,7)=vertex(1,5); vertex(5,8)=vertex(1,7);
vertex(6,5)=vertex(1,2); vertex(6,7)=vertex(1,3); vertex(6,8)=vertex(1,4);
vertex(7,5)=vertex(1,5); vertex(7,7)=vertex(1,7); vertex(7,8)=vertex(1,8);
vertex(8,5)=vertex(1,3); vertex(8,7)=vertex(1,4); vertex(8,8)=vertex(1,2);
vertex(9,5)=vertex(1,7); vertex(9,7)=vertex(1,8); vertex(9,8)=vertex(1,5);
vertex(10,5)=vertex(1,4); vertex(10,7)=vertex(1,2); vertex(10,8)=vertex(1,3);
vertex(11,5)=vertex(1,8); vertex(11,7)=vertex(1,5); vertex(11,8)=vertex(1,7);
vertex(12,5)=vertex(1,2); vertex(12,7)=vertex(1,3); vertex(12,8)=vertex(1,4);

for i=13:24,
vertex(i,1)=vertex(i-12,4); vertex(i,2)=vertex(i-12,2);
vertex(i,3)=vertex(i-12,3); vertex(i,4)=vertex(i-12,1); vertex(i,5)=vertex(i-12,6);
vertex(i,6)=vertex(i-12,5); vertex(i,7)=vertex(i-12,7); vertex(i,8)=vertex(i-12,8);
end %for i
for i=25:36
vertex(i,1)=vertex(i-24,8); vertex(i,2)=vertex(i-24,2);
vertex(i,3)=vertex(i-24,6); vertex(i,4)=vertex(i-24,4); vertex(i,5)=vertex(i-24,5);
vertex(i,6)=vertex(i-24,3); vertex(i,7)=vertex(i-24,7); vertex(i,8)=vertex(i-24,1);
end %for i
for i=37:48
vertex(i,1)=vertex(i-36,2); vertex(i,2)=vertex(i-36,1);
vertex(i,3)=vertex(i-36,3); vertex(i,4)=vertex(i-36,4); vertex(i,5)=vertex(i-36,5);
vertex(i,6)=vertex(i-36,7); vertex(i,7)=vertex(i-36,6); vertex(i,8)=vertex(i-36,8);
end %for i
end %if type

if type~=0 & type~=1 & type~=2 & type~=3
%generate all possible permutations
vertex(2,1)=vertex(1,1); vertex(2,2)=vertex(1,4); vertex(2,3)=vertex(1,2); vertex(2,4)=vertex(1,3);
vertex(3,1)=vertex(1,1); vertex(3,2)=vertex(1,3); vertex(3,3)=vertex(1,4); vertex(3,4)=vertex(1,2);
vertex(4,1)=vertex(1,3); vertex(4,2)=vertex(1,2); vertex(4,3)=vertex(1,4); vertex(4,4)=vertex(1,1);
vertex(5,1)=vertex(1,4); vertex(5,2)=vertex(1,2); vertex(5,3)=vertex(1,1); vertex(5,4)=vertex(1,3);
vertex(6,1)=vertex(1,4); vertex(6,2)=vertex(1,1); vertex(6,3)=vertex(1,3); vertex(6,4)=vertex(1,2);
vertex(7,1)=vertex(1,2); vertex(7,2)=vertex(1,4); vertex(7,3)=vertex(1,3); vertex(7,4)=vertex(1,1);
vertex(8,1)=vertex(1,3); vertex(8,2)=vertex(1,1); vertex(8,3)=vertex(1,2); vertex(8,4)=vertex(1,4);
vertex(9,1)=vertex(1,2); vertex(9,2)=vertex(1,3); vertex(9,3)=vertex(1,1); vertex(9,4)=vertex(1,4);
vertex(10,1)=vertex(1,8); vertex(10,2)=vertex(1,7); vertex(10,3)=vertex(1,6); vertex(10,4)=vertex(1,5);
vertex(11,1)=vertex(1,6); vertex(11,2)=vertex(1,5); vertex(11,3)=vertex(1,8); vertex(11,4)=vertex(1,7);
```

```
vertex(12,1)=vertex(1,5); vertex(12,2)=vertex(1,7); vertex(12,3)=vertex(1,8); vertex(12,4)=vertex(1,6);
vertex(13,1)=vertex(1,6); vertex(13,2)=vertex(1,8); vertex(13,3)=vertex(1,7); vertex(13,4)=vertex(1,5);
vertex(14,1)=vertex(1,6); vertex(14,2)=vertex(1,7); vertex(14,3)=vertex(1,5); vertex(14,4)=vertex(1,8);
vertex(15,1)=vertex(1,7); vertex(15,2)=vertex(1,6); vertex(15,3)=vertex(1,8); vertex(15,4)=vertex(1,5);
vertex(16,1)=vertex(1,5); vertex(16,2)=vertex(1,8); vertex(16,3)=vertex(1,6); vertex(16,4)=vertex(1,7);
vertex(17,1)=vertex(1,8); vertex(17,2)=vertex(1,5); vertex(17,3)=vertex(1,7); vertex(17,4)=vertex(1,6);
vertex(18,1)=vertex(1,7); vertex(18,2)=vertex(1,5); vertex(18,3)=vertex(1,6); vertex(18,4)=vertex(1,8);
vertex(19,1)=vertex(1,8); vertex(19,2)=vertex(1,6); vertex(19,3)=vertex(1,5); vertex(19,4)=vertex(1,7);
vertex(20,1)=vertex(1,5); vertex(20,2)=vertex(1,6); vertex(20,3)=vertex(1,7); vertex(20,4)=vertex(1,8);
vertex(21,1)=vertex(1,7); vertex(21,2)=vertex(1,8); vertex(21,3)=vertex(1,5); vertex(21,4)=vertex(1,6);
vertex(22,1)=vertex(1,2); vertex(22,2)=vertex(1,1); vertex(22,3)=vertex(1,4); vertex(22,4)=vertex(1,3);
vertex(23,1)=vertex(1,4); vertex(23,2)=vertex(1,3); vertex(23,3)=vertex(1,2); vertex(23,4)=vertex(1,1);
vertex(24,1)=vertex(1,3); vertex(24,2)=vertex(1,4); vertex(24,3)=vertex(1,1); vertex(24,4)=vertex(1,2);
vertex(25,1)=vertex(1,6); vertex(25,2)=vertex(1,7); vertex(25,3)=vertex(1,8); vertex(25,4)=vertex(1,5);
vertex(26,1)=vertex(1,3); vertex(26,2)=vertex(1,4); vertex(26,3)=vertex(1,2); vertex(26,4)=vertex(1,1);
vertex(27,1)=vertex(1,4); vertex(27,2)=vertex(1,3); vertex(27,3)=vertex(1,1); vertex(27,4)=vertex(1,2);
vertex(28,1)=vertex(1,3); vertex(28,2)=vertex(1,1); vertex(28,3)=vertex(1,4); vertex(28,4)=vertex(1,2);
vertex(29,1)=vertex(1,2); vertex(29,2)=vertex(1,4); vertex(29,3)=vertex(1,1); vertex(29,4)=vertex(1,3);
vertex(30,1)=vertex(1,2); vertex(30,2)=vertex(1,3); vertex(30,3)=vertex(1,4); vertex(30,4)=vertex(1,1);
vertex(31,1)=vertex(1,4); vertex(31,2)=vertex(1,1); vertex(31,3)=vertex(1,2); vertex(31,4)=vertex(1,3);
vertex(32,1)=vertex(1,6); vertex(32,2)=vertex(1,8); vertex(32,3)=vertex(1,5); vertex(32,4)=vertex(1,7);
vertex(33,1)=vertex(1,6); vertex(33,2)=vertex(1,5); vertex(33,3)=vertex(1,7); vertex(33,4)=vertex(1,8);
vertex(34,1)=vertex(1,5); vertex(34,2)=vertex(1,7); vertex(34,3)=vertex(1,6); vertex(34,4)=vertex(1,8);
vertex(35,1)=vertex(1,8); vertex(35,2)=vertex(1,7); vertex(35,3)=vertex(1,5); vertex(35,4)=vertex(1,6);
vertex(36,1)=vertex(1,7); vertex(36,2)=vertex(1,5); vertex(36,3)=vertex(1,8); vertex(36,4)=vertex(1,6);
vertex(37,1)=vertex(1,5); vertex(37,2)=vertex(1,6); vertex(37,3)=vertex(1,8); vertex(37,4)=vertex(1,7);
vertex(38,1)=vertex(1,7); vertex(38,2)=vertex(1,8); vertex(38,3)=vertex(1,6); vertex(38,4)=vertex(1,5);
vertex(39,1)=vertex(1,8); vertex(39,2)=vertex(1,6); vertex(39,3)=vertex(1,7); vertex(39,4)=vertex(1,5);
vertex(40,1)=vertex(1,7); vertex(40,2)=vertex(1,6); vertex(40,3)=vertex(1,5); vertex(40,4)=vertex(1,8);
vertex(41,1)=vertex(1,8); vertex(41,2)=vertex(1,5); vertex(41,3)=vertex(1,6); vertex(41,4)=vertex(1,7);
vertex(42,1)=vertex(1,5); vertex(42,2)=vertex(1,8); vertex(42,3)=vertex(1,7); vertex(42,4)=vertex(1,6);
vertex(43,1)=vertex(1,1); vertex(43,2)=vertex(1,4); vertex(43,3)=vertex(1,3); vertex(43,4)=vertex(1,2);
vertex(44,1)=vertex(1,3); vertex(44,2)=vertex(1,2); vertex(44,3)=vertex(1,1); vertex(44,4)=vertex(1,4);
vertex(45,1)=vertex(1,1); vertex(45,2)=vertex(1,3); vertex(45,3)=vertex(1,2); vertex(45,4)=vertex(1,4);
vertex(46,1)=vertex(1,4); vertex(46,2)=vertex(1,2); vertex(46,3)=vertex(1,3); vertex(46,4)=vertex(1,1);
vertex(47,1)=vertex(1,1); vertex(47,2)=vertex(1,2); vertex(47,3)=vertex(1,4); vertex(47,4)=vertex(1,3);
vertex(48,1)=vertex(1,2); vertex(48,2)=vertex(1,1); vertex(48,3)=vertex(1,3); vertex(48,4)=vertex(1,4);


vertex(2,5)=vertex(1,8); vertex(2,6)=vertex(1,6); vertex(2,7)=vertex(1,5); vertex(2,8)=vertex(1,7);
vertex(3,5)=vertex(1,7); vertex(3,6)=vertex(1,6); vertex(3,7)=vertex(1,8); vertex(3,8)=vertex(1,5);
vertex(4,5)=vertex(1,6); vertex(4,6)=vertex(1,8); vertex(4,7)=vertex(1,7); vertex(4,8)=vertex(1,5);
vertex(5,5)=vertex(1,8); vertex(5,6)=vertex(1,5); vertex(5,7)=vertex(1,7); vertex(5,8)=vertex(1,6);
vertex(6,5)=vertex(1,7); vertex(6,6)=vertex(1,5); vertex(6,7)=vertex(1,6); vertex(6,8)=vertex(1,8);
vertex(7,5)=vertex(1,6); vertex(7,6)=vertex(1,7); vertex(7,7)=vertex(1,5); vertex(7,8)=vertex(1,8);
vertex(8,5)=vertex(1,5); vertex(8,6)=vertex(1,8); vertex(8,7)=vertex(1,6); vertex(8,8)=vertex(1,7);
vertex(9,5)=vertex(1,5); vertex(9,6)=vertex(1,7); vertex(9,7)=vertex(1,8); vertex(9,8)=vertex(1,6);
vertex(10,5)=vertex(1,4); vertex(10,6)=vertex(1,3); vertex(10,7)=vertex(1,2); vertex(10,8)=vertex(1,1);
vertex(11,5)=vertex(1,2); vertex(11,6)=vertex(1,1); vertex(11,7)=vertex(1,4); vertex(11,8)=vertex(1,3);
vertex(12,5)=vertex(1,1); vertex(12,6)=vertex(1,4); vertex(12,7)=vertex(1,2); vertex(12,8)=vertex(1,3);
vertex(13,5)=vertex(1,4); vertex(13,6)=vertex(1,1); vertex(13,7)=vertex(1,3); vertex(13,8)=vertex(1,2);
vertex(14,5)=vertex(1,3); vertex(14,6)=vertex(1,1); vertex(14,7)=vertex(1,2); vertex(14,8)=vertex(1,4);
vertex(15,5)=vertex(1,4); vertex(15,6)=vertex(1,2); vertex(15,7)=vertex(1,1); vertex(15,8)=vertex(1,3);
vertex(16,5)=vertex(1,2); vertex(16,6)=vertex(1,4); vertex(16,7)=vertex(1,3); vertex(16,8)=vertex(1,1);
vertex(17,5)=vertex(1,1); vertex(17,6)=vertex(1,3); vertex(17,7)=vertex(1,4); vertex(17,8)=vertex(1,2);
vertex(18,5)=vertex(1,3); vertex(18,6)=vertex(1,2); vertex(18,7)=vertex(1,4); vertex(18,8)=vertex(1,1);
```

```
vertex(19,5)=vertex(1,2); vertex(19,6)=vertex(1,3); vertex(19,7)=vertex(1,1); vertex(19,8)=vertex(1,4);
vertex(20,5)=vertex(1,3); vertex(20,6)=vertex(1,4); vertex(20,7)=vertex(1,1); vertex(20,8)=vertex(1,2);
vertex(21,5)=vertex(1,1); vertex(21,6)=vertex(1,2); vertex(21,7)=vertex(1,3); vertex(21,8)=vertex(1,4);
vertex(22,5)=vertex(1,8); vertex(22,6)=vertex(1,7); vertex(22,7)=vertex(1,6); vertex(22,8)=vertex(1,5);
vertex(23,5)=vertex(1,6); vertex(23,6)=vertex(1,5); vertex(23,7)=vertex(1,8); vertex(23,8)=vertex(1,7);
vertex(24,5)=vertex(1,7); vertex(24,6)=vertex(1,8); vertex(24,7)=vertex(1,5); vertex(24,8)=vertex(1,6);
vertex(25,5)=vertex(1,4); vertex(25,6)=vertex(1,1); vertex(25,7)=vertex(1,2); vertex(25,8)=vertex(1,3);
vertex(26,5)=vertex(1,6); vertex(26,6)=vertex(1,8); vertex(26,7)=vertex(1,5); vertex(26,8)=vertex(1,7);
vertex(27,5)=vertex(1,7); vertex(27,6)=vertex(1,5); vertex(27,7)=vertex(1,8); vertex(27,8)=vertex(1,6);
vertex(28,5)=vertex(1,7); vertex(28,6)=vertex(1,8); vertex(28,7)=vertex(1,6); vertex(28,8)=vertex(1,5);
vertex(29,5)=vertex(1,8); vertex(29,6)=vertex(1,7); vertex(29,7)=vertex(1,5); vertex(29,8)=vertex(1,6);
vertex(30,5)=vertex(1,6); vertex(30,6)=vertex(1,7); vertex(30,7)=vertex(1,8); vertex(30,8)=vertex(1,5);
vertex(31,5)=vertex(1,8); vertex(31,6)=vertex(1,5); vertex(31,7)=vertex(1,6); vertex(31,8)=vertex(1,7);
vertex(32,5)=vertex(1,2); vertex(32,6)=vertex(1,1); vertex(32,7)=vertex(1,3); vertex(32,8)=vertex(1,4);
vertex(33,5)=vertex(1,3); vertex(33,6)=vertex(1,1); vertex(33,7)=vertex(1,4); vertex(33,8)=vertex(1,2);
vertex(34,5)=vertex(1,3); vertex(34,6)=vertex(1,4); vertex(34,7)=vertex(1,2); vertex(34,8)=vertex(1,1);
vertex(35,5)=vertex(1,1); vertex(35,6)=vertex(1,3); vertex(35,7)=vertex(1,2); vertex(35,8)=vertex(1,4);
vertex(36,5)=vertex(1,1); vertex(36,6)=vertex(1,2); vertex(36,7)=vertex(1,4); vertex(36,8)=vertex(1,3);
vertex(37,5)=vertex(1,2); vertex(37,6)=vertex(1,4); vertex(37,7)=vertex(1,1); vertex(37,8)=vertex(1,3);
vertex(38,5)=vertex(1,4); vertex(38,6)=vertex(1,2); vertex(38,7)=vertex(1,3); vertex(38,8)=vertex(1,1);
vertex(39,5)=vertex(1,4); vertex(39,6)=vertex(1,3); vertex(39,7)=vertex(1,1); vertex(39,8)=vertex(1,2);
vertex(40,5)=vertex(1,3); vertex(40,6)=vertex(1,2); vertex(40,7)=vertex(1,1); vertex(40,8)=vertex(1,4);
vertex(41,5)=vertex(1,2); vertex(41,6)=vertex(1,3); vertex(41,7)=vertex(1,4); vertex(41,8)=vertex(1,1);
vertex(42,5)=vertex(1,1); vertex(42,6)=vertex(1,4); vertex(42,7)=vertex(1,3); vertex(42,8)=vertex(1,2);
vertex(43,5)=vertex(1,7); vertex(43,6)=vertex(1,6); vertex(43,7)=vertex(1,5); vertex(43,8)=vertex(1,8);
vertex(44,5)=vertex(1,5); vertex(44,6)=vertex(1,8); vertex(44,7)=vertex(1,7); vertex(44,8)=vertex(1,6);
vertex(45,5)=vertex(1,5); vertex(45,6)=vertex(1,6); vertex(45,7)=vertex(1,8); vertex(45,8)=vertex(1,7);
vertex(46,5)=vertex(1,6); vertex(46,6)=vertex(1,5); vertex(46,7)=vertex(1,7); vertex(46,8)=vertex(1,8);
vertex(47,5)=vertex(1,8); vertex(47,6)=vertex(1,6); vertex(47,7)=vertex(1,7); vertex(47,8)=vertex(1,5);
vertex(48,5)=vertex(1,5); vertex(48,6)=vertex(1,7); vertex(48,7)=vertex(1,6); vertex(48,8)=vertex(1,8);
end %if type

ss=size(vertex,1);
for vv=1:ss
%calculate shape measure
newalledges=zeros(nr,nr);
diff8d4d=zeros(nr,nr); diff8c2v=zeros(nr,nr); diff8d2d=zeros(nr,nr);
diff8oh=zeros(nr,nr); diff8d6h=zeros(nr,nr); diff8d3h=zeros(nr,nr);
 for i=1:nr,
  for j=1:nr,
  newalledges(i,j)=alledges(vertex(vv,i),vertex(vv,j));
  end %for j
 end %for i
newalledges=triu(newalledges);
 for i=1:nr,
  for j=1:nr,
   if newalledges(i,j)==1
   angle=degallangles(vertex(vv,i),vertex(vv,j));
    if angle==0
    angle=degallangles(vertex(vv,j),vertex(vv,i));
    end %if angle
   diff8d4d(i,j)=ideal8d4d(i,j)-angle;
   diff8c2v(i,j)=ideal8c2v(i,j)-angle;
   diff8d2d(i,j)=ideal8d2d(i,j)-angle;
   diff8oh(i,j)=ideal8oh(i,j)-angle;
```

```matlab
  diff8d6h(i,j)=ideal8d6h(i,j)-angle;
  diff8d3h(i,j)=ideal8d3h(i,j)-angle;
   end %if
  end %for j
 end %for i
 for i=1:nr,
  for j=1:nr,
   if diff8d4d(i,j)==0 & ideal8d4d(i,j)~=0
   diff8d4d(i,j)=ideal8d4d(i,j);
    end %if
   if diff8c2v(i,j)==0 & ideal8c2v(i,j)~=0
   diff8c2v(i,j)=ideal8c2v(i,j);
    end %if
   if diff8d2d(i,j)==0 & ideal8d2d(i,j)~=0
   diff8d2d(i,j)=ideal8d2d(i,j);
    end %if
   if diff8oh(i,j)==0 & ideal8oh(i,j)~=0
   diff8oh(i,j)=ideal8oh(i,j);
    end %if
   if diff8d6h(i,j)==0 & ideal8d6h(i,j)~=0
   diff8d6h(i,j)=ideal8d6h(i,j);
    end %if
   if diff8d3h(i,j)==0 & ideal8d3h(i,j)~=0
   diff8d3h(i,j)=ideal8d3h(i,j);
    end %if
  end %for j
 end %for i
 sum8d4d(vv)=sum(sum(diff8d4d.^2));
 sum8c2v(vv)=sum(sum(diff8c2v.^2));
 sum8d2d(vv)=sum(sum(diff8d2d.^2));
 sum8d6h(vv)=sum(sum(diff8d6h.^2));
 sum8oh(vv)=sum(sum(diff8oh.^2));
 sum8d3h(vv)=sum(sum(diff8d3h.^2));
end %for vv

%load the shape minimized alignments
ii=0; jj=0; kk=0; mm=0; nn=0;
for vv=1:ss
 if sum8d6h(1,vv)==min(sum8d6h)
 ii=vv;
  end %if
 if sum8d3h(1,vv)==min(sum8d3h)
 jj=vv;
  end %if
 if sum8c2v(1,vv)==min(sum8c2v)
 mm=vv;
  end %if
 if sum8d4d(1,vv)==min(sum8d4d)
 nn=vv;
  end %if
 if sum8d2d(1,vv)==min(sum8d2d)
 kk=vv;
  end %if
 end %for vv
 for vv=1:8
```

```
if abs(min(sum8d2d)-min(sum8d2d(1,vv))) <=0.001
kk=vv;
 end %if
end %for vv
for vv=1:ss
 if abs(sum8d2d(1,vv)-min(sum8d2d)+sum8c2v(1,vv)-min(sum8c2v))<=0.001
kk=vv;
 mm=vv;
 end %if
end %for vv
if abs(sum8d4d(1,kk)-min(sum8d4d))<=0.001
nn=kk;
end %if
if abs(sum8d6h(1,kk)-min(sum8d6h))<=0.001
ii=kk;
end %if
if abs(sum8d3h(1,kk)-min(sum8d3h))<=0.001
jj=kk;
end %if

if type==0
%calculate theta twist angle
centroidA1=(P(vertex(kk,1),:)+P(vertex(kk,2),:))/2;
centroidB1=(P(vertex(kk,6),:)+P(vertex(kk,7),:))/2;
centroidA2=(P(vertex(kk,3),:)+P(vertex(kk,4),:))/2;
centroidB2=(P(vertex(kk,5),:)+P(vertex(kk,8),:))/2;
vector1=cross(centroidA1-P(vertex(kk,2),:),centroidB1-centroidA1);
vector2=cross(centroidB1-P(vertex(kk,6),:),centroidB1-centroidA1);
vector3=cross(centroidA2-P(vertex(kk,4),:),centroidB2-centroidA2);
vector4=cross(centroidB2-P(vertex(kk,8),:),centroidB2-centroidA2);
twist(1,1)=acos((vector1*vector2')/(norm(vector1)*norm(vector2)))*180/pi;
twist(1,2)=acos((vector3*vector4')/(norm(vector3)*norm(vector4)))*180/pi;
end %if type==0

%sort the measured shape angles
finalangles=zeros(nr,nr);
for i=1:nr,
 for j=1:nr,
 newalledges(i,j)=alledges(vertex(kk,i),vertex(kk,j));
 end %for j
end %for i
newalledges=triu(newalledges);
for i=1:nr,
 for j=1:nr,
 if newalledges(i,j)==1
 angle=degallangles(vertex(kk,i),vertex(kk,j));
  if angle==0
  angle=degallangles(vertex(kk,j),vertex(kk,i));
  end %if angle
  finalangles(i,j)=angle;
 end %if newalledges
 end %for j
end %for i

%sort the c2v ideal angles
```

```
newideal8c2v=zeros(nr,nr);
for i=1:nr,
 for j=1:nr,
  if ideal8c2v(i,j)~=0
   for m=1:nr
    for n=1:nr
     if vertex(mm,i)==vertex(kk,m) & vertex(mm,j)==vertex(kk,n)
           newideal8c2v(m,n)=ideal8c2v(i,j);
           newideal8c2v(n,m)=ideal8c2v(i,j);
     end %if
    end %for n
   end %for m
  end %if newalledges1
 end %for j
end %for i
newideal8c2v=triu(newideal8c2v);

%sort the d4d ideal angles
newideal8d4d=zeros(nr,nr);
for i=1:nr,
 for j=1:nr,
  if ideal8d4d(i,j)~=0
   for m=1:nr
    for n=1:nr
     if vertex(nn,i)==vertex(kk,m) & vertex(nn,j)==vertex(kk,n)
           newideal8d4d(m,n)=ideal8d4d(i,j);
           newideal8d4d(n,m)=ideal8d4d(i,j);
     end %if
    end %for n
   end %for m
  end %if newalledges1
 end %for j
end %for i
newideal8d4d=triu(newideal8d4d);

%sort the d6h ideal angles
newideal8d6h=zeros(nr,nr);
for i=1:nr,
 for j=1:nr,
  if ideal8d6h(i,j)~=0
   for m=1:nr
    for n=1:nr
     if vertex(ii,i)==vertex(kk,m) & vertex(ii,j)==vertex(kk,n)
           newideal8d6h(m,n)=ideal8d6h(i,j);
           newideal8d6h(n,m)=ideal8d6h(i,j);
     end %if
    end %for n
   end %for m
  end %if newalledges1
 end %for j
end %for i
newideal8d6h=triu(newideal8d6h);

%sort the d3h ideal angles
newideal8d3h=zeros(nr,nr);
```

```
for i=1:nr,
 for j=1:nr,
  if ideal8d3h(i,j)~=0
   for m=1:nr
    for n=1:nr
     if vertex(jj,i)==vertex(kk,m) & vertex(jj,j)==vertex(kk,n)
          newideal8d3h(m,n)=ideal8d3h(i,j);
          newideal8d3h(n,m)=ideal8d3h(i,j);
     end %if
    end %for n
   end %for m
  end %if newalledges1
 end %for j
end %for i
newideal8d3h=triu(newideal8d3h);

%print results
sindex(1,1)=sqrt(min(sum8d4d)/18);
sindex(1,2)=sqrt(min(sum8c2v)/18);
sindex(1,3)=sqrt(min(sum8d2d)/18);
sindex(1,4)=sqrt(min(sum8oh)/18);
sindex(1,5)=sqrt(min(sum8d6h)/18);
sindex(1,6)=sqrt(min(sum8d3h)/18);

sindex1(1,1)=finalangles(5,6); sindex1(2,1)=finalangles(7,8); sindex1(3,1)=finalangles(5,7);
sindex1(4,1)=finalangles(6,8); sindex2(1,1)=finalangles(1,2); sindex2(2,1)=finalangles(3,4);
sindex2(3,1)=finalangles(1,5); sindex2(4,1)=finalangles(4,6); sindex2(5,1)=finalangles(2,8);
sindex2(6,1)=finalangles(3,7); sindex2(7,1)=finalangles(2,5); sindex2(8,1)=finalangles(3,6);
sindex2(9,1)=finalangles(1,8); sindex2(10,1)=finalangles(4,7); sindex2(11,1)=finalangles(1,7);
sindex2(12,1)=finalangles(4,8); sindex2(13,1)=finalangles(2,6); sindex2(14,1)=finalangles(3,5);
sindex2(15,1)=finalangles(1,3); sindex2(16,1)=finalangles(1,4); sindex2(17,1)=finalangles(6,7);
sindex2(18,1)=finalangles(2,3); sindex2(19,1)=finalangles(2,4); sindex2(20,1)=finalangles(5,8);

sindex3(1,1)=newideal8d4d(5,6); sindex3(2,1)=newideal8d4d(7,8); sindex3(3,1)=newideal8d4d(5,7);
sindex3(4,1)=newideal8d4d(6,8); sindex4(1,1)=newideal8d4d(1,2); sindex4(2,1)=newideal8d4d(3,4);
sindex4(3,1)=newideal8d4d(1,5); sindex4(4,1)=newideal8d4d(4,6); sindex4(5,1)=newideal8d4d(2,8);
sindex4(6,1)=newideal8d4d(3,7); sindex4(7,1)=newideal8d4d(2,5); sindex4(8,1)=newideal8d4d(3,6);
sindex4(9,1)=newideal8d4d(1,8); sindex4(10,1)=newideal8d4d(4,7); sindex4(11,1)=newideal8d4d(1,7);
sindex4(12,1)=newideal8d4d(4,8); sindex4(13,1)=newideal8d4d(2,6); sindex4(14,1)=newideal8d4d(3,5);
sindex4(15,1)=newideal8d4d(1,3); sindex4(16,1)=newideal8d4d(1,4); sindex4(17,1)=newideal8d4d(6,7);
sindex4(18,1)=newideal8d4d(2,3); sindex4(19,1)=newideal8d4d(2,4); sindex4(20,1)=newideal8d4d(5,8);

sindex5(1,1)=newideal8c2v(5,6); sindex5(2,1)=newideal8c2v(7,8); sindex5(3,1)=newideal8c2v(5,7);
sindex5(4,1)=newideal8c2v(6,8); sindex6(1,1)=newideal8c2v(1,2); sindex6(2,1)=newideal8c2v(3,4);
sindex6(3,1)=newideal8c2v(1,5); sindex6(4,1)=newideal8c2v(4,6); sindex6(5,1)=newideal8c2v(2,8);
sindex6(6,1)=newideal8c2v(3,7); sindex6(7,1)=newideal8c2v(2,5); sindex6(8,1)=newideal8c2v(3,6);
sindex6(9,1)=newideal8c2v(1,8); sindex6(10,1)=newideal8c2v(4,7); sindex6(11,1)=newideal8c2v(1,7);
sindex6(12,1)=newideal8c2v(4,8); sindex6(13,1)=newideal8c2v(2,6); sindex6(14,1)=newideal8c2v(3,5);
sindex6(15,1)=newideal8c2v(1,3); sindex6(16,1)=newideal8c2v(1,4); sindex6(17,1)=newideal8c2v(6,7);
sindex6(18,1)=newideal8c2v(2,3); sindex6(19,1)=newideal8c2v(2,4); sindex6(20,1)=newideal8c2v(5,8);

sindex7(1,1)=ideal8d2d(5,6); sindex7(2,1)=ideal8d2d(7,8); sindex7(3,1)=ideal8d2d(5,7);
sindex7(4,1)=ideal8d2d(6,8); sindex8(1,1)=ideal8d2d(1,2); sindex8(2,1)=ideal8d2d(3,4);
sindex8(3,1)=ideal8d2d(1,5); sindex8(4,1)=ideal8d2d(4,6); sindex8(5,1)=ideal8d2d(2,8);
sindex8(6,1)=ideal8d2d(3,7); sindex8(7,1)=ideal8d2d(2,5); sindex8(8,1)=ideal8d2d(3,6);
```

```
sindex8(9,1)=ideal8d2d(1,8); sindex8(10,1)=ideal8d2d(4,7); sindex8(11,1)=ideal8d2d(1,7);
sindex8(12,1)=ideal8d2d(4,8); sindex8(13,1)=ideal8d2d(2,6); sindex8(14,1)=ideal8d2d(3,5);
sindex8(15,1)=ideal8d2d(1,3); sindex8(16,1)=ideal8d2d(1,4); sindex8(17,1)=ideal8d2d(6,7);
sindex8(18,1)=ideal8d2d(2,3); sindex8(19,1)=ideal8d2d(2,4); sindex8(20,1)=ideal8d2d(5,8);

sindex9(1,1)=ideal8oh(5,6); sindex9(2,1)=ideal8oh(7,8); sindex9(3,1)=ideal8oh(5,7);
sindex9(4,1)=ideal8oh(6,8); sindex10(1,1)=ideal8oh(1,2); sindex10(2,1)=ideal8oh(3,4);
sindex10(3,1)=ideal8oh(1,5); sindex10(4,1)=ideal8oh(4,6); sindex10(5,1)=ideal8oh(2,8);
sindex10(6,1)=ideal8oh(3,7); sindex10(7,1)=ideal8oh(2,5); sindex10(8,1)=ideal8oh(3,6);
sindex10(9,1)=ideal8oh(1,8); sindex10(10,1)=ideal8oh(4,7); sindex10(11,1)=ideal8oh(1,7);
sindex10(12,1)=ideal8oh(4,8); sindex10(13,1)=ideal8oh(2,6); sindex10(14,1)=ideal8oh(3,5);
sindex10(15,1)=ideal8oh(1,3); sindex10(16,1)=ideal8oh(1,4); sindex10(17,1)=ideal8oh(6,7);
sindex10(18,1)=ideal8oh(2,3); sindex10(19,1)=ideal8oh(2,4); sindex10(20,1)=ideal8oh(5,8);

sindex11(1,1)=newideal8d6h(5,6); sindex11(2,1)=newideal8d6h(7,8); sindex11(3,1)=newideal8d6h(5,7);
sindex11(4,1)=newideal8d6h(6,8); sindex12(1,1)=newideal8d6h(1,2); sindex12(2,1)=newideal8d6h(3,4);
sindex12(3,1)=newideal8d6h(1,5); sindex12(4,1)=newideal8d6h(4,6); sindex12(5,1)=newideal8d6h(2,8);
sindex12(6,1)=newideal8d6h(3,7); sindex12(7,1)=newideal8d6h(2,5); sindex12(8,1)=newideal8d6h(3,6);
sindex12(9,1)=newideal8d6h(1,8); sindex12(10,1)=newideal8d6h(4,7); sindex12(11,1)=newideal8d6h(1,7);
sindex12(12,1)=newideal8d6h(4,8); sindex12(13,1)=newideal8d6h(2,6); sindex12(14,1)=newideal8d6h(3,5);
sindex12(15,1)=newideal8d6h(1,3); sindex12(16,1)=newideal8d6h(1,4); sindex12(17,1)=newideal8d6h(6,7);
sindex12(18,1)=newideal8d6h(2,3); sindex12(19,1)=newideal8d6h(2,4); sindex12(20,1)=newideal8d6h(5,8);

sindex13(1,1)=newideal8d3h(5,6); sindex13(2,1)=newideal8d3h(7,8); sindex13(3,1)=newideal8d3h(5,7);
sindex13(4,1)=newideal8d3h(6,8); sindex14(1,1)=newideal8d3h(1,2); sindex14(2,1)=newideal8d3h(3,4);
sindex14(3,1)=newideal8d3h(1,5); sindex14(4,1)=newideal8d3h(4,6); sindex14(5,1)=newideal8d3h(2,8);
sindex14(6,1)=newideal8d3h(3,7); sindex14(7,1)=newideal8d3h(2,5); sindex14(8,1)=newideal8d3h(3,6);
sindex14(9,1)=newideal8d3h(1,8); sindex14(10,1)=newideal8d3h(4,7); sindex14(11,1)=newideal8d3h(1,7);
sindex14(12,1)=newideal8d3h(4,8); sindex14(13,1)=newideal8d3h(2,6); sindex14(14,1)=newideal8d3h(3,5);
sindex14(15,1)=newideal8d3h(1,3); sindex14(16,1)=newideal8d3h(1,4); sindex14(17,1)=newideal8d3h(6,7);
sindex14(18,1)=newideal8d3h(2,3); sindex14(19,1)=newideal8d3h(2,4); sindex14(20,1)=newideal8d3h(5,8);

if type==3
sindex2(21,1)=finalangles(4,5); sindex4(21,1)=newideal8d4d(4,5); sindex6(21,1)=newideal8c2v(4,5);
sindex8(21,1)=ideal8d2d(4,5); sindex10(21,1)=ideal8oh(4,5);
sindex12(21,1)=newideal8d6h(4,5); sindex14(21,1)=newideal8d3h(4,5);
end %if

shapeangles=[sindex1,sindex3,sindex5,sindex7,sindex9,sindex11,sindex13];
otherangles=[sindex2,sindex4,sindex6,sindex8,sindex10,sindex12,sindex14];
format bank
disp(['Shape Analysis of ', title,' is:']);
disp('   D4d   C2v   D2d    Oh   D6h   D3h'); disp(sindex);
disp(' ');
if longanalysis == 1
if type==0
disp('Shape Determining Angles:');
disp(['Measured',' D4d ',' C2v ',' D2d',   Oh ',' D6h',' D3h']);
disp(shapeangles);
disp(' ');
disp('Other Angles:');
disp(['Measured',   D4d ',' C2v ',' D2d',   Oh ',' D6h',' D3h']);
disp(otherangles);
disp(' ');
disp('Phi Twist Angles:');
```

```
disp(twist);
end %if type==0
if type~=0
disp('Delta Angles:');
disp(['Measured','    D4d ','  C2v ','  D2d','    Oh ','  D6h','   D3h']);
disp([shapeangles;otherangles]);
end %if type~=0
end %if longanalysis
end %if nr==8


%--------------------------------------------------
%Section J: 9-Coordinate Shape Analysis
%--------------------------------------------------

if nr==9
%find the three 4-edge vertices
for i=1:nr,
 if sum(alledges(i,:))==4
  for j=1:nr,
   if i~=j & sum(alledges(j,:))==4
    for k=1:nr,
     if i~=k & j~=k & sum(alledges(k,:))==4
     vertex(1,3)=i;
     vertex(1,2)=j;
     vertex(1,1)=k;
     end %if
    end %for k
   end %if
  end %for j
 end %if sum
end %for i

%generate all possible permutations
vertex(2,1)=vertex(1,2); vertex(2,2)=vertex(1,3);
vertex(2,3)=vertex(1,1); vertex(3,1)=vertex(1,3);
vertex(3,2)=vertex(1,1); vertex(3,3)=vertex(1,2);

%find the 5-edge vertices by connectivity
for vv=1:3,
 for i=1:nr,
  if alledges(i,vertex(vv,1))==1 & alledges(i,vertex(vv,2))==1
  vertex(vv,4)=i;
  end %if
 end %for i
 for i=1:nr,
  if alledges(i,vertex(vv,1))==1 & alledges(i,vertex(vv,2))==1 & alledges(i,vertex(vv,4))==1
  vertex(vv,5)=i;
  end %if
 end %for i
 for i=1:nr,
  if alledges(i,vertex(vv,2))==1 & alledges(i,vertex(vv,3))==1 & alledges(i,vertex(vv,4))==1
  vertex(vv,6)=i;
  end %if
  if alledges(i,vertex(vv,2))==1 & alledges(i,vertex(vv,3))==1 & alledges(i,vertex(vv,5))==1
  vertex(vv,7)=i;
```

```
  end %if
 if alledges(i,vertex(vv,1))==1 & alledges(i,vertex(vv,3))==1 & alledges(i,vertex(vv,4))==1
 vertex(vv,8)=i;
  end %if
 if alledges(i,vertex(vv,1))==1 & alledges(i,vertex(vv,3))==1 & alledges(i,vertex(vv,5))==1
 vertex(vv,9)=i;
  end %if
 end %for i

%calculate shape measure
newalledges=zeros(9);
 for i=1:nr,
  for j=1:nr,
  newalledges(i,j)=alledges(vertex(vv,i),vertex(vv,j));
  end %for j
 end %for i
newalledges=triu(newalledges);
 for i=1:nr,
  for j=1:nr,
   if newalledges(i,j)==1
   angle=degallangles(vertex(vv,i),vertex(vv,j));
    if angle==0
    angle=degallangles(vertex(vv,j),vertex(vv,i));
    end %if angle
   diff9c4v(i,j)=ideal9c4v(i,j)-angle;
   diff9d3h(i,j)=ideal9d3h(i,j)-angle;
    end %if
  end %for j
 end %for i
sum9c4v(vv)=sum(sum(diff9c4v.^2));
sum9d3h(vv)=sum(sum(diff9d3h.^2));
 end %for vv

%load the shape minimized alignment
kk=0;
i=min(sum9c4v);
j=min(sum9d3h);
for vv=1:3
 if (sum9c4v(1,vv)-i+sum9d3h(1,vv)-j)<=.000001 & (sum9c4v(1,vv)-i+sum9d3h(1,vv)-j)>=-.000001
 kk=vv;
 end %if
end %for vv
for i=1:nr,
 for j=1:nr,
 newalledges(i,j)=alledges(vertex(kk,i),vertex(kk,j));
 end %for j
end %for i
newalledges=triu(newalledges);
for i=1:nr,
 for j=1:nr,
  if newalledges(i,j)==1
  angle=degallangles(vertex(kk,i),vertex(kk,j));
   if angle==0
   angle=degallangles(vertex(kk,j),vertex(kk,i));
   end %if angle
```

168

```
   finalangles(i,j)=angle;
  end %if newalledges
 end %for j
end %for i

%print results
sindex(1,1)=sqrt(min(sum9d3h)/21);
sindex(1,2)=sqrt(min(sum9c4v)/21);

sindex1(1,1)=finalangles(6,7); sindex1(2,1)=finalangles(4,5); sindex1(3,1)=finalangles(8,9);
sindex1(4,1)=finalangles(4,8); sindex1(5,1)=finalangles(5,9); sindex2(1,1)=finalangles(4,6);
sindex2(2,1)=finalangles(6,8); sindex2(3,1)=finalangles(5,7); sindex2(4,1)=finalangles(7,9);
sindex2(5,1)=finalangles(3,8); sindex2(6,1)=finalangles(3,9); sindex2(7,1)=finalangles(2,4);
sindex2(8,1)=finalangles(2,5); sindex2(9,1)=finalangles(1,8); sindex2(10,1)=finalangles(1,9);
sindex2(11,1)=finalangles(1,4); sindex2(12,1)=finalangles(1,5); sindex2(13,1)=finalangles(3,6);
sindex2(14,1)=finalangles(3,7); sindex2(15,1)=finalangles(2,6); sindex2(16,1)=finalangles(2,7);

sindex3(1,1)=ideal9d3h(6,7); sindex3(2,1)=ideal9d3h(4,5); sindex3(3,1)=ideal9d3h(8,9);
sindex3(4,1)=ideal9d3h(4,8); sindex3(5,1)=ideal9d3h(5,9); sindex4(1,1)=ideal9d3h(4,6);
sindex4(2,1)=ideal9d3h(6,8); sindex4(3,1)=ideal9d3h(5,7); sindex4(4,1)=ideal9d3h(7,9);
sindex4(5,1)=ideal9d3h(3,8); sindex4(6,1)=ideal9d3h(3,9); sindex4(7,1)=ideal9d3h(2,4);
sindex4(8,1)=ideal9d3h(2,5); sindex4(9,1)=ideal9d3h(1,8); sindex4(10,1)=ideal9d3h(1,9);
sindex4(11,1)=ideal9d3h(1,4); sindex4(12,1)=ideal9d3h(1,5); sindex4(13,1)=ideal9d3h(3,6);
sindex4(14,1)=ideal9d3h(3,7); sindex4(15,1)=ideal9d3h(2,6); sindex4(16,1)=ideal9d3h(2,7);

sindex5(1,1)=ideal9c4v(6,7); sindex5(2,1)=ideal9c4v(4,5); sindex5(3,1)=ideal9c4v(8,9);
sindex5(4,1)=ideal9c4v(4,8); sindex5(5,1)=ideal9c4v(5,9); sindex6(1,1)=ideal9c4v(4,6);
sindex6(2,1)=ideal9c4v(6,8); sindex6(3,1)=ideal9c4v(5,7); sindex6(4,1)=ideal9c4v(7,9);
sindex6(5,1)=ideal9c4v(3,8); sindex6(6,1)=ideal9c4v(3,9); sindex6(7,1)=ideal9c4v(2,4);
sindex6(8,1)=ideal9c4v(2,5); sindex6(9,1)=ideal9c4v(1,8); sindex6(10,1)=ideal9c4v(1,9);
sindex6(11,1)=ideal9c4v(1,4); sindex6(12,1)=ideal9c4v(1,5); sindex6(13,1)=ideal9c4v(3,6);
sindex6(14,1)=ideal9c4v(3,7); sindex6(15,1)=ideal9c4v(2,6); sindex6(16,1)=ideal9c4v(2,7);

shapeangles=[sindex1,sindex3,sindex5];
otherangles=[sindex2,sindex4,sindex6];
format bank
disp(['Shape Analysis of ', title,' is:']);
disp('   D3h   C4v'); disp(sindex);
disp(' ');
if longanalysis == 1
disp('Shape Determining Angles:');
disp(['Measured',' D3h ',' C4v ']);
disp(shapeangles);
disp(' ');
disp('Other Angles:');
disp(['Measured',' D3h ',' C4v ']);
disp(otherangles);
end %if
end %if nr==9
```

Chapter 3 Appendix

**Luminescence Data, SIR Mixing Times, Probe Temperature Correction
^{1}H-NMR, COSY and EXSY Spectra, and XRD Data**
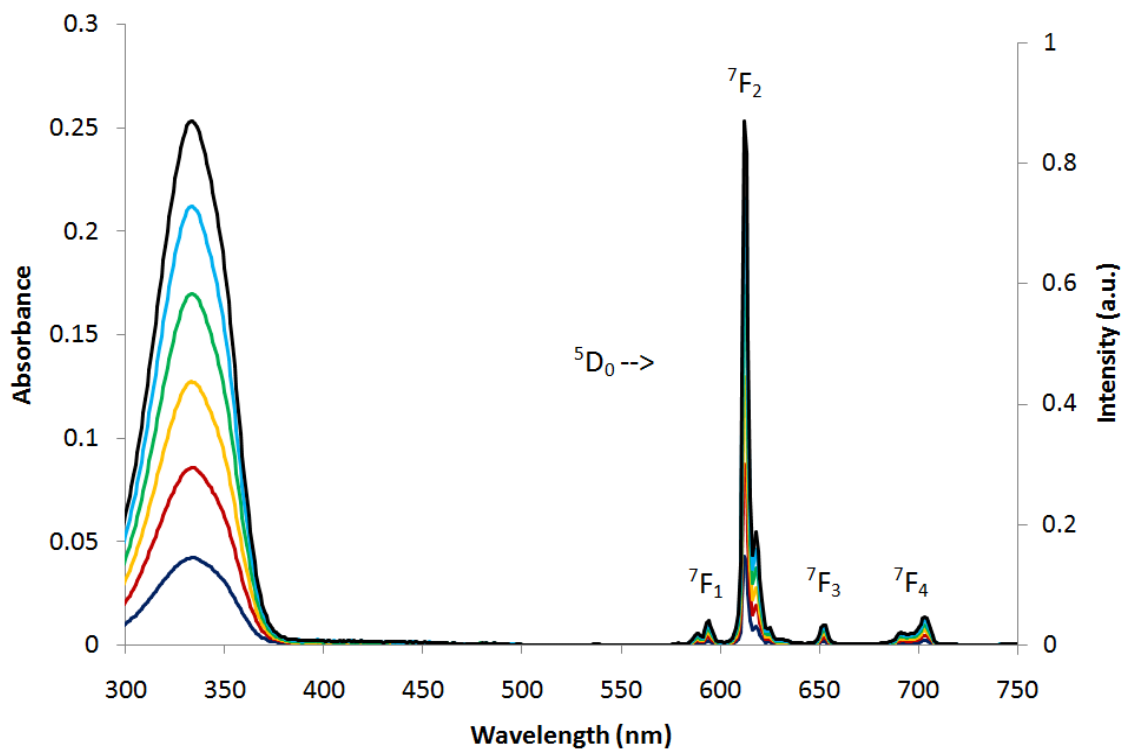
Figure A3.1. UV-vis absorption and visible luminescence of **Eu** in aqueous buffer
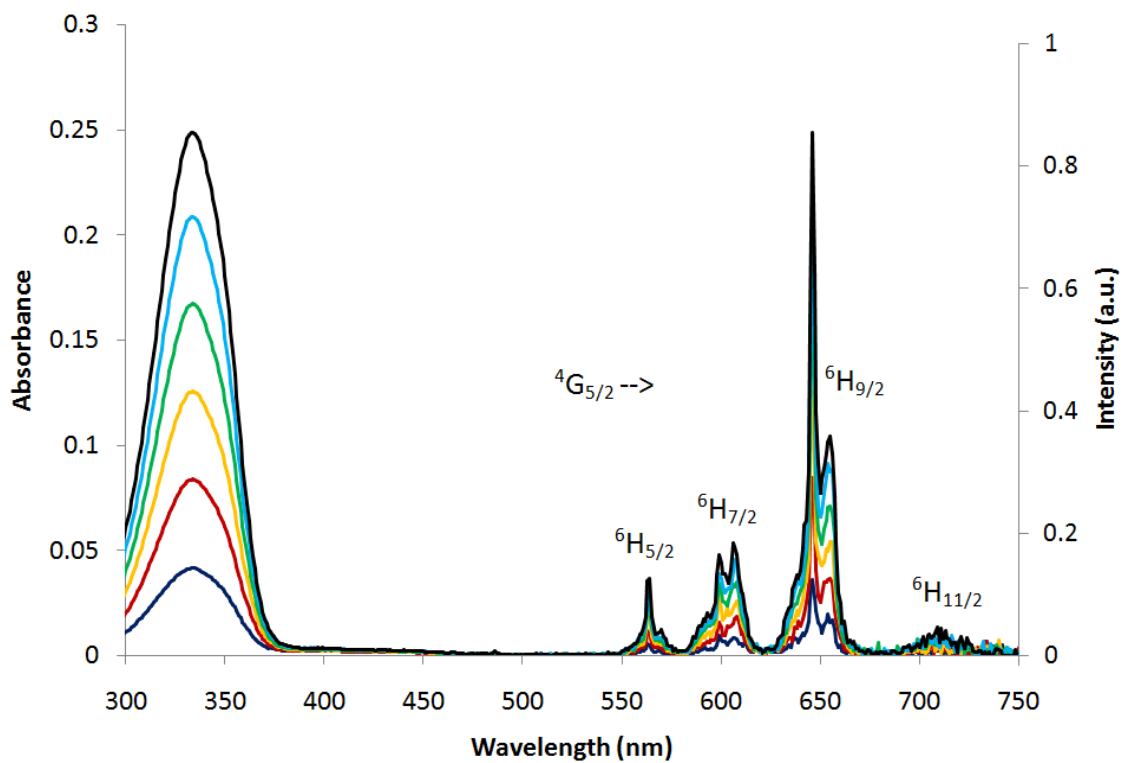
Figure A3.2. UV-vis absorption and visible luminescence of **Sm** in aqueous buffer
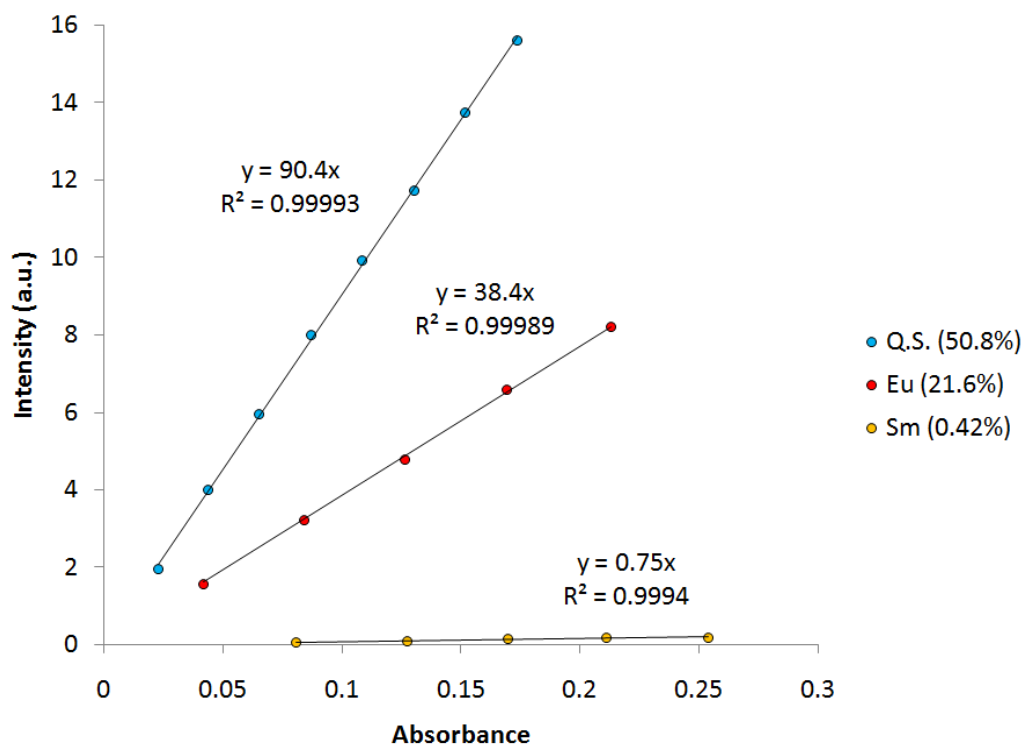
Figure A3.3. Quantum yield determination (**Eu** and **Sm**)- Day 1
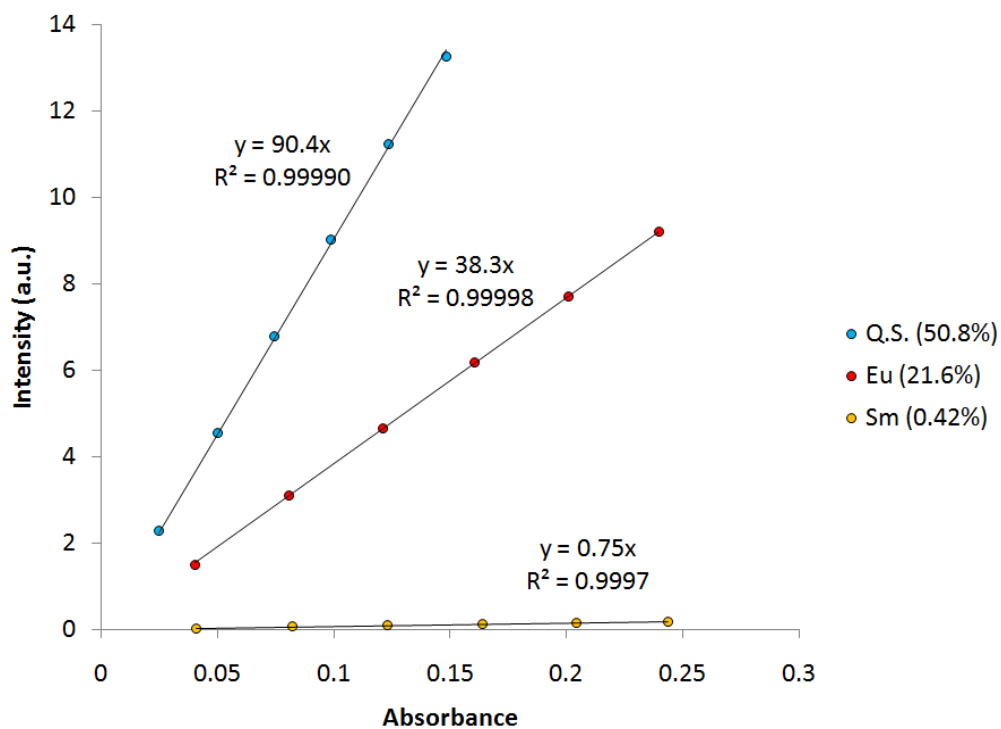
Figure A3.4. Quantum yield determination (**Eu** and **Sm**)- Day 2
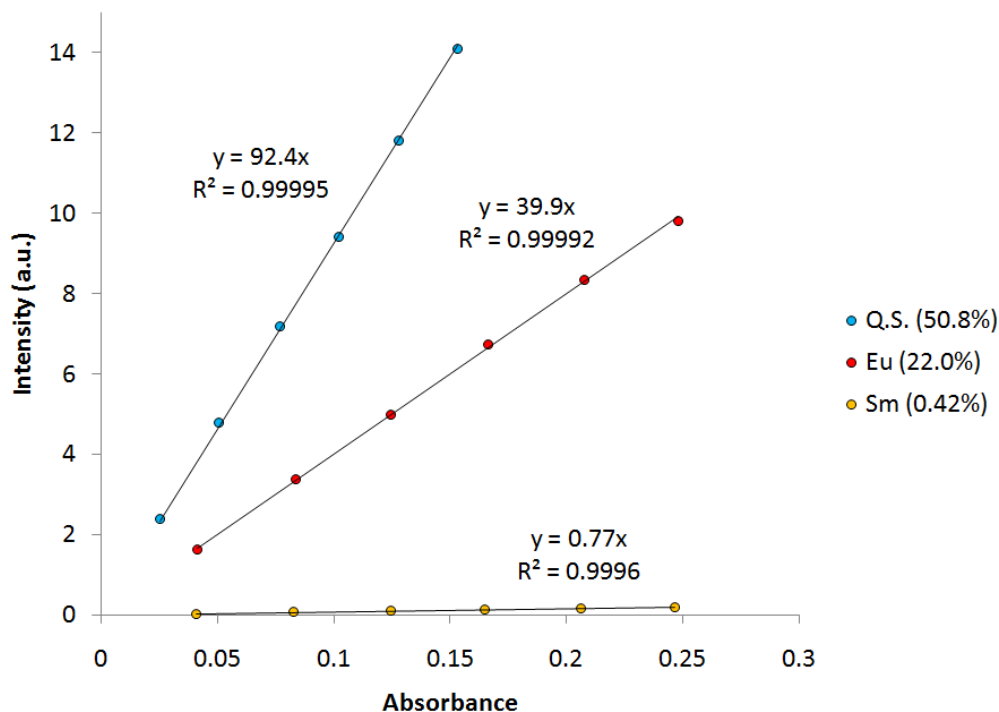
Figure A3.5. Quantum yield determination (**Eu** and **Sm**)- Day 3

Table A3.1. Variable delay list (in seconds) used for each complex in the SIR experiments

Lu, Eu, Sm	Yb	Er, Tm	Dy, Ho, Tb
0.00003	0.0005	0.0005	0.0005
0.0005	0.001	0.001	0.001
0.005	0.0015	0.0015	0.0015
0.015	0.002	0.002	0.002
0.025	0.0025	0.0025	0.0025
0.035	0.003	0.003	0.003
0.05	0.004	0.0035	0.0035
0.065	0.005	0.004	0.004
0.085	0.006	0.0045	0.0045
0.1	0.007	0.005	0.005
0.125	0.008	0.006	0.0055
0.16	0.009	0.007	0.006
0.2	0.01	0.008	0.0065
0.25	0.015	0.009	0.007
0.3	0.02	0.01	0.0075
0.35	0.025	0.011	0.008
0.4	0.03	0.012	0.0085
0.45	0.04	0.013	0.009
0.5	0.05	0.014	0.0095
0.55	0.06	0.015	0.01
0.6	0.07	0.016	0.011
0.65	0.08	0.018	0.012
0.7	0.09	0.02	0.013
0.75	0.1	0.022	0.014
0.8	0.15	0.025	0.015

0.85	0.2	0.03	0.016
0.9	0.25	0.035	0.017
1	0.3	0.04	0.018
1.25	0.4	0.045	0.019
1.5	0.5	0.05	0.02
1.75	0.6	0.055	0.025
2	0.7	0.06	0.03
2.5	0.8	0.065	0.035
3	0.9	0.07	0.04
4	1	0.075	0.045
5	1.1	0.08	0.05
6	1.2	0.085	0.055
8	1.3	0.09	0.06
10	1.4	0.1	0.07
12	1.5	0.125	0.1
15	2	0.15	0.2
18	3	0.2	0.5

$$y = 1.0329x - 0.2181$$
$$R^2 = 0.99995$$
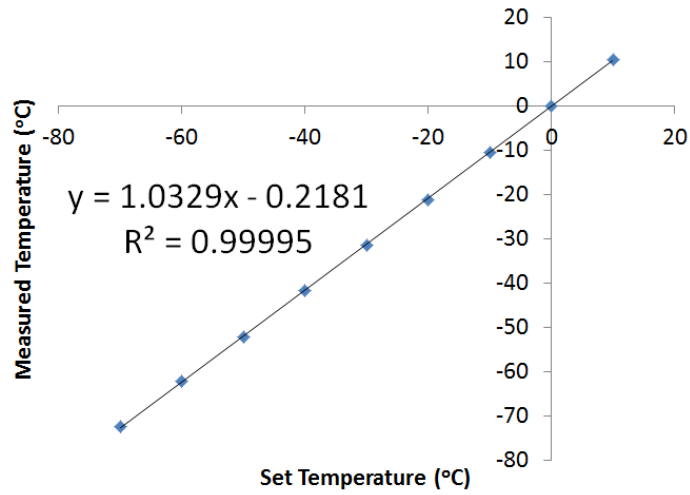
Figure A3.6. Variable temperature probe calibration used to correct SIR data
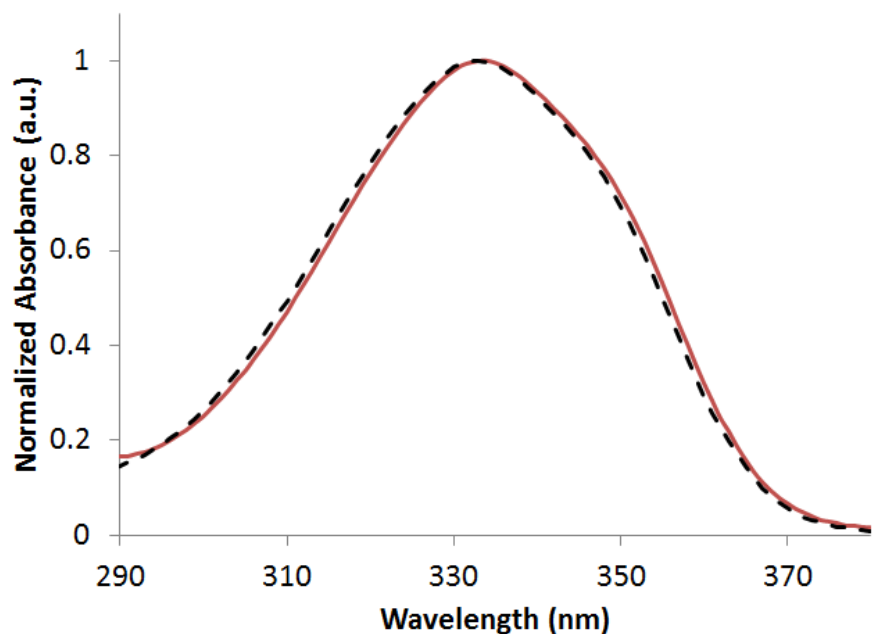
Figure A3.7. Overlay of **Eu** and [Eu(5LIO-1,2-HOPO)$_2$]$^-$ absorption spectra
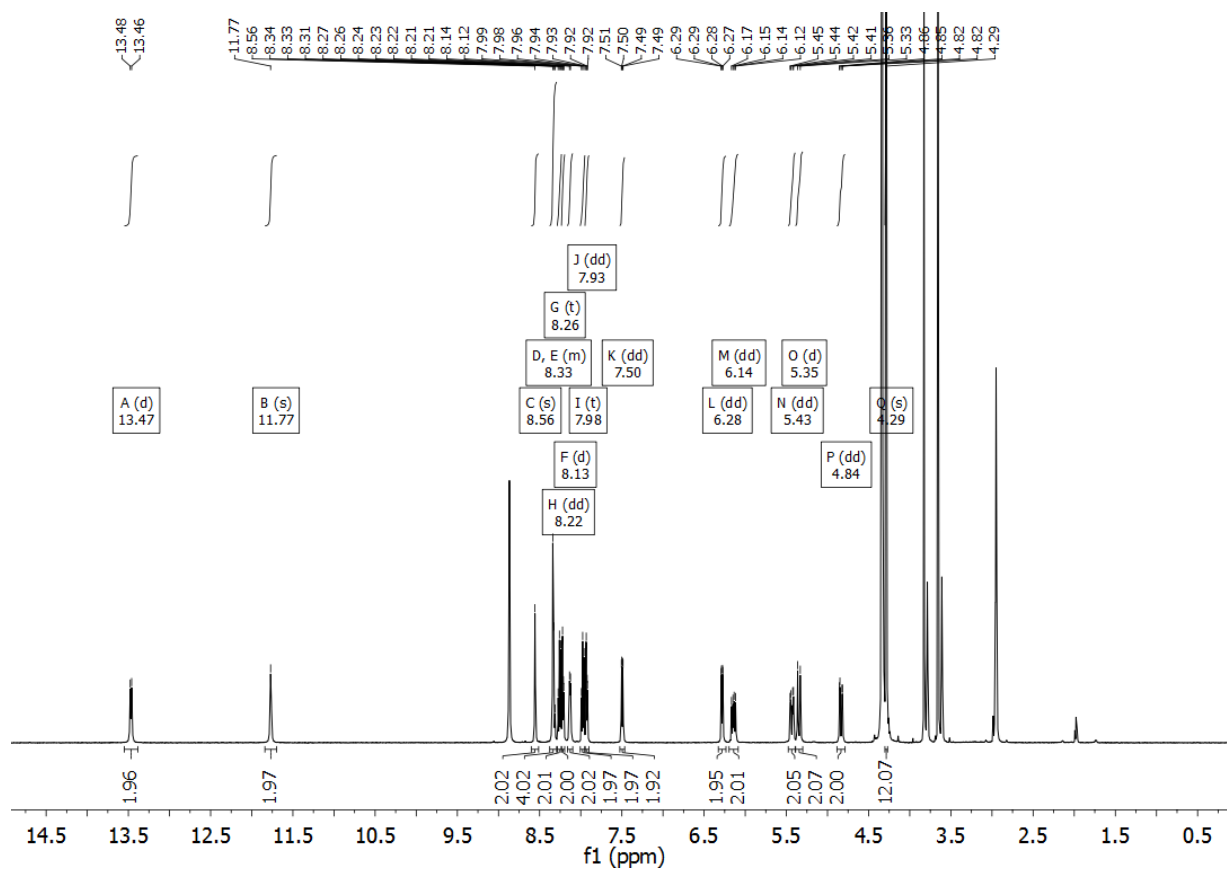
Figure A3.8. ^{1}H-NMR Spectrum of **Lu**
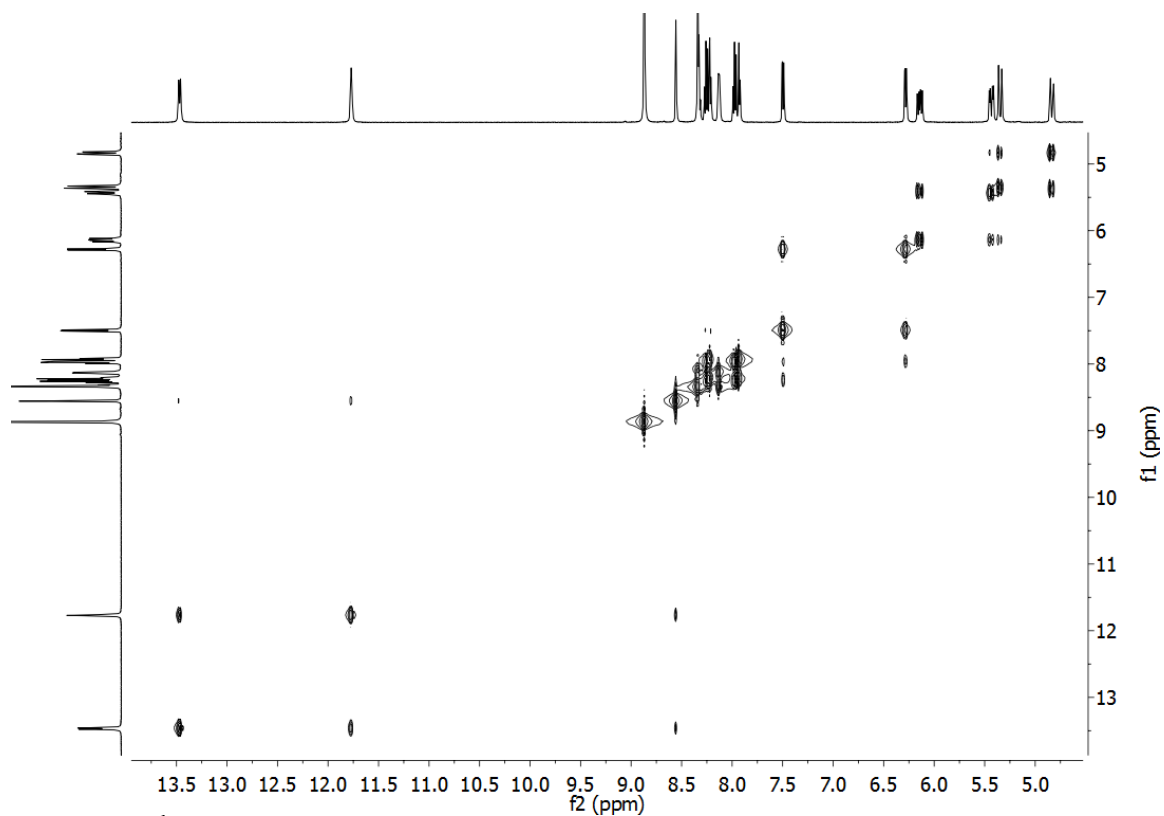
Figure A3.9. ^{1}H-NMR EXSY Spectrum of **Lu**
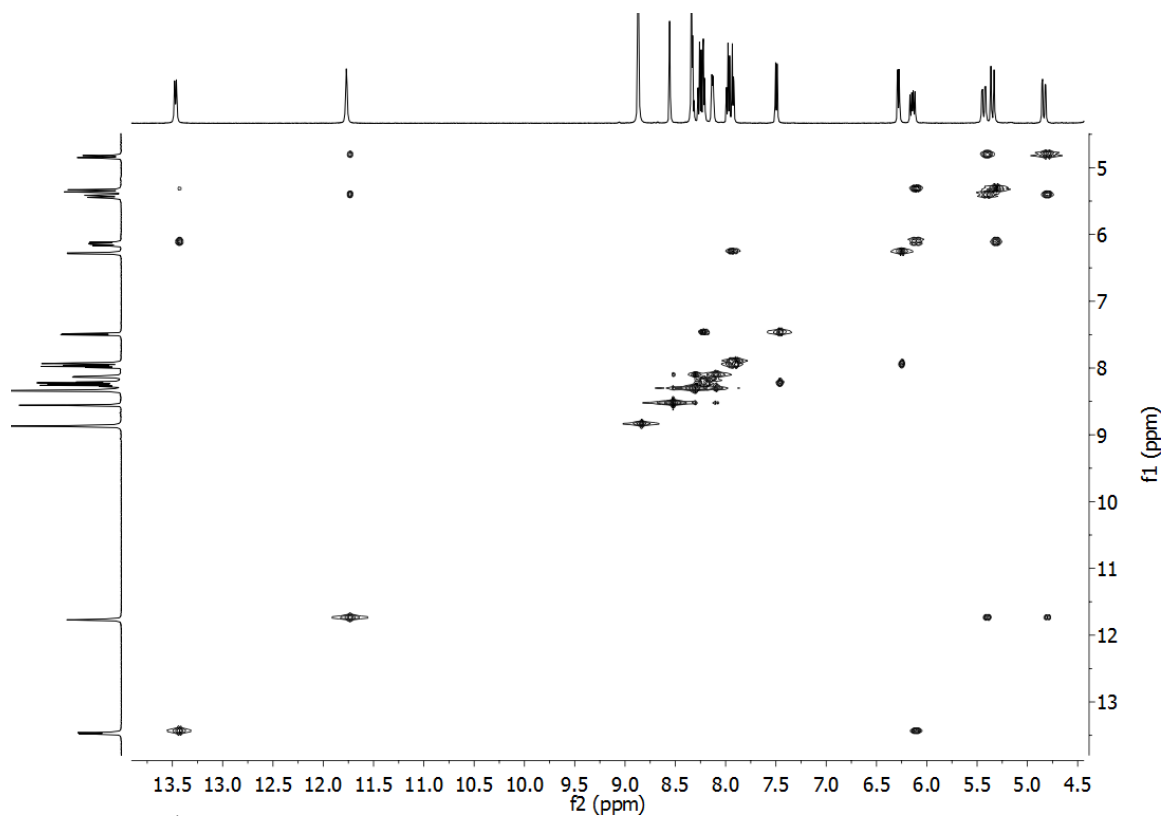
Figure A3.10. ^{1}H-NMR COSY Spectrum of **Lu**
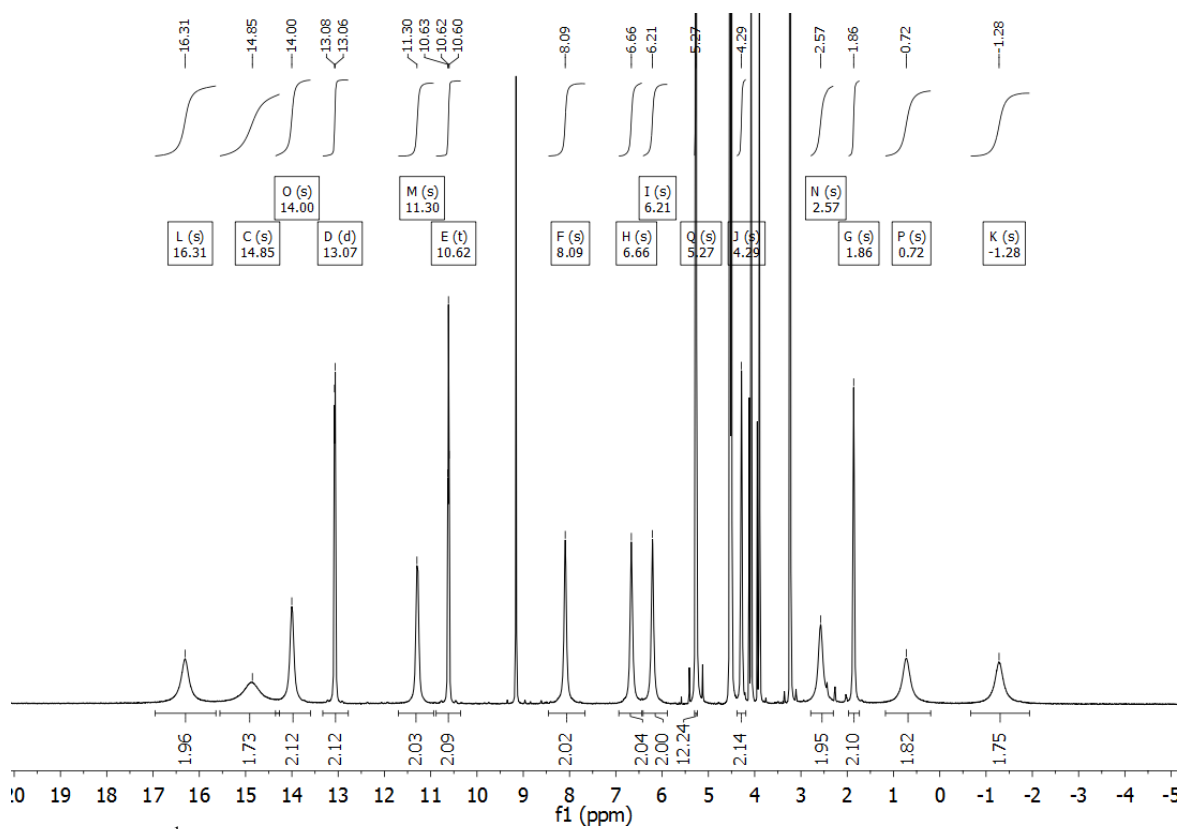
Figure A3.11. ^{1}H-NMR Spectrum of **Yb**
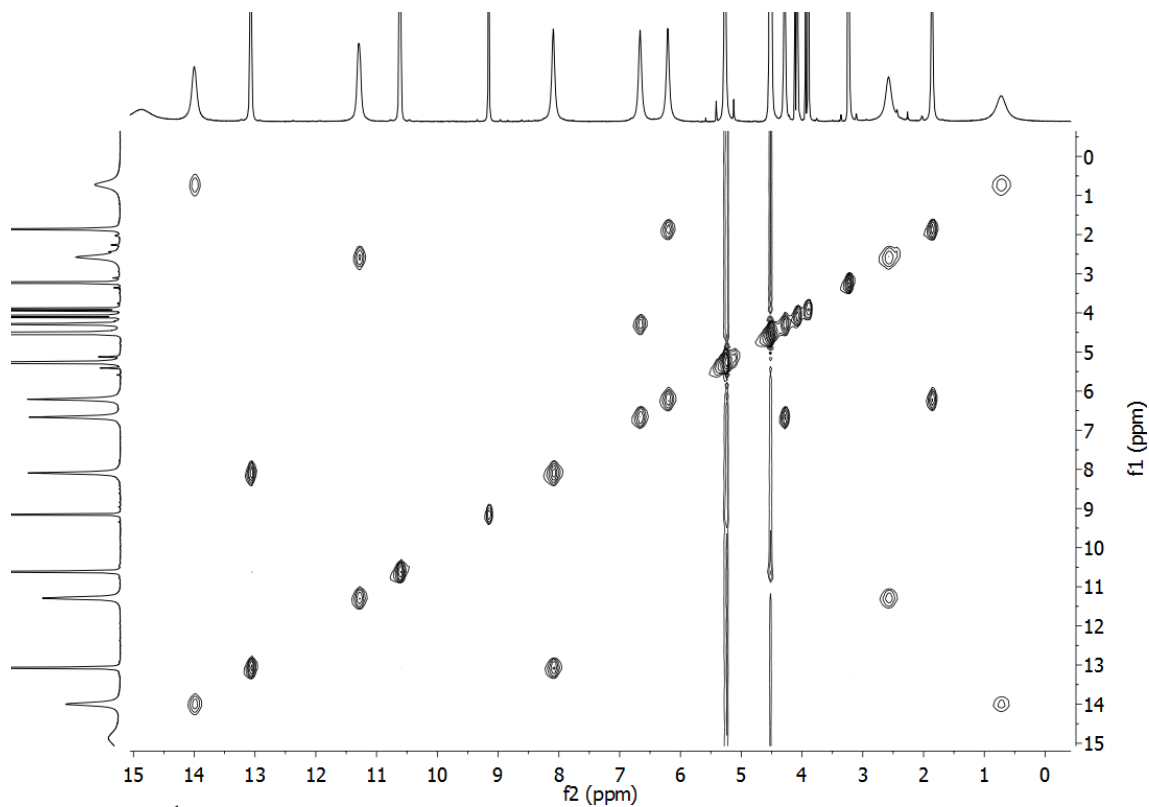
Figure A3.12. ^{1}H-NMR EXSY Spectrum of **Yb**
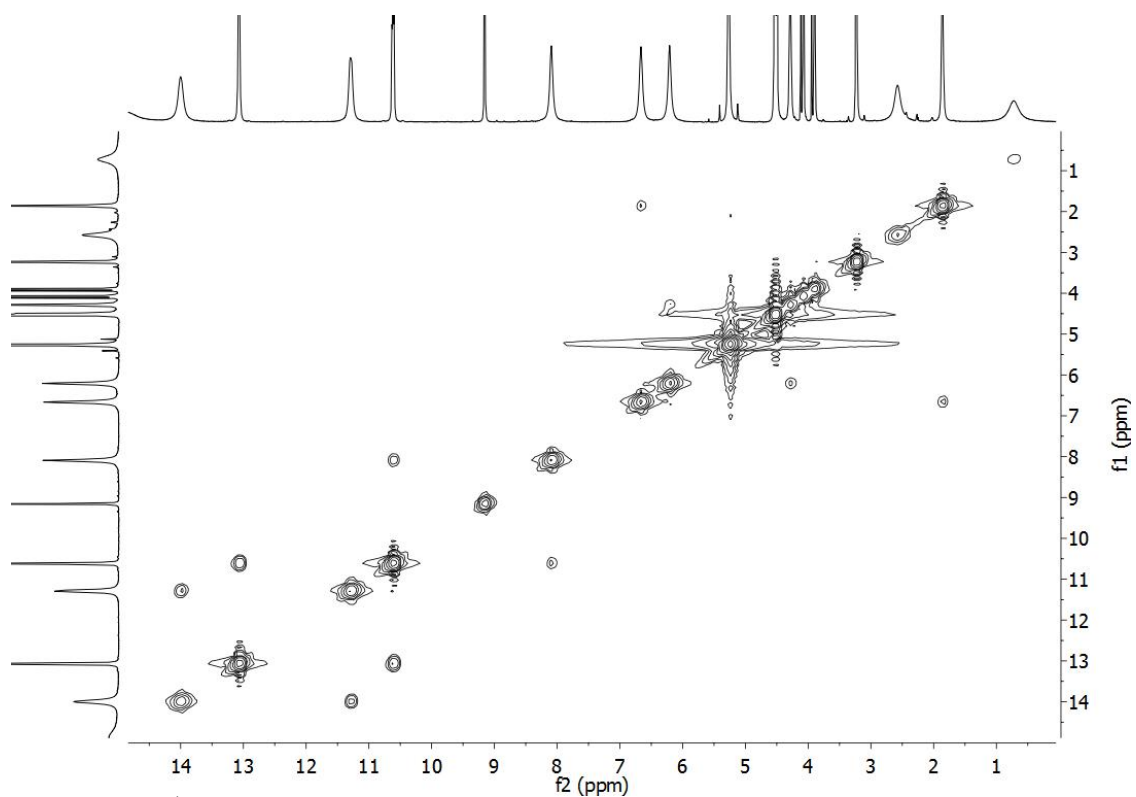
Figure A3.13. ^{1}H-NMR COSY Spectrum of **Yb**
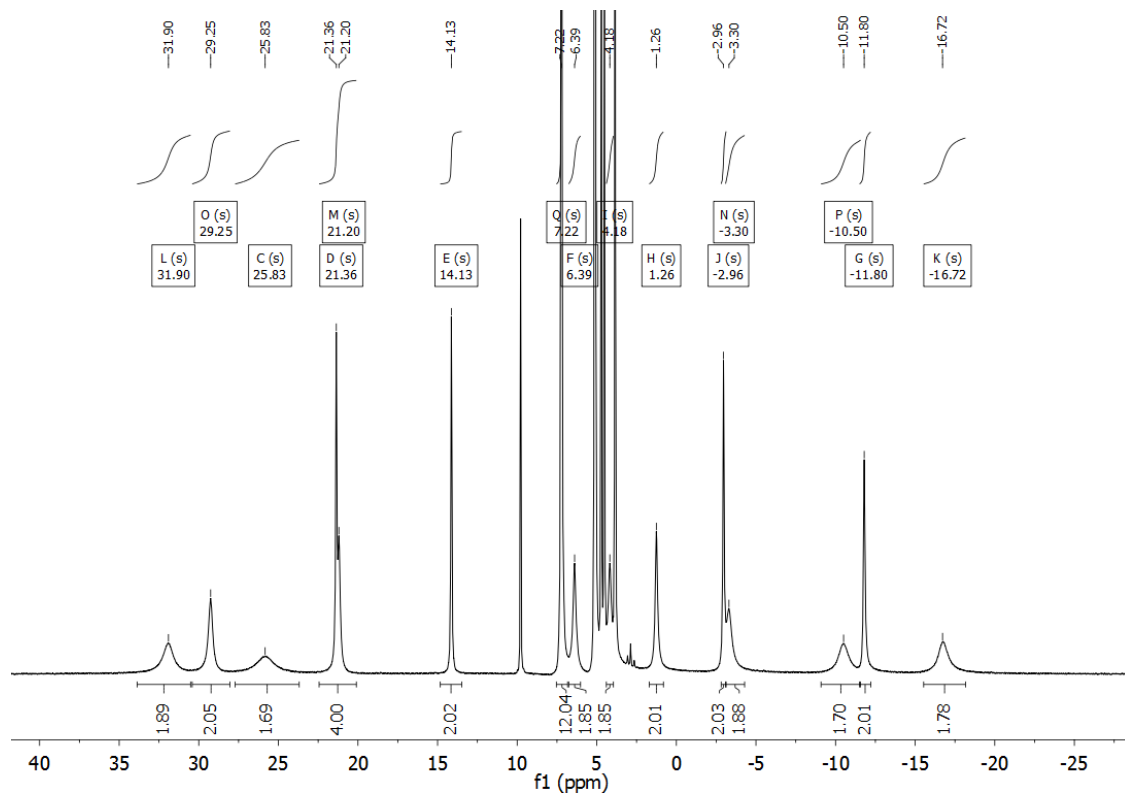
Figure A3.14. ^{1}H-NMR Spectrum of **Tm**

178
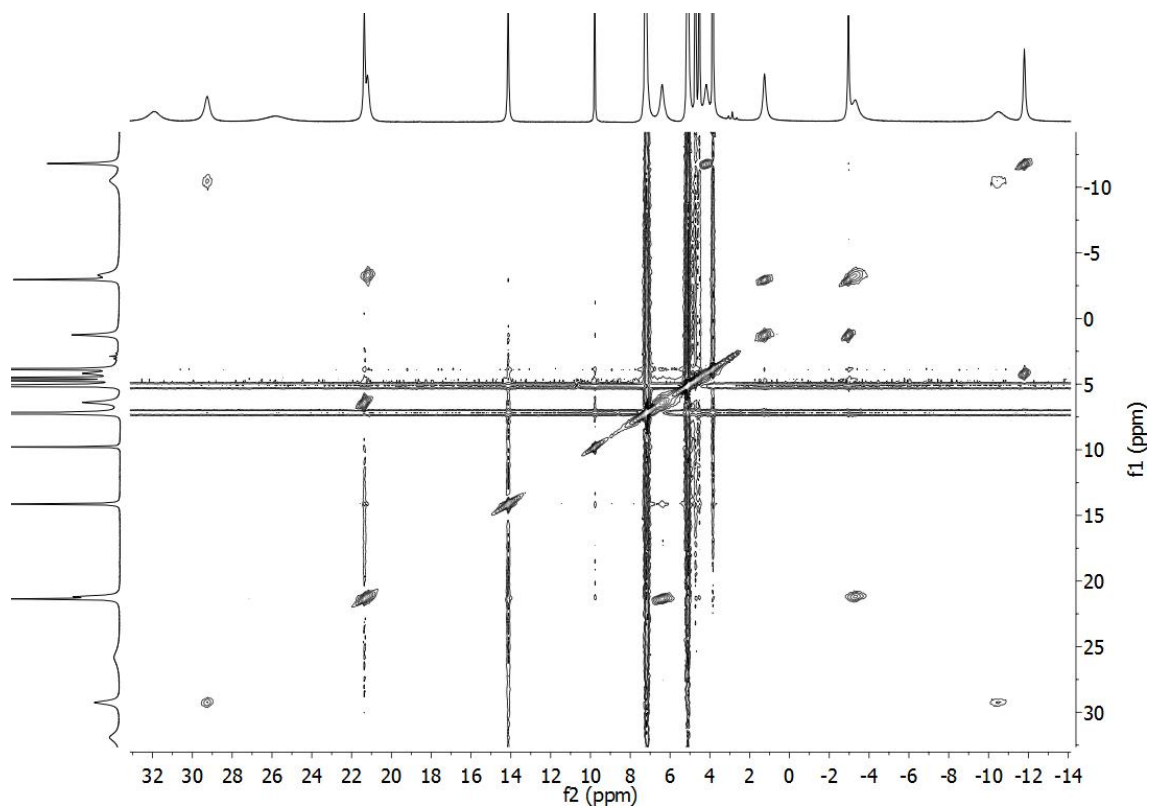
Figure A3.15. ^{1}H-NMR EXSY Spectrum of **Tm**
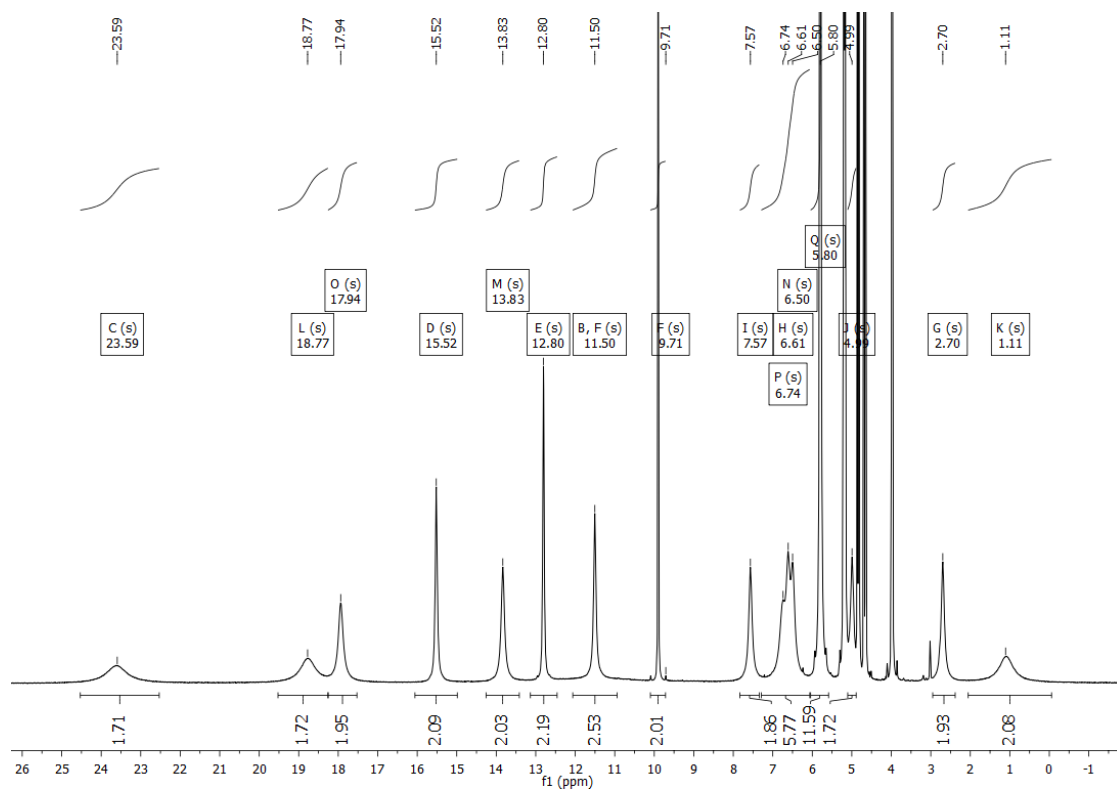
Figure A3.16. ^{1}H-NMR Spectrum of **Er**
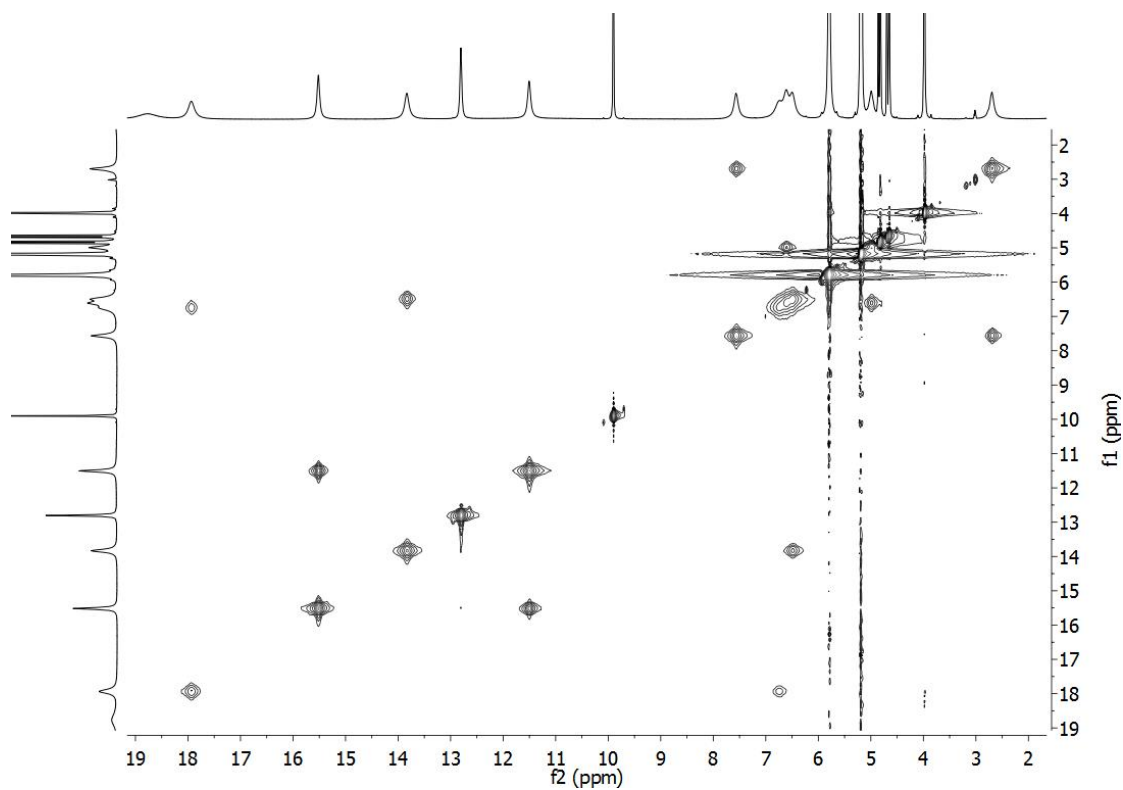
Figure A3.17. ^{1}H-NMR EXSY Spectrum of **Er**
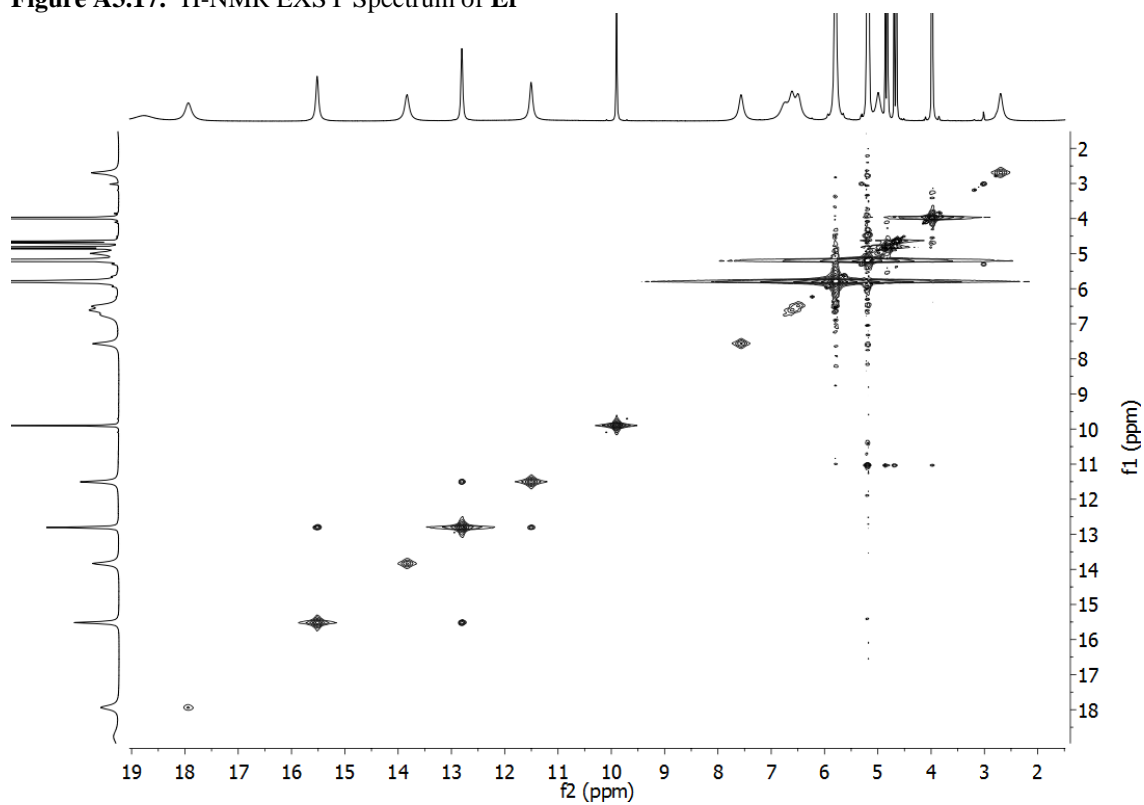
Figure A3.18. ^{1}H-NMR COSY Spectrum of **Er**
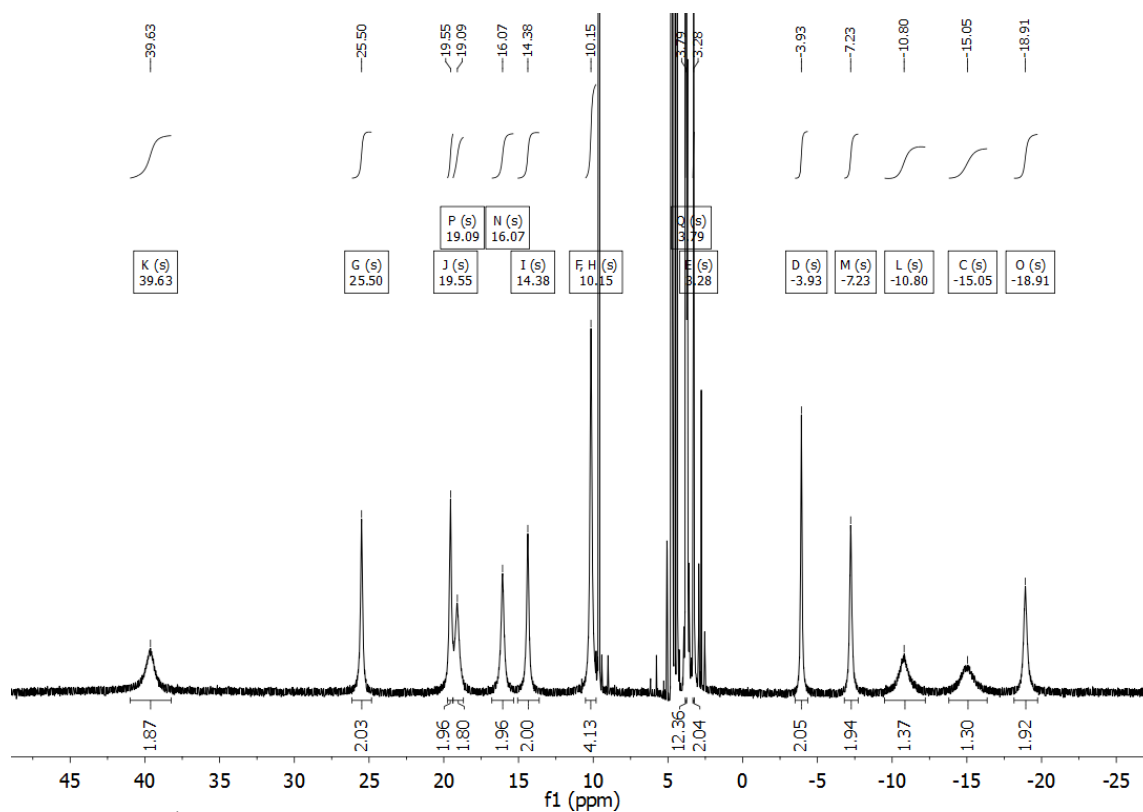
Figure A3.19. ^{1}H-NMR Spectrum of **Ho**
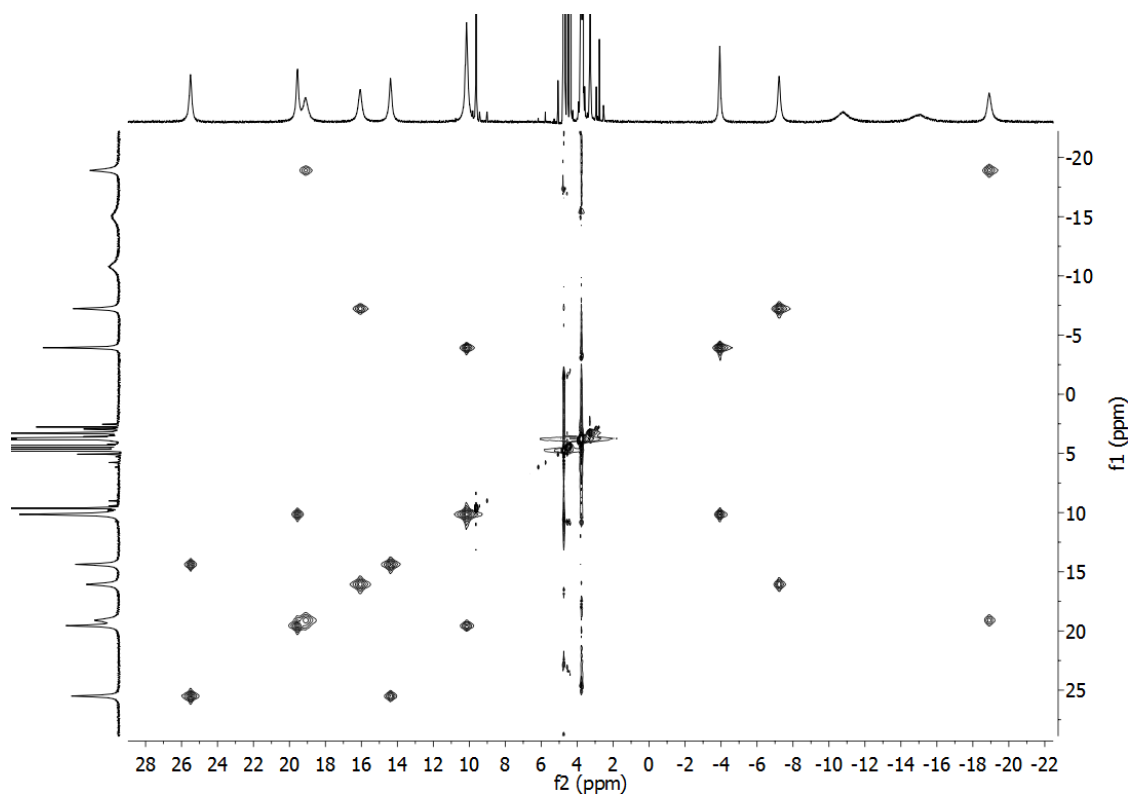
Figure A3.20. ^{1}H-NMR EXSY Spectrum of **Ho**

181
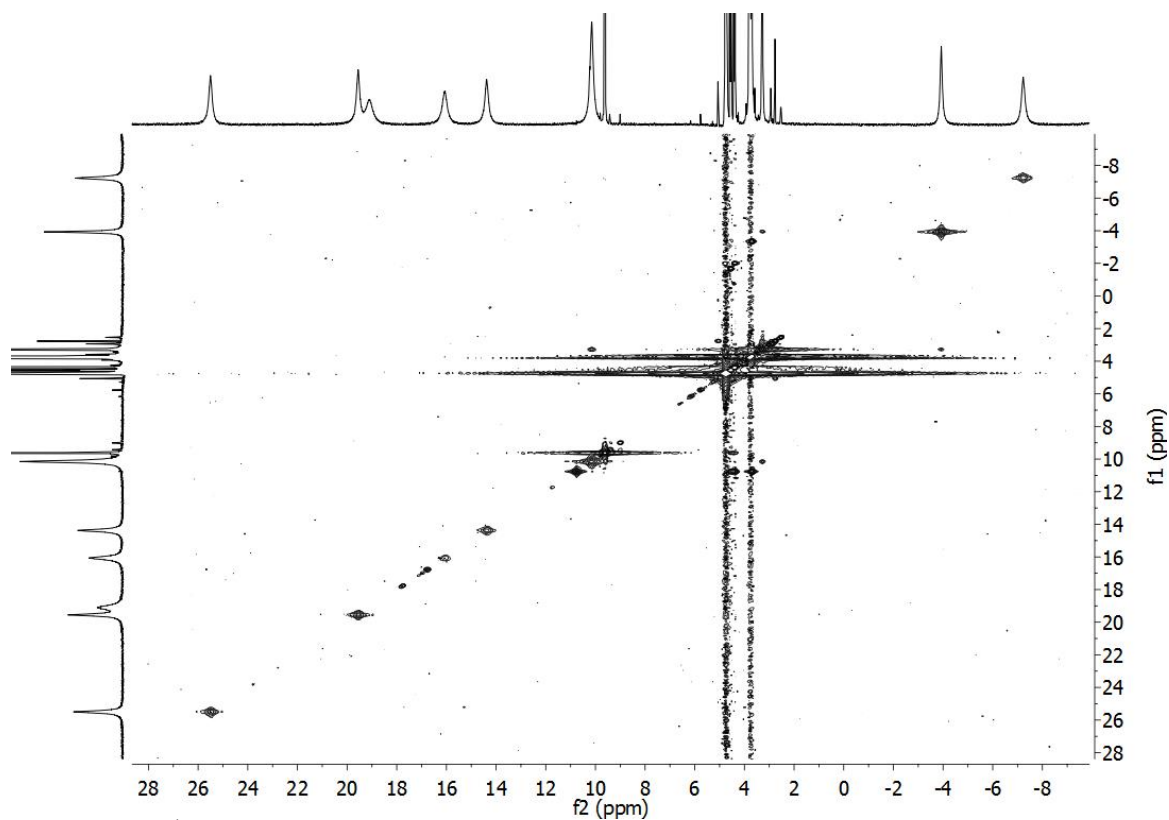
Figure A3.21. ^{1}H-NMR COSY Spectrum of **Ho**
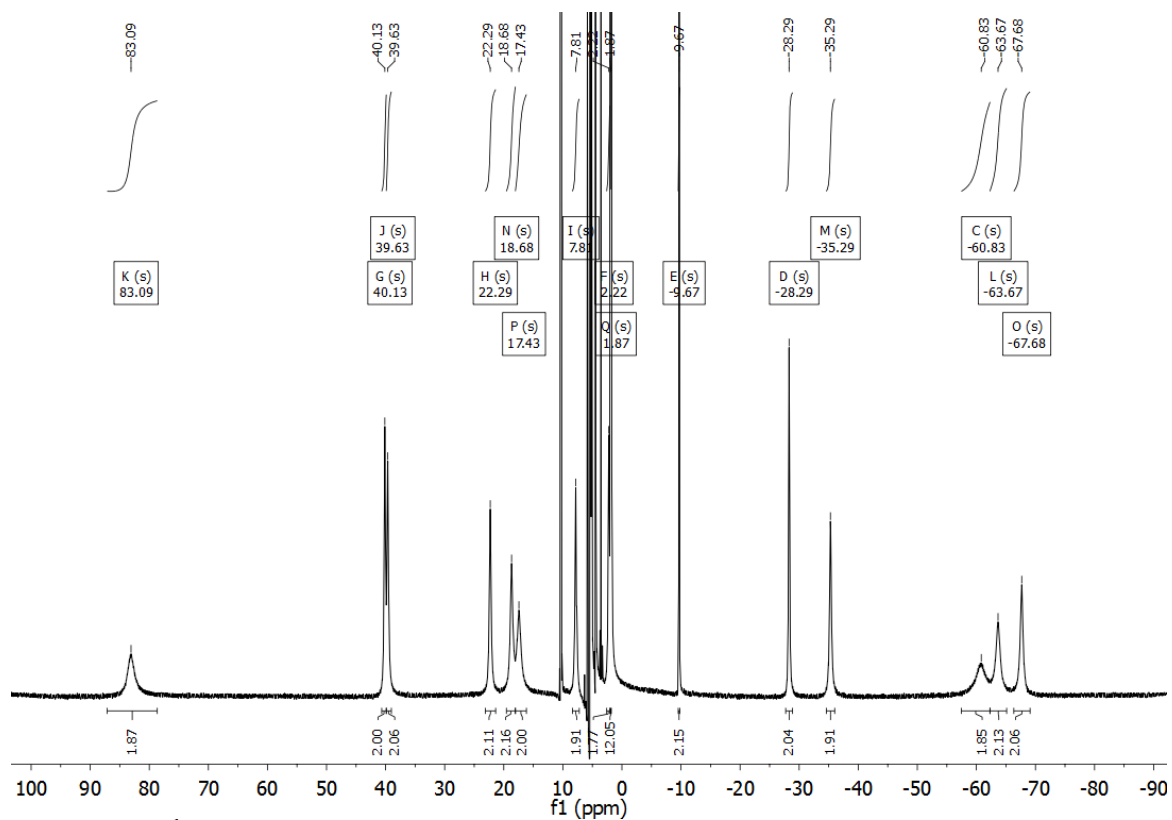
Figure A3.22. ^{1}H-NMR Spectrum of **Dy**
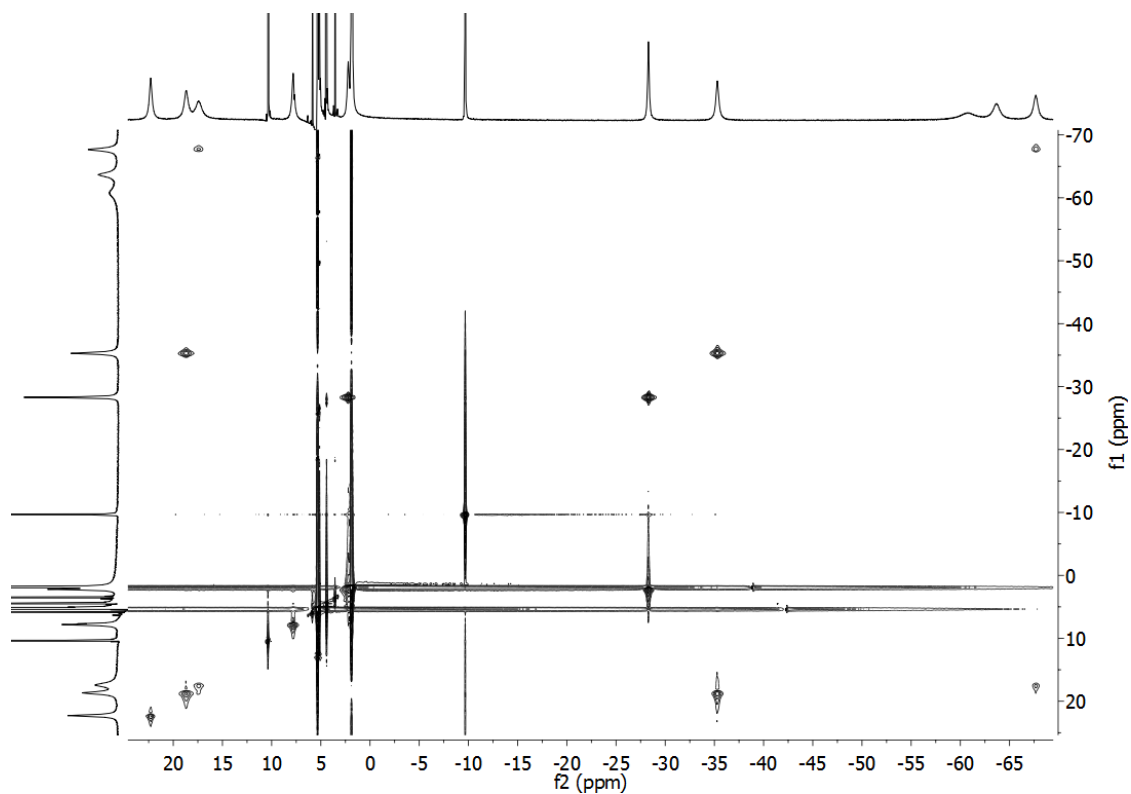
Figure A3.23. ^{1}H-NMR EXSY Spectrum of **Dy**
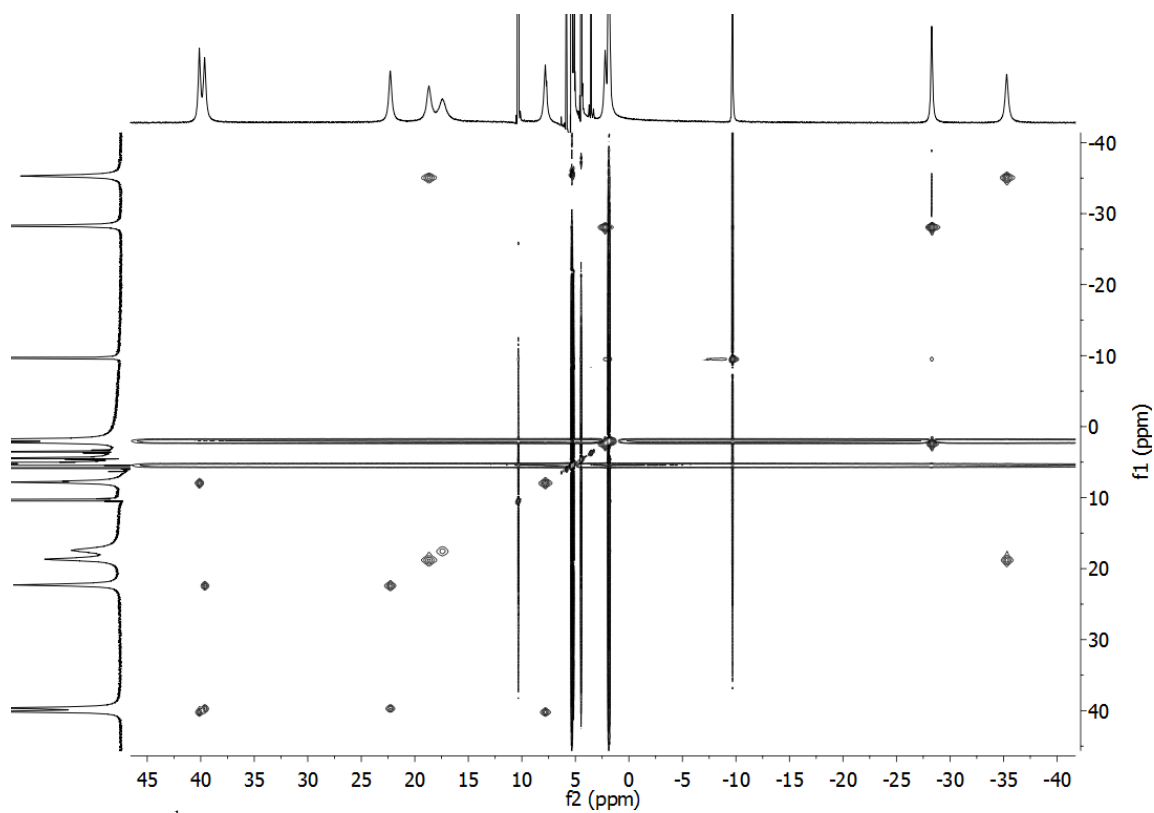
Figure A3.24. ^{1}H-NMR EXSY Spectrum of **Dy**
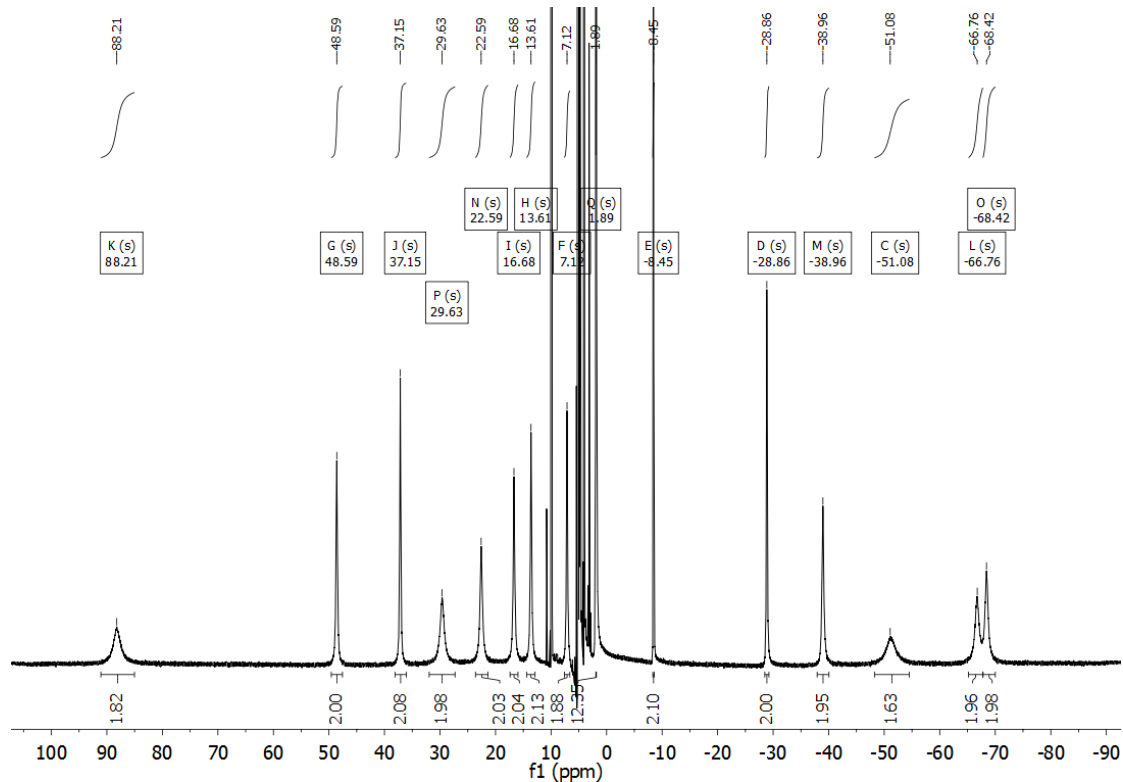
Figure A3.25. ^{1}H-NMR Spectrum of **Tb**
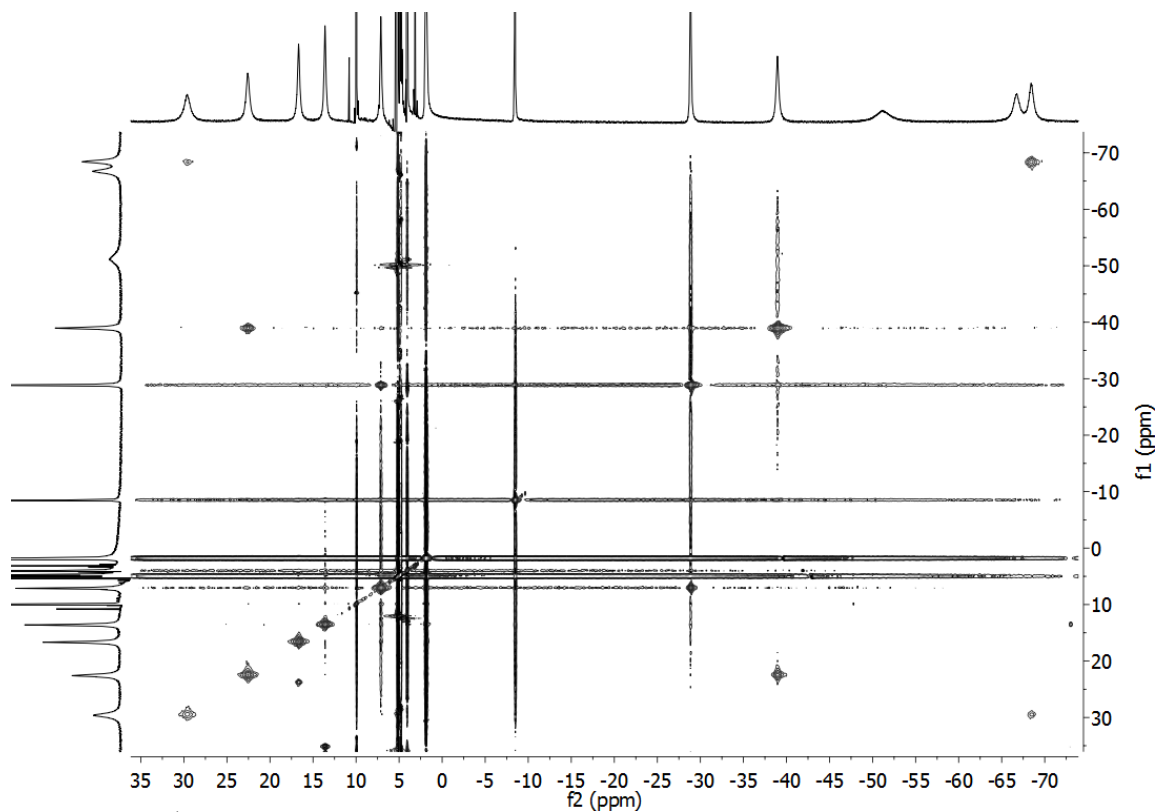
Figure A3.26. ^{1}H-NMR EXSY Spectrum of **Tb**
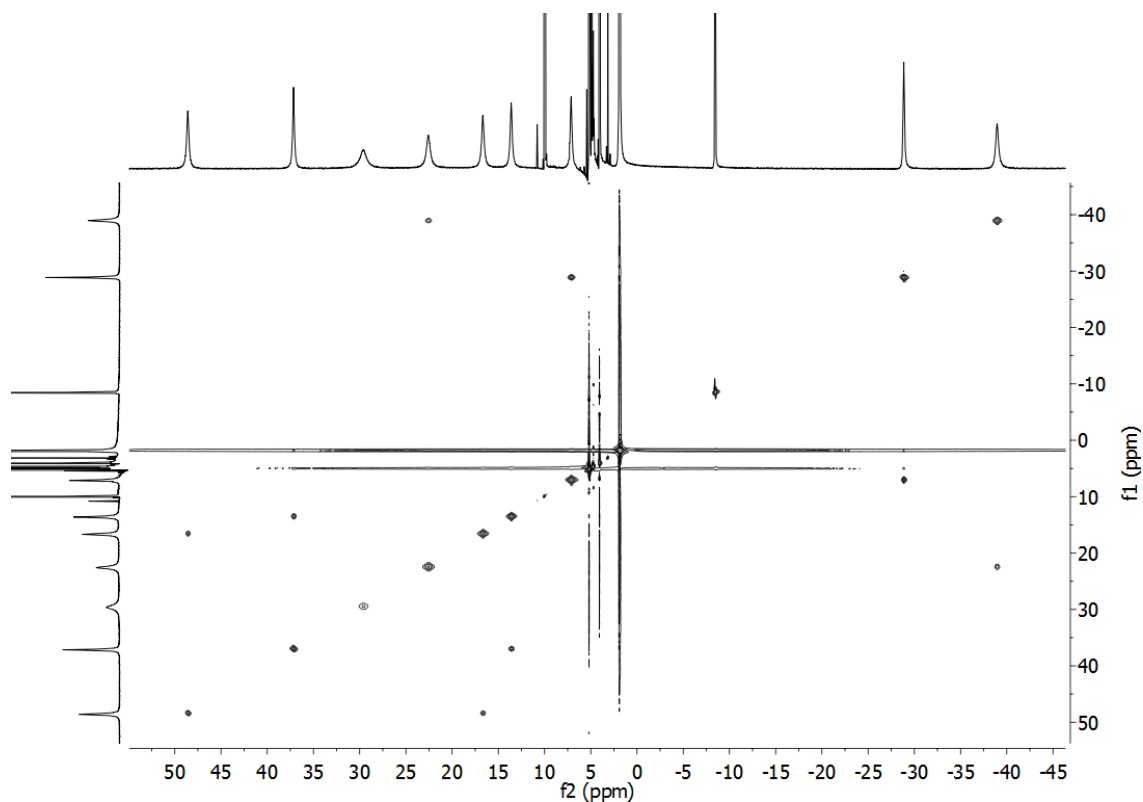
Figure A3.27. ^{1}H-NMR EXSY Spectrum of **Tb**
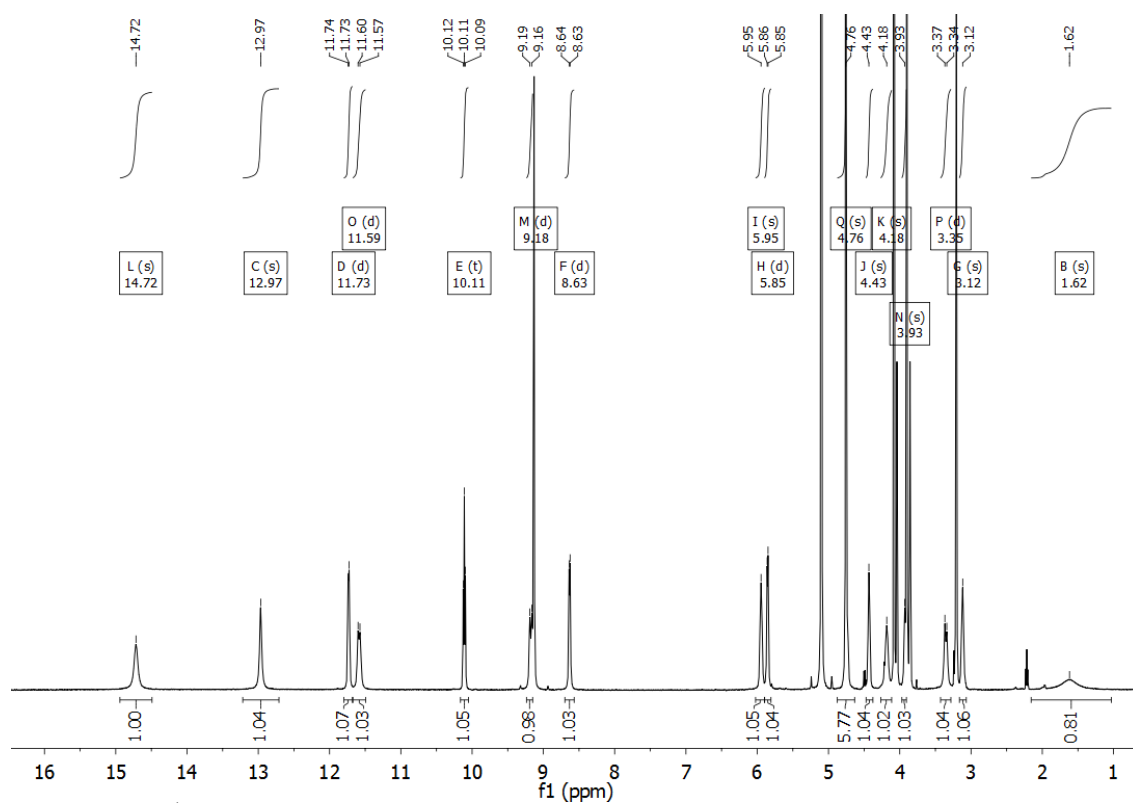
Figure A3.28. ^{1}H-NMR Spectrum of **Eu**
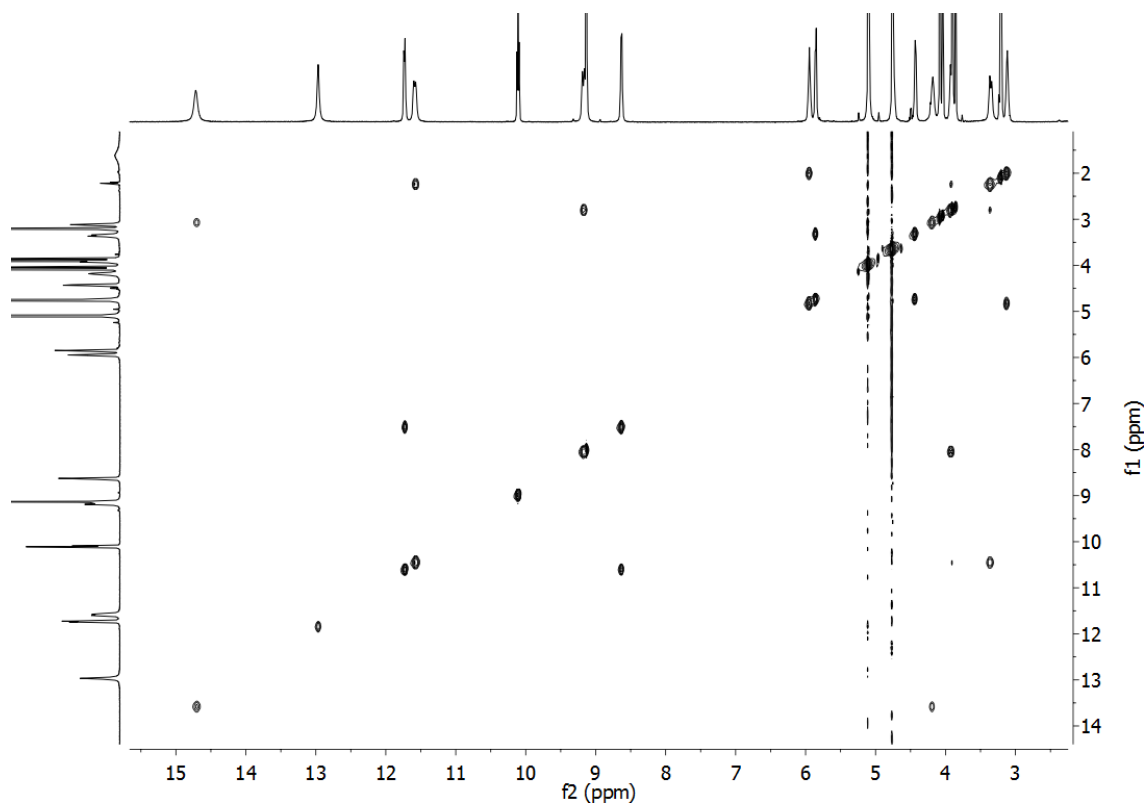
Figure A3.29. ^{1}H-NMR EXSY Spectrum of **Eu**
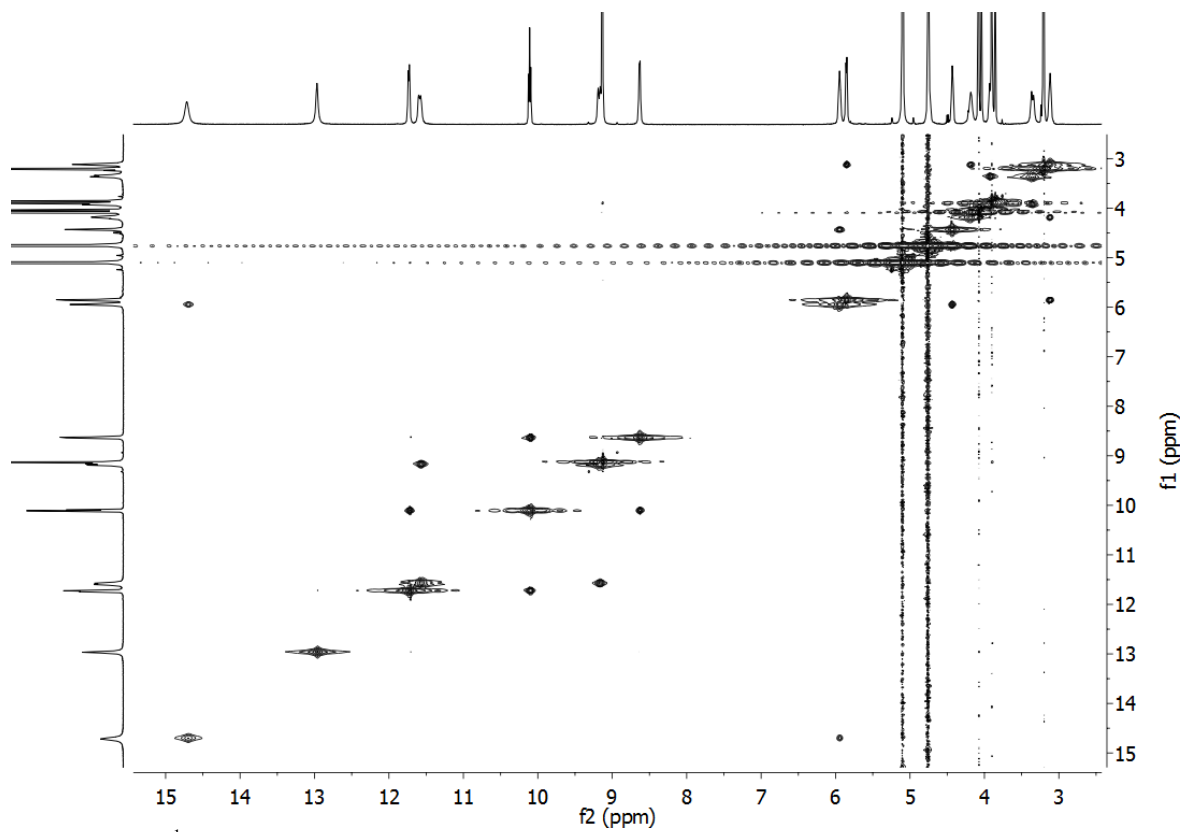
Figure A3.30. ^{1}H-NMR COSY Spectrum of **Eu**

Figure A3.31. ^{1}H-NMR Spectrum of **Sm**

Figure A3.32. ^{1}H-NMR EXSY Spectrum of **Sm**
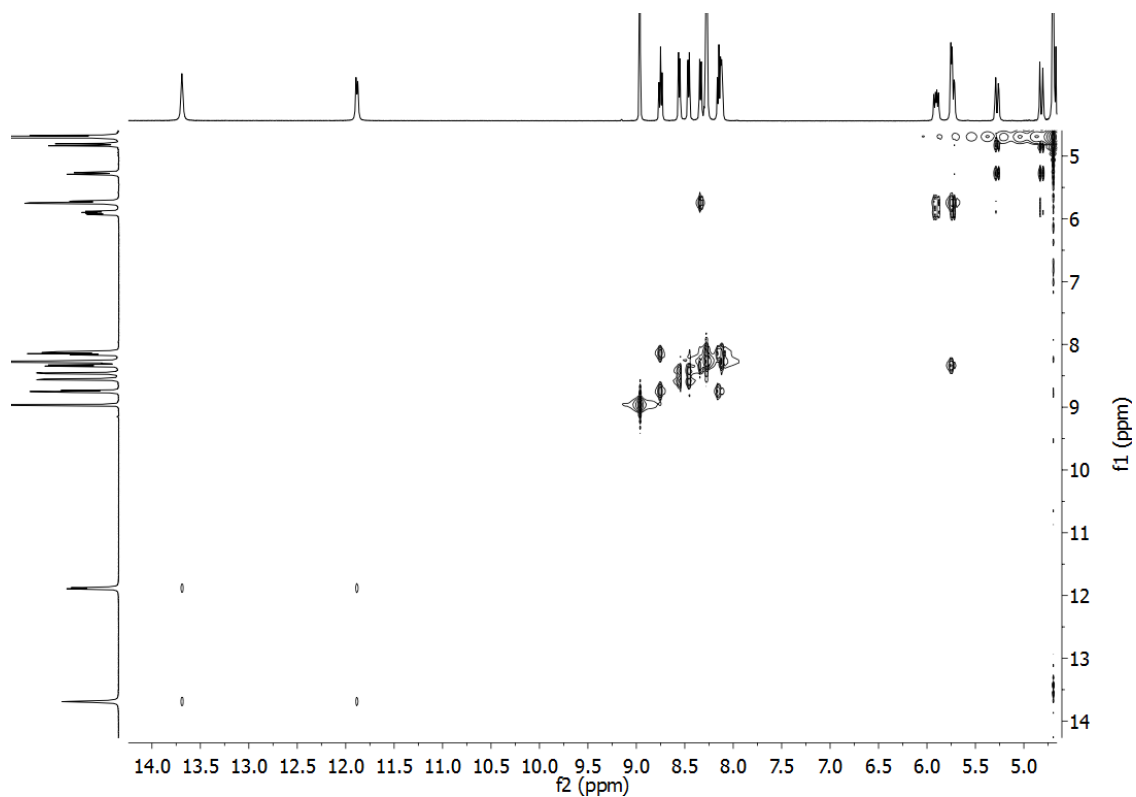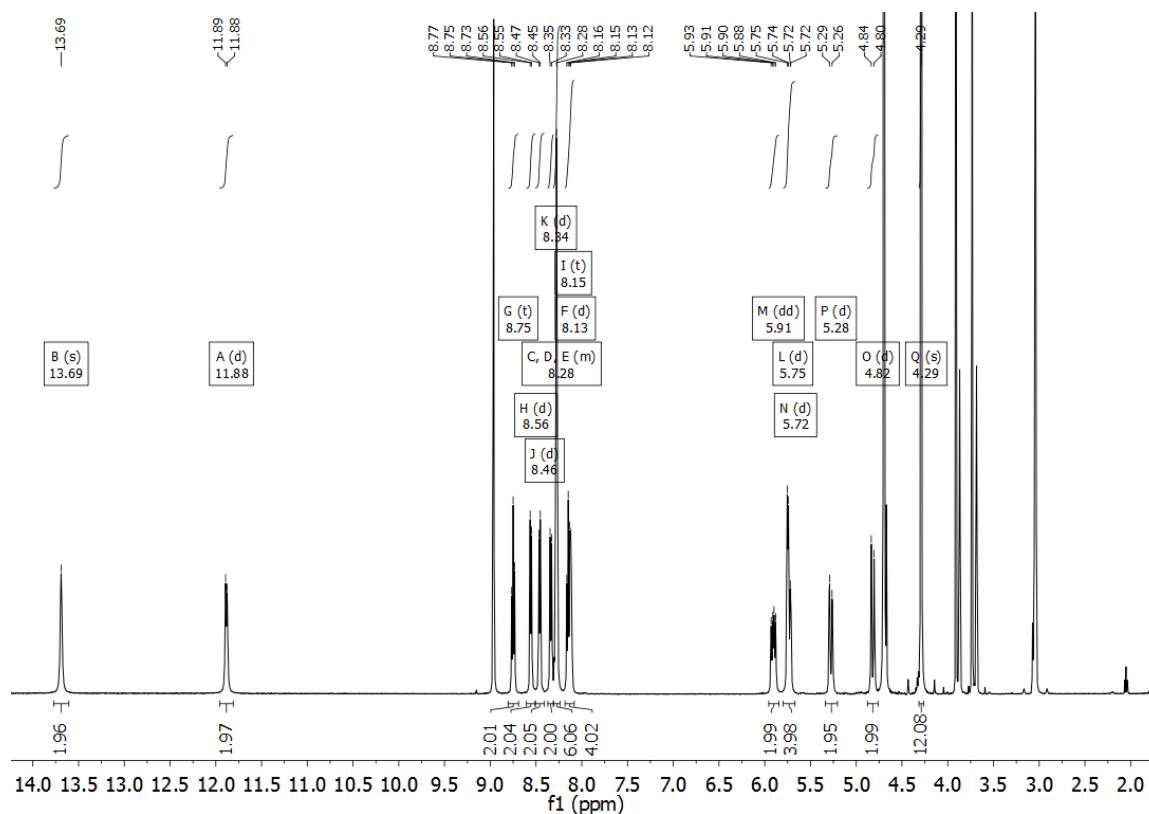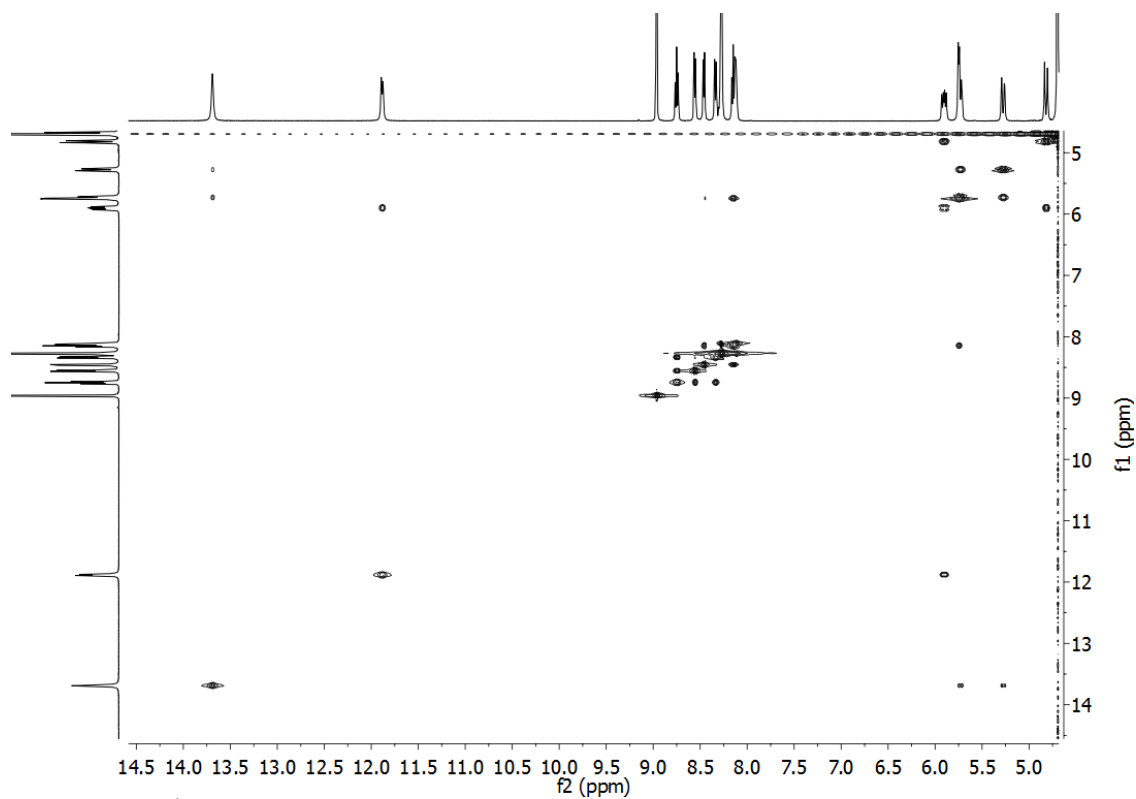
Figure A3.33. ^{1}H-NMR COSY Spectrum of **Sm**
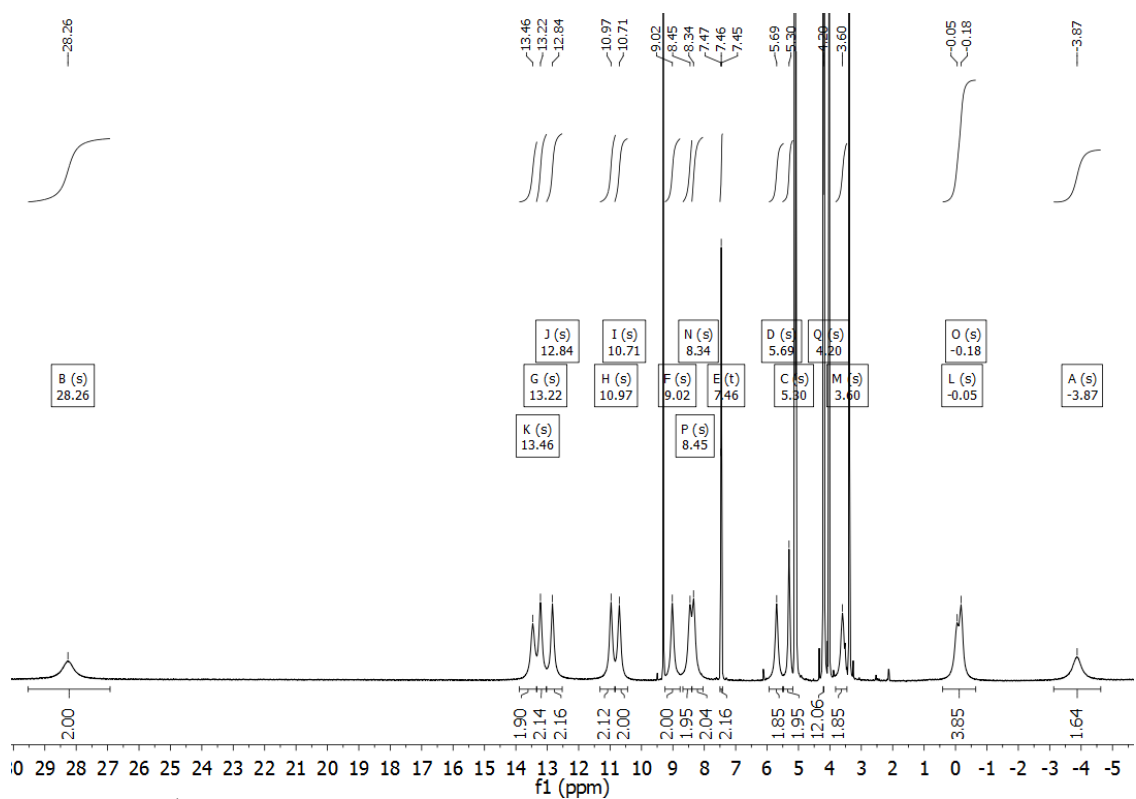
Figure A3.34. ^{1}H-NMR Spectrum of **Nd**
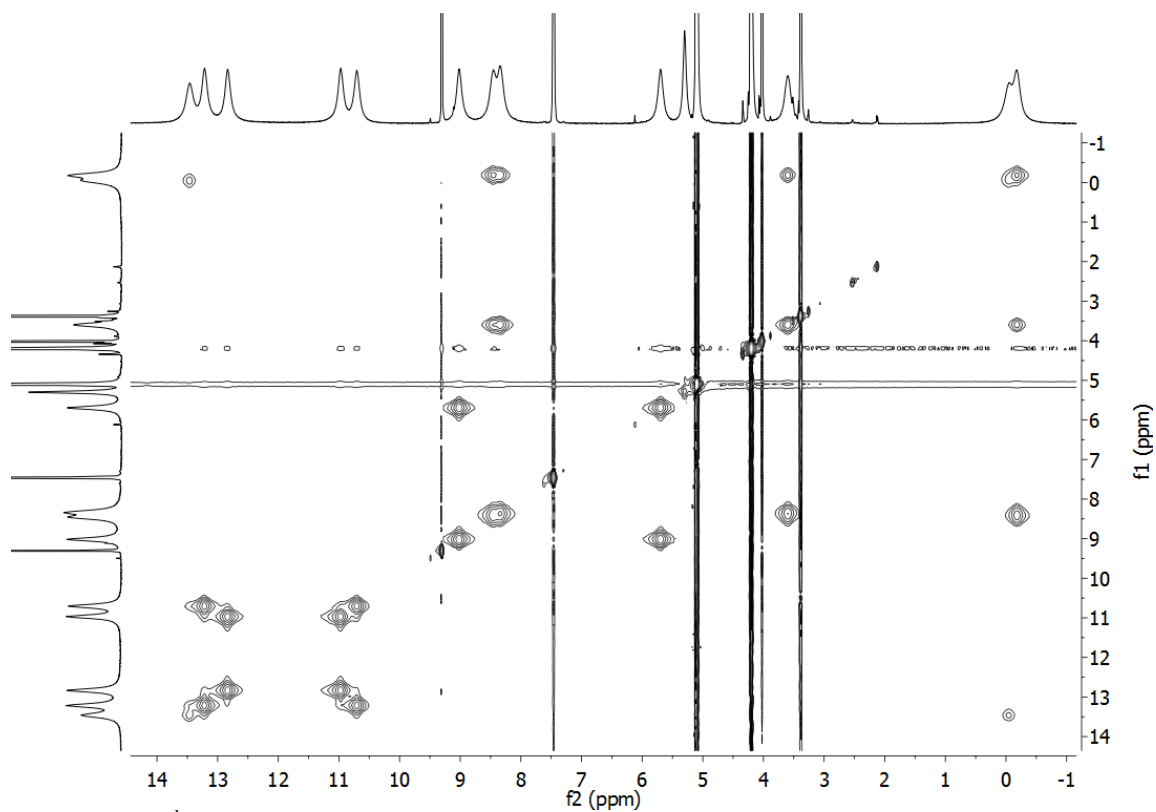
Figure A3.35. ^{1}H-NMR EXSY Spectrum of **Nd**
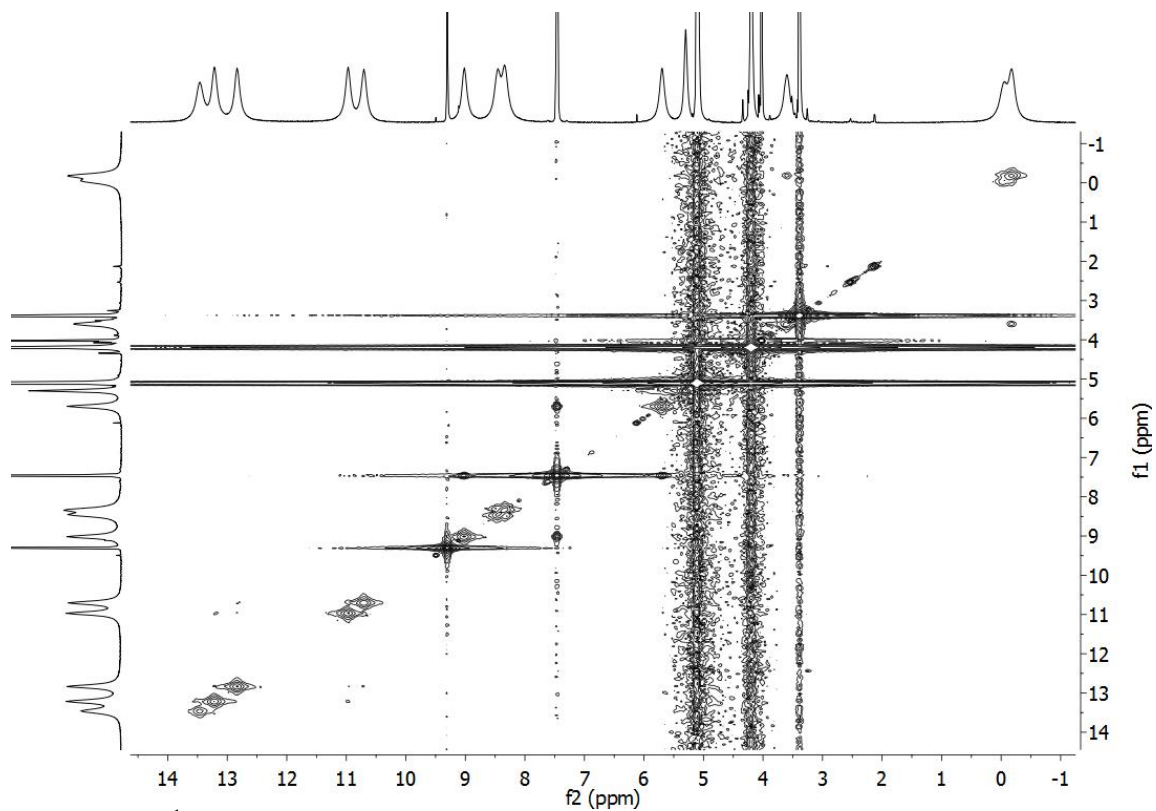
Figure A3.36. ^{1}H-NMR COSY Spectrum of **Nd**
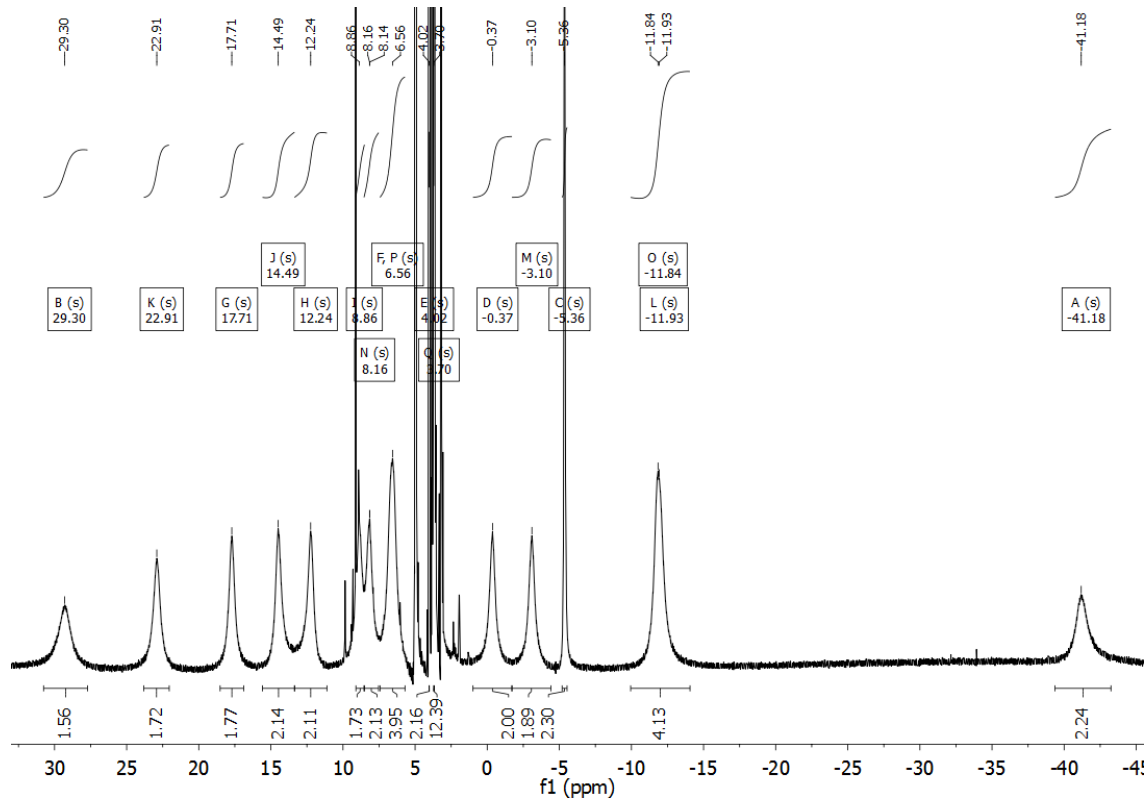
Figure A3.37. ^{1}H-NMR Spectrum of **Pr**
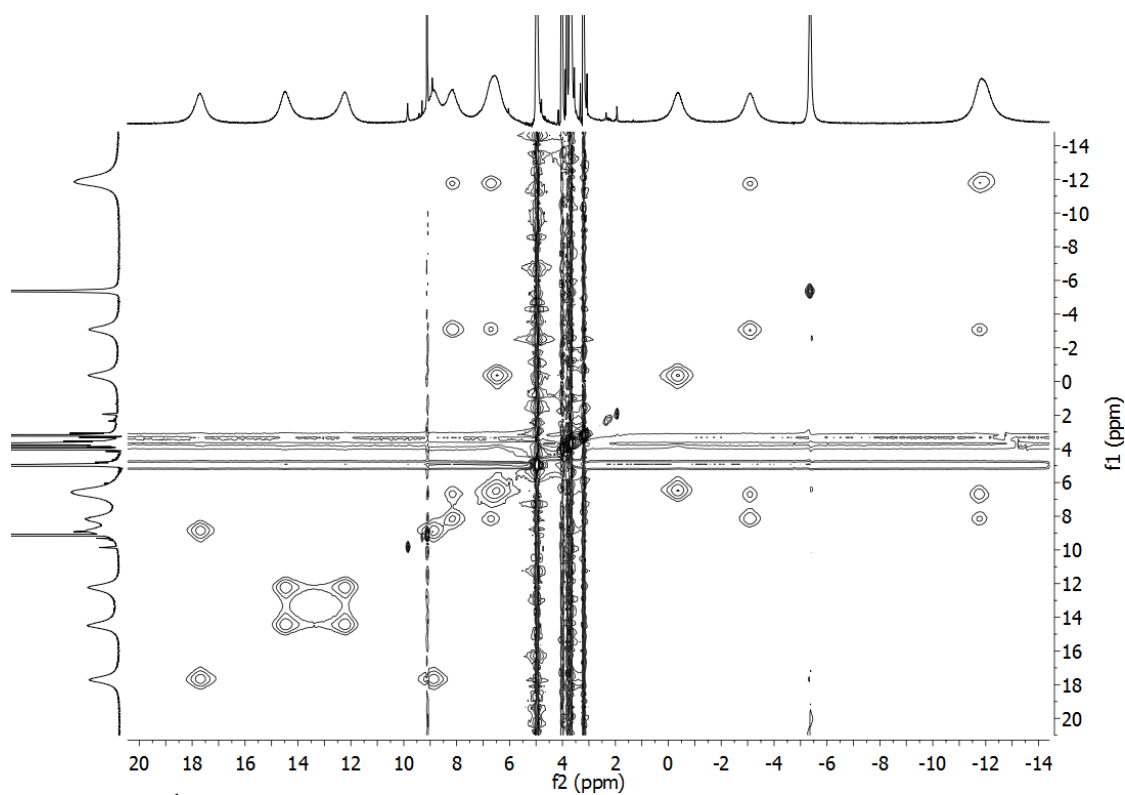
Figure A3.38. ^{1}H-NMR EXSY Spectrum of **Pr**
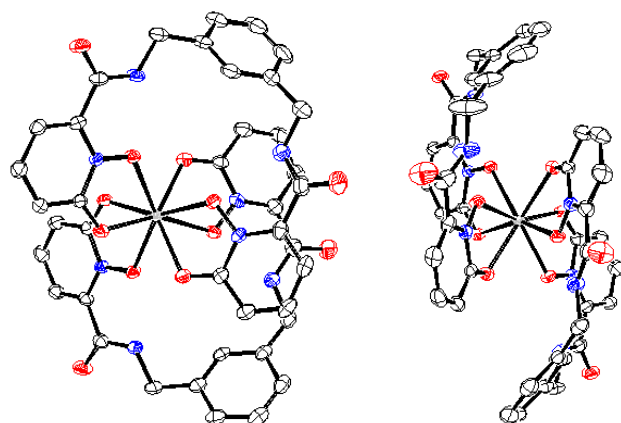
Figure A3.39. ORTEP of **Lu**.

Table A3.2. Crystal data and structure refinement for **Lu**.

Identification code	[Lu(5LImXy-1,2-HOPO)$_2$][NMe$_4$]
Empirical formula	C44 H44 Lu N9 O12
Formula weight	1065.85
Temperature	100(2) K
Wavelength	0.71073 Å
Crystal system	Monoclinic
Space group	P2(1)/c
Unit cell dimensions	a = 14.6313(11) Å α= 90°.
	b = 14.7507(11) Å β= 101.1900(10)°.
	c = 24.8902(18) Å γ = 90°.
Volume	5269.7(7) Å^3
Z	4
Density (calculated)	1.343 Mg/m^3
Absorption coefficient	1.936 mm^{-1}
F(000)	2152
Crystal size	0.21 x 0.19 x 0.03 mm^3
Theta range for data collection	1.42 to 25.36°.
Index ranges	-17<=h<=17, -17<=k<=17, -29<=l<=29
Reflections collected	58364
Independent reflections	9645 [R(int) = 0.0333]
Completeness to theta = 25.00°	99.9 %
Absorption correction	Semi-empirical from equivalents
Max. and min. transmission	0.9442 and 0.6867
Refinement method	Full-matrix least-squares on F^2
Data / restraints / parameters	9645 / 0 / 599
Goodness-of-fit on F^2	1.066
Final R indices [I>2sigma(I)]	R1 = 0.0257, wR2 = 0.0548
R indices (all data)	R1 = 0.0312, wR2 = 0.0570
Largest diff. peak and hole	1.382 and -0.692 e.Å^{-3}

191
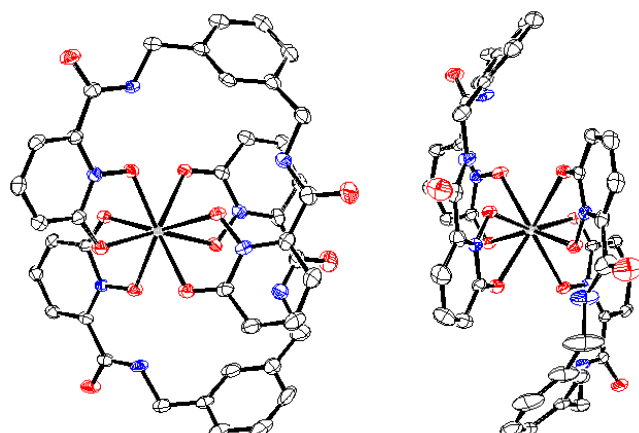
Figure A3.40. ORTEP of **Yb**.

Table A3.3. Crystal data and structure refinement for **Yb**.

Identification code	[Yb(5LImXy-1,2-HOPO)$_2$][NMe$_4$]
Empirical formula	C44 H44 N9 O12 Yb
Formula weight	1063.92
Temperature	100(2) K
Wavelength	0.71073 Å
Crystal system	Monoclinic
Space group	P2(1)/c
Unit cell dimensions	a = 14.6265(7) Å α= 90°.
	b = 14.7386(6) Å β= 101.1920(10)°.
	c = 24.9100(11) Å γ = 90°.
Volume	5267.8(4) Å^3
Z	4
Density (calculated)	1.341 Mg/m^3
Absorption coefficient	1.838 mm^{-1}
F(000)	2148
Crystal size	0.10 x 0.10 x 0.02 mm^3
Theta range for data collection	1.42 to 25.37°.
Index ranges	-17<=h<=17, -17<=k<=17, -29<=l<=30
Reflections collected	106349
Independent reflections	9651 [R(int) = 0.0599]
Completeness to theta = 25.00°	99.9 %
Absorption correction	Semi-empirical from equivalents
Max. and min. transmission	0.9642 and 0.8376
Refinement method	Full-matrix least-squares on F^2
Data / restraints / parameters	9651 / 0 / 599
Goodness-of-fit on F^2	1.048
Final R indices [I>2sigma(I)]	R1 = 0.0270, wR2 = 0.0609
R indices (all data)	R1 = 0.0343, wR2 = 0.0633
Largest diff. peak and hole	0.823 and -0.579 e.Å^{-3}
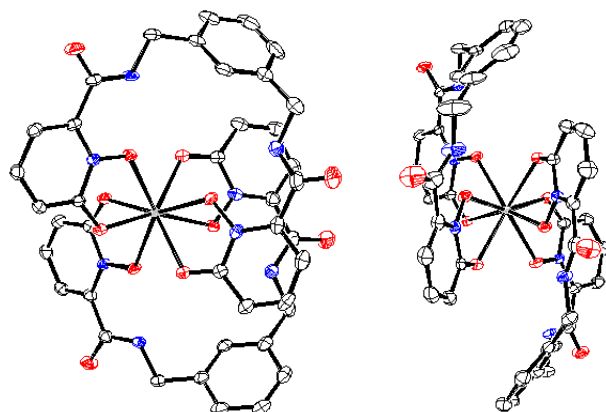
Figure A3.41. ORTEP of **Tm**.

Table A3.4. Crystal data and structure refinement for **Tm**.

Identification code	[Tm(5LImXy-1,2-HOPO)$_2$][NMe$_4$]
Empirical formula	C44 H44 N9 O12 Tm
Formula weight	1059.81
Temperature	100(2) K
Wavelength	0.71073 Å
Crystal system	Monoclinic
Space group	P2(1)/c
Unit cell dimensions	a = 14.6284(8) Å α= 90°.
	b = 14.7262(8) Å β= 101.1758(11)°.
	c = 24.9658(13) Å γ = 90°.
Volume	5276.2(5) Å^3
Z	4
Density (calculated)	1.334 Mg/m^3
Absorption coefficient	1.744 mm^{-1}
F(000)	2144
Crystal size	0.15 x 0.12 x 0.06 mm^3
Theta range for data collection	1.42 to 25.37°.
Index ranges	-17<=h<=17, -17<=k<=17, -30<=l<=25
Reflections collected	74002
Independent reflections	9648 [R(int) = 0.0301]
Completeness to theta = 25.00°	99.8 %
Absorption correction	Semi-empirical from equivalents
Max. and min. transmission	0.9026 and 0.7799
Refinement method	Full-matrix least-squares on F^2
Data / restraints / parameters	9648 / 0 / 599
Goodness-of-fit on F^2	1.049
Final R indices [I>2sigma(I)]	R1 = 0.0241, wR2 = 0.0568
R indices (all data)	R1 = 0.0271, wR2 = 0.0582
Largest diff. peak and hole	0.537 and -0.586 e.Å^{-3}

193
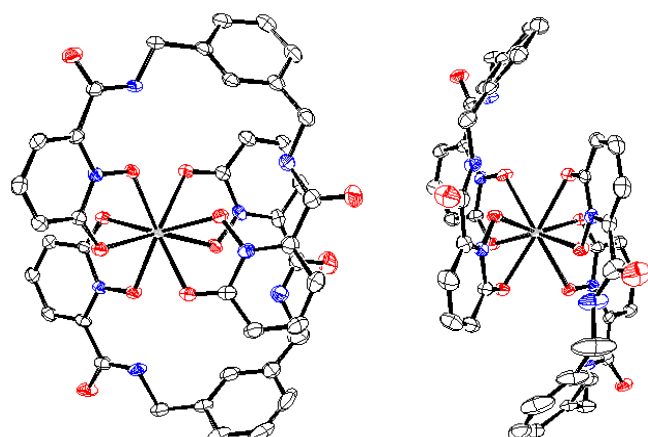
Figure A3.42. ORTEP of **Er**.

Table A3.5. Crystal data and structure refinement for **Er**.

Identification code	[Er(5LImXy-1,2-HOPO)$_2$][NMe$_4$]
Empirical formula	C44 H44 Er N9 O12
Formula weight	1058.14
Temperature	100(2) K
Wavelength	0.71073 Å
Crystal system	Monoclinic
Space group	P2(1)/c
Unit cell dimensions	a = 14.6597(7) Å $\quad$ α= 90°.
	b = 14.7216(7) Å $\quad$ β= 101.1080(10)°.
	c = 24.9678(11) Å $\quad$ γ = 90°.
Volume	5287.5(4) Å^3
Z	4
Density (calculated)	1.329 Mg/m^3
Absorption coefficient	1.649 mm^{-1}
F(000)	2140
Crystal size	0.20 x 0.14 x 0.02 mm^3
Theta range for data collection	1.42 to 25.38°.
Index ranges	-17<=h<=17, -17<=k<=17, -30<=l<=30
Reflections collected	158373
Independent reflections	9698 [R(int) = 0.0382]
Completeness to theta = 25.00°	100.0 %
Absorption correction	Semi-empirical from equivalents
Max. and min. transmission	0.9678 and 0.7339
Refinement method	Full-matrix least-squares on F^2
Data / restraints / parameters	9698 / 0 / 599
Goodness-of-fit on F^2	1.053
Final R indices [I>2sigma(I)]	R1 = 0.0237, wR2 = 0.0546
R indices (all data)	R1 = 0.0257, wR2 = 0.0555
Largest diff. peak and hole	0.508 and -0.579 e.Å^{-3}
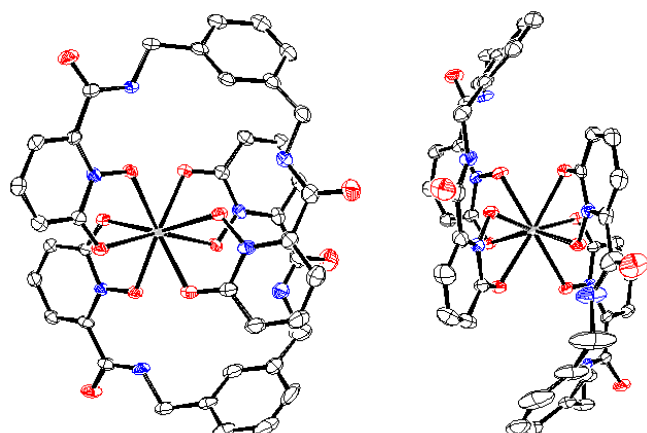
Figure A3.43. ORTEP of **Ho**.

Table A3.6. Crystal data and structure refinement for **Ho**.

Identification code	[Ho(5LImXy-1,2-HOPO)$_2$][NMe$_4$]
Empirical formula	C44 H44 Ho N9 O12
Formula weight	1055.81
Temperature	100(2) K
Wavelength	0.71073 Å
Crystal system	Monoclinic
Space group	P2(1)/c
Unit cell dimensions	a = 14.6557(9) Å α= 90°.
	b = 14.7227(9) Å β= 101.0810(10)°.
	c = 24.9594(15) Å γ = 90°.
Volume	5285.1(6) Å^3
Z	4
Density (calculated)	1.327 Mg/m^3
Absorption coefficient	1.559 mm^{-1}
F(000)	2136
Crystal size	0.40 x 0.30 x 0.06 mm^3
Theta range for data collection	1.42 to 25.37°.
Index ranges	-17<=h<=17, -17<=k<=17, -30<=l<=29
Reflections collected	147016
Independent reflections	9688 [R(int) = 0.0329]
Completeness to theta = 25.00°	100.0 %
Absorption correction	Semi-empirical from equivalents
Max. and min. transmission	0.9123 and 0.5744
Refinement method	Full-matrix least-squares on F^2
Data / restraints / parameters	9688 / 0 / 599
Goodness-of-fit on F^2	1.075
Final R indices [I>2sigma(I)]	R1 = 0.0237, wR2 = 0.0538
R indices (all data)	R1 = 0.0251, wR2 = 0.0545
Largest diff. peak and hole	0.535 and -0.533 e.Å^{-3}
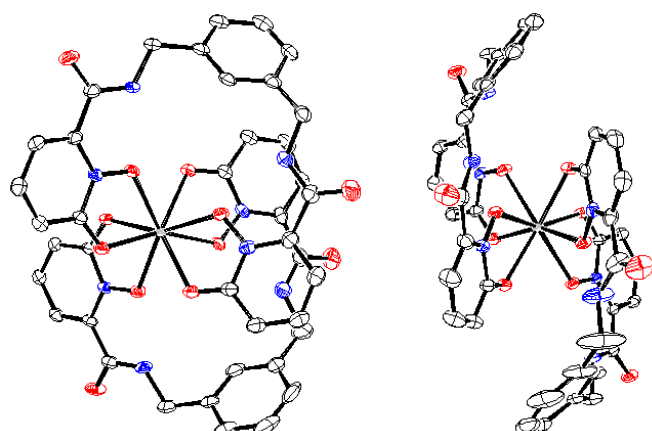
Figure A3.44. ORTEP of **Dy**.

Table A3.7. Crystal data and structure refinement for **Dy**.

Identification code	[Dy(5LImXy-1,2-HOPO)$_2$][NMe$_4$]
Empirical formula	C44 H44 Dy N9 O12
Formula weight	1053.38
Temperature	100(2) K
Wavelength	0.71073 Å
Crystal system	Monoclinic
Space group	P2(1)/c
Unit cell dimensions	a = 14.6814(7) Å α= 90°.
	b = 14.7194(7) Å β= 101.0430(10)°.
	c = 25.0388(12) Å γ = 90°.
Volume	5310.7(4) Å^3
Z	4
Density (calculated)	1.317 Mg/m^3
Absorption coefficient	1.469 mm^{-1}
F(000)	2132
Crystal size	0.15 x 0.12 x 0.06 mm^3
Theta range for data collection	1.41 to 25.35°.
Index ranges	-17<=h<=17, -17<=k<=17, -30<=l<=30
Reflections collected	72756
Independent reflections	9712 [R(int) = 0.0350]
Completeness to theta = 25.00°	100.0 %
Absorption correction	Semi-empirical from equivalents
Max. and min. transmission	0.9170 and 0.8098
Refinement method	Full-matrix least-squares on F^2
Data / restraints / parameters	9712 / 0 / 599
Goodness-of-fit on F^2	1.063
Final R indices [I>2sigma(I)]	R1 = 0.0233, wR2 = 0.0539
R indices (all data)	R1 = 0.0263, wR2 = 0.0553
Largest diff. peak and hole	0.496 and -0.530 e.Å^{-3}
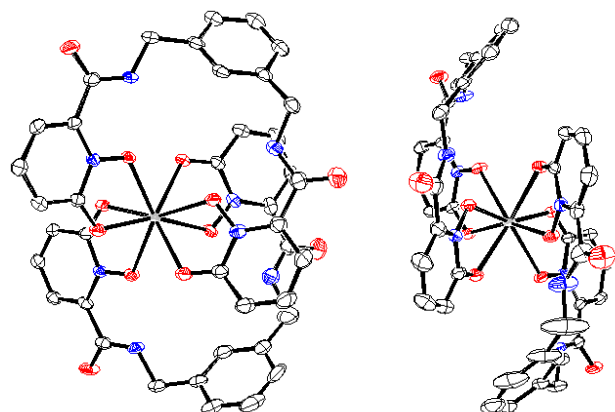
Figure A3.45. ORTEP of **Tb**.

Table A3.8. Crystal data and structure refinement for **Tb**.

Identification code	[Tb(5LImXy-1,2-HOPO)$_2$][NMe$_4$]
Empirical formula	C44 H44 N9 O12 Tb
Formula weight	1049.80
Temperature	100(2) K
Wavelength	0.71073 Å
Crystal system	Monoclinic
Space group	P2(1)/c
Unit cell dimensions	a = 14.6862(12) Å α= 90°.
	b = 14.7523(12) Å β= 101.017(2)°.
	c = 25.005(2) Å γ = 90°.
Volume	5317.7(7) Å^3
Z	4
Density (calculated)	1.311 Mg/m^3
Absorption coefficient	1.392 mm^{-1}
F(000)	2128
Crystal size	0.24 x 0.16 x 0.06 mm^3
Theta range for data collection	1.41 to 25.36°.
Index ranges	-17<=h<=17, -17<=k<=17, -30<=l<=30
Reflections collected	161370
Independent reflections	9744 [R(int) = 0.0465]
Completeness to theta = 25.00°	100.0 %
Absorption correction	Semi-empirical from equivalents
Max. and min. transmission	0.9212 and 0.7312
Refinement method	Full-matrix least-squares on F^2
Data / restraints / parameters	9744 / 0 / 599
Goodness-of-fit on F^2	0.977
Final R indices [I>2sigma(I)]	R1 = 0.0263, wR2 = 0.0656
R indices (all data)	R1 = 0.0306, wR2 = 0.0678
Largest diff. peak and hole	0.475 and -0.556 e.Å^{-3}
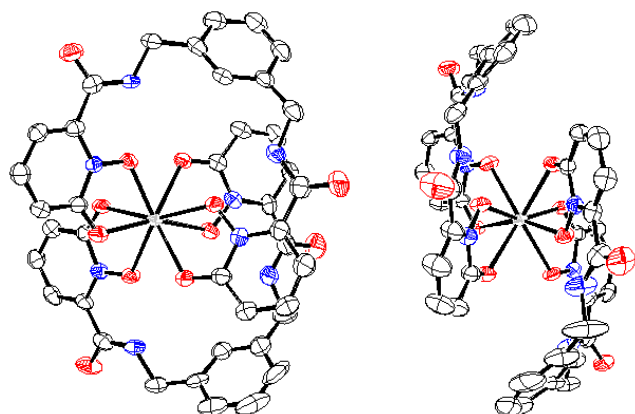
Figure A3.46. ORTEP of **Eu**.

Table A3.9. Crystal data and structure refinement for **Eu**.

Identification code	[Eu(5LImXy-1,2-HOPO)$_2$][NMe$_4$]
Empirical formula	C44 H44 Eu N9 O12
Formula weight	1042.84
Temperature	137(2) K
Wavelength	0.71073 Å
Crystal system	Monoclinic
Space group	P2(1)/c
Unit cell dimensions	a = 14.781(5) Å α= 90°.
	b = 14.868(5) Å β= 100.493(5)°.
	c = 25.106(8) Å γ = 90°.
Volume	5425(3) Å^3
Z	4
Density (calculated)	1.277 Mg/m^3
Absorption coefficient	1.217 mm^{-1}
F(000)	2120
Crystal size	0.20 x 0.15 x 0.04 mm^3
Theta range for data collection	1.40 to 25.31°.
Index ranges	-17<=h<=17, -17<=k<=17, -30<=l<=30
Reflections collected	57544
Independent reflections	9841 [R(int) = 0.0916]
Completeness to theta = 25.00°	99.9 %
Absorption correction	Semi-empirical from equivalents
Max. and min. transmission	0.9529 and 0.7929
Refinement method	Full-matrix least-squares on F^2
Data / restraints / parameters	9841 / 0 / 599
Goodness-of-fit on F^2	0.923
Final R indices [I>2sigma(I)]	R1 = 0.0445, wR2 = 0.0869
R indices (all data)	R1 = 0.0763, wR2 = 0.0956
Largest diff. peak and hole	1.487 and -0.716 e.Å^{-3}
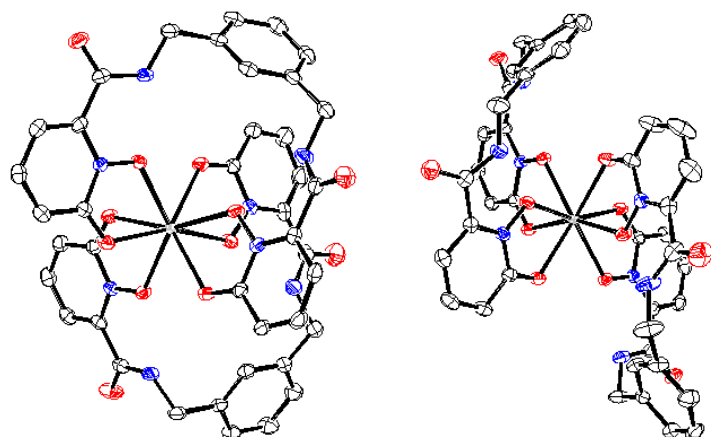
Figure A3.47. ORTEP of **Sm**.

Table A3.10. Crystal data and structure refinement for **Sm**.

Identification code	$[Sm(5LImXy-1,2-HOPO)_2][NMe_4] \cdot 3DMF$
Empirical formula	C53 H65 N12 O15 Sm
Formula weight	1260.52
Temperature	100(2) K
Wavelength	0.71069 Å
Crystal system	Monoclinic
Space group	P2(1)/n
Unit cell dimensions	a = 16.584(5) Å $\qquad$ α= 90.000(5)°.
	b = 14.226(5) Å $\qquad$ β= 100.088(5)°.
	c = 24.031(5) Å $\qquad$ γ = 90.000(5)°.
Volume	5582(3) Å^3
Z	4
Density (calculated)	1.500 Mg/m^3
Absorption coefficient	1.130 mm^{-1}
F(000)	2596
Crystal size	0.60 x 0.45 x 0.27 mm^3
Theta range for data collection	2.41 to 25.53°.
Index ranges	-20<=h<=19, -17<=k<=17, -29<=l<=29
Reflections collected	77521
Independent reflections	10332 [R(int) = 0.0254]
Completeness to theta = 25.00°	99.8 %
Absorption correction	Semi-empirical from equivalents
Max. and min. transmission	0.7500 and 0.5504
Refinement method	Full-matrix least-squares on F^2
Data / restraints / parameters	10332 / 0 / 740
Goodness-of-fit on F^2	1.098
Final R indices [I>2sigma(I)]	R1 = 0.0234, wR2 = 0.0545
R indices (all data)	R1 = 0.0303, wR2 = 0.0585
Largest diff. peak and hole	1.287 and -0.557 e.Å^{-3}
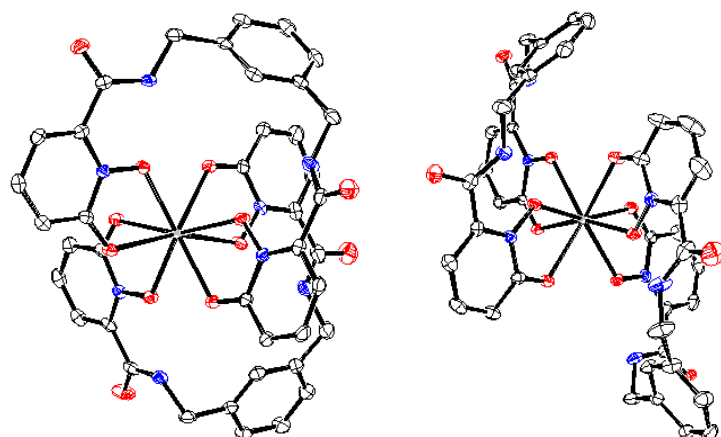
Figure A3.48. ORTEP of **Nd**.

Table A3.11. Crystal data and structure refinement for **Nd**.

Identification code	[Nd(5LImXy-1,2-HOPO)$_2$][NMe$_4$]·3DMF
Empirical formula	C53 H65 N12 Nd O15
Formula weight	1254.41
Temperature	100(2) K
Wavelength	0.71073 Å
Crystal system	Monoclinic
Space group	P2(1)/n
Unit cell dimensions	a = 16.5333(8) Å α= 90°.
	b = 14.2313(7) Å β= 99.9220(10)°.
	c = 23.9795(11) Å γ = 90°.
Volume	5557.8(5) Å^3
Z	4
Density (calculated)	1.499 Mg/m^3
Absorption coefficient	1.013 mm^{-1}
F(000)	2588
Crystal size	0.30 x 0.25 x 0.12 mm^3
Theta range for data collection	1.39 to 25.38°.
Index ranges	-19<=h<=19, -17<=k<=17, -28<=l<=28
Reflections collected	58047
Independent reflections	10200 [R(int) = 0.0289]
Completeness to theta = 25.00°	100.0 %
Absorption correction	Semi-empirical from equivalents
Max. and min. transmission	0.8881 and 0.7509
Refinement method	Full-matrix least-squares on F^2
Data / restraints / parameters	10200 / 0 / 740
Goodness-of-fit on F^2	1.064
Final R indices [I>2sigma(I)]	R1 = 0.0242, wR2 = 0.0567
R indices (all data)	R1 = 0.0294, wR2 = 0.0600
Largest diff. peak and hole	0.782 and -0.409 e.Å^{-3}
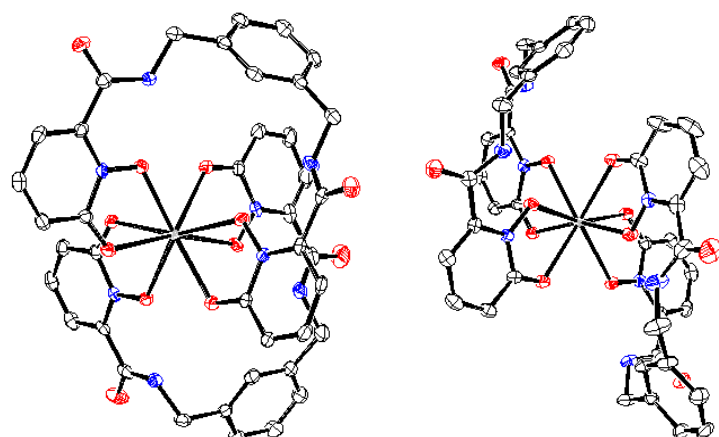
Figure A3.49. ORTEP of **Pr**.

Table A3.12. Crystal data and structure refinement for **Pr**.

Identification code	[Pr(5LImXy-1,2-HOPO)$_2$][NMe$_4$]·3DMF
Empirical formula	C53 H65 N12 O15 Pr
Formula weight	1251.08
Temperature	100(2) K
Wavelength	0.71073 Å
Crystal system	Monoclinic
Space group	P2(1)/n
Unit cell dimensions	a = 16.5300(7) Å α= 90°.
	b = 14.2860(6) Å β= 99.8055(9)°.
	c = 23.9746(10) Å γ = 90°.
Volume	5578.8(4) Å^3
Z	4
Density (calculated)	1.490 Mg/m^3
Absorption coefficient	0.952 mm^{-1}
F(000)	2584
Crystal size	0.10 x 0.08 x 0.06 mm^3
Theta range for data collection	1.39 to 25.38°.
Index ranges	-19<=h<=19, -17<=k<=17, -28<=l<=28
Reflections collected	84428
Independent reflections	10239 [R(int) = 0.0444]
Completeness to theta = 25.00°	100.0 %
Absorption correction	Semi-empirical from equivalents
Max. and min. transmission	0.9451 and 0.9108
Refinement method	Full-matrix least-squares on F^2
Data / restraints / parameters	10239 / 0 / 740
Goodness-of-fit on F^2	1.103
Final R indices [I>2sigma(I)]	R1 = 0.0302, wR2 = 0.0713
R indices (all data)	R1 = 0.0414, wR2 = 0.0791
Largest diff. peak and hole	1.745 and -0.550 e.Å^{-3}
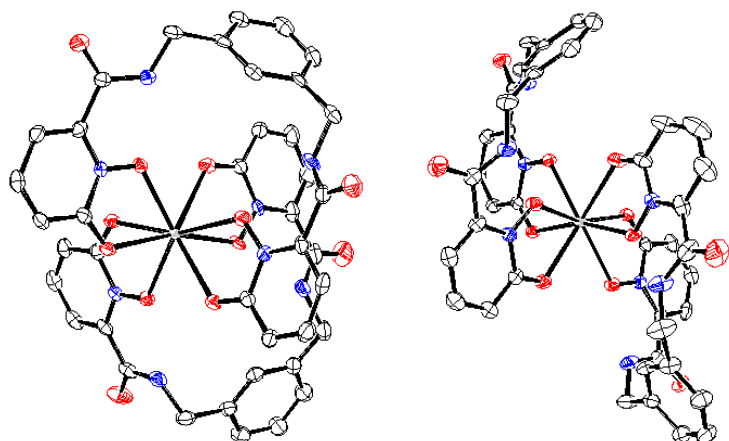
Figure A3.50. ORTEP of **Ce**.

Table A3.13. Crystal data and structure refinement for **Ce**.

Identification code	[Ce(5LImXy-1,2-HOPO)$_2$][NMe$_4$]·3DMF
Empirical formula	C53 H65 Ce N12 O15
Formula weight	1250.29
Temperature	293(2) K
Wavelength	0.71073 Å
Crystal system	Monoclinic
Space group	P2(1)/n
Unit cell dimensions	a = 16.5219(7) Å α= 90°.
	b = 14.2382(6) Å β= 99.962(2)°.
	c = 24.0395(11) Å γ = 90°.
Volume	5569.8(4) Å^3
Z	4
Density (calculated)	1.491 Mg/m^3
Absorption coefficient	0.896 mm^{-1}
F(000)	2580
Crystal size	0.09 x 0.07 x 0.04 mm^3
Theta range for data collection	1.39 to 25.44°.
Index ranges	-19<=h<=16, -17<=k<=17, -28<=l<=22
Reflections collected	66237
Independent reflections	10184 [R(int) = 0.0486]
Completeness to theta = 25.00°	99.7 %
Absorption correction	Semi-empirical from equivalents
Max. and min. transmission	0.9651 and 0.9237
Refinement method	Full-matrix least-squares on F^2
Data / restraints / parameters	10184 / 0 / 740
Goodness-of-fit on F^2	1.108
Final R indices [I>2sigma(I)]	R1 = 0.0483, wR2 = 0.1202
R indices (all data)	R1 = 0.0653, wR2 = 0.1319
Largest diff. peak and hole	2.416 and -1.041 e.Å^{-3}
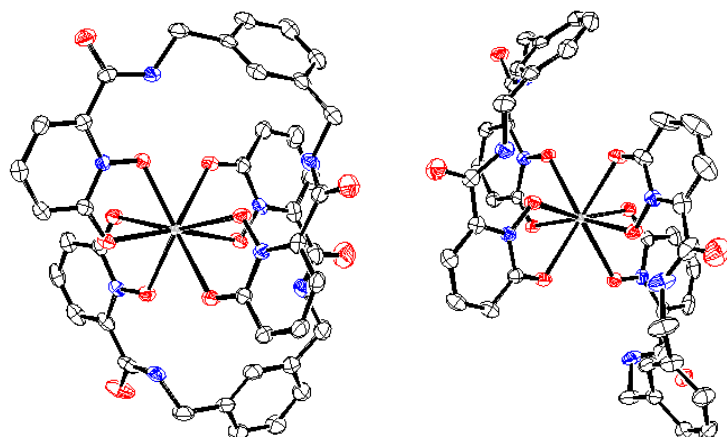
Figure A3.51. ORTEP of **La**.

Table A3.14. Crystal data and structure refinement for **La**.

Identification code	[La(5LImXy-1,2-HOPO)$_2$][NMe$_4$]·3DMF
Empirical formula	C53 H65 La N12 O15
Formula weight	1249.08
Temperature	100(2) K
Wavelength	0.71073 Å
Crystal system	Monoclinic
Space group	P2(1)/n
Unit cell dimensions	a = 16.5163(9) Å α= 90°.
	b = 14.2923(8) Å β= 100.1150(10)°.
	c = 24.0229(13) Å γ = 90°.
Volume	5582.6(5) Å^3
Z	4
Density (calculated)	1.486 Mg/m^3
Absorption coefficient	0.844 mm^{-1}
F(000)	2576
Crystal size	0.22 x 0.22 x 0.10 mm^3
Theta range for data collection	1.64 to 25.38°.
Index ranges	-19<=h<=19, -17<=k<=17, -28<=l<=28
Reflections collected	74193
Independent reflections	10248 [R(int) = 0.0453]
Completeness to theta = 25.00°	100.0 %
Absorption correction	Semi-empirical from equivalents
Max. and min. transmission	0.9204 and 0.8362
Refinement method	Full-matrix least-squares on F^2
Data / restraints / parameters	10248 / 0 / 740
Goodness-of-fit on F^2	1.058
Final R indices [I>2sigma(I)]	R1 = 0.0306, wR2 = 0.0760
R indices (all data)	R1 = 0.0442, wR2 = 0.0839
Largest diff. peak and hole	1.059 and -0.456 e.Å^{-3}

Table A3.15. DFT Calculated structure of **Ho** used for fitting the isotropic shifts ^{1}H-NMR Data

Atom Label	X	Y	Z	Atom Label	X	Y	Z
C	-1.974	1.796126	-1.82363	C	-4.17	-1.12451	-5.32907
C	-2.657	2.38477	-2.91819	H	-5.25	-1.07673	-5.21779
H	-2.301	2.121106	-3.90715	C	-3.534	-0.35872	-6.3071
C	-3.725	3.23691	-2.7155	H	-4.121	0.281281	-6.96104
H	-4.235	3.678249	-3.56767	C	-2.146	-0.39512	-6.43342
C	-4.157	3.524524	-1.41674	H	-1.651	0.21802	-7.18308
H	-4.993	4.176599	-1.19984	C	-1.378	-1.20941	-5.59101
C	-3.514	2.951408	-0.32917	C	-2.03	-1.98299	-4.62499
C	-4.068	3.261919	1.046474	H	-1.439	-2.60608	-3.96037
C	-4.113	2.79299	3.4289	C	0.133	-1.25792	-5.7491
H	-5.189	2.584152	3.422915	H	0.432	-2.07412	-6.41606
H	-4.02	3.859809	3.678156	H	0.474	-0.32416	-6.21647
C	-3.423	1.944364	4.475975	C	1.755	-2.44165	-4.34307
C	-4.17	1.124513	5.329069	C	2.289	-2.66775	-2.94047
H	-5.25	1.076729	5.217791	C	3.285	-3.62029	-2.78059
C	-3.534	0.358724	6.307099	H	3.629	-4.12209	-3.67554
H	-4.121	-0.28128	6.961045	C	3.784	-3.9021	-1.50443
C	-2.146	0.39512	6.433422	H	4.566	-4.64569	-1.38036
H	-1.651	-0.21802	7.183077	C	3.28	-3.24138	-0.40039
C	-1.378	1.209412	5.59101	H	3.632	-3.43561	0.605845
C	-2.03	1.982993	4.624992	C	2.257	-2.26902	-0.53358
H	-1.439	2.606084	3.960372	N	-2.447	2.120624	-0.54321
C	0.133	1.257923	5.749101	N	-3.568	2.574828	2.096167
H	0.432	2.074122	6.416064	H	-2.799	1.930014	1.90111
H	0.474	0.324163	6.216465	N	0.817	1.477571	4.492367
C	1.755	2.441647	4.343075	H	0.552	0.9753	3.638272
C	2.289	2.667746	2.94047	N	1.812	2.00809	1.839231
C	3.285	3.620294	2.78059	N	-2.447	-2.12062	0.543215
H	3.629	4.122088	3.675536	N	-3.568	-2.57483	-2.09617
C	3.784	3.902101	1.504435	H	-2.799	-1.93001	-1.90111
H	4.566	4.645691	1.380355	N	0.817	-1.47757	-4.49237
C	3.28	3.241377	0.400393	H	0.552	-0.9753	-3.63827
H	3.632	3.435606	-0.60585	N	1.812	-2.00809	-1.83923
C	2.257	2.269018	0.533579	O	-0.986	1.011129	-1.90637
C	-1.974	-1.79613	1.823626	O	-1.774	1.564305	0.470526
C	-2.657	-2.38477	2.918189	O	-0.986	-1.01113	1.906367
H	-2.301	-2.12111	3.907148	O	-1.774	-1.5643	-0.47053
C	-3.725	-3.23691	2.715499	O	0.87	1.067137	1.936897
H	-4.235	-3.67825	3.567671	O	1.716	1.620316	-0.40702
C	-4.157	-3.52452	1.416742	O	0.87	-1.06714	-1.9369
H	-4.993	-4.1766	1.199838	O	1.716	-1.62032	0.40702
C	-3.514	-2.95141	0.329171	O	-4.974	4.093205	1.160794
C	-4.068	-3.26192	-1.04647	O	2.181	3.140584	5.266659
C	-4.113	-2.79299	-3.4289	O	-4.974	-4.09321	-1.16079
H	-5.189	-2.5838	-3.42198	O	2.181	-3.14058	-5.26666
H	-4.02	-3.85981	-3.67816	Ho	0	0	0
C	-3.423	-1.94436	-4.47598				

Chapter 4 Appendix

^{1}H-NMR, COSY and EXSY Spectra for 2LImTHF-1,2-HOPO Complexes
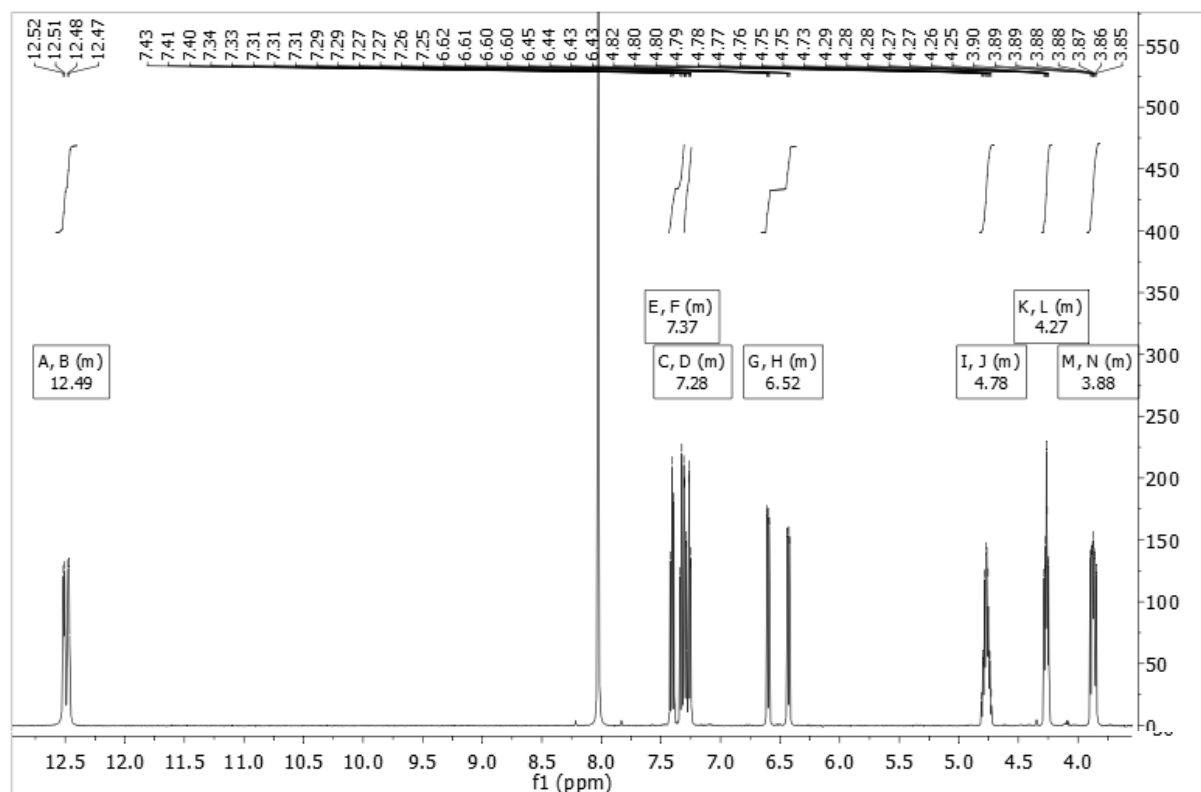
Figure A4.1. ^{1}H-NMR Spectrum of [Lu(2LImTHF-1,2-HOPO)$_2$][NMe$_4$]
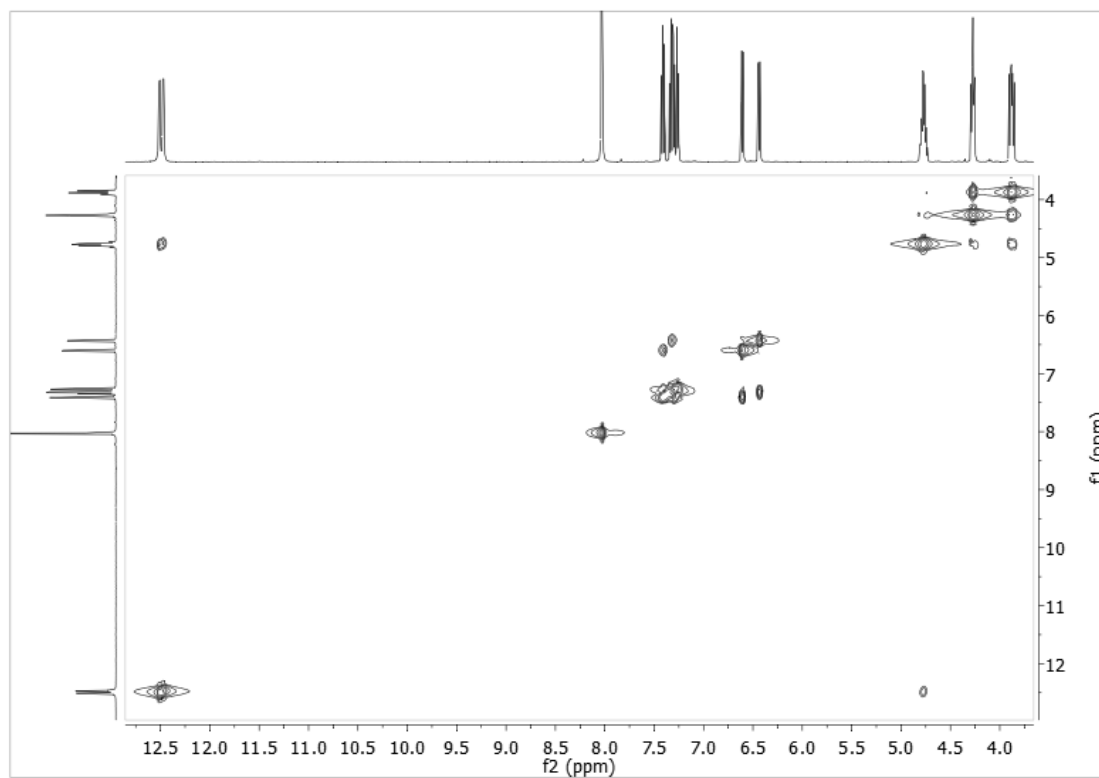
Figure A4.2. ^{1}H-NMR COSY Spectrum of [Lu(2LImTHF-1,2-HOPO)$_2$][NMe$_4$]
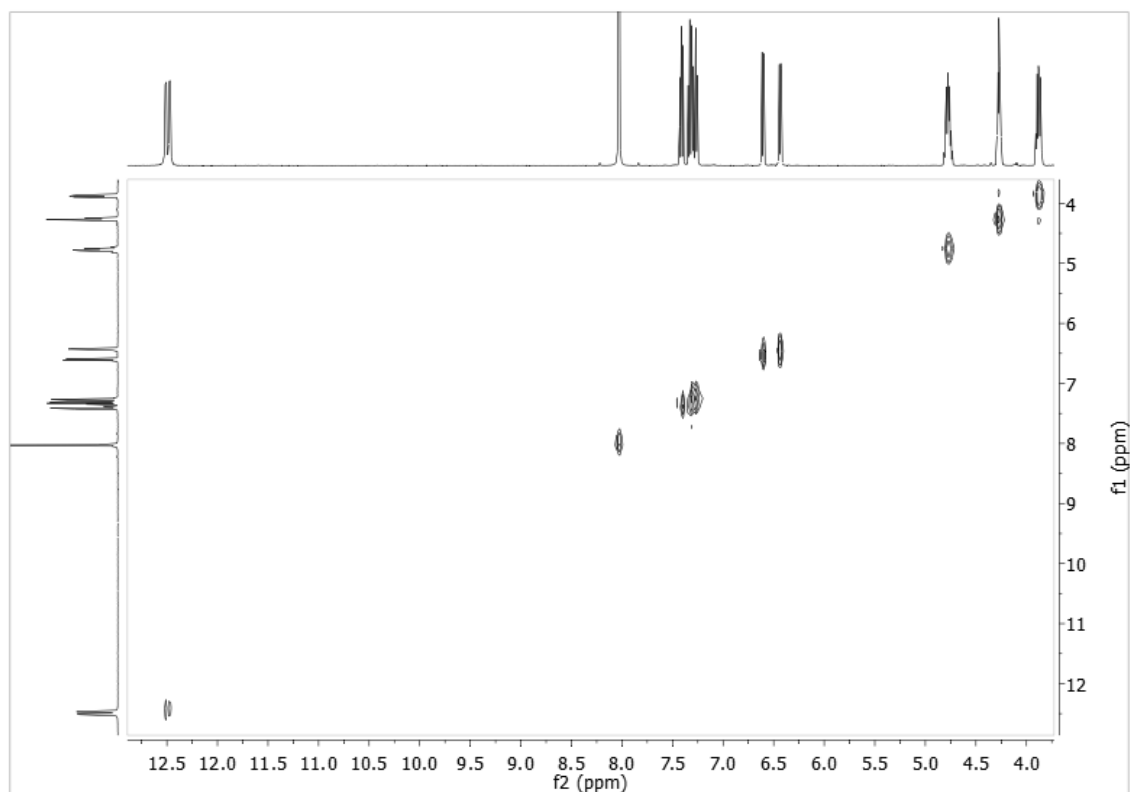
Figure A4.3. ^{1}H-NMR EXSY Spectrum of [Lu(2LImTHF-1,2-HOPO)$_2$][NMe$_4$]
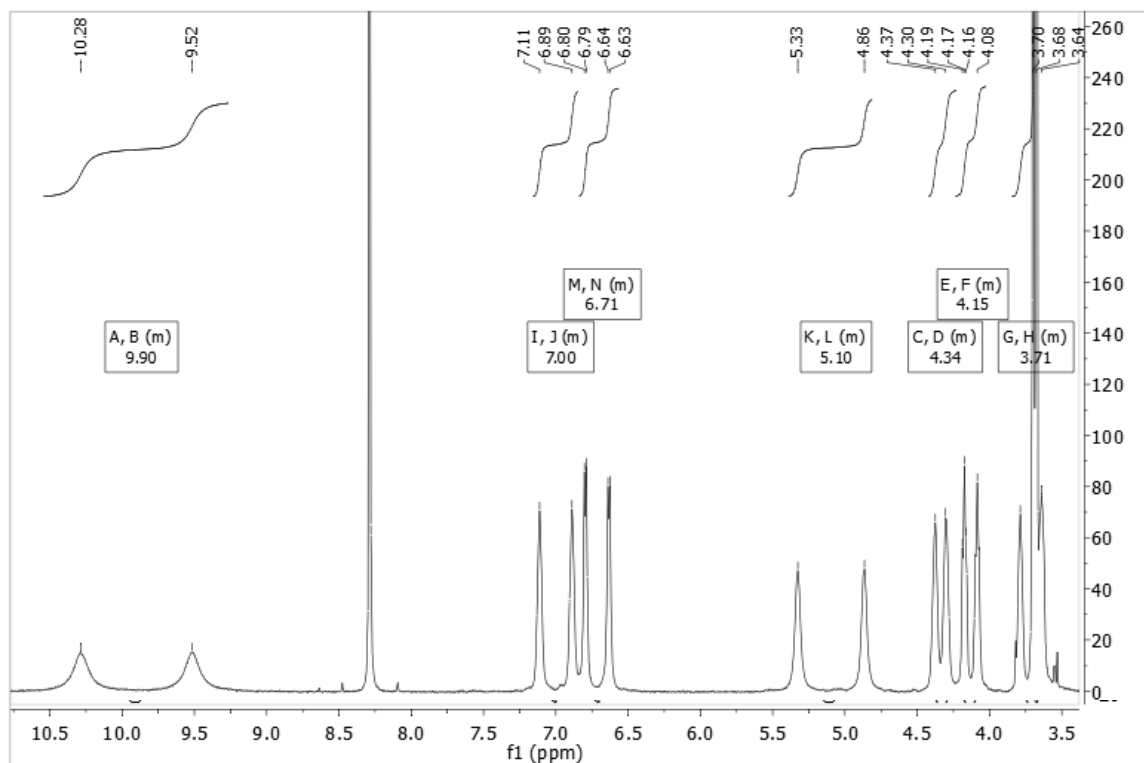
Figure A4.4. ^{1}H-NMR Spectrum of [Yb(2LImTHF-1,2-HOPO)$_2$][NMe$_4$]

207
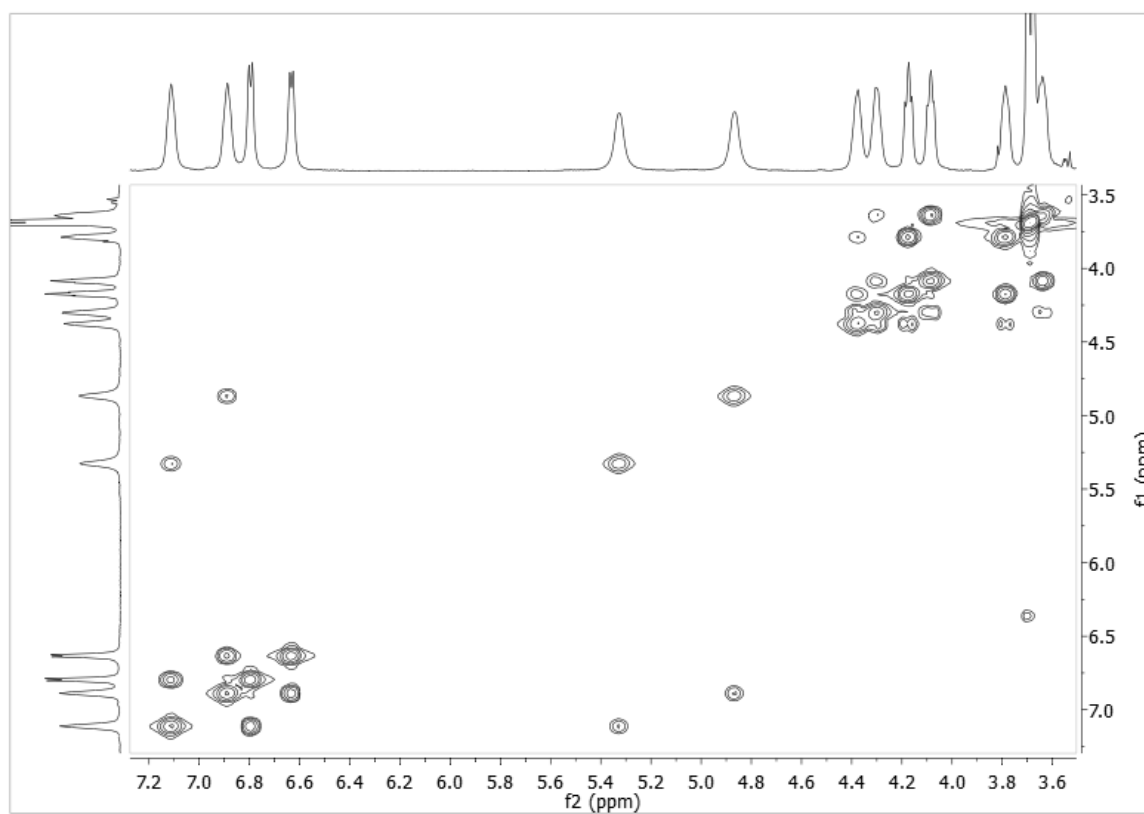
Figure A4.5. ^{1}H-NMR COSY Spectrum of [Yb(2LImTHF-1,2-HOPO)$_2$][NMe$_4$]
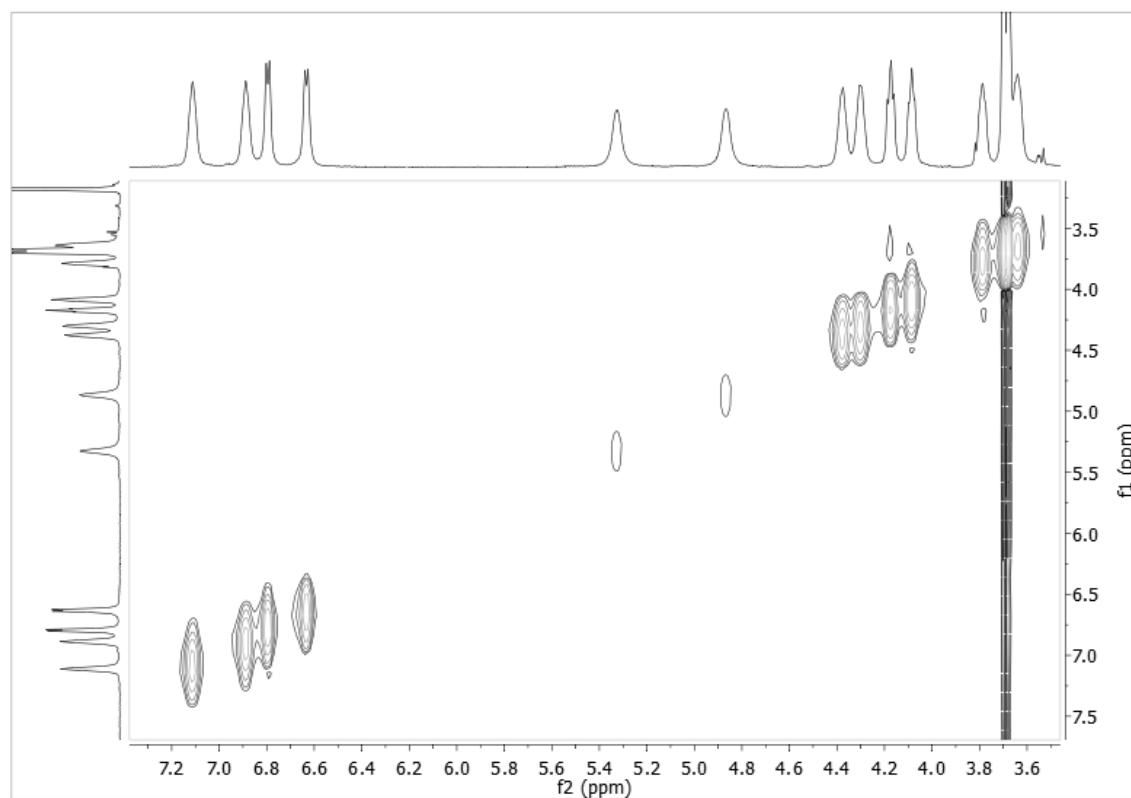
Figure A4.6. ^{1}H-NMR EXSY Spectrum of [Yb(2LImTHF-1,2-HOPO)$_2$][NMe$_4$]
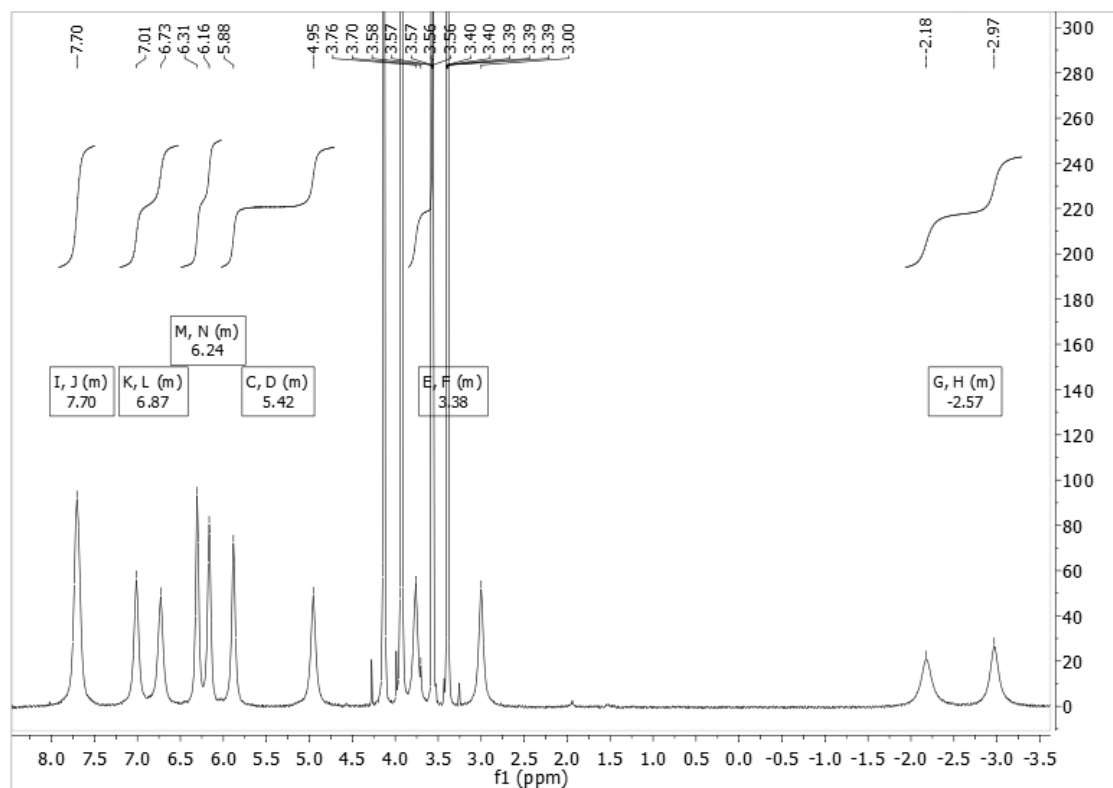
Figure A4.7. ^{1}H-NMR Spectrum of [Tm(2LImTHF-1,2-HOPO)$_2$][NMe$_4$]
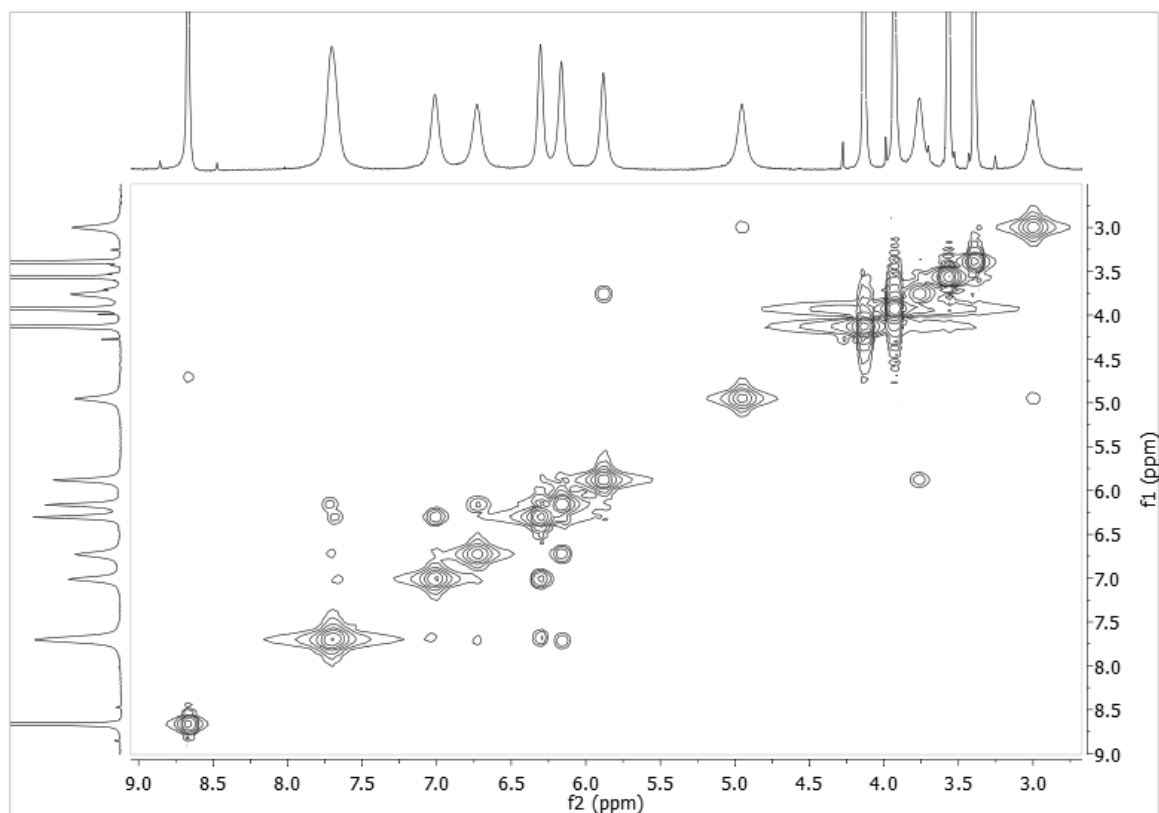
Figure A4.8. ^{1}H-NMR COSY Spectrum of [Tm(2LImTHF-1,2-HOPO)$_2$][NMe$_4$]
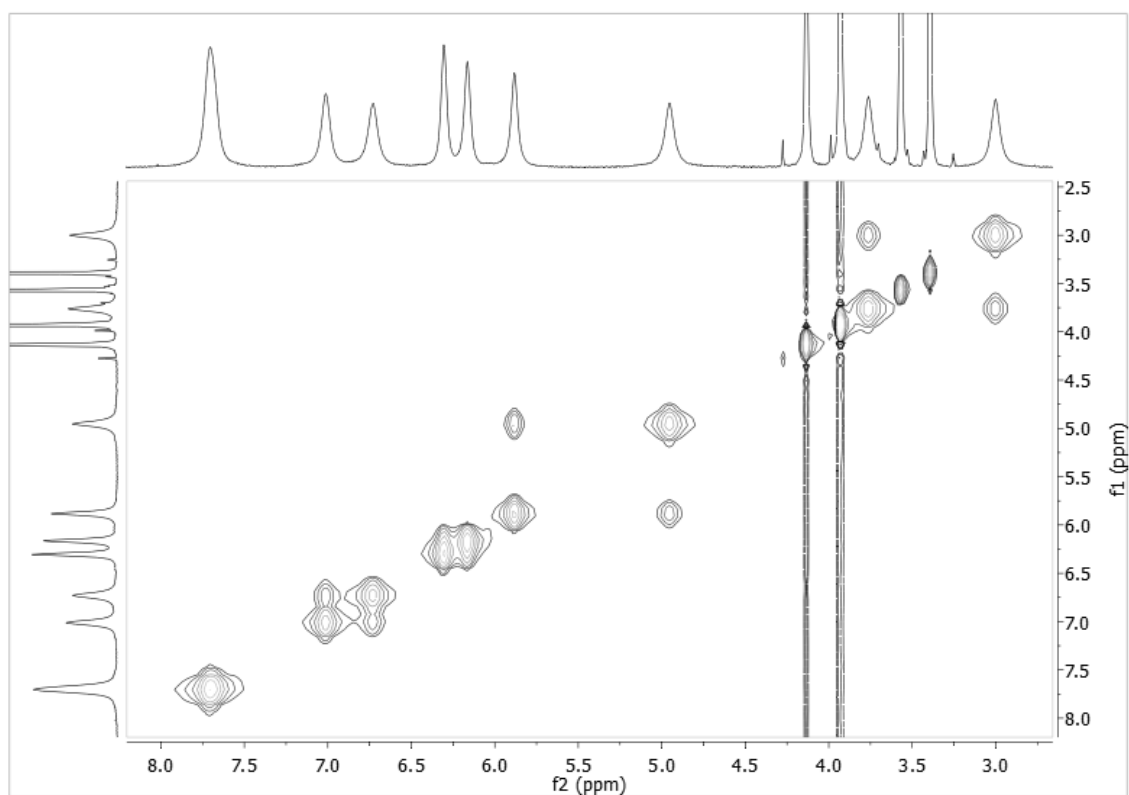
Figure A4.9. ^{1}H-NMR EXSY Spectrum of [Tm(2LImTHF-1,2-HOPO)$_2$][NMe$_4$]
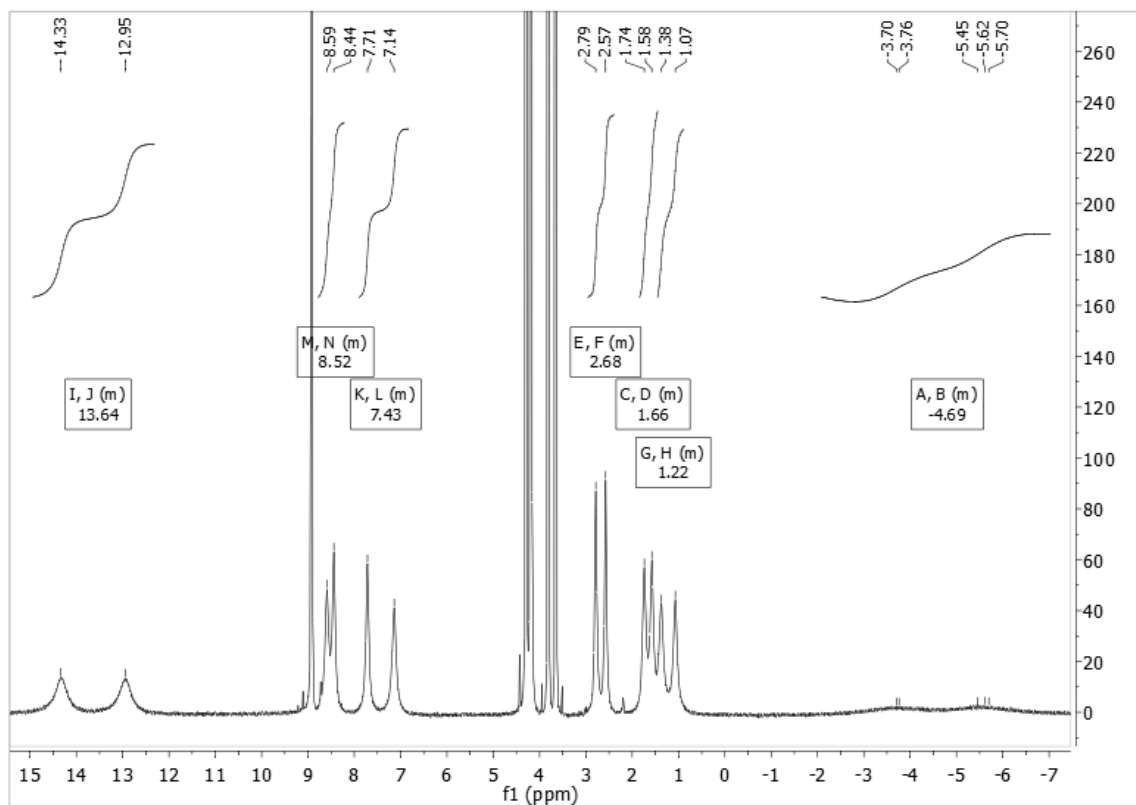
Figure A4.10. ^{1}H-NMR Spectrum of [Er(2LImTHF-1,2-HOPO)$_2$][NMe$_4$]
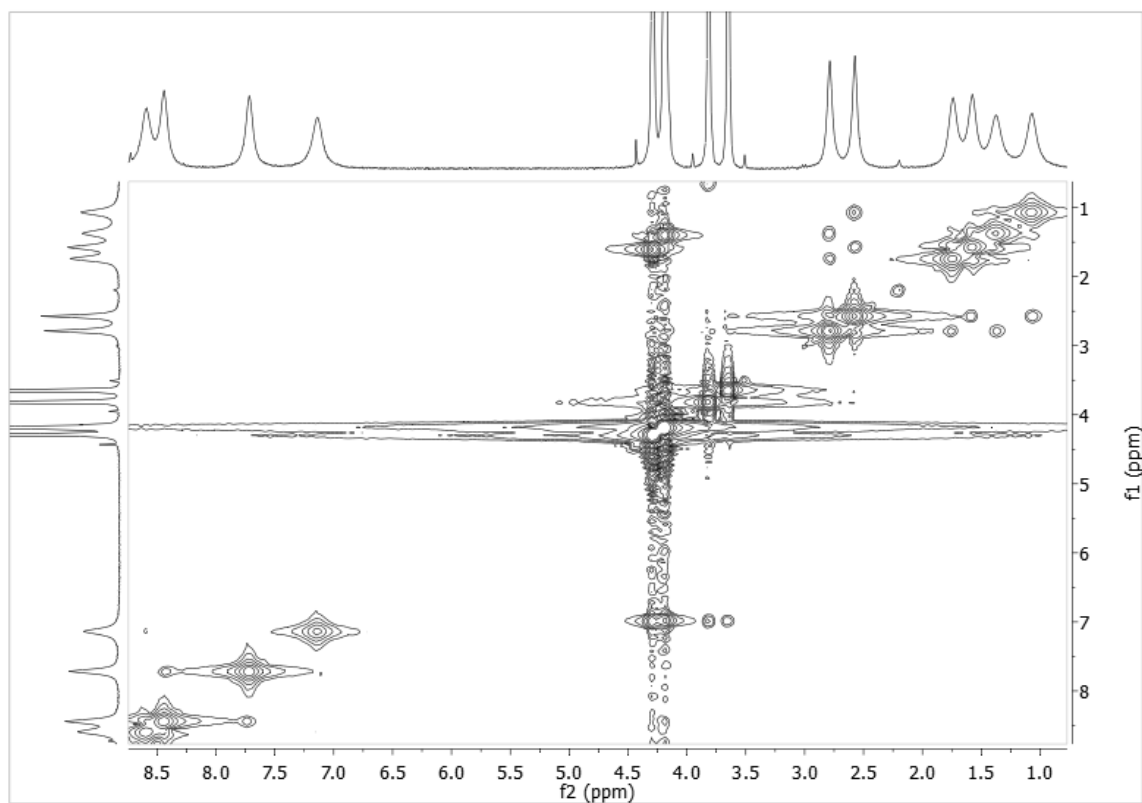
Figure A4.11. ^{1}H-NMR COSY Spectrum of [Er(2LImTHF-1,2-HOPO)$_2$][NMe$_4$]
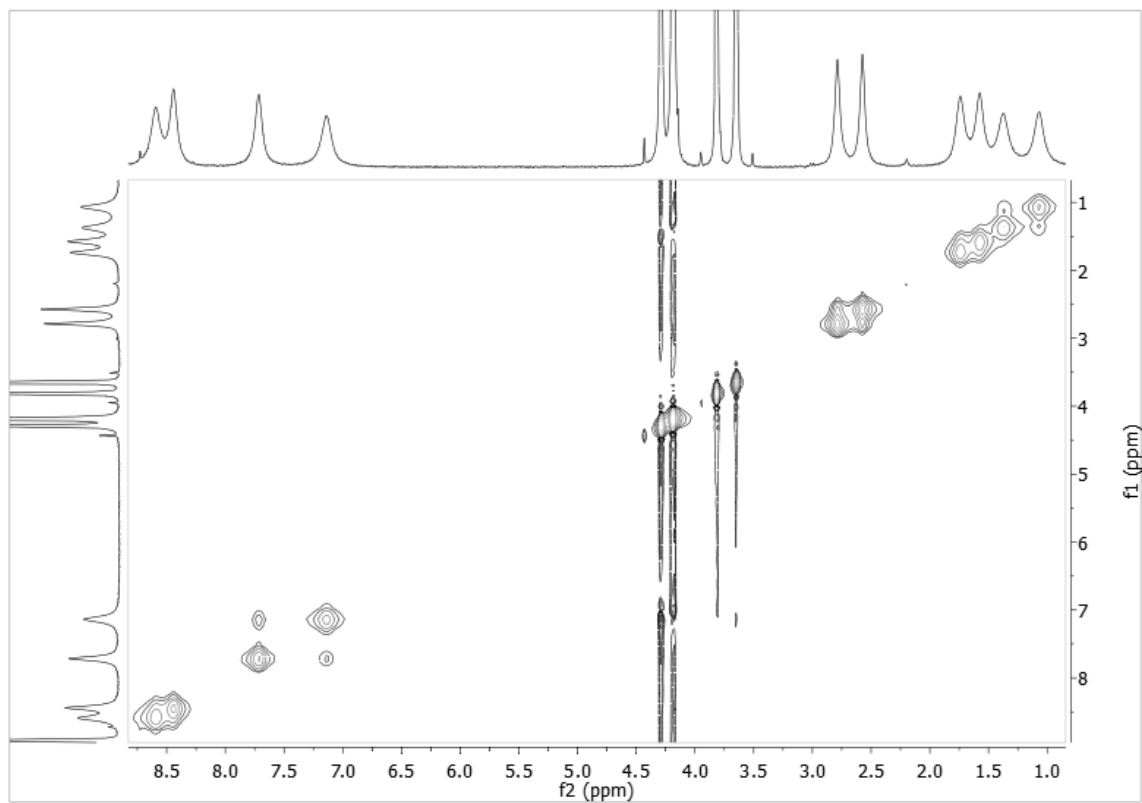
Figure A4.12. ^{1}H-NMR EXSY Spectrum of [Er(2LImTHF-1,2-HOPO)$_2$][NMe$_4$]
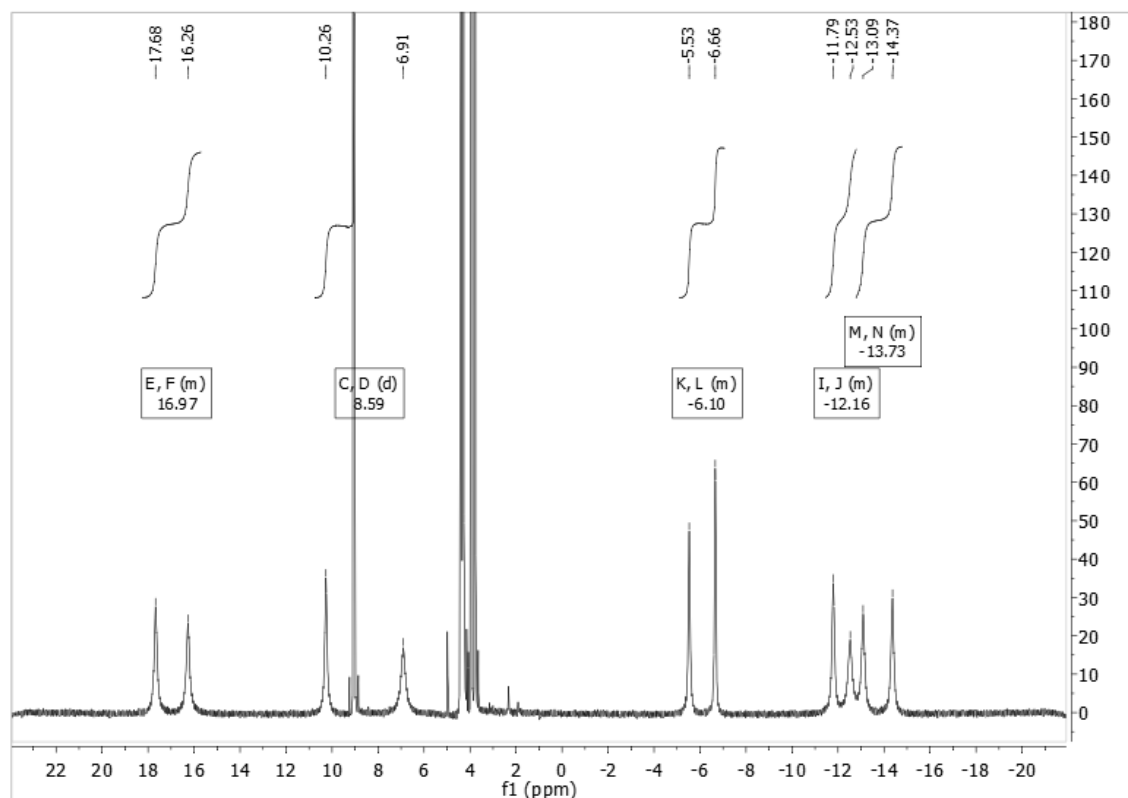
Figure A4.13. ^{1}H-NMR Spectrum of [Dy(2LImTHF-1,2-HOPO)$_2$][NMe$_4$]
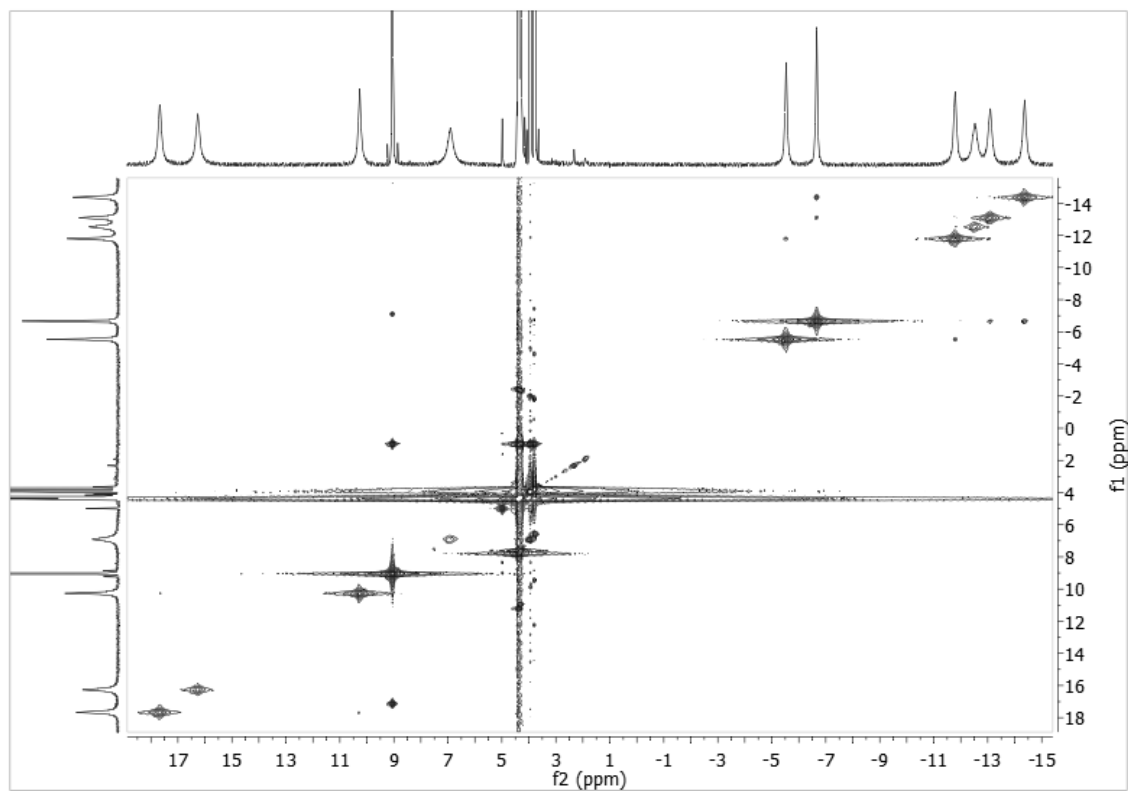
Figure A4.14. ^{1}H-NMR COSY Spectrum of [Dy(2LImTHF-1,2-HOPO)$_2$][NMe$_4$]
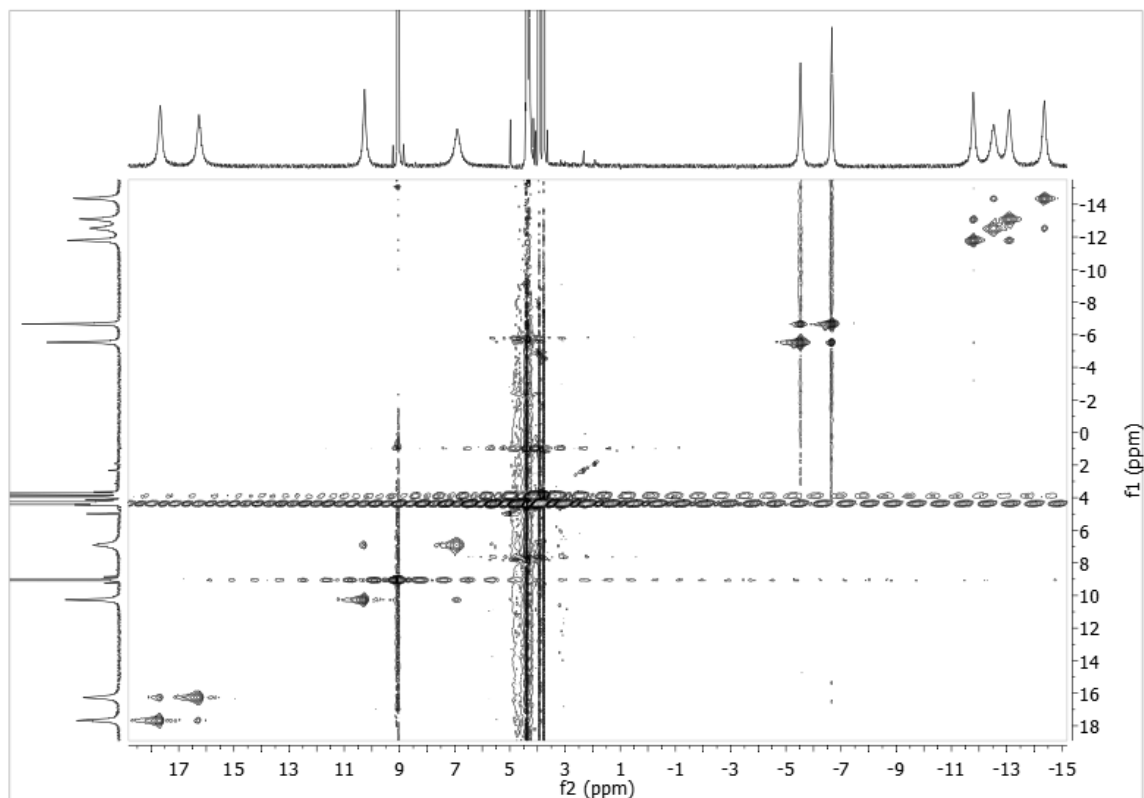
Figure A4.15. ^{1}H-NMR EXSY Spectrum of [Dy(2LImTHF-1,2-HOPO)$_2$][NMe$_4$]
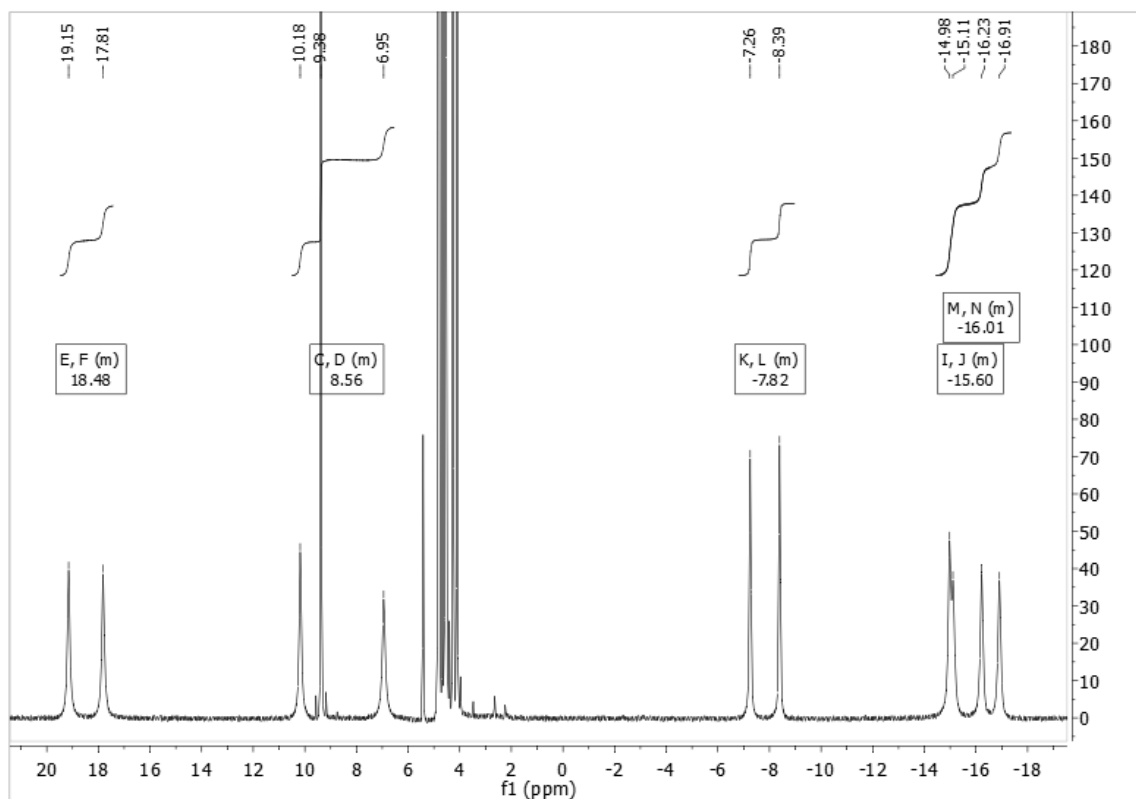
Figure A4.16. ^{1}H-NMR Spectrum of [Tb(2LImTHF-1,2-HOPO)$_2$][NMe$_4$]

213
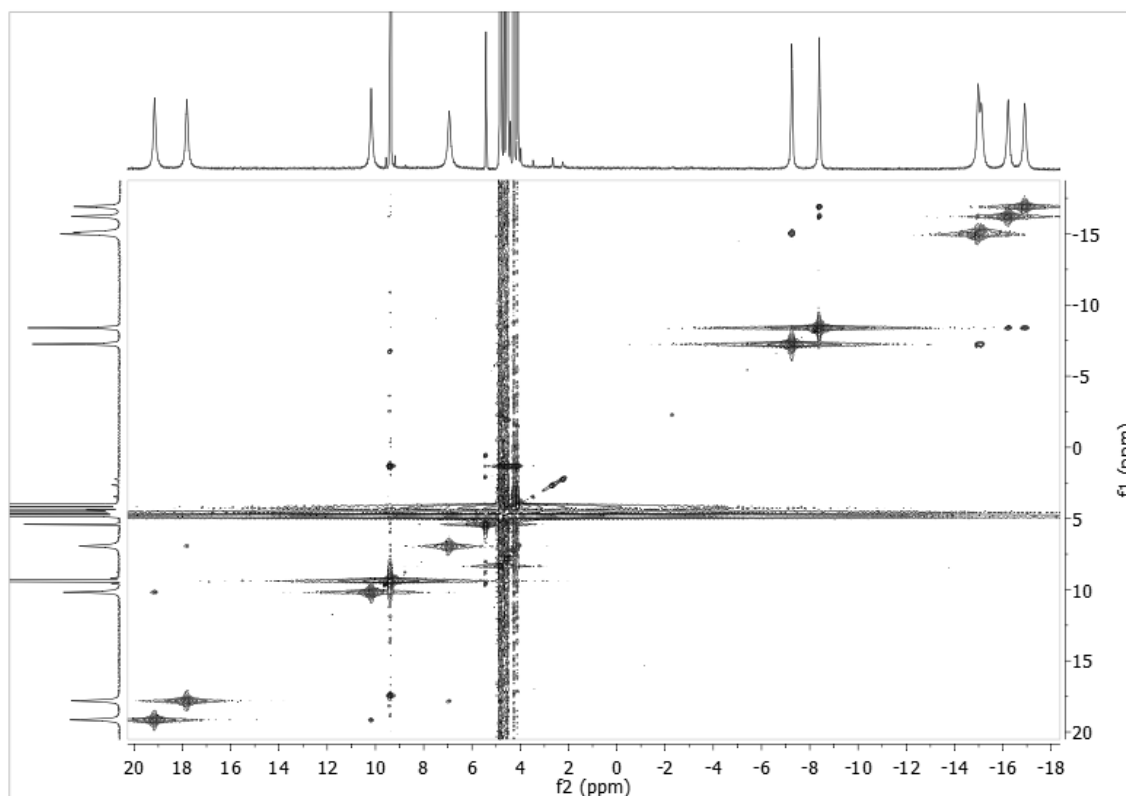
Figure A4.17. ^{1}H-NMR COSY Spectrum of [Tb(2LImTHF-1,2-HOPO)$_2$][NMe$_4$]
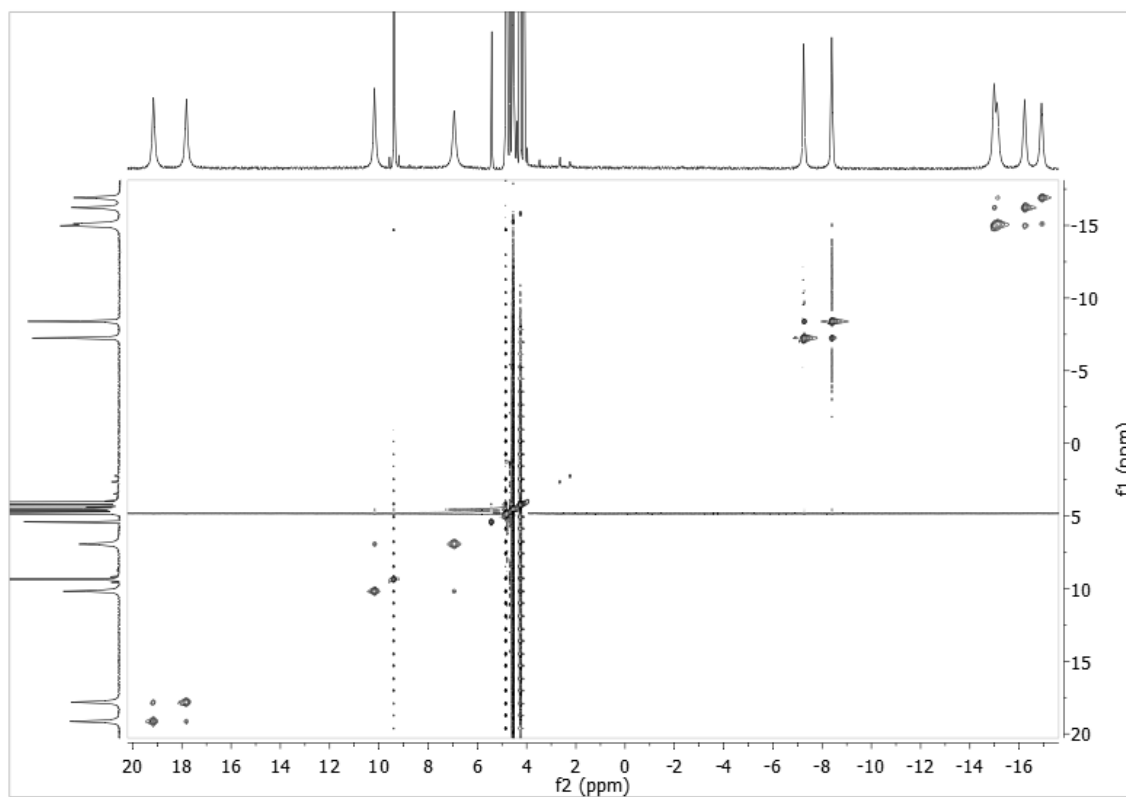
Figure A4.18. ^{1}H-NMR EXSY Spectrum of [Tb(2LImTHF-1,2-HOPO)$_2$][NMe$_4$]

214
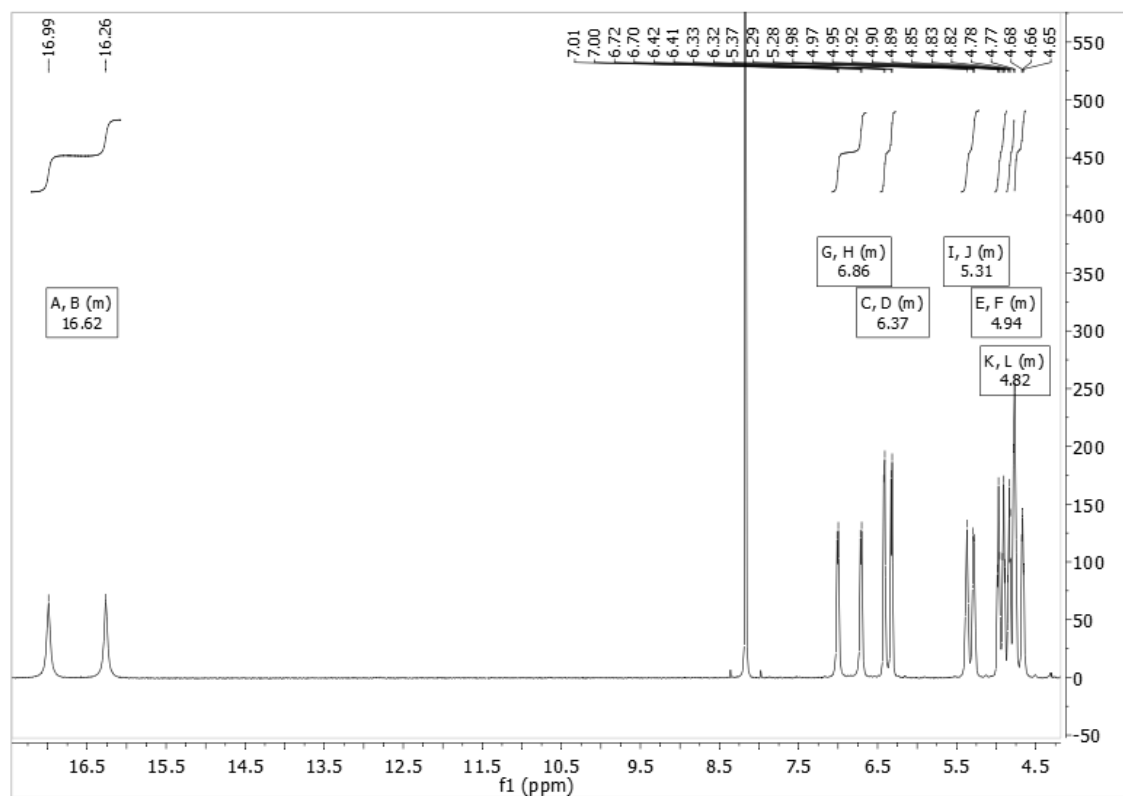
Figure A4.19. ^{1}H-NMR Spectrum of [Eu(2LImTHF-1,2-HOPO)$_2$][NMe$_4$]
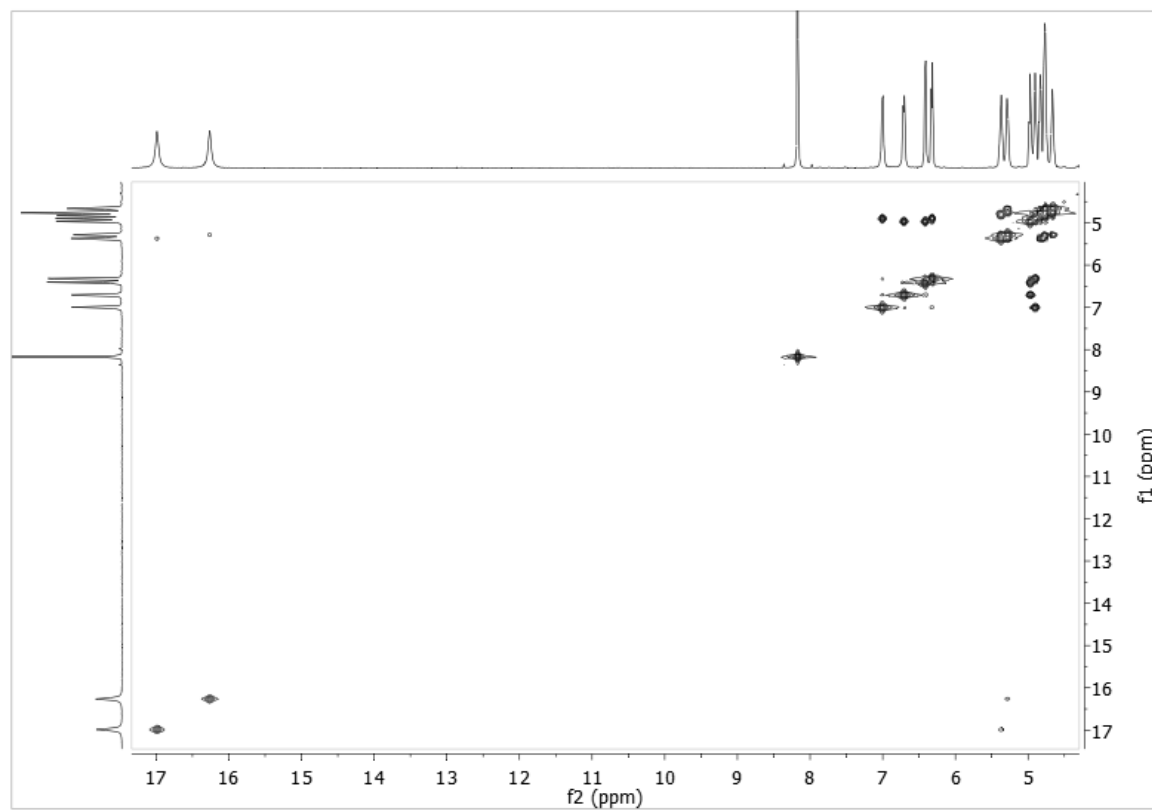
Figure A4.20. ^{1}H-NMR COSY Spectrum of [Eu(2LImTHF-1,2-HOPO)$_2$][NMe$_4$]
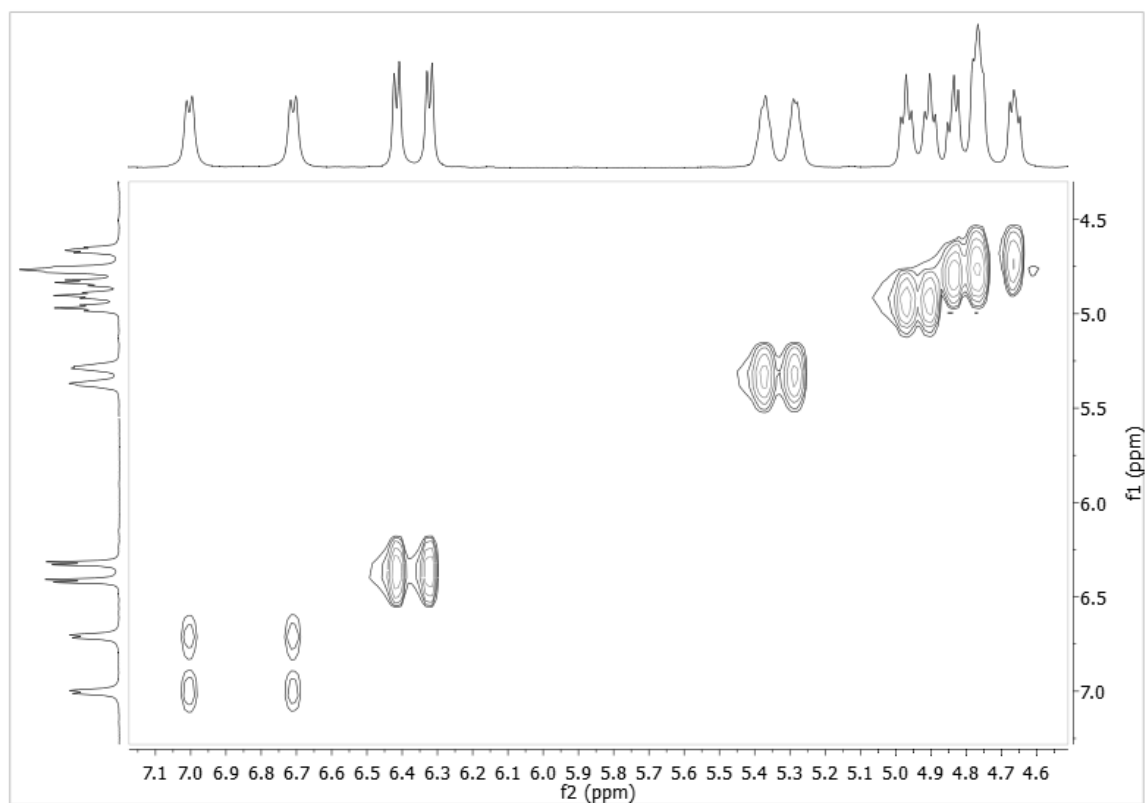
Figure A4.21. ^{1}H-NMR EXSY Spectrum of [Eu(2LImTHF-1,2-HOPO)₂][NMe₄]
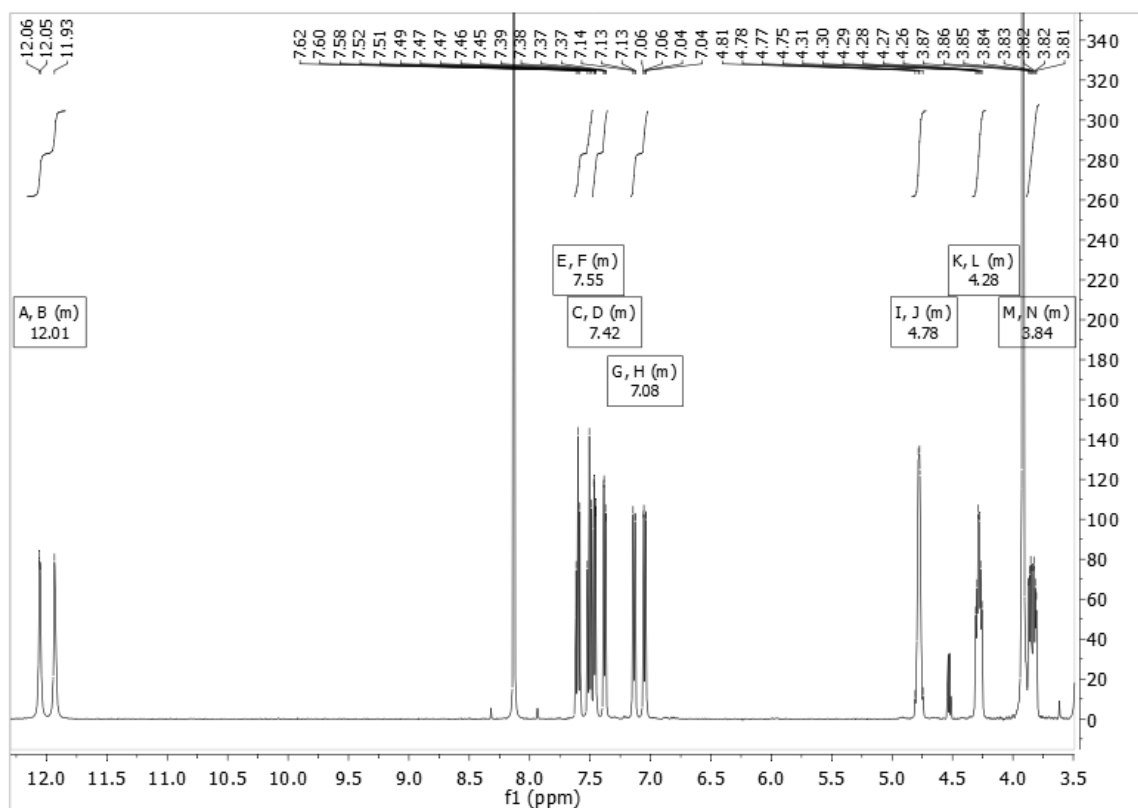
Figure A4.22. ^{1}H-NMR Spectrum of [Sm(2LImTHF-1,2-HOPO)₂][NMe₄]
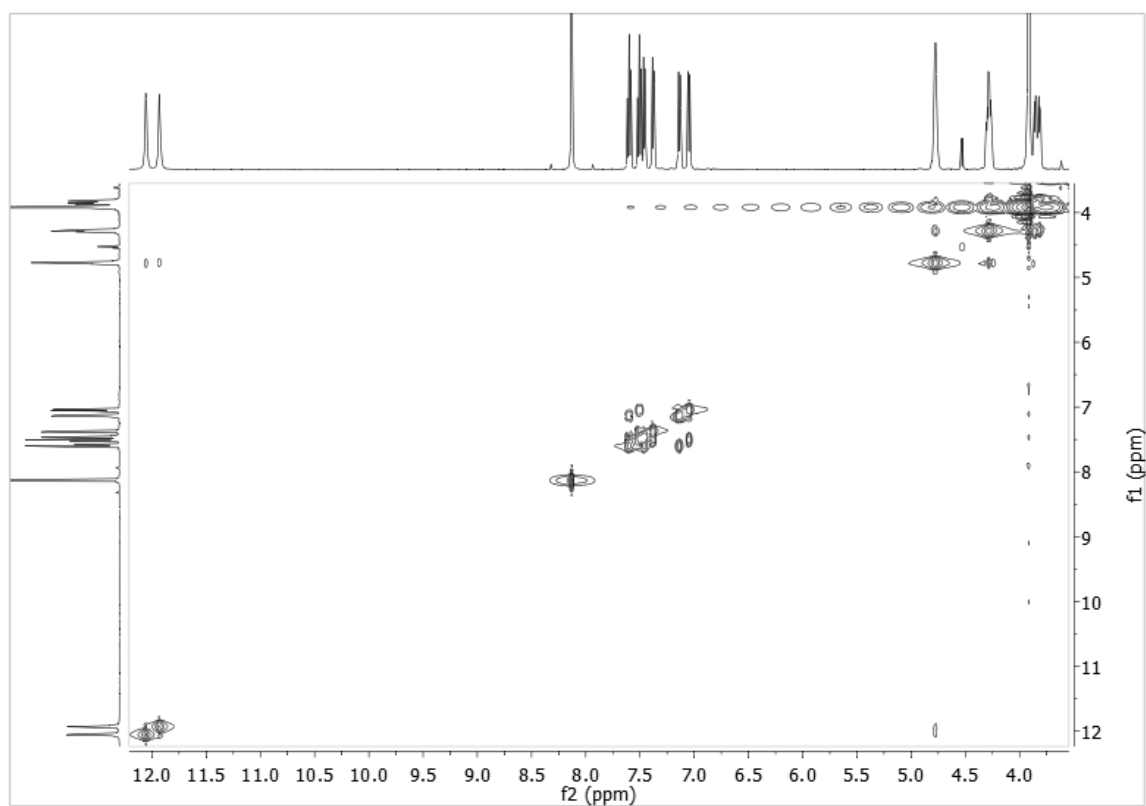
Figure A4.23. ^{1}H-NMR COSY Spectrum of [Sm(2LImTHF-1,2-HOPO)$_2$][NMe$_4$]
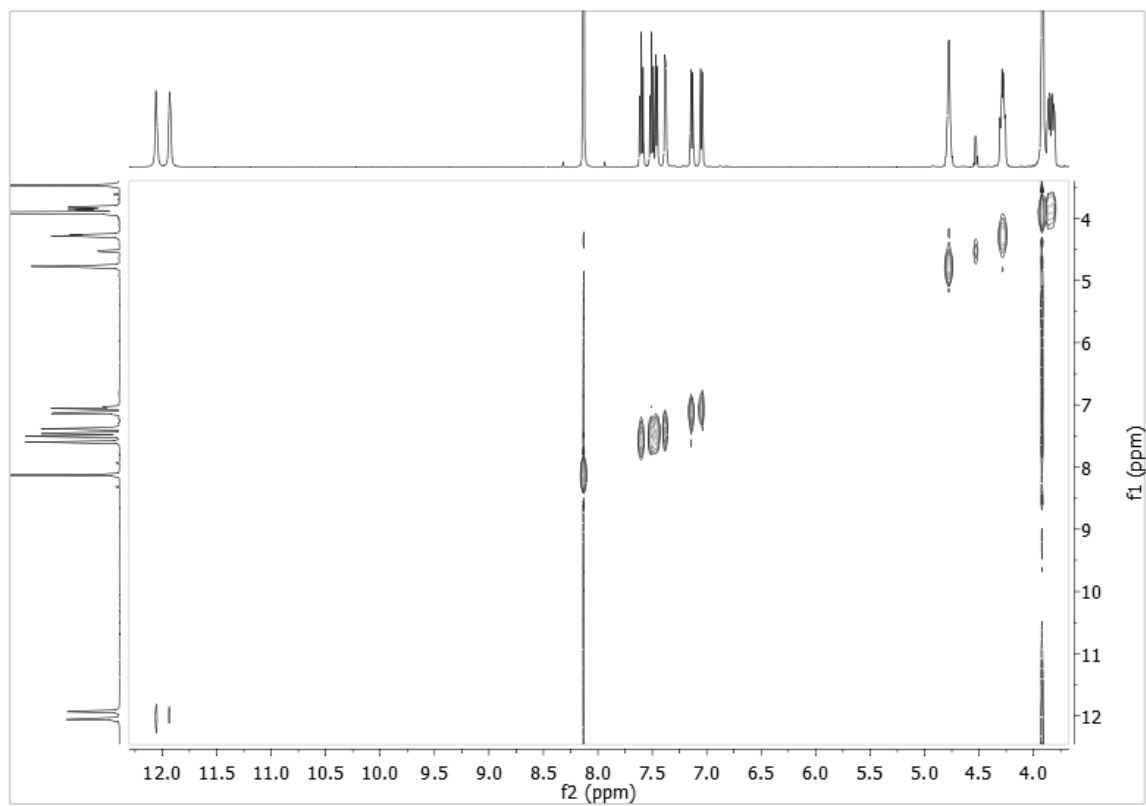
Figure A4.24. ^{1}H-NMR EXSY Spectrum of [Sm(2LImTHF-1,2-HOPO)$_2$][NMe$_4$]

217
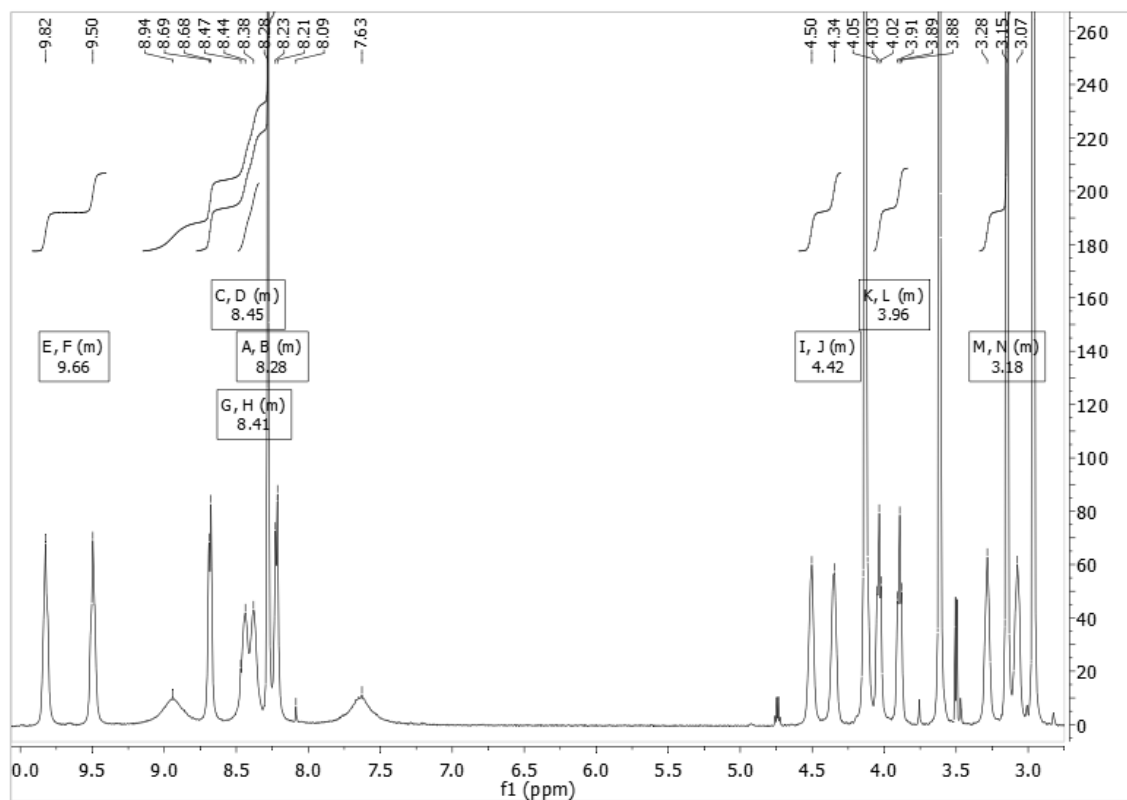
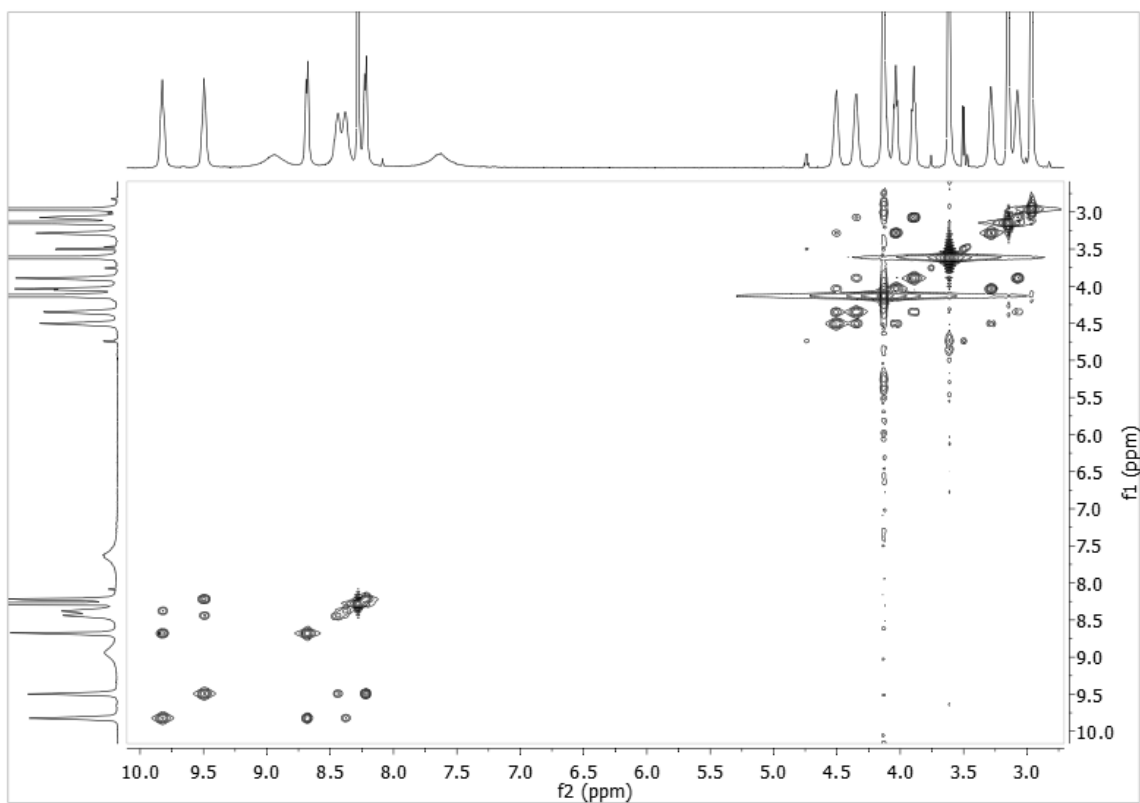**Figure A4.25.** ^{1}H-NMR Spectrum of [Nd(2LImTHF-1,2-HOPO)$_2$][NMe$_4$]

Figure A4.26. ^{1}H-NMR COSY Spectrum of [Nd(2LImTHF-1,2-HOPO)$_2$][NMe$_4$]
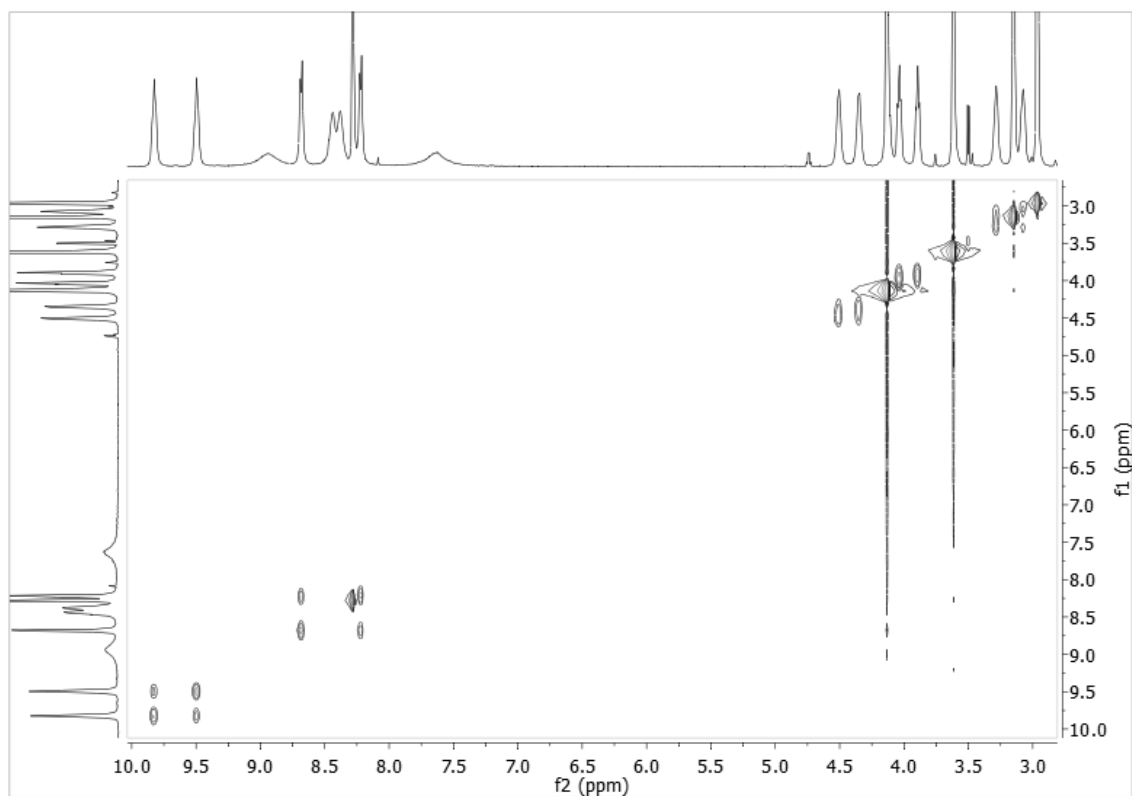
Figure A4.27. ^{1}H-NMR EXSY Spectrum of [Nd(2LImTHF-1,2-HOPO)$_2$][NMe$_4$]
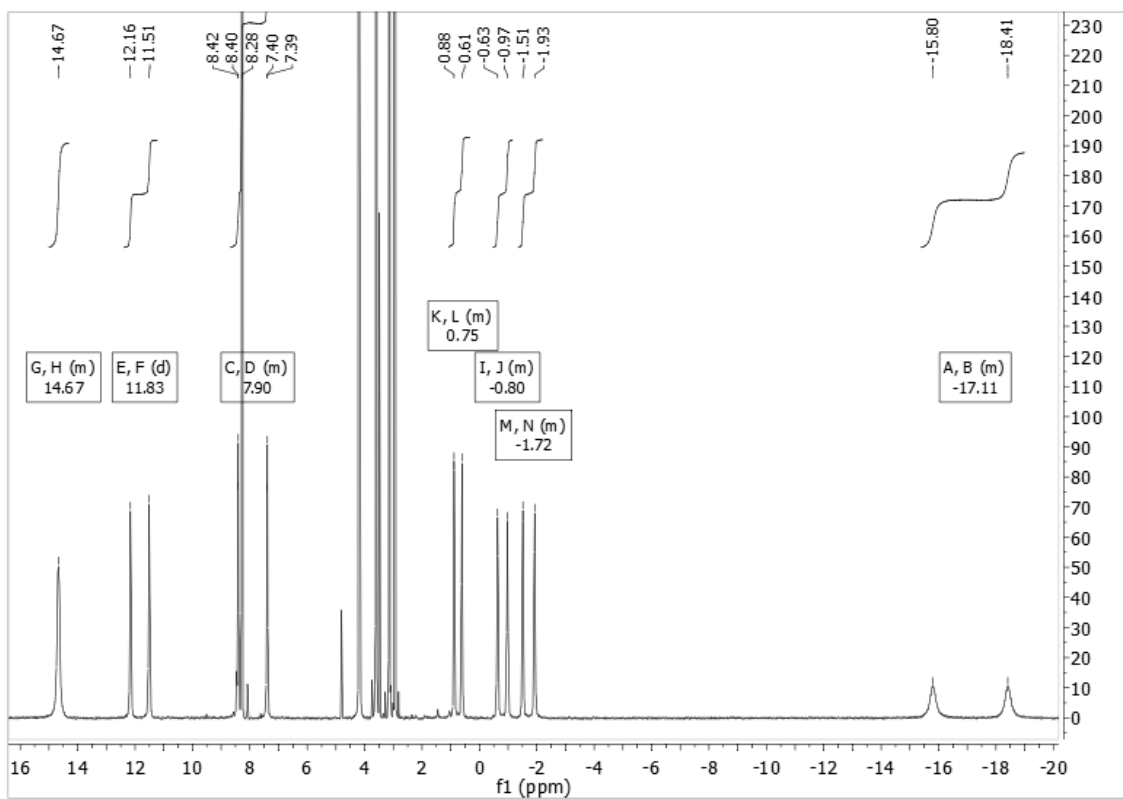
Figure A4.28. ^{1}H-NMR Spectrum of [Pr(2LImTHF-1,2-HOPO)$_2$][NMe$_4$]

219
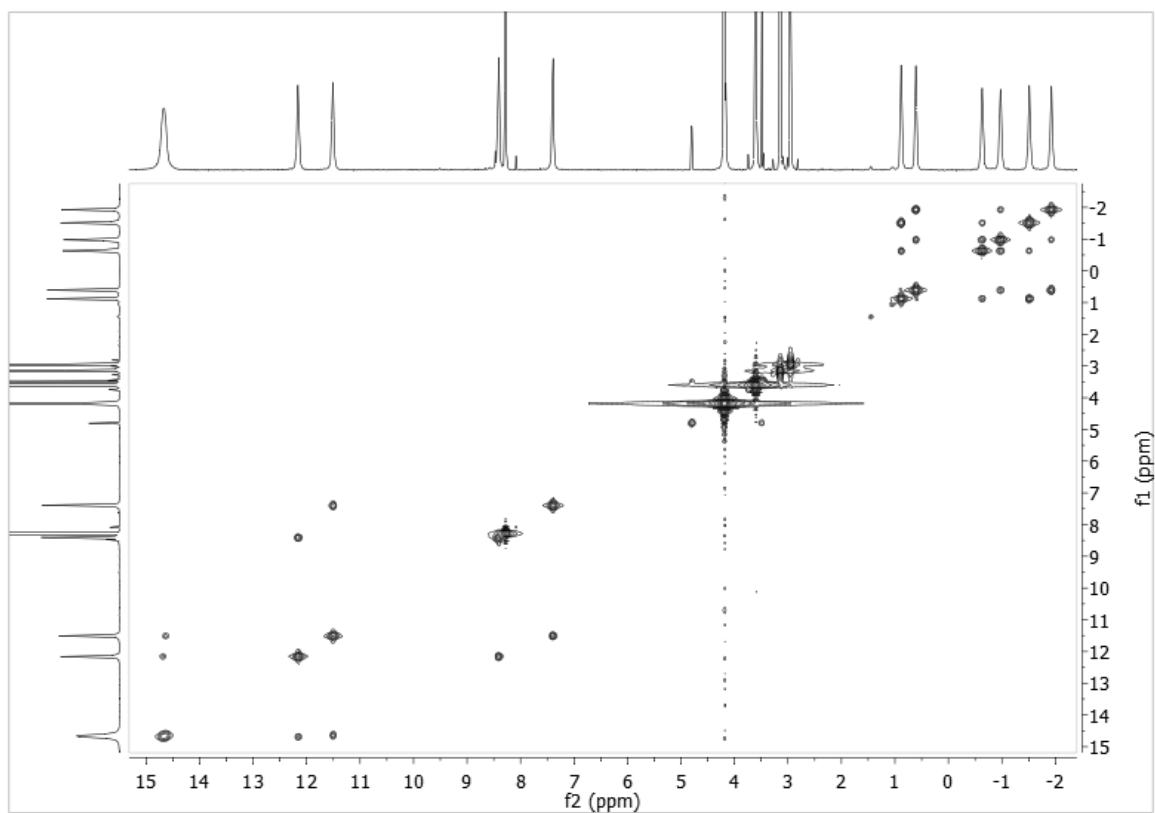
Figure A4.29. ^{1}H-NMR COSY Spectrum of [Pr(2LImTHF-1,2-HOPO)$_2$][NMe$_4$]
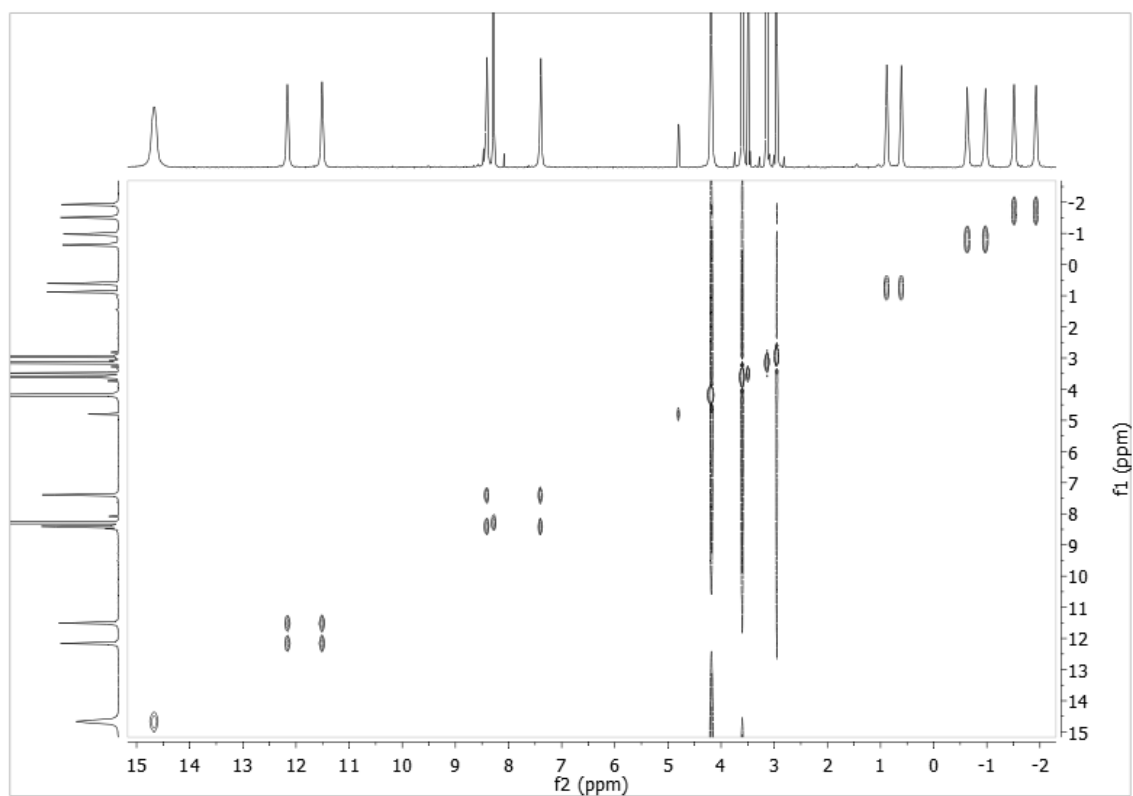
Figure A4.30. ^{1}H-NMR EXSY Spectrum of [Pr(2LImTHF-1,2-HOPO)$_2$][NMe$_4$]
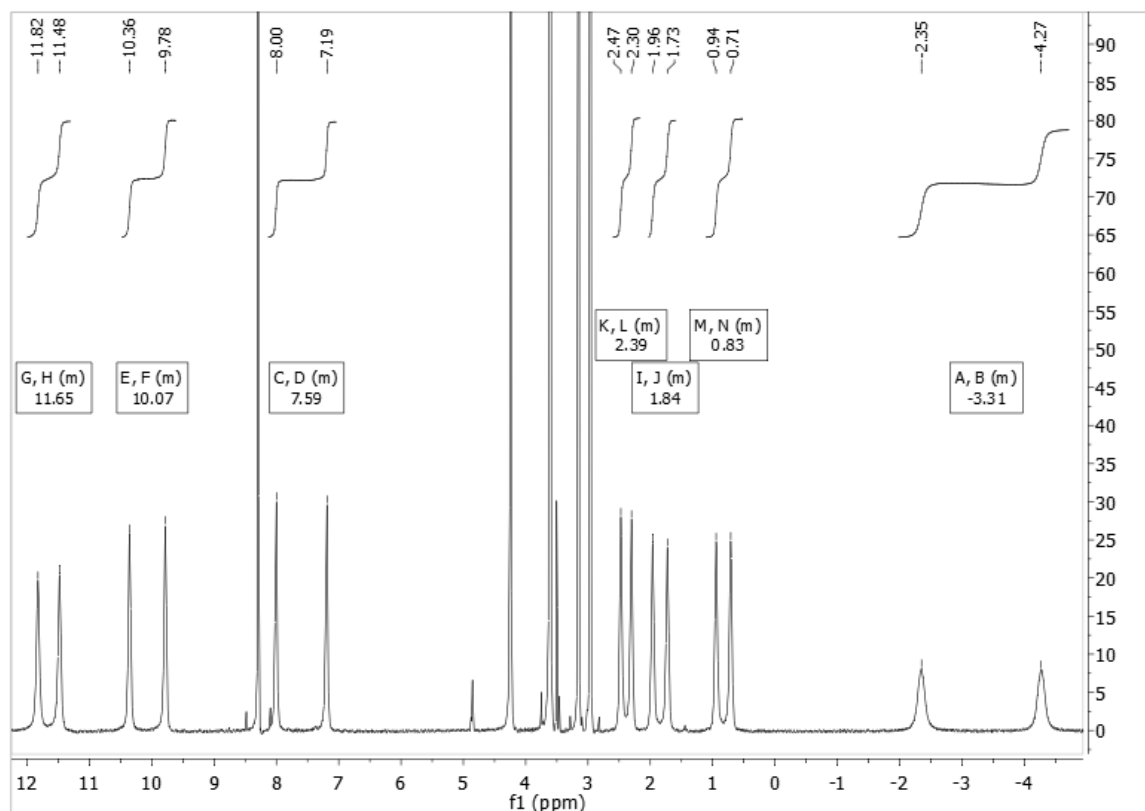
Figure A4.31. ^{1}H-NMR Spectrum of [Ce(2LImTHF-1,2-HOPO)$_2$][NMe$_4$]
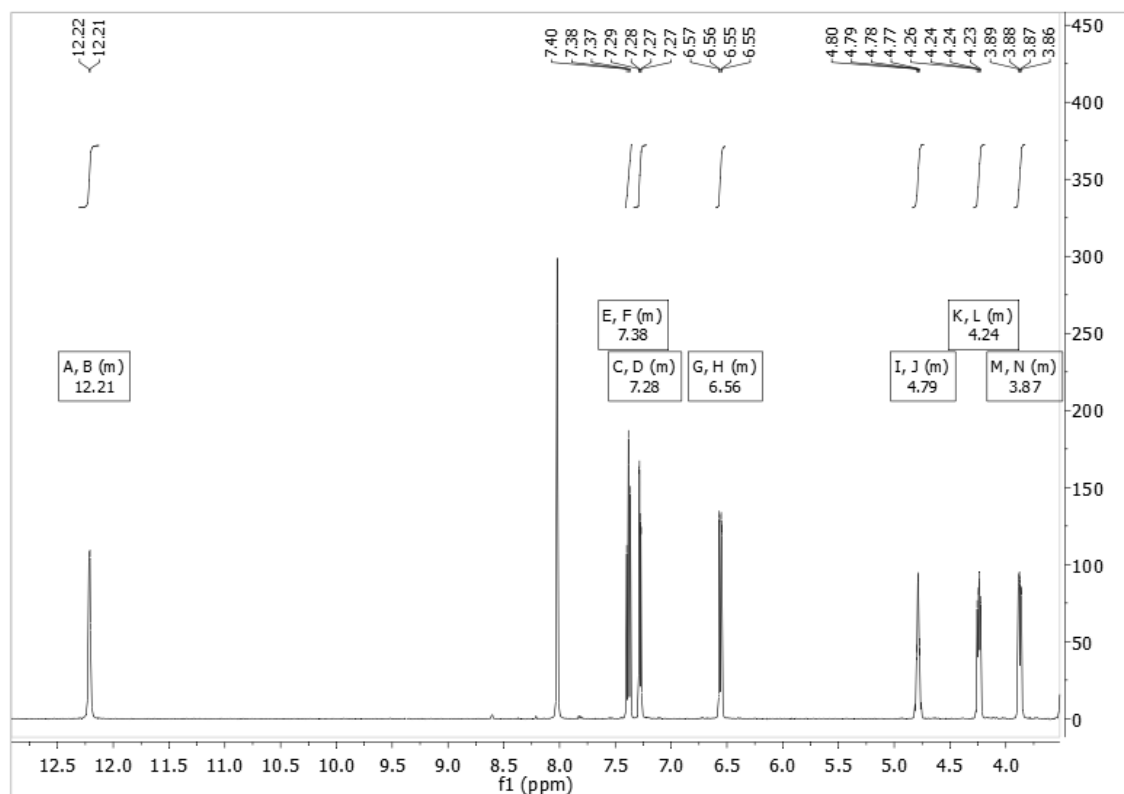
Figure A4.32. ^{1}H-NMR Spectrum of [La(2LImTHF-1,2-HOPO)$_2$][NMe$_4$]

221
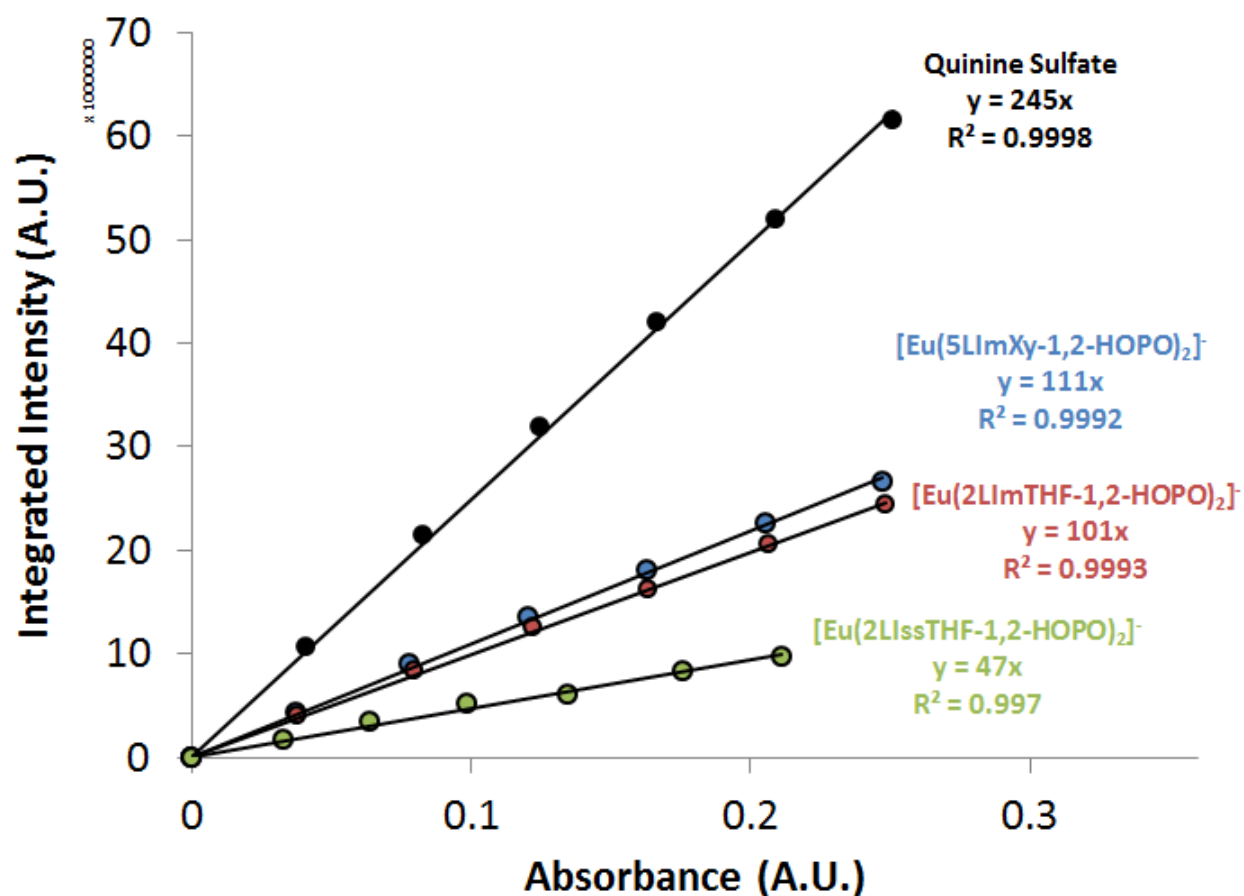
Figure A4.33. Quantum Yield Determination of [Eu(2LImTHF-1,2-HOPO)₂]⁻ and [Eu(2LIssTHF-1,2-HOPO)₂]⁻

Table A4.1. DFT calculated structure of [Ho(2LImTHF-1,2-HOPO)₂]⁻ used to fit the ¹H-NMR isotropic shifts

Atom Label	X	Y	Z	Atom Label	X	Y	Z
N	-1.715	2.081253	1.855153	H	-3.418	-3.65448	0.583045
N	1.068	-0.69618	4.579888	C	4.101	2.172164	-3.07324
H	0.564	-0.7215	3.686114	H	4.644	2.281447	-4.0027
N	2.117	-1.43264	1.994777	C	-2.143	-2.76436	-2.96189
O	3.09	-1.27581	5.485248	C	-1.676	-2.444	-4.36942
N	-0.877	1.36426	4.529784	C	2.34	1.169906	-4.51292
H	-0.523	0.967218	3.654282	C	-3.052	-3.80015	-2.80398
O	-2.058	3.152852	5.306604	H	-3.363	-4.31834	-3.70203
C	-3.522	4.12889	1.528198	C	-3.522	-4.12889	-1.5282
H	-4.236	4.938803	1.406162	H	-4.236	-4.9388	-1.40616
C	2.601	-1.76978	0.721336	C	0.465	-0.30961	5.831376
C	-2.143	2.764356	2.961886	H	1.275	-0.23015	6.559382
C	-2.145	2.371747	0.55229	C	-0.331	1.034047	5.837785
C	-3.08	3.428761	0.421805	H	0.307	1.858342	6.178048
H	-3.418	3.654479	-0.58304	C	0.465	0.309613	-5.83138
C	3.883	-2.37392	0.679692	H	1.275	0.230147	-6.55938
H	4.254	-2.65474	-0.29926	C	-0.331	-1.03405	-5.83778
C	-3.052	3.800149	2.803984	H	0.307	-1.85834	-6.17805
H	-3.363	4.318339	3.702033	C	-0.574	1.30224	-6.38411

C	2.84	-1.59772	3.145311	H	-0.119	2.19207	-6.82842
C	2.34	-1.16991	4.512916	H	-1.27	1.614843	-5.58721
C	-1.676	2.443996	4.36942	C	-1.452	-0.74835	-6.88348
C	4.101	-2.17216	3.073239	H	-1.437	-1.44743	-7.72212
H	4.644	-2.28145	4.002704	H	-2.433	-0.80932	-6.39718
C	4.617	-2.56875	1.834579	C	-0.574	-1.30224	6.384106
H	5.602	-3.02351	1.779151	H	-0.119	-2.19207	6.828421
N	2.117	1.432643	-1.99478	H	-1.27	-1.61484	5.587212
N	-0.877	-1.36426	-4.52978	C	-1.452	0.748354	6.883475
H	-0.523	-0.96722	-3.65428	H	-1.437	1.447434	7.722122
N	-1.715	-2.08125	-1.85515	H	-2.433	0.80932	6.397179
O	-2.058	-3.15285	-5.3066	O	-1.229	0.568917	-7.40262
N	1.068	0.696176	-4.57989	O	-1.229	-0.56892	7.402618
H	0.564	0.721505	-3.68611	O	-0.833	-1.08338	-1.94687
O	3.09	1.275808	-5.48525	O	-1.665	-1.67462	0.388827
C	4.617	2.56875	-1.83458	O	-0.833	1.083375	1.94687
H	5.602	3.023513	-1.77915	O	-1.665	1.674619	-0.38883
C	-2.145	-2.37175	-0.55229	O	0.885	-0.91691	2.009285
C	2.84	1.597722	-3.14531	O	1.864	-1.50815	-0.27331
C	2.601	1.769778	-0.72134	O	0.885	0.916907	-2.00928
C	3.883	2.373921	-0.67969	O	1.864	1.508148	0.273306
H	4.254	2.654735	0.299264	Ho	0	0	0
C	-3.08	-3.42876	-0.42181				

Chapter 5 Appendix
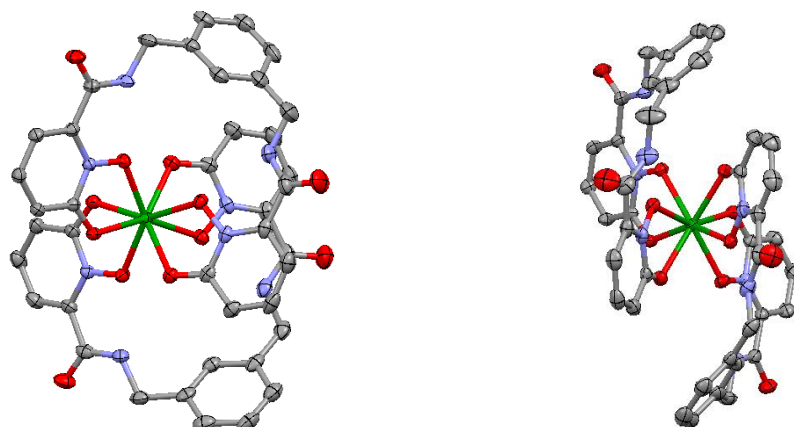
XRD Data and DFT Coordinates

Figure A5.1. ORTEP of **Sc** (solvent, counterion, and hydrogens removed for clarity).

Table A5.1. Crystal data and structure refinement for **Sc**.

|	
Identification code	[Sc(5LImXy-1,2-HOPO)$_2$][NMe$_4$]
Empirical formula	C44 H44 N9 O12 Sc
Formula weight	1008.94
Temperature	100(2) K
Wavelength	0.71073 Å
Crystal system	Monoclinic
Space group	P2(1)/c
Unit cell dimensions	a = 14.6094(6) Å $\alpha = 90°$.
	b = 14.7981(6) Å $\beta = 101.2280(10)°$.
	c = 24.6083(10) Å $\gamma = 90°$.
Volume	5218.3(4) Å^3
Z	4
Density (calculated)	1.284 Mg/m^3
Absorption coefficient	0.211 mm^{-1}
F(000)	2112
Crystal size	0.30 x 0.22 x 0.11 mm^3
Theta range for data collection	1.61 to 25.35°.
Index ranges	-17<=h<=17, -15<=k<=17, -29<=l<=29
Reflections collected	43301
Independent reflections	9555 [R(int) = 0.0267]
Completeness to theta = 25.00°	100.0 %
Absorption correction	Semi-empirical from equivalents
Max. and min. transmission	0.9772 and 0.9394
Refinement method	Full-matrix least-squares on F^2
Data / restraints / parameters	9555 / 0 / 646
Goodness-of-fit on F^2	1.007
Final R indices [I>2sigma(I)]	R1 = 0.0421, wR2 = 0.1080
R indices (all data)	R1 = 0.0527, wR2 = 0.1146
Largest diff. peak and hole	0.484 and -0.327 e.Å^{-3}
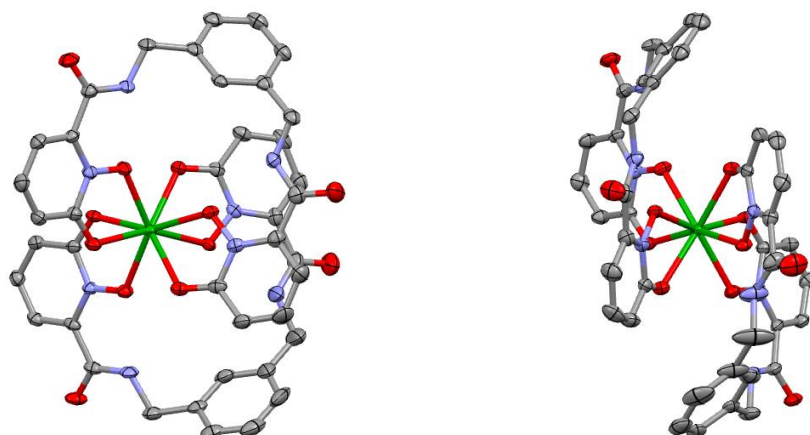
Figure A5.2. ORTEP of **Y** (solvent, counterion, and hydrogens removed for clarity).

Table A5.2. Crystal data and structure refinement for **Y**.

|	
Identification code	[Y(5LImXy-1,2-HOPO)$_2$][NMe$_4$]
Empirical formula	C44 H44 N9 O12 Y
Formula weight	979.79
Temperature	100(2) K
Wavelength	0.71073 Å
Crystal system	Monoclinic
Space group	P2(1)/c
Unit cell dimensions	a = 14.6265(11) Å $\alpha= 90°$.
	b = 14.7375(11) Å $\beta= 101.1190(10)°$.
	c = 24.9826(19) Å $\gamma = 90°$.
Volume	5284.1(7) Å^3
Z	4
Density (calculated)	1.232 Mg/m^3
Absorption coefficient	1.166 mm^{-1}
F(000)	2024
Crystal size	0.30 x 0.10 x 0.07 mm^3
Theta range for data collection	1.61 to 25.37°.
Index ranges	-17<=h<=17, -17<=k<=17, -30<=l<=30
Reflections collected	62193
Independent reflections	9684 [R(int) = 0.0478]
Completeness to theta = 25.00°	100.0 %
Absorption correction	Semi-empirical from equivalents
Max. and min. transmission	0.9228 and 0.7212
Refinement method	Full-matrix least-squares on F^2
Data / restraints / parameters	9684 / 0 / 599
Goodness-of-fit on F^2	1.052
Final R indices [I>2sigma(I)]	R1 = 0.0381, wR2 = 0.0900
R indices (all data)	R1 = 0.0512, wR2 = 0.0942
Largest diff. peak and hole	0.391 and -0.377 e.Å^{-3}
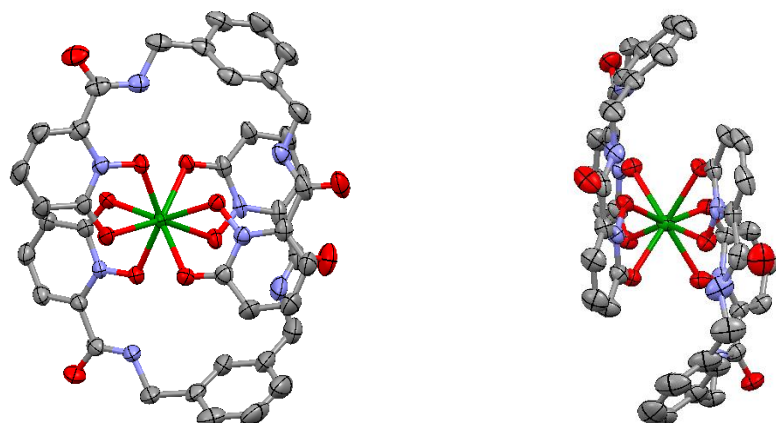
Figure A5.3. ORTEP of **In** (solvent, counterion, and hydrogens removed for clarity).

Table A5.3. Crystal data and structure refinement for **In**.

|	
Identification code	[In(5LImXy-1,2-HOPO)$_2$][NMe$_4$]
Empirical formula	C44 H44 In N9 O12
Formula weight	1005.70
Temperature	100(2) K
Wavelength	0.71073 Å
Crystal system	Monoclinic
Space group	P2(1)/c
Unit cell dimensions	a = 14.796(3) Å α= 90°.
	b = 15.042(3) Å β= 101.734(3)°.
	c = 24.057(5) Å γ = 90°.
Volume	5242.3(19) Å^3
Z	4
Density (calculated)	1.274 Mg/m^3
Absorption coefficient	0.514 mm^{-1}
F(000)	2064
Crystal size	0.30 x 0.27 x 0.22 mm^3
Theta range for data collection	1.61 to 25.40°.
Index ranges	-16<=h<=17, -18<=k<=18, -28<=l<=28
Reflections collected	91918
Independent reflections	9639 [R(int) = 0.0305]
Completeness to theta = 25.00°	100.0 %
Absorption correction	Semi-empirical from equivalents
Max. and min. transmission	0.8954 and 0.8612
Refinement method	Full-matrix least-squares on F^2
Data / restraints / parameters	9639 / 0 / 599
Goodness-of-fit on F^2	1.062
Final R indices [I>2sigma(I)]	R1 = 0.0363, wR2 = 0.0937
R indices (all data)	R1 = 0.0416, wR2 = 0.0981
Largest diff. peak and hole	0.802 and -0.577 e.Å^{-3}
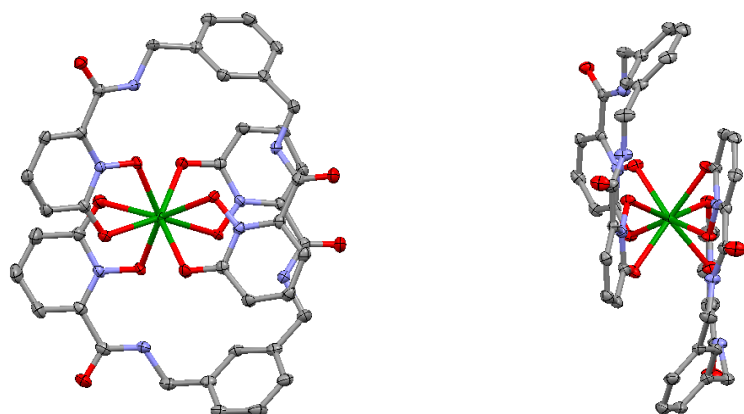
Figure A5.4. ORTEP of **Tl** (solvent, counterion, and hydrogens removed for clarity).

Table A5.4. Crystal data and structure refinement for **Tl**.

|	
Identification code	[Tl(5LImXy-1,2-HOPO)$_2$][NMe$_4$]
Empirical formula	C44 H44 N9 O12 Tl
Formula weight	1095.25
Temperature	100(2) K
Wavelength	0.71073 Å
Crystal system	Monoclinic
Space group	P2(1)/n
Unit cell dimensions	a = 17.1508(8) Å α= 90°.
	b = 10.7064(5) Å β= 96.2040(10)°.
	c = 28.8293(14) Å γ = 90°.
Volume	5262.7(4) Å^3
Z	4
Density (calculated)	1.382 Mg/m^3
Absorption coefficient	3.131 mm^{-1}
F(000)	2192
Crystal size	0.34 x 0.15 x 0.10 mm^3
Theta range for data collection	1.45 to 25.36°.
Index ranges	-20<=h<=20, -12<=k<=12, -34<=l<=34
Reflections collected	114286
Independent reflections	9631 [R(int) = 0.0316]
Completeness to theta = 25.00°	100.0 %
Absorption correction	Semi-empirical from equivalents
Max. and min. transmission	0.7448 and 0.4157
Refinement method	Full-matrix least-squares on F^2
Data / restraints / parameters	9631 / 0 / 599
Goodness-of-fit on F^2	1.129
Final R indices [I>2sigma(I)]	R1 = 0.0205, wR2 = 0.0519
R indices (all data)	R1 = 0.0227, wR2 = 0.0528
Largest diff. peak and hole	0.641 and -0.387 e.Å^{-3}
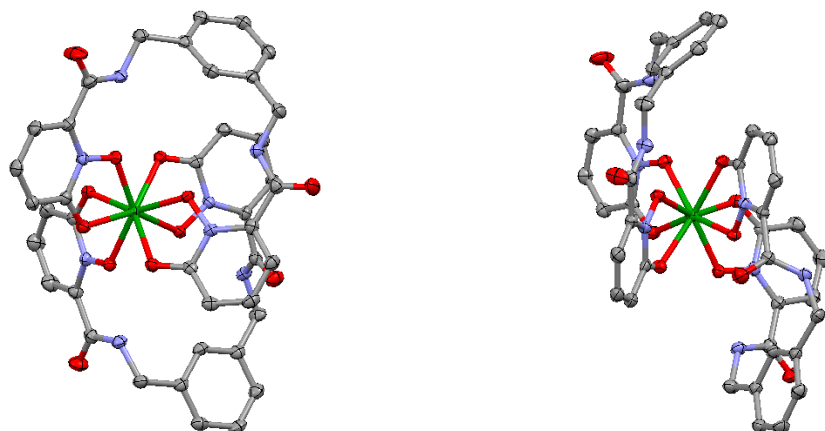
Figure A5.5. ORTEP of **Ti** (hydrogens removed for clarity).

Table A5.5. Crystal data and structure refinement for **Ti**.

|	
Identification code	[Ti(5LImXy-1,2-HOPO)$_2$]
Empirical formula	C40 H32 N8 O12 Ti
Formula weight	864.64
Temperature	100(2) K
Wavelength	0.71073 Å
Crystal system	Monoclinic
Space group	P2(1)/c
Unit cell dimensions	a = 12.0736(8) Å α= 90°.
	b = 19.3293(12) Å β= 105.0010(10)°.
	c = 16.0885(10) Å γ = 90°.
Volume	3626.7(4) Å^3
Z	4
Density (calculated)	1.584 Mg/m^3
Absorption coefficient	0.318 mm^{-1}
F(000)	1784
Crystal size	0.27 x 0.19 x 0.13 mm^3
Theta range for data collection	1.68 to 25.35°.
Index ranges	-14<=h<=14, -21<=k<=23, -19<=l<=19
Reflections collected	42958
Independent reflections	6643 [R(int) = 0.0319]
Completeness to theta = 25.00°	100.0 %
Absorption correction	Semi-empirical from equivalents
Max. and min. transmission	0.9598 and 0.9190
Refinement method	Full-matrix least-squares on F^2
Data / restraints / parameters	6643 / 0 / 550
Goodness-of-fit on F^2	1.053
Final R indices [I>2sigma(I)]	R1 = 0.0373, wR2 = 0.0940
R indices (all data)	R1 = 0.0446, wR2 = 0.0984
Largest diff. peak and hole	0.638 and -0.385 e.Å^{-3}
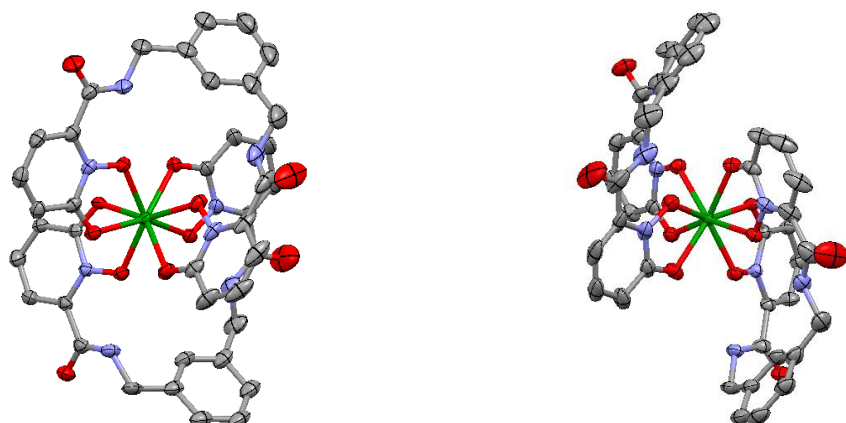
Figure A5.6. ORTEP of **Zr** (solvent and hydrogens removed for clarity).

Table A5.6. Crystal data and structure refinement for **Zr**.

|	
Identification code	[Zr(5LImXy-1,2-HOPO)$_2$]
Empirical formula	C40 H32 N8 O12 Zr
Formula weight	907.96
Temperature	100(2) K
Wavelength	0.71073 Å
Crystal system	Monoclinic
Space group	P2(1)/c
Unit cell dimensions	a = 12.9852(5) Å α= 90°.
	b = 16.8744(7) Å β= 106.438(2)°.
	c = 18.5054(8) Å γ = 90°.
Volume	3889.1(3) Å^3
Z	4
Density (calculated)	1.551 Mg/m^3
Absorption coefficient	0.360 mm^{-1}
F(000)	1856
Crystal size	0.08 x 0.06 x 0.01 mm^3
Theta range for data collection	1.67 to 25.51°.
Index ranges	-14<=h<=15, -19<=k<=20, -22<=l<=16
Reflections collected	26694
Independent reflections	7164 [R(int) = 0.0426]
Completeness to theta = 25.00°	99.6 %
Absorption correction	Semi-empirical from equivalents
Max. and min. transmission	0.9964 and 0.9718
Refinement method	Full-matrix least-squares on F^2
Data / restraints / parameters	7164 / 0 / 550
Goodness-of-fit on F^2	0.989
Final R indices [I>2sigma(I)]	R1 = 0.0423, wR2 = 0.0947
R indices (all data)	R1 = 0.0675, wR2 = 0.1031
Largest diff. peak and hole	0.424 and -0.311 e.Å^{-3}
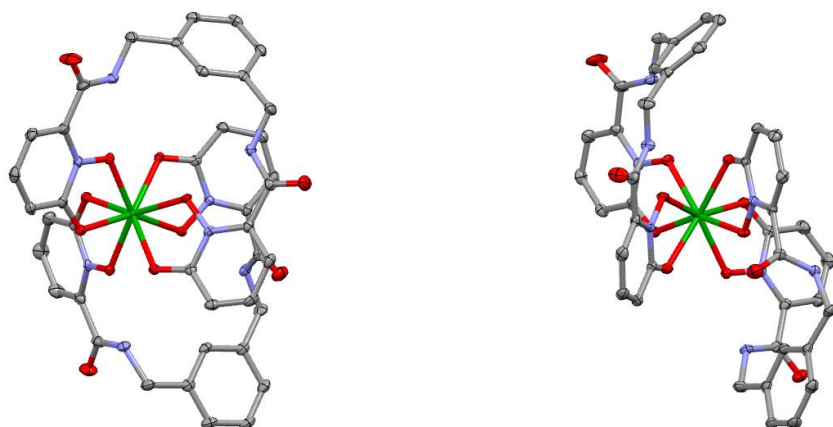
Figure A5.7. ORTEP of **Hf** (hydrogens removed for clarity).

Table A5.7. Crystal data and structure refinement for **Hf**.

|	
Identification code	[Hf(5LImXy-1,2-HOPO)$_2$]
Empirical formula	C40 H32 Hf N8 O12
Formula weight	995.23
Temperature	100(2) K
Wavelength	0.71073 Å
Crystal system	Monoclinic
Space group	P2(1)/c
Unit cell dimensions	a = 12.097(3) Å $\quad$ α= 90°.
	b = 19.590(4) Å $\quad$ β= 104.525(9)°.
	c = 16.135(4) Å $\quad$ γ = 90°.
Volume	3701.5(14) Å^3
Z	4
Density (calculated)	1.786 Mg/m^3
Absorption coefficient	2.899 mm^{-1}
F(000)	1984
Crystal size	0.07 x 0.06 x 0.05 mm^3
Theta range for data collection	1.67 to 25.40°.
Index ranges	-14<=h<=14, -23<=k<=23, -19<=l<=19
Reflections collected	51679
Independent reflections	6815 [R(int) = 0.0275]
Completeness to theta = 25.00°	100.0 %
Absorption correction	Semi-empirical from equivalents
Max. and min. transmission	0.8686 and 0.8228
Refinement method	Full-matrix least-squares on F^2
Data / restraints / parameters	6815 / 0 / 550
Goodness-of-fit on F^2	1.143
Final R indices [I>2sigma(I)]	R1 = 0.0203, wR2 = 0.0458
R indices (all data)	R1 = 0.0216, wR2 = 0.0463
Largest diff. peak and hole	0.710 and -0.681 e.Å^{-3}
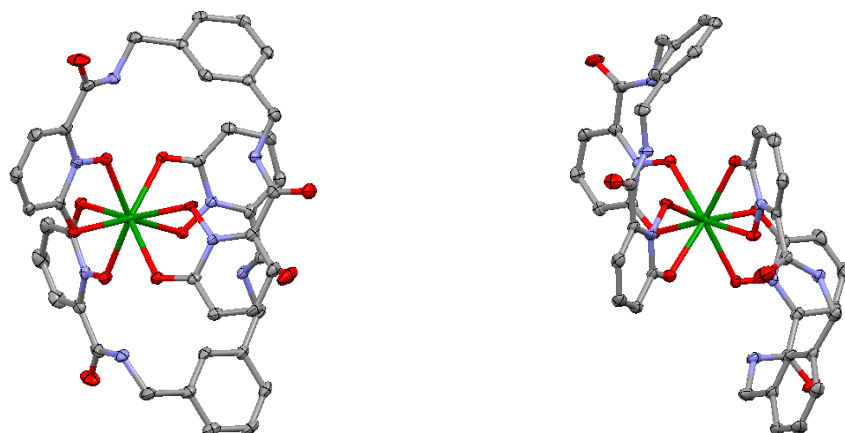
Figure A5.8. ORTEP of **Ce^IV** (hydrogens removed for clarity).

Table A5.8. Crystal data and structure refinement for **Ce^IV**.

|	
Identification code	[Ce(5LImXy-1,2-HOPO)$_2$]
Empirical formula	C40 H32 Ce N8 O12
Formula weight	956.86
Temperature	100(2) K
Wavelength	0.71073 Å
Crystal system	Monoclinic
Space group	P2(1)/c
Unit cell dimensions	a = 12.1717(4) Å α= 90°.
	b = 19.9261(6) Å β= 103.590(2)°.
	c = 16.1952(5) Å γ = 90°.
Volume	3817.9(2) Å^3
Z	4
Density (calculated)	1.665 Mg/m^3
Absorption coefficient	1.271 mm^{-1}
F(000)	1928
Crystal size	0.06 x 0.04 x 0.03 mm^3
Theta range for data collection	1.65 to 25.41°.
Index ranges	-14<=h<=14, -23<=k<=24, -19<=l<=19
Reflections collected	47485
Independent reflections	7013 [R(int) = 0.0343]
Completeness to theta = 25.00°	100.0 %
Absorption correction	Semi-empirical from equivalents
Max. and min. transmission	0.9629 and 0.9277
Refinement method	Full-matrix least-squares on F^2
Data / restraints / parameters	7013 / 0 / 550
Goodness-of-fit on F^2	1.027
Final R indices [I>2sigma(I)]	R1 = 0.0237, wR2 = 0.0530
R indices (all data)	R1 = 0.0302, wR2 = 0.0559
Largest diff. peak and hole	0.582 and -0.484 e.Å^{-3}
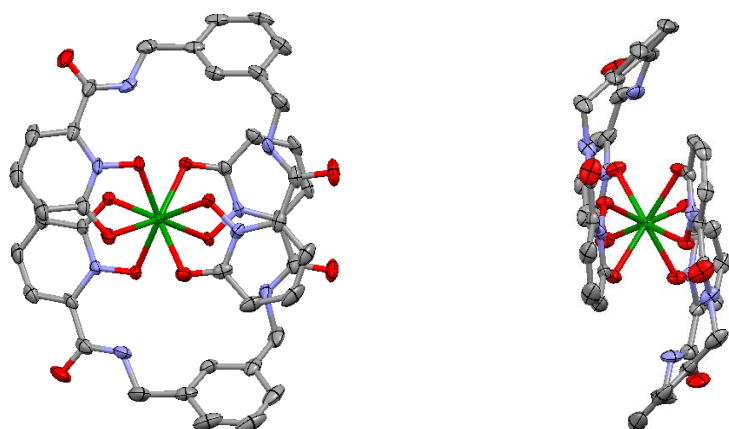
Figure A5.9. ORTEP of **Sn** (solvent and hydrogens removed for clarity).

Table A5.9. Crystal data and structure refinement for **Sn**.

Identification code	[Sn(5LImXy-1,2-HOPO)$_2$]
Empirical formula	C40 H32 N8 O12 Sn
Formula weight	935.43
Temperature	100(2) K
Wavelength	0.71073 Å
Crystal system	Monoclinic
Space group	C2/c
Unit cell dimensions	a = 23.6140(8) Å $\qquad$ α= 90°.
	b = 14.3621(5) Å $\qquad$ β= 90.980(2)°.
	c = 24.3046(8) Å $\qquad$ γ = 90°.
Volume	8241.6(5) Å^3
Z	8
Density (calculated)	1.508 Mg/m^3
Absorption coefficient	0.693 mm^{-1}
F(000)	3792
Crystal size	0.12 x 0.06 x 0.04 mm^3
Theta range for data collection	1.66 to 25.42°.
Index ranges	-28<=h<=28, -17<=k<=17, -29<=l<=28
Reflections collected	37894
Independent reflections	7548 [R(int) = 0.0409]
Completeness to theta = 25.00°	99.5 %
Absorption correction	Semi-empirical from equivalents
Max. and min. transmission	0.9728 and 0.9215
Refinement method	Full-matrix least-squares on F^2
Data / restraints / parameters	7548 / 0 / 550
Goodness-of-fit on F^2	1.072
Final R indices [I>2sigma(I)]	R1 = 0.0344, wR2 = 0.0837
R indices (all data)	R1 = 0.0430, wR2 = 0.0881
Largest diff. peak and hole	1.146 and -0.770 e.Å^{-3}

Table A5.10. DFT Coordinates of the **Ti** transition state as a representative sample

Atom Label	X	Y	Z	Atom Label	X	Y	Z
Ti	0	0	0.069	C	3.602	-0.451	-3.351
O	-0.695	-1.186	1.588	C	3.948	-1.926	2.499
O	1.707	-0.982	0.858	O	-4.798	2.63	3.039
O	-0.18	-1.93	-0.765	O	-4.508	0.798	-4.108
O	1.374	-0.084	-1.457	O	4.501	-0.792	-4.117
O	-1.376	0.086	-1.455	O	4.803	-2.634	3.028
O	0.179	1.931	-0.763	H	-3.466	0.277	1.398
O	-1.706	0.981	0.862	H	-2.756	-0.912	-2.114
O	0.697	1.184	1.588	H	2.753	0.914	-2.117
C	-2.48	2.279	2.691	H	3.469	-0.279	1.392
C	-0.134	1.876	2.277	N	-4.224	0.769	1.861
C	0.196	2.764	3.321	N	-3.518	-0.771	-2.773
C	-0.809	3.406	4.021	N	4.227	-0.772	1.853
C	-2.152	3.149	3.718	N	3.514	0.775	-2.777
H	1.248	2.909	3.539	C	-5.192	-0.773	-0.461
H	-0.557	4.093	4.822	C	-5.253	-1.829	-1.373
H	-2.975	3.589	4.266	C	-5.883	-3.018	-0.985
C	-1.706	3.731	-3.273	C	-6.433	-3.137	0.292
C	-2.613	2.716	-3.611	C	-6.34	-2.082	1.202
C	-2.542	1.481	-2.99	C	-5.715	-0.888	0.831
C	-0.66	2.256	-1.665	H	-4.707	0.154	-0.751
C	-0.743	3.512	-2.309	H	-5.935	-3.854	-1.678
H	-1.767	4.695	-3.768	H	-6.916	-4.064	0.587
H	-3.401	2.85	-4.339	H	-6.746	-2.191	2.204
H	-0.027	4.269	-2.013	C	-5.597	0.271	1.796
C	2.537	-1.477	-2.996	H	-6.248	1.103	1.497
C	2.607	-2.711	-3.618	H	-5.93	-0.03	2.797
C	1.7	-3.726	-3.281	C	-4.649	-1.685	-2.764
C	0.739	-3.509	-2.314	H	-4.337	-2.668	-3.136
C	0.658	-2.254	-1.669	H	-5.382	-1.285	-3.471
H	3.394	-2.844	-4.349	C	6.433	3.136	0.285
H	1.761	-4.69	-3.777	C	5.881	3.019	-0.99
H	0.023	-4.266	-2.018	C	5.25	1.831	-1.379
C	0.137	-1.878	2.274	C	5.191	0.773	-0.469
C	2.484	-2.282	2.684	C	5.716	0.886	0.823
C	2.158	-3.154	3.71	C	6.342	2.08	1.194
C	0.815	-3.411	4.015	H	6.917	4.063	0.581
C	-0.191	-2.768	3.318	H	5.933	3.856	-1.683
H	2.981	-3.595	4.256	H	4.705	-0.153	-0.759
H	0.564	-4.1	4.816	H	6.75	2.188	2.196
H	-1.242	-2.914	3.537	C	5.6	-0.274	1.787
N	-1.467	1.717	1.965	H	6.25	-1.105	1.485
N	-1.569	1.287	-2.046	H	5.935	0.026	2.787
N	1.47	-1.719	1.961	C	4.644	1.689	-2.769
N	1.565	-1.284	-2.05	H	4.332	2.672	-3.139
C	-3.944	1.922	2.508	H	5.376	1.289	-3.478
C	-3.608	0.455	-3.345				

Chapter 6 Appendix

DFT Calculations, XANES Details, Laser-Induced Damage Analysis, and FEFF calculations

DFT Calculations

Ground state geometry optimization and frequency calculations were performed using Gaussian 09 at the Molecular Graphics and Computation Facility at University of California, Berkeley, CA.[1] The B3LYP functional[2,3] was used, treating the light atoms with the 6-31G(d,p) basis set[4-6] and the Eu^{III} atoms with the quasi relativistic effective core pseudopotential ECP52MWB (Gaussian Keyword MWB52).[7,8] All calculations were run with no symmetry constraints. Frequency calculations were inspected to ensure the absence of imaginary frequencies, confirming the structures minimized to a ground state. In all cases, input coordinates were originally taken from the appropriate crystal structures.[9-11] Coordinates for the singlet-triplet structural comparison were superimposed in Accelrys Discovery Studio Viewer v3.5 using the metal and first coordination sphere as tether points. Molecular graphics were rendered in POV-RAY.[12] Ground state geometry minimizations of the XRD crystal structure coordinates are shown in the following figure.
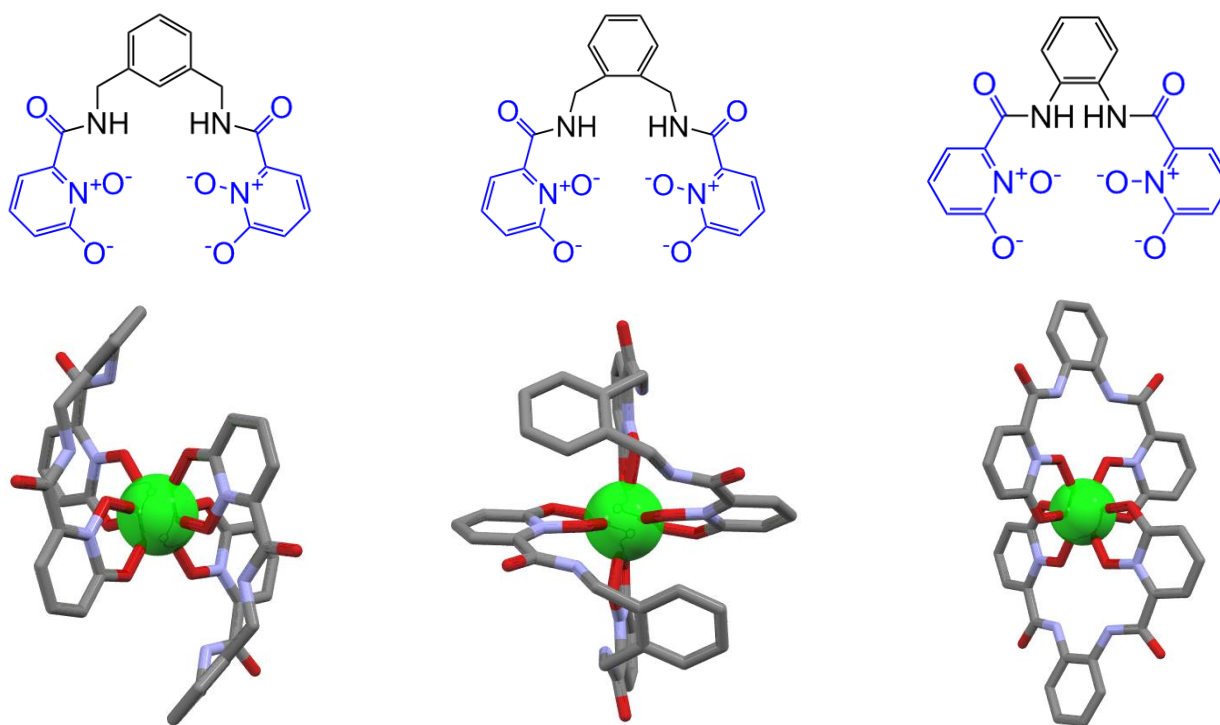
Figure A6.1. DFT geometry optimized structures of [Eu(L^1)$_2$]$^-$ (left), [Eu(L^2)$_2$]$^-$ (middle), and [Eu(L^3)$_2$]$^-$ right

The DFT minimizations of the XRD crystal structures are shown, viewed along the apparent C$_2$ symmetry axis that relates the two ligands. The shape of the eight coordinating oxygen atoms is closest to a D$_{2d}$ trigonal face dodecahedron in all three cases. The 1,2-HOPO chelates span the *m* edges and the connecting backbones span either *g* edges (for [Eu(L^1)$_2$]$^-$ and [Eu(L^2)$_2$]$^-$) or *a* edges ([Eu(L^3)$_2$]$^-$). However, we know from the q-value of [Eu(L^2)$_2$]$^-$ (see Materials and Methods section of the main text) that [Eu(L^2)$_2$]$^-$ is not 8-coordinate in aqueous solution. Addition of the 9th oxygen-containing ligand was modeled as a molecule of DMSO in these gas phase DFT calculations. DMSO was chosen instead of water for the purposes of calculation, since optimizations using water were skewed by the strong hydrogen bonding

between the water protons and the anionic HOPO oxygens, an effect that is exacerbated by the lack of solvent treatments in these gas-phase calculations.
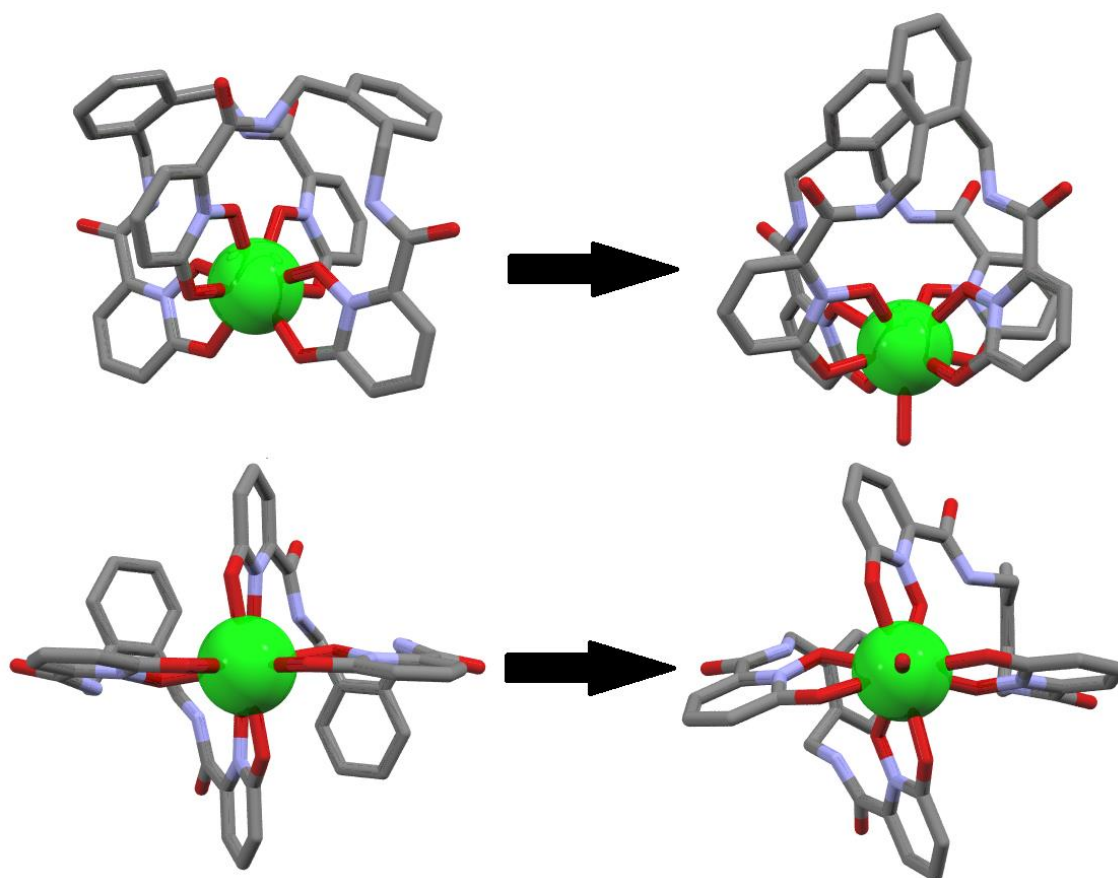

Figure A6.2. Two views of the DFT geometry optimized structures of $[Eu(L^2)_2]^-$ (left) and $[Eu(L^2)_2DMSO]^-$ (right), hydrogens and DMSO atoms (except coordinating oxygen) were removed for clarity.
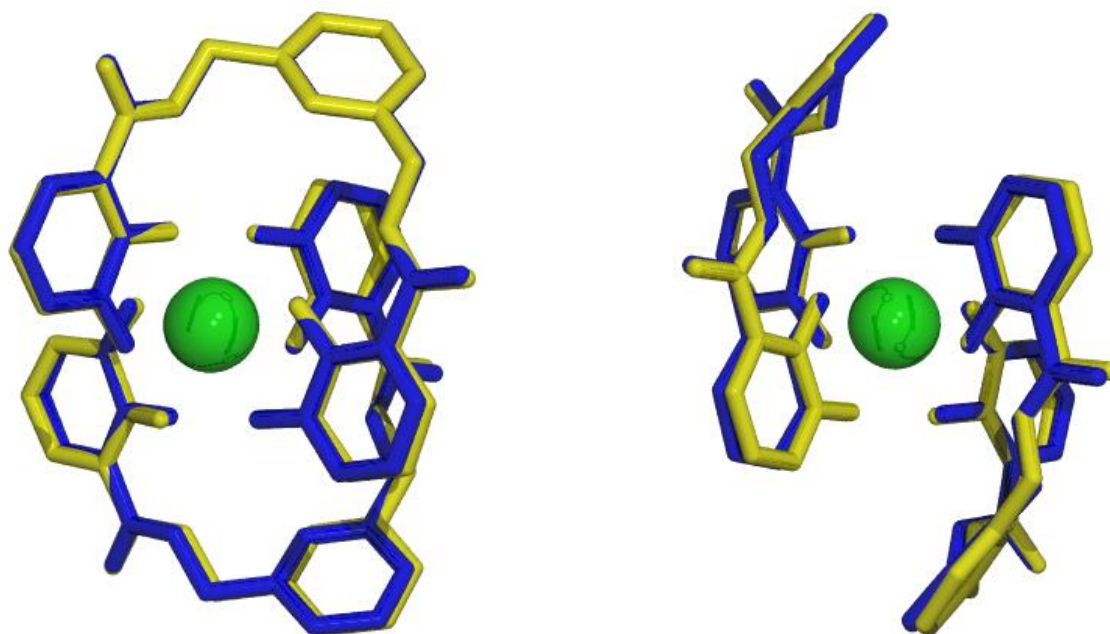
Figure A6.3. Two views of singlet (blue) and triplet (yellow) $[Eu(L^1)_2]^-$ superimposed to demonstrate similarity

Superimposing the singlet and triplet state DFT minimized structures for $[Eu(L^1)_2]^-$ reveals that the structures are nearly identical. The average M-O bond distances were found to be 0.004 Å longer in the triplet state structure, which is an extremely small difference. Note that the triplet excited state calculated here is not the state that can be observed by our time resolved XANES signal. The ligand-centered singlet and triplet excited states are short lived in aqueous solution at room temperature, even more so in the presence of an accepting state on the Eu^{III}. The ligand is expected to quickly relax to the ground state structure once the energy has been transferred onto the Eu^{III} center. We therefore expect that the structures of the ground state and *4f* metal-centered excited state are even more closely matched than the two structures shown above.

Collection of Time-Resolved XANES

Laser pump/X-ray probe experiments were carried out at beamline 11-ID-D of the Advanced Photon Source (APS). The X-ray beam at this station has a flux of 5×10^{12} photons/second at the sample position, after focusing with a toroidal mirror to measure approximately 2 mm (H) by 50 μm (V). The APS produced X-ray pulses approximately 80 ps wide at 153 ns intervals. The sample was excited with an Nd:YLF regenerative amplified laser (repetition rate 1.6 kHz, FWHM 5 ps); a frequency-tripling crystal was used to produce a 351 nm-wavelength beam. The laser spot, approximately 750 microns in diameter, was centered over the X-ray spot at the sample position. Neutral density filters were used to attenuate the laser, with the resulting fluence per shot incident on the sample varying between 1.6 and 40 mJ/cm^2.

We used a flowing jet of solution with diameter 0.5 mm. Assuming laminar flow, the linear speed of material in the jet can be estimated from the cross-sectional area and the volume flow rate. We found that (by adjusting the pump speed) the linear speed could be varied from 2.7 m/s to 3.5 m/s; the jet became visibly unstable outside this range. This means that after each laser pulse, the UV-illuminated volume of sample flowed past the X-ray beam within ~150

microseconds, which is less than the luminescence lifetime of all the samples studied here (see Table 1 in the main text). We consequently found that the apparent decay rate of the TR-XANES signal depended on the flow speed. This constitutes a limitation on the measurement, as we cannot directly compare the decay rate of the TR-XANES signal with the known lifetime of the 4f intrashell excitation that we claim to observe. However, we note that there is no other excitation with a comparable lifetime (on the order of 100 μs) in the systems being studied here. Fig. S4 shows the apparent decay rate of the signal from complex $[Eu(L^1)_2]^-$ with the jet speed set to 3 m/s (this flow speed was used during collection of all the data presented here).

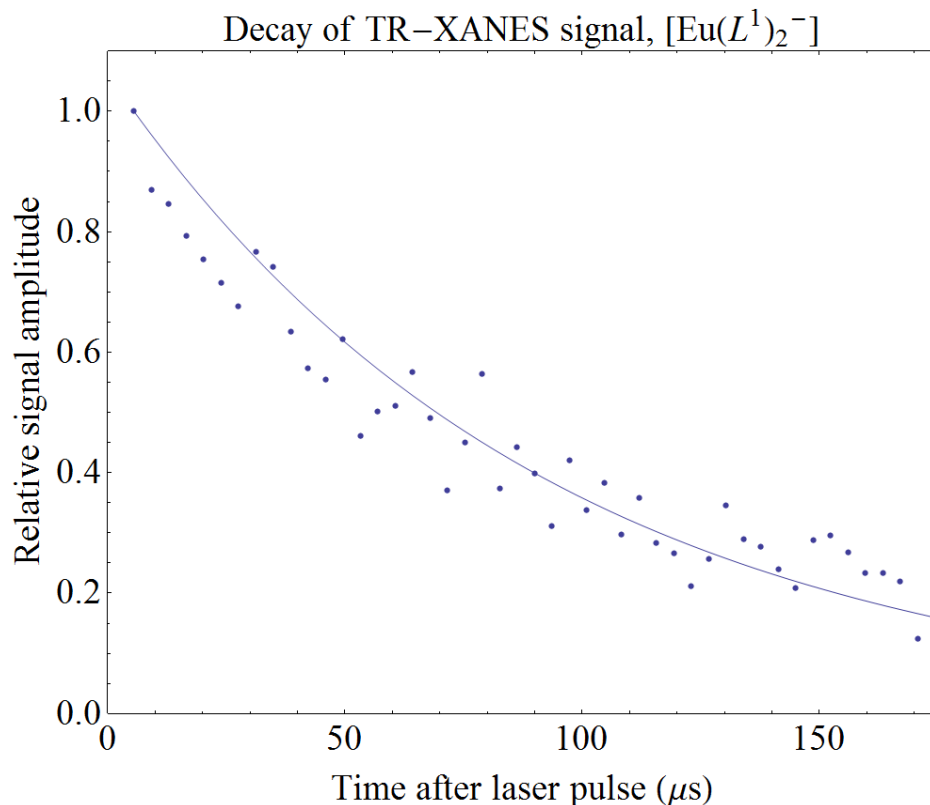**Figure A6.4**. Time-dependence of the relative amplitude of the TR-XANES signal from complex $[Eu(L^1)_2]^-$ (dots), showing an apparent lifetime of 92 μs (solid line).

Sample concentrations ranged from 0.3 mM to 1 mM in pure water or aqeuous TRIS buffer (0.01 M, pH 7.4), with up to 15% DMSO by volume as a cosolvent. Solutions were prepared by dissolving each solid sample in DMSO and then diluting with either water or TRIS buffer. Spectral features were unaffected by these variations in solvent chemistry. We also compared solutions of complex $[Eu(L^1)_2]^-$ prepared from crystallizations with two counter-ions, py^+ and $NMe4^+$. The two transient XANES signals are shown in Fig. S5.

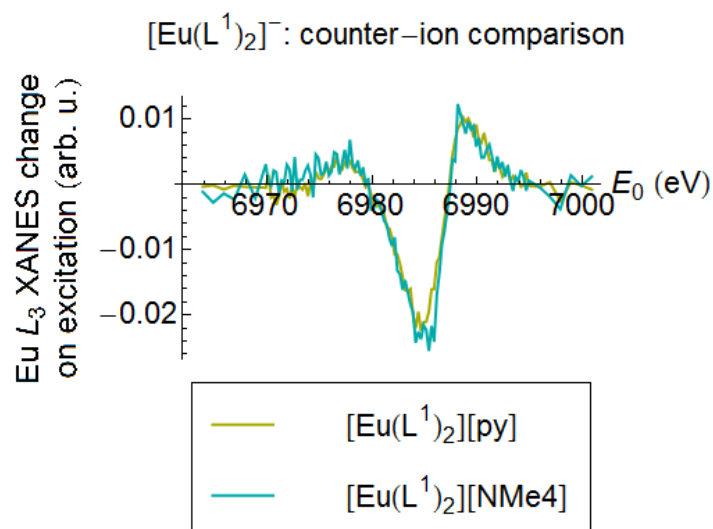**Figure A6.5**. Transient XANES signals obtained from solutions of $[Eu(L^1)_2]^-$ with two counter-ions.

The data taken from the solution of $[Eu(L^1)_2][NMe4]$ show higher noise, since a smaller quantity of sample was used. Otherwise, we observe no significant difference as a result of the change in counterion, especially when compared to the much larger variations among the three signals shown in Fig. 3 of the main text. The similarities of the XANES signals are consistent with the fact that the luminescence behavior of the representative complex is unaffected by the counterion. For the sake of consistency, however, we have only used data collected from solutions of the pyridinium salts for making Fig. 3 of the main text.

To clearly show the correlation between the observed XANES signal and the known efficiency for excitation of the EuIII ion, the sensitization efficiency ηsens (see Table 1 of the main text) is plotted against the integrated TR-XANES signals (Fig. 3b) of the three complexes (see S6 below).
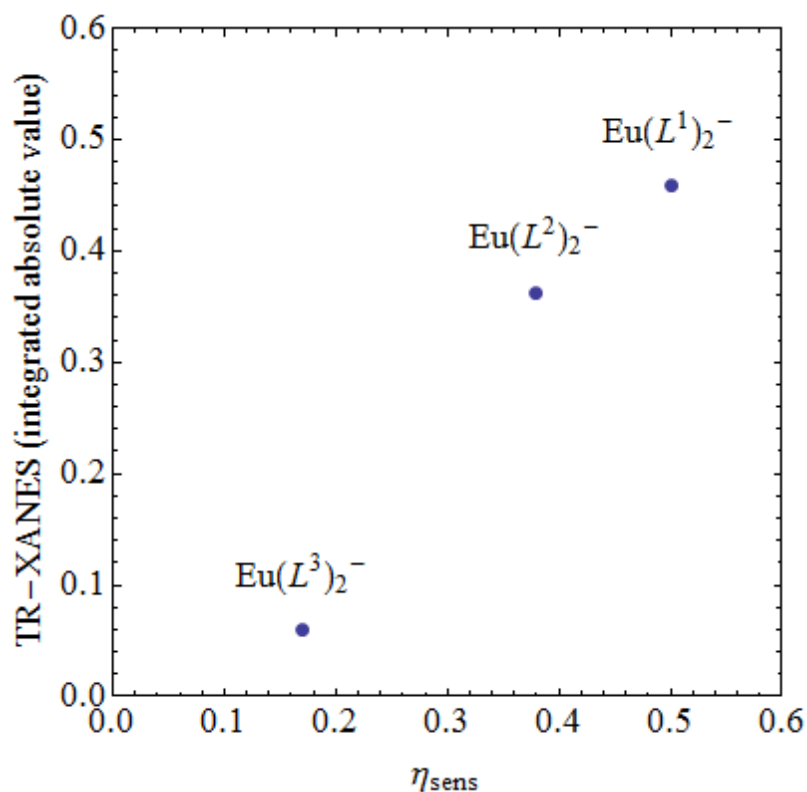
Figure A6.6. Correlation between ηsens and integrated TR-XANES signals.

Laser-Induced Damage

We used two criteria to assess sample damage: visual inspection of the sample solutions for precipitate and discoloration, and systematic drifts of the ground-state XANES. X-ray exposure caused no visible change in the samples, and correspondingly, we found no significant change in the ground-state XANES over 1 hour of exposure to the X-rays alone (Fig. S7a). Exposure to the pump laser caused both precipitation of unidentified Eu-containing material out of solution and a gradual decrease in the ground-state XANES intensity (Fig. S7b). For comparison of this systematic drift with the transient signal, Fig. S7c shows the excited – ground state difference from a single scan, plotted against the difference in the ground state spectra from two consecutive scans (i.e., the systematic drift induced by 10 minutes of exposure to the pump laser). Note that the systematic drift is uniform across the scan range, and smaller in magnitude than the transient signal.
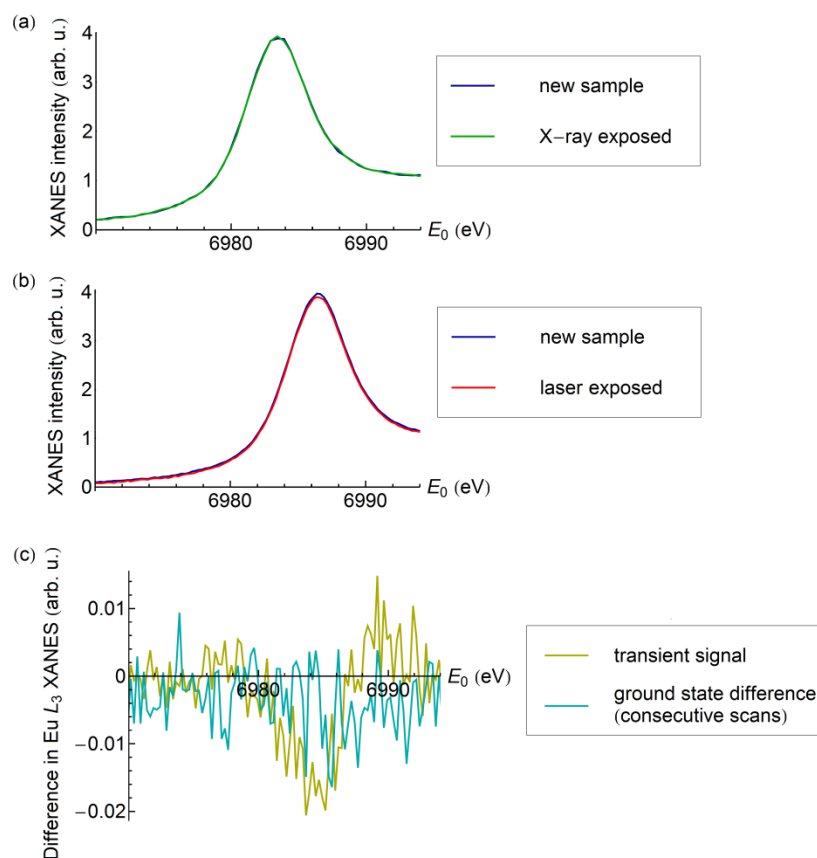
Figure A6.7. (a) Ground-state XANES collected from a new solution of $[Eu(L^1)_2]^-$ and from the same solution after 1 hour of exposure to the X-ray beam. Each scan required approximately 10 minutes of collection time. (b) Ground-state XANES collected from a second solution of $[Eu(L^1)_2]^-$ and from the same solution after 1 hour of simultaneous exposure to the X-ray beam and pump laser (12 mJ/cm² fluence per shot at 1.6 kHz). (c) Comparison of the transient signal with the systematic scan-to-scan drift.

FEFF calculations

Using FEFF9[13], we performed ab initio calculations of the *l*-projected density of states and multiple scattering calculations of the *L*3 edge XANES for the EuIII ion in the DFT-minimized structure of the ground state of complex $[Eu(L^1)_2]^-$. Self-consistent scattering potentials were calculated while including the effect of the *f* electrons (using the UNFREEZEF card). The results are shown in Figure S8. In the pre-edge region (below 6980 eV), the features of the *d*-DOS and *f*-DOS are closely aligned, a signature of the expected (static) 4*f*-5*d* hybridization common in lanthanide materials. The calculated XANES shown includes both electric dipole and electric quadrupole transitions (specified in the MULTIPOLE card). The contribution from quadrupole transitions alone, i.e. the expected position of 2*p* → 4*f* transitions, is shown in the same panel. We note that both the large *f*-dos peak and the contribution to the XANES from quadrupole transitions have maxima in the same region as the TR-XANES signal at 6977 eV, providing evidence that the TR-XANES signal at this energy is associated with a change in either a mixed *f-d* state or a pure 4*f* state.
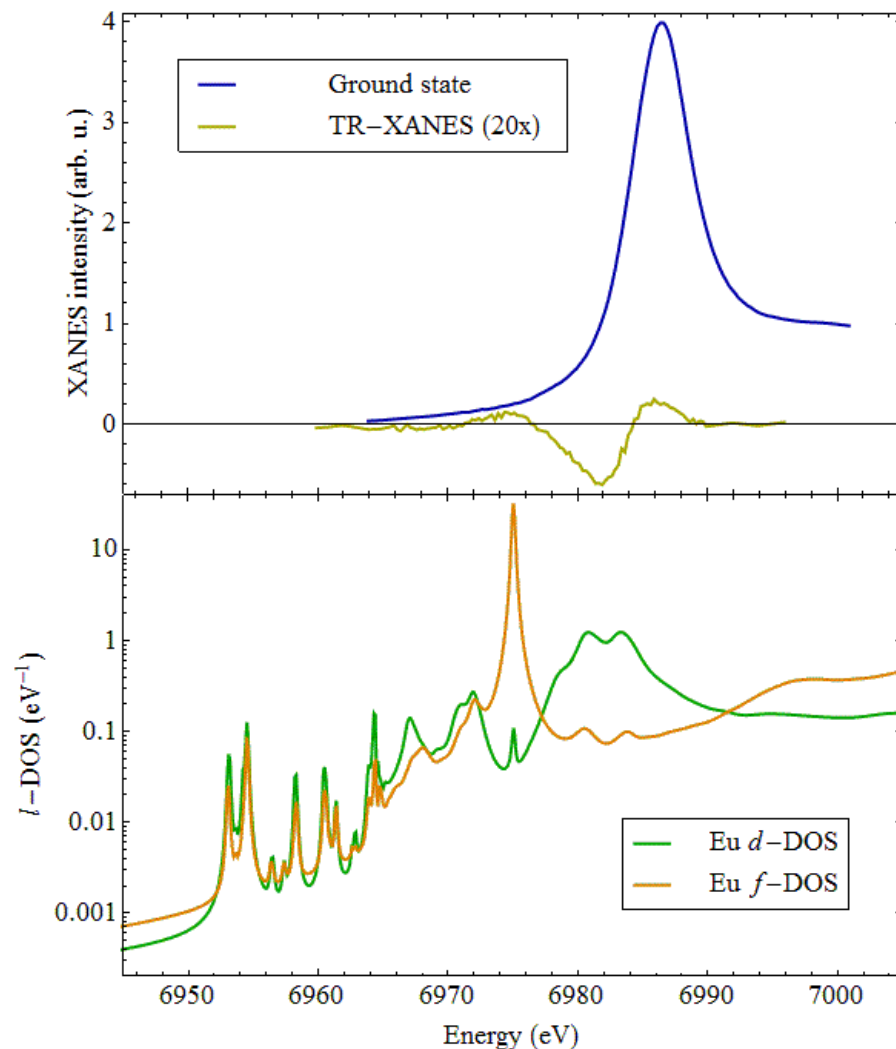
Figure A6.8. Experimental ground-state and TR-XANES signals from $[Eu(L^1)_2]^-$ (upper panel; TR-XANES signal scaled vertically for clarity) and FEFF calculations of the *l*-projected density of states for the central Eu^{III} (lower panel).

References

1. Gaussian 09, Revision A.02, M. J. Frisch, G. W. Trucks, H. B. Schlegel, G. E. Scuseria, M. A. Robb, J. R. Cheeseman, G. Scalmani, V. Barone, B. Mennucci, G. A. Petersson, H. Nakatsuji, M. Caricato, X. Li, H. P. Hratchian, A. F. Izmaylov, J. Bloino, G. Zheng, J. L. Sonnenberg, M. Hada, M. Ehara, K. Toyota, R. Fukuda, J. Hasegawa, M. Ishida, T. Nakajima, Y. Honda, O. Kitao, H. Nakai, T. Vreven, J. A. Montgomery, Jr., J. E. Peralta, F. Ogliaro, M. Bearpark, J. J. Heyd, E. Brothers, K. N. Kudin, V. N. Staroverov, R. Kobayashi, J. Normand, K. Raghavachari, A. Rendell, J. C. Burant, S. S. Iyengar, J. Tomasi, M. Cossi, N. Rega, J. M. Millam, M. Klene, J. E. Knox, J. B. Cross, V. Bakken, C. Adamo, J. Jaramillo, R. Gomperts, R. E. Stratmann, O. Yazyev, A. J. Austin, R. Cammi, C. Pomelli, J. W. Ochterski, R. L. Martin, K. Morokuma, V. G.

Zakrzewski, G. A. Voth, P. Salvador, J. J. Dannenberg, S. Dapprich, A. D. Daniels, O. Farkas, J. B. Foresman, J. V. Ortiz, J. Cioslowski, and D. J. Fox, Gaussian, Inc., Wallingford CT, 2009.

2. Becke, A. D. *J. Chem. Phys.* **1993**, *98*, 5648-5652.

3. Stephens, P. J.; Devlin, F. J.; Chabalowski, C. F.; Frisch, M. J. *J. Phys. Chem.* **1994**, *98,* 11623-11627.

4. Ditchfield, R.; Hehre, W. J.; Pople, J. A. *J. Chem. Phys.* **1971**, *54*, 724-728.

5. Hehre, W. J.; Ditchfield, R.; Pople, J. A. *J. Chem. Phys.* **1972**, *56*, 2257-2261.

6. Gordon, M. S. *Chem. Phys. Lett.* **1980**, *76*, 163-168.

7. Dolg, M.; Stoll, H.; Savin, A.; Preuss, H. *Theor. Chim. Acta* **1989,** *75*, 173.

8. Dolg, M.; Stoll, H.; Preuss, H. *Theor. Chim. Acta* **1993,** *85,* 441.

9. D'Aléo, A.; Xu, J.; Moore, E. G.; Jocher, C. J.; Raymond, K. N. *Inorg. Chem.* **2008**, *47*, 6109-6111.

10. D'Aléo, A.; Moore, E. G.; Szigethy, G.; Xu, J.; Raymond, K. N. *Inorg. Chem.* **2009**, *48*, 9316-9324.

11. Tatum, D. *in preparation* **2013**.

12. Persistence of Vision Pty. Ltd. (2004) Persistence of Vision Raytracer (Version 3.6) [Computer software]. Retrieved from http://www.povray.org/download/

13. Rehr, J.J.; Kas, J.J.; Prange, M.P.; Sorini, A,P.; Takimoto, Y.; Vila, F.; *Comptes Rendus Physique* **2009**, *10* (6) 548-559.